This is to certify that the

dissertation entitled

STOCHASTIC SIMULATION OF SEPARATION SYSTEMS

presented by

Peter Edward Krouskop

has been accepted towards fulfillment
of the requirements for

PhD degree in Chemistry

Victoria McGuffin
Major professor

Date 1/7/2002

STOCHASTIC SIMULATION OF SEPARATION SYSTEMS

VOLUME 1

By

Peter Edward Krouskop

A DISSERTATION

Submitted to
Michigan State University
in partial fulfillment of the requirements
for the degree of

DOCTOR OF PHILOSOPHY

Department of Chemistry

2002

ABSTRACT

STOCHASTIC SIMULATION OF SEPARATION SYSTEMS

By

Peter Edward Krouskop

A three-dimensional stochastic simulation of chromatography has been developed and used to study absorption chromatography, adsorption chromatography, and reactive chromatography. The trajectories of individual molecules are tracked as the processes of absorption, adsorption, chemical reaction, diffusion, electrophoretic migration, and laminar or electroosmotic flow are simulated. The macroscopic and molecular abilities of the simulation are used to study the effects of the radii of the fluid and surface phases, the diffusion coefficients in the fluid and surface phases, and the absorption coefficient on the rate of molecular transfer between the fluid and surface phases. The data collected from the simulation are used to develop an empirical equation relating the parameters listed above to the mass transfer rate constants. The effects of heterogeneous surfaces on absorption systems are also investigated. It is determined that heterogeneities that cause differences in the absorption coefficient result in a system that behaves as a homogeneous system with an absorption coefficient equal to the average absorption coefficient. Differences in the diffusion coefficient and the interfacial barrier to mass transfer cause noticeable changes in the kinetic behavior of the system, but do not affect the long-time or steady-state behavior of the system.

The computer algorithm for the simulation of linear adsorption chromatography is developed and validated. The algorithm is independent of the time increment of the

simulation. The adsorption process is treated as a second order reaction between the adsorbate and the surface, and desorption is treated as a first-order reaction. The kinetic and steady-state behavior of adsorption systems are investigated and the simulation is shown to be in good agreement with established theories of adsorption chromatography.

Finally, systems in which reaction and separation occur concurrently (reactive separations) are considered. The simulation of an absorption chromatography column in which a reaction occurs in the fluid or surface phase is presented. The responses of reactive separation systems with irreversible and reversible reactions to changes in the absorption coefficient, the diffusion coefficient, and the reaction rate are studied. The statistical moments of the reactant and product zones are shown to be in agreement with established theories. The data also suggests that the mass transfer and reaction rates affect the system response in a dependent manner. The data show that separation of the reactant and product species is possible while the system is not at steady state. The yield and purity of the product is shown to increase for systems in which the absorption coefficient of the product is smaller than the absorption coefficient of the reactant.

This dissertation presents the depth of information obtainable from the stochastic model of separation systems. The simulation bridges molecular descriptions of the system (e.g. *ab initio* and molecular dynamics simulations) to macroscopic descriptions of the system (e.g. mass balance equations). Hence, a unified treatment of separation systems is presented for the study of the effects of molecular interactions on the macroscopic system.

ACKNOWLEDGMENTS

I would like to express my appreciation to my advisor, Dr. Victoria McGuffin, for helping me to develop into the scientist that I am. I would also like to thank the other members of my committee, Dr. Cukier, Dr. Hunt, and Dr. Pinnavaia, for never giving up hope. I have learned the role of scientist and an educator from them. I hope to become as good at it as they are.

I would like to thank those that have provided money so that I could conduct my research: The American Chemical Society, Division of Analytical Chemistry, ACS summer fellowship sponsored by the Dow Chemical Company Foundation, the Dow Chemical Foundation Fellowship, and the Walter and Margaret Yates Memorial Scholarship.

I thank my family and friends for the support and encouragement that they have given to me. My wife, Marilyn, has helped me get through the tough times with her smiles and laughter. My lab mates, John Goodpaster and Sam Howerton, and I have become good friends as we have helped each other through the trials of graduate school. I am thankful to have met them and to have had the privilege of working around them. I wish them the best in all that they endeavor to do in this life. I am glad that Carl Newman joined the group when he did. Now there is someone else who understands the potential of "Sam's World" to wreak havoc on the rest of humanity. I wish him the best in his studies. Finally, I would like to acknowledge all the other people that I have been

privileged to meet and work with throughout the department. Thank you for the kind encouragement and support.

TABLE OF CONTENTS

LIST OF TABLES

LIST OF FIGURES

Chapter 1

Models of Chromatography

1.1 Introduction.

There have been many different models applied to chromatographic systems to gain an understanding of the processes involved in this separation method. The models can be broadly grouped into three categories. The first category is based on mass balance equations. Partial differential equations are used to describe the movement of the analyte through the chromatographic system. The solutions of these equations provide zone profiles of the analyte as a function of time or distance. The second category is based on molecular dynamic simulations of the molecules in the separation system. By applying these methods of simulation to chromatography, the molecular nature of the separation processes can be observed. The third category is based on the stochastic nature of the separation process. The probability of an adsorption or absorption (partition) event occurring for a single analyte molecule is used to determine the probability distribution for an ensemble of molecules. The probability distribution is then used to obtain the zone profile of the analyte as a function of time or distance. All three of these types of models have been applied to homogeneous and heterogeneous chromatographic systems with linear and non-linear isotherms.

This chapter will discuss in detail the different models that have been used to study linear adsorption and absorption chromatography. The benefits and limitations of the models will be presented.

1.2 Mass Balance Models of Separation Systems.

A general mass balance equation that describes the processes in a separation system is

$$v_0 \frac{\partial C}{\partial z} + \frac{\partial C}{\partial T} + \beta \frac{\partial q}{\partial T} = D \frac{\partial^2 C}{\partial z^2} \qquad [1.1]$$

where v_0 is the average velocity of the fluid phase, C is the concentration of solute in the fluid phase, q is the concentration of solute in the surface phase, T is time, z is the distance coordinate in the axial direction, β is the ratio of the surface phase volume to the fluid phase volume, and D is the axial dispersion coefficient.

Solutions to Equation [1.1] become very difficult to obtain as more detail about the system is placed in the model. Thus, these models are usually solved with some assumption(s) made about the system. Golshan-Shirazi and Guiochon have reviewed these models for both linear and non-linear chromatography.[1,2] The classification scheme presented by Golshan-Shirazi and Guiochon for linear isotherm systems is used herein.

1.2.1 Plate Models.

The first models of chromatography were based on the idea of several extraction stages placed in series. The Craig model is based on this idea of discrete stages.[3] Each stage is assumed to reach equilibrium before a finite amount of the mobile phase is moved from one stage to the next in a stepwise fashion. A model presented by Martin and Synge uses the same approach, but allows continuous flow to occur between the stages of the separation.[4] These models have had a lasting impact on chromatography. It

is from these models that plate height and the number of theoretical plates were defined as a measure of the separation ability of a column. The number of theoretical plates directly corresponds to the number of equilibrium stages, and the plate height is the length of the column divided by the number of theoretical plates. The plate models have been used widely as a method of comparing one separation system to another, but the models are not predictive. Hence, these models can not be used to determine the molecular and system responses caused by changes in the fluid or surface phase characteristics. Recent work has shown that the more complex models of separation systems discussed below can be reduced to these simple models, and the relationships between the system parameters and the plate models can be determined.[5,6]

1.2.2 Equilibrium-Dispersive Models.

The category of equilibrium-dispersive models includes all models that assume equilibrium to exist between the fluid and surface phases. The $\partial q/\partial T$ term in Equation [1.1] is replaced by an expression that describes the steady-state or equilibrium relationship of the solute concentration in the fluid and surface phases. The broadening of the zone profile due to the processes of axial dispersion, mass transfer and adsorption/desorption kinetics is accounted for through an apparent dispersion coefficient. The apparent dispersion coefficient is system specific, and is usually determined empirically. Taylor and Aris use this type of model to study zone profiles that occur when a system is at steady state.[7,8] Equilibrium-dispersive models have more

predictive power than the plate models,[9,10] but still depend on empirical data to determine the value of the apparent dispersion coefficient.

1.2.3 Lumped Kinetic Models.

The lumped kinetic models study the limiting processes that produce broadening in the analyte zone and combine the other processes that occur on a faster time scale into a single term. For example, reaction-dispersive models assume that the mass transfer to and from the interface of the fluid and surface phases is fast and at equilibrium when compared to the reaction, and the processes of absorption or adsorption and desorption are studied in detail.[5,9] Transport-dispersive models study the mass transfer to and from the interface of the fluid and surface phases in detail, and assume the processes of absorption or adsorption and desorption are fast and at equilibrium when compared to the transport processes.[6,11-15] These models provide more information about the effects of the various processes within chromatography than the previously mentioned equilibrium models. For example, Golay used moment analysis of a transport-dispersive model to determine the effect of system shape and size as well as diffusion and partition coefficients on the broadening of zones.[12] Other workers have examined the effects of boundary conditions on the moments obtained from transport-dispersive systems.[14,15] Finally, Frey and Grushka use a combination of the Craig model and a lumped kinetic model to arrive at a numerical solution of the mass balance equations for the separation system.[6] However, a disadvantage of these models is that the dependence of the system on both slow mass transfer and slow reaction kinetics cannot be studied simultaneously.

1.2.4 General Rate Models.

Finally, there are predictive mass balance models that make no assumptions about the system.[16-21] These models, called general rate models, describe the processes of mass transport in the fluid and surface phases, axial dispersion, and absorption or adsorption and desorption kinetics within the system. These models can be used to study systems in which the mass transfer and surface interaction processes occur on the same time scale. Also, since no assumption about equilibrium or steady-state conditions are made, the progression of the system from some initial condition to steady state can be studied in detail. Unfortunately, these systems are usually not solvable analytically, and are almost always simplified by making assumptions about the system. If assumptions are not made, numerical means must be used to obtain the predicted zone profile[20] or the moments of the zones.[16-19,21]

1.3 Molecular Models.

The second approach to modeling separation systems is based on molecular modeling through *ab initio* and molecular dynamic simulations.[22] Since the simulations are done on a true atomic or molecular level, very detailed and accurate descriptions of the system can be obtained. This molecular approach has been applied to study the adsorption and desorption processes on heterogeneous surfaces.[23-25] Catalytic systems have been studied using these methods as well.[26] Molecular dynamic methods have also been used to study the surface phase of absorption chromatography.[27-29] Molecular dynamics simulations have also investigated the effects of chain length and density on the

structure of the surface phase.[30] Temperature effects on the behavior of the surface phase have also been studied.[31] Simulations of the transfer process between the fluid and surface phases have been done to study the retention process within absorption chromatography.[32,33] While these simulations have given very detailed information about the surface phase and the retention process, the simulations represent small time scales (e.g. 1.0×10^{-9} s) and short distances (e.g. 1.0×10^{-6} m) when compared to a real chromatographic system.

1.4 Stochastic Models of Separation Systems.

The third approach to describing separation systems is based on the stochastic nature of the separation process. The retention probability for an individual molecule is determined and used to predict the retention behavior of an ensemble of molecules. There are two methods that have been employed to model the systems in this manner. The methods can be distinguished from one another by the method in which the retention probability is used within the model.

1.4.1 Probability Distribution Models.

The first theory based on probability methods was presented by Giddings and Eyring.[34] This approach views the retention processes as a series of interactions that can be described by the laws of statistics. The probability that a molecule will elute from a column within a time T and T + ΔT is developed and then used to obtain a zone profile. This model has been extensively used to study adsorption chromatography.[34-37] This model has also been adapted to study the effects of heterogeneous surface phases in

adsorption chromatography.[38-41] This kind of stochastic model has also been derived from non-equilibrium statistical mechanics which has provided a basis on which to gain an understanding of the mathematical and physical meanings of dispersion coefficients.[42,43] Recently, this model has been extended to study systems in which the adsorption and desorption kinetics are on the same time scale as the mass transfer processes.[44] It has also been used to develop a model of non-linear chromatography.[45] These models provide information about the behavior of an ensemble of molecules in a chromatographic system, but molecular-level information about the chromatographic system cannot be elucidated from these models.

1.4.2 Random-Walk Molecular Models.

The second kind of stochastic model of chromatography simulates individual molecules as they progress through the system. These models use Monte Carlo techniques to apply the processes of mass transfer and reaction kinetics to individual molecules. Recently, these models have been employed to study a wide variety of systems in separation science, including flow injection analysis,[46-48] field-flow fractionation,[49,50] electrophoresis,[51,52] and chromatography.[53-55] An advantage of such methods is that they deal with the behavior of individual molecules, rather than the average behavior of an ensemble. By monitoring the positions or trajectories of these molecules in space and time, a direct and detailed description of physical and chemical phenomena is possible. Stochastic simulations require few, if any, simplifying assumptions and can be designed to include all relevant mass transport processes in a single unified model. These simulation methods can be applied to homogeneous systems

or to systems with physical and chemical heterogeneity at the molecular, microscopic, or macroscopic level. The systems may be near to or far from steady-state or equilibrium conditions. Consequently, these simulation methods are a powerful and versatile means to model complex separation systems. Finally, stochastic simulations can provide the connection between molecular-level models, such as *ab initio* quantum mechanics or molecular dynamics calculations (Section 1.3) , and the classical theoretical models (Section 1.2), or experiments that investigate the macroscopic or bulk behavior of the system.

There are several distinctions among the various stochastic simulations that have been developed to date. In these simulations, the fundamental equations of motion for each relevant mass transport process are applied independently to each molecule as shown in Figure 1.1. The simulations range in complexity from one-dimensional models with finite step size[56,57] to three-dimensional models with variable step size.[46-48,52,54,55] The more rigorous and comprehensive models generally provide the most detailed insight as well as the greatest accuracy and precision. The transport algorithms may be implemented by uniformly incrementing time and calculating the distance traveled,[46-48,52,54,55] or by incrementing distance and calculating the time required to traverse that distance.[49-51] Although these approaches may seem equivalent, there is an important difference in the statistical distribution of error. No matter how large the number of molecules or how small the time or distance increment, there is a lower limit to the statistical error. If time is the incremental variable then its uncertainty or imprecision is controlled and the remaining imprecision is contained in the distance. Conversely, if distance is the incremental variable, then the uncontrolled imprecision is contained in the

Figure 1.1 Schematic representation of the trajectories of three molecules during four sequential time increments of the stochastic simulation. Diffusion is illustrated as a sphere of randomly varying radial distance (ρ) with a vector indicating the randomly selected spherical coordinate angles (ϕ,θ). Axial displacement due to laminar or electroosmotic convection is illustrated as a dashed line. Surface interaction is shown for a molecule that is retained by the surface phase (top) and a molecule that is not retained and undergoes an elastic collision at the interface (bottom).

Figure 1.1

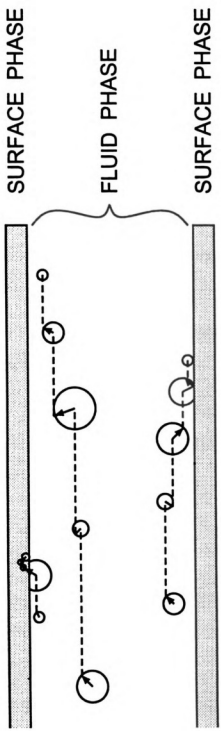

time (or velocity). Each of these approaches has conditions under which it is advantageous; for example, controlled precision in the distance domain is most beneficial when there is spatial heterogeneity in the system.

Another distinction is that some stochastic simulations are performed by advancing each molecule individually through the separation system,[49-51] whereas other simulations advance all molecules simultaneously in each time or distance increment.[46-48,52,54,55] The former approach has the advantage that it can be performed until a given number of molecules have been simulated or until a desired level of precision has been achieved. This approach has the potential to be faster because it utilizes no more than the requisite minimum number of molecules. However, this approach does not easily provide both spatial and temporal distributions of the molecules. Furthermore, this approach is not suitable for modeling transport processes that are dependent upon the local number or concentration of molecules, such as those involving interconversion of the solute by acid/base or complexation reactions, nonideal solute-solute interactions, and nonlinear absorption or adsorption isotherms. For the proper implementation of such processes, all molecules must be advanced simultaneously through the system.

1.5 Conclusions.

The model used in this dissertation is a three-dimensional computer simulation based on the stochastic principles presented in Section 1.4.2. This approach provides a very robust model with few assumptions, allowing complex systems to be investigated

with ease. Chapter 2 discusses the algorithms of the simulation in detail. The relationship between the mass transfer rates and the shape of the zone profiles is investigated in Chapter 3 for systems representative of gas chromatography, supercritical fluid chromatography, enhanced fluidity liquid chromatography, and liquid chromatography. The model is then used to determine an empirical relationship between the system and molecular parameters and the observed rate of mass transfer between the fluid and surface phases in an absorption (partition) system under diffusion-limited conditions in Chapter 4. The simulation is also employed to study absorption systems with a heterogeneous surface phase. The adaptation of the simulation to model a heterogeneous surface phase and the results of the studies are discussed in Chapter 5. Chapter 6 presents the development, validation, and initial application of a novel adsorption algorithm. Chapters 7 and 8 discuss the application of the simulation to systems in which chemical reaction and separation occur concurrently. The benefits of applying a stochastic model with molecular-level detail to such systems are elucidated as well. Finally, Chapter 9 presents the conclusions of the work detailed in the intervening chapters and discusses some of the future work that is possible with this simulation.

1.6 References.

1. Golshan-Shirazi, S.; Guiochon, G.; in Theoretical Advancement in Chromatography and Related Separation Techniques, Dondi, F.; Guiochon, G. Eds.; Kluwer, Amsterdam, the Netherlands, 1992; pp. 61-92.

2. Golshan-Shirazi, S.; Guiochon, G.; J. Chromatogr. 1992, 603, 1.

3. Craig, L.C.; J. Biol. Chem. 1944, 155, 519.

4. Martin, A.J.P.; Synge, R.L.M.; Biochem. J. 1941, 35, 1358.

5. Karol, P.J.; Anal. Chem. 1989, 61, 1937.

6. Frey, G.L.; Grushka, E.; Anal. Chem. 1996, 68, 2147.

7. Taylor, G.; Proc. Roy. Soc. A 1953, 219, 186.

8. Aris, R.; Proc. Roy. Soc. A 1956, A235, 67.

9. Lapidus, L.; Amundson, N.R.; J. Phys. Chem. 1952, 56, 984.

10. Villermaux, J.; Van Swaaj, W.P.M.; Chem. Eng. Sci. 1969, 24, 1097.

11. Giddings, J.C.; J. Chem. Phys. 1959, 31, 1462.

12. Golay, M.J.E. in Gas Chromatography 1958, Desty, D.H. Ed.; Academic Press: New York, NY, 1958; p. 36.

13. Jönsson, J.A.; Chromatographia, 1984, 427.

14. Karol, P.J.; J. Chromatogr. 1988, 445, 207.

15. Karol, P.J.; J. Chromatogr. 1991, 550, 247.

16. Kucera, E.; J. Chromatogr. 1965, 19, 237.

17. Grushka, E.; J. Phys. Chem. 1972, 76, 2586.

18. Villermaux, J.; J. Chromatogr. Sci. 1974, 12, 822.

19. Lenhoff, A.M.; J. Chromatogr. 1987, 384, 285.

20. Row, K.H.; Choi, D.K.; Sep. Sci. Technol. 1995, 30, 3615.

21. Gotmar, G.; Fornstedt, T.; Guiochon, G.; J. Chromatogr. A. 1999, 831, 17.

22. Schure, M.R.; in Advances in Chromatography Vol. 39, Brown, P.R.; Grushka, E. Eds.; Marcel Dekker: New York, NY, 1998; p.139.

23. Lehner, B.; Hohage, M.; Zeppenfeld, P.; Chem. Phys. Lett. 2001, 336, 123.

24. Borowko, M.; Patrykiejew, A.; Rzysko, W.; Sokolowski, S.; Langmuir 1997, 13, 1073.

25. Riccardo, J.L.; Steel, W.A.; Ramirez Cuesta, A.J.; Zgrablich, G.; Langmuir 1997, 13, 1064.

26. Bates, S.P.; Van Santen, R.A.; Advances in Catalysis, Vol. 42; Academic Press, 1998; 1.

27. Slusher, J.T.; Mountain, R.D.; J. Phys. Chem. B 1999, 103, 1354.

28. Klatte, S.J.; Beck, T.L.; J. Phys. Chem. 1995, 99, 16024.

29. Yarovsky, I.; Aguilar, M.I.; Hearn, M.T.W.; J. Chromatogr. A 1994, 660, 75.

30. Yarovsky, I.; Aguilar, M.I.; Hearn, M.T.W.; Anal. Chem. 1995, 67, 2145.

31. Klatte, S.J.; Beck, T.L.; J. Phys. Chem. 1993, 97, 5727.

32. Klatte, S.J.; Beck, T.L.; J. Phys. Chem. 1996, 100, 5931.

33. Wheeler, J.F.; Beck, T.L; Klatte, S.J.; Cole, L.A.; Dorsey, J.G.; J. Chromatogr. A 1993, 656, 317.

34. Giddings, J.C.; Eyring, H.; J. Phys. Chem. 1955, 59, 416.

35. Giddings, J.C.; J. Chem. Phys. 1957, 26, 169.

36. McQuarrie, D.A.; J. Chem. Phys. 1963, 38, 437.

37. Oxtoby, J.C.; J. Chem. Phys. 1969, 51, 3886.

38. Giddings, J.C.; Anal. Chem. 1963, 35, 1999.

39. Weiss, G.H.; Sep. Sci. 1970, 5, 51.

40. Cavazzini, A.; Remelli, M.; Dondi, F.; J. Microcolumn Sep. 1997, 9, 295.

41. Cavazzini, A.; Remelli, M.; Dondi, F.; Felinger, A.; Anal. Chem. 1999, 71, 3453.

42. DeClerk, K.; Smuts, T.W.; Pretorius, V.; Sep. Sci. 1966, 1, 443.

43. Weiss, G.H.; Sep. Sci. 1967, 2, 551.

44. Felinger, A.; Cavazzini, A.; Remelli, M.; Dondi, F.; Anal. Chem. 1999, 71, 4472.

45. Dondi, F.; Munari, P.; Remelli, M.; Cavazzini, A.; Anal. Chem. 2000, 72, 4353.

46. Betteridge, D.; Marczewski, C.Z.; Wade, A.P.; Anal. Chim. Acta 1984, 165, 227.

47. Crowe, C.D.; Levin, H.W.; Betteridge, D.; Wade, A.P.; Anal. Chim. Acta 1987, 194, 49.

48. Wentzell, P.D.; Bowridge, M.R.; Taylor, E.L.; MacDonald, C.; Anal. Chim. Acta 1993, 278, 293.

49. Schure, M.R.; Anal. Chem. 1988, 60, 1109.

50. Schure, M.R.; Weeratunga, S.K.; Anal. Chem. 1991, 63, 2614.

51. Schure, M.R.; Lenhoff, A.M.; Anal. Chem. 1993, 65, 3024.

52. Hopkins, D.L.; McGuffin, V.L.; Anal. Chem. 1998, 70, 1066.

53. Guell, O.A.; Holcombe, J.A.; Anal. Chem. 1990, 62, 529A.

54. McGuffin, V.L.; Wu, P.; J. Chromatogr. A 1996, 722, 3.

55. McGuffin, V.L.; Krouskop, P.E.; Wu, P.; J. Chromatogr. A 1998, 828, 37.

56. Giddings, J.C.; J. Chem. Ed. 1958, 35, 588.

57. Chen, J.; Weber, S.G.; Anal. Chem. 1983, 55, 127.

Chapter 2

Three-Dimensional Stochastic Simulation

2.1 Introduction.

The three-dimensional molecular simulation program presented in this dissertation is written in the FORTRAN 90 programming language and is optimized for execution on an International Business Machines (IBM) RS/6000 Model 580 computer as well as R10000 Silicon Graphics, Inc. (SGI) workstations and a SGI Origin 2400 server with thirty-two 300 MHz R12000 processors. This program incorporates algorithms for the processes of diffusion, convection by laminar and electroosmotic flow, electrophoretic migration, and surface interaction by an absorption (partition) or adsorption mechanism, as shown schematically in Figure 2.1. These processes are applied to each molecule at each time increment (t) until the total simulation time (T) is reached. The simulation may be performed in Cartesian global coordinates, which is most appropriate for separations in planar media, or alternatively in cylindrical global coordinates for separations in capillary tubes, membranes, or fibers. Because of its mathematical simplicity, the latter case will be described in detail. This chapter will discuss the algorithms used in the simulation for diffusion, convection, electrophoretic migration, absorption (partition), adsorption, and chemical reaction.

2.2 Simulation Input.

The input parameters required for the simulation may be divided into three general categories, as summarized in Table 2.1.

Figure 2.1: Flowchart of the stochastic simulation.

Figure 2.1

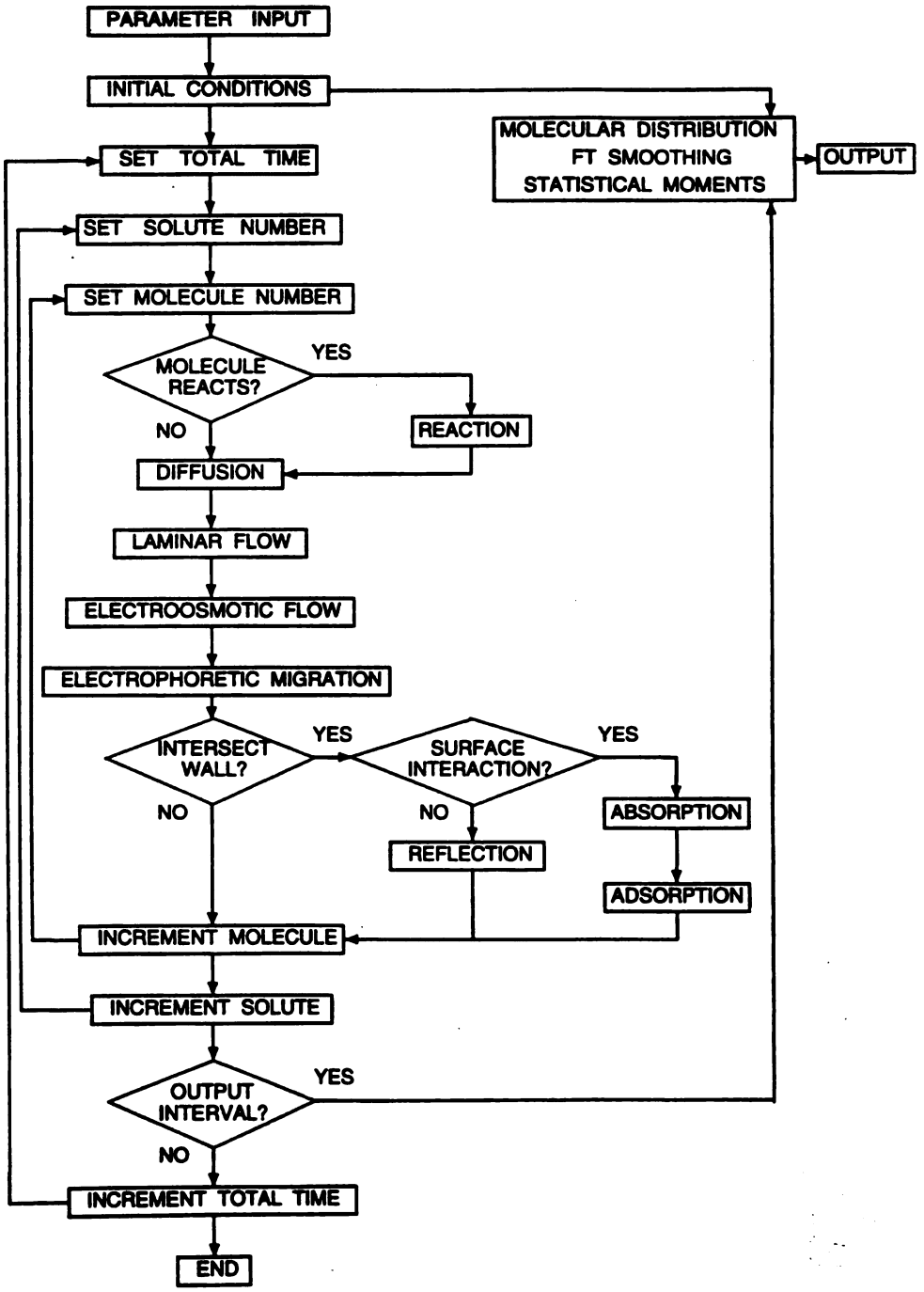
PARAMETER INPUT
INITIAL CONDITIONS
SET TOTAL TIME
SET SOLUTE NUMBER
SET MOLECULE NUMBER
MOLECULE REACTS?
YES
NO
REACTION
DIFFUSION
LAMINAR FLOW
ELECTROOSMOTIC FLOW
ELECTROPHORETIC MIGRATION
INTERSECT WALL?
YES
NO
SURFACE INTERACTION?
YES
NO
ABSORPTION
REFLECTION
ADSORPTION
INCREMENT MOLECULE
INCREMENT SOLUTE
OUTPUT INTERVAL?
YES
NO
INCREMENT TOTAL TIME
END
MOLECULAR DISTRIBUTION
FT SMOOTHING
STATISTICAL MOMENTS
OUTPUT

Table 2.1 Input Parameter for the Stochastic Simulation Program.

System Parameters	Symbol
Radius of fluid phase	R_f
Radius of surface phase	R_s
Length of fluid/surface phase	L
Position of injection	L_{inj}
Length, variance of injection zone	l_{inj}, σ_{inj}
Position of detector	L_{det}
Number of surface different adsorption or absorption sites	n
Fractional coverage of surface site i	P_i
Zeta potential of surface phase	ζ
Velocity of fluid phase	v_0
pH of fluid phase	pH
pC of complexing agent in fluid phase	pC
Ionic strength of fluid phase	I
Viscosity of fluid phase	η
Dielectric constant of fluid phase	ε
Temperature	T_0
Pressure	P
Voltage	V
Molecular Parameters	**Symbol**
Diffusion coefficient in fluid phase	D_f
Diffusion coefficient in surface phase for interaction i	$D_{s,i}$
Equilibrium constant for acid/base reaction	K_a
Equilibrium constant for complexation reaction	K_c
Absorption coefficient for interaction i	$K_{abs,i}$
Adsorption rate constant for interaction i	$k_{a,i}$
Desorption rate constant for interaction i	$k_{d,i}$
Reaction rate constant for reaction i	$k_{r,i}$
Electrophoretic mobility	μ
Charge	$z_\pm$
Computational Parameters	**Symbol**
Number of molecules	N
Time increment	t
Total simulation time	T
Molecular coordinate systems	
Spherical coordinates	ρ,ϕ,θ
Cartesian coordinates	x,y,z
Global coordinate systems	
Cylindrical coordinates	R,Θ,Z
Cartesian coordinates	X,Y,Z

The system parameters describe properties of the fluid and the surface, as well as the spatial dimensions of the separation system to be simulated. The molecular parameters describe attributes of the solute molecules or ions. The values of these parameters may be systematically chosen to characterize the behavior of the system or may be derived from ab initio calculation or from experiment. On the basis of these input parameters, an array is created that contains the properties and coordinates of each molecule. To initialize the simulation, the molecules are distributed randomly with a delta, rectangular, or Gaussian profile of specified variance at a specified mean distance in the global coordinate frame. The molecules may be distributed entirely in the fluid phase, entirely in the surface phase, or at equilibrium between the phases.

2.3 Simulation Output.

The simulation program allows the molecular zone profile to be examined as the distance distribution at specified times or, correspondingly, as the time distribution at specified distances. The statistical moments of the molecular distribution are then calculated in either the distance or time domain.[1-3] For example, the first statistical moment or mean is calculated as

$$M_1 = \frac{\sum_{i=1}^{N} x_i}{N} \qquad [2.1]$$

where x_i is the time or distance datum of an individual molecule and N is the total number of molecules. The higher order central moments are calculated as

$$M_y = \frac{\sum_{i=1}^{N}(x_i - M_1)^y}{N} \qquad [2.2]$$

where the second moment or variance is obtained when y = 2, the third moment is obtained when y = 3, etc. These statistical moments, as well as the chromatographic or electrophoretic figures of merit derived therefrom, are stored in a standard data file at each specified time (or distance). For example, the capacity factor, effective mobility, velocity, plate height, skew, etc. can be calculated since the beginning of the simulation (net average) or since the most recent data file output (local average). Other information such as the number of molecules in the fluid and surface phases, the time spent by each molecule in each phase, and the number of transitions between phases are also recorded in the standard data file.

In addition to these numerical output parameters, the molecular population is summed in discrete segments and then smoothed by Fourier transform methods[4] to provide a continuous zone profile for graphical display. Because the molecular distribution may be examined at any time (or distance), these output routines provide an extensive visual and numerical record of transport processes throughout the simulation.

2.4 Diffusion.

Molecular diffusion is simulated by using a three-dimensional extension of the Einstein-Smoluchowski equation.[5-7] The radial distance ρ traveled during the time increment t is selected randomly from the following probability distribution

$$P_\rho = \frac{\rho^2}{\sqrt{4\pi D_{f,s}\, t}} \exp\left(\frac{-\rho^2}{4 D_{f,s}\, t}\right) \qquad [2.3]$$

where $D_{f,s}$ represents the binary diffusion coefficient of the molecule in the fluid or surface phase, as appropriate. This approach provides a variable step size derived from a normal (Gaussian) distribution, where the direction of travel is subsequently randomized through the spherical coordinate angles (ϕ,θ). The coordinate increments in the molecular frame are used to calculate the new molecular position in the global coordinate frame.

To verify the accuracy of the diffusion algorithm, the zone distance and variance for an ensemble of 750 molecules were monitored as a function of the simulation time. These results were compared with classical mass balance models based on the Einstein equation.[5] Excellent agreement was observed for the range of diffusion coefficients from 10^{-1} to 10^{-10} cm^2 s^{-1}, with average relative errors for the zone distance and variance of 0.81% and 3.67%, respectively.[1,8]

2.5 Convection.

Molecular convection in the fluid phase may be induced by means of a pressure or electrical field gradient applied tangential to the surface. The axial distance z traveled by a molecule in time increment t is given by

$$z = v\, t \qquad [2.4]$$

The following convection algorithms may be used individually or in combination to simulate a wide variety of hydrodynamic conditions for chromatography, electrophoresis, or electrochromatography.

2.5.1 Pressure-Induced Flow.

For pressure-induced flow under fully developed laminar conditions, the radial velocity profile in the cylindrical global frame is given by the Taylor-Aris equation[9,10]

$$v = 2 v_0 \left(1 - \frac{R^2}{R_f^2} \right) \qquad [2.5]$$

$$v_0 = \frac{R_f^2 P}{8 \eta L} \qquad [2.6]$$

The mean velocity v_0 may be specified as an input parameter or may be calculated from the Hagen-Poiseuille equation,[11-14] where P is the applied pressure, η is the viscosity of the fluid phase, R_f and L are the radius and length. The coordinate increment in the molecular frame determined from Equations [2.4] and [2.5] is used to calculate the new molecular position in the global coordinate frame.

To verify the accuracy of the laminar convection algorithm, the zone distance and variance for an ensemble of 750 molecules were monitored as a function of the simulation time. These results were compared with classical mass balance models based on the Taylor-Aris equation[9,10] with both diffusion and resistance to mass transfer in the fluid phase. Excellent agreement was observed for the range of linear velocities from 0.001 to 100 cm s^{-1}, with average relative errors for the zone distance and variance of 0.49% and 2.24%, respectively.[2]

2.5.2 Electroosmotic flow.

For electric field-induced flow due to electroosmosis, the radial velocity profile in the cylindrical global frame is given by the Rice-Whitehead equation[15,16]

$$v = v_0\left(1 - \frac{I_0(\kappa R)}{I_0(\kappa R_f)}\right) \qquad [2.7]$$

$$v_0 = \frac{\varepsilon \zeta V}{4\pi\eta L} \qquad [2.8]$$

where κ^{-1} is the Debye length, and I_0 is the zero-order modified Bessel function of the first kind. The maximum velocity v_0 may be specified as an input parameter or may be calculated from the Helmholtz-Smoluchowski equation,[17,18] where ε is the permittivity of the fluid phase, ζ is the zeta potential of the fluid-surface interface, and V is the applied voltage. The coordinate increment in the molecular frame determined from Equations [2.4] and [2.7] is used to calculate the new molecular position in the global coordinate frame.

To verify the accuracy of the electroosmotic convection algorithm, the zone distance and variance for an ensemble of 500 molecules were monitored as a function of the simulation time. These results were compared with classical mass balance models based on the analytical solution of the Rice-Whitehead equation by McEldoon and Datta.[19] Excellent agreement was observed for the range of linear velocities from 0.01 to 1.0 cm s^{-1}, with average relative errors for the zone distance and variance of 0.12% and 4.42%, respectively.[1]

2.6 Electrophoretic Migration.

For charged molecules under the influence of an applied electric field,[20] the velocity of electrophoretic migration is given by

$$v = \frac{\mu V}{L} \qquad [2.9]$$

The electrophoretic mobility μ is corrected by means of the modified Onsager equation[21] to the specified ionic strength of the fluid phase.

If the molecule exists as a single species, the mobility is constant. This convection algorithm provides equal displacement of all molecules during each time increment according to Equations [2.4] and [2.9]. The axial coordinate increment in the molecular frame is used to calculate the new position for each molecule in the global frame.

If the molecule exists as n multiple species in dynamic equilibrium (e.g., phosphate may exist as H_3PO_4, $H_2PO_4^-$, HPO_4^{2-}, or PO_4^{3-}), the mobility of an individual molecule is determined from statistical probability at each time increment. The fraction α_i of each species i is calculated from the appropriate equilibrium constants for acid/base or complexation reactions, which are corrected for ionic strength by means of the Davies equation.[22,23] The identity of a molecule is determined by selecting a random number, χ, between zero and one to establish the value of i that satisfies the relationship

$$1 - \sum_{j=1}^{n-i} \alpha_{n-j} < \chi \leq \sum_{j=1}^{i+1} \alpha_{j-1} \qquad [2.10]$$

The molecule is then assigned the mobility μ_i corresponding to species i during that time increment and its electrophoretic migration is calculated via Equations [2.4] and [2.9]. The resulting migration of the zone is similar, but not identical, to that for a single species whose average mobility is given by

$$\mu = \sum_{i=0}^{n} \alpha_i \mu_i \qquad [2.11]$$

To verify the accuracy of the electrophoretic migration algorithms corresponding to a single species and n multiple species, the zone distance and variance for an ensemble of 500 molecules were monitored as a function of the simulation time. These results were compared with classical models. Excellent agreement was observed for single species with positive and negative electrophoretic mobilities in the range from $+10^{-3}$ to -10^{-3} $cm^2\ V^{-1}\ s^{-1}$, with average relative errors for the zone distance and variance of 0.04% and 2.67%, respectively.[1] The agreement is similarly good for multiple species, with average relative errors for the zone distance and variance of 0.01% and 3.38%, respectively, for phosphate at pH values from 3.0 to 9.0.[1]

2.7 Surface Interaction.

Molecular interaction with a stationary surface is simulated as an absorption process if the surface is permeable (e.g., thin polymer film or chemically bonded organic ligands) or as an adsorption process if the surface is solid (e.g., silica or alumina). The surface may be homogeneous, or heterogeneous. If the surface has more than one kind of absorption (or adsorption) site present ($n > 1$), then the fraction (P_i) of the surface covered

by each site is input. When a solute molecule intersects the boundary between the fluid and surface phases, a random number is used to determine which site is to be chosen. The appropriate molecular parameters are then chosen for the solute molecule, and the algorithm for absorption (or adsorption) is then initiated. The processes is repeated each time the molecule intersects the interface from the mobile phase side.

2.7.1 Absorption or Partition.

For the absorption process, the probability of transport between the fluid and surface phases at a given partition site i is given by

$$P_{fs,i} = \mathrm{Min}\left(a_i \, K_{abs,i} \sqrt{\frac{D_{s,i}}{D_f}}, a_i \right) \qquad [2.12]$$

$$P_{sf,i} = \mathrm{Min}\left(a_i, \frac{a_i}{K_{abs,i}} \sqrt{\frac{D_f}{D_{s,i}}} \right) \qquad [2.13]$$

where $K_{abs,i}$ is the absorption coefficient and the constant a_i represents the fraction of effective collisions with the interface, which is equal to unity when there is no barrier to transport (diffusion-limited case). When a molecule in the fluid phase encounters the fluid-surface interface during the simulation, a random number between zero and one is selected. If the selected number is less than or equal to the probability $P_{fs,i}$ given by Equation [2.12], the molecule will be transferred to the surface phase. Otherwise, the molecule will remain in the fluid phase and will undergo an elastic collision at the interface. A similar routine is performed when a molecule in the surface phase encounters the interface, except that the random number is compared with the probability

$P_{sf,i}$ given in Equation [2.13]. Finally, when a molecule in the fluid or surface phase encounters a physical boundary of the system, an elastic collision is performed.

To verify the accuracy of the absorption algorithm, the zone distance and variance for an ensemble of 750 molecules were monitored as a function of the simulation time. These results were compared with classical mass balance models based on the extended Golay equation including both diffusion and resistance to mass transfer in the fluid and surface phases.[24] The first and second moments for a homogeneous surface phase are predicted to be

$$M_1 = \frac{v_0 T}{1+k'} \qquad [2.14]$$

$$M_2 = \left(\frac{2D_f}{v_0} + \frac{2k'D_s}{v_0} + \frac{\left(1+6k'+11k'^2\right)R_f^2 v_0}{24(1+k')^2 D_f} + \frac{k'R_s^2 v_0}{(1+k')^2 D_s} \right) M_1 \qquad [2.15]$$

where M_1 and M_2 are the first and second moments in distance at time T, k' is the capacity factor (defined as $K_{abs}(V_s/V_f)$ where V_s and V_f are the volumes of the surface and fluid phases, respectively), and all other symbols are as defined in Table 2.1. Excellent agreement was observed for the range of absorption coefficients from 0.01 to 100.0, with average relative errors for the zone distance and variance of 0.55% and 4.02%, respectively.[2]

2.7.2 Adsorption.

The process of adsorption can occur for any molecule that interacts with the interface of the fluid and surface phases. The final phase of the molecule is determined

by comparing a random number to the probability that a molecule will adsorb at the time of the collision (Equation [2.16]).

$$P_{ads,i} = \left(1 - \exp\left(-k'_{a,i}\, t\right)\right) \qquad [2.16]$$

$$k'_{a,i} = k_{a,i}\,[S] \qquad [2.17]$$

where $k'_{a,i}$ is the pseudo-first-order reaction rate constant for adsorption on site i, t is the time increment of the simulation, $k_{a,i}$ is the second-order adsorption rate constant, and [S] is the number of surface sites in the system (discussed further in Chapter 6). If the random number is less then the probability, the molecule adsorbs, otherwise the molecule elastically collides with the interface.

Desorption is treated as a first-order reaction. The reaction is simulated by randomly assigning each adsorbed molecule a lifetime based on the desorption rate constant ($k_{d,i}$) of the site chosen as previously described.[25] The lifetimes are determined by

$$\lambda_i = \frac{-1}{k_{d,i}} \log(\chi) \qquad [2.18]$$

where λ_i is the adsorbed lifetime of the molecule, and χ is a random number between zero and one. The molecule then remains adsorbed for the entire assigned lifetime. At the end of the assigned lifetime, the molecule desorbs and diffuses back into the fluid phase.

To verify the accuracy of the adsorption algorithm, the zone distance and variance for an ensemble of 750 molecules were monitored as a function of the simulation time. These results were compared with classical mass balance models for a homogeneous surface phase based on the following equations proposed by Giddings[26]

$$M_1 = \frac{v_0 T}{(1+K_{ads})} \qquad [2.19]$$

$$M_2 = \left(\frac{2D_f}{v_0} + \frac{(1+6K_{ads}+11K_{ads}^2)R_f^2 v_0}{24(1+K_{ads})^2 D_f} + \frac{2k' v_0}{(1+K_{ads})^2 k_d} \right) M_1 \qquad [2.20]$$

where M_1 and M_2 are the first and second moments in distance at time T, K_{ads} is equal to k_a/k_d, and all other symbols are as defined in Table 2.1. Excellent agreement was observed for the range of distribution coefficients from 0.01 to 100.0, with average relative errors for the zone distance and variance of ± 0.784% and ± 6.46%, respectively.[27]

2.8 Chemical Reaction.

Chemical reactions can be modeled to occur in the fluid phase, the surface phase, or both. The simulation models first-order and pseudo-first-order reversible and irreversible kinetics that describe systems ranging from one simple reaction to those as complex as three sequential reactions with one side reaction. To simulate the reaction, when the molecule enters the reacting phase it is assigned a random lifetime (λ_r) using Equation [2.18] with $k_{d,i}$ replaced with the appropriate reaction rate constant $k_{r,i}$. If the molecule then remains in the reacting phase for an accumulated time that is equal to or greater than the assigned lifetime, the molecule is converted to the new species with all of its respective properties. In the case of a branching reaction, a lifetime is randomly selected for each reaction and that with the shortest lifetime is assigned to the molecule. To properly simulate reactions that are faster than the time increment of the simulation,

the algorithm calculates lifetimes that sum to equal or exceed the time increment of the simulation. A time-weighted average of the molecular properties is then used to determine the diffusion and electromigration steps. This process allows the reactions to be simulated with finer precision than the discrete time intervals used within the simulation. In essence, the time increment of the simulation is contracted and expanded, as necessary, to allow reactions to be modeled accurately. The reaction algorithm has been validated for kinetic rate constants over the range of 1.0×10^{-8} to 1.0×10^{10} s^{-1} and for equilibrium constants over the range of 1.0×10^{-18} to 1.0×10^{18}.[25]

2.9 Conclusions.

The algorithms that have been described in this chapter model the respective processes to within 5% error of what is theoretically expected. The processes of mass transfer (diffusion, convection, electrophoretic migration, absorption, and adsorption) are modeled within a framework that allows any combination of the processes to be investigated. Chemical reaction is also modeled to allow the investigation of the interconversion of species in electrophoresis, electrochromatography, and reactive separations. This allows a unified study of the basic separation techniques of analytical scientists.

2.10 References.

1. Hopkins, D.L.; McGuffin, V.L.; Anal. Chem. 1998, 70, 1066.

2. McGuffin, V.L.; Wu, P.; J. Chromatogr. A 1996, 722, 3.

3. McGuffin, V.L.; Krouskop, P.E.; Wu, P.; J. Chromatogr. A 1998, 828, 37.

4. Press, W.H.; Flannery, B.P.; Teukolsky, S.A.; Vetterling, W.T.; Numerical Recipes: The Art of Scientific Computing; Cambridge University Press: Cambridge, England, 1989.

5. Einstein, A.; Ann. Phys. 1905, 17, 549.

6. Reid, R.C.; Prausnitz, J.M.; Sherwood, T.K.; The Properties of Gases and Liquids; McGraw-Hill: New York, NY, 1977.

7. Feller, W.; Probability Theory and its Application; Wiley: New York, NY, 1950; Chapter 14.

8. Krouskop, P.E.; unpublished research, Michigan State University, East Lansing, MI 1998.

9. Taylor, G.; Proc. Roy. Soc. (London) 1953, A219, 186.

10. Aris, R.; Proc. Roy. Soc. (London) 1956, A235, 67.

11. Bird, R.B.; Stewart, W.E.; Lightfoot, E.N.; Transport Phenomena; Wiley: New York, NY, 1960.

12. Sherwood, T.K.; Pigford, R.L.; Wilke, C.R.; Mass Transfer; McGraw-Hill: New York, NY, 1975.

13. Hines, A.L.; Maddox, R.N.; Mass Transfer: Fundamentals and Applications; Prentice-Hall: Englewood Cliffs, NJ, 1985.

14. Karger, B.L.; Snyder, L.R.; Horvath, C.; An Introduction to Separation Science; Wiley: New York, NY, 1973.

15. Rice, C.L.; Whitehead, R.; J. Phys. Chem. 1965, 69, 4017.

16. Martin, M.; Guiochon, G.; Anal. Chem. 1984, 56, 614.

17. von Smoluchowski, M.; Bull. Intern. Acad. Sci. Cracovic 1903, 1903, 184.

18. Huckel, E.; Physik Z. 1924, 25, 204.

19. McEldoon, J.P.; Datta, R.; Anal. Chem. 1992, 64, 230.

20. Atkins, P.W.; Physical Chemistry; W.H. Freeman: San Francisco, CA, 1978.

21. Robinson, R.A.; Stokes, R.H.; Electrolyte Solutions: The Measurement and Interpretation of Conductance, Chemical Potental, and Diffusion in Solutions of Simple Electrolytes; Butterworths: London, England, 1959.

22. Butler, J.N.; Ionic Equilibrium: A Mathematical Approach; Addison-Wesley: Reading, MA, 1964.

23. Laitinen, H.A.; Harris, W.E.; Chemical Analysis, 2nd Ed.; McGraw-Hill: New York, NY, 1975.

24. Golay, M.J.E.; in Gas Chromatography 1958; Desty, D.H. Ed.; Academic Press: New York, NY, 1958; p. 36.

25. Hopkins, D.L.; McGuffin, V.L.; unpublished research, Michigan State University, East Lansing, MI 1998.

26. Giddings, J.C.; Dynamics of Chromatography; Marcel Dekker: New York, NY, 1965; Chp. 3.

27. Krouskop, P.E.; McGuffin, V.L.; Anal. Chem. manuscript in preparation, 2001.

Chapter 3

Three-Dimensional Stochastic Simulation for the Unified Treatment of Chromatographic and Electrophoretic Separations

3.1 Introduction.

In this chapter, the three-dimensional stochastic simulation of Chapter 2 is used for the unified treatment of chromatography, electrophoresis, and electrochromatography. In this simulation, the migration of individual molecules or ions is established through the processes of diffusion and convection by laminar, electroosmotic, and electrophoretic flow. Molecular retention arises from absorption (partition) into permeable surfaces. The molecular distribution and the corresponding zone profile may be examined and characterized at any specified time or spatial position during the simulation. The effects of diffusion in the fluid and surface phases as well as interfacial resistance to mass transport in a unified study of chromatography systems are presented below.

3.2 Selected Applications of the Stochastic Simulation.

Some applications have been selected to illustrate the capabilities and versatility of the stochastic simulation approach. The kinetic and equilibrium behavior are characterized for a model chromatographic system with a simple absorption mechanism under diffusion-limited conditions. In the first series of simulations, the behavior is examined as a function of the diffusion coefficient in the fluid phase. In the second series of simulations, the effect of the diffusion coefficient in the surface phase is similarly

explored. Finally, the influence of interfacial resistance to mass transport between the fluid and surface phases is examined.

For each of these cases, the kinetic behavior of the system is elucidated by monitoring the number of molecules in the fluid phase as a function of the simulation time. These data are analyzed by means of nonlinear regression to the following equation

$$\frac{N_f}{N} = \frac{k_{sf} + k_{fs}\exp\left(-(k_{fs} + k_{sf})T\right)}{k_{fs} + k_{sf}} \qquad [3.1]$$

in order to determine the pseudo first-order rate constants for transport from the fluid to the surface phase (k_{fs}) and from the surface to the fluid phase (k_{sf}). By using this approach, the rate constants k_{fs} and k_{sf} can typically be determined with ±0.49% relative standard deviation and the ratio of the rate constants k_{fs}/k_{sf} with ±0.70% relative standard deviation and ±2.25% relative error.[1,2] The characteristic time τ is given by

$$\tau = \frac{1}{k_{fs} + k_{sf}} \qquad [3.2]$$

The equilibrium behavior of the system is elucidated by monitoring the number of molecules in the fluid and surface phases at equilibrium, $\tilde{N}_f$ and $\tilde{N}_s$, respectively. The ratio of the number of molecules can typically be determined with ±0.29% relative standard deviation and ±0.39% relative error.[1] The kinetic and equilibrium descriptions of the system are related in the following manner:

$$\frac{k_{fs}}{k_{sf}} = \frac{\tilde{N}_s}{\tilde{N}_f} = \frac{K_{abs} V_s}{V_f} = k' \qquad [3.3]$$

where the volumes of the fluid and surface phases are given as $V_f = \pi R_f^2 L$ and $V_s = \pi (R_s^2 + 2 R_s R_f) L$, respectively, and k' is the capacity factor.

Finally, for each case, the hydrodynamic behavior of the system is elucidated under laminar flow conditions. In the presence of flow, the characteristic time τ will influence the appearance of the solute zones. If τ is sufficiently small, the system will be nearly at equilibrium and the zone profile will be a symmetric Gaussian distribution. Under these conditions, the profile will be well described by classical equations of mass balance based on the equilibrium-dispersive model, such as the Golay equation (Equations [2.14] and [2.15]).[3] As τ increases, however, the system may depart from equilibrium and the zone profile may become highly asymmetric. As a measure of the degree of departure from equilibrium for convective systems, we may use the inverse of the Stanton number (St^{-1}) defined as

$$\frac{1}{St} = \frac{\tau}{T} = \frac{\tau v_0}{d} \qquad [3.4]$$

where τ is equal to $1/(k_{fs} + k_{sf})$, T is time, d is distance, and v_0 is the linear velocity. This parameter directly reflects the sources of kinetic stress that are placed on the system and will approach a limiting value of zero for a system that is at equilibrium. For each of the cases outlined above, the solute zone profiles are simulated at fixed times from 0 to 30 s. The first moment (mean zone distance) and second moment (variance) are determined by means of Equations [2.1] and [2.2] as a function of the simulation time and are compared with classical theoretical models.[3]

3.2.1 Effect of the Fluid-Phase Diffusion Coefficient.

The stochastic simulation method is especially well suited for the unified treatment of chromatographic separations. To illustrate this capability, we have simulated systems that are representative of gas, dense gas, supercritical fluid, enhanced fluidity liquid, and liquid chromatography. The kinetic behavior of these systems is illustrated in Figure 3.1. The gas, dense gas, and supercritical fluid are compared as fluid phases in an open-tubular column with radius R_f of 50.0×10^{-1} cm and surface phase R_s of 2.5×10^{-2} cm, resulting in a volumetric phase ratio V_f/V_s of 100. As shown in Figure 3.1A, the kinetic behavior of the system is nearly indistinguishable, despite the significant change in diffusion coefficients D_f from 1.0×10^{-1} to 1.0×10^{-3} cm^2 s^{-1} for these fluid phases. This observation is confirmed by the rate constants k_{fs} and k_{sf}, which were determined by nonlinear regression of the simulation data to Equation [3.1] and are summarized in Table 3.1. There is a small but statistically significant decrease in both k_{fs} and k_{sf} with decreasing diffusion coefficient in the fluid phase. The overall transport rate, as represented by the characteristic time τ in Equation [3.2], is controlled by the rate constant for transport from the surface to fluid phase (k_{sf}) which is one-hundred-fold larger than that from fluid to surface phase (k_{fs}). It is evident that the characteristic time τ is very small (~10^{-5} s), which indicates that equilibrium is rapidly achieved within this system for all of the fluid phases. Finally, the ratio of the rate constants k_{fs}/k_{sf} and the ratio of the number of molecules at equilibrium $\tilde{N}_s/\tilde{N}_f$ are in good agreement with the theoretically predicted value of K_{abs} $V_s/V_f = 0.01$ given by Equation [3.3].

Figure 3.1: Kinetic evolution of the absorption process with varying diffusion coefficients in the fluid phase representative of (A) gas, dense gas, and supercritical fluid chromatography, (B) supercritical fluid, enhanced fluidity liquid, and liquid chromatography. Simulation conditions: (A) $N = 1.0\times10^{5}$; $t = 1.0\times10^{-7}$ s; $T = 20\ \tau$; $R_f = 5.0\times10^{-3}$ cm; $R_s = 2.5\times10^{-5}$ cm; $D_f = 1.0\times10^{-1}$ cm^2 s^{-1} (∇), 1.0×10^{-2} cm^2 s^{-1} ($\diamond$), 1.0×10^{-3} cm^2 s^{-1} ($\triangle$); $D_s = 1.0\times10^{-5}$ cm^2 s^{-1}; $K_{abs} = 1.0$. (B) $N = 1.0\times10^{4}$; $t = 1.0\times10^{-5}$ s; $T = 20\ \tau$; $R_f = 2.0\times10^{-3}$ cm; $R_s = 8.28\times10^{-4}$ cm; $D_f = 1.0\times10^{-3}$ cm^2 s^{-1} ($\triangle$), 1.0×10^{-4} cm^2 s^{-1} ($\square$), 1.0×10^{-5} cm^2 s^{-1} ($\bigcirc$); $D_s = 1.0\times10^{-5}$ cm^2 s^{-1}; $K_{abs} = 1.0$.

Figure 3.1

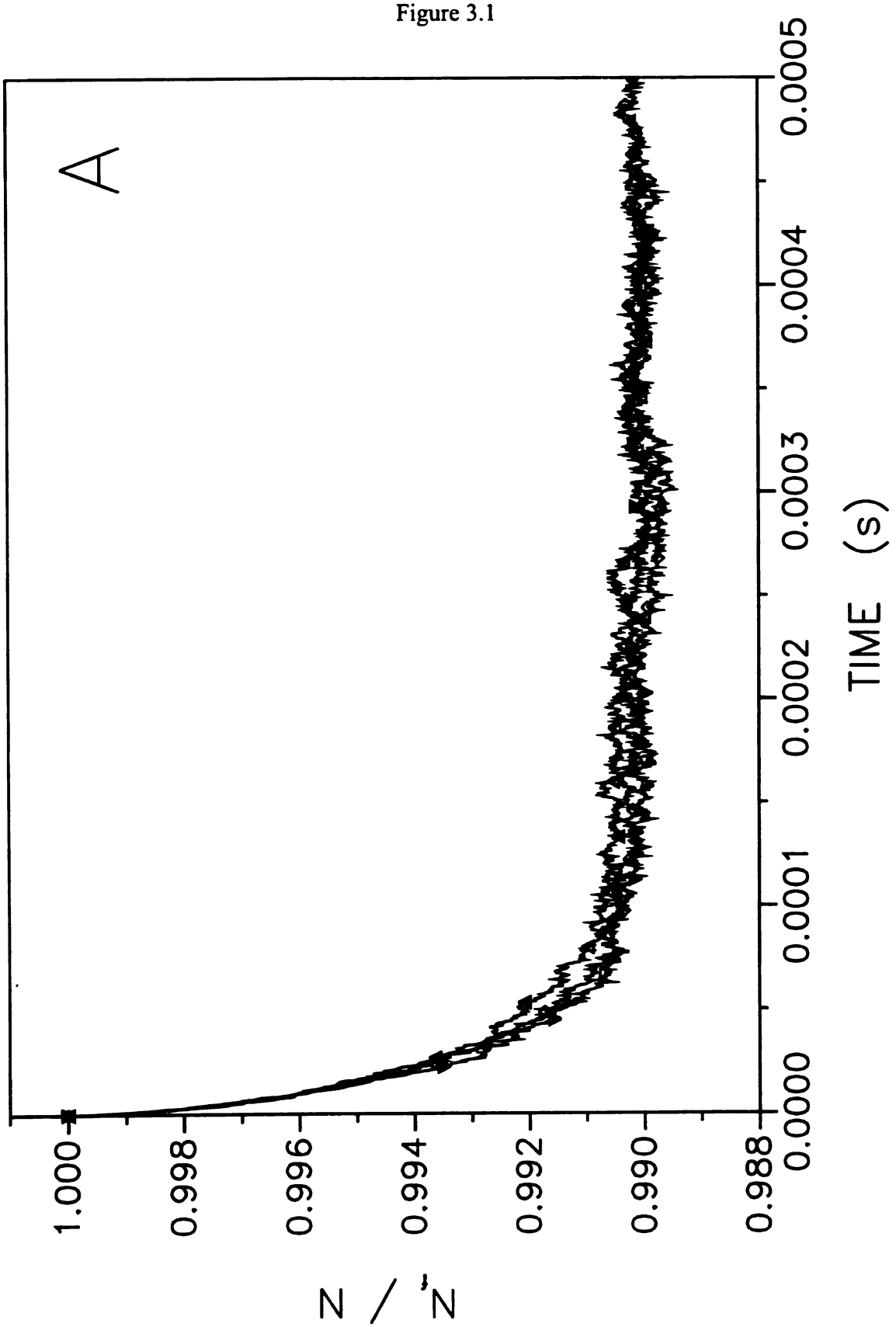
A
1.000
0.998
0.996
0.994
0.992
0.990
0.988
N / N'
0.0000
0.0001
0.0002
0.0003
0.0004
0.0005
TIME (s)

Figure 3.1 cont.

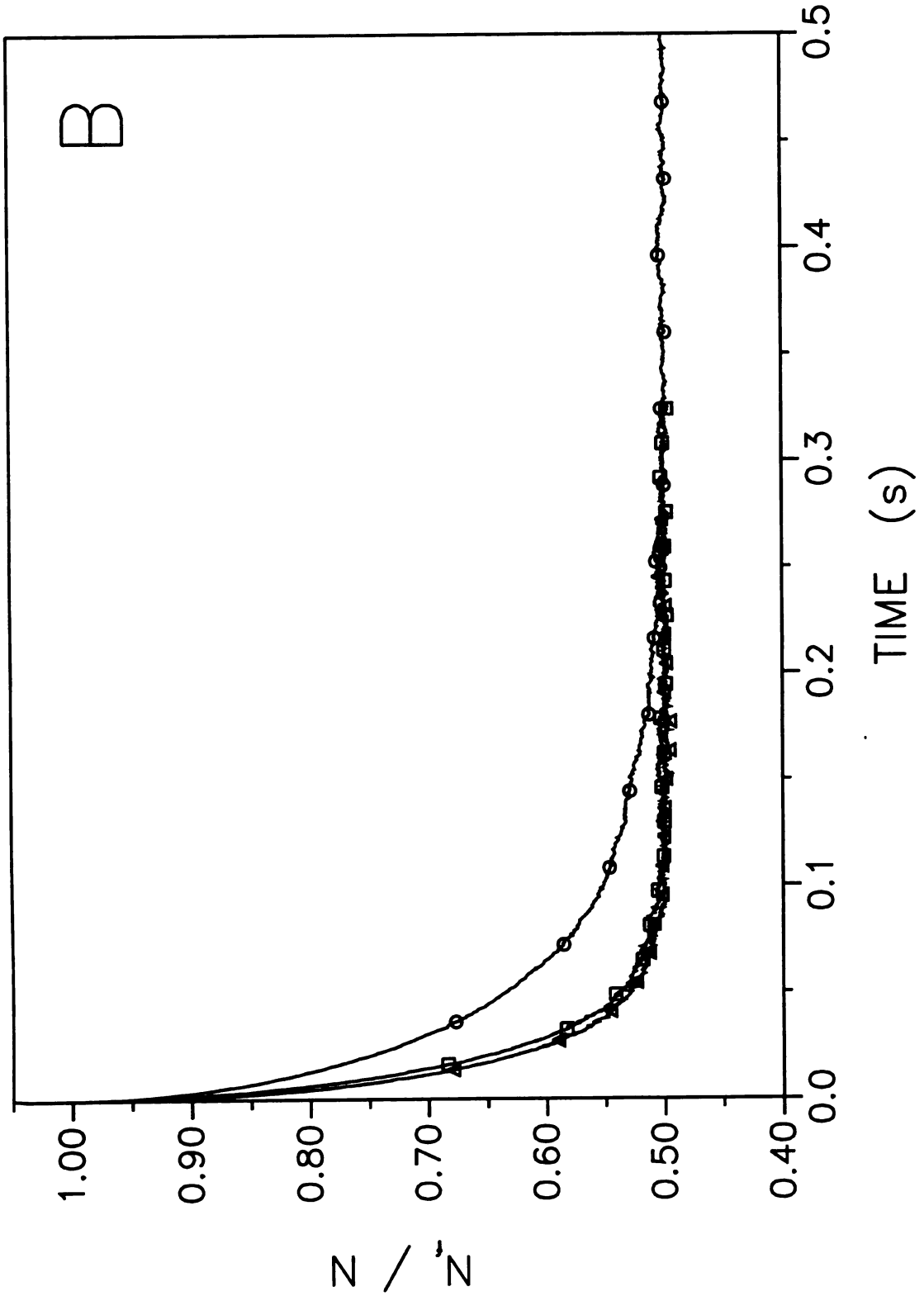

Table 3.1 Effect of Fluid-Phase Diffusion Coefficient on Rate Constants.

D_f ($cm^2\ s^{-1}$)	k_{fs} (s^{-1})	k_{sf} (s^{-1})	τ (s)	k_{fs}/k_{sf}	$\tilde{N}_s/\tilde{N}_f$
1.00×10^{-1} [a]	442	44000	2.25×10^{-5}	0.01006	0.01021
1.00×10^{-2} [a]	407	40700	2.44×10^{-5}	0.01000	0.00996
1.00×10^{-3} [a]	367	37200	2.66×10^{-5}	0.00986	0.01000
1.00×10^{-3} [b]	36.6	37.0	0.014	0.989	0.995
1.00×10^{-4} [b]	30.5	30.7	0.016	0.993	1.003
1.00×10^{-5} [b]	13.74	13.87	0.036	0.991	0.997

[a] Simulation conditions: $N = 1.0\times10^{5}$; $t = 1.0\times10^{-7}$ s; $T = 20\ \tau$; $R_f = 5.0\times10^{-3}$ cm; $R_s = 2.5\times10^{-5}$ cm; $D_s = 1.0\times10^{-5}$ $cm^2\ s^{-1}$; $K_{abs} = 1.0$.

[b] Simulation conditions: $N = 1.0\times10^{4}$; $t = 1.0\times10^{-5}$ s; $T = 20\ \tau$; $R_f = 2.0\times10^{-3}$ cm; $R_s = 8.28\times10^{-4}$ cm; $D_s = 1.0\times10^{-5}$ $cm^2\ s^{-1}$; $K_{abs} = 1.0$.

The supercritical fluid, enhanced fluidity liquid, and liquid are compared as fluid phases in an open-tubular column with radius R_f of 20.0×10^{-1} cm and surface phase R_s of 8.28×10^{-1} cm, resulting in a volumetric phase ratio V_f/V_s of 1.0. As shown in Figure 3.1B, the kinetic behavior of the system is somewhat more distinguishable for these fluid phases with diffusion coefficients D_f from 1.0×10^{-3} to 1.0×10^{-5} $cm^2\ s^{-1}$. The rate constants derived from these data are summarized in Table 3.1. The rate constants k_{fs} and k_{sf} are approximately equal, as expected from Equation [3.3], and are several orders of magnitude smaller than those determined for the system described above. The characteristic time τ is significantly larger ($\sim10^{-2}$ s), so that equilibrium is much more slowly achieved than in the system above.

The liquid chromatography case may be used as a representative example to illustrate other kinetic and equilibrium information that can be derived from the stochastic simulation approach. During the kinetic process shown in Figure 3.1, the

system gradually evolves from the initial condition, where all molecules are uniformly distributed in the fluid phase, to the equilibrium condition, where $\tilde{N}_f = N (K_{abs} V_s/V_f)/(1 + K_{abs} V_s/V_f)$ molecules are uniformly distributed in the fluid phase and $\tilde{N}_s = N/(1 + K_{abs} V_s/V_f)$ molecules are uniformly distributed in the surface phase. The radial distribution of solute molecules is illustrated in Figure 3.2 at times corresponding to 0.0 τ, 0.1 τ, 0.2 τ, 0.5 τ, 1.0 τ, 2.0 τ, and 5.0 τ, where τ is 0.036 s for the liquid chromatography system. At these times, the system has achieved 0%, 9.5%, 18.1%, 39.4%, 63.2%, 86.5%, and 99.3%, respectively, of the molecular distribution at equilibrium. Once the system has achieved equilibrium ($T > 20\ \tau$), we may further characterize the transport between the fluid and surface phases. The residence time distribution for a single sojourn of a molecule in the fluid and surface phases is shown in Figure 3.3. From this distribution, the average residence time is 1.9×10^{-3} s and the standard deviation is 1.1×10^{-3} s. However the most probable residence time is one time constant, with approximately 30% of the molecules residing just 1.0×10^{-5} s before transferring to the opposite phase. The molecules are transferred between phases an average of 284 times per second at equilibrium. The standard deviation is 76 s^{-1}, which suggests that 95% of the molecules are transferred between phases from 135 to 433 times per second.

The effect of the fluid-phase diffusion coefficient on the fluid dynamic behavior of the system has also been examined. The solute zone profiles for supercritical fluid, enhanced fluidity liquid, and liquid chromatography at a mean linear velocity of 0.10 cm s^{-1} are shown in Figure 3.4. Since the simulation time T is much greater than the characteristic time τ in all cases, the system is nearly at equilibrium according to Equation

Figure 3.2: Radial solute distribution profiles during the kinetic evolution of chromatographic systems. Simulation conditions: $N = 1.0\times10^{4}$; $t = 1.0\times10^{-5}$ s; $T = 0.0\ \tau$ ($\bigcirc$), $0.1\ \tau$ ($\square$), $0.2\ \tau$ ($\triangle$), $0.5\ \tau$ ($\diamond$), $1.0\ \tau$ ($\triangledown$), $2.0\ \tau$ (+), $5.0\ \tau$ ($\times$), where $\tau = 0.036$ s; $R_f = 2.0\times10^{-3}$ cm; $R_s = 8.28\times10^{-4}$ cm; $D_f = 1.0\times10^{-5}$ cm^2 s^{-1}; $D_s = 1.0\times10^{-5}$ cm^2 s^{-1}; $K_{abs} = 1.0$.

Figure 3.2

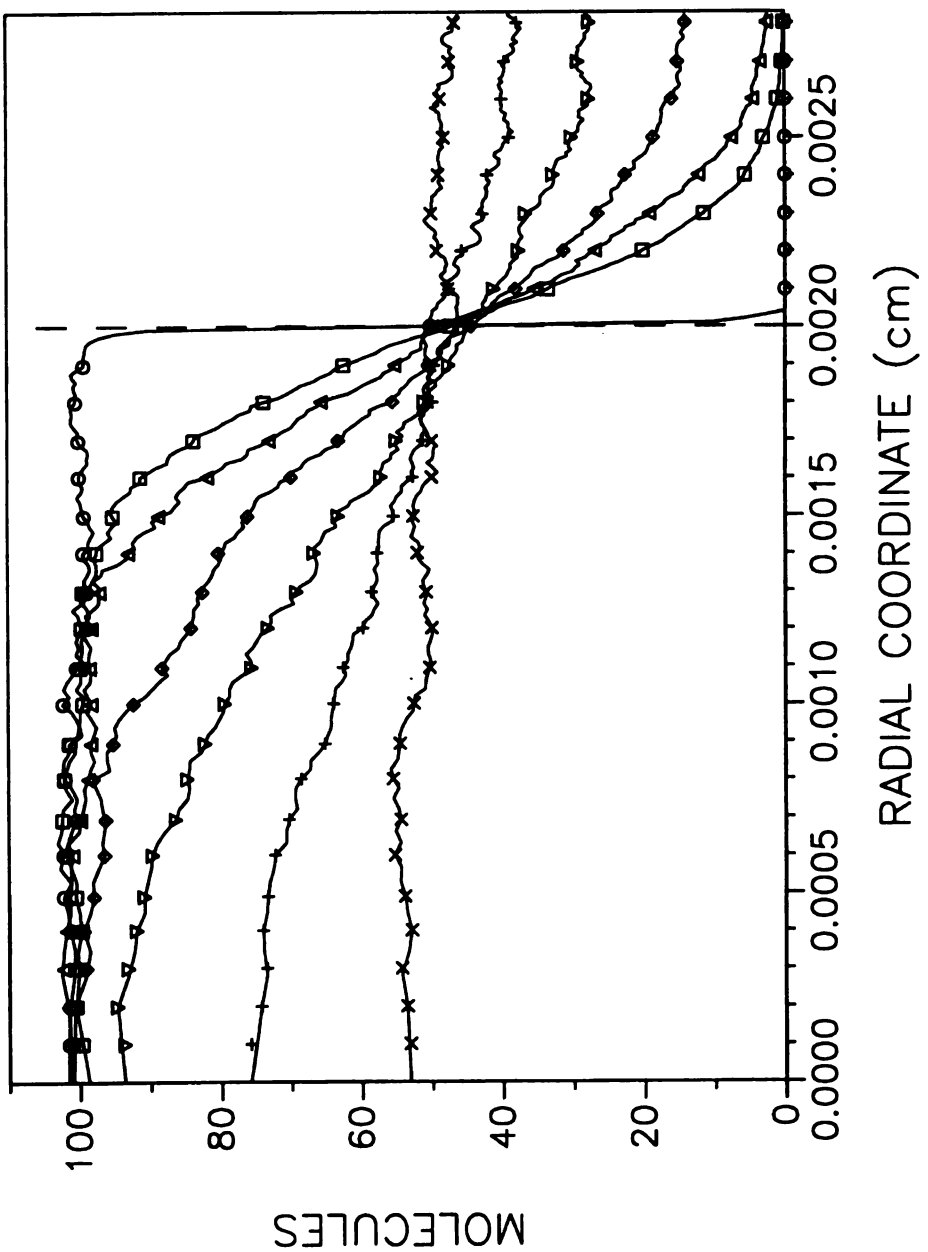
MOLECULES
100
80
60
40
20
0
0.0000
0.0005
0.0010
0.0015
0.0020
0.0025
RADIAL COORDINATE (cm)

Figure 3.3: Residence time distribution for a single sojourn in the fluid phase (A) and surface phase (B) under equilibrium conditions. Simulation conditions: $T > 20\ \tau$, where $\tau = 0.036$ s; other conditions as given in Figure 3.2.

Figure 3.3

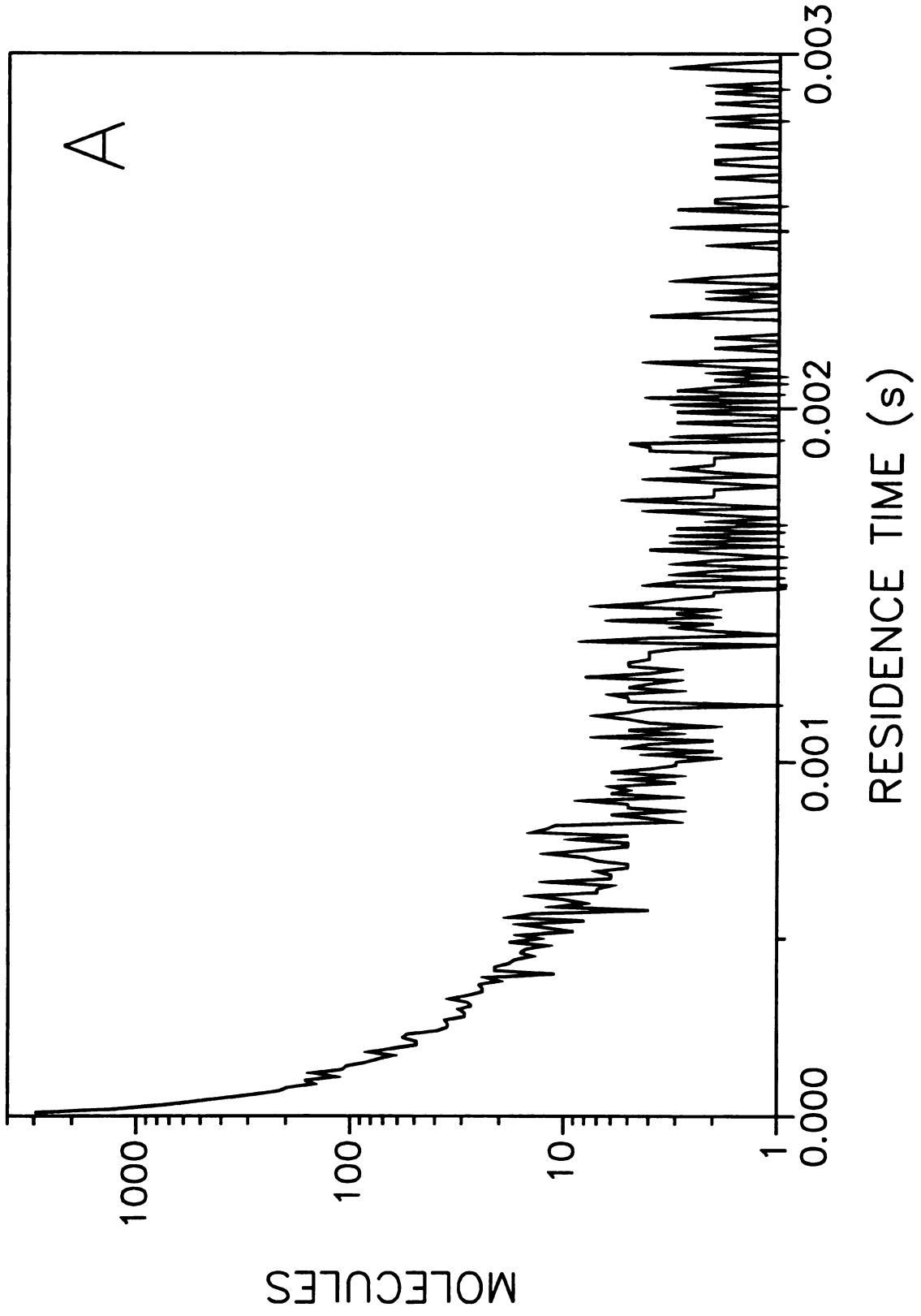
A
MOLECULES
1000
100
10
1
0.000
0.001
0.002
0.003
RESIDENCE TIME (s)

Figure 3.3 cont.

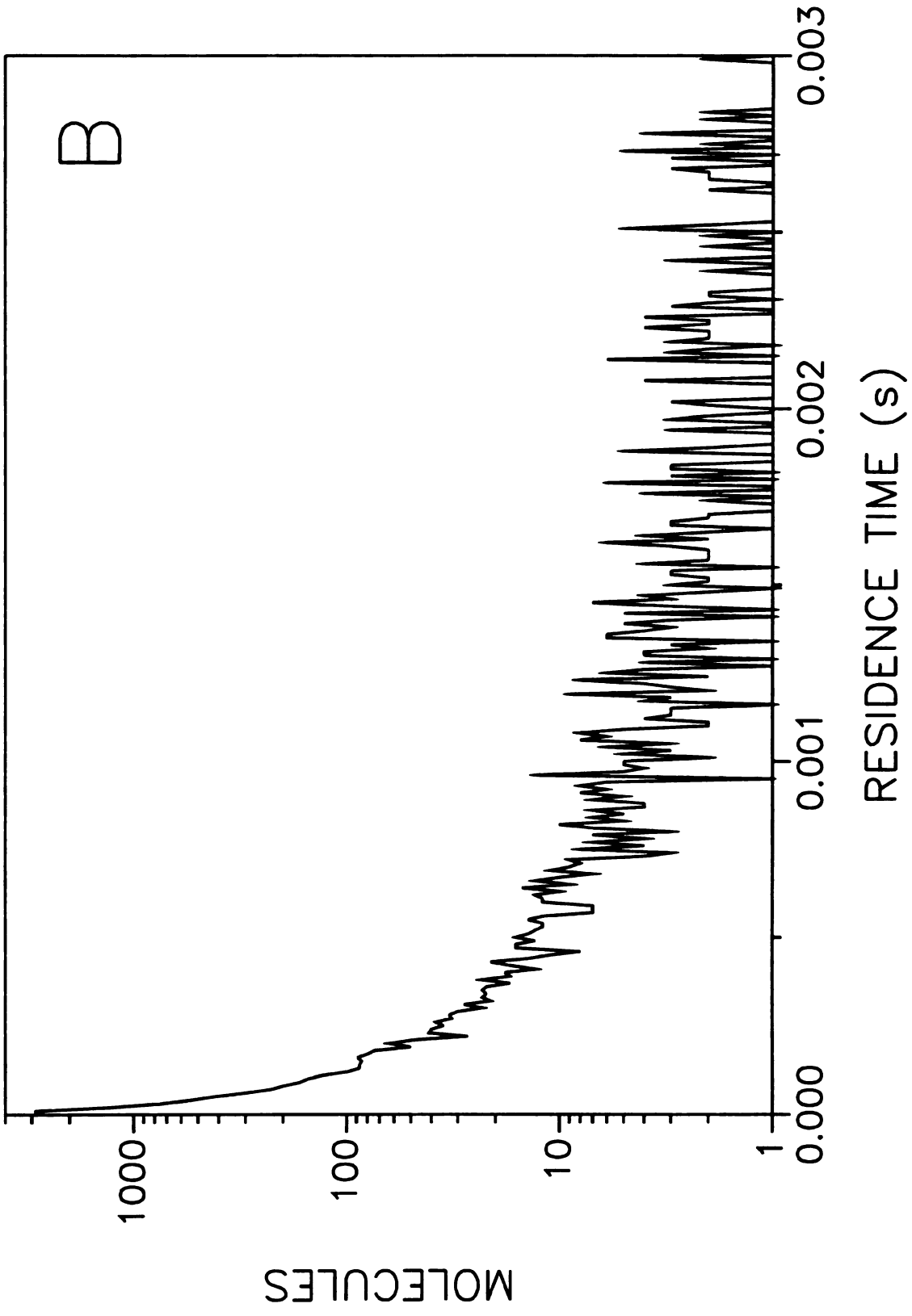

Figure 3.4: Evolution of the solute zone profile with varying diffusion coefficients in the fluid phase representative of (A) supercritical fluid, (B) enhanced fluidity liquid, and (C) liquid chromatography. Simulation conditions: $N = 1.0\times10^{3}$; $t = 1.0\times10^{-5}$ s; T = 5, 10, 15, 20, 25, 30 s (left to right); $R_f = 2.0\times10^{-3}$ cm; $Rs = 8.28\times10^{-4}$ cm; $D_f = 1.0\times10^{-3}$ cm^2 s^{-1} (A), 1.0×10^{-4} cm^2 s^{-1} (B), 1.0×10^{-5} cm^2 s^{-1} (C); $D_s = 1.0\times10^{-5}$ cm^2 s^{-1}; $K_{abs} = 1.0$, v_0 =0.10 cm s^{-1}.

Figure 3.4

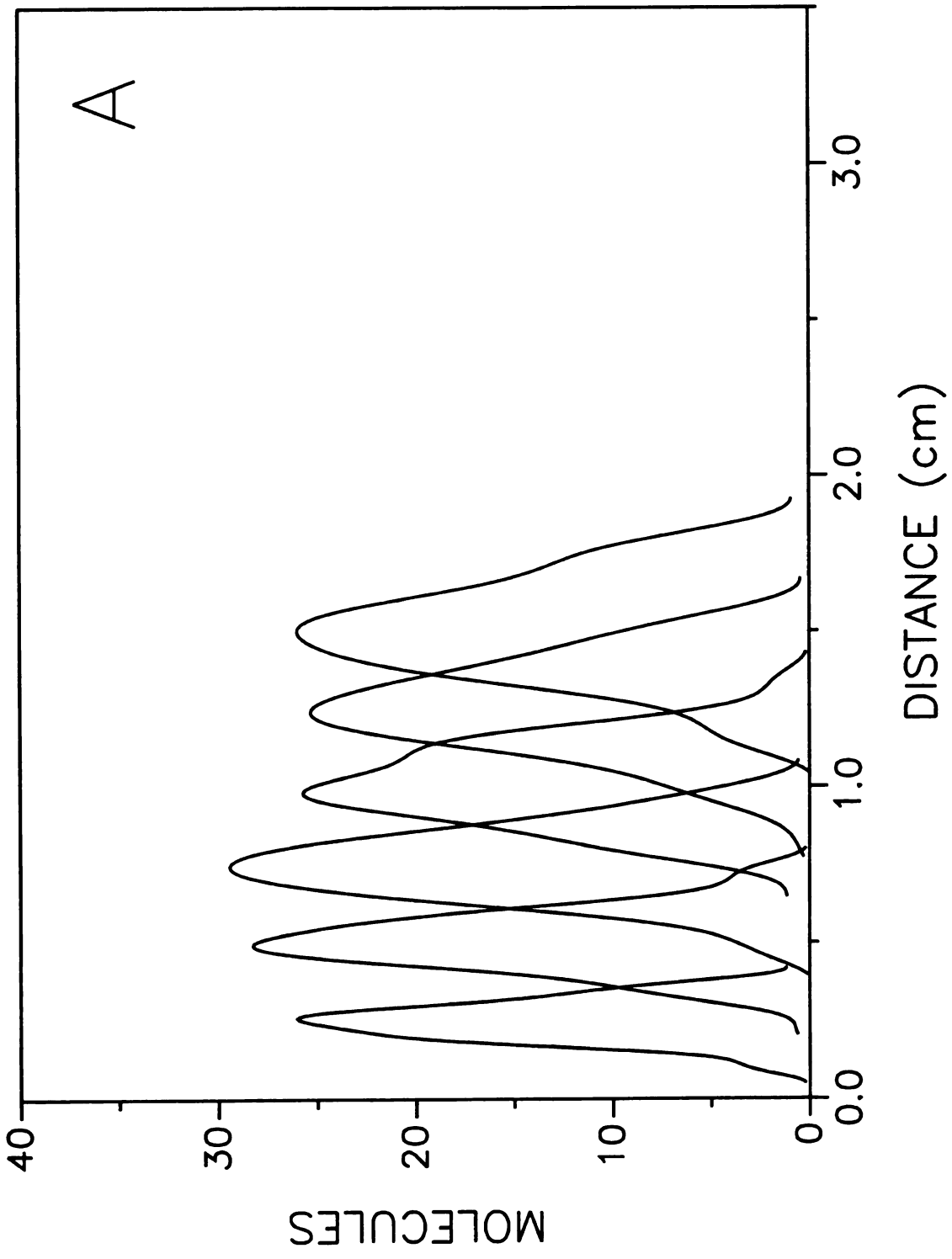

Figure 3.4 cont.

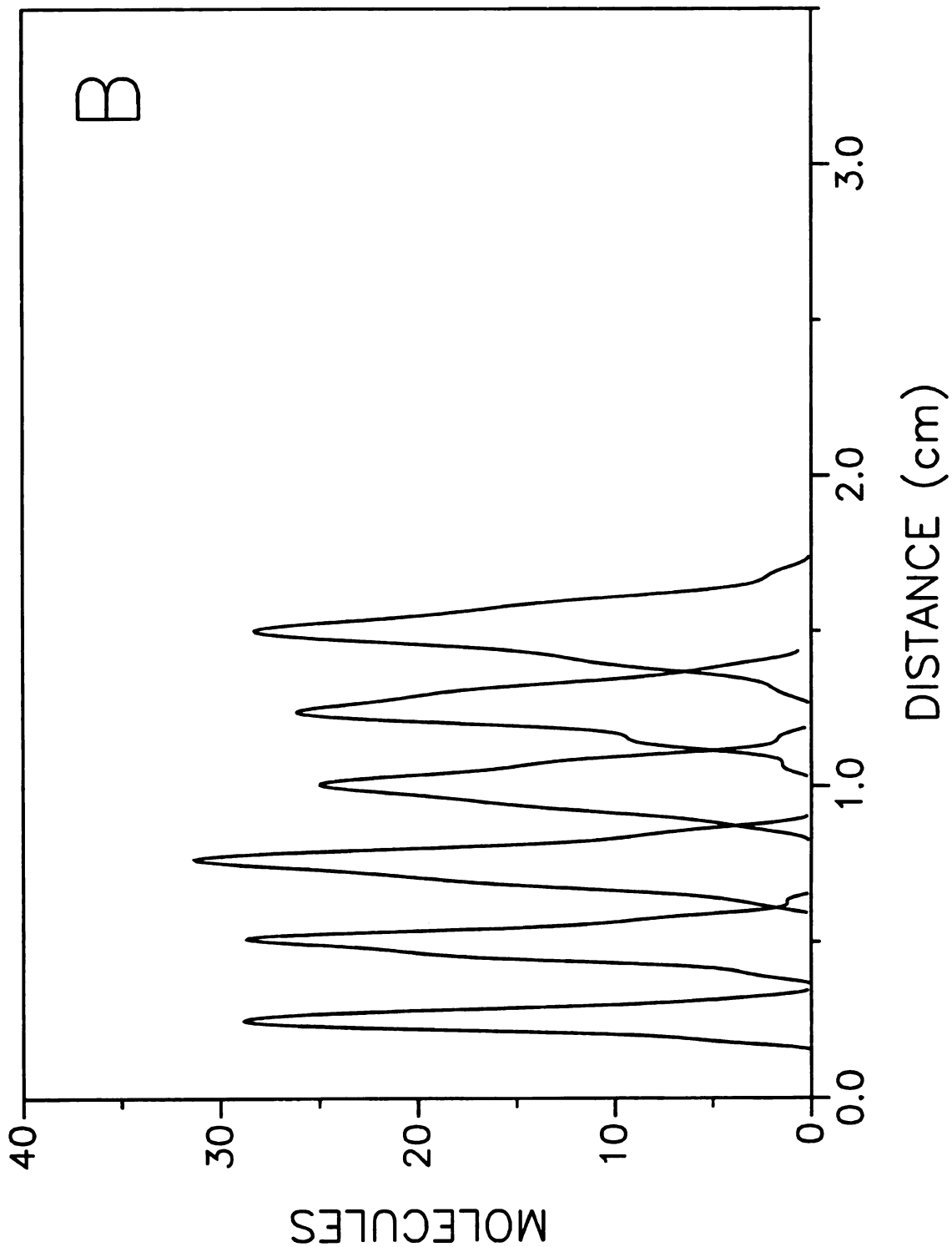

Figure 3.4 cont.

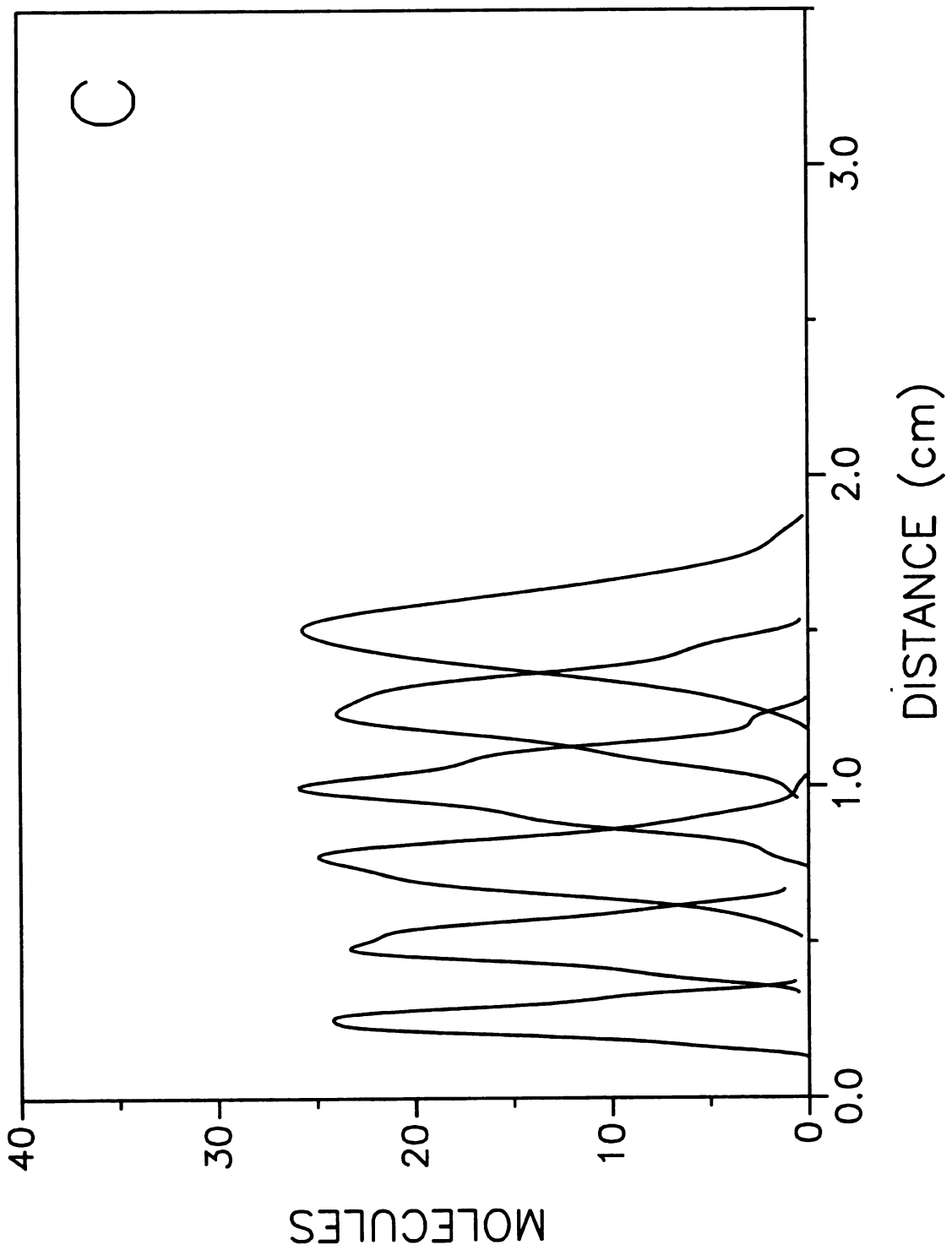

[3.4] and the zone profiles are symmetric. The statistical moments of these zone profiles calculated by means of Equations [2.1] and [2.2] are shown as a function of the simulation time in Figure 3.5. The first statistical moment or mean distance coincides with the theoretically expected value of $M_1 = v_0 T/(1 + K_{abs} V_s/V_f)$ for all fluid phases. The second statistical moment or variance also agrees well with the extended Golay equation (Equation 2.15),[3] which includes dispersion arising from axial diffusion in the fluid and surface phases and resistance to mass transfer in the fluid and surface phases. The variance for enhanced fluidity liquid chromatography is the smallest because the selected velocity of 0.10 cm s^{-1} is near the optimum value of 0.11 cm s^{-1} for this system. For liquid chromatography, the selected velocity is greater than the optimum value of 0.022 cm s^{-1} and the variance has a correspondingly larger contribution from resistance to mass transfer in the fluid phase. For supercritical fluid chromatography, the selected velocity is less than the optimum value of 0.41 cm s^{-1} and the variance has a correspondingly larger contribution from axial diffusion in the fluid phase. In all cases, however, there is excellent agreement between the simulation results and the extended Golay equation[3] because the system is nearly at equilibrium.

The liquid chromatography case may again be used as a representative example to illustrate other hydrodynamic information that can be derived from the stochastic simulation approach. Consider the final zone profile in Figure 3.4C, where each molecule has traveled for a fixed total time of 30.0 s. Of this total time, each molecule has spent some time in the fluid phase and the remainder in the surface phase. The residence time distribution in each phase is shown in Figure 3.6. It is evident that the

Figure 3.5: Mean distance (A) and variance (B) of the solute zone profile with varying diffusion coefficients in the fluid phase. Simulation conditions: $D_f = 1.0\times10^{-3}$ cm^2 s^{-1} (△), 1.0×10^{-4} cm^2 s^{-1} (□), 1.0×10^{-5} cm^2 s^{-1} (○); other conditions as given in Figure 3.4C. (—) Theory according to the extended Golay equation.[3]

Figure 3.5

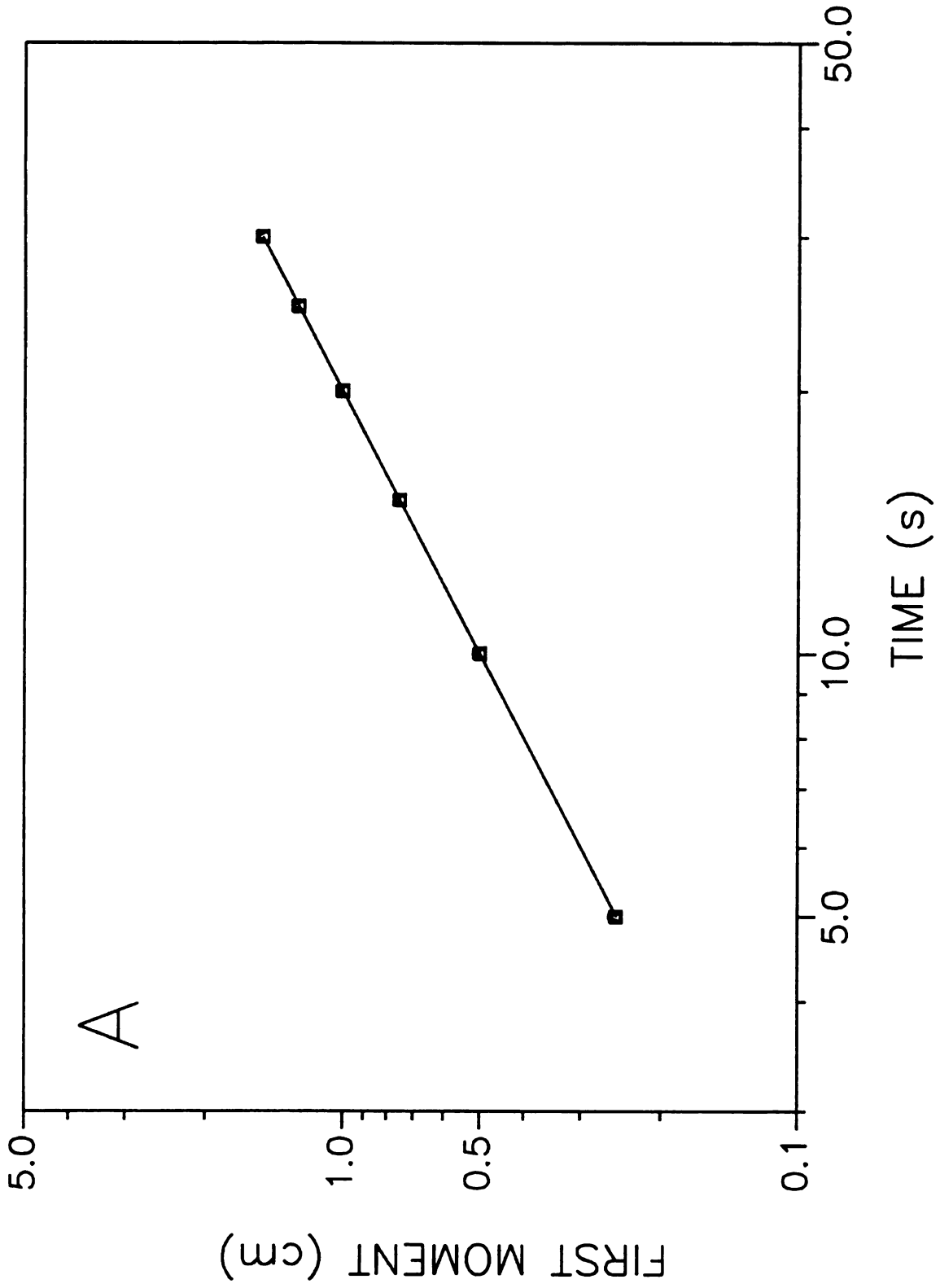

Figure 3.5 cont.

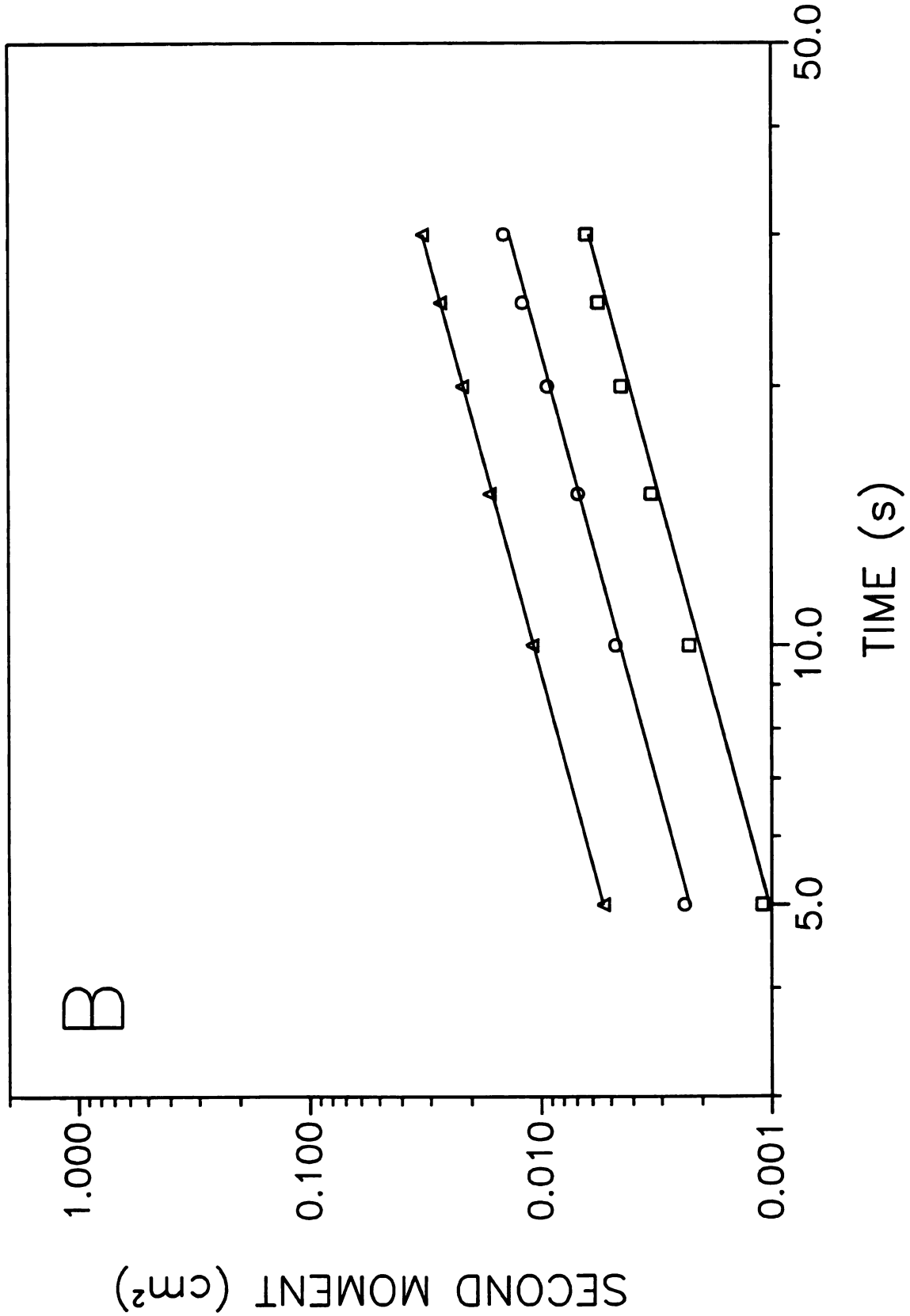

Figure 3.6: Residence time distribution for total time spent in the fluid phase (A) and surface phase (B). Simulation conditions as given in Figure 3.4C.

Figure 3.6

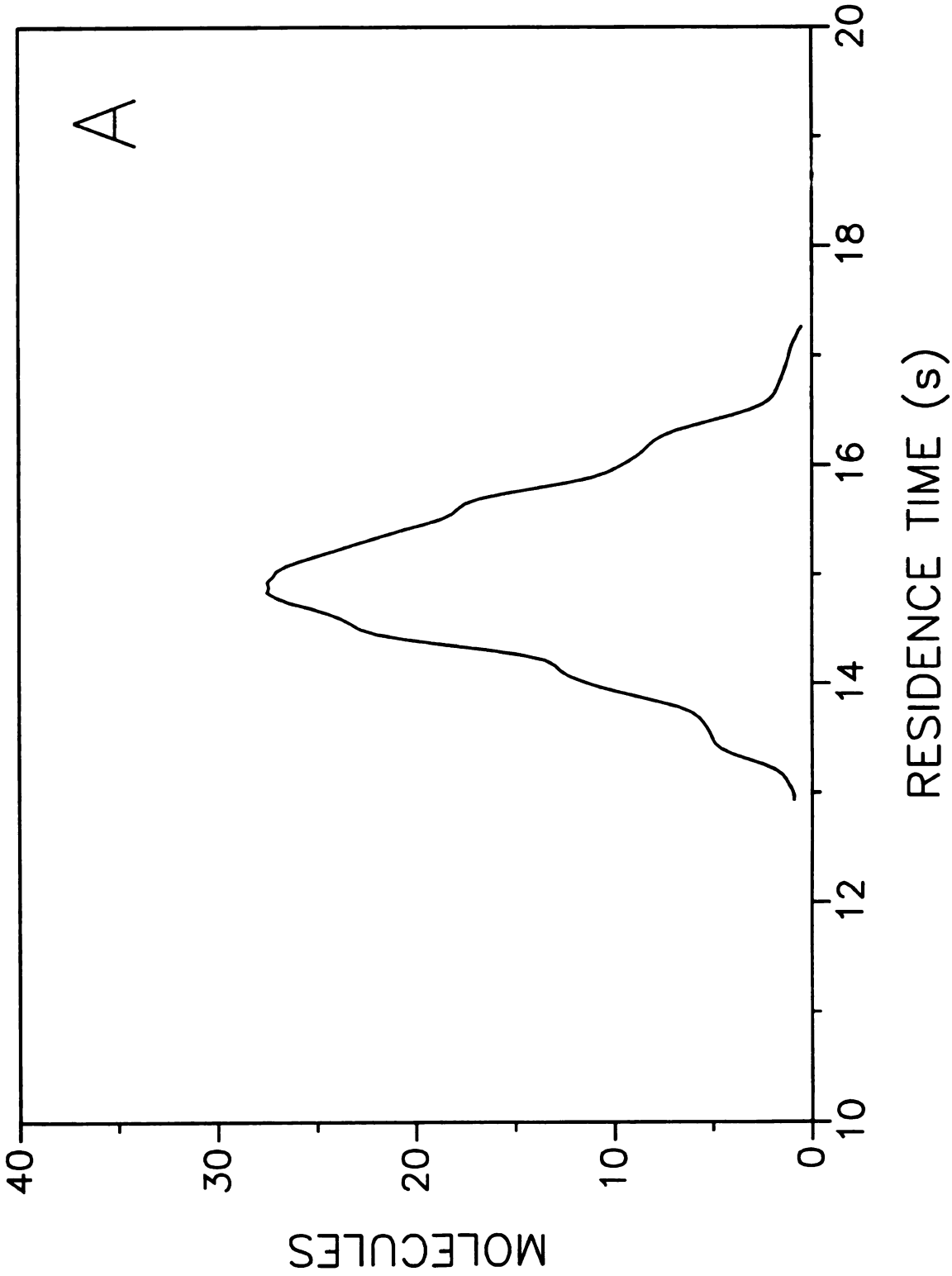

Figure 3.6 cont.

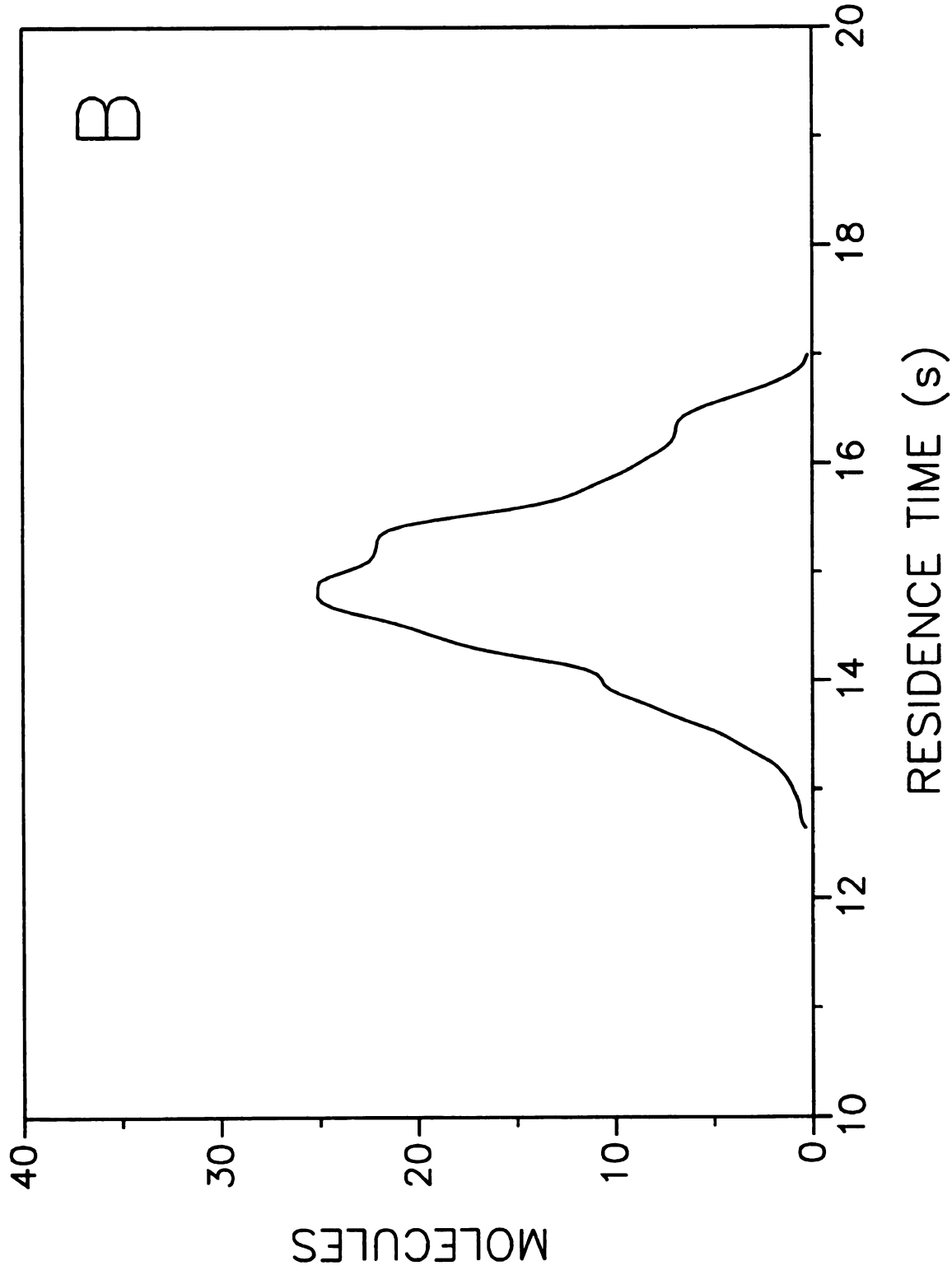

residence time distribution in the fluid phase is symmetric and the mean value of 15.0 s coincides with the theoretically expected value of $T_f = T /(1 + K_{abs} V_s/V_f) = 15.0$ s. Similarly, the mean residence time in the surface phase of 15.0 s coincides with the expected value of $T_s = T (K_{abs} V_s/V_f)/(1 + K_{abs} V_s/V_f) = 15.0$ s. The standard deviation of these residence time distributions is 0.77 s, which suggests that 95% of the molecules have spent from 13.5 to 16.5 s in each phase. This information can also be used to calculate the capacity factor (k′) for each molecule as T_s/T_f. These calculations suggest that the mean capacity factor is 1.00, the standard deviation is 0.10, and 95% of the molecules have capacity factors ranging from 0.80 to 1.20. Finally, it is instructive to graph the residence time in each phase *versus* the distance traveled for each molecule, as shown in Figure 3.7. This graph confirms that molecules at the front of the zone have spent the greatest time in the fluid phase and the least time in the surface phase, whereas the converse is true for molecules at the rear of the zone. The relationship between residence time and distance traveled appears to be linear with slopes of 6.00 and -6.00 s cm^{-1} for the fluid and surface phases, respectively. This slope is a direct measure of the extent of deviation from equilibrium across the solute zone. The steeper the slope, which is related to the variables in Equation [3.4] such as characteristic time τ, velocity, and distance traveled, the greater is the nonequilibrium. Moreover, the broader the solute zone for a given slope, the greater is the nonequilibrium. The data in Figure 3.7 also suggest that there is significant variation in the behavior of individual molecules. For example, molecules at the center of the zone that have traveled the mean distance of 1.5

Figure 3.7: Relationship between total time spent in fluid phase (A) and surface phase (B) and the distance traveled by individual molecules. Simulation conditions as given in Figure 3.4C.

Figure 3.7

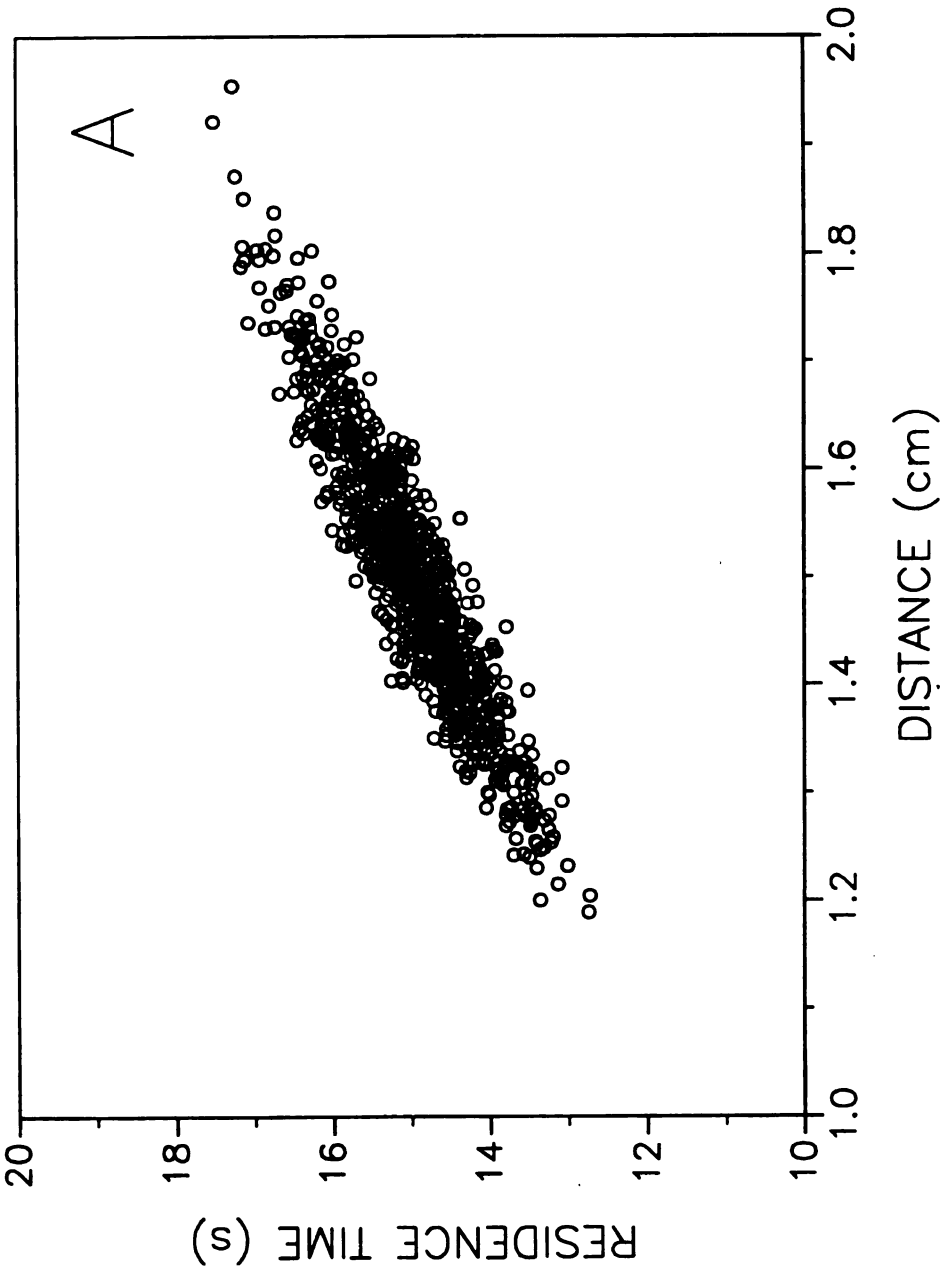

Figure 3.7 cont.

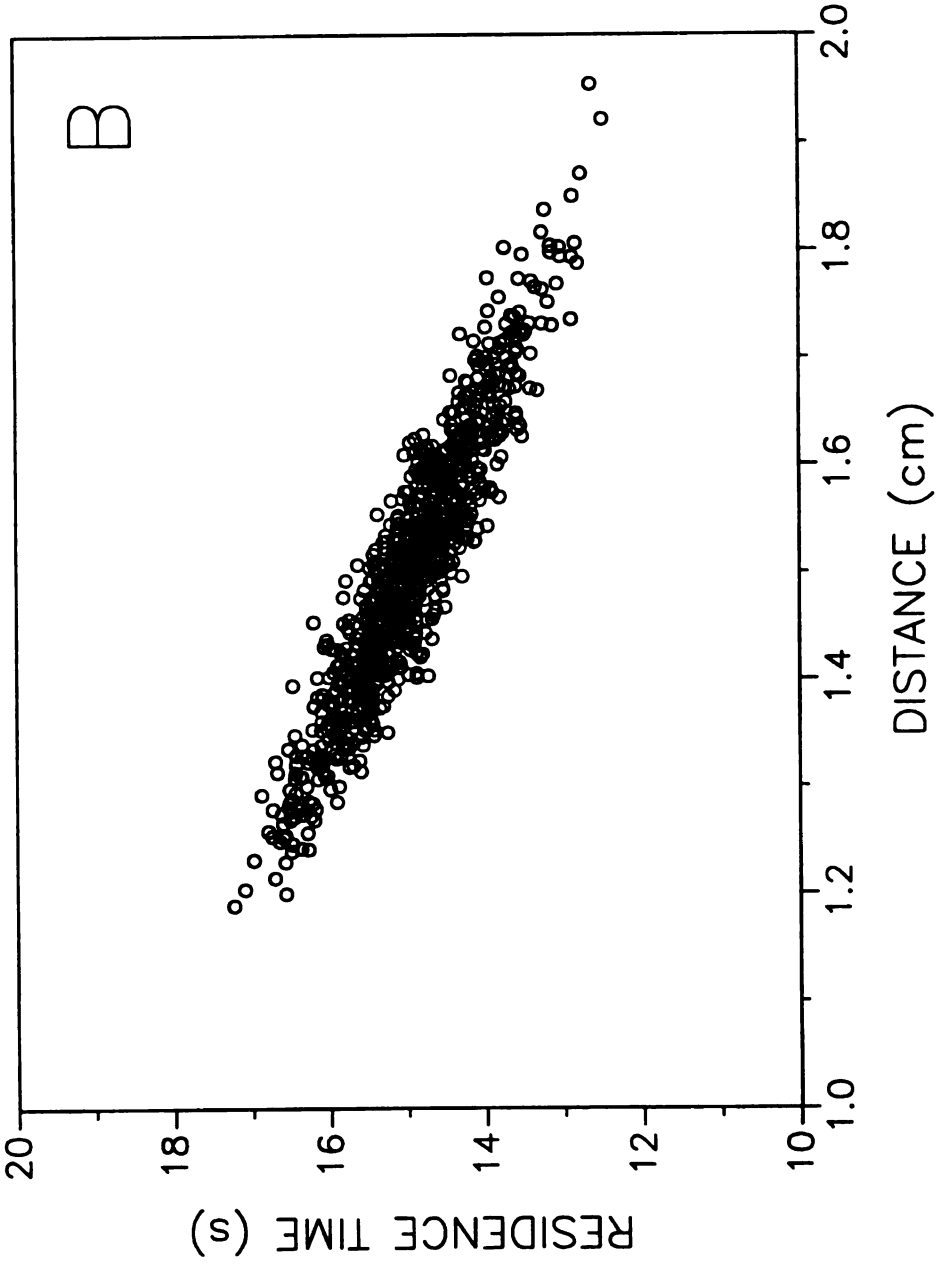

cm may have spent from 14.4 to 15.6 s in the fluid and surface phases and may have capacity factors ranging from 0.91 to 1.07 (95% confidence level). These descriptions and characterizations of molecular behavior appear to be typical of solute zones in systems that are nearly at equilibrium.

3.2.2 Effect of the Surface-Phase Diffusion Coefficient.

Using the liquid chromatography case as a representative example, the diffusion coefficient in the surface phase was varied from 1.0×10^{-5} to 1.0×10^{-8} $cm^2\ s^{-1}$. The kinetic behavior of the system is summarized in Table 3.2 and Figure 3.8.

Table 3.2 Effect of the Surface-Phase Diffusion Coefficient on Rate Constants.[a]

D_s ($cm^2\ s^{-1}$)	k_{fs} (s^{-1})	k_{sf} (s^{-1})	τ (s)	k_{fs}/k_{sf}	$\tilde{N}_s/\tilde{N}_f$
1.00×10^{-5}	13.74	13.87	0.036	0.991	0.997
1.00×10^{-6}	3.076	3.102	0.162	0.991	1.006
1.00×10^{-7}	0.353	0.357	1.41	0.989	0.999
1.00×10^{-8}	0.038	0.039	13.05	0.986	0.999

[a] Simulation conditions: $N = 1.0\times10^{4}$; $t = 1.0\times10^{-5}$ s; $T = 20\ \tau$; $R_f = 2.0\times10^{-3}$ cm; $R_s = 8.28\times10^{-4}$ cm; $D_f = 1.0\times10^{-5}$ $cm^2\ s^{-1}$; $K_{abs} = 1.0$.

It is apparent from the rate constants and the characteristic time τ that the kinetic behavior is reasonably rapid for the diffusion coefficient of 1.0×10^{-5} $cm^2\ s^{-1}$, slightly slower for 1.0×10^{-6} $cm^2\ s^{-1}$, and significantly slower for 1.0×10^{-7} and 1.0×10^{-8} $cm^2\ s^{-1}$.

In order to understand the effect of the diffusion coefficients in the fluid and surface phases on the rate constants, it is helpful to represent the data in Tables 3.1 and 3.2 graphically. As shown in Figure 3.9, the rate constants are intrinsically related to the

Figure 3.8: Kinetic evolution of the absorption process with varying diffusion coefficients in the surface phase for liquid chromatography. Simulation conditions: $D_f = 1.0\times10^{-5}$ cm^2 s^{-1}; $D_s = 1.0\times10^{-5}$ cm^2 s^{-1} (○), 1.0×10^{-6} cm^2 s^{-1} (□), 1.0×10^{-7} cm^2 s^{-1} (△), 1.0×10^{-8} cm^2 s^{-1} (◇); other conditions as given in Figure 3.1B.

Figure 3.8

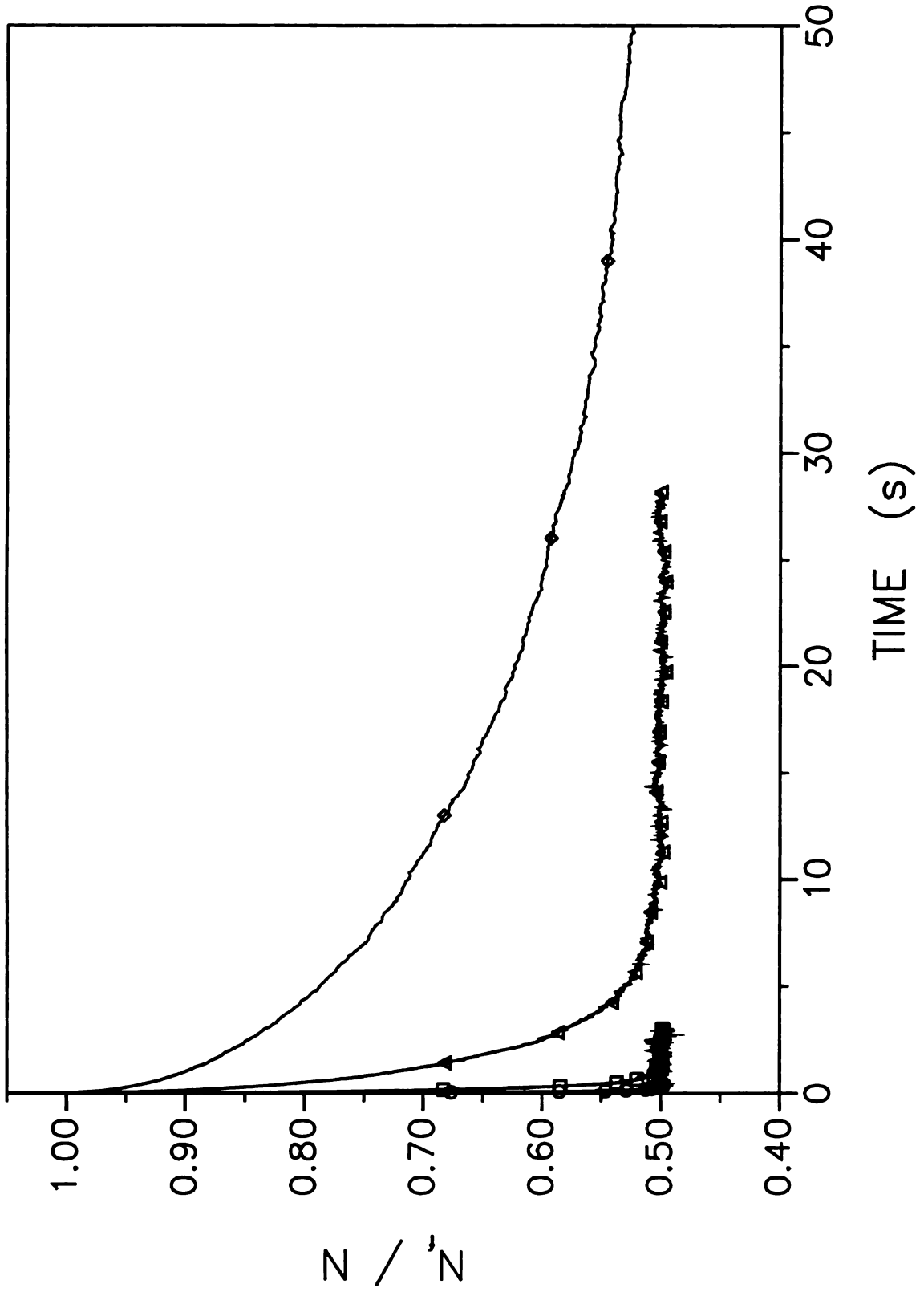

Figure 3.9: Effect of the reduced diffusion coefficient on rate constants k_{fs} (○) and k_{sf} (●). Simulation conditions as given in Tables 3.1 and 3.2.

Figure 3.9

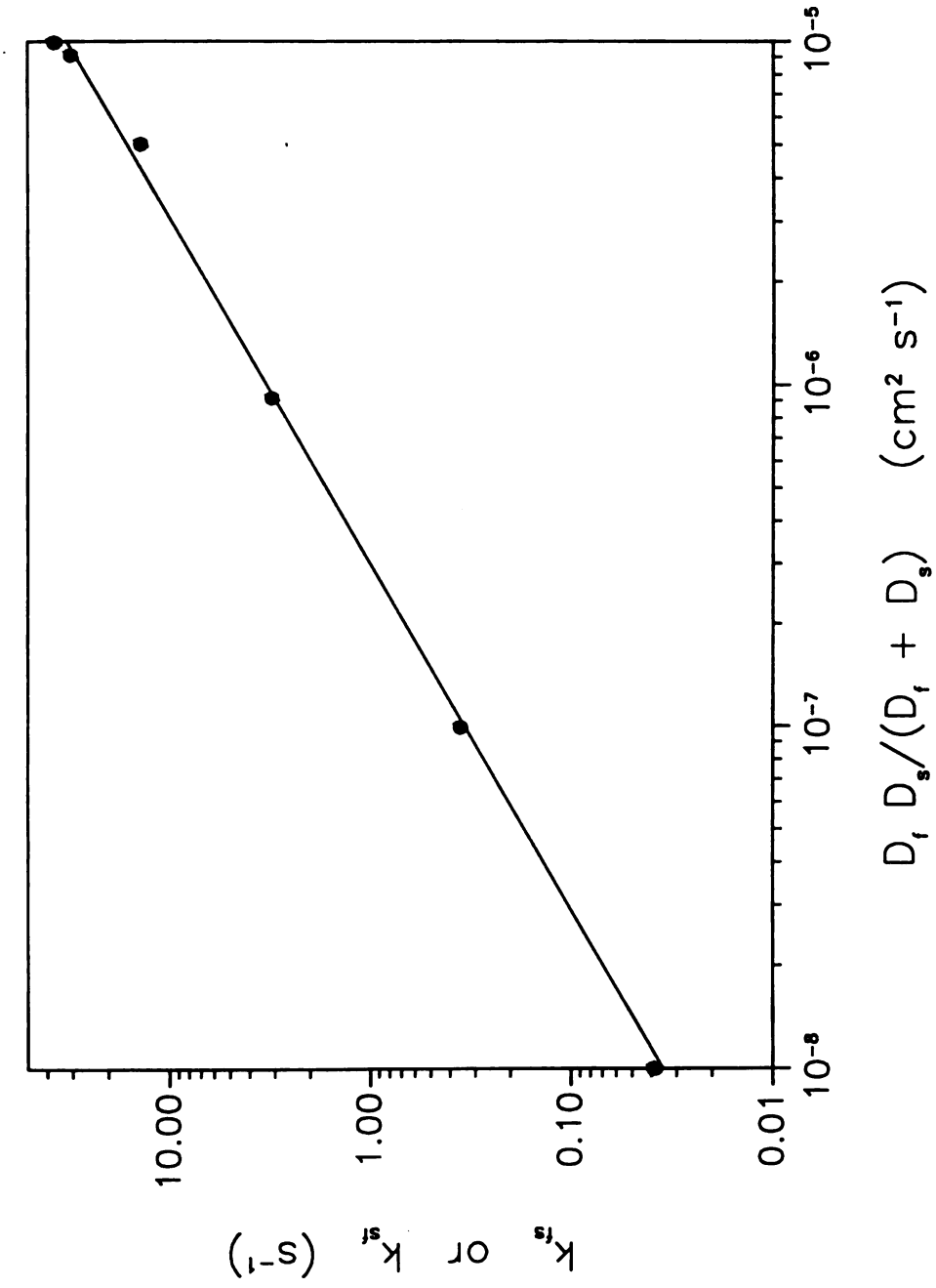

reduced diffusion coefficient $D = D_f D_s/(D_f + D_s)$ for the system.[1] When the diffusion coefficients are comparable in magnitude, they both influence the kinetic behavior of the system. However, when one diffusion coefficient is significantly smaller than the other, it serves to limit the overall rate of transport in the system. The consequences of this dependence on the reduced diffusion coefficient were observed in Figure 3.1 and Table 3.1 above. Because the diffusion coefficient in the surface phase was significantly smaller (1.0×10^{-5} cm^2 s^{-1}), the fluid phases of gas, dense gas, and supercritical fluid had little effect on the kinetic behavior. The practical implications of this statement are clear: In the development of unified chromatography, we cannot simply be concerned with the properties of the fluid phase. We must also concomitantly increase the diffusion coefficients in the surface phase so that they are maintained within approximately two orders of magnitude of those in the fluid phase in order to derive the full benefits of the improved kinetic behavior.

The effect of the surface phase diffusion coefficient on the fluid dynamic behavior of the system has also been examined. The solute zone profiles obtained at a mean linear velocity of 0.10 cm s^{-1} are shown in Figure 3.10. For the diffusion coefficient of 1.0×10^{-5} cm^2 s^{-1}, the ratio of the characteristic time τ to the simulation time T ranges from 0.007 to 0.001 for simulation times from 5 to 30 s, respectively. Consequently, this system is nearly at equilibrium according to Equation [3.4] and all of the zone profiles are symmetric. Similarly for the diffusion coefficient of 1.0×10^{-6} cm^2 s^{-1}, the inverse of the Stanton number (St^{-1})ranges from 0.032 to 0.005 and all of the solute zones appear to be symmetric. However, for the diffusion coefficient of 1.0×10^{-7} cm^2 s^{-1}, the value of St^{-1} is

Figure 3.10: Evolution of the solute zone profile with varying diffusion coefficients in the surface phase for liquid chromatography. Simulation conditions:

$D_f = 1.0\times10^{-5}$ cm^2 s^{-1}; $D_s = 1.0\times10^{-5}$ cm^2 s^{-1} (A), 1.0×10^{-6} cm^2 s^{-1} (B),

1.0×10^{-7} cm^2 s^{-1} (C), 1.0×10^{-8} cm^2 s^{-1} (D); other conditions as given in Figure 3.4C.

Figure 3.10

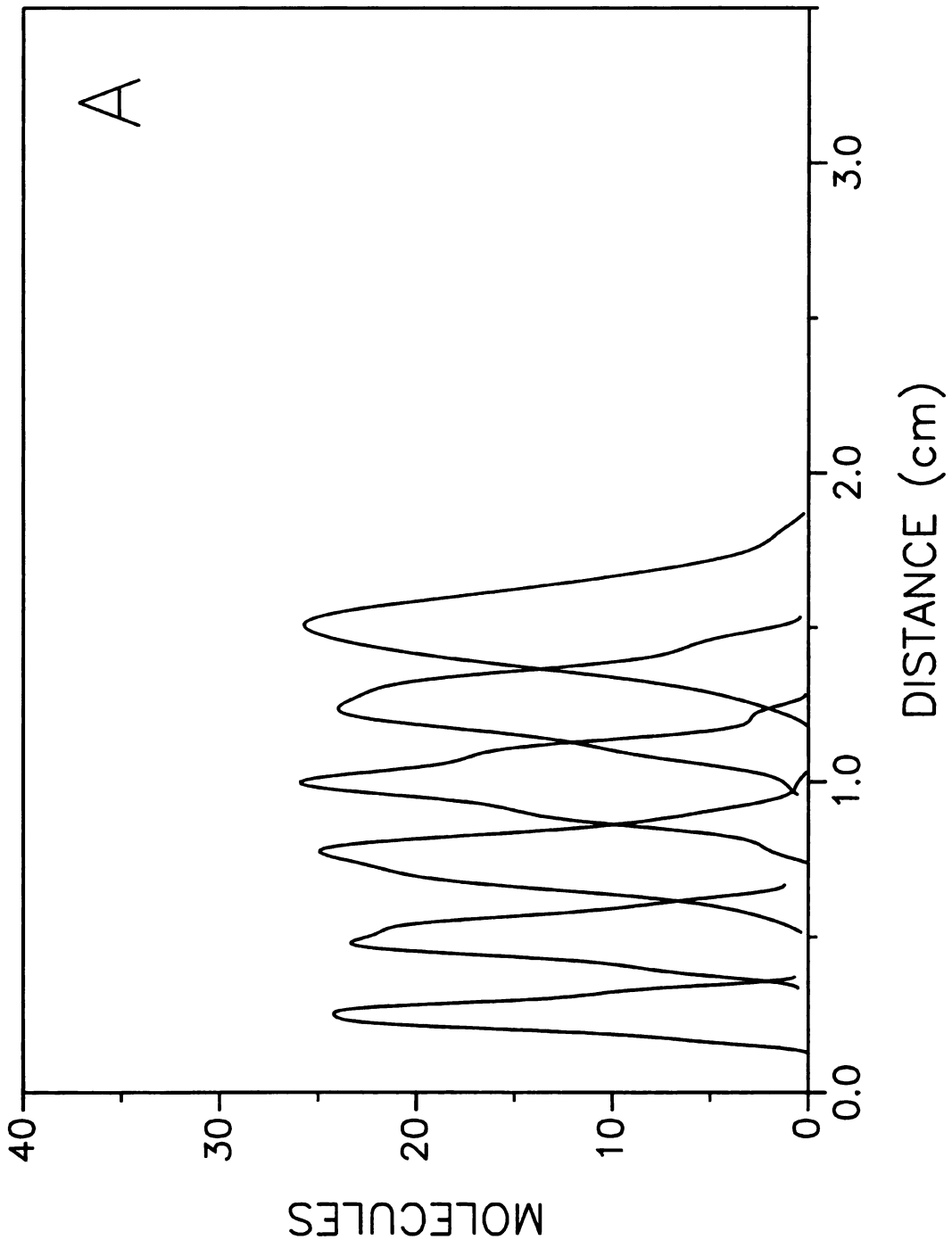

Figure 3.10 cont.

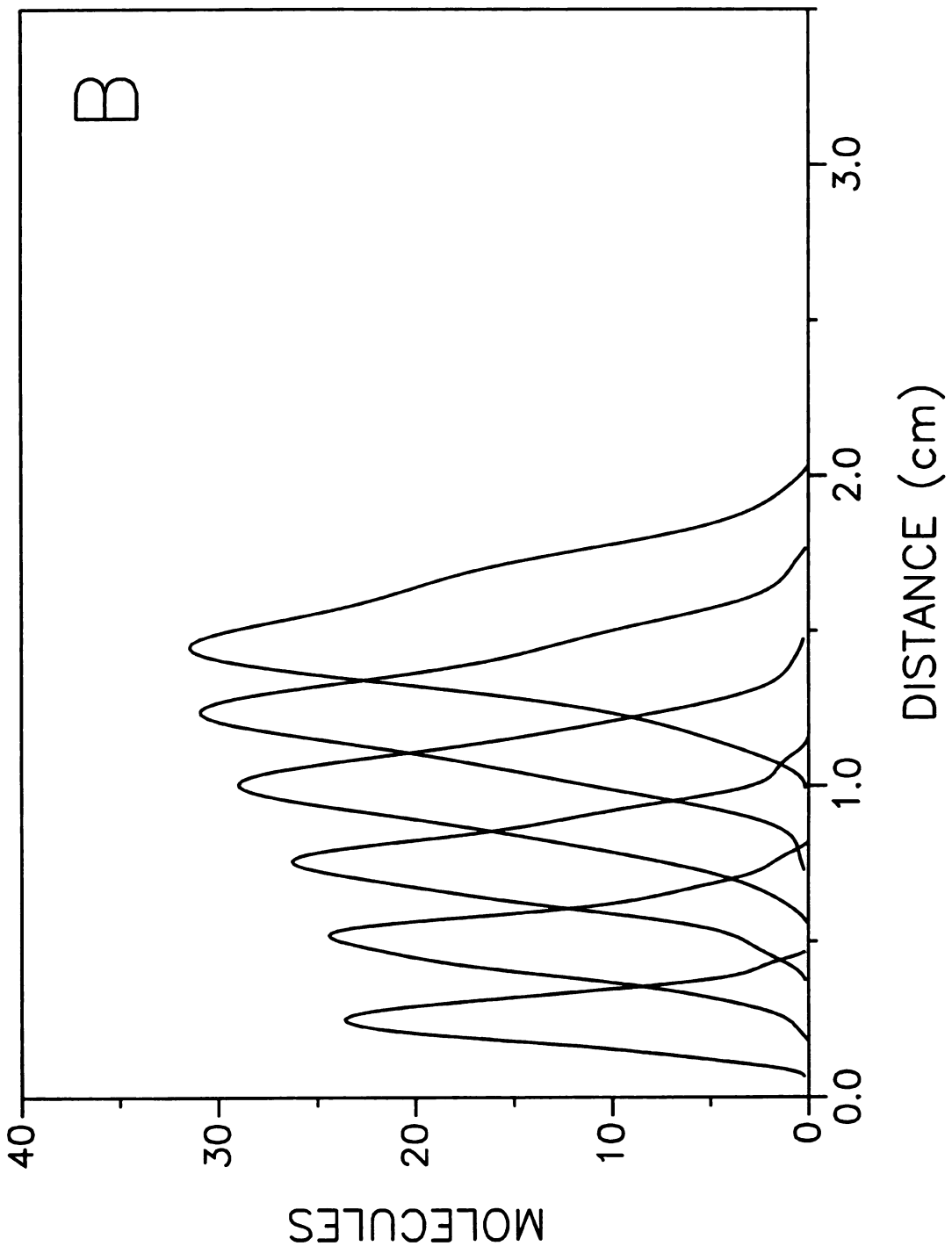

Figure 3.10 cont.

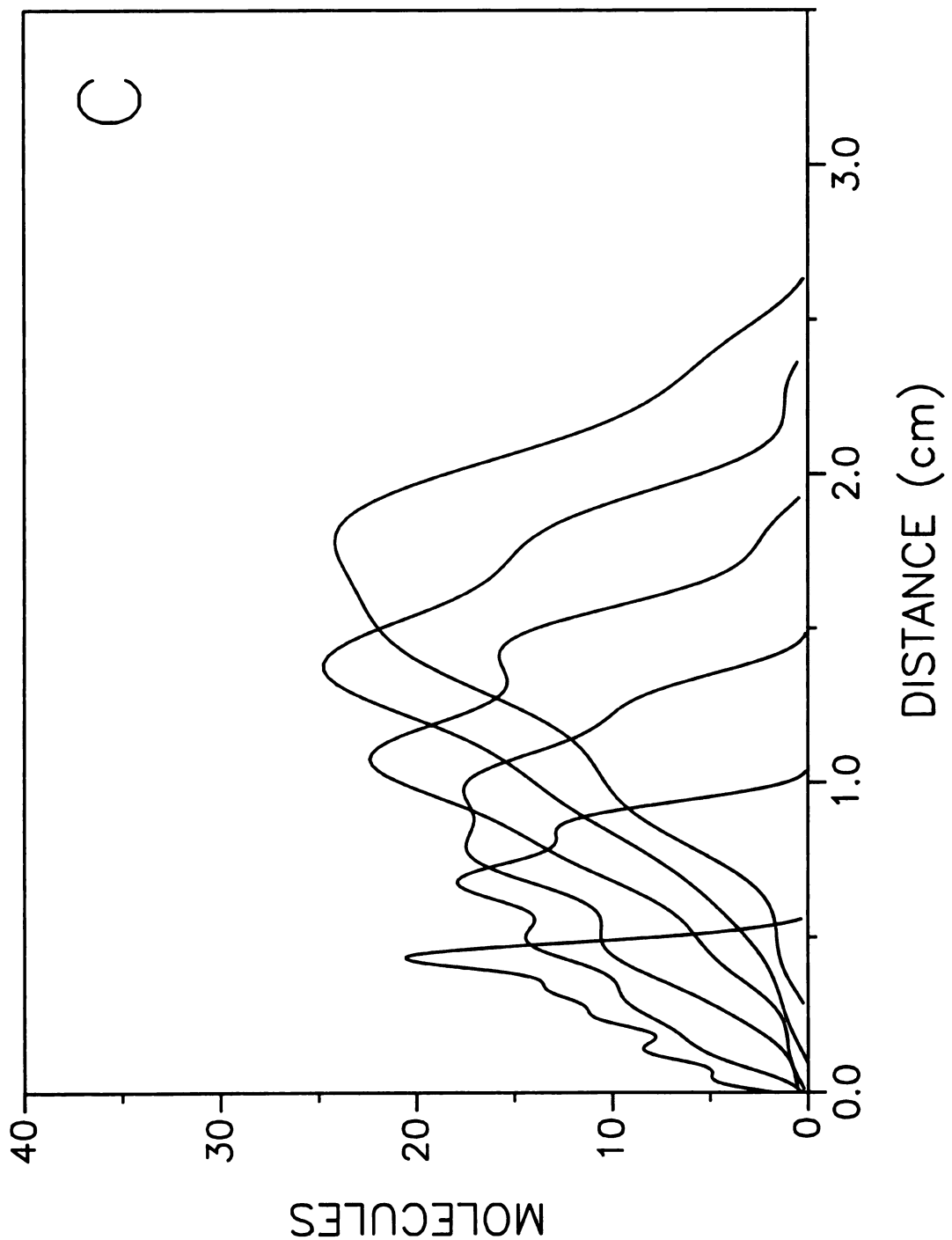

Figure 3.10 cont.

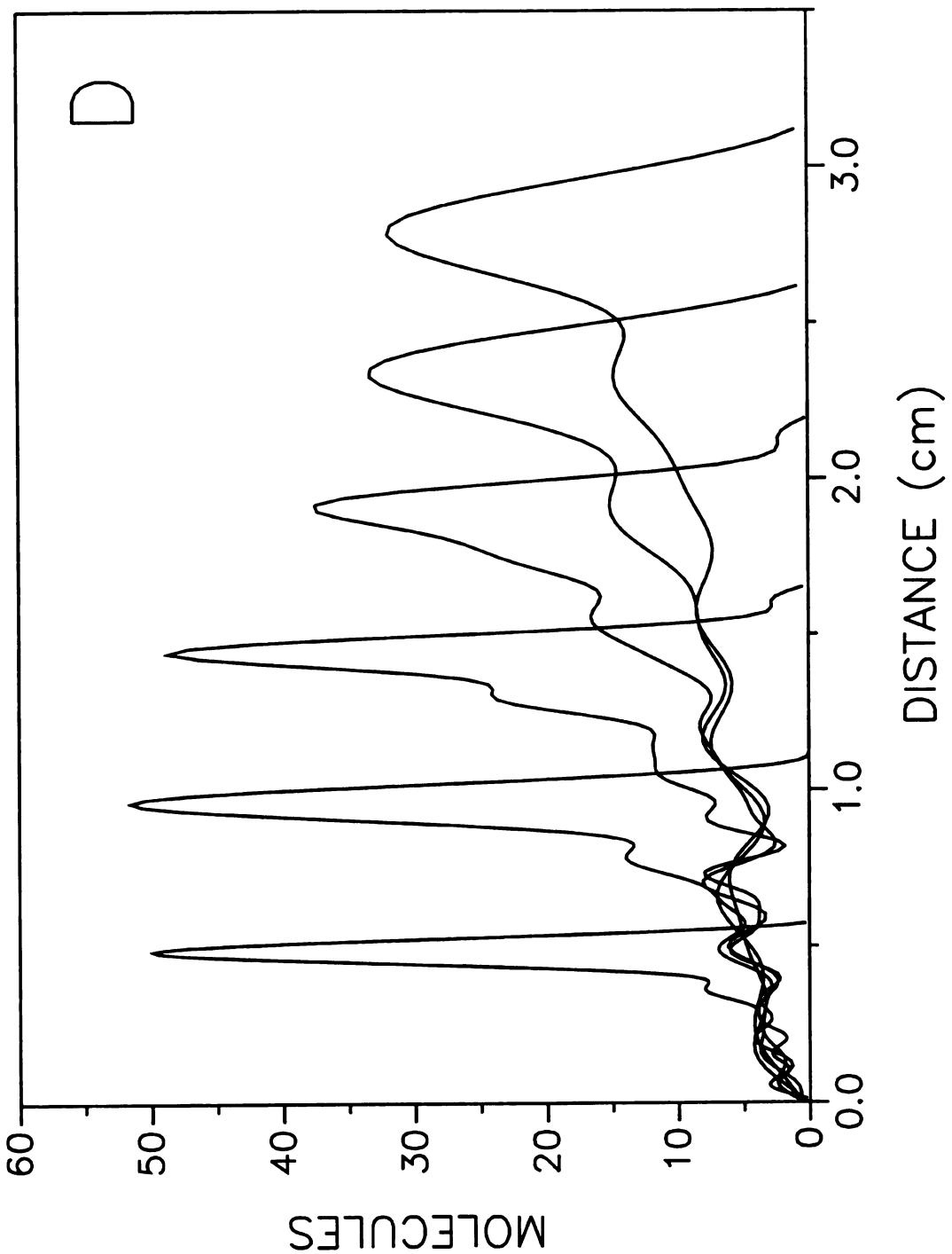

significantly larger and ranges from 0.28 to 0.047. The zone profiles initially deviate from equilibrium and are asymmetric but progressively become more symmetric. The deviations from equilibrium are even more problematic for the diffusion coefficient of 1.0×10^{-8} cm^2 s^{-1}, where the value of St^{-1} ranges from 2.61 to 0.44 and all of the profiles are markedly asymmetric.

The statistical moments of the solute zone profiles are shown as a function of the simulation time in Figure 3.11. For the diffusion coefficient of 1.0×10^{-5} cm^2 s^{-1}, the mean distance and variance agree well with the theoretically expected values from the extended Golay equation.[3] However, as the diffusion coefficient in the surface phase decreases and the system deviates from equilibrium behavior, the mean zone distance increases because the molecules have proportionately greater residence time in the fluid phase. The variance also increases because the resistance to mass transfer in the surface phase has an additional contribution from slow kinetics. When the molecular zone begins migration from the initial nonequilibrium state, the variance increases as the square of the simulation time (as evident for the diffusion coefficient of 1.0×10^{-8} cm^2 s^{-1}). As the system gradually evolves toward the steady state, the variance progressively changes until it increases linearly with the simulation time (as evident for the diffusion coefficient of 1.0×10^{-7} cm^2 s^{-1}). As shown in Figure 3.11, the slow kinetics of the system influence the time required for the onset of steady-state conditions and the variance incurred during this transition as well as the variance per unit time (or length) once steady-state conditions have been achieved. The extended Golay equation[3] and other equilibrium-dispersive models cannot be used to predict the behavior of such systems.

Figure 3.11: Mean distance (A) and variance (B) of the solute zone profile with varying diffusion coefficients in the surface phase. Simulation conditions: $D_f = 1.0\times10^{-5}$ cm^2 s^{-1}; $D_s = 1.0\times10^{-5}$ cm^2 s^{-1} (○), 1.0×10^{-6} cm^2 s^{-1} (□), 1.0×10^{-7} cm^2 s^{-1} (△), 1.0×10^{-8} cm^2 s^{-1} (◇); other conditions as given in Figure 3.4C. (—) Theory according to the extended Golay equation.[3]

Figure 3.11

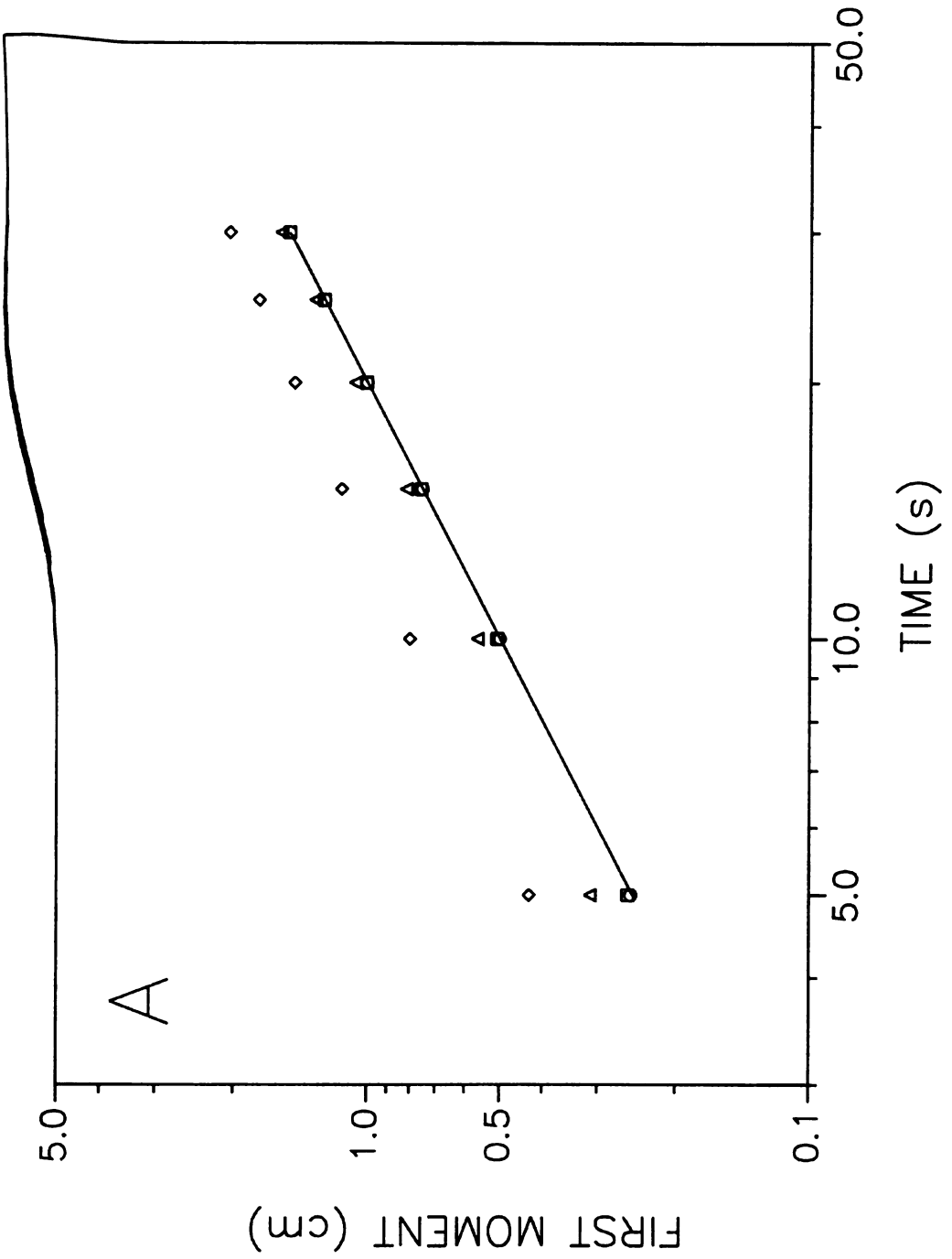

Figure 3.11 cont.

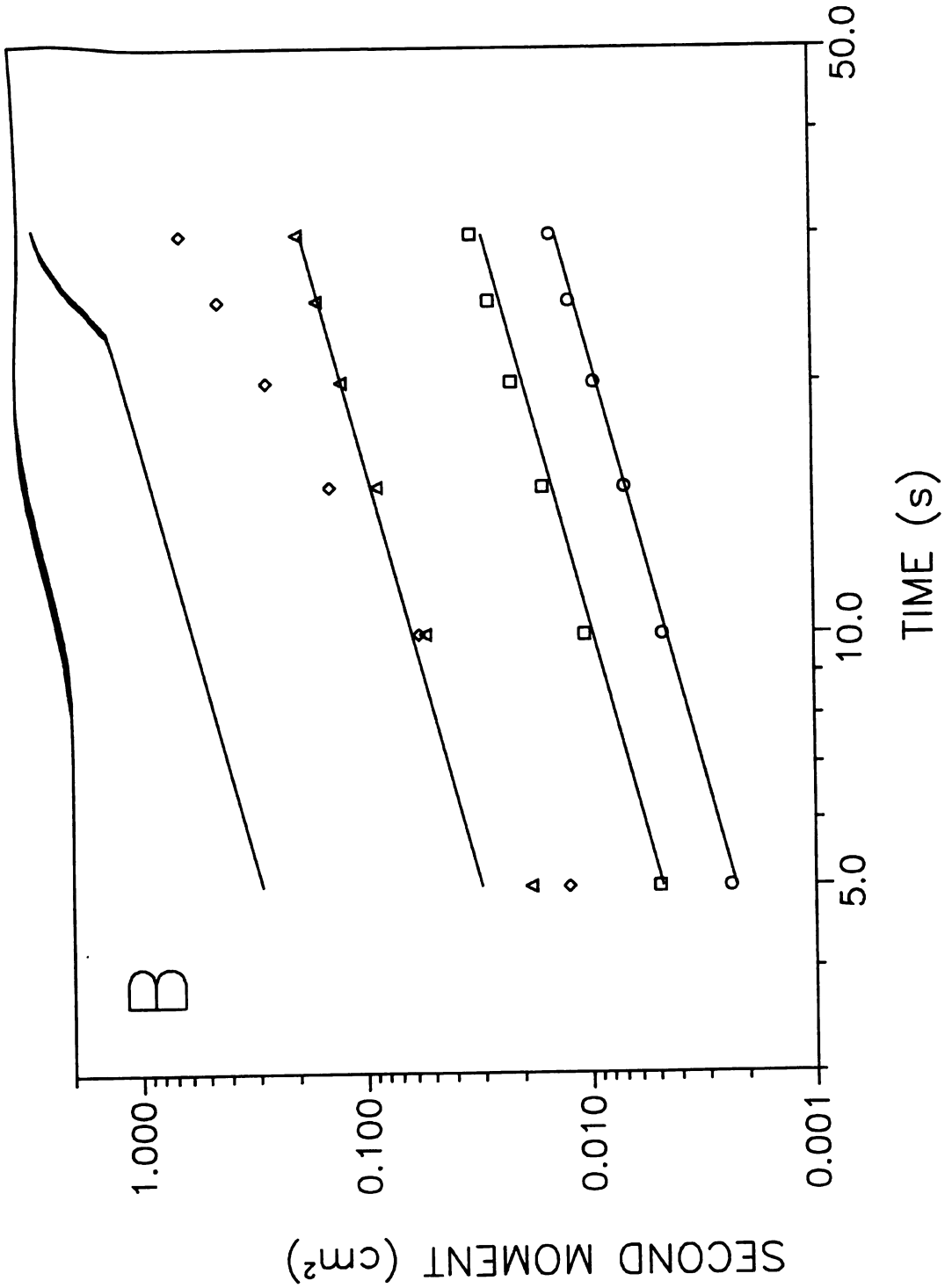

3.2.3 Effect of Interfacial Resistance to Mass Transport.

It is possible to extend this simulation approach to consider the situation where there is some resistance to mass transport at the interface and all collisions are not sufficiently energetic to overcome this barrier. To represent this situation, the constant *a* in the probability expressions of Equations [2.12] and [2.13] was varied from 1.0 to 0.001 for the case of liquid chromatography. The kinetic behavior of the system is summarized in Table 3.3 and Figure 3.12.

Table 3.3 Effect of Interfacial Resistance to Mass Transport on Rate Constants.[a]

a	k_{fs} (s^{-1})	k_{sf} (s^{-1})	τ (s)	k_{fs}/k_{sf}	N_s/N_f
1.0	13.74	13.87	0.036	0.991	0.997
0.5	11.60	11.73	0.043	0.989	0.997
0.1	2.509	2.509	0.199	1.000	1.001
0.05	1.301	1.302	0.384	0.999	0.998
0.01	0.273	0.272	1.84	1.004	1.008
0.005	0.137	0.137	3.65	1.001	1.002
0.001	0.028	0.028	18.02	0.992	1.005

[a] Simulation conditions: $N = 1.0\times10^{4}$; $t = 1.0\times10^{-5}$ s; $T = 20\ \tau$; $R_f = 2.0\times10^{-3}$ cm; $R_s = 8.28\times10^{-4}$ cm; $D_f = 1.0\times10^{-5}$ $cm^2\ s^{-1}$; $D_s = 1.0\times10^{-5}$ $cm^2\ s^{-1}$; $K_{abs} = 1.0$.

It is apparent from the rate constants and the characteristic time τ that the kinetic behavior is reasonably rapid for $a = 1.0$, slightly slower for $a = 0.5$, and significantly slower for smaller values of *a*.

The trends may be more clearly illustrated in graphical form, as shown in Figure 3.13. The rate constants increase linearly with the constant *a* up to approximately 0.5, whereafter the system becomes diffusion limited for these simulation conditions. From the rate constants given in Table 3.3, we can estimate the barrier to interfacial transport

Figure 3.12: Kinetic evolution of the absorption process with varying interfacial resistance to mass transport. Simulation conditions: $D_f = 1.0\times10^{-5}$ cm^2 s^{-1}; $D_s = 1.0\times10^{-5}$ cm^2 s^{-1}; a = 1.0 (○), 0.1 (□), 0.01 (△), 0.001 (◇); other conditions as given in Figure 3.1B.

Figure 3.12

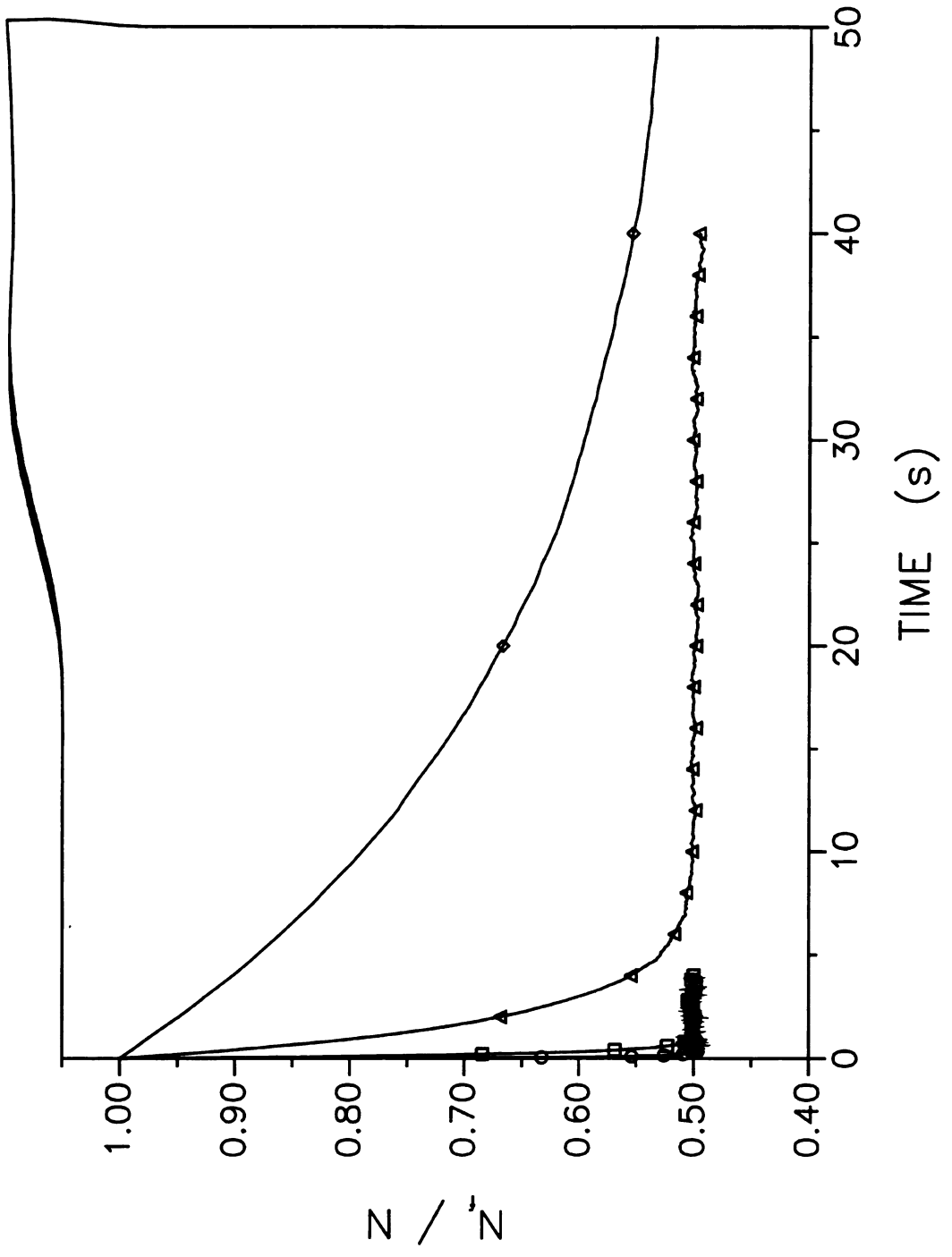

Figure 3.13: Effect of interfacial resistance to mass transport on rate constants k_{fs} (○) and k_{sf} (●). Simulation conditions as given in Table 3.3.

Figure 3.13

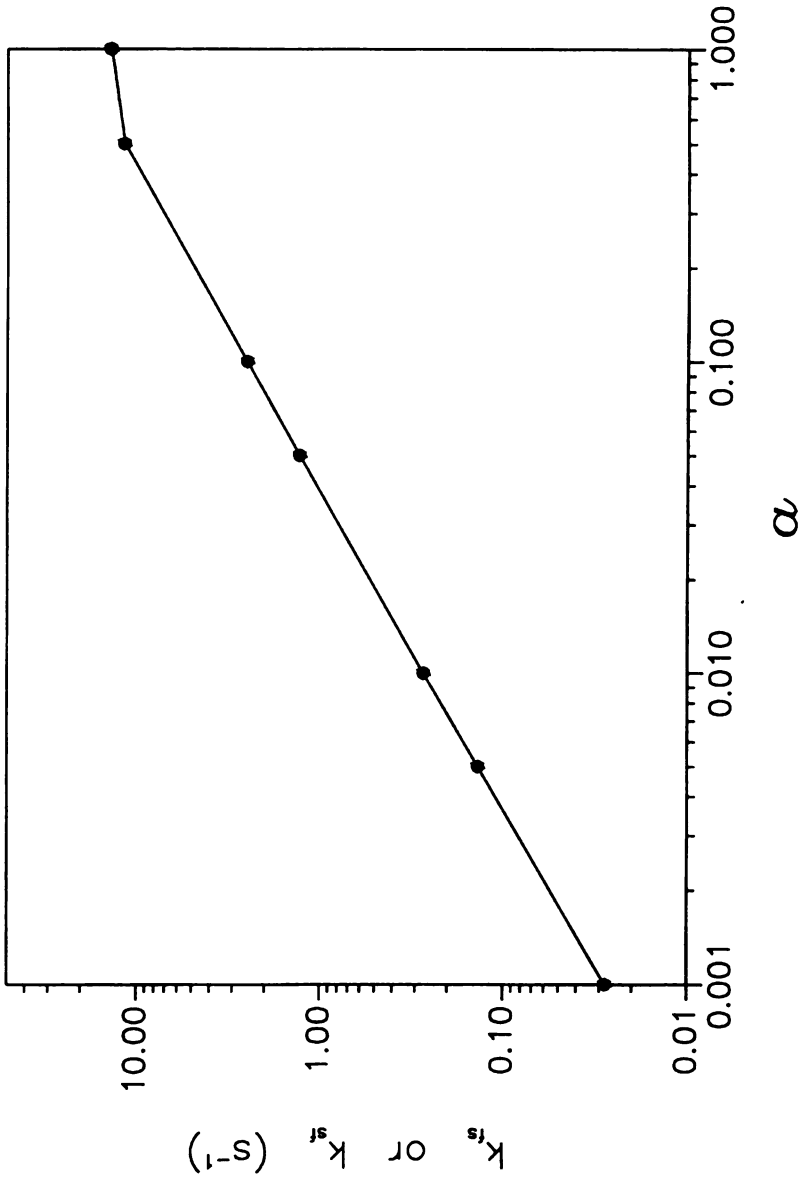

relative to the diffusion-limited case (a = 1.0). These barriers correspond to 0.17 k_B T_0 for a = 0.5, 1.70 k_B T_0 for a = 0.1, 2.36 k_B T_0 for a = 0.05, 3.92 k_B T_0 for a = 0.01, 4.61 k_B T_0 for a = 0.005, and 6.20 k_B T_0 for a = 0.001 where k_B is the Boltzman constant, and T_0 is the temperature. From these calculations, it is evident that relatively small barriers can have a significant effect upon the kinetic behavior of the system. Consequently, we must seek to minimize sources of interfacial resistance to mass transport in order to develop unified chromatographic systems with optimal kinetic performance. This may involve minimizing surface tension effects, minimizing configurational or orientational effects, and choosing fluid-phase solvents and modifiers that can be easily and rapidly disassociated from solute molecules at the interface.

The effect of interfacial resistance to mass transfer on the fluid dynamic behavior of the system has also been examined. The solute zone profiles obtained at a mean linear velocity of 0.10 cm s^{-1} are shown in Figure 3.14 for values of the constant a of 1.0, 0.1, 0.01, and 0.001. Although the characteristic time τ is very similar for these values of the constant a and for diffusion coefficients in the surface phase from 1.0×10^{-5} to 1.0×10^{-8} cm^2 s^{-1} shown in Table 3.2, there is a marked difference in the solute zone profiles in Figures 3.10 and 3.14. The profiles for decreasing values of the constant a broaden but remain symmetric regardless of the magnitude of the characteristic time τ. Symmetry is preserved because the constant a influences both P_{fs} and P_{sf} in Equations [2.12] and [2.13] in the same manner. In contrast, the diffusion coefficients influence only one of the probability expressions in Equations [2.12] and [2.13] and mass transport in only one

Figure 3.14: Evolution of the solute zone profile with varying interfacial resistance to mass transport for liquid chromatography. Simulation conditions: $D_f = 1.0\times10^{-5}$ cm^2 s^{-1}; $D_s = 1.0\times10^{-5}$ cm^2 s^{-1}; a = 1.0 (A), 0.1 (B), 0.01 (C), 0.001 (D); other conditions as given in Figure 3.4C.

Figure 3.14

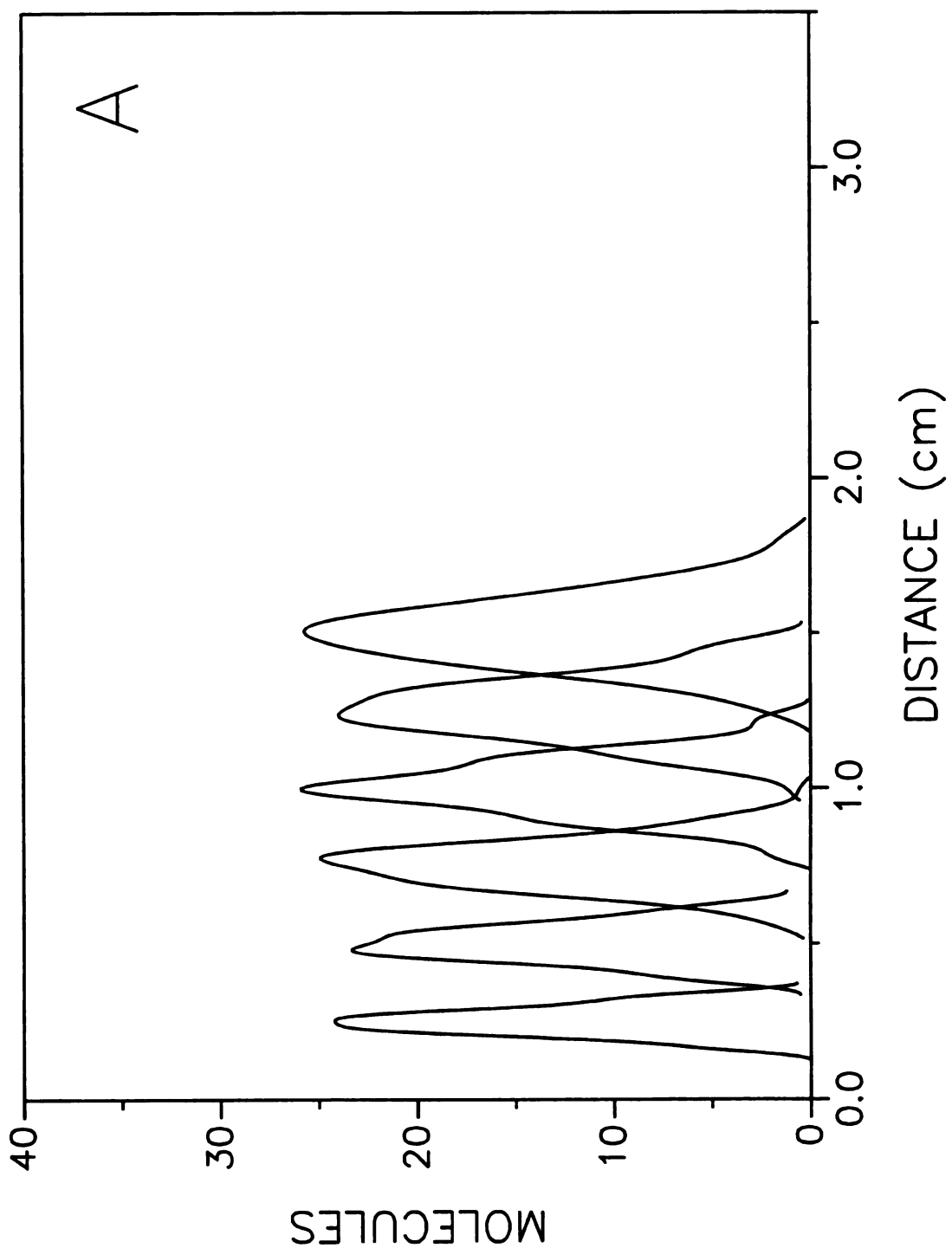

Figure 3.14 cont.

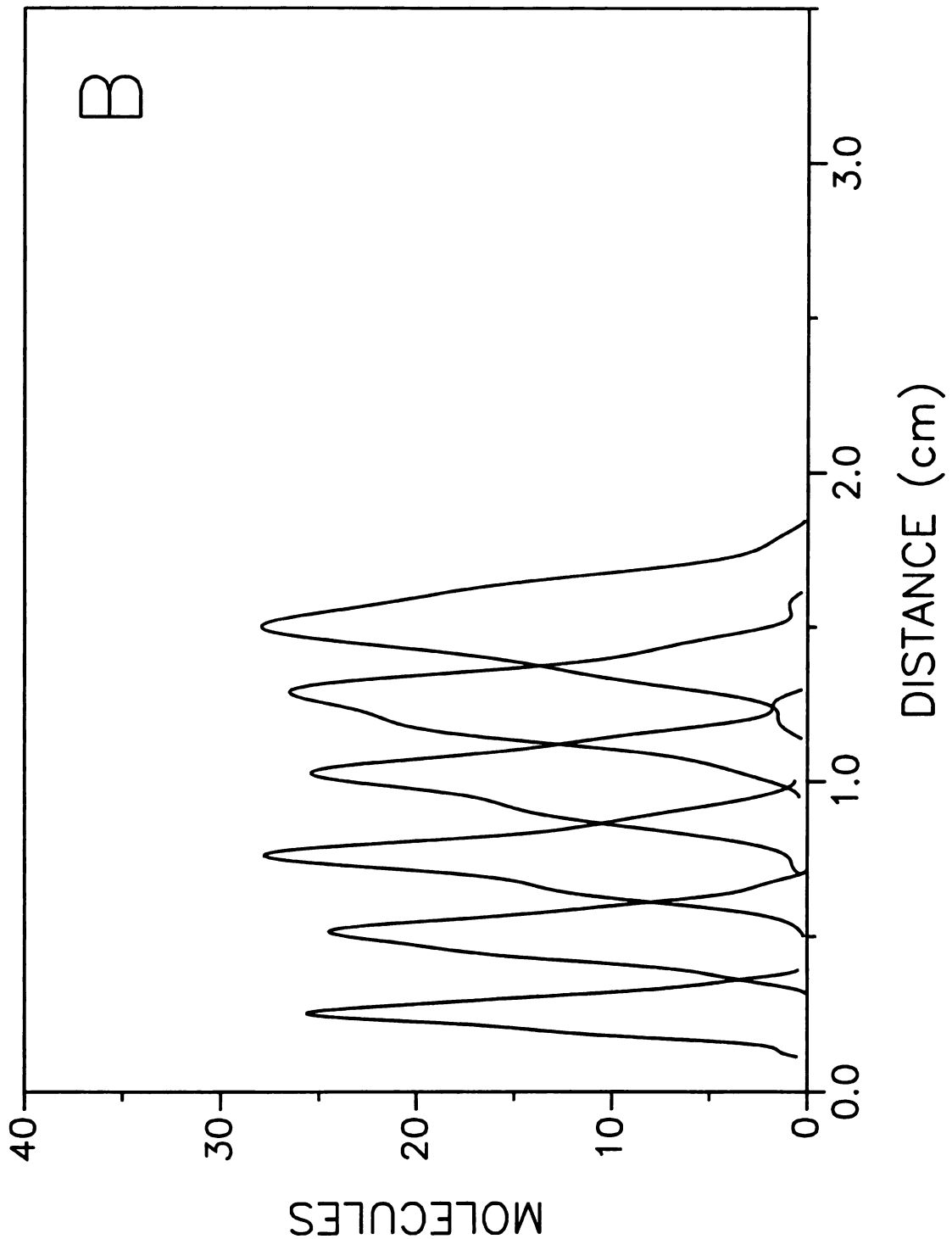

Figure 3.14 cont.

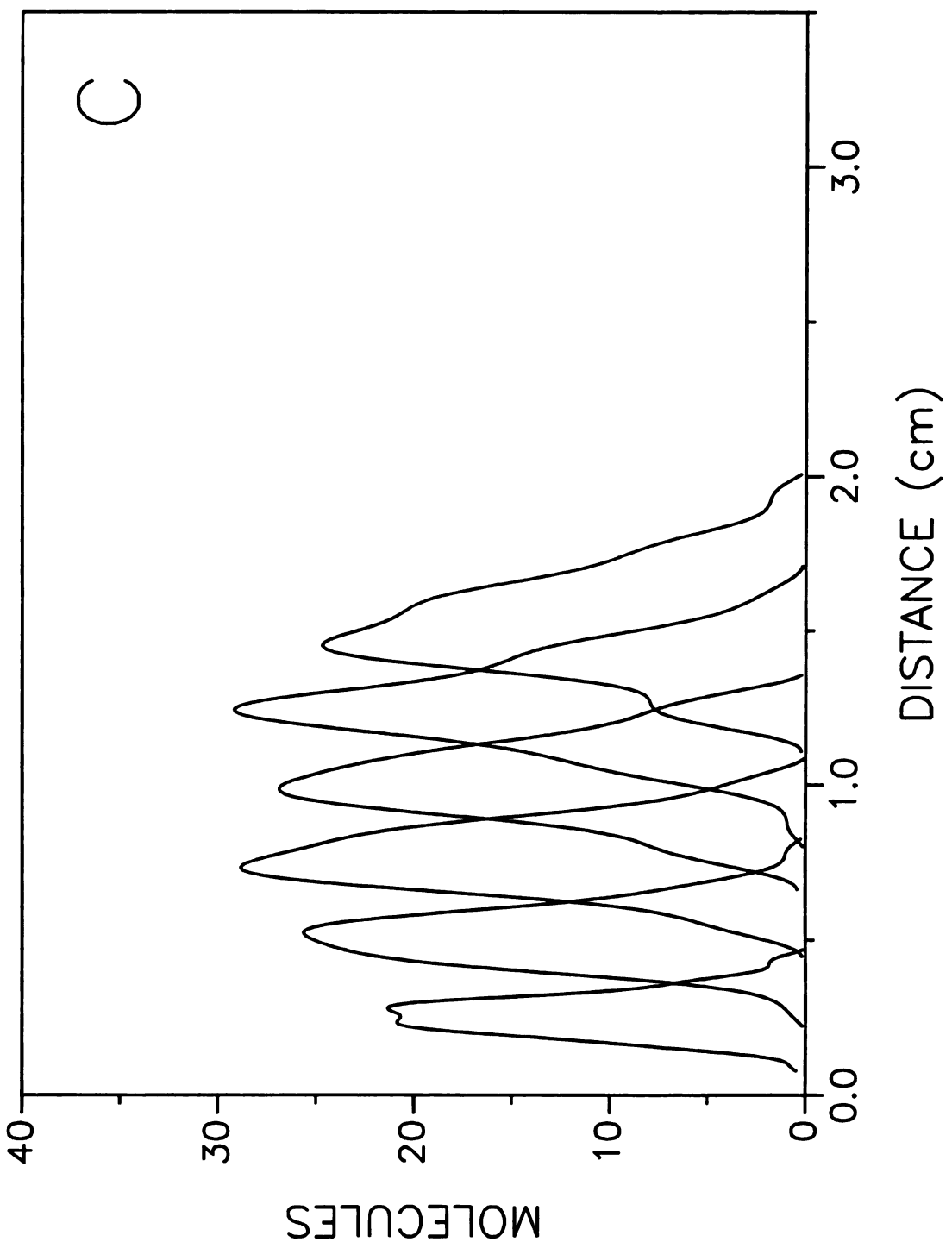

Figure 3.14 cont.

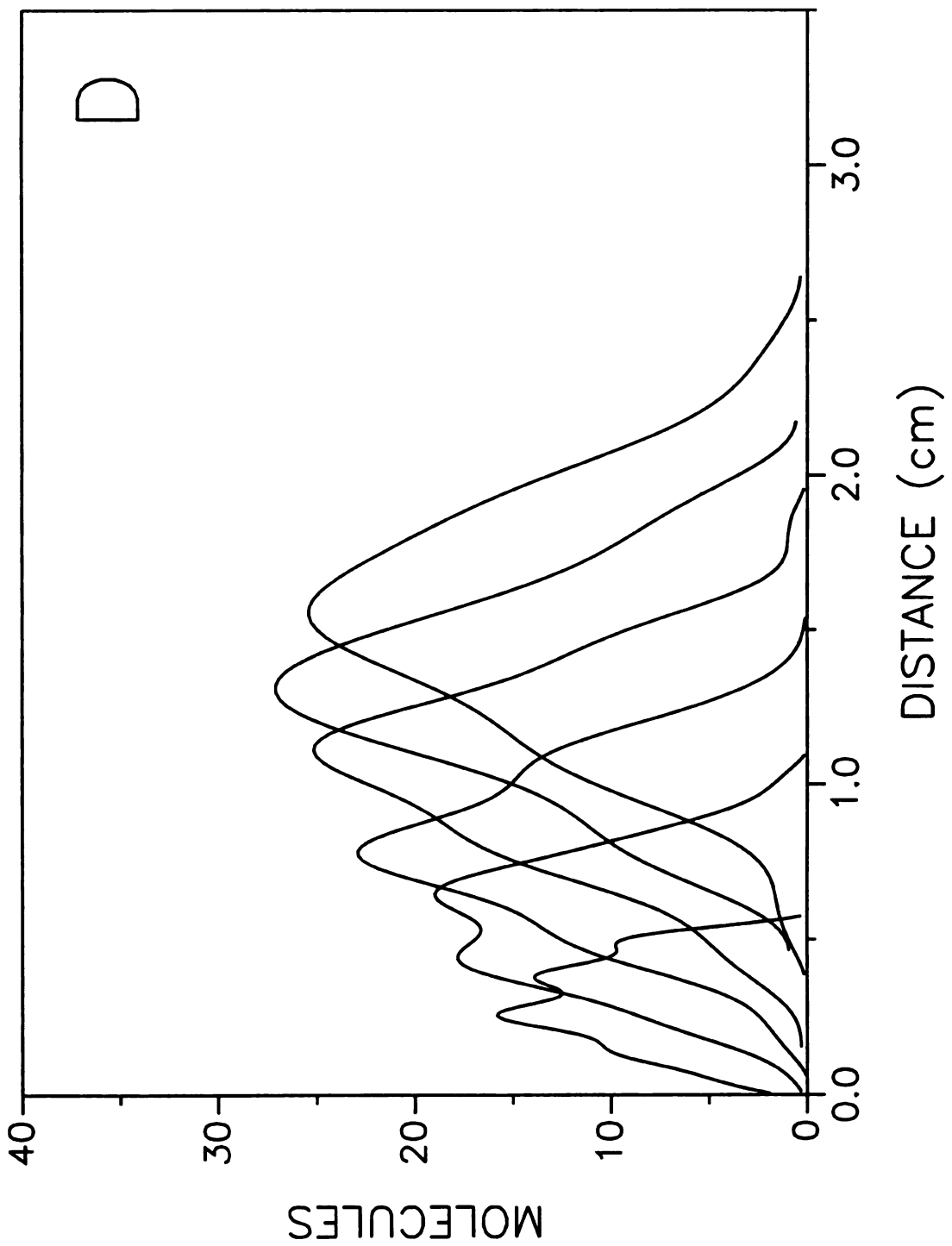

phase, resulting in zone profiles that are broader and more asymmetric as the characteristic time τ increases.

The statistical moments of the solute zone profiles are shown as a function of the simulation time in Figure 3.15. For the constant $a = 1.0$, the mean distance and variance agree well with the theoretically expected values. As the constant a decreases, the mean distance increases slightly because the molecules spend more time in the fluid phase before an effective transfer can occur at the interface. In general, the mean distance agrees reasonably well with the theoretically expected value for all except the smallest value of $a = 0.001$. However, the variance of the zone increases significantly as the constant a decreases. Only for the case of $a = 1.0$ does the variance conform to the extended Golay equation.[3] This is because the Golay equation assumes that equilibrium conditions exist at the interface and does not consider the effects of slow interfacial mass transfer. These contributions rapidly become important as the constant a decreases and become predominant for values of a less than 0.01. It is also noteworthy that these contributions to variance increase linearly with simulation time, suggesting that steady-state conditions have been achieved. Clearly, interfacial resistance to mass transport in chromatographic systems is important and merits further study and more detailed characterization.

3.3 Conclusions.

A three-dimensional stochastic simulation has been developed for the unified treatment of separation systems for chromatography, electrophoresis, and

Figure 3.15: Mean distance (A) and variance (B) of the solute zone profile with varying interfacial resistance to mass transport. Simulation conditions: $D_f = 1.0\times10^{-5}$ cm^2 s^{-1}; $D_s = 1.0\times10^{-5}$ cm^2 s^{-1}; a = 1.0 (○), 0.1 (□), 0.01 (△), 0.001 (◇); other conditions as given in Figure 3.4C. (—) Theory according to the extended Golay equation.[3]

Figure 3.15

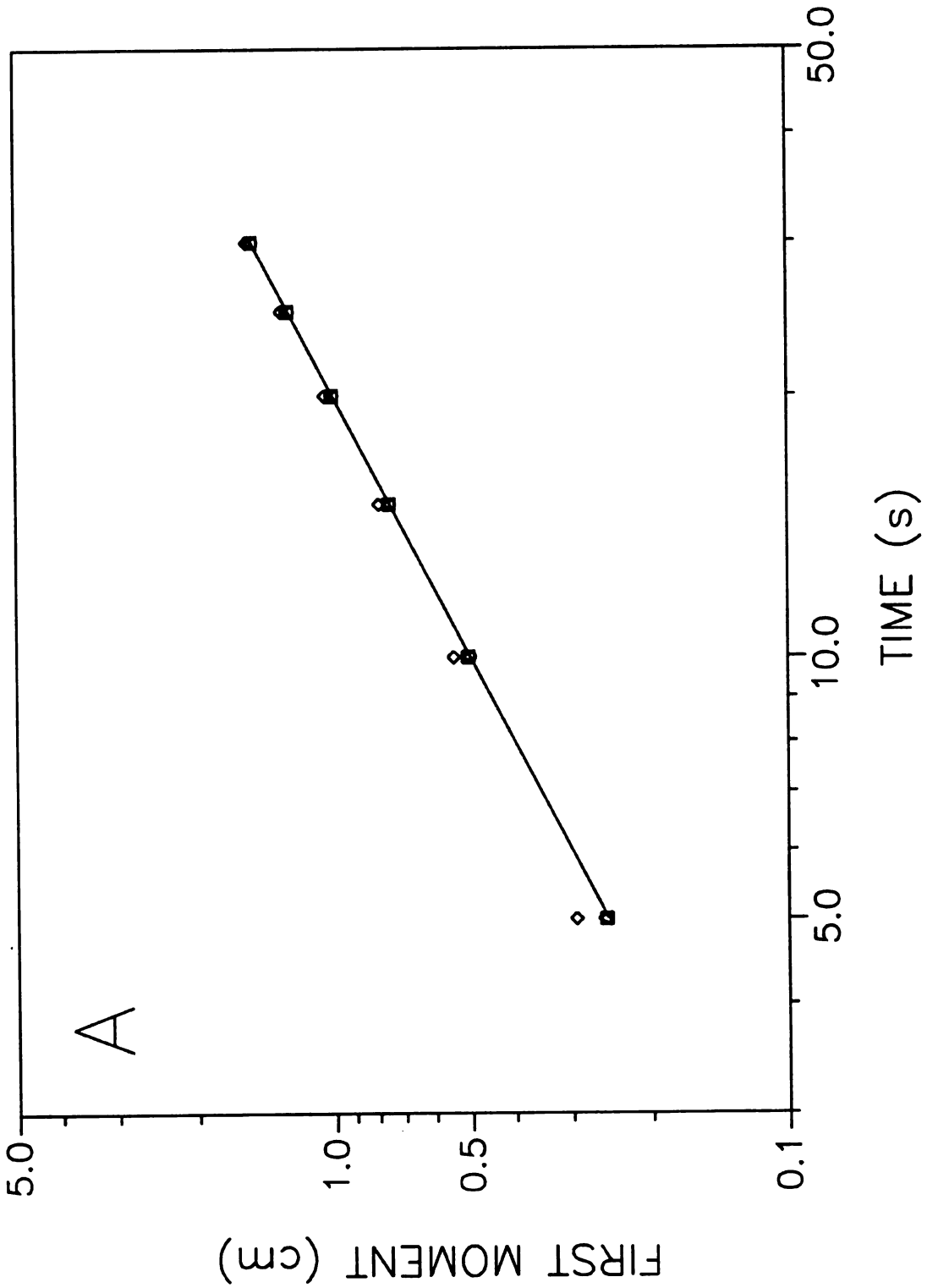

Figure 3.15 cont.

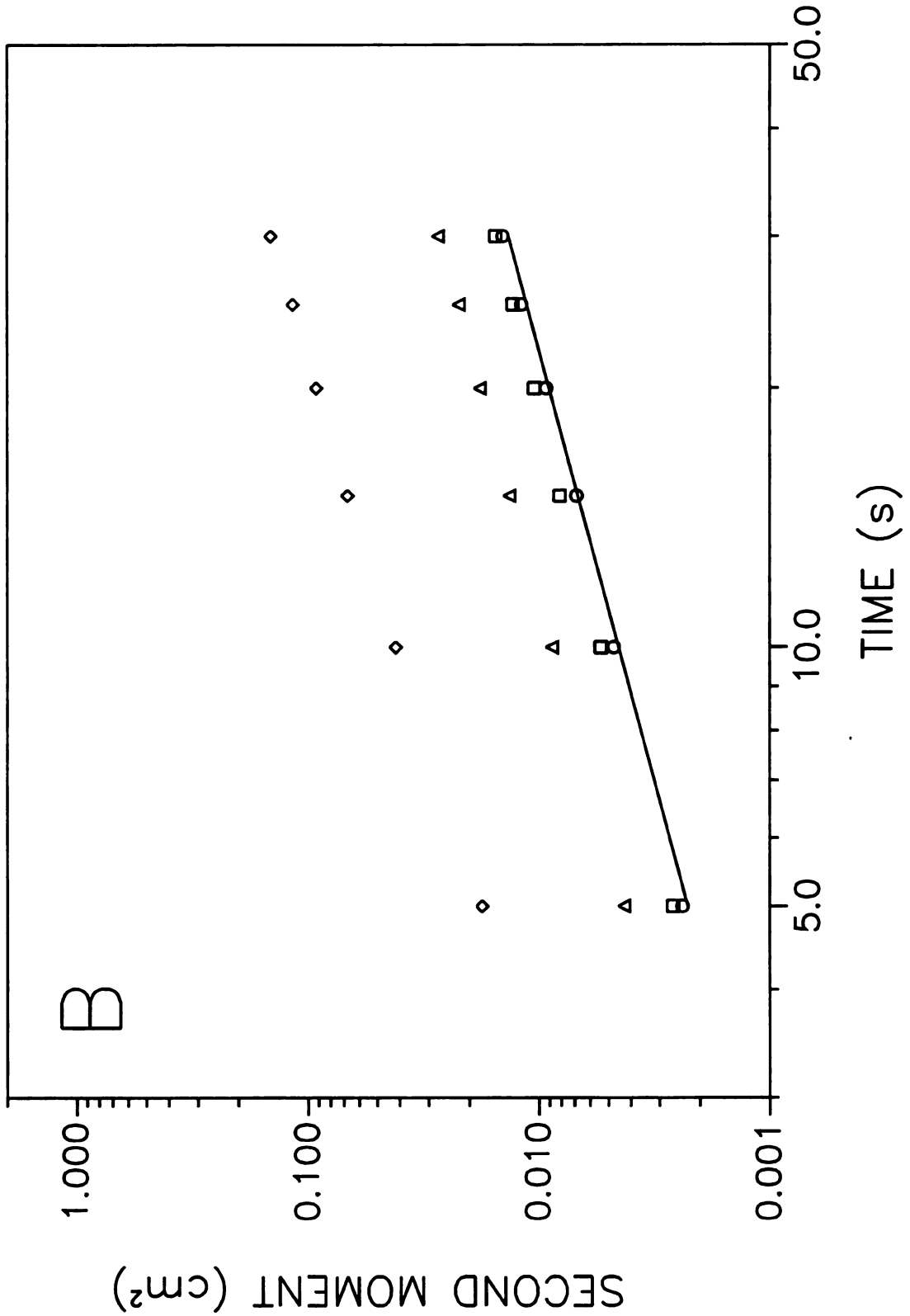

electrochromatography. This simulation follows the trajectories of individual molecules through the mass transport processes of diffusion, convection by laminar and electroosmotic flow, electrophoretic migration, and surface interaction by absorption and adsorption mechanisms. This simulation provides the opportunity to perform hypothetical experiments and to make observations that may not be possible with classical theoretical models or experiments.

In this chapter, the simulation has been used to characterize the absorption mechanism between homogeneous fluid and surface phases for chromatography. The kinetic and equilibrium properties as well as the fluid dynamic behavior were examined as a function of the diffusion coefficient in the fluid and surface phases and the interfacial resistance to mass transport. These results suggest that an increase in surface phase diffusion coefficients and a reduction of interfacial resistance are the most critical factors in the development of more rapid separation systems.

3.4 References.

1. McGuffin, V.L.; Krouskop, P.E.; Wu, P.; J. Chromatogr. A 1998, 828, 37.

2. Wu, P.; McGuffin, V.L.; AIChE J. 1998, 44, 2053.

3. Golay, M.J.E.; in Gas Chromatography 1958; Desty, D.H., Ed.; Academic Press: New York, NY, 1958; p.36.

Chapter 4

Stochastic Simulation of the Absorption Mechanism Under Diffusion-Limited Conditions in Chromatography and Electrochromatography

4.1 Introduction.

In a chromatography or electrochromatography system, molecules that are at the front edge of the solute zone in the fluid phase enter a new, previously unoccupied region of the column. Because there are no solute molecules in the surface phase, reequilibration must occur such that the activity or, more simply, the concentration in each phase is in correspondence with the absorption coefficient. At the rear edge of the zone, the complementary process occurs. Solute molecules in the surface phase are left behind, so that there is an activity or concentration deficiency in the fluid phase that must be reequilibrated. In each of these processes, a finite time is required for solute molecules to diffuse, dissolve, absorb, or adsorb in the proper phase. During this time, the solute zone continues to advance and thereby perpetuates and exacerbates the problem. As a result, the solute zone remains in a continuous state of nonequilibrium. The importance of nonequilibrium and kinetics in separation science has been recognized since the pioneering work of Giddings.[1-5] A detailed understanding of kinetic effects is necessary to identify and to characterize the rate-limiting processes, so that separation speed can be increased without sacrificing efficiency. This understanding is especially important for condensed-phase separations because of the inherently small diffusion coefficients and slow separation speed.

The goals of this chapter are as follows: 1) to perform stochastic simulations of the absorption process under diffusion-limited conditions in a system with homogeneous fluid and surface phases and to determine the kinetic rate constants, 2) to elucidate the relationships between the rate constants and the fundamental parameters of the system, including the absorption coefficient of the solute between the fluid and surface phases, the diffusion coefficient of the solute in each phase, and the radial dimensions of each phase, and 3) to examine the relationship between the rate constants and the solute zone profiles in chromatography and electrochromatography.

4.2 Results and Discussion.

In the absorption process, the solute X is distributed between the fluid (f) and surface (s) phases:

$$X_f \underset{k_{sf}}{\overset{k_{fs}}{\longleftrightarrow}} X_s \qquad [4.1]$$

where k_{fs} and k_{sf} are the pseudo-first-order rate constants. Under these conditions, the distribution of solute molecules can be described by a simple kinetic model of reversible reactions.[6,7] The net rate of change in the number of molecules in the fluid and surface phases (N_f and N_s, respectively) is governed by the following system of ordinary differential equations:

$$\frac{dN_f}{dT} = -k_{fs} N_f + k_{sf} N_s \qquad [4.2]$$

$$\frac{dN_s}{dT} = k_{fs} N_f - k_{sf} N_s \qquad [4.3]$$

If all molecules initially reside in the fluid phase, then the solution of Equations [4.2] and [4.3] is given by

$$\frac{N_f}{N} = \frac{k_{sf} + k_{fs}\exp\left(-(k_{fs} + k_{sf})T\right)}{(k_{fs} + k_{sf})} \qquad [4.4]$$

$$\frac{N_s}{N} = \frac{k_{fs} - k_{fs}\exp\left(-(k_{fs} + k_{sf})T\right)}{(k_{fs} + k_{sf})} \qquad [4.5]$$

From Equations [4.4] and [4.5], it follows directly that

$$\tilde{N}_f = \lim_{T\to\infty} N_f = \frac{k_{sf}\,N}{(k_{fs} + k_{sf})} \qquad [4.6]$$

$$\tilde{N}_s = \lim_{T\to\infty} N_s = \frac{k_{fs}\,N}{(k_{fs} + k_{sf})} \qquad [4.7]$$

where $\tilde{N}_f$ and $\tilde{N}_s$ represent the number of molecules in the fluid and surface phases at equilibrium. Hence, the ratio of the number of molecules $\tilde{N}_s/\tilde{N}_f$ under the equilibrium definition is equal to the ratio of the rate constants k_{fs}/k_{sf} under the kinetic definition:

$$\frac{\tilde{N}_s}{\tilde{N}_f} = \frac{k_{fs}}{k_{sf}} = k' = \frac{K_{abs}\,V_s}{V_f} \qquad [4.8]$$

Furthermore, this ratio defines the capacity factor (k′), which represents the absorption coefficient (K_{abs}) adjusted for the volumes of the fluid and surface phases (V_f and V_s, respectively). For the cylindrical model system, these volumes are given by

$$V_f = \pi R_f^2 L \qquad [4.9]$$

$$V_s = \pi\left[(R_f + R_s)^2 - R_f^2\right]L \qquad [4.10]$$

To examine the kinetic and equilibrium behavior of the model system, the number of molecules in the fluid phase is monitored as a function of time during the stochastic simulation. Three to five repetitive simulations with 10,000 molecules are averaged to obtain the simulation data (T, N_f/N). The kinetic rate constants are then determined by nonlinear regression of the simulation data to Equation [4.4], as illustrated in Figure 4.1. In addition, the ratio of the number of molecules $\tilde{N}_s/\tilde{N}_f$ is calculated after equilibrium has been attained.[8]

4.2.1 Effect of Parameters on Equilibrium Processes.

As noted above, the ratio of the number of molecules in the fluid and surface phases $\tilde{N}_s/\tilde{N}_f$ reflects the equilibrium behavior of the system. This ratio was determined by stochastic simulation as a function of the absorption coefficient (Table 4.1), the diffusion coefficients in the fluid and surface phases (Table 4.2), and the radial depth of the fluid and surface phases (Table 4.3). The theoretically expected relationship between the $\tilde{N}_s/\tilde{N}_f$ ratio and these parameters is given in Equations [4.8], [4.9], and [4.10]. The simulation data show excellent agreement with this theoretical relationship, as verified in Figure 4.2. The $\tilde{N}_s/\tilde{N}_f$ ratio is determined with ±0.29% average relative standard deviation and ±0.39% average relative error.

4.2.2 Effect of Parameters on Kinetic Processes.

The kinetic rate constants k_{fs} and k_{sf} were also determined as a function of the absorption coefficient (Table 4.1), the diffusion coefficients in the fluid and surface phases

Figure 4.1: Kinetic evolution of the absorption process by monitoring the relative number of molecules in the fluid phase (N_f/N) as a function of simulation time (T). Simulation conditions: N = 10,000, t = 5.0×10^{-4} s, $D_f = 1.0\times10^{-5}$ cm^2 s^{-1}, $D_s = 1.0\times10^{-7}$ cm^2 s^{-1}, $R_f = 2.00\times10^{-3}$ cm, $R_s = 8.28\times10^{-4}$ cm, $K_{abs} = 1.0$. (——) Nonlinear regression analysis according to Equation [4.4], yielding rate constants $k_{fs} = 0.353\pm0.001$, $k_{sf} = 0.357\pm0.001$ ($r^2 = 0.974$).

Figure 4.1

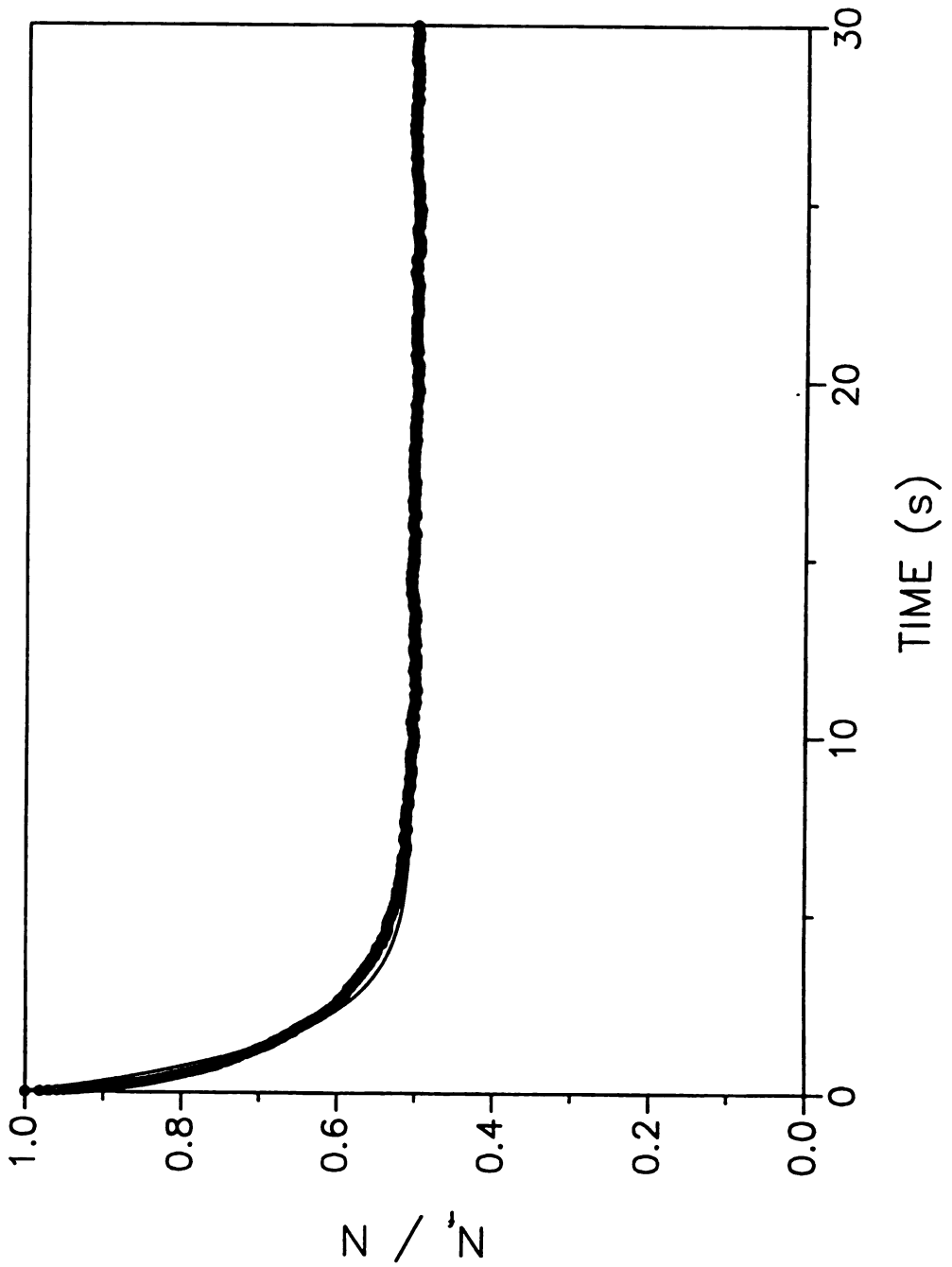

Table 4.1 Kinetic Rate Constants k_{fs} and k_{sf} and Steady-State Distribution $\tilde{N}_s/\tilde{N}_f$ as a Function of the Absorption Coefficient.[a]

K_{abs}	k_{fs} (s^{-1})	k_{sf} (s^{-1})	k_{fs}/k_{sf}	$\tilde{N}_s/\tilde{N}_f$
0.1	2.765 ± 0.011	27.78 ± 0.112	0.1	0.1
0.2	4.988 ± 0.017	25.00 ± 0.090	0.2	0.2
0.5	9.495 ± 0.041	19.10 ± 0.086	0.497	0.504
1.0	13.74 ± 0.069	13.87 ± 0.074	0.991	0.999
2.0	16.43 ± 0.078	8.363 ± 0.044	1.965	1.992
5.0	17.95 ± 0.081	3.713 ± 0.022	4.836	4.954
10.0	18.37 ± 0.083	1.971 ± 0.016	9.323	9.924

[a] Values of k_{fs} and k_{sf} determined by nonlinear regression of the simulation data to Equation [4.4]. Simulation conditions: N = 10,000, t = 5.0×10^{-4} s, $D_f = 1.0\times10^{-5}$ cm^2 s^{-1}, $D_s = 1.0\times10^{-5}$ cm^2 s^{-1}, $R_f = 2.00\times10^{-3}$ cm, $R_s = 8.28\times10^{-4}$ cm.

Table 4.2 Kinetic Rate Constants k_{fs} and k_{sf} and Steady-State Distribution $\tilde{N}_s/\tilde{N}_f$ as a Function of the Fluid and Surface Phase Diffusion Coefficients.[a]

D_f (cm^2 s^{-1})	D_s (cm^2 s^{-1})	k_{fs} (s^{-1})	k_{sf} (s^{-1})	k_{fs}/k_{sf}	$\tilde{N}_s/\tilde{N}_f$
1.0×10^{-4}	1.0×10^{-5}	30.94 ± 0.09	31.25 ± 0.10	0.990	1.008
1.0×10^{-4}	1.0×10^{-6}	3.635 ± 0.016	3.690 ± 0.017	0.985	0.988
1.0×10^{-4}	1.0×10^{-7}	0.366 ± 0.001	0.363 ± 0.002	1.009	1.023
1.0×10^{-5}	1.0×10^{-4}	21.49 ± 0.097	21.95 ± 0.106	0.979	1.000
1.0×10^{-5}	1.0×10^{-5}	13.74 ± 0.069	13.87 ± 0.074	0.991	0.999
1.0×10^{-5}	1.0×10^{-6}	3.076 ± 0.010	3.102 ± 0.011	0.991	1.006
1.0×10^{-5}	1.0×10^{-7}	0.353 ± 0.001	0.357 ± 0.001	0.989	0.999
1.0×10^{-5}	1.0×10^{-8}	0.0380 ± 0.0002	0.0386 ± 0.0002	0.986	0.999
1.0×10^{-5}	1.0×10^{-9}	0.00388 ± 0.00001	0.00377 ± 0.00001	1.027	1.020
1.0×10^{-5}	1.0×10^{-10}	0.00040 ± 0.000001	0.00041 ± 0.000001	0.982	0.951
1.0×10^{-6}	1.0×10^{-4}	2.199 ± 0.011	2.238 ± 0.012	0.983	0.988
1.0×10^{-6}	1.0×10^{-5}	2.204 ± 0.011	2.265 ± 0.012	0.973	1.001
1.0×10^{-6}	1.0×10^{-6}	1.381 ± 0.004	1.391 ± 0.004	0.993	1.008
1.0×10^{-6}	1.0×10^{-7}	0.308 ± 0.001	0.306 ± 0.001	1.006	0.979
1.0×10^{-6}	1.0×10^{-8}	0.0370 ± 0.0001	0.0381 ± 0.0001	0.972	1.001
1.0×10^{-7}	1.0×10^{-5}	0.233 ± 0.001	0.240 ± 0.001	0.972	1.001
1.0×10^{-7}	1.0×10^{-6}	0.221 ± 0.001	0.225 ± 0.001	0.982	0.976

[a] Values of k_{fs} and k_{sf} determined by nonlinear regression of the simulation data to Equation [4.4]. Simulation conditions: N = 10,000, t = 5.0×10^{-4} s, $R_f = 2.00\times10^{-3}$ cm, $R_s = 8.28\times10^{-4}$ cm, $K_{abs} = 1.0$.

Table 4.3 Kinetic Rate Constants k_{fs} and k_{sf} and Steady-State Distribution $\tilde{N}_s/\tilde{N}_f$ as a Function of the Fluid and Surface Phase Radii.[a]

R_f (cm)	R_s (cm)	k_{fs} (s^{-1})	k_{sf} (s^{-1})	k_{fs}/k_{sf}	$\tilde{N}_s/\tilde{N}_f$
1.13×10^{-3}	8.28×10^{-4}	32.90 ± 0.088	16.59 ± 0.050	1.983	2.008
2.00×10^{-3}	8.28×10^{-4}	13.74 ± 0.069	13.87 ± 0.074	0.991	0.999
3.69×10^{-3}	8.28×10^{-4}	5.279 ± 0.026	10.72 ± 0.055	0.492	0.500
8.68×10^{-3}	8.28×10^{-4}	1.615 ± 0.014	8.332 ± 0.076	0.194	0.200
1.70×10^{-2}	8.28×10^{-4}	0.721 ± 0.006	7.686 ± 0.069	0.094	0.098
3.35×10^{-2}	8.28×10^{-4}	0.337 ± 0.003	7.186 ± 0.063	0.047	0.049
8.33×10^{-2}	8.28×10^{-4}	0.128 ± 0.001	6.811 ± 0.059	0.019	0.020
2.00×10^{-3}	9.76×10^{-5}	52.27 ± 0.40	533.8 ± 4.4	0.094	0.098
2.00×10^{-3}	1.91×10^{-4}	28.49 ± 0.18	144.9 ± 0.95	0.197	0.199
2.00×10^{-3}	4.49×10^{-4}	18.03 ± 0.079	36.69 ± 0.17	0.491	0.498
2.00×10^{-3}	1.46×10^{-3}	10.69 ± 0.036	5.410 ± 0.020	1.977	1.980
2.00×10^{-3}	2.90×10^{-3}	7.753 ± 0.029	1.587 ± 0.007	4.885	4.960
2.00×10^{-3}	4.63×10^{-3}	6.469 ± 0.030	0.718 ± 0.005	9.014	10.028

[a] Values of k_{fs} and k_{sf} determined by nonlinear regression of the simulation data to Equation [4.4]. Simulation conditions: N = 10,000, $t = 5.0\times10^{-4}$ s, $D_f = 1.0\times10^{-5}$ cm^2 s^{-1}, $D_s = 1.0\times10^{-5}$ cm^2 s^{-1}, $K_{abs} = 1.0$.

Figure 4.2: Relationship between the ratio of molecules in the fluid and surface phases at equilibrium ($\tilde{N}_s/\tilde{N}_f$) and the absorption coefficient (K_{abs}) and the radius of the fluid and surface phases (R_f and R_s, respectively). (——) Theory according to Equations [4.8] to [4.10] ($r^2 = 1.000$). Simulation conditions given in Tables 4.1 to 4.3.

Figure 4.2

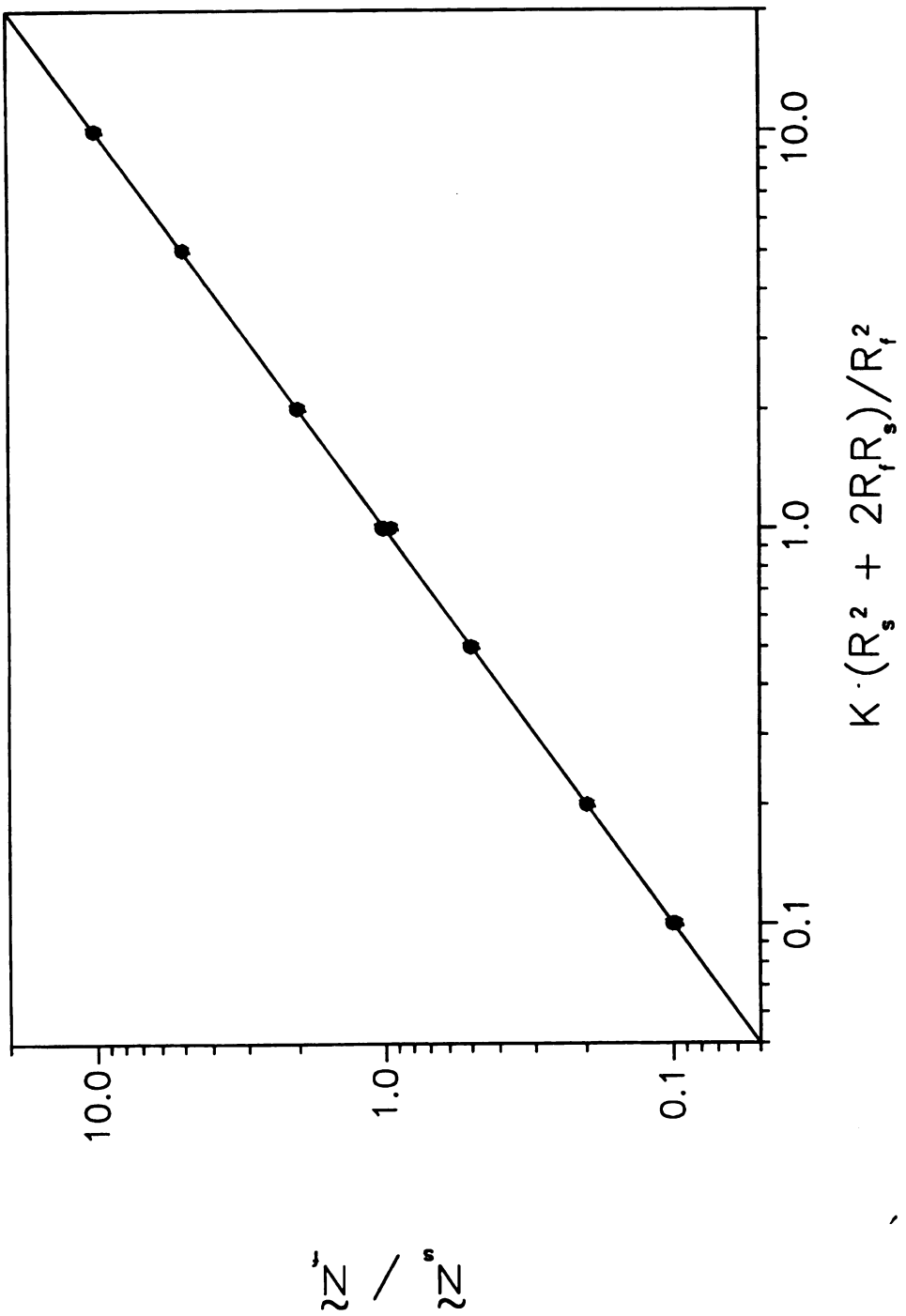

(Table 4.2), and the radial depth of the fluid and surface phases (Table 4.3). The theoretically expected relationship between the ratio of the rate constants k_{fs}/k_{sf} and these parameters is given in Equations [4.8], [4.9], and [4.10]. The simulation data show excellent agreement with this theoretical relationship, as verified in Figure 4.3. The individual rate constants k_{fs} and k_{sf} are determined with ±0.49% average relative standard deviation, and the ratio of the rate constants k_{fs}/k_{sf} with ±0.70% average relative standard deviation and ±2.25% average relative error.

Although the ratio of the rate constants k_{fs}/k_{sf} can be readily predicted by Equation [4.8], there is no theoretical model presently available to determine the magnitude of the individual rate constants k_{fs} and k_{sf}. For this reason, the stochastic simulation approach has been used to elucidate the relationships between the diffusion-limited rate constants and the fundamental parameters of the system.

The absorption coefficient was varied from 0.1 to 10.0, with all other parameters remaining constant. The effect of the variation in absorption coefficient on the individual rate constants is summarized in Table 4.1. It is apparent that k_{fs} increases nonlinearly whereas k_{sf} decreases nonlinearly with an increase in absorption coefficient. Upon detailed examination, the following relationships appear to be applicable:

$$k_{fs} \propto \left(\frac{K_{abs}}{1+K_{abs}} \right) \qquad [4.11]$$

$$k_{sf} \propto \left(\frac{1}{1+K_{abs}} \right) \qquad [4.12]$$

These relationships suggest that the rate constant for transport from the fluid to surface phase is controlled by the fraction of molecules in the surface phase at equilibrium and,

Figure 4.3: Relationship between the ratio of the rate constants (k_{fs}/k_{sf}) and the absorption coefficient (K_{abs}) and the radius of the fluid and surface phases (R_f and R_s, respectively). (——) Theory according to Equations [4.8] to [4.10] ($r^2 = 0.999$). Simulation conditions given in Tables 4.1 to 4.3.

Figure 4.3

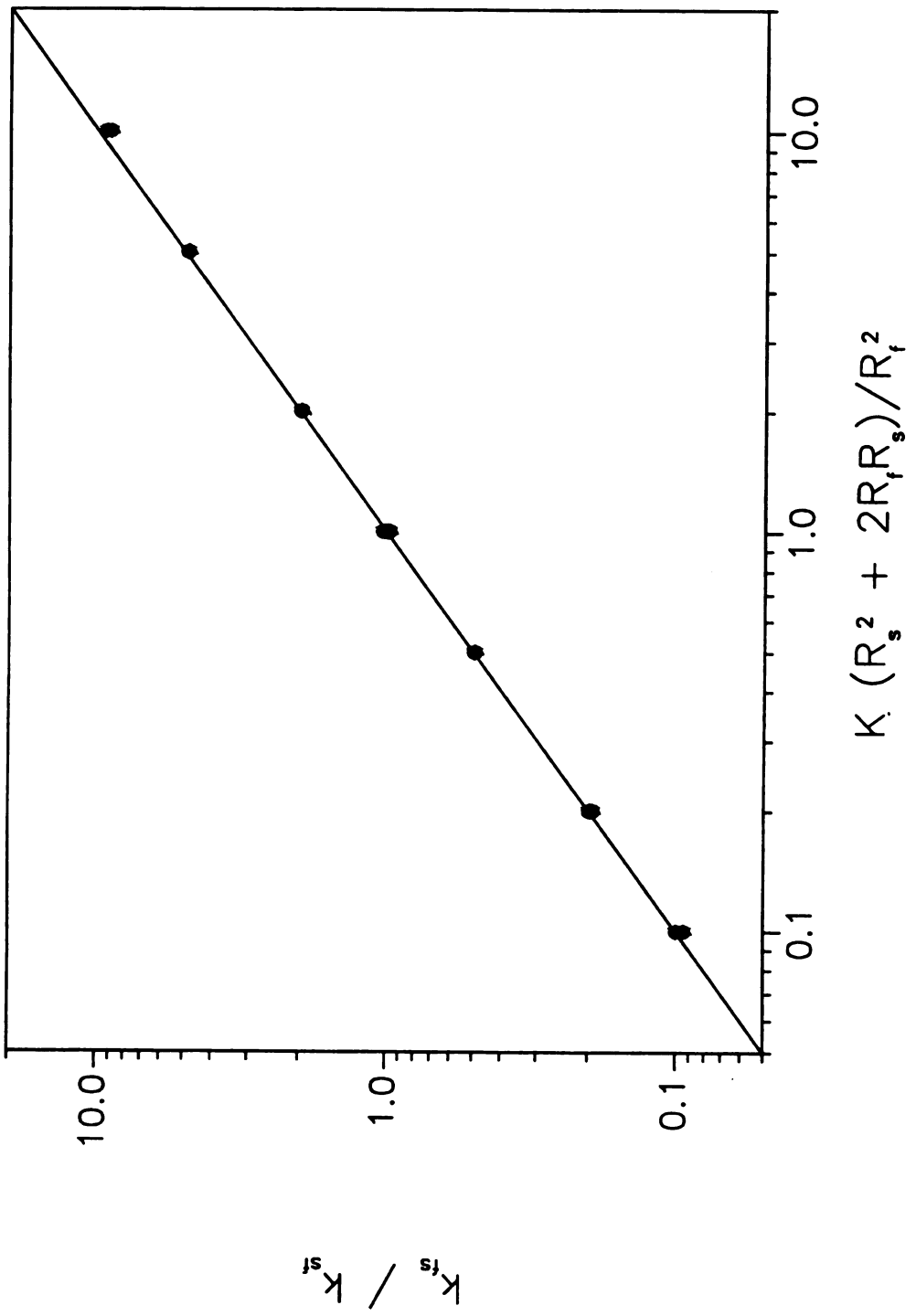

conversely, the rate constant for transport from the surface to fluid phase is dictated by the fraction of molecules in the fluid phase at equilibrium.

The diffusion coefficient in the fluid phase was varied from 1.0×10^{-4} to 1.0×10^{-7} cm^2 s^{-1} and the diffusion coefficient in the surface phase was varied from 1.0×10^{-4} to 1.0×10^{-10} cm^2 s^{-1}, with all other parameters remaining constant. The effect of the variation in diffusion coefficient on the individual rate constants is summarized in Table 4.2. It is apparent that both k_{fs} and k_{sf} increase with an increase in the diffusion coefficients in the fluid and surface phases. Upon detailed examination, the following relationships are elucidated:

$$k_{fs} \propto \left(\frac{1}{D_f}+\frac{1}{D_s}\right)^{-1} \qquad [4.13]$$

$$k_{sf} \propto \left(\frac{1}{D_f}+\frac{1}{D_s}\right)^{-1} \qquad [4.14]$$

These relationships indicate that the rate constants are controlled by the reduced diffusion coefficient of the system. When the diffusion coefficients in the surface and fluid phases are of comparable magnitude, both have a manifest influence upon the rate constants. However, when one diffusion coefficient is notably smaller than the other, it serves to limit the overall transport rate.

The radius of the fluid phase was varied from 1.13×10^{-3} to 8.33×10^{-2} cm and the radius of the surface phase was varied from 9.76×10^{-5} to 4.63×10^{-3} cm, with all other parameters remaining constant. These radii result in a volume ratio of the fluid and surface phases (V_s/V_f) ranging from 0.02 to 10.0. The effect of the variation in radius on

the individual rate constants is summarized in Table 4.3. Both k_{fs} and k_{sf} decrease in a complex manner with an increase in the radius of either the fluid or surface phase. The following relationships appear to be applicable:

$$k_{fs} \propto \left(\frac{2R_f R_s + R_s^2}{R_f^2 + 2R_f R_s + R_s^2} \right) \left(\frac{(R_f + \pi R_s)^2}{\sqrt{(\pi R_f + \pi R_s) R_f^3 \; R_s^2}} \right) \qquad [4.15]$$

$$k_{sf} \propto \left(\frac{R_f^2}{R_f^2 + 2R_f R_s + R_s^2} \right) \left(\frac{(R_f + \pi R_s)^2}{\sqrt{(\pi R_f + \pi R_s) R_f^3 \; R_s^2}} \right) \qquad [4.16]$$

These relationships suggest that there are two important radius-dependent contributions, one of which is common and the other specific to the individual rate constants. The specific contribution, shown in the left-hand term of Equations [4.15] and [4.16], indicates that the rate of transport from fluid to surface phase depends on the volume ratio of the surface phase to the total system. Conversely, the rate of transport from surface to fluid phase depends on the volume ratio of the fluid phase to the total system. The common contribution, shown in the right-hand term of Equations [4.15] and [4.16], suggests that the radii of the fluid and surface phases operate in a concerted manner if they are of comparable magnitude. However, if one radius is notably larger than the other, it predominantly controls the overall transport rate.

Upon appropriate combination of Equations [4.11] through [4.16], the following expressions for the rate constants are obtained:

$$k_{fs} = \left(\frac{K_{abs}\left(2R_f R_s + R_s^2\right)}{R_f^2 + K_{abs}\left(2R_f R_s + R_s^2\right)} \right) \times \left(\sqrt{\frac{1}{D_f} + \frac{1}{D_s}} \right)^{-1} \left(\sqrt{\frac{\pi R_f}{D_f} + \frac{\pi R_s}{D_s}} \right)^{-1} \left(\frac{\left(R_f + \pi R_s\right)^2}{\sqrt{R_f^3 R_s^2}} \right) \quad [4.17]$$

$$k_{sf} = \left(\frac{R_f^2}{R_f^2 + K_{abs}\left(2R_f R_s + R_s^2\right)} \right) \times \left(\sqrt{\frac{1}{D_f} + \frac{1}{D_s}} \right)^{-1} \left(\sqrt{\frac{\pi R_f}{D_f} + \frac{\pi R_s}{D_s}} \right)^{-1} \left(\frac{\left(R_f + \pi R_s\right)^2}{\sqrt{R_f^3 R_s^2}} \right) \quad [4.18]$$

These equations indicate that the term involving the absorption coefficient in Equations [4.11] and [4.12] is coupled with that for the volume of the fluid and surface phases in Equations [4.15] and [4.16]. This coupling is intuitively meaningful, since the capacity factor in Equation [4.8] is defined by this relationship. In addition, the reduced diffusion coefficient in Equations [4.13] and [4.14] is coupled, in part, to the reduced radius in Equations [4.15] and [4.16]. This coupling is also meaningful, since it denotes the rate of diffusion relative to the distance over which that diffusion occurs. Figures 4.4A and 4.4B demonstrate the excellent agreement obtained between the rate constants determined by the stochastic simulation and those predicted by Equations [4.17] and [4.18] over the entire range of parameters given in Tables 4.1 to 4.3. From linear regression analysis of k_{fs} and k_{sf} according to Equations [4.17] and [4.18], the slopes are 1.01 and 1.11, respectively, the intercepts are -0.02 and -0.60, respectively, and the square of the linear correlation coefficients (r^2) are 0.989 and 0.999, respectively. Because the slopes appear to be nearly unity and the intercepts appear to be nearly zero, this suggests that all important parameters have been considered. In addition, the ratio of the rate constants

Figure 4.4: Relationship between the individual rate constants k_{fs} (A) and k_{sf} (B) determined by stochastic simulation and predicted by Equations [4.17] and [4.18]. (——) represents the expected line with a slope one and an intercept of zero. Simulation conditions given in Tables 4.1 to 4.3.

Figure 4.4

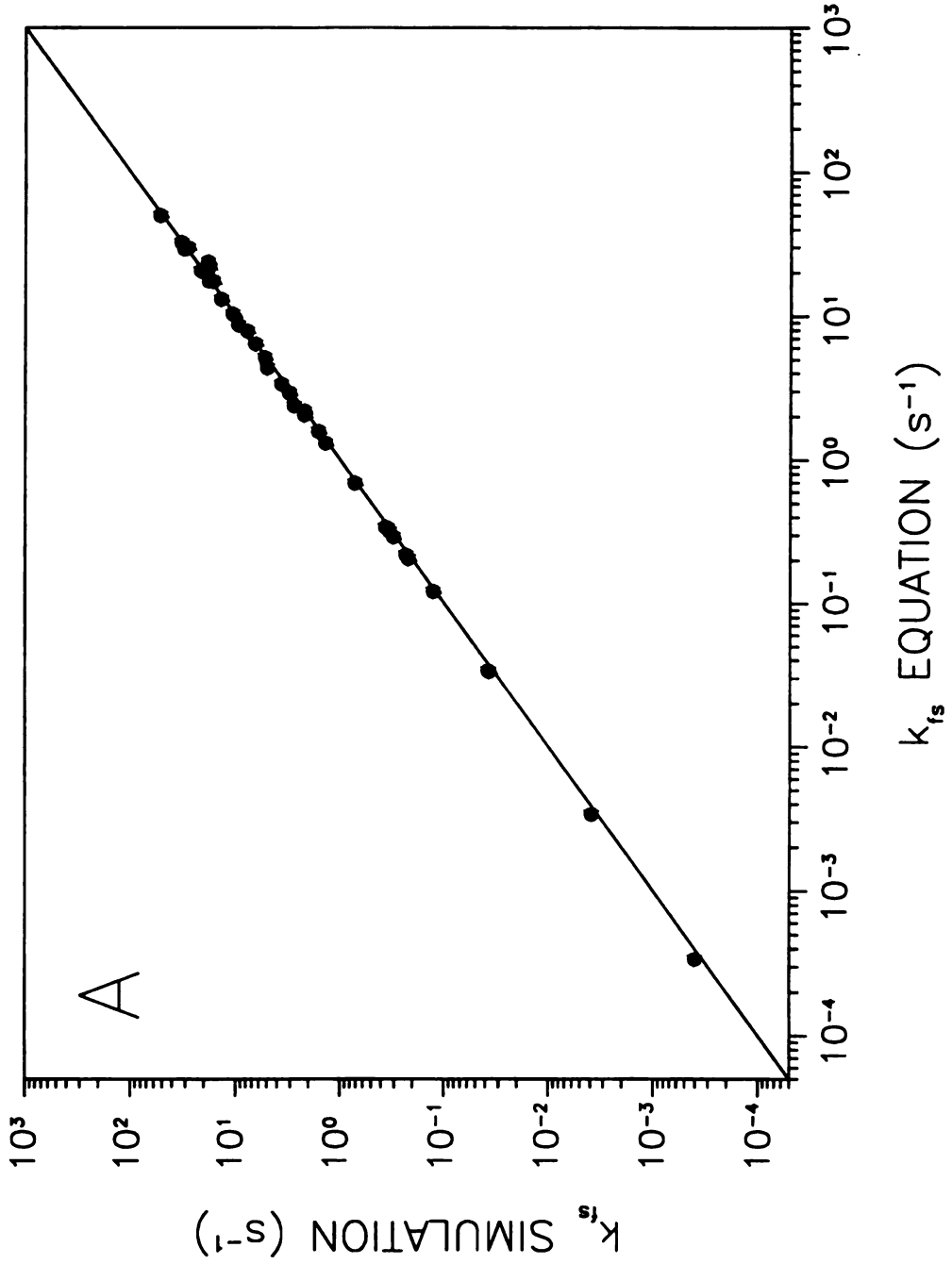
A
k_{fs} SIMULATION (s^{-1})
k_{fs} EQUATION (s^{-1})
10^{3}
10^{2}
10^{1}
10^{0}
10^{-1}
10^{-2}
10^{-3}
10^{-4}

Figure 4.4 cont.

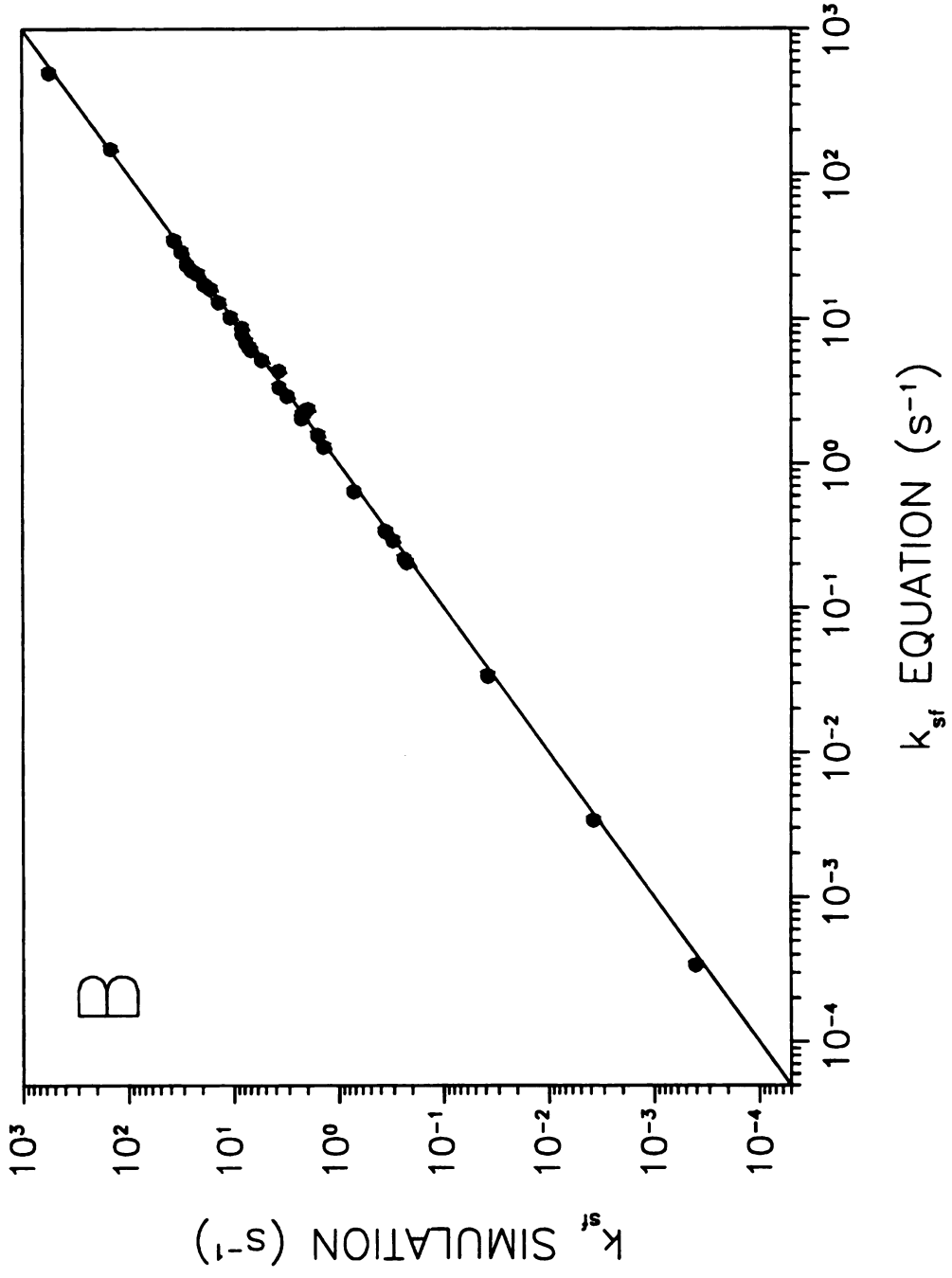

k_{fs}/k_{sf} evaluated by using Equation [4.17] and [4.18] is equivalent to $K_{abs}\ V_s/V_f$, as given by Equations [4.8], [4.9] and [4.10]. Thus, we may conclude that the relationships for the rate constants in a homogeneous fluid and surface phase under diffusion-limited conditions have been fully resolved. The individual rate constants k_{fs} and k_{sf} can be predicted by using Equations [4.17] and [4.18] with average relative errors of ±4.36% and ±6.59%, respectively, in the range from 1×10^{-3} to $1\times10^{3}\ s^{-1}$.

The overall kinetic behavior of the system can be described in terms of the characteristic time τ. This represents the time required for the number of molecules in the fluid phase N_f/N to reach $1 - (1/e)$ of the number at equilibrium $\tilde{N}_f/N$. For the reversible pseudo-first-order system in Equation [4.1], the characteristic time is given by

$$\tau = \left(\frac{1}{k_{fs} + k_{sf}} \right) \qquad [4.19]$$

which can be readily evaluated by substitution of k_{fs} and k_{sf} from Equations [4.17] and [4.18].

Finally, it is desirable to evaluate the sensitivity of the rate constants k_{fs} and k_{sf} as well as the characteristic time τ to changes in the various parameters. This can be easily achieved by calculating the partial derivatives of Equations [4.17], [4.18] and [4.19], e.g. $\partial k_{fs}/\partial K_{abs}$, $\partial k_{sf}/\partial K_{abs}$, $\partial \tau/\partial K_{abs}$, etc., as summarized in Appendix A. It is noteworthy that the derivatives of the rate constants k_{fs} and k_{sf} with respect to the absorption coefficient K_{abs} are opposite in sign. These contributions balance such that the characteristic time τ is independent of K_{abs}. The derivatives of both rate constants with respect to the diffusion coefficients D_f and D_s are positive, leading to a strong negative dependence of the

characteristic time τ. Finally, the derivatives of both rate constants with respect to the radii R_f and R_s are negative, leading to a strong positive dependence of the characteristic time τ. These conclusions are in accord with the general trends observed in Tables 4.1 to 4.3.

4.2.3 Effect of Kinetic Rate Constants on Zone Profiles in Chromatography and Electrochromatography.

In the presence of convective flow, the characteristic time τ will influence the appearance of the solute zone profiles. If τ is sufficiently small, the system will be nearly at equilibrium and the zone profile will be a symmetric Gaussian distribution. Under these conditions, the profile will be well described by the classical equations of mass balance using the equilibrium-dispersive model.[9-12] As τ increases, however, the system may depart from equilibrium and the zone profile may become highly asymmetric. As a measure of the degree of departure from equilibrium for convective systems, we may define a unitless kinetic parameter as the inverse of the Stanton number (St^{-1}) as given in Equation [3.4] This parameter directly reflects the sources of kinetic stress that are placed on the system and will approach a limiting value of zero for a system that is at equilibrium. It is apparent from this definition that kinetic stress arises from the characteristic time τ as well as the linear velocity and the distance traveled.

In order to examine the influence of each of these sources of kinetic stress, a standard system has been selected for stochastic simulation. For a solute with an absorption coefficient $K_{abs} = 1.0$, diffusion coefficients $D_f = 1.0\times10^{-5}$ cm^2 s^{-1} and $D_s =$

1.0×10^{-7} cm^2 s^{-1}, and radii $R_f = 2.00\times10^{-3}$ cm and $R_s = 8.28\times10^{-4}$ cm, the characteristic time τ shown graphically in Figure 4.1 is 1.408 s. The evolution of the corresponding solute zone profile for this system is shown as a function of distance traveled in Figure 4.5A for laminar flow at a fixed linear velocity of 0.1 cm s^{-1}. The initial profile, which is obtained at a distance of 0.1 cm ($St^{-1} = \tau = 1.408$), appears to be highly asymmetric. The degree of asymmetry gradually decreases as the solute zone travels distances of 0.2 cm ($St^{-1} = \tau/2 = 0.704$), 0.5 cm ($St^{-1} = \tau/5 = 0.282$), 1.0 cm ($St^{-1} = \tau/10 = 0.141$), and 2.0 cm ($St^{-1} = \tau/20 = 0.070$). At the final distance of 5.0 cm ($St^{-1} = \tau/50 = 0.028$), there is only a slight appearance of asymmetry. The evolution of the solute zone profile is shown in Figure 4.5B for electroosmotic flow at a fixed linear velocity of 0.1 cm s^{-1}. Again, the degree of asymmetry is high in the initial profile and gradually decreases until it is only slightly apparent in the final profile. The statistical moments of these zone profiles are calculated by means of Equations [2.1] and [2.2], and are shown as a function of distance traveled in Figure 4.6. The first statistical moment, which represents the mean retention time, increases in the theoretically expected linear manner with distance. The second and third statistical moments, which represent the variance and asymmetry, also increase linearly with distance. The skew of the zone profile, represented as $M_3/\sqrt{(M_2)^3}$,[13,14] must therefore decrease with the square root of distance. In other words, the solute zone becomes broader but more symmetric as it traverses the chromatography or electrochromatography system. It is noteworthy that the profiles with laminar flow are not visibly broader or less symmetric than those with electroosmotic flow (*vide infra*).

Figure 4.5: Evolution of the solute zone profile as a function of distance with laminar flow (A) and electroosmotic flow (B). Simulation conditions: $N = 1000$, $t = 5.0\times10^{-5}$ s, $D_f = 1.0\times10^{-5}$ cm^2 s^{-1}, $D_s = 1.0\times10^{-7}$ cm^2 s^{-1}, $R_f = 2.00\times10^{-3}$ cm, $R_s = 8.28\times10^{-4}$ cm, $v_0 = 0.1$ cm s^{-1}, $K_{abs} = 1.0$, $L_{det} = 0.1, 0.2, 0.5, 1.0, 2.0, 5.0$ cm (left to right).

Figure 4.5

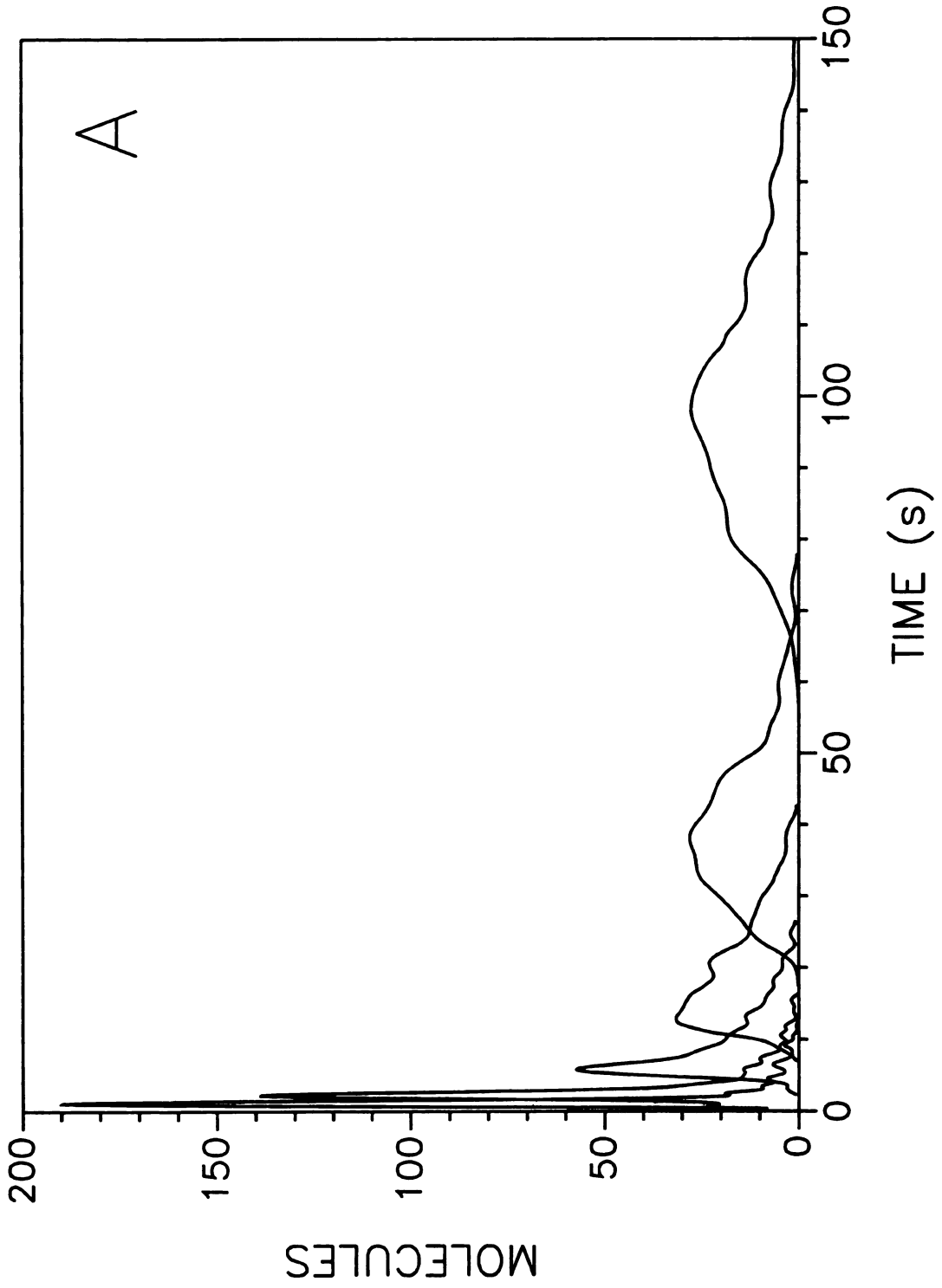

Figure 4.5 cont.

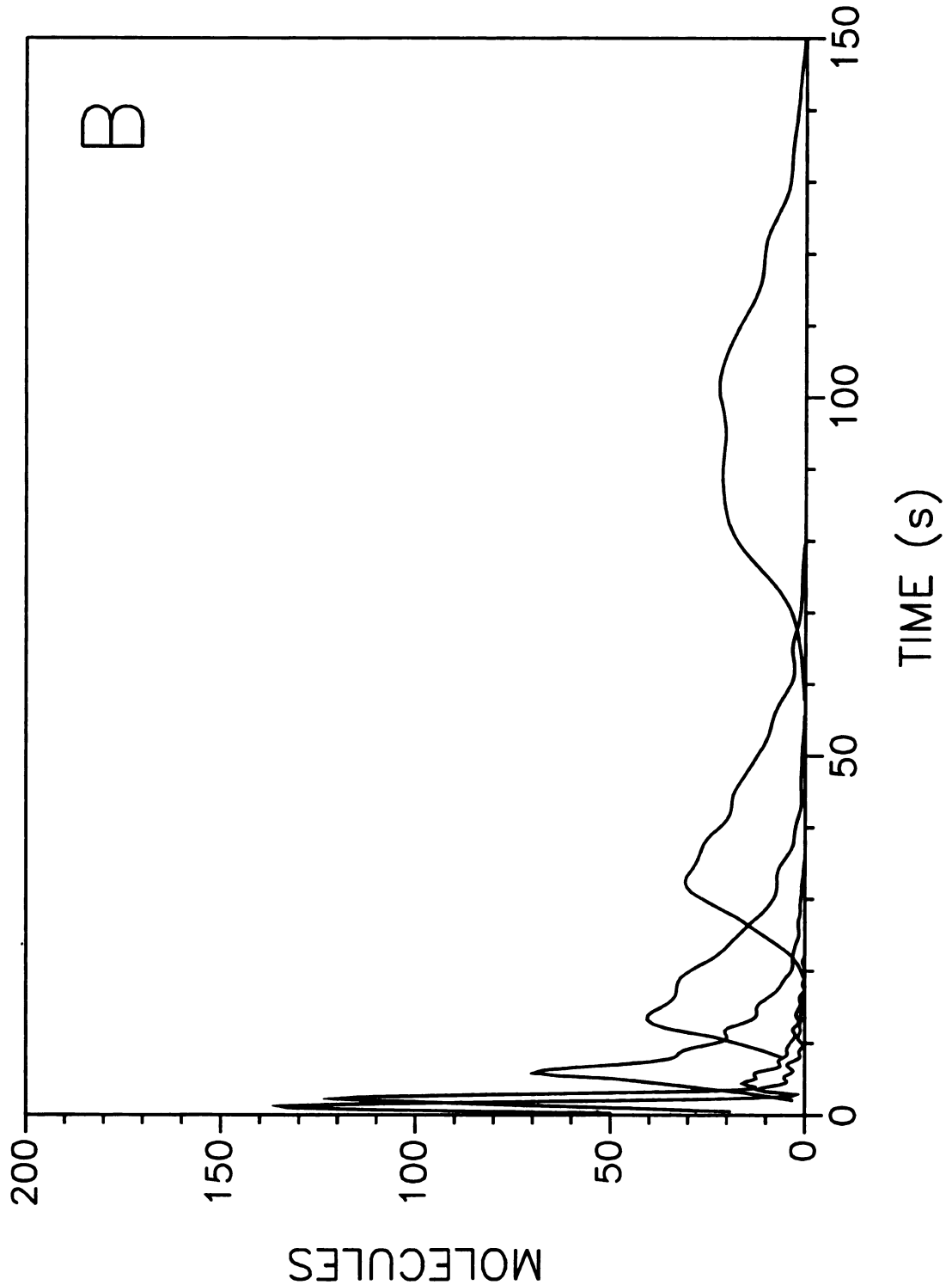

Figure 4.6: First (A), second (B), and third (C) statistical moments of the solute zone profiles as a function of the distance traveled for laminar flow (○) and electroosmotic flow (□). Simulation conditions given in Figure 4.5.

Figure 4.6

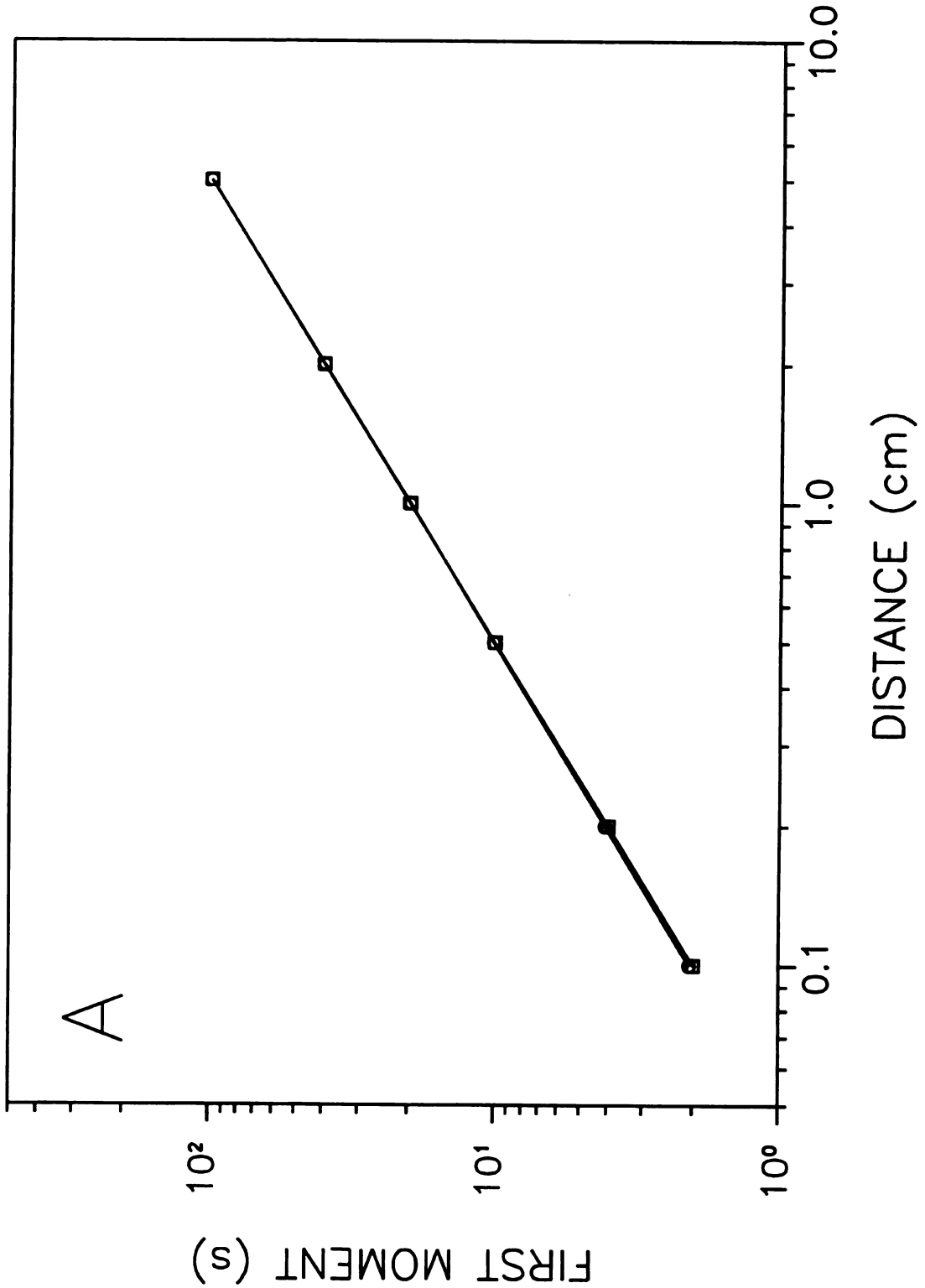

Figure 4.6 cont.

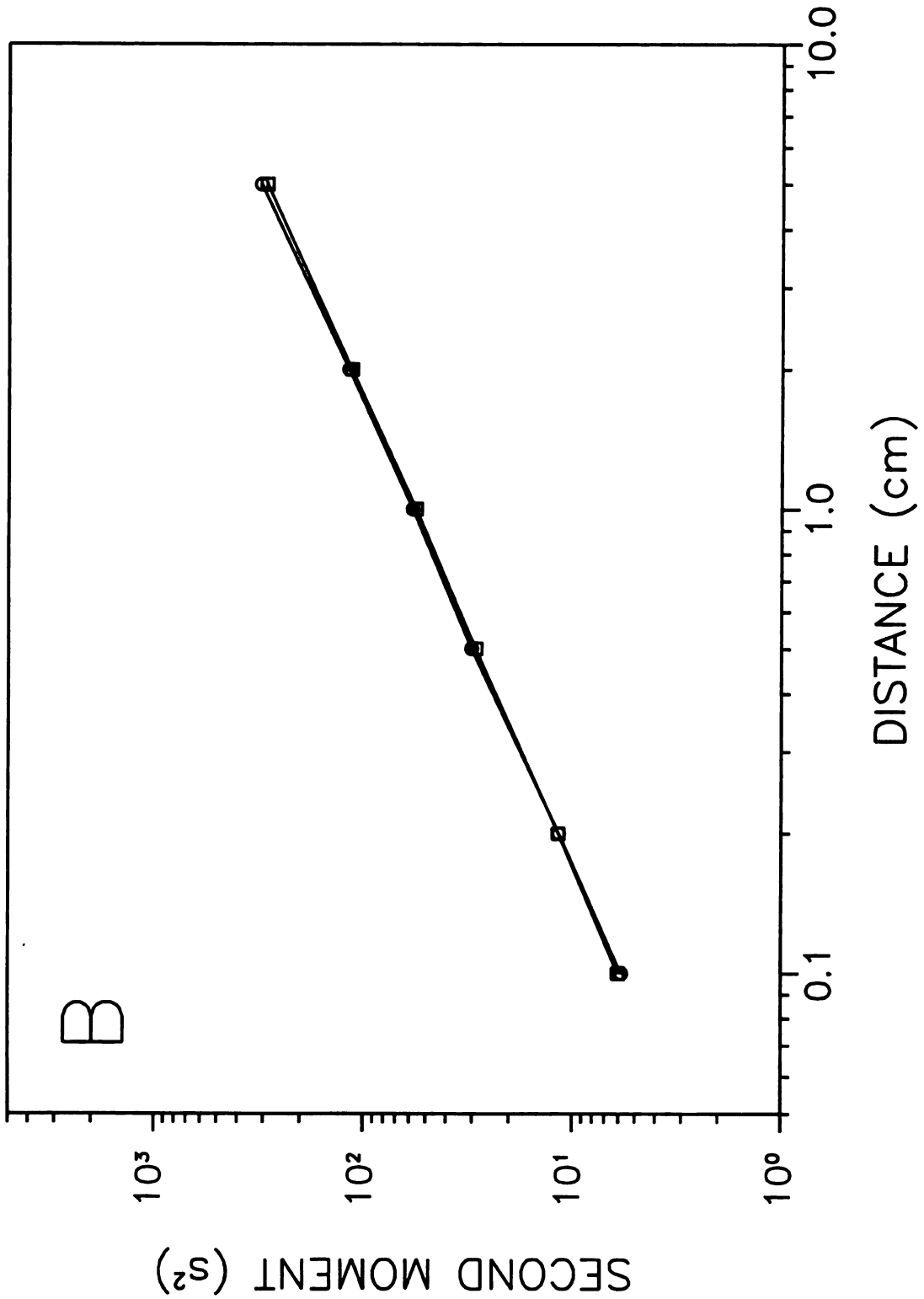

Figure 4.6 cont.

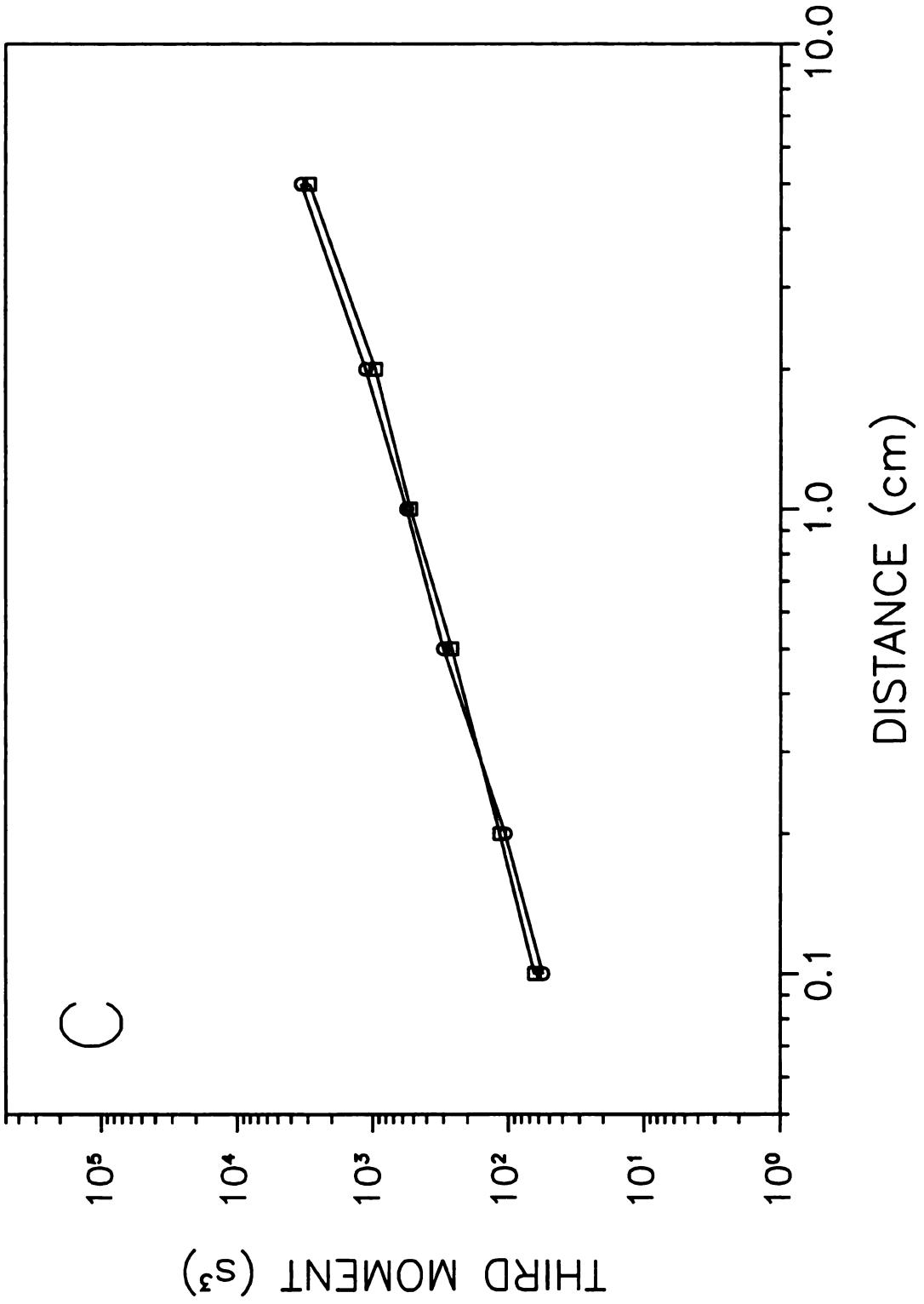

The effect of the linear velocity has been examined at a fixed distance of 5.0 cm and a fixed characteristic time τ for the standard system described above. As shown in Figure 4.7, the solute zone profile becomes increasingly asymmetric as the linear velocity is increased from 0.1 cm s^{-1} ($St^{-1} = \tau/50 = 0.028$) to 1.0 cm s^{-1} ($St^{-1} = \tau/5 = 0.282$). These zone profiles are characterized by means of the statistical moments in Figure 4.8 for both laminar and electroosmotic flow. The first moment varies in the theoretically expected inverse manner with velocity. The second and third moments also vary inversely with velocity. Consequently, the skew $M_3/\sqrt{(M_2)^3}$ must increase with the square root of the velocity. In other words, the solute zone becomes less broad but more skewed as the linear velocity increases.

The effect of the characteristic time τ has been examined at a fixed linear velocity of 0.1 cm s^{-1} and a fixed distance of 5.0 cm. Although any of the parameters in Equations [4.17] and [4.18] may be used, we have chosen to vary the parameter that has the greatest influence upon τ. By evaluation of the partial derivatives given in the Appendix under the conditions of the standard system, $\partial\tau/\partial K_{abs} = 0$, $\partial\tau/\partial D_f = -2.5\times10^3$, $\partial\tau/\partial D_s = -1.5\times10^7$, $\partial\tau/\partial R_f = 4.8\times10^2$, and $\partial\tau/\partial R_s = 6.0\times10^3$. From this analysis, it is apparent that the diffusion coefficient in the surface phase has the most significant effect. As shown in Figure 4.9, the solute zone profile is symmetric for diffusion coefficients of 1.0×10^{-5} cm^2 s^{-1} ($St^{-1} = 0.0007$) and 1.0×10^{-6} cm^2 s^{-1} ($St^{-1} = 0.003$), becomes slightly asymmetric for 1.0×10^{-7} cm^2 s^{-1} ($St^{-1} = 0.028$), and highly asymmetric for 1.0×10^{-8} cm^2 s^{-1} ($St^{-1} = 0.261$). These zone profiles are characterized by means of the statistical moments in Figure 4.10

Figure 4.7: Solute zone profile as a function of the linear velocity of laminar flow.

Simulation conditions: $N = 1000$, $t = 5.0\times10^{-5}$ s, $D_f = 1.0\times10^{-5}$ cm^2 s^{-1}, $D_s = 1.0\times10^{-7}$ cm^2 s^{-1}, $R_f = 2.00\times10^{-3}$ cm, $R_s = 8.28\times10^{-4}$ cm, $K_{abs} = 1.0$, $v_0 = 0.1$ cm s^{-1} (—), 0.2 cm s^{-1} (— — —), 0.5 cm s^{-1} (– – –), 1.0 cm s^{-1} (- - -), $L_{det} = 5.0$ cm.

Figure 4.7

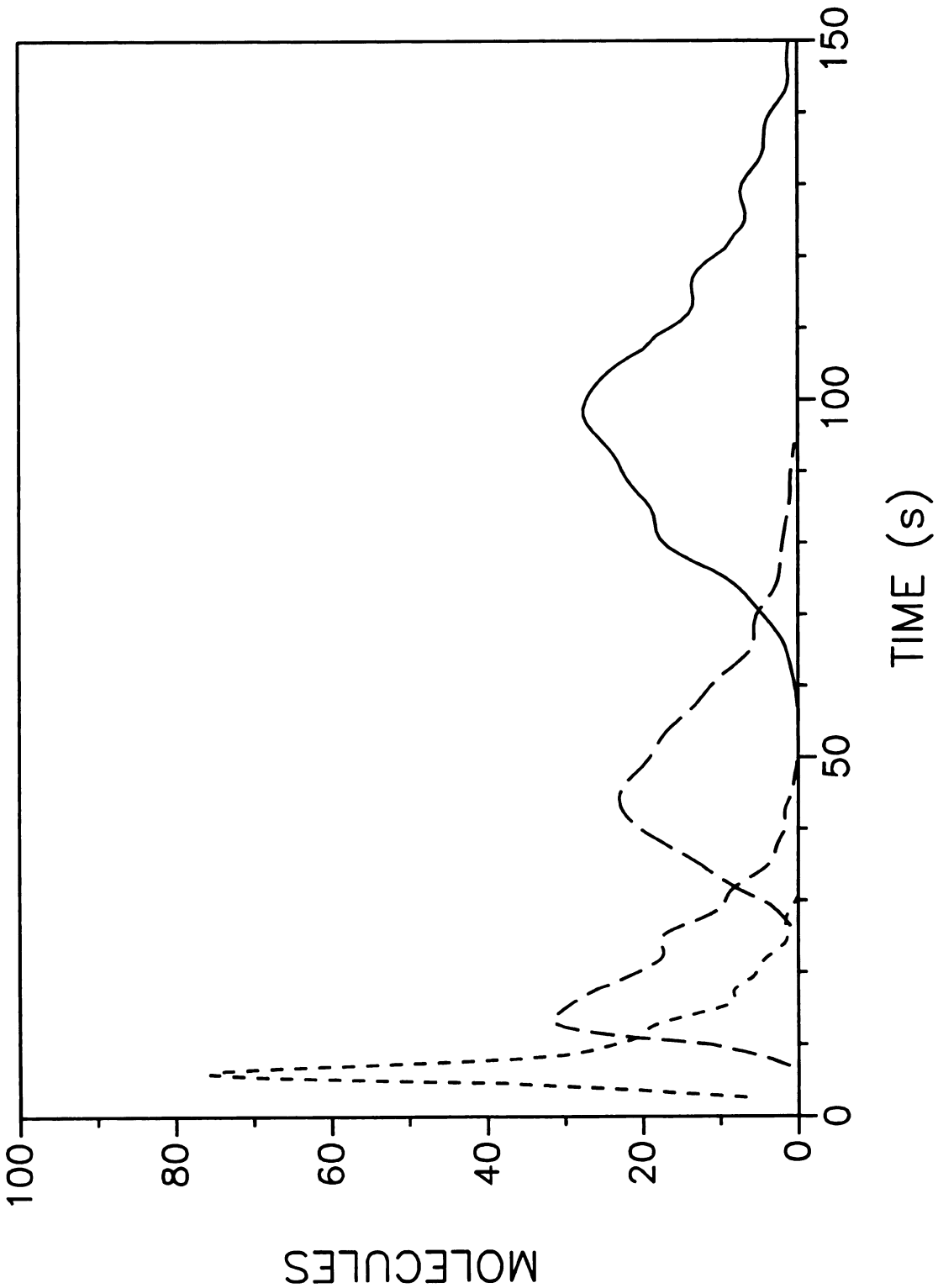

Figure 4.8: First (A), second (B), and third (C) statistical moments of the solute zone profiles as a function of the linear velocity for laminar flow (○) and electroosmotic flow (□). Simulation conditions given in Figure 4.7.

Figure 4.8

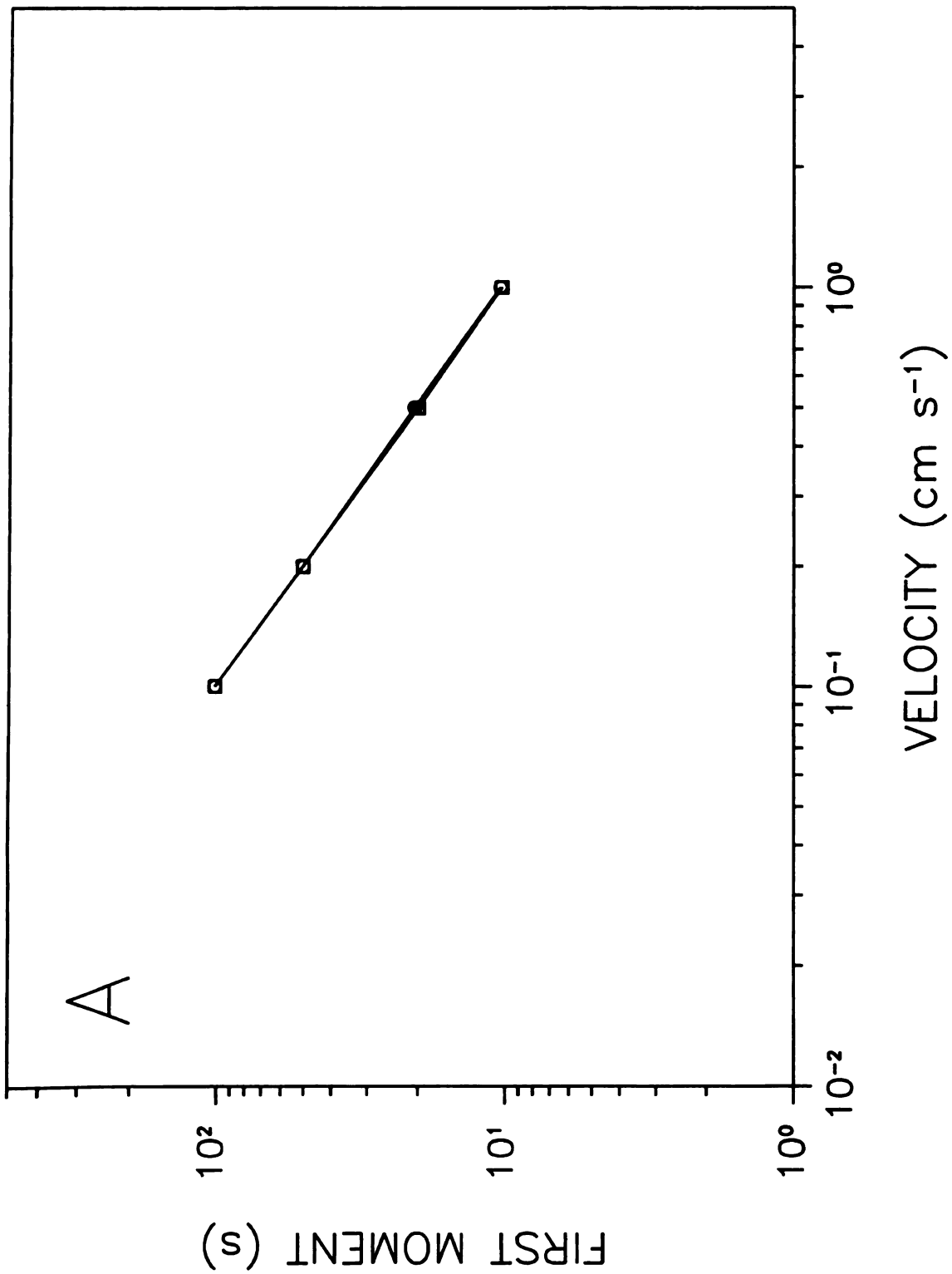

Figure 4.8 cont.

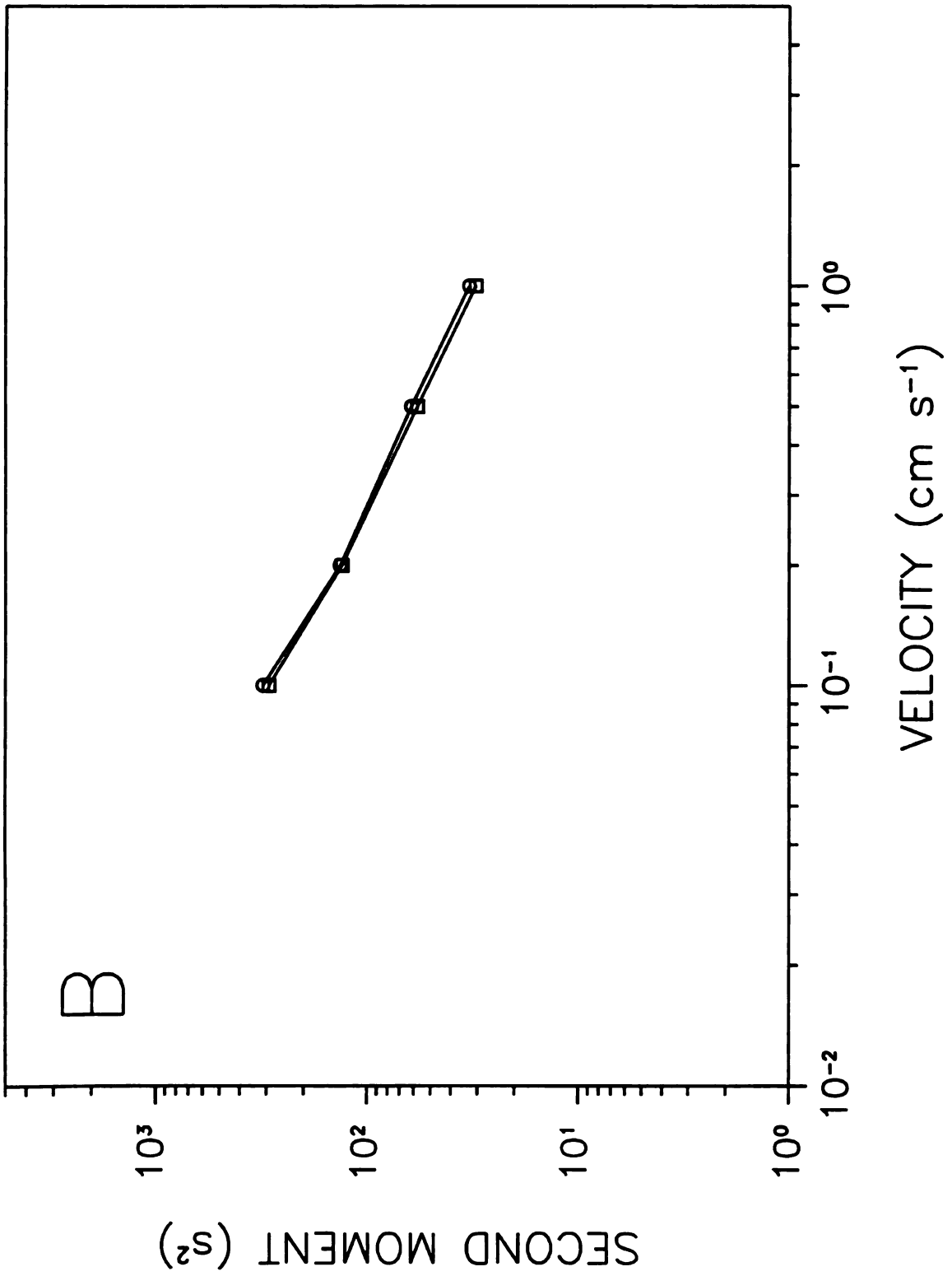

Figure 4.8 cont.

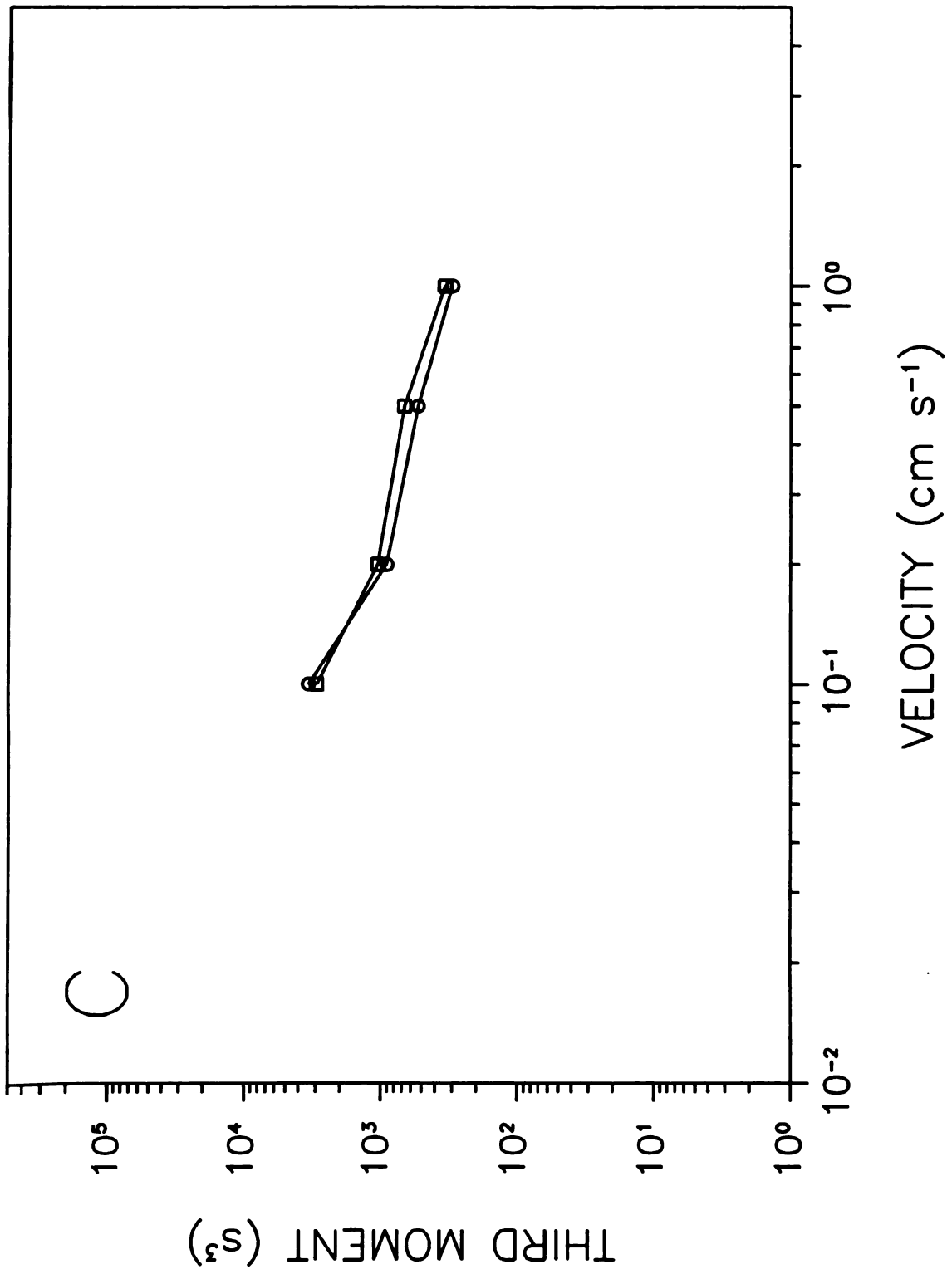

Figure 4.9: Solute zone profile as a function of the diffusion coefficient in the surface phase. Simulation conditions: $N = 1000$, $t = 5.0\times10^{-5}$ s, $D_f = 1.0\times10^{-5}$ cm^2 s^{-1}, $D_s = 1.0\times10^{-5}$ cm^2 s^{-1} (- - -), 1.0×10^{-6} cm^2 s^{-1} (– – –), 1.0×10^{-7} cm^2 s^{-1} (—), 1.0×10^{-8} cm^2 s^{-1} (— — —), $R_f = 2.00\times10^{-3}$ cm, $R_s = 8.28\times10^{-4}$ cm, $K_{abs} = 1.0$, $v_0 = 0.1$ cm s^{-1}, $L_{det} = 5.0$ cm.

Figure 4.9

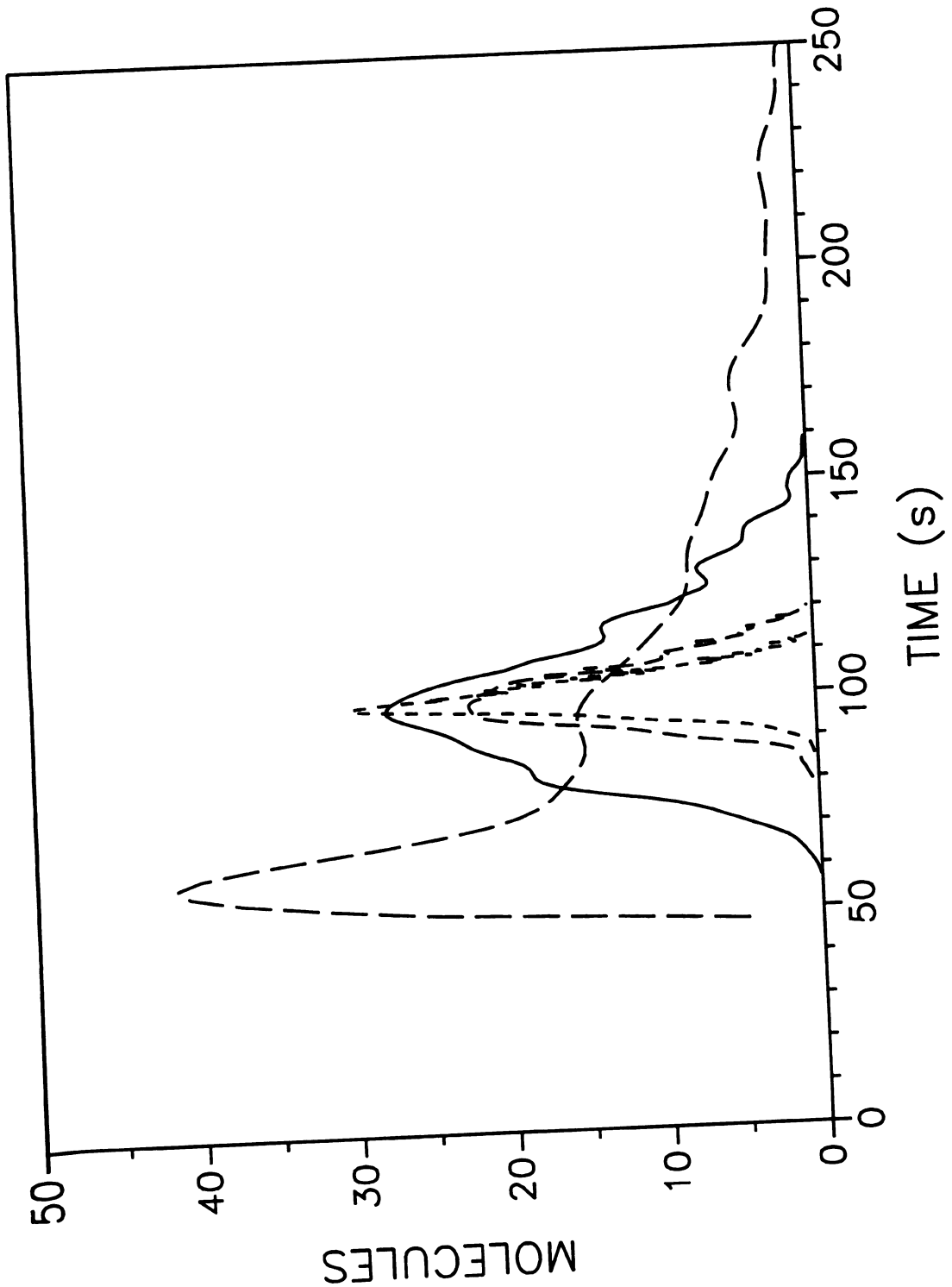

Figure 4.10: First (A), second (B), and third (C) statistical moments of the solute zone profiles as a function of the characteristic time τ for laminar flow (○) and electroosmotic flow (□). Simulation conditions given in Figure 4.9.

Figure 4.10

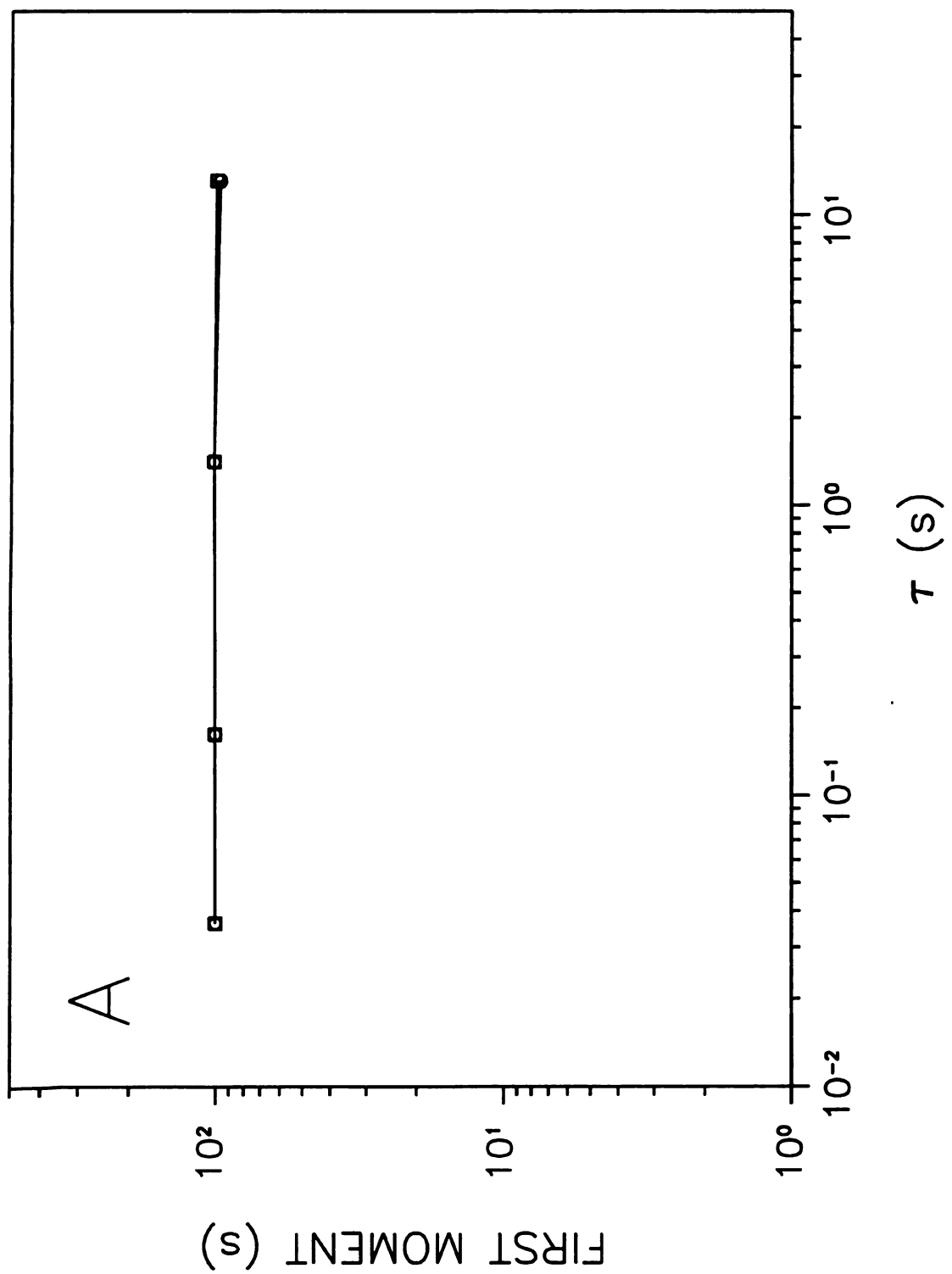

Figure 4.10 cont.

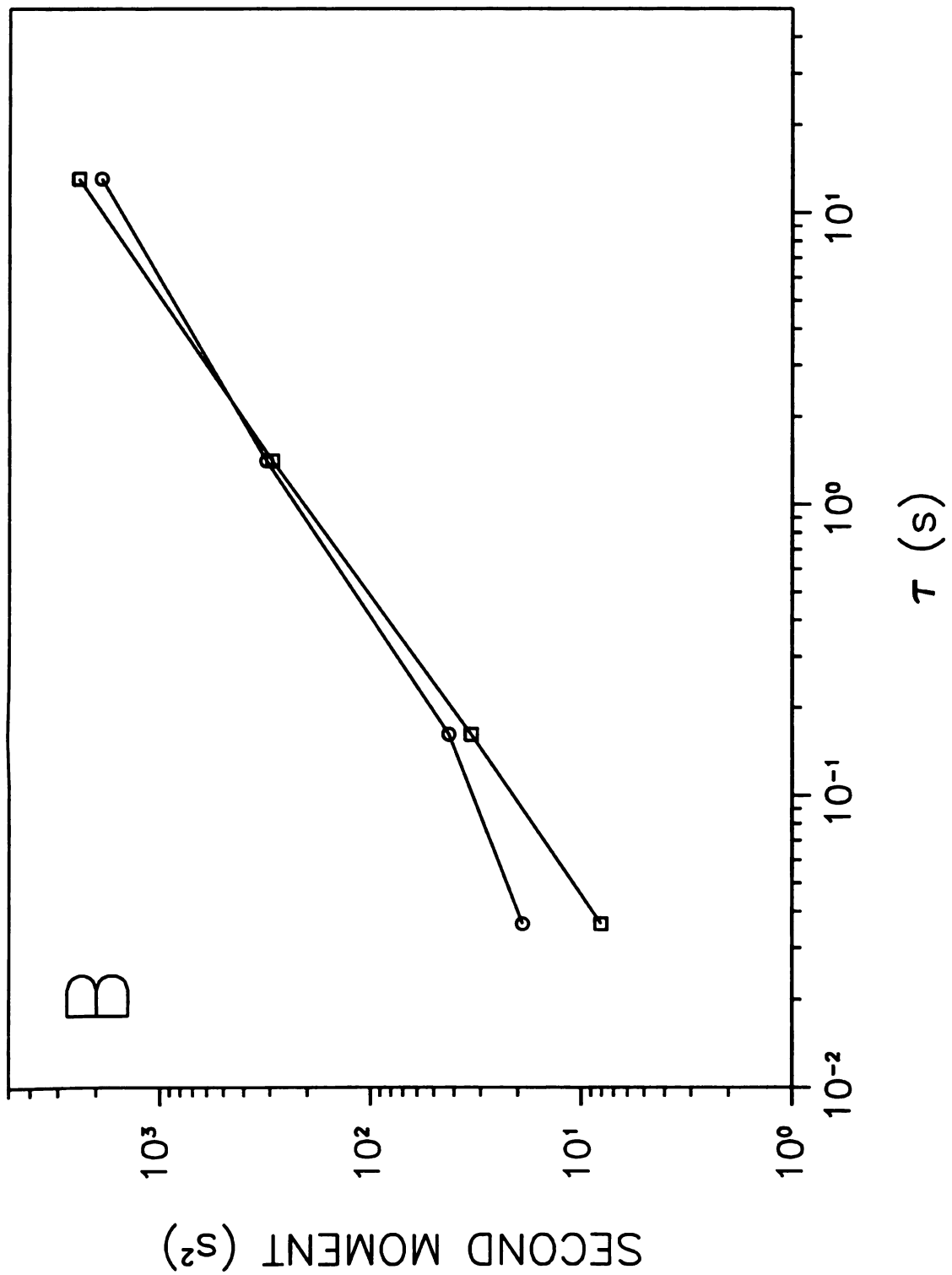

Figure 4.10 cont.

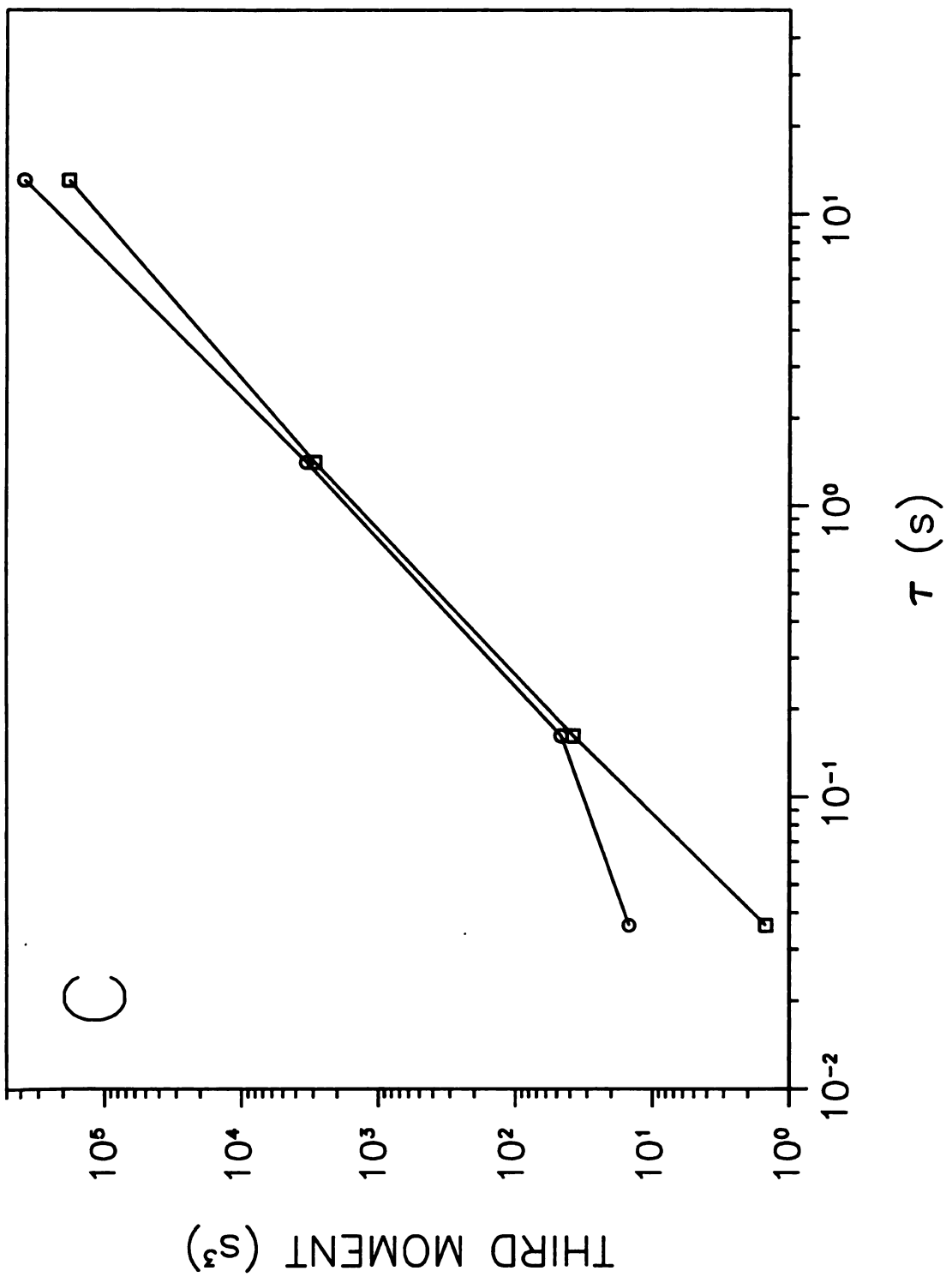

for both laminar and electroosmotic flow. The first moment is independent of the characteristic time τ. The second moment increases linearly with τ and the third moment increases with the square of τ. Consequently, the skew $M_3/\sqrt{(M_2)^3}$ must increase with the square root of τ. Thus, the solute zone will become broader and more skewed as the characteristic time τ increases and will have the relationships given in Equations [4.17] and [4.18] to the parameters of the system.

As noted previously, the solute zone profiles with laminar and electroosmotic flow are indistinguishable at higher values of τ (Figure 4.10). At the lowest value of τ, however, the radial flow profile begins to have a manifest influence. The parabolic flow profile characteristic of laminar flow causes a greater increase in variance and asymmetry than the nearly flat flow profile of electroosmotic flow. It is noteworthy that this influence is only discernible for diffusion coefficients in the stationary phase on the order of 1.0×10^{-5} cm^2 s^{-1} for the system examined here. For more typical values of the diffusion coefficient, on the order of 1.0×10^{-7} to 1.0×10^{-9} cm^2 s^{-1},[15-17] dispersion arising from the radial flow profile is negligible in comparison with that from kinetic contributions. Hence, it seems prudent to reevaluate the potential benefits to be gained by electrochromatography compared with traditional chromatography as well as the requisite conditions for their achievement.[18]

4.3 Conclusions.

From the stochastic simulation approach, a greatly improved understanding is derived of the kinetic processes involved in the absorption mechanism. The diffusion-

limited rate constants can now be predicted via Equations [4.17] and [4.18] for any simple system consisting of a homogeneous fluid phase in contact with a homogeneous surface phase. In addition, the effect of these rate constants on the solute zone profile (mean, variance, and asymmetry) can be readily predicted. This simulation approach can now be applied to more complex separation mechanisms, such as absorption or adsorption at multiple sites or a combined absorption-adsorption mechanism. These types of studies are essential if the retention and dispersion processes inherent in complex chromatographic and electrophoretic systems are to be understood and controlled.

4.4 References.

1. Giddings, J.C.; J. Chromatogr. 1959, 2, 44.
2. Giddings, J.C.; J. Chem. Phys. 1959, 31 1462.
3. Giddings, J.C.; J. Chromatogr. 1960, 3 , 443.
4. Giddings, J.C.; J. Chromatogr. 1961, 5, 61.
5. Giddings, J.C.; Dynamics of Chromatography; Marcel Dekker: New York, NY, 1965.
6. Steinfeld, J.I.; Francisco, J.S.; Hase, W.L.; Chemical Kinetics and Dynamics; Prentice Hall: Englewood Cliffs, NJ, 1989.
7. Benson, S.W.; Foundations of Chemical Kinetics; McGraw-Hill: New York, NY, 1960.
8. Wu, P.; McGuffin, V.L.; AIChE J. 1998, 44, 2053.
9. Bird, R.B.; Stewart, W.E.; Lightfoot, E.N.; Transport Phenomena; Wiley: New York, NY, 1960.
10. Sherwood, T.K.; Pigford, R.L.; Wilke, C.R.; Mass Transfer; McGraw-Hill: New York, NY, 1975.

11. Hines, A.L.; Maddox, R.N.; Mass Transfer: Fundamentals and Applications; Prentice-Hall: Englewood Cliffs, NJ, 1985.

12. Golshan-Shirazi, S.; Guiochon, G.; in Theoretical Advancement in Chromatography and Related Separation Techniques, Dondi, F.; Guiochon, G. Eds.; Kluwer: Amsterdam, 1992; pp. 61-92.

13. Cramer, H.; Mathematical Methods of Statistics; Princeton University Press: Princeton, NJ, 1946.

14. Grushka, E.; J. Phys. Chem. 1972, 76, 2586.

15. Bogar, R.G.; Thomas, J.C.; Callis, J.B.; Anal. Chem. 1984, 56, 1080.

16. Zuli, S.L.; Kovaleski, J.M.; Zhu, X.R.; Harris, J.M.; Wirth, M.J.; Anal. Chem. 1994, 66, 1708.

17. Hansen, R.L.; Harris, J.M.; Anal. Chem. 1995, 67, 492.

18. Robson, M.M.; Cikalo, M.G.; Myers, P.; Euerby, M.R.; Bartle, K.D.; J. Microcolumn Sep. 1997, 9, 357.

Appendix A

Derivatives of the Mass-Transfer Rate Constants k_{fs} and k_{sf} With Respect to Molecular and System Parameters

The derivative of the characteristic time τ with respect to any variable x is obtained by applying the chain rule:

$$\frac{\partial \tau}{\partial x} = \frac{\partial \tau}{\partial k_{fs}} \frac{\partial k_{fs}}{\partial x} + \frac{\partial \tau}{\partial k_{sf}} \frac{\partial k_{sf}}{\partial x} \qquad [A.1]$$

From Equation [A.1], it can easily be shown that the derivative of t with respect to the individual rate constants k_{fs} and k_{sf} is given by

$$\frac{\partial \tau}{\partial k_{fs}} = \frac{\partial \tau}{\partial k_{sf}} = \frac{-1}{\left(k_{fs} + k_{sf}\right)^2} = -\tau^2 \qquad [A.2]$$

By replacing x in Equation [A.1] with one of the system parameters from Equations [3.17] or [3.18], the effect of the parameter on the magnitude of τ can be evaluated. The resulting derivatives of the rate constants with respect to each of the system parameters are given below. For the absorption coefficient K_{abs}:

$$\frac{\partial k_{fs}}{\partial K_{abs}} = \left(\frac{R_f^2 \left(2 R_f R_s + R_s^2\right)}{\left[R_f^2 + K_{abs}\left(2 R_f R_s + R_s^2\right)\right]^2} \right) \times \left(\sqrt{\frac{1}{D_f} + \frac{1}{D_s}} \right)^{-1} \left(\sqrt{\frac{\pi R_f}{D_f} + \frac{\pi R_s}{D_s}} \right)^{-1} \left(\frac{\left(R_f + \pi R_s\right)^2}{\sqrt{R_f^3 R_s^2}} \right) \qquad [A.3]$$

$$\frac{\partial k_{sf}}{\partial K_{abs}} = \left(\frac{-R_f^2\left(2R_f R_s + R_s^2\right)}{\left[R_f^2 + K_{abs}\left(2R_f R_s + R_s^2\right)\right]^2} \right) \times$$
$$\left(\sqrt{\frac{1}{D_f} + \frac{1}{D_s}} \right)^{-1} \left(\sqrt{\frac{\pi R_f}{D_f} + \frac{\pi R_s}{D_s}} \right)^{-1} \left(\frac{(R_f + \pi R_s)^2}{\sqrt{R_f^3 R_s^2}} \right) \qquad [A.4]$$

For the diffusion coefficient in the fluid phase D_f:

$$\frac{\partial k_{fs}}{\partial D_f} = \left(\frac{K_{abs}\left(2R_f R_s + R_s^2\right)}{R_f^2 + K_{abs}\left(2R_f R_s + R_s^2\right)} \right) \times$$
$$\left(\frac{D_s^2\left[2\pi R_f D_s + \pi D_f (R_f + R_s)\right]}{2\sqrt{\left[(D_f + D_s)(\pi R_f D_s + \pi R_s D_f)\right]^3}} \right) \left(\frac{(R_f + \pi R_s)^2}{\sqrt{R_f^3 R_s^2}} \right) \qquad [A.5]$$

$$\frac{\partial k_{sf}}{\partial D_f} = \left(\frac{R_f^2}{R_f^2 + K_{abs}\left(2R_f R_s + R_s^2\right)} \right) \times$$
$$\left(\frac{D_s^2\left[2\pi R_f D_s + \pi D_f (R_f + R_s)\right]}{2\sqrt{\left[(D_f + D_s)(\pi R_f D_s + \pi R_s D_f)\right]^3}} \right) \left(\frac{(R_f + \pi R_s)^2}{\sqrt{R_f^3 R_s^2}} \right) \qquad [A.6]$$

For the diffusion coefficient in the surface phase D_s:

$$\frac{\partial k_{fs}}{\partial D_s} = \left(\frac{K_{abs}\left(2R_f R_s + R_s^2\right)}{R_f^2 + K_{abs}\left(2R_f R_s + R_s^2\right)} \right) \times$$
$$\left(\frac{D_f^2\left[2\pi R_s D_f + \pi D_s (R_f + R_s)\right]}{2\sqrt{\left[(D_f + D_s)(\pi R_f D_s + \pi R_s D_f)\right]^3}} \right) \left(\frac{(R_f + \pi R_s)^2}{\sqrt{R_f^3 R_s^2}} \right) \qquad [A.7]$$

$$\frac{\partial k_{sf}}{\partial D_s} = \left(\frac{R_f^2}{R_f^2 + K_{abs}\left(2R_f R_s + R_s^2\right)} \right) \times$$

$$\left(\frac{D_f^2\left[2\pi R_s D_f + \pi D_s\left(R_f + R_s\right)\right]}{2\sqrt{\left[\left(D_f + D_s\right)\left(\pi R_f D_s + \pi R_s D_f\right)\right]^3}} \right) \left(\frac{\left(R_f + \pi R_s\right)^2}{\sqrt{R_f^3 R_s^2}} \right) \qquad [A.8]$$

For the radius of the fluid phase R_f:

$$\frac{\partial k_{fs}}{\partial R_f} = k_{fs}\left(-\frac{3}{2R_f} + \frac{2}{R_f + \pi R_s} + \frac{2\pi R_s}{2R_f R_s + R_s^2} \right.$$

$$\left. - \frac{2\pi\left(R_f + K_{abs} R_s\right)}{R_f^2 + K_{abs}\left(2R_f R_s + R_s^2\right)} - \frac{\pi D_s}{2\pi\left(R_f D_s + R_s D_f\right)} \right) \qquad [A.9]$$

$$\frac{\partial k_{sf}}{\partial R_f} = k_{sf}\left(\frac{1}{2R_f} + \frac{2}{R_f + \pi R_s} \right.$$

$$\left. - \frac{2\pi\left(R_f + K_{abs} R_s\right)}{R_f^2 + K_{abs}\left(2R_f R_s + R_s^2\right)} - \frac{\pi D_s}{2\pi\left(R_f D_s + R_s D_f\right)} \right) \qquad [A.10]$$

For the radius of the surface phase R_s:

$$\frac{\partial k_{fs}}{\partial R_s} = k_{fs}\left(-\frac{2}{R_s} + \frac{2\pi}{R_f + \pi R_s} + \frac{2\pi\left(R_f + R_s\right)}{2R_f R_s + R_s^2} \right.$$

$$\left. - \frac{2\pi K_{abs}\left(R_f + R_s\right)}{R_f^2 + K_{abs}\left(2R_f R_s + R_s^2\right)} - \frac{\pi D_f}{2\pi\left(R_f D_s + R_s D_f\right)} \right) \qquad [A.11]$$

$$\frac{\partial k_{sf}}{\partial R_s} = k_{sf}\left(-\frac{2}{R_f} + \frac{2\pi}{R_f + \pi R_s} \right.$$

$$\left. - \frac{2\pi K_{abs}\left(R_f + R_s\right)}{R_f^2 + K_{abs}\left(2R_f R_s + R_s^2\right)} - \frac{\pi D_f}{2\pi\left(R_f D_s + R_s D_f\right)} \right) \qquad [A.12]$$

where k_{fs} and k_{sf} are given by Equations [3.17] and [3.18]. Equations [4.3] through [4.12] can be substituted into Equation [4.1] to obtain $\partial\tau/\partial x$, the slope of the graph of the characteristic time τ with respect to the chosen parameter.

Chapter 5

Stochastic Simulation of the Absorption Mechanism in Chromatography With a Heterogeneous Surface Phase

5.1 Introduction.

It has long been recognized that surfaces are not homogeneous. This fact has been considered in many models of adsorption chromatography.[1-6] Interestingly, no model of heterogeneous phases has been applied to an absorption system. Yet, there are many circumstances when the stationary phase may be considered inhomogeneous in absorption systems. In some cases, the heterogeneity is introduced intentionally. For example, mixtures of different stationary phases have been used for both gas chromatography[7,8] and liquid chromatography.[9-11] In other cases, the heterogeneity is an unintentional and often undesirable aspect of the system. Such heterogeneities have been found through surface studies of the chromatographic stationary phases. Lochmuller *et al.* have studied alkyl chain organization on silica supports and found that, for low coverage of the support, the chains tend to group together and form islands.[12] Other studies have examined the selectivity[13] as well as the possibility of phase transitions[14] in stationary phases of different bonding density. Molecular dynamics methods have also been applied to tethered alkyl chains and have shown that the mobile phase as well as the surface phase show inhomogeneities based on radial position.[15-21] Thus, the fluid and surface phases in real absorption systems are likely to be heterogeneous. The many different interactions may affect the retention of solute molecules in both beneficial and detrimental ways.

Such chromatographic systems are not accurately modeled by assuming a homogenous phase, so interest has moved toward development of appropriate models.

This chapter presents a three-dimensional stochastic (Monte Carlo) simulation of absorption chromatography that has been adapted to allow multiple interactions with a randomly mixed heterogeneous surface. Each surface phase interaction has a defined value for the absorption coefficient, diffusion coefficient, and interfacial resistance to mass transfer. The simulation is used to study the effects of multiple surface interactions on the overall system performance of absorption chromatography.

5.2 Simulation.

The algorithms presented in Chapter 2 are used to model absorption chromatography with heterogeneous surface phases. The program has been modified to randomly selects from multiple surface interactions. The number of different types of interaction sites (n) and the relative proportion or probability of encountering those sites in the surface phase (P_i) are input parameters for the simulation, as shown previously in Table 2.1. When a fluid phase molecule intersects the boundary between the fluid and surface phases, a random number (χ) is selected and compared to the relative proportion of the surface sites. The type of surface site (i) is determined when the random number satisfies the relationship

$$1 - \sum_{j=0}^{n-i} P_{n-j} < \chi \leq \sum_{j=1}^{i} P_j \qquad [5.1]$$

Once the type of site has been chosen, the probability that a molecule will be transferred across the interface is calculated by using Equations [2.12] and [2.13]. A second random number is selected and compared to the calculated probability. If the random number is less than or equal to the calculated value, the appropriate transfer occurs. If the random number is greater than the calculated probability, then no transfer occurs and the molecule undergoes an elastic collision with the interface. This approach results in completely independent interactions for the molecule each time the interface is encountered.

5.3 Results.

In this work, the stochastic simulation is used to study the effects of multiple absorption pathways on the chromatographic process. The system studied is an open tubular column with a fluid-phase radius of 2.0×10^{-3} cm and a surface-phase film thickness of 8.24×10^{-4} cm. These values are used so that the volume phase ratio β is equal to 1.0. The system contains two absorption pathways that are used to study the overall effects of differences in absorption coefficient ($K_{abs,i}$), surface-phase diffusion coefficient ($D_{s,i}$), and interfacial resistance to mass transfer coefficient (a_i). The simulation is performed for a total time necessary for all molecules to elute from column lengths of 0.1, 0.3, 0.5, 1.0, 3.0, and 5.0 cm. During the simulation time, distance data are collected at 5 s intervals. The observed kinetics of the system, chromatographic zone profiles, and statistical moments are presented and discussed below.

5.3.1 Effect of Differences in the Absorption Coefficient.

To explore the effects of differing absorption coefficients, a series of systems is simulated in which the average absorption coefficient is held constant, while the difference between the values is varied. The average absorption coefficient is determined by $K_{abs,avg} = P_1 K_{abs,1} + P_2 K_{abs,2}$, where $K_{abs,1}$ and $K_{abs,2}$ are the respective absorption coefficients. With a probability of 0.5 for each type of surface interaction, the ratio $(K_{abs,2} - K_{abs,1})/ K_{abs,avg}$ was varied while holding $K_{abs,avg}$ constant at a value of 1.0. The steady-state and kinetic data for these systems as well as for a single site with an absorption coefficient of 1.0 are presented at the top of Table 5.1. The ratio of the number of molecules in the surface and fluid phases ($\tilde{N}_s/\tilde{N}_f$) indicates that the steady-state distribution for these systems is similar and is determined by the average absorption coefficient (Equation [4.8]). The mass transfer curves for these systems are fit to Equation [4.5] by using nonlinear regression. The acquired kinetic rate constants for mass transfer are approximately equal for all four systems. The degree of fit to Equation [4.5], as shown by the square of the correlation coefficient (R^2), is comparable for all four systems as well. The ratio of the mass transfer rate constants (k_{fs}/k_{sf}) is also equal to the average absorption coefficient. The values of the characteristic times that correspond to 50% (T_{50}), 90% (T_{90}), and 95% (T_{95}) of the change between the initial and steady-state conditions are also similar. This implies that these four systems, which have the same average absorption coefficient, are equivalent. In fact, the rate constants, R^2 values, and characteristic times are all statistically equal at the 95% confidence level.

Table 5.1 Rate Constants (k_{fs}, k_{sf}),[a] Characteristic Times (T_{50}, T_{90}, T_{95}), and Steady-State Distributions ($\tilde{N}_s/\tilde{N}_f$) for Mass Transfer Processes as a Function of Absorption Coefficient and Probability of Absorption Sites.[b]

$K_{abs,1}$	$K_{abs,2}$	P_1	P_2	$\tilde{N}_s/\tilde{N}_f$	k_{fs}/k_{sf}	k_{fs} (s^{-1})	k_{sf} (s^{-1})	R^2	T_{50} (s)	T_{90} (s)	T_{95} (s)
1.0	—	1.0	—	0.995 ± 0.002	0.988 ±0.005	0.366 ± 0.003	0.371 ± 0.005	0.966 ± 0.001	0.74 ± 0.02	3.63 ± 0.08	4.9 ± 0.2
1.0	1.0	0.5	0.5	1.008 ± 0.005	0.992 ± 0.003	0.370 ± 0.006	0.373 ± 0.006	0.965 ± 0.001	0.75 ± 0.01	3.93 ± 0.09	5.3 ± 0.2
0.75	1.25	0.5	0.5	1.002 ± 0.002	0.991 ± 0.002	0.370 ± 0.003	0.374 ± 0.003	0.965 ± 0.002	0.74 ± 0.01	3.79 ± 0.09	5.0 ± 0.1
0.5	1.5	0.5	0.5	0.995 ± 0.002	0.986 ± 0.002	0.367 ± 0.004	0.372 ± 0.004	0.967 ± 0.001	0.75 ± 0.02	3.74 ± 0.07	5.2 ± 0.2
0.5	—	1.0	—	0.499 ± 0.001	0.498 ± 0.002	0.183 ± 0.002	0.367 ± 0.006	0.973 ± 0.002	1.06 ± 0.02	4.8 ± 0.1	6.7 ± 0.4
0.25	0.75	0.5	0.5	0.499 ± 0.001	0.497 ± 0.002	0.179 ± 0.002	0.359 ± 0.005	0.974 ± 0.002	1.10 ± 0.01	4.9 ± 0.1	6.2 ± 0.1
1.0	—	1.0	—	0.995 ± 0.002	0.988 ± 0.005	0.366 ± 0.003	0.371 ± 0.005	0.966 ± 0.001	0.74 ± 0.02	3.63 ± 0.08	4.9 ± 0.2
0.5	1.5	0.5	0.5	0.995 ± 0.002	0.986 ± 0.002	0.367 ± 0.004	0.372 ± 0.004	0.967 ± 0.001	0.75 ± 0.02	3.74 ± 0.07	5.2 ± 0.2
5.0	—	1.0	—	4.98 ± 0.02	4.38 ± 0.02	2.17 ± 0.01	0.495 ± 0.004	0.898 ± 0.003	0.174 ± 0.003	1.52 ± 0.04	2.31 ± 0.04
2.5	7.5	0.5	0.5	5.03 ± 0.03	4.36 ± 0.03	2.20 ± 0.03	0.506 ± 0.008	0.896 ± 0.001	0.172 ± 0.002	1.52 ± 0.03	2.28 ± 0.04
1.0	1.0	0.5	0.5	1.008 ± 0.005	0.992 ± 0.003	0.370 ± 0.006	0.373 ± 0.006	0.965 ± 0.001	0.75 ± 0.01	3.93 ± 0.09	5.3 ± 0.2
0.1	10.0	0.909	0.091	0.988 ±0.003	0.988 ± 0.008	0.365 ± 0.006	0.369 ± 0.009	0.965 ± 0.003	0.74 ± 0.02	3.73 ± 0.06	4.98 ± 0.04
0.01	10.0	0.901	0.099	0.990 ± 0.004	0.983 ± 0.001	0.372 ± 0.004	0.378 ± 0.004	0.963 ± 0.002	0.723 ± 0.003	3.76 ± 0.08	5.1 ± 0.1

[a] Determined by nonlinear regression according to Equation [4.5] with square of the correlation coefficient R^2.

[b] Simulation conditions: $N = 10000$, $R_f = 2.0 \times 10^{-3}$ cm, $R_s = 8.28 \times 10^{-4}$ cm, $a_1 = a_2 = 1.0$, $D_f = 1.0 \times 10^{-5}$ cm^2 s^{-1}, $D_{s,1} = D_{s,2} = 1.0 \times 10^{-7}$ cm^2 s^{-1}, $t = 1.0 \times 10^{-3}$ s, $T = 20\,\tau$.

To further test this phenomenon, three systems are simulated such that the ratio $(K_{abs,2} - K_{abs,1})/ K_{abs,avg}$ is constant with a value of 1.0 and $K_{abs,avg}$ is varied. Corresponding systems with a single site are also presented for comparison. The steady-state behavior ($\tilde{N}_s/\tilde{N}_f$) of the multiple-site systems is the same as the corresponding single site system over the range of $K_{abs,avg}$ from 0.5 to 5.0, as seen in the middle of Table 5.1. The kinetic behavior of the multiple site systems is also equivalent to that of the single site systems. The rate constants, R^2 values, and characteristic times for these systems are statistically equal at the 95% confidence level.

Finally, the absorption coefficients and probabilities of each site are varied while holding $K_{abs,avg}$ at a constant value of 1.0. The steady-state and kinetic behavior of these systems is statistically identical to the others with a value of 1.0 for $K_{abs,avg}$, as seen at the bottom of Table 5.1. Even the system in which the absorption coefficients differ by three orders of magnitude does not deviate from the observed trend. Thus, it appears that the systems truly behave as a system with a single site having an absorption coefficient equal to $K_{abs,avg}$ (*vide infra*). This suggests that the kinetics of the overall system cannot be used to determine the number of sites or the strength of their interaction with the solute if the only difference between the sites is the absorption coefficient.

To further study the effects of the absorption coefficient, the fluid dynamic behavior of the systems at the top of Table 5.1 is simulated with a fluid-phase velocity (v_0) of 0.1 cm s^{-1}. The zone profiles produced at column lengths from 0.1 to 5.0 cm are shown in Figure 5.1. It can be seen that the three systems appear similar. This is the result of the similar mass transfer kinetics and equilibrium behavior seen previously in

Figure 5.1: Zone profiles for systems with laminar flow and two absorption sites with (A) $K_{abs,1} = K_{abs,2} = 1.0$, (B) $K_{abs,1} = 0.75$, $K_{abs,2} = 1.25$, (C) $K_{abs,1} = 0.5$, $K_{abs,2} = 1.5$. Column lengths of 0.1, 0.2, 0.5, 1.0, 2.0, and 5.0 cm. Simulation conditions: N = 1000, t = 5.0×10^{-5} s, $R_f = 2.0 \times 10^{-3}$ cm, $R_s = 8.28 \times 10^{-4}$ cm, $v_0 = 0.1$ cm s^{-1}, $D_f = 1.0 \times 10^{-5}$ cm^2 s^{-1}, $D_{s,1} = D_{s,2} = 1.0 \times 10^{-7}$ cm^2 s^{-1}, $P_1 = P_2 = 0.5$, $a_1 = a_2 = 1.0$.

Figure 5.1

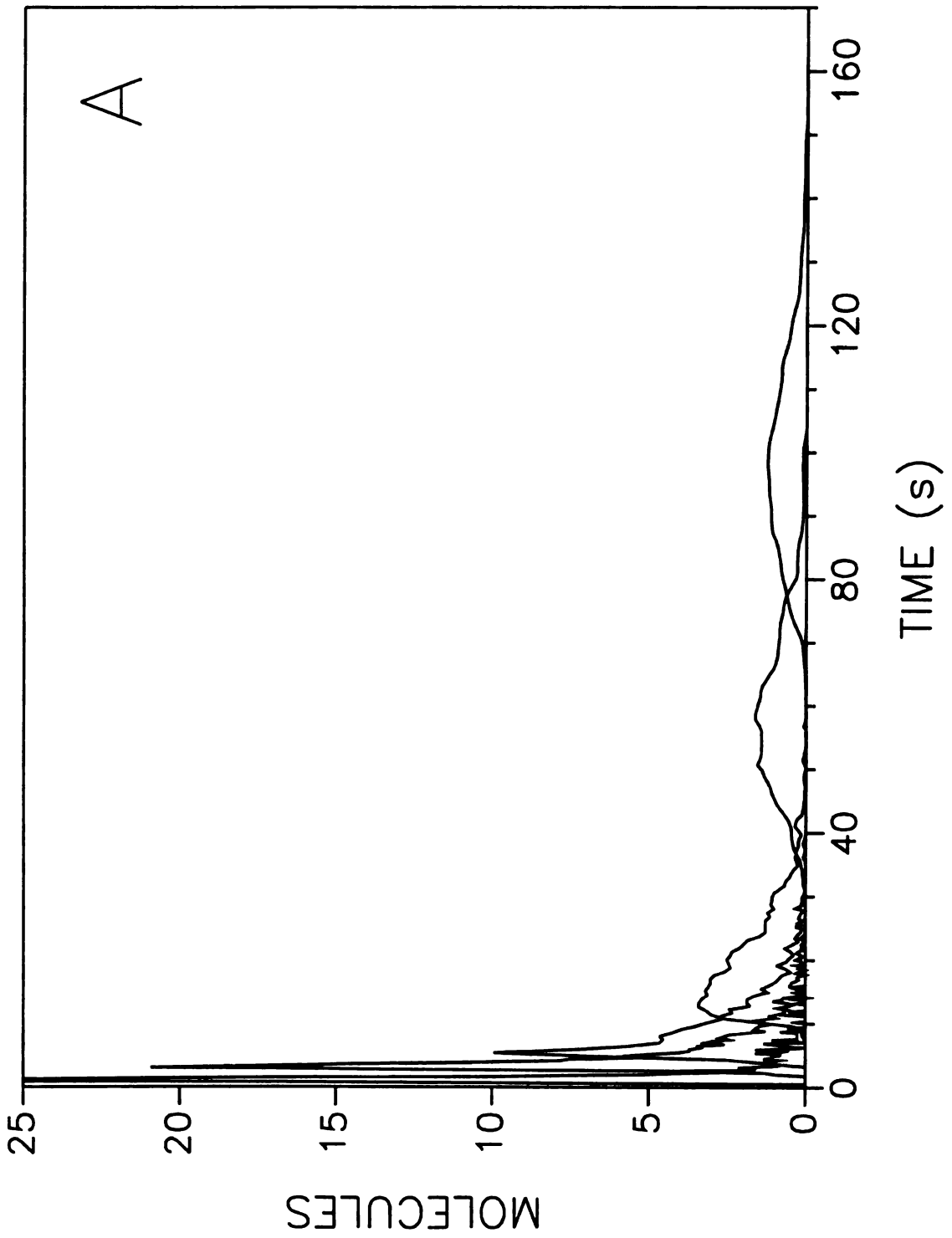

Figure 5.1 cont.

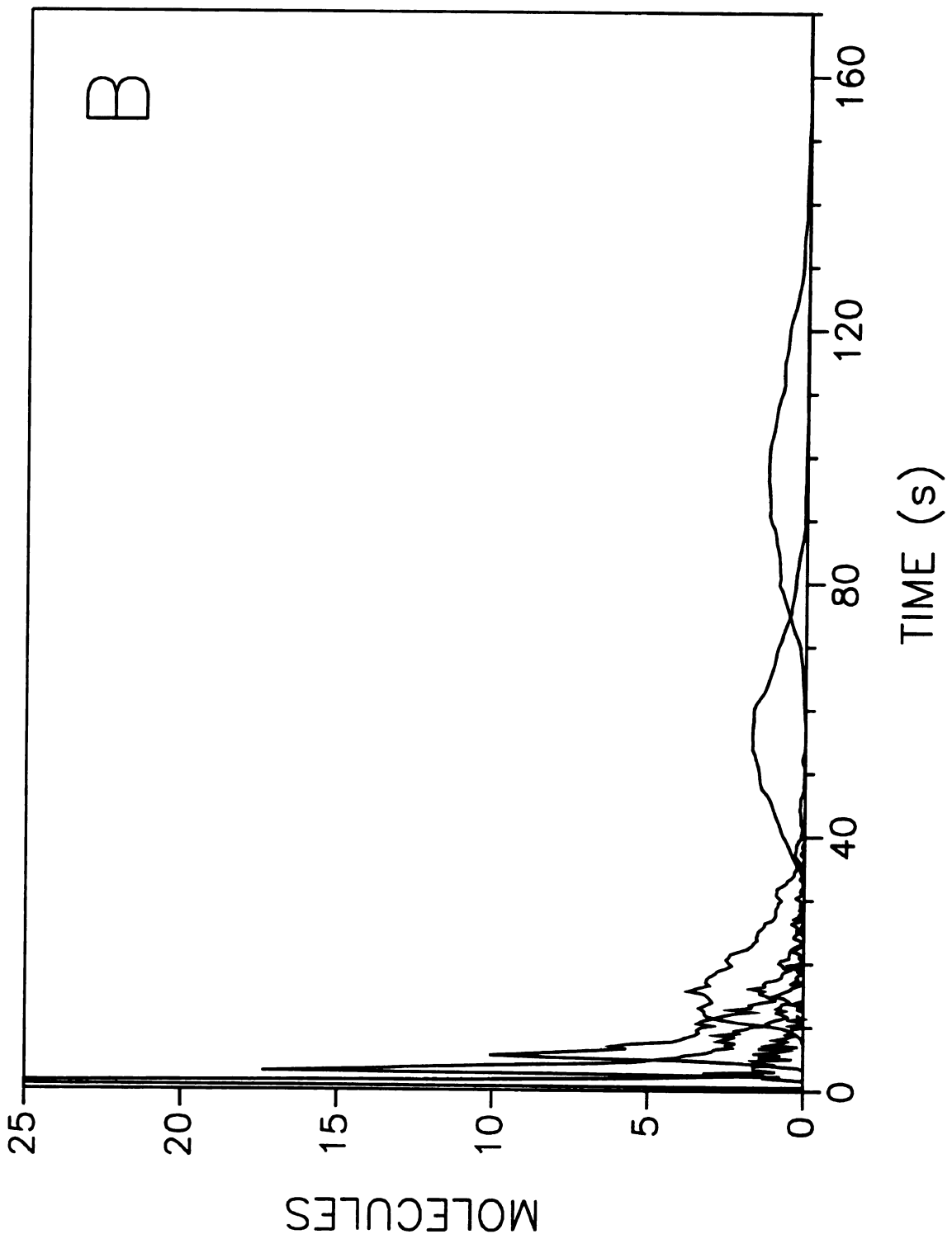

Figure 5.1 cont.

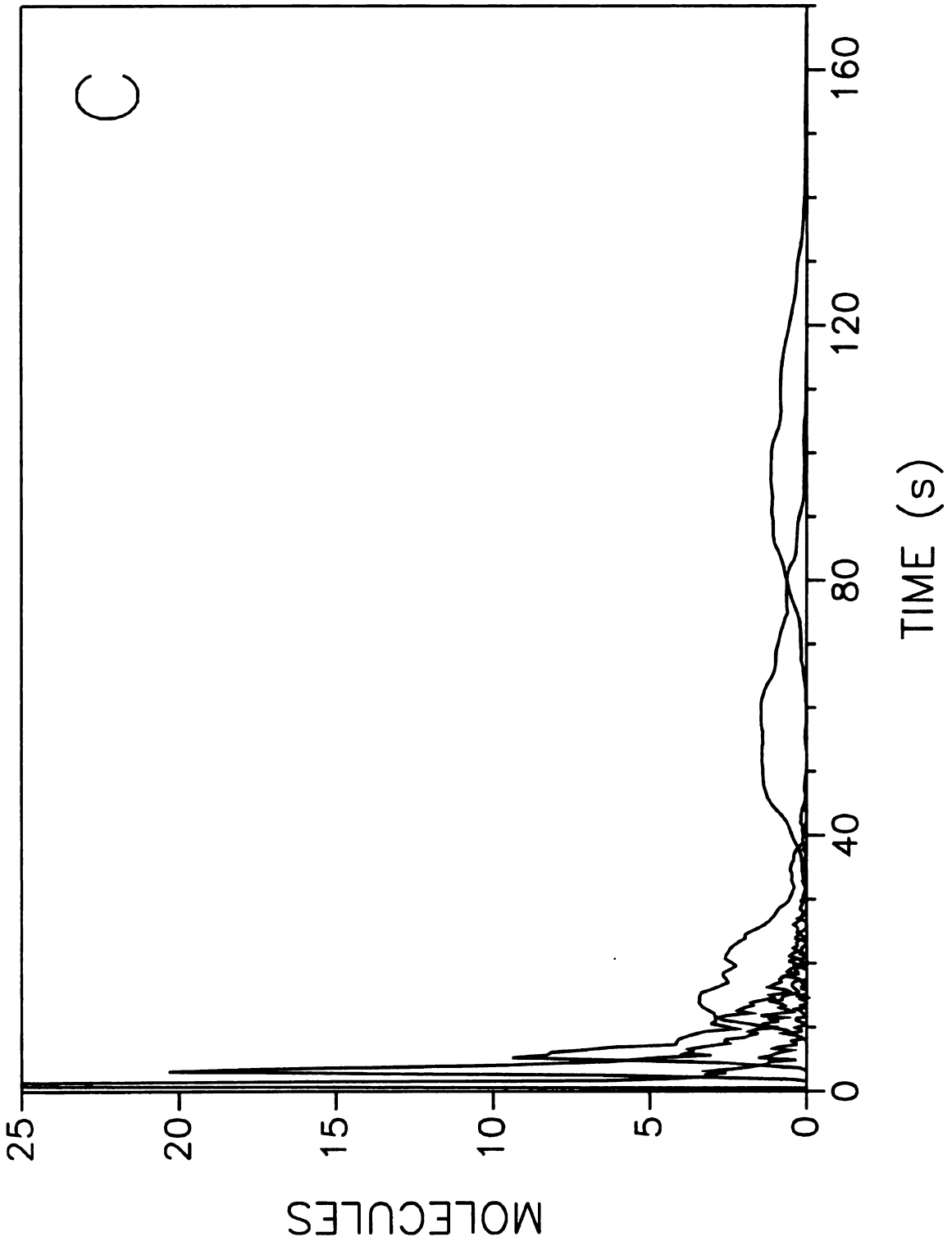

Table 5.1. The maxima of the zone profiles at each column length occur at the same point in time and have the same magnitude for all three systems. The first two profiles show a large front followed by a very small tail that grows and can be easily seen in the third and fourth profiles. The tail then diminishes as the last two zone profiles become symmetric.

The systems discussed above can be quantitatively compared by means of the statistical moments of the zone profiles. The moments were calculated in time and distance using Equations [2.1] and [2.2]. Figure 5.2A displays the first moment in time, or mean elution time, at each column length, and Figure 5.3A shows the corresponding first moment in distance, or mean zone position. The first moments in time and distance are linear and equal in magnitude. The linearity of the first moments in both domains implies that the systems are at steady state. The fact that the systems are equal in magnitude indicates that the systems are independent of the changes in absorption coefficient. The slope of the first moment in either the time or distance domain is related to the absorption coefficient as shown below for a system with a single site at steady state

$$M_{1,t} = \frac{(1 + K_{abs}\,\beta)}{v} L \qquad [5.2]$$

$$M_{1,d} = \frac{v}{(1 + K_{abs}\,\beta)} T \qquad [5.3]$$

Equation [5.2] shows the relationship between the first moment in time as a function of distance (L), velocity (v_0), and volume phase ratio (β). Equation [5.3] shows the corresponding relationship between the first moment in distance as a function of time (T). The first moments of these systems all have the same slope in Figures 5.2A and 5.3A,

Figure 5.2: The calculated (A) first moment, (B) second moment, and (C) third moment in time as a function of distance for systems with ($\triangle$) $K_{abs,1} = K_{abs,2} = 1.0$; ($\bigcirc$) $K_{abs,1} = 0.75$, $K_{abs,2} = 1.25$; ($\square$) $K_{abs,1} = 0.5$, $K_{abs,2} = 1.5$. All other conditions as given in Figure 5.1.

Figure 5.2

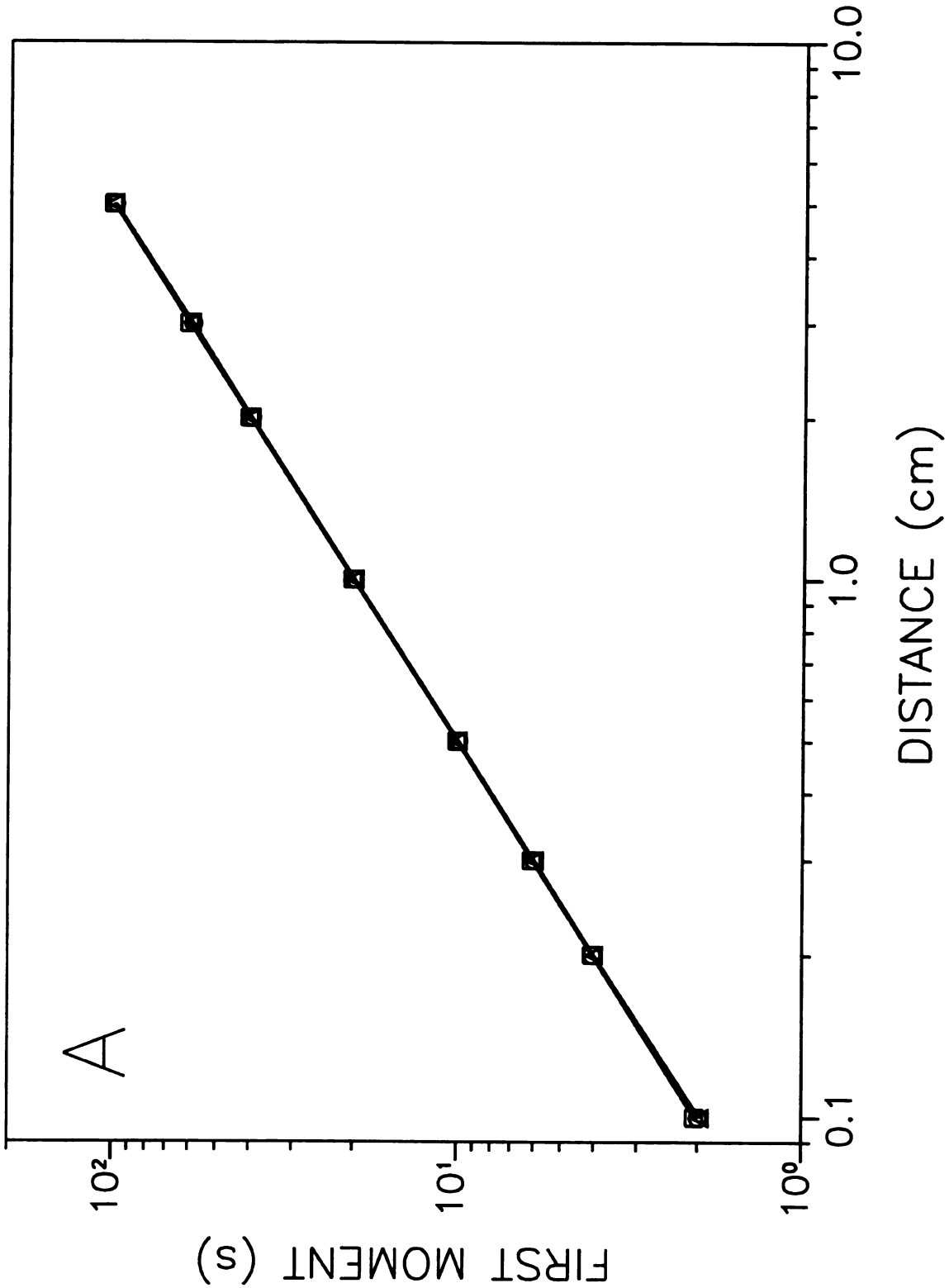

Figure 5.2 cont.

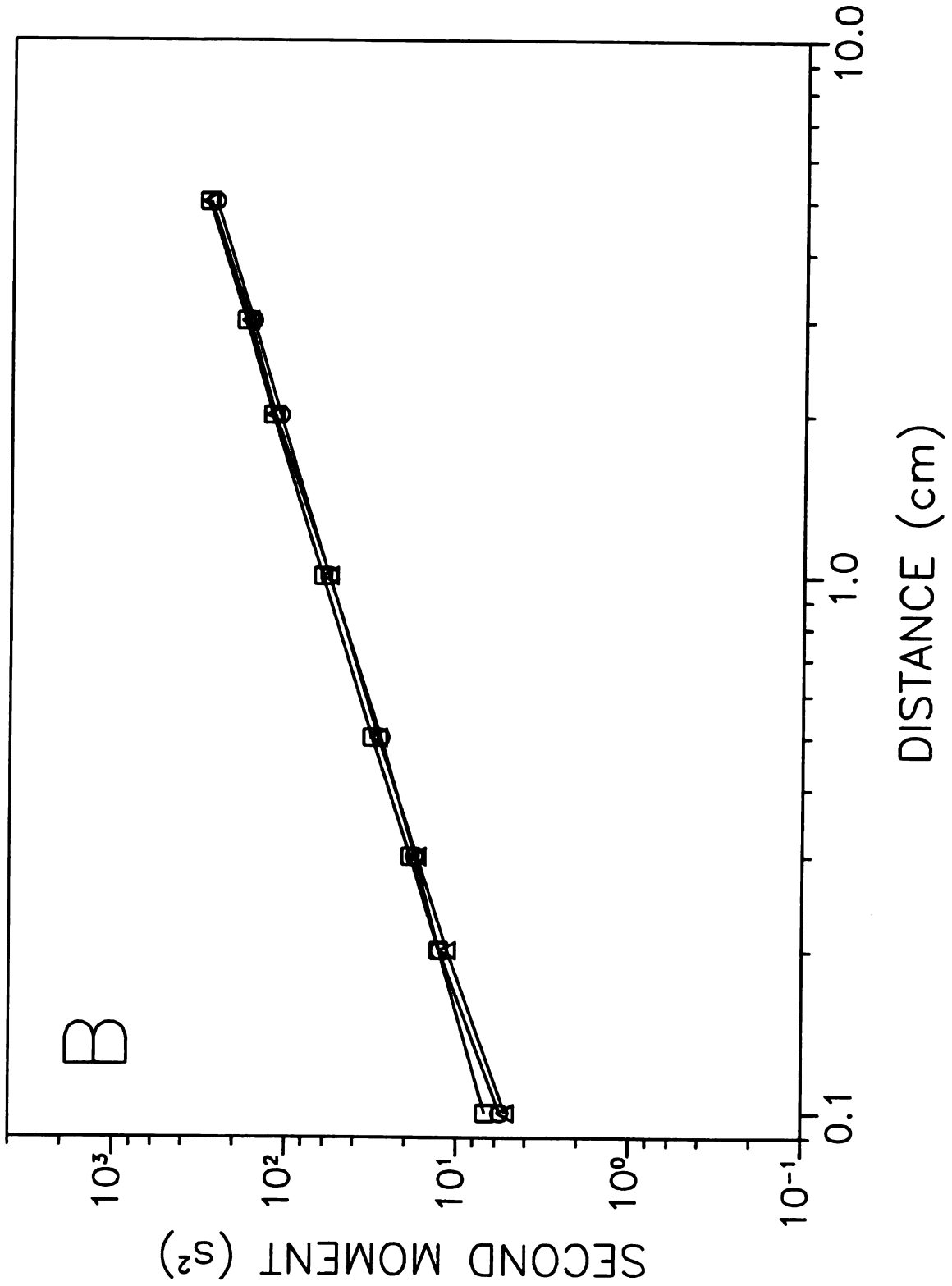

Figure 5.2 cont.

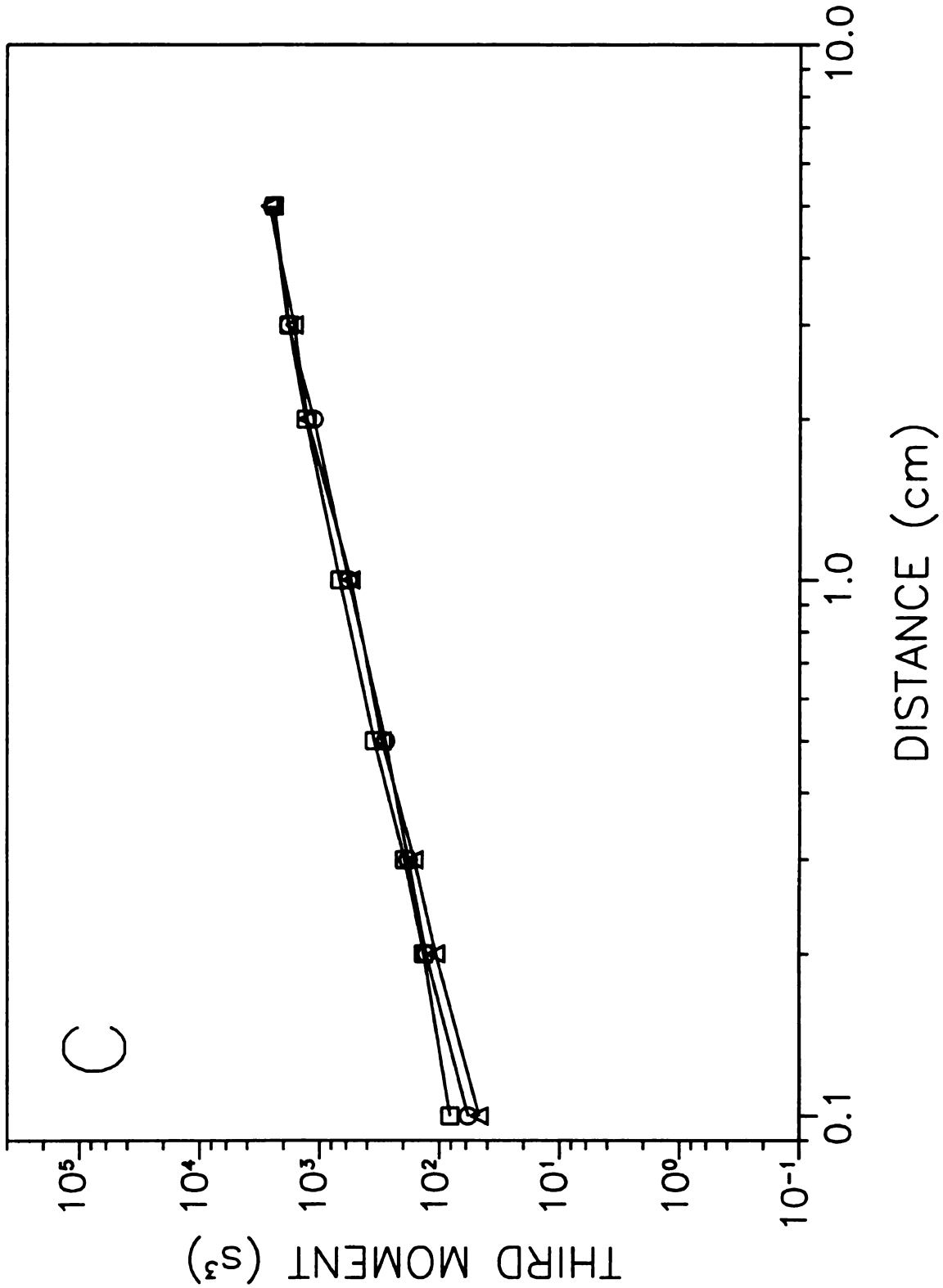

Figure 5.3: The calculated (A) first moment, (B) second moment, and (C) third moment in distance as a function of time for systems with ($\triangle$) $K_{abs,1} = K_{abs,2} = 1.0$; ($\bigcirc$) $K_{abs,1} = 0.75$, $K_{abs,2} = 1.25$; ($\square$) $K_{abs,1} = 0.5$, $K_{abs,2} = 1.5$. All other conditions as given in Figure 5.1.

Figure 5.3

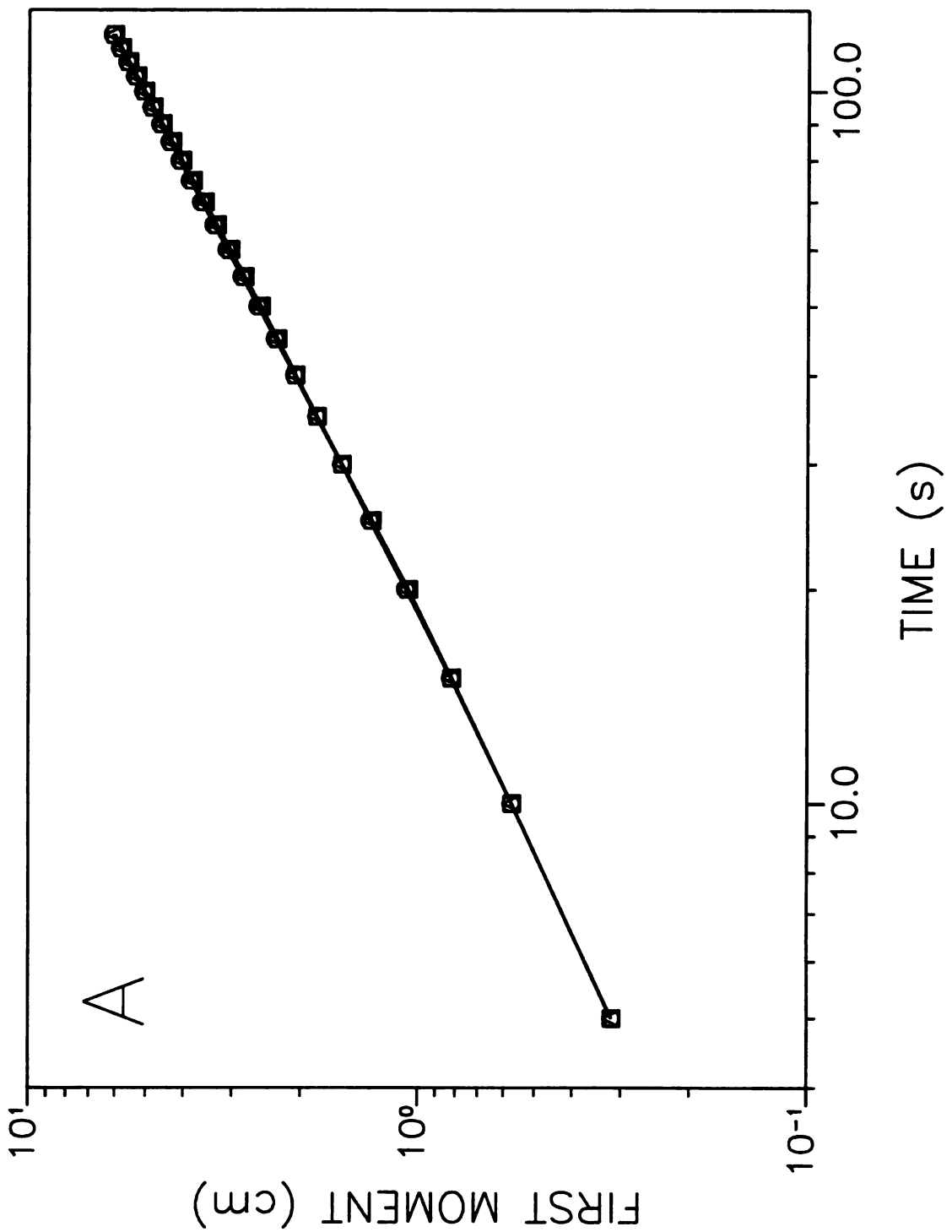

Figure 5.3 cont.

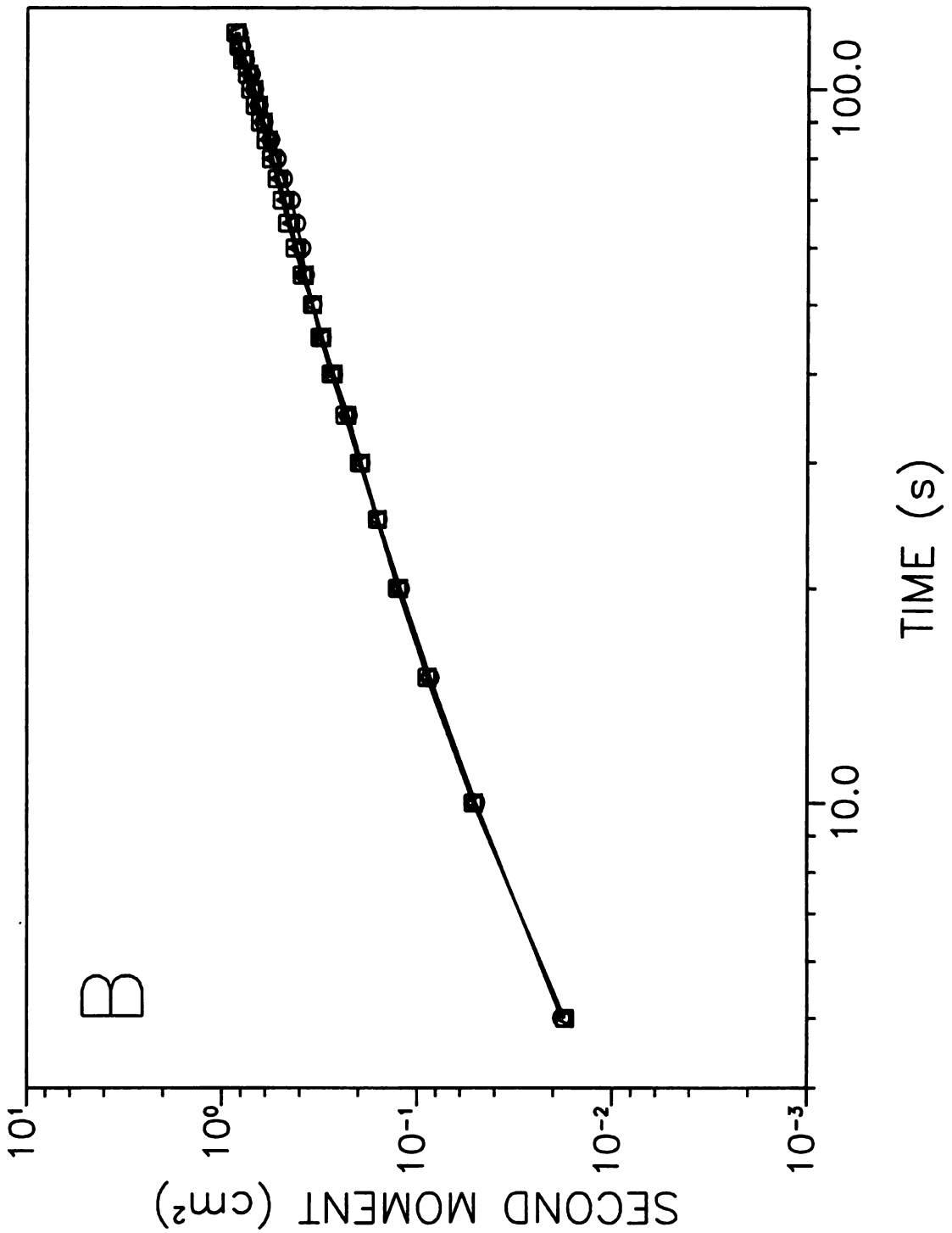

Figure 5.3 cont.

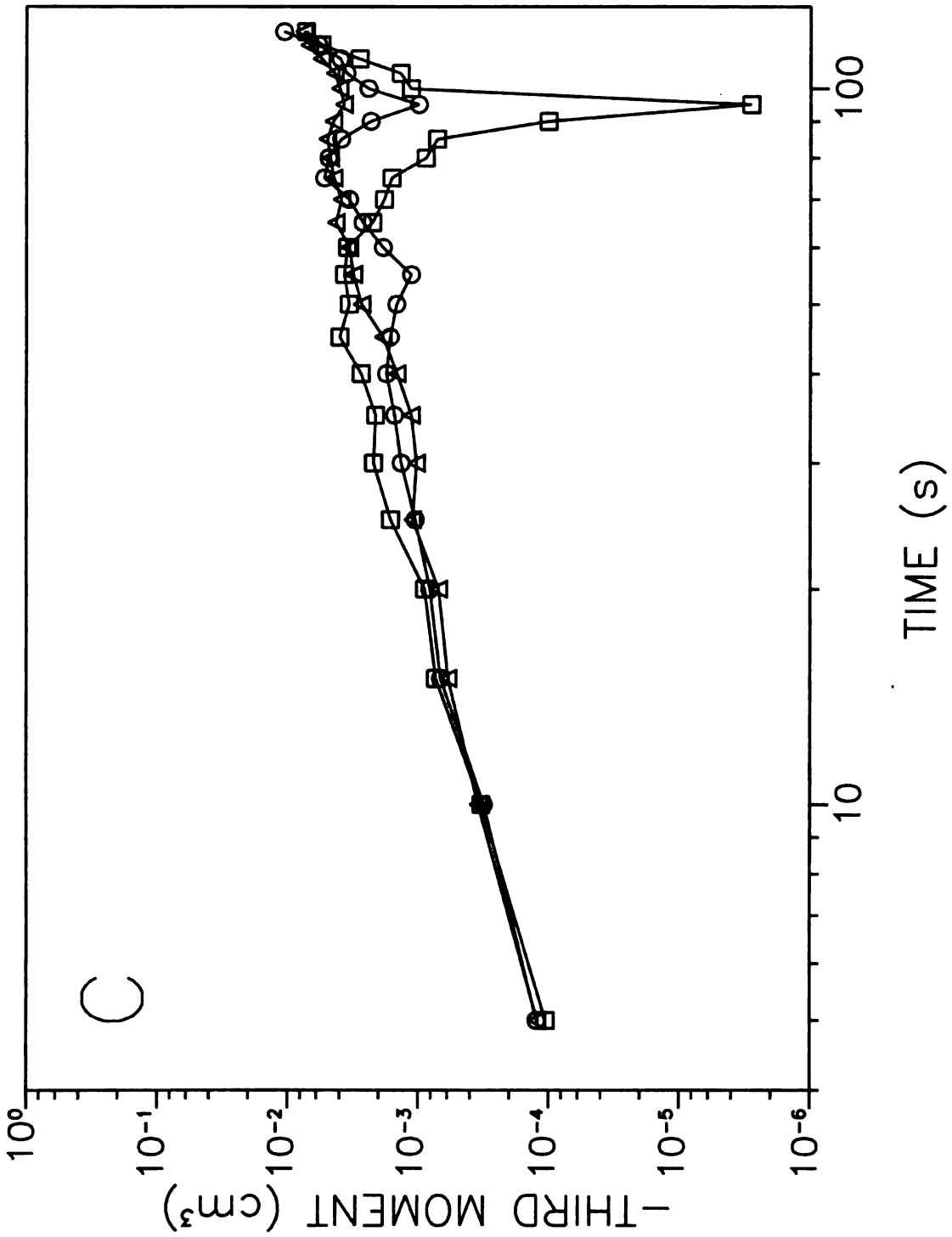

implying that the systems have the same average absorption coefficient. The overall response of each system is equivalent to a system with a single site having the same absorption coefficient. In these graphs, the observed equivalent absorption coefficient is equal to 1.0. This leads to the conclusion that differences in the absorption coefficient of the sites on the surface is not sufficient to cause a difference in the mean response of the system.

Figures 5.2B and 5.3B show the second moment or variance in time and distance, respectively. The data in Figure 5.2B are linear and show small differences in variance at short distances that disappear as distance increases. In Figure 5.3B, the moments are linear and show no difference in variance between the systems. These observations imply that the variance in the profiles is not affected by the differences in the absorption coefficients of the two sites. For a system with a single site at steady state, the variance can be calculated by the modified Golay equation[22]

$$M_{2,t} = \left(\frac{2D_f}{v^3} + \frac{2K_{abs}\beta D_s}{v^3} + \frac{\left(1+6K_{abs}\beta+11(K_{abs}\beta)^2\right)R_f^2}{24(1+K_{abs}\beta)^2 D_f v} + \frac{2K_{abs}\beta R_s^2}{3(1+K_{abs}\beta)^2 D_s v} \right) L \qquad [5.4]$$

$$M_{2,d} = \left(\frac{2D_f}{(1+K_{abs}\beta)} + \frac{2K_{abs}\beta D_s}{(1+K_{abs}\beta)} + \frac{\left(1+6K_{abs}\beta+11(K_{abs}\beta)^2\right)R_f^2 v^2}{24(1+K_{abs}\beta)^3 D_f v} + \frac{2K_{abs}\beta R_s^2 v^2}{3(1+K_{abs}\beta)^3 D_s} \right) T \qquad [5.5]$$

Equation [5.4] shows the relationship between the absorption coefficient and the second moment in time as a function of distance. The relationship between the second moment in distance as a function of time and the absorption coefficient is shown in Equation [5.5]. The first two terms of Equations [5.4] and [5.5] represent diffusional broadening in the fluid and surface phases, whereas the last two terms represent resistance to mass transfer in the fluid and surface phases. Thus, changes in the absorption coefficient would be expected to cause changes in the amount of broadening produced by the systems. The linearity of the graphs indicates that the steady-state conditions of the Golay equation are applicable to the systems. The common line shared by the systems in each graph confirms that the mass transfer within the different systems is equivalent because the average absorption coefficient is the same.

The third moments in time and distance are displayed in Figures 5.2C and 5.3C, respectively. The third moments in both time and distance increase linearly and are similar in magnitude for all systems. These observations indicate that the systems are at steady state and the asymmetry is not dependent on the different absorption coefficients. The third moments in time as a function of distance are positive, while the third moments in distance as a function of time are negative because zone profiles that are tailing in one domain are fronting in the other.

The fluid dynamic behavior of these systems, as presented in the zone profiles and moments, do not show any dependence on the difference in the absorption coefficient between the two sites. The systems respond as a system with a single site having the

same average absorption coefficient. This is in agreement with the kinetic observations presented earlier.

5.3.2 Effect of Differences in the Diffusion Coefficient.

The simulation is used to study the effects of two different surface-phase diffusion coefficients on the mass transfer rate and the zone profiles of multiple-site absorption systems. The diffusion coefficient of one surface phase site is 1.0×10^{-7} cm^2 s^{-1}, and the diffusion coefficient for the other site is varied from 1.0×10^{-5} to 1.0×10^{-8} cm^2 s^{-1}. All other parameters remain constant. The steady-state distribution of molecules between the fluid and surface phases ($\tilde{N}_s/\tilde{N}_f$) in Table 5.2 is independent of the changes in diffusion coefficient and, as expected, is equal to 1.0 for these systems. However, the mass transfer rate constants in Table 5.2 vary from 2.6 s^{-1} for the largest diffusion coefficient to 0.129 s^{-1} for the smallest diffusion coefficient of the second site. The degree of fit with Equation [4.5] is best for the systems where the diffusion coefficients of the two sites are equal ($D_f = D_s = 1.0 \times 10^{-7}$ cm^2 s^{-1}). The larger the difference in the diffusion coefficients between the two sites, the lower the R^2 value because the system response no longer appears to be a single exponential decay. The characteristic times are useful in observing the trend toward two independent rates of transfer across the phase boundary of the system. The changes in T_{50}, T_{90}, and T_{95} indicate that the larger diffusion coefficient controls the short-time behavior and the smaller diffusion coefficient controls the long-time behavior of these systems. Based on

Table 5.2 Rate Constants (k_{fs}, k_{sf}),[a] Characteristic Times (T_{50}, T_{90}, T_{95}), and Steady-State Distributions ($\tilde{N}_s/\tilde{N}_f$) for Mass Transfer Processes as a Function of Diffusion Coefficient.[b]

$D_{s,1}$ ($cm^2\ s^{-1}$)	$D_{s,2}$ ($cm^2\ s^{-1}$)	$\tilde{N}_s/\tilde{N}_f$	k_{fs}/k_{sf}	k_{fs} (s^{-1})	k_{sf} (s^{-1})	R^2	T_{50} (s)	T_{90} (s)	T_{95} (s)
1.0×10^{-7}	1.0×10^{-5}	0.992 ± 0.004	0.960 ± 0.002	2.51 ± 0.07	2.61 ± 0.07	0.43 ± 0.01	0.042 ± 0.003	2.41 ± 0.03	3.75 ± 0.05
1.0×10^{-7}	1.0×10^{-6}	0.987 ± 0.003	0.973 ± 0.002	1.16 ± 0.03	1.20 ± 0.03	0.82 ± 0.02	0.190 ± 0.002	2.1 ± 0.1	3.8 ± 0.1
1.0×10^{-7}	1.0×10^{-7}	1.008 ± 0.005	0.992 ± 0.003	0.370 ± 0.006	0.373 ± 0.006	0.965 ± 0.001	0.75 ± 0.01	3.93 ± 0.09	5.3 ± 0.2
1.0×10^{-7}	1.0×10^{-8}	0.996 ± 0.004	0.972 ± 0.007	0.129 ± 0.002	0.133 ± 0.003	0.780 ± 0.004	1.83 ± 0.03	26 ± 3	46 ± 3

[a] Determined by nonlinear regression according to Equation [4.5] with square of the correlation coefficient R^2.

[b] Simulation conditions: N = 10000, $R_f = 2.0 \times 10^{-3}$ cm, $R_s = 8.28 \times 10^{-4}$ cm, $a_1 = a_2 = 1.0$, $P_1 = P_2 = 0.5$, $K_{abs,1} = K_{abs,2} = 1.0$, $D_f = 1.0 \times 10^{-5}\ cm^2\ s^{-1}$, $t = 1.0 \times 10^{-3}$ s, $T = 20\ \tau$.

these kinetic data, it is expected that changes in the diffusion coefficient will affect the fluid dynamic behavior of the system.

The effects of the changes in the mass transfer rate can be easily seen in the zone profiles of the systems. Figure 5.4 shows the zone profiles for the systems presented in Table 5.2 at columns lengths of 0.1 to 5.0 cm. The height of the profiles decreases and the width increases as the column length increases for all the systems. It is also noticeable that the profiles at the longest column length become wider and shorter as the diffusion coefficient of the second site decreases. The increase in width is predicted by chromatographic theory for a single site (Equations [5.4] and [5.5]),[22] and the decrease in height occurs because the area remains constant (i.e., there is no change in the number of solute molecules). Also, the first four profiles for each system are noticeably asymmetric. The asymmetry decreases as the column length increases. For a fixed column length, the asymmetry also decreases as the diffusion coefficient of the second site increases.

The statistical moments for the zone profiles in time and distance are presented in Figures 5.5 and 5.6, respectively. Two series of systems are presented. In one series, which has already been shown in Table 5.2 and Figure 5.4, the diffusion coefficient of the first site is held constant at 1.0×10^{-7} cm^2 s^{-1} and the diffusion coefficient of the second site is varied from 1.0×10^{-5} to 1.0×10^{-8} cm^2 s^{-1}. In the other series, the diffusion coefficient of the first site is held constant at 1.0×10^{-6} cm^2 s^{-1} and the diffusion coefficient of the second site ranges from 1.0×10^{-5} to 1.0×10^{-8} cm^2 s^{-1}. The first moments in time as a function of distance shown in Figure 5.5A are linear and equal in magnitude. These observations again imply that the movement of the zones has reached

Figure 5.4: Zone profiles for systems with laminar flow and two absorption sites with (A) $D_{s,1} = 1.0 \times 10^{-5}$ cm^2 s^{-1}, $D_{s,2} = 1.0 \times 10^{-7}$ cm^2 s^{-1}; (B) $D_{s,1} = 1.0 \times 10^{-6}$ cm^2 s^{-1}, $D_{s,2} = 1.0 \times 10^{-7}$ cm^2 s^{-1}; (C) $D_{s,1} = 1.0 \times 10^{-7}$ cm^2 s^{-1}, $D_{s,2} = 1.0 \times 10^{-7}$ cm^2 s^{-1}; (D) $D_{s,1} = 1.0 \times 10^{-8}$ cm^2 s^{-1}, $D_{s,2} = 1.0 \times 10^{-7}$ cm^2 s^{-1}. Column lengths of 0.1, 0.2, 0.5, 1.0, 2.0, and 5.0 cm. All other parameters as follows: N=1000, $t = 5.0 \times 10^{-5}$ s, $R_f = 2.0 \times 10^{-3}$ cm, $R_s = 8.28 \times 10^{-4}$ cm, $v_0 = 0.1$ cm s^{-1}, $D_f = 1.0 \times 10^{-5}$ cm^2 s^{-1}, $P_1 = P_2 = 0.5$, $a_1 = a_2 = 1.0$, $K_{abs,1} = K_{abs,2} = 1.0$.

Figure 5.4

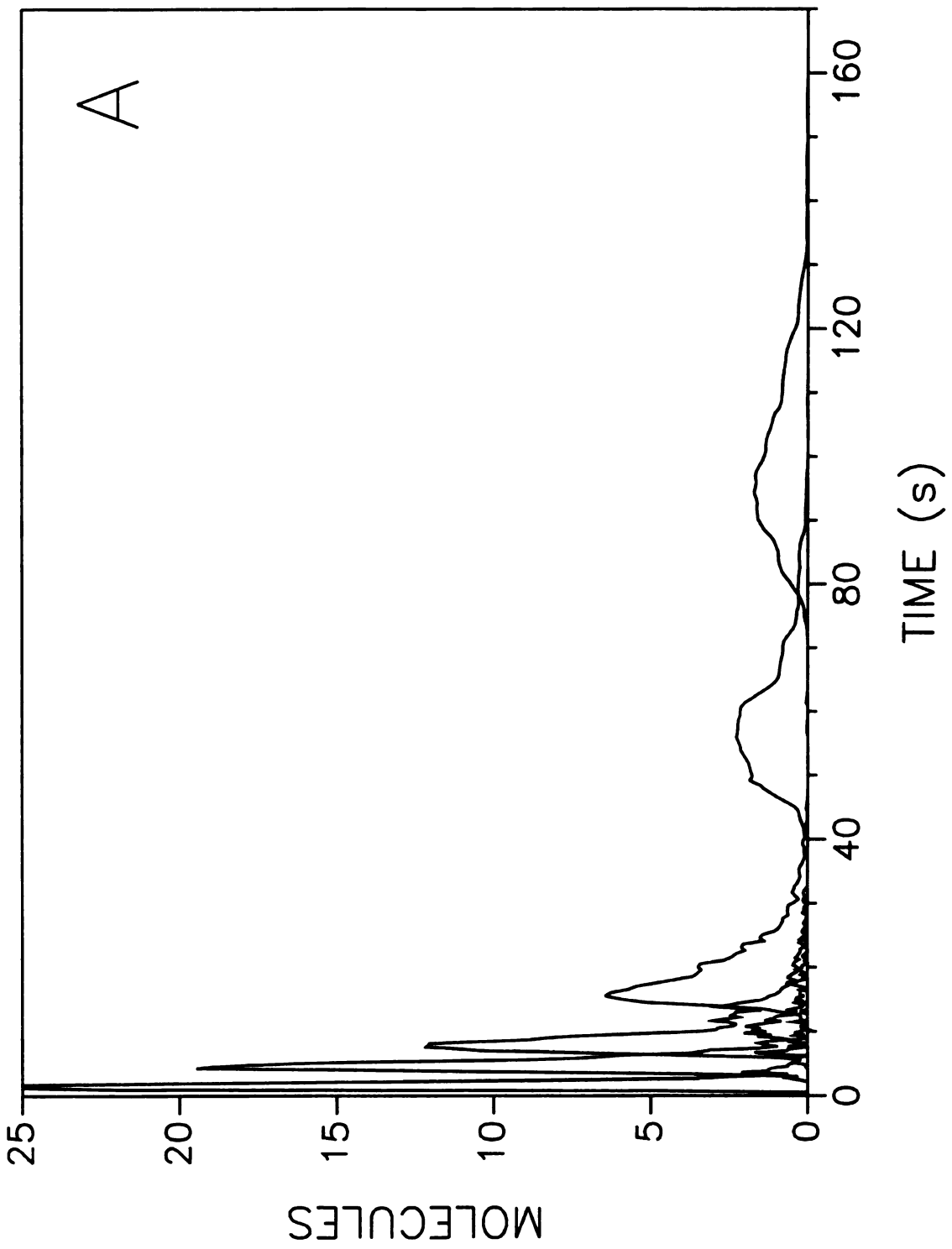

Figure 5.4 cont.

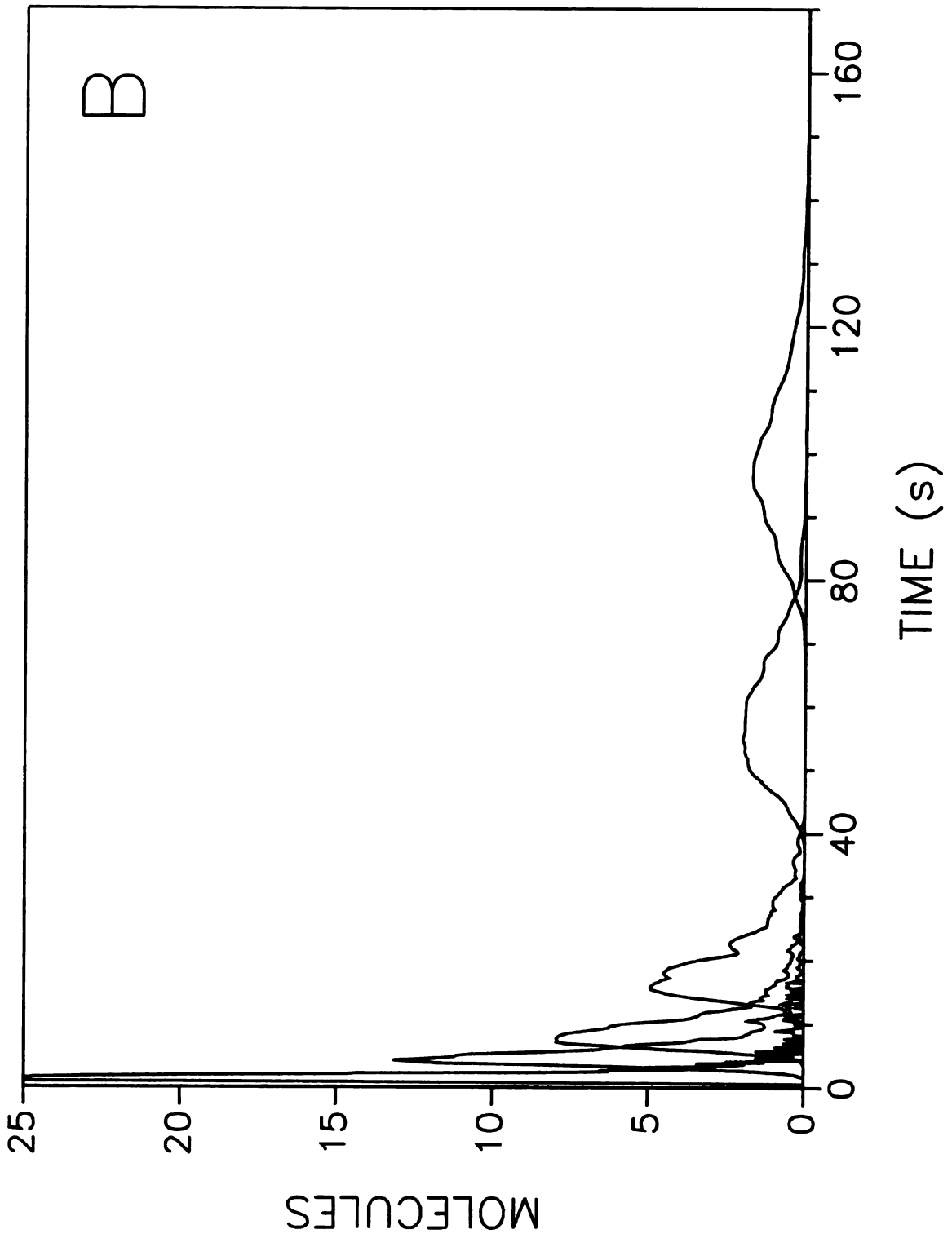

Figure 5.4 cont.

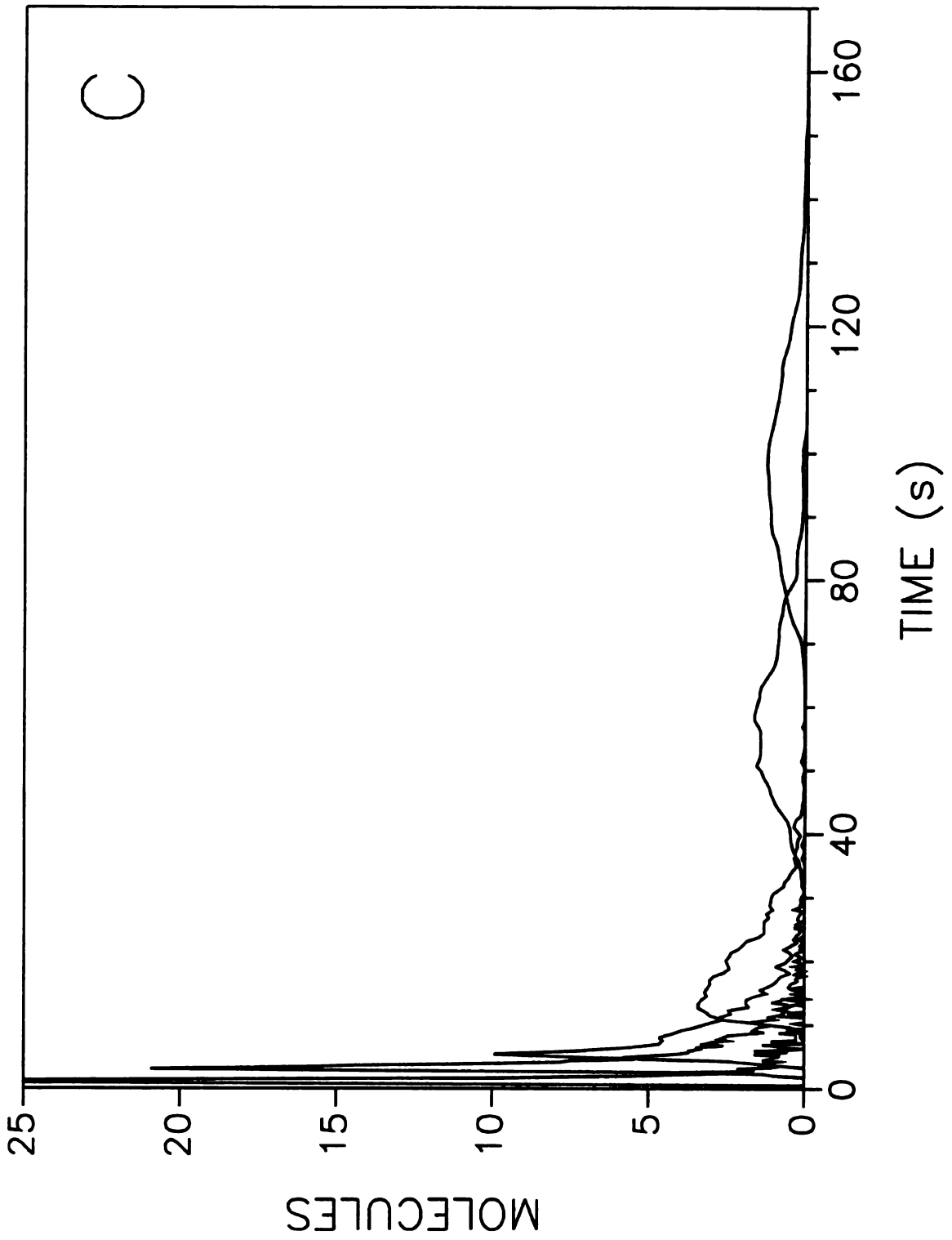

Figure 5.4 cont.

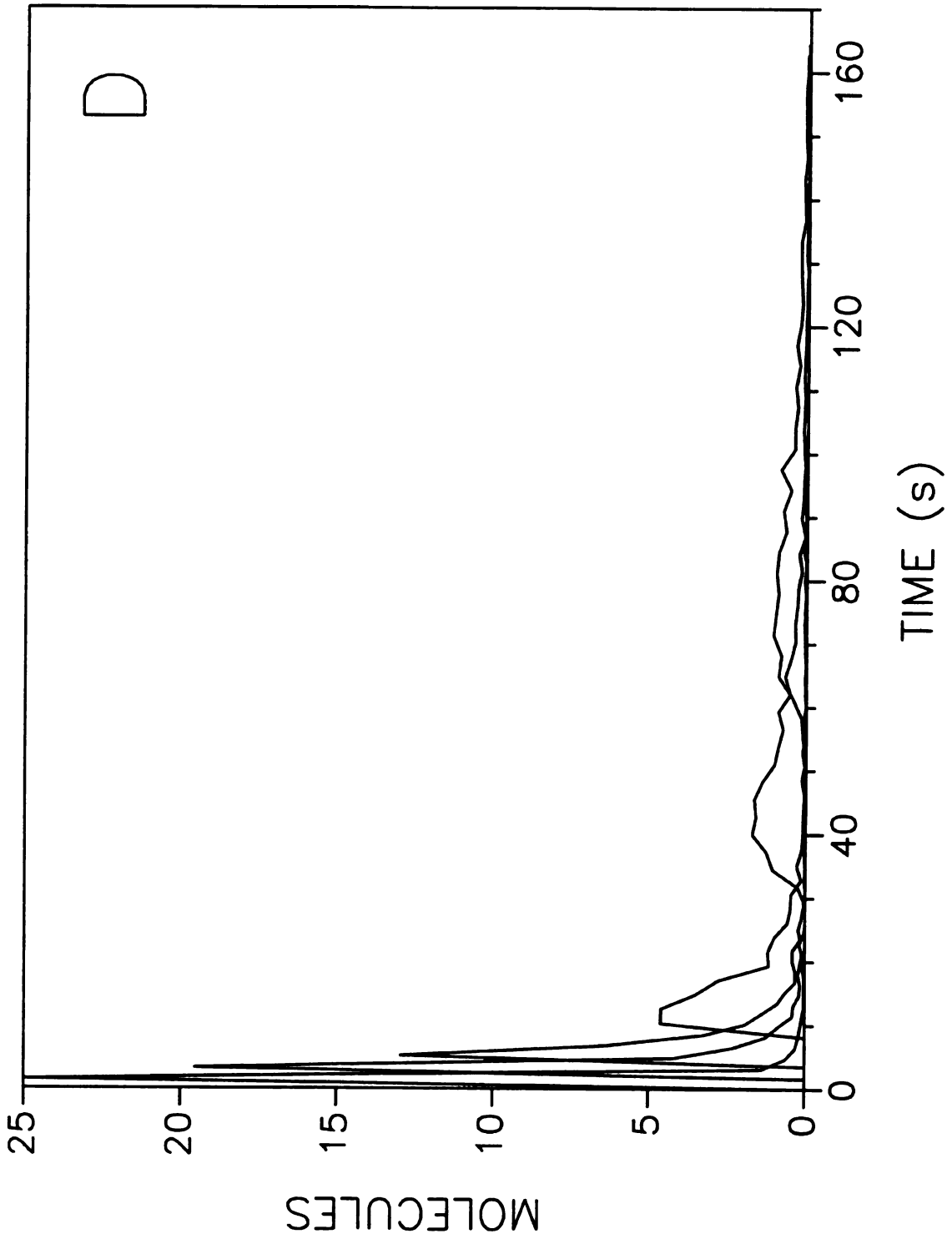

Figure 5.5: The calculated (A) first moment, (B) second moment, and (C) third moment in distance as a function of time for systems with (□) $D_{s,1} = 1.0 \times 10^{-5}$ cm^2 s^{-1}, $D_{s,2} = 1.0 \times 10^{-6}$ cm^2 s^{-1}; (○) $D_{s,1} = 1.0 \times 10^{-5}$ cm^2 s^{-1}, $D_{s,2} = 1.0 \times 10^{-7}$ cm^2 s^{-1}; (△) $D_{s,1} = 1.0 \times 10^{-6}$ cm^2 s^{-1}, $D_{s,2} = 1.0 \times 10^{-6}$ cm^2 s^{-1}; (◇) $D_{s,1} = 1.0 \times 10^{-6}$ cm^2 s^{-1}, $D_{s,2} = 1.0 \times 10^{-7}$ cm^2 s^{-1}; (●) $D_{s,1} = 1.0 \times 10^{-6}$ cm^2 s^{-1}, $D_{s,2} = 1.0 \times 10^{-8}$ cm^2 s^{-1}; (■) $D_{s,1} = 1.0 \times 10^{-7}$ cm^2 s^{-1}, $D_{s,2} = 1.0 \times 10^{-7}$ cm^2 s^{-1}; (▲) $D_{s,1} = 1.0 \times 10^{-7}$ cm^2 s^{-1}, $D_{s,2} = 1.0 \times 10^{-8}$ cm^2 s^{-1}. All other conditions as given in Figure 5.4.

Figure 5.5

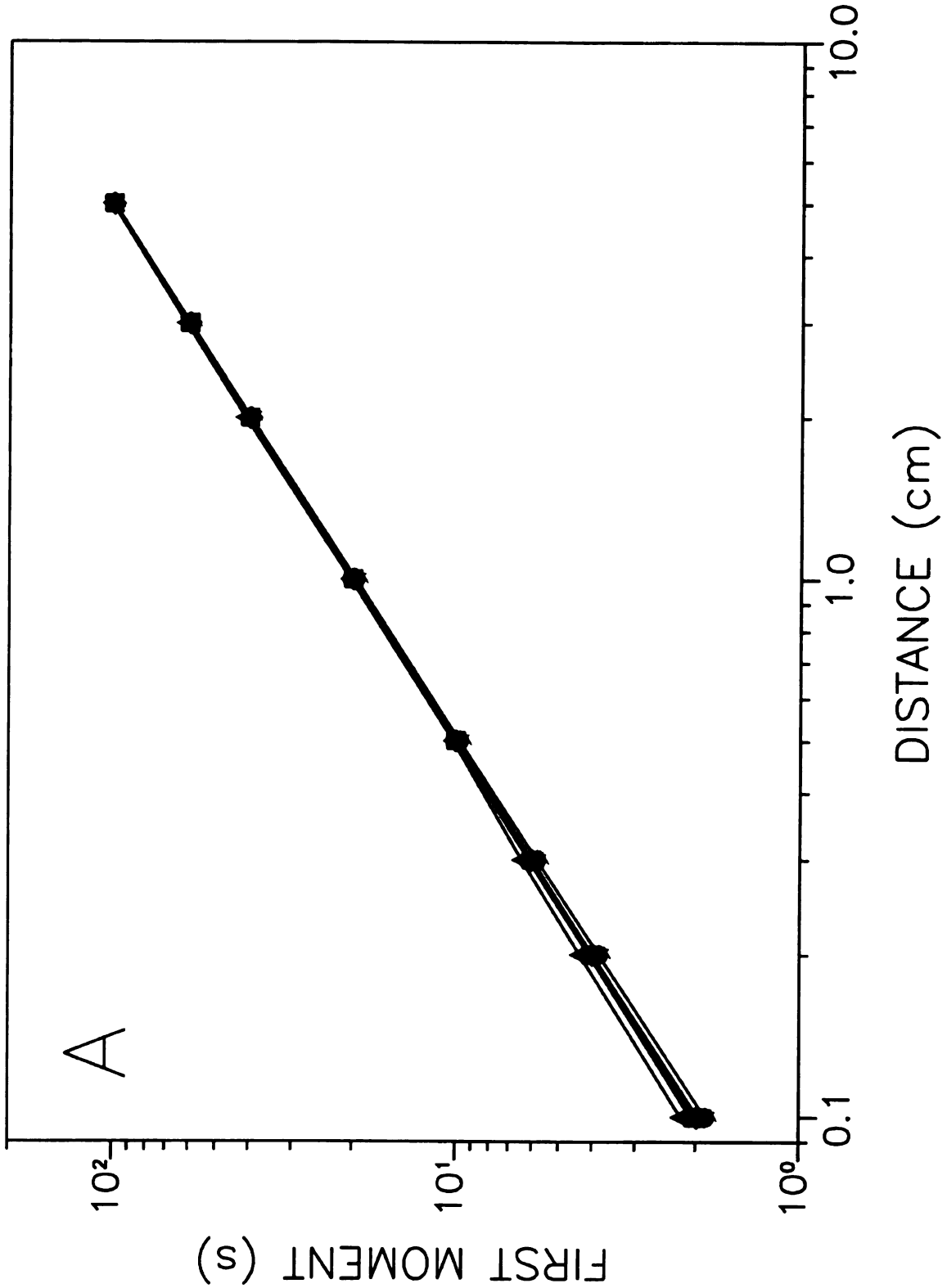

Figure 5.5 cont.

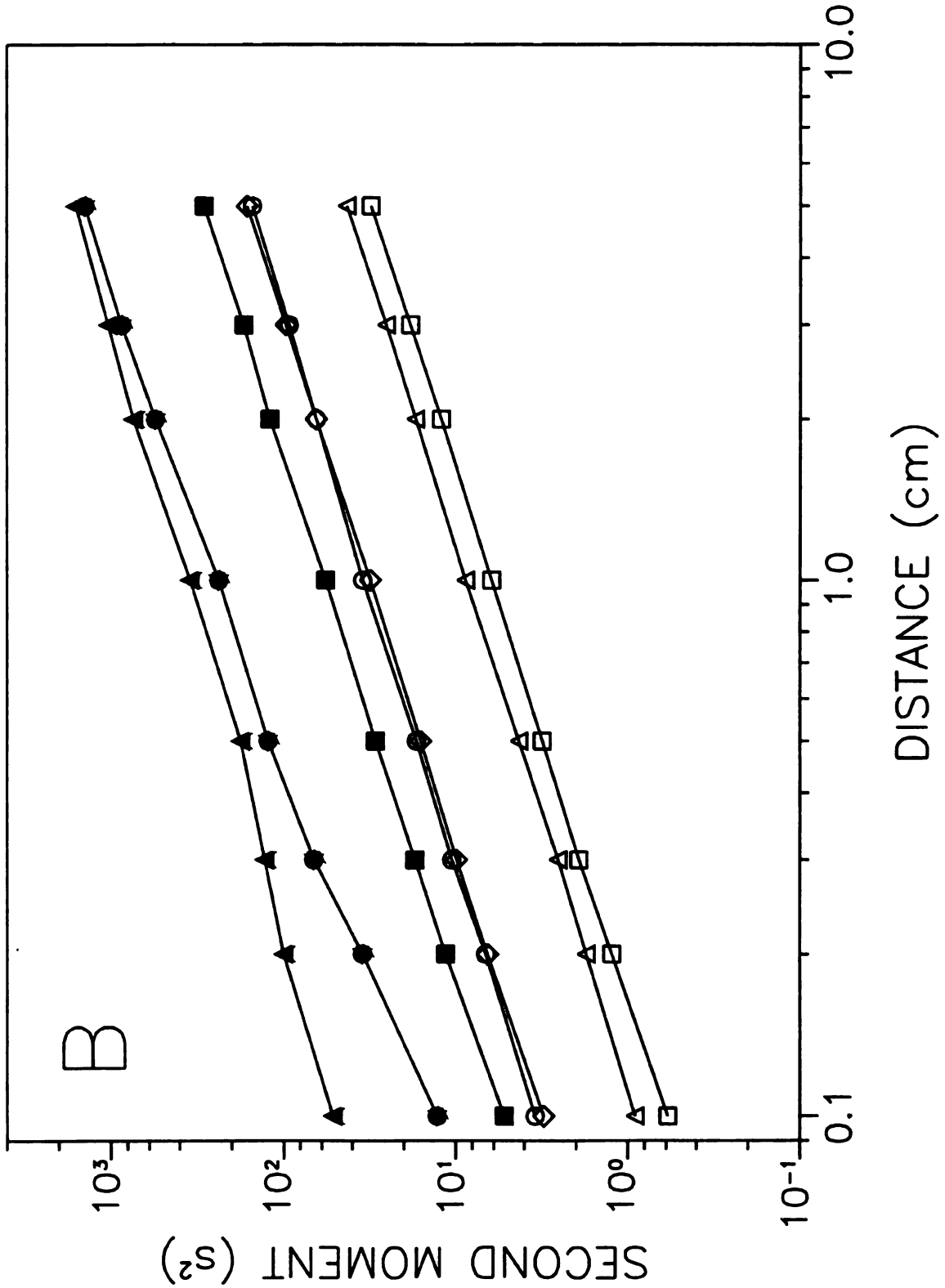

Figure 5.5 cont.

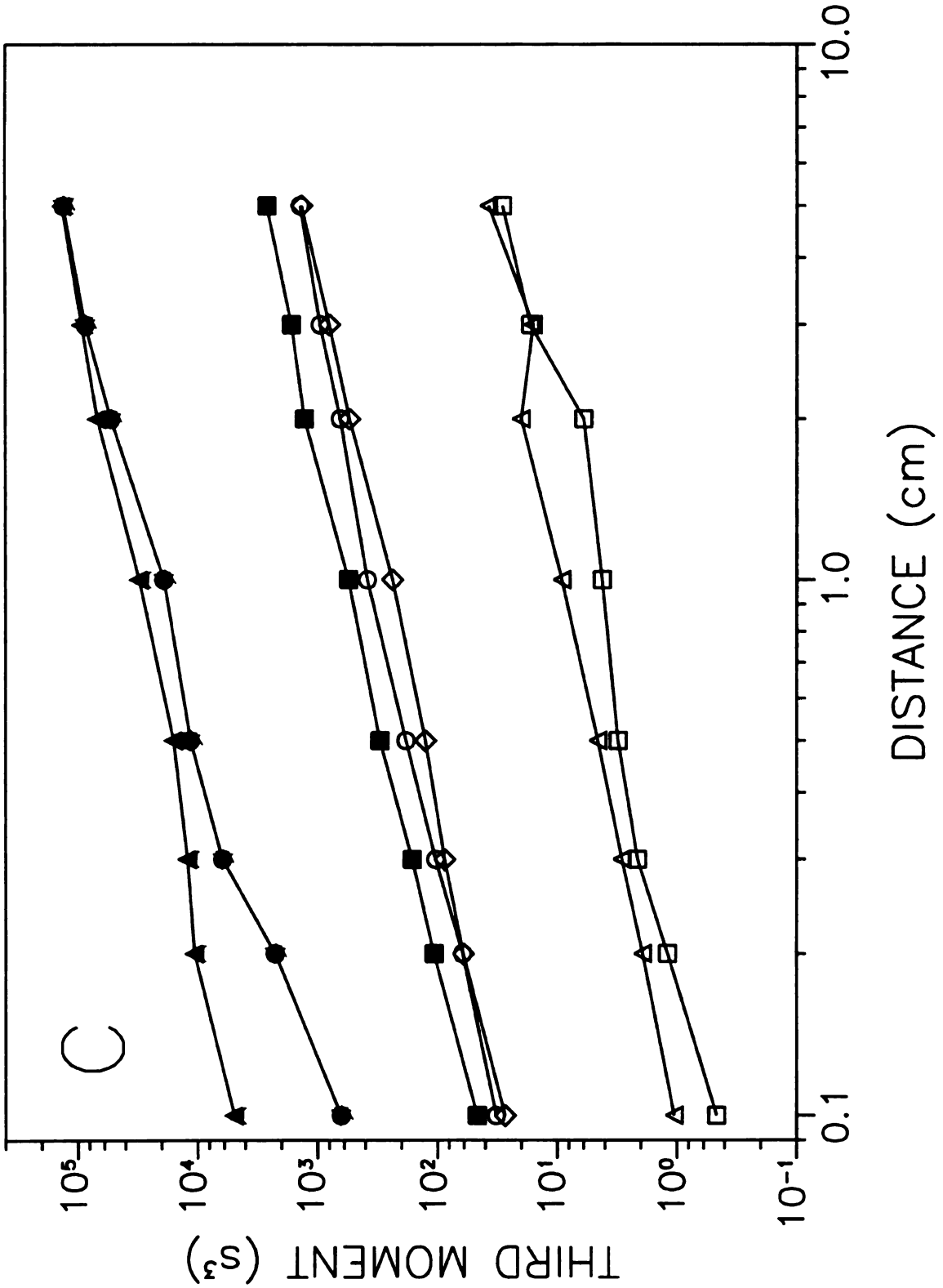

Figure 5.6: The calculated (A) first moment, (B) second moment, and (C) third moment in time as a function of distance for systems with (□) $D_{s,1} = 1.0 \times 10^{-5}$ cm^2 s^{-1}, $D_{s,2} = 1.0 \times 10^{-6}$ cm^2 s^{-1}; (○) $D_{s,1} = 1.0 \times 10^{-5}$ cm^2 s^{-1}, $D_{s,2} = 1.0 \times 10^{-7}$ cm^2 s^{-1}; (△) $D_{s,1} = 1.0 \times 10^{-6}$ cm^2 s^{-1}, $D_{s,2} = 1.0 \times 10^{-6}$ cm^2 s^{-1}; (◇) $D_{s,1} = 1.0 \times 10^{-6}$ cm^2 s^{-1}, $D_{s,2} = 1.0 \times 10^{-7}$ cm^2 s^{-1}; (●) $D_{s,1} = 1.0 \times 10^{-6}$ cm^2 s^{-1}, $D_{s,2} = 1.0 \times 10^{-8}$ cm^2 s^{-1}; (■) $D_{s,1} = 1.0 \times 10^{-7}$ cm^2 s^{-1}, $D_{s,2} = 1.0 \times 10^{-7}$ cm^2 s^{-1}; (▲) $D_{s,1} = 1.0 \times 10^{-7}$ cm^2 s^{-1}, $D_{s,2} = 1.0 \times 10^{-8}$ cm^2 s^{-1}. All other conditions as given in Figure 5.4.

Figure 5.6

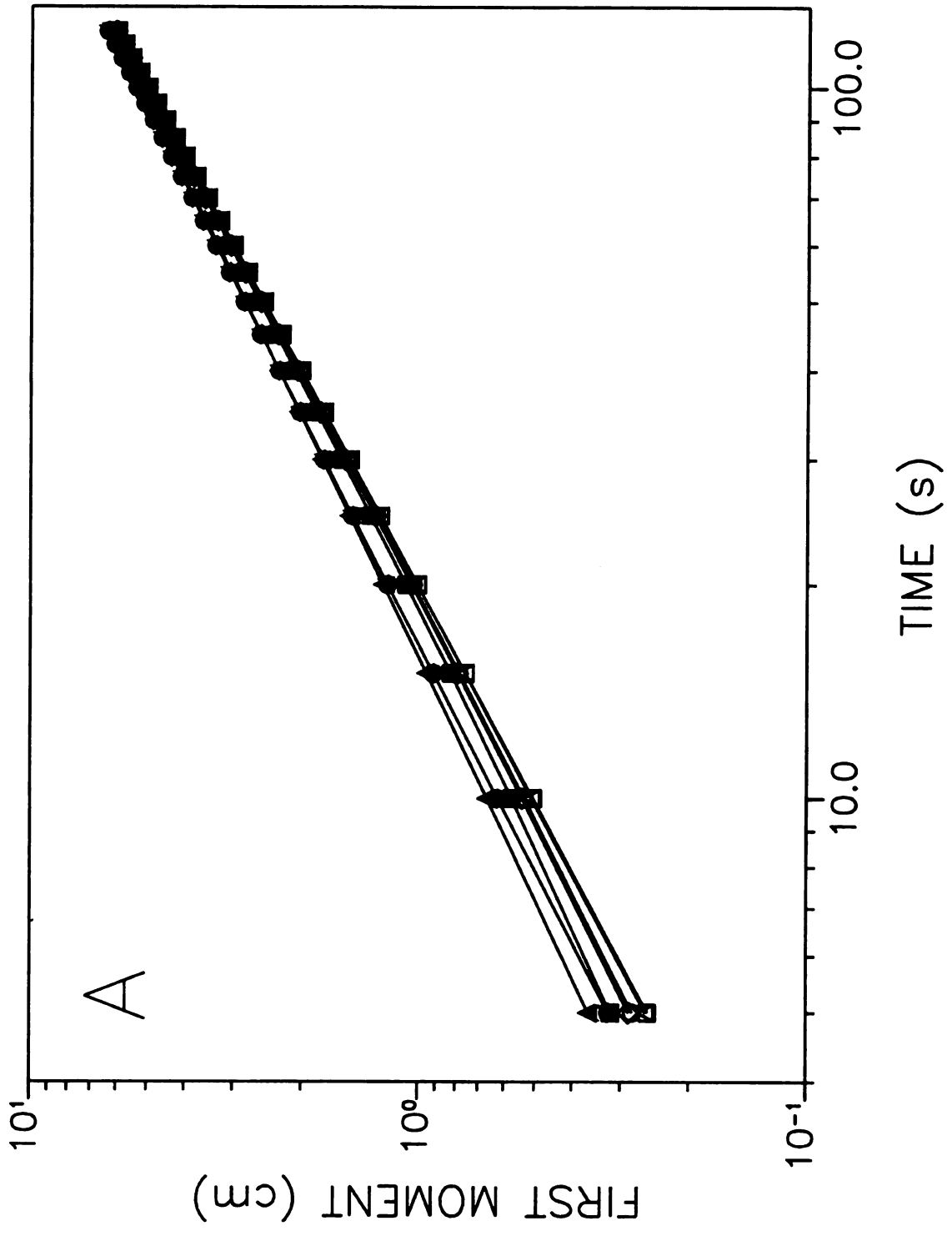

Figure 5.6 cont.

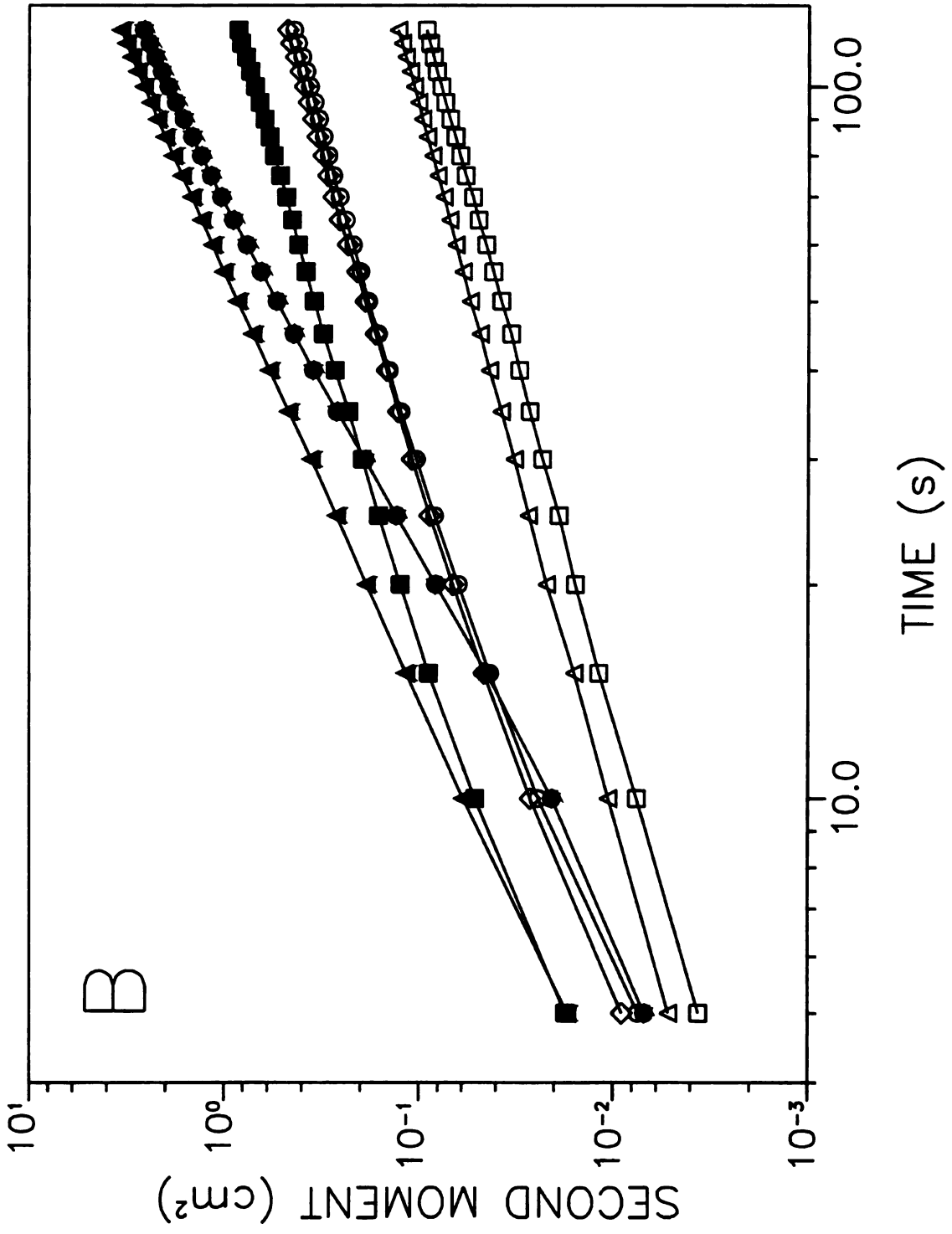

Figure 5.6 cont.

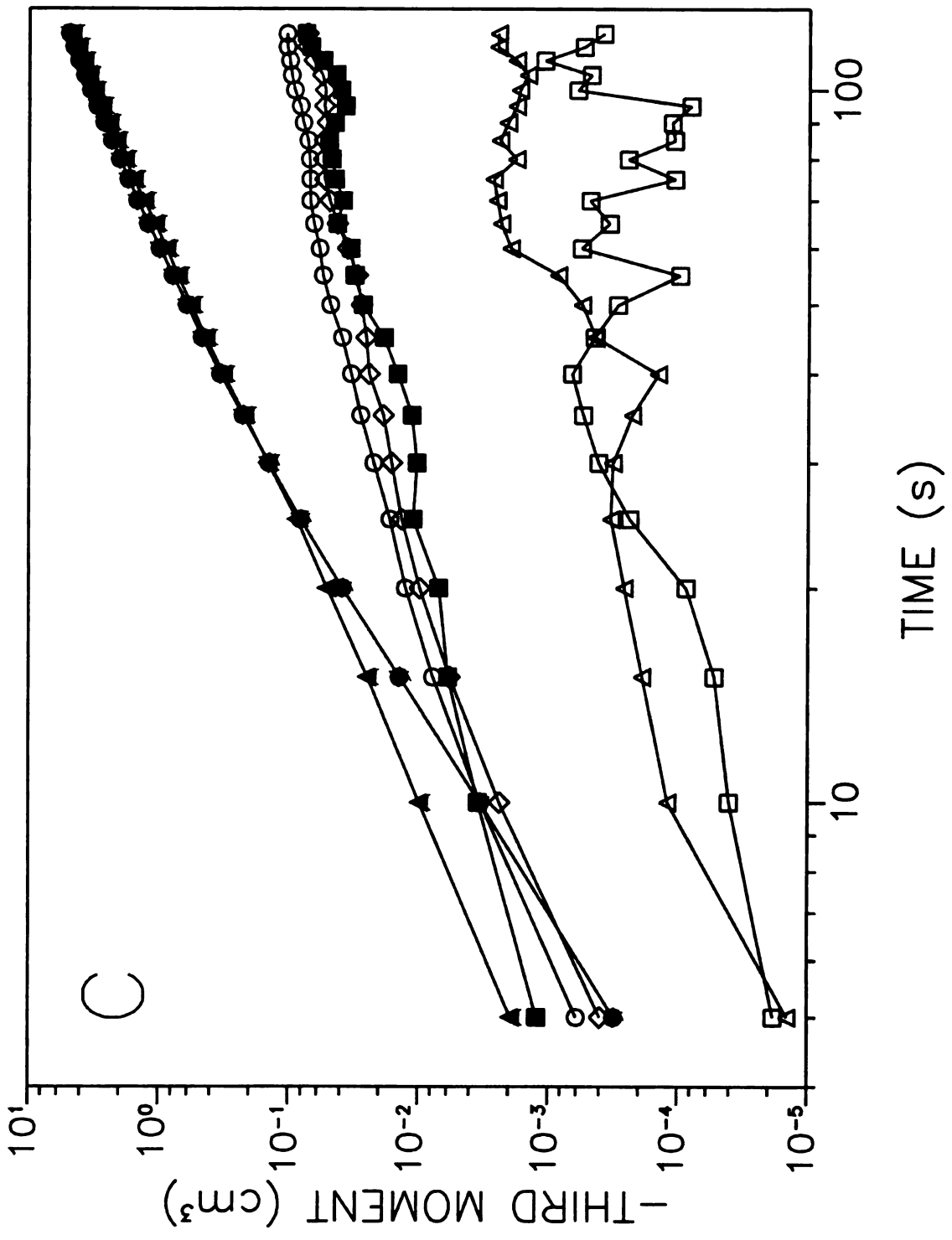

steady state and that the different mass transfer rates have no effect on the average system response. The first moments in distance as a function of time in Figure 5.6A show a different result. While the first moments are linear, they are not equal in magnitude. The first moments in distance increase as the diffusion coefficient of the second site decreases. The observed separation of first moments is the result of different rates of zone movement through the system. The deviations, easily seen in Figure 5.6A for the diffusion coefficient combinations of $D_{s,1} = 1.0 \times 10^{-6}$ and $D_{s,2} = 1.0 \times 10^{-8}$ cm^2 s^{-1} or $D_{s,1} = 1.0 \times 10^{-7}$ and $D_{s,2} = 1.0 \times 10^{-8}$ cm^2 s^{-1} can best be described by the slow kinetics of mass transfer observed for these systems (Table 5.2). The solute molecules were all started in the mobile phase and, because of the slow kinetics to enter the surface phase, the velocity of the solute zone is faster than the steady-state velocity. The zone then travels farther down the column than expected from equilibrium theories. As the system relaxes over time, a steady state is established and the average velocity of the analyte molecules approaches that predicted by theory. However, there is a constant offset in the first moment due to the initial period of non-equilibrium. Longer periods of non-equilibrium associated with smaller diffusion coefficients of the second site produce larger offsets as seen in Figure 5.6A.

The second moment or variance in time as a function of distance is shown in Figure 5.5B. The graphs are linear but vary in magnitude and can be separated into three distinct groups. The systems with a value of 1.0×10^{-6} cm^2 s^{-1} as the smallest diffusion coefficient have the fastest mass transfer rates and, correspondingly, the smallest values of the second moment. Systems with a value of 1.0×10^{-7} cm^2 s^{-1} as the smallest

diffusion coefficient appear in the middle of the graph, indicating that the zones have broadened more due to the slower mass transfer rates. The systems with the largest second moments have a diffusion coefficient of 1.0×10^{-8} cm^2 s^{-1}. These results suggest that the systems behave as if limited by the smallest diffusion coefficient. The larger diffusion coefficient of the pair does not change the system response appreciably at long distances. However at short distances, the site with the larger diffusion coefficient does influence the system response, as seen for the systems with $D_{s,1} = 1.0 \times 10^{-6}$ and $D_{s,2} = 1.0 \times 10^{-8}$ cm^2 s^{-1} or $D_{s,1} = 1.0 \times 10^{-7}$ and $D_{s,2} = 1.0 \times 10^{-8}$ cm^2 s^{-1}. Figure 5.6B shows the variance in distance as a function of time for these systems. Some of the general trends in Figure 5.5B are observed here as well. The variance of the systems appears to increase as the smallest diffusion coefficient decreases. The systems also show the same tendency to form groups according to the smallest diffusion coefficient in the pair. There are also some very noticeable differences. The systems with a value of 1.0×10^{-6} cm^2 s^{-1} as the smallest diffusion coefficient are linear. These systems equilibrate quickly and show no deviation from the trend expected from equilibrium theory. However, the systems that have a value of 1.0×10^{-7} cm^2 s^{-1} as the smallest diffusion coefficient show slight curvature over short times, but become linear over long times. These systems reach steady state over the course of the simulation and behave as theory predicts. The systems with a value of 1.0×10^{-8} cm^2 s^{-1} for the smallest diffusion coefficient initially show curvature and appear to reach a linear relationship with time, but with a steeper slope. This greater dependence on time is believed to occur because the systems do not reach steady state within the time simulated (*vide infra*). The

increased slope indicates that the zones broaden more than predicted by equilibrium theories because of the slow mass transfer kinetics of the second site.

The third moments in time and distance are presented in Figures 5.5C and 5.6C, respectively. The third moments display trends similar to those of the second moments in both time and distance. The third moments in time are linear, whereas those in distance are not. For both time and distance domains, a decrease in the diffusion coefficient causes an increase in the third moment or asymmetry. It appears that the smallest diffusion coefficient is the controlling factor for the asymmetry, just as it was for the variance. It is interesting to note again that the third moments in time and distance are opposite in sign. The moments in time as a function of distance are positive (tailing profiles) while the moments in distance as a function of time are negative (fronting profiles).

5.3.3. Effect of Differences in Interfacial Resistance to Mass Transfer.

The final parameter studied is the barrier to mass transport across the interface between the fluid and surface phases. The *a* parameter in Equations [2.12] and [2.13] is maintained constant at 1.0 for one surface site, while the other site is varied from 1.0 to 0.001. The steady-state distribution of molecules between the surface and fluid phases as well as the mass transfer rate constants for these systems are recorded in Table 5.3. The ratio of the number of molecules in the surface and fluid phases appears to be similar for all of these systems. This implies that the steady-state behavior is not affected by the *a* parameter. However, the kinetics show a reduction in the rate constants as the *a*

Table 5.3 Rate Constants (k_{fs}, k_{sf}),[a] Characteristic Times (T_{50}, T_{90}, T_{95}), and Steady-State Distributions ($\tilde{N}_s/\tilde{N}_f$) for Mass Transfer Processes as a Function of the Interfacial Resistance to Mass Transfer (a).[b]

a_1	a_2	$\tilde{N}_s/\tilde{N}_f$	k_{fs}/k_{sf}	k_{fs} (s^{-1})	k_{sf} (s^{-1})	R^2	T_{50} (s)	T_{90} (s)	T_{95} (s)
1.0	1.0	1.008 ± 0.005	0.992 ± 0.003	0.370 ± 0.006	0.373 ± 0.006	0.965 ± 0.001	0.75 ± 0.01	3.93 ± 0.09	5.3 ± 0.2
1.0	0.1	0.998 ± 0.007	0.995 ± 0.002	0.37 ± 0.02	0.37 ± 0.02	0.924 ± 0.004	0.83 ± 0.02	3.6 ± 0.1	4.8 ± 0.3
1.0	0.01	0.993 ± 0.010	0.985 ± 0.008	0.23 ± 0.02	0.24 ± 0.02	0.963 ± 0.008	1.53 ± 0.07	6.7 ± 0.1	9.23 ± 0.03
1.0	0.001	0.986 ± 0.006	0.880 ± 0.008	0.099 ± 0.003	0.112 ± 0.004	0.77 ± 0.01	2.33 ± 0.03	37.2 ± 0.6	55 ± 9

[a] Determined by nonlinear regression according to Equation [4.5] with square of the correlation coefficient R^2.

[b] Simulation conditions: $N = 10000$, $R_f = 2.0 \times 10^{-3}$ cm, $R_s = 8.28 \times 10^{-4}$ cm, $P_1 = P_2 = 0.5$, $K_{abs,1} = K_{abs,2} = 1.0$, $D_f = 1.0 \times 10^{-5}$ cm^2 s^{-1}, $D_{s,1} = D_{s,2} = 1.0 \times 10^{-7}$ cm^2 s^{-1}, $t = 1.0 \times 10^{-3}$ s, $T = 20\,\tau$.

parameter is reduced. This indicates that as the resistance to mass transfer increases (*a* decreases), the rate of mass transfer across the interface decreases. As the *a* parameter is reduced to 0.001, the systems appear to change from single exponential kinetics to biexponential kinetics. This change in kinetic behavior can be seen in the values of the square of the correlation coefficient (R^2) of the fit to Equation [4.5] as well as the characteristic times. The values of T_{50} show a steady increase as the *a* parameter decreases, but T_{90} and T_{95} show more substantial changes for the value of 0.001. This trend in the characteristic times indicates that the long-time response becomes dominated by the slow mass transfer of the surface site with the small value for the *a* parameter, while the short time behavior is dominated by the faster mass transfer of the other site.

The effect of the barrier to interfacial mass transfer on the fluid dynamic behavior can be seen in Figure 5.7. This figure shows the zone profiles for the systems presented in Table 5.3 at columns lengths of 0.1 to 5.0 cm. Each system shows a decrease in the height of the zone profile, an increase in the width, and a decrease in the asymmetry as the column length increases. This is the same trend that is seen for the previous studies (Figures 5.1 and 5.4) as well as for systems with homogeneous surfaces (Chapters 3 and 4).[23,24] It can be seen that as the two values of the *a* parameter diverge, the asymmetry in the zone profile at 5.0 cm increases. The asymmetry is most noticeable for the system with $a_1 = 1.0$ and $a_2 = 0.001$, since it has the largest difference in the *a* parameter.

The moments of these systems in time and distance are shown Figures 5.8 and 5.9, respectively. The first moments in time as a function of distance (Figure 5.8A) are linear and equal in magnitude. This indicates that the *a* parameter does not affect the mean

Figure 5.7: Zone profiles for systems with laminar flow and two absorption sites with (A) $a_1 = a_2 = 1.0$; (B) $a_1 = 1.0$, $a_2 = 0.1$; (C) $a_1 = 1.0$, $a_2 = 0.01$; (D) $a_1 = 1.0$, $a_2 = 0.001$. Column lengths of 0.1, 0.2, 0.5, 1.0, 2.0, and 5.0 cm. All other parameters as follows: $N = 1000$, $t = 5.0 \times 10^{-5}$ s, $R_f = 2.0 \times 10^{-3}$ cm, $R_s = 8.28 \times 10^{-4}$ cm, $v_0 = 0.1$ cm s^{-1}, $P_1 = P_2 = 0.5$, $K_{abs,1} = K_{abs,2} = 1.0$, $D_f = 1.0 \times 10^{-5}$ cm^2 s^{-1}, $D_{s,1} = D_{s,2} = 1.0 \times 10^{-7}$ cm^2 s^{-1}.

Figure 5.7

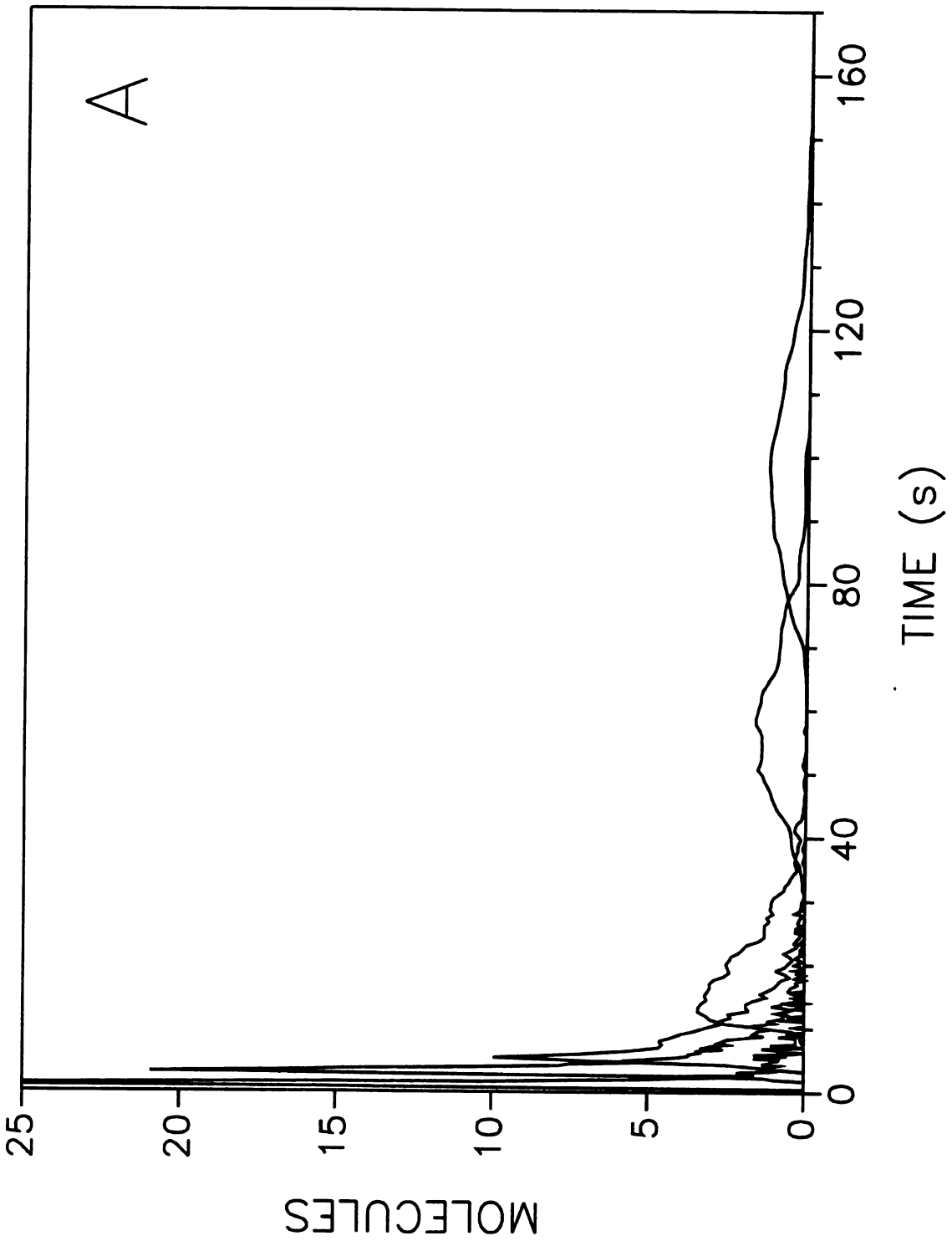

Figure 5.7 cont.

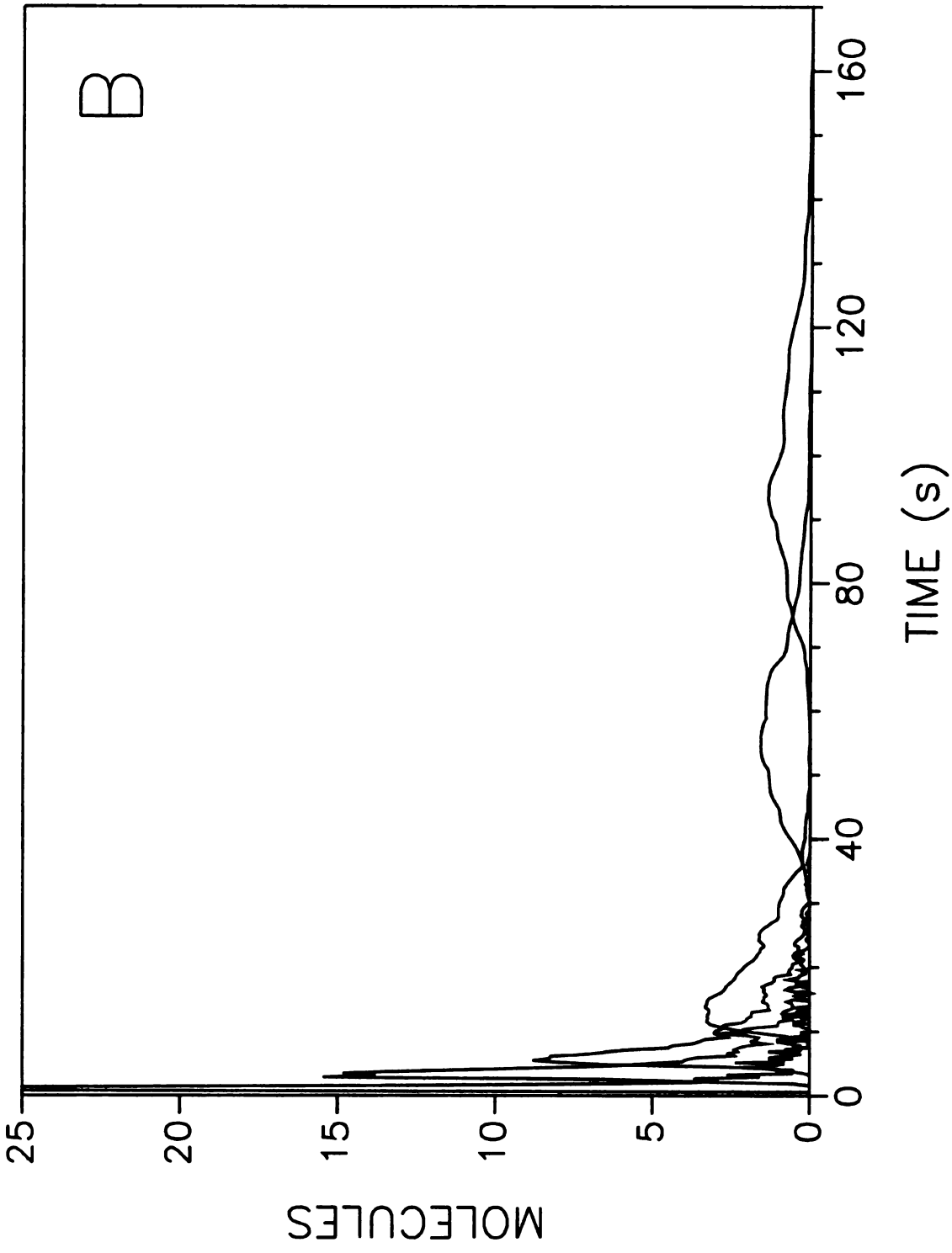

Figure 5.7 cont.

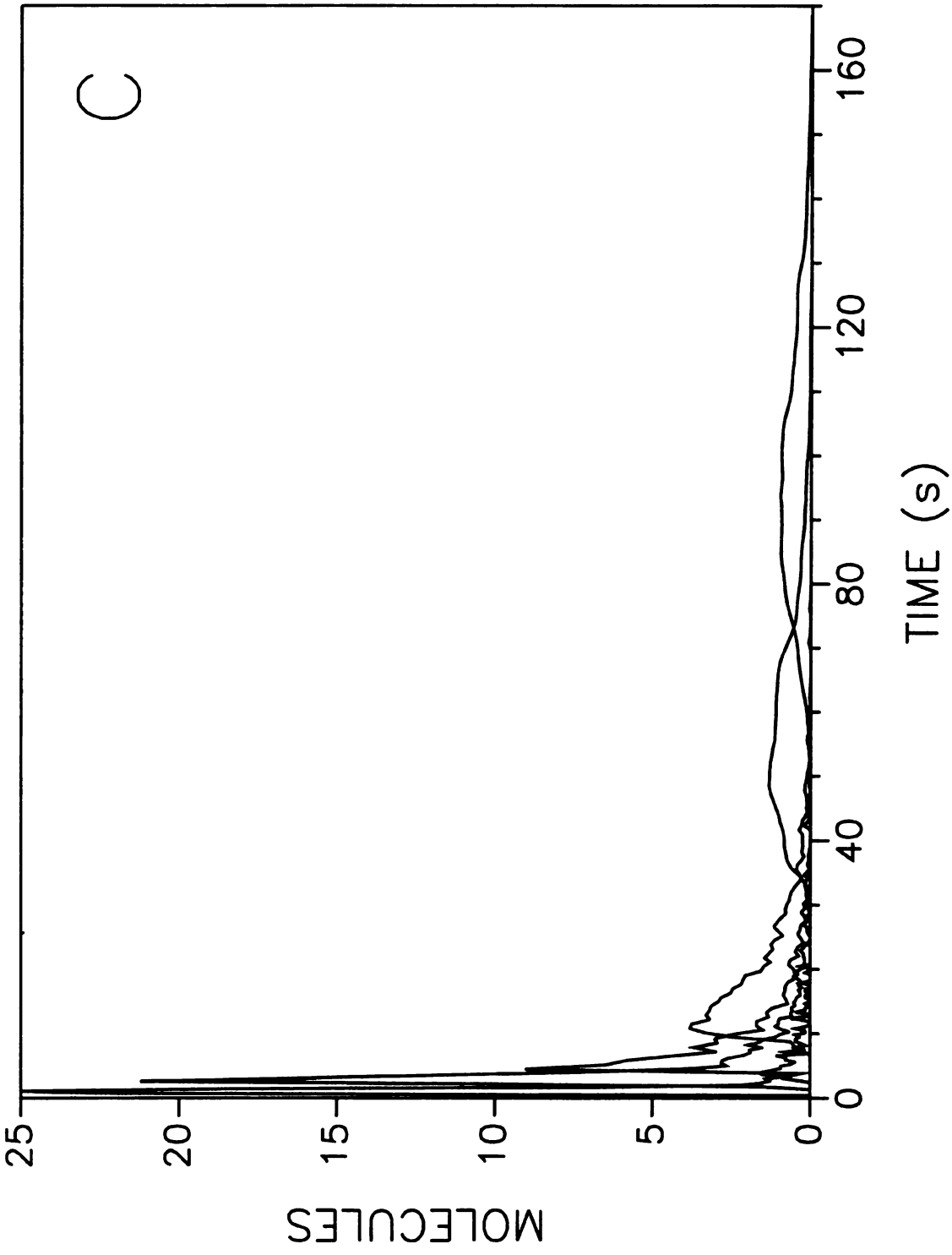

Figure 5.7 cont.

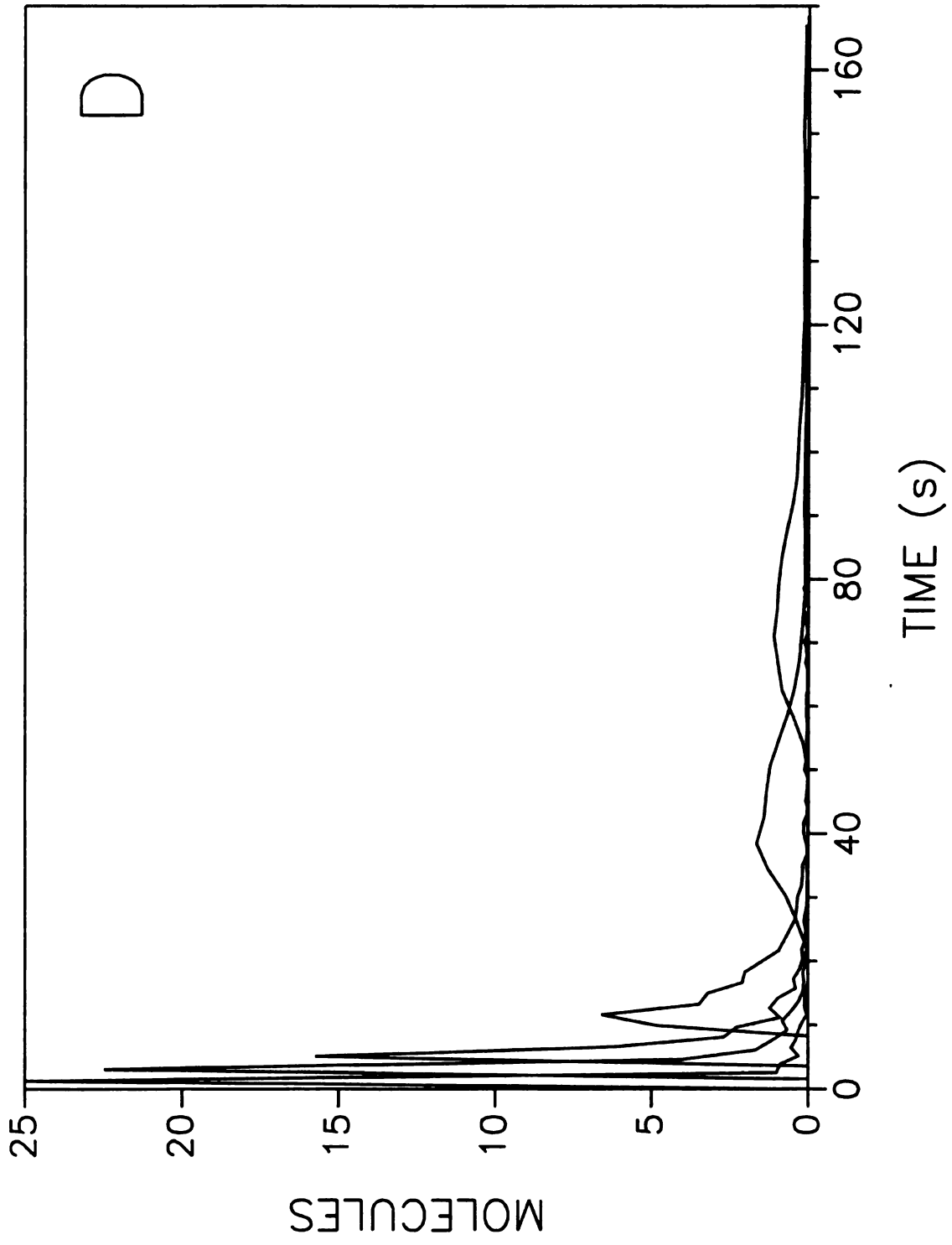

Figure 5.8: The calculated (A) first moment, (B) second moment, and (C) third moment in time as a function of distance for systems with (○) $a_1 = a_2 = 1.0$; (□) $a_1 = 1.0$, $a_2 = 0.1$; (△) $a_1 = 1.0$, $a_2 = 0.01$; (◇) $a_1 = 1.0$, $a_2 = 0.001$. All other conditions as given in Figure 5.7.

Figure 5.8

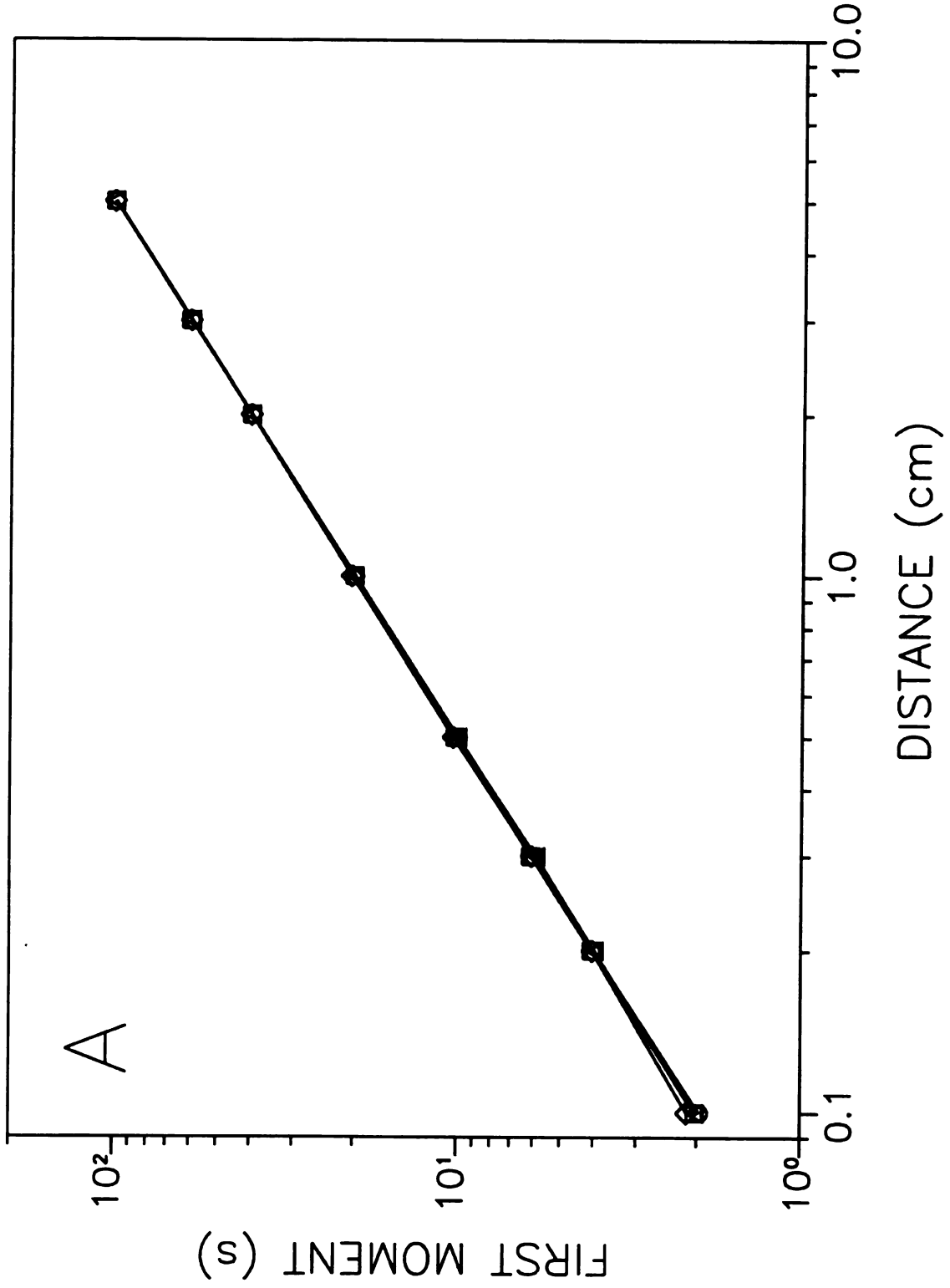

Figure 5.8 cont.

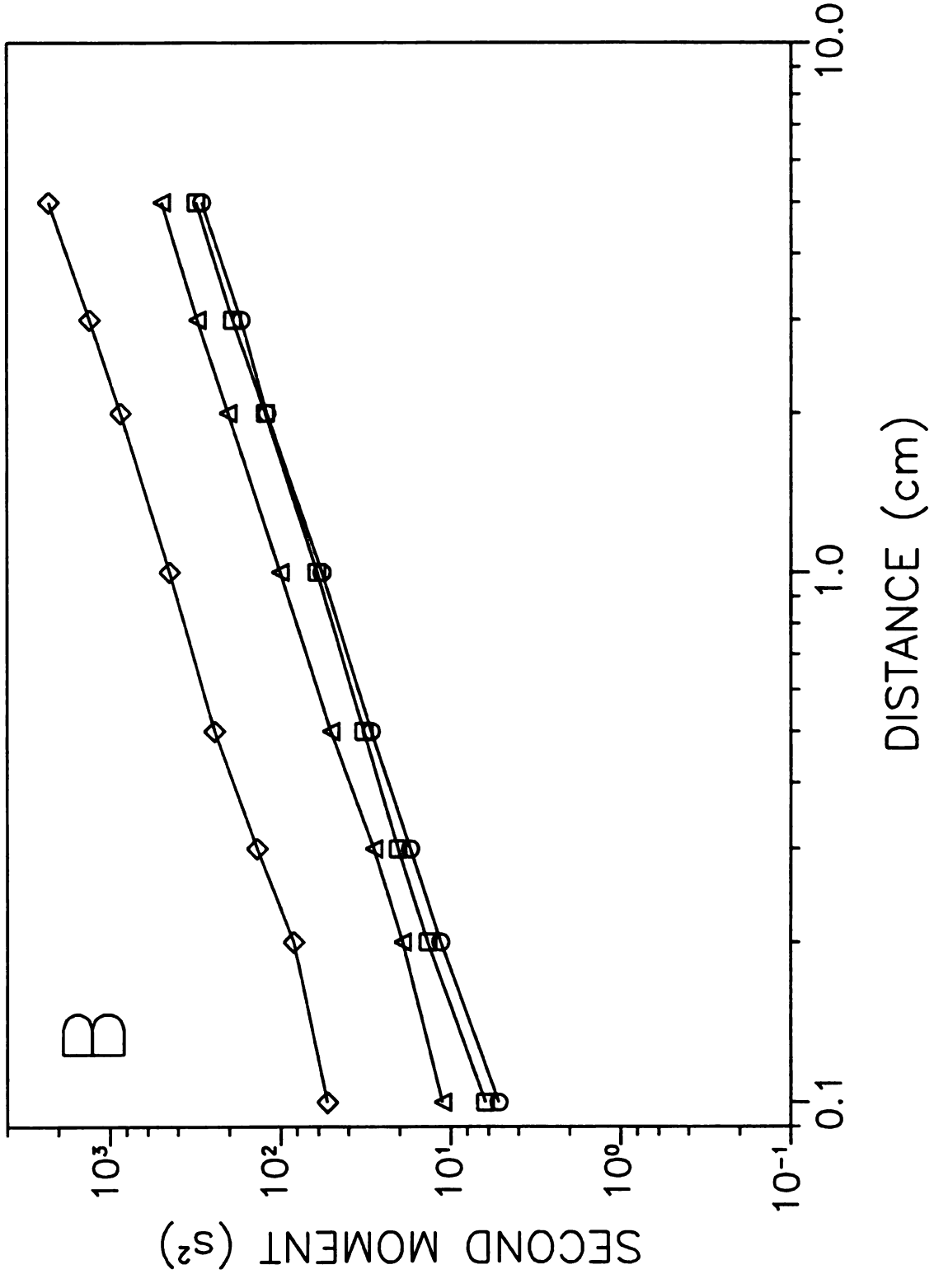

Figure 5.8 cont.

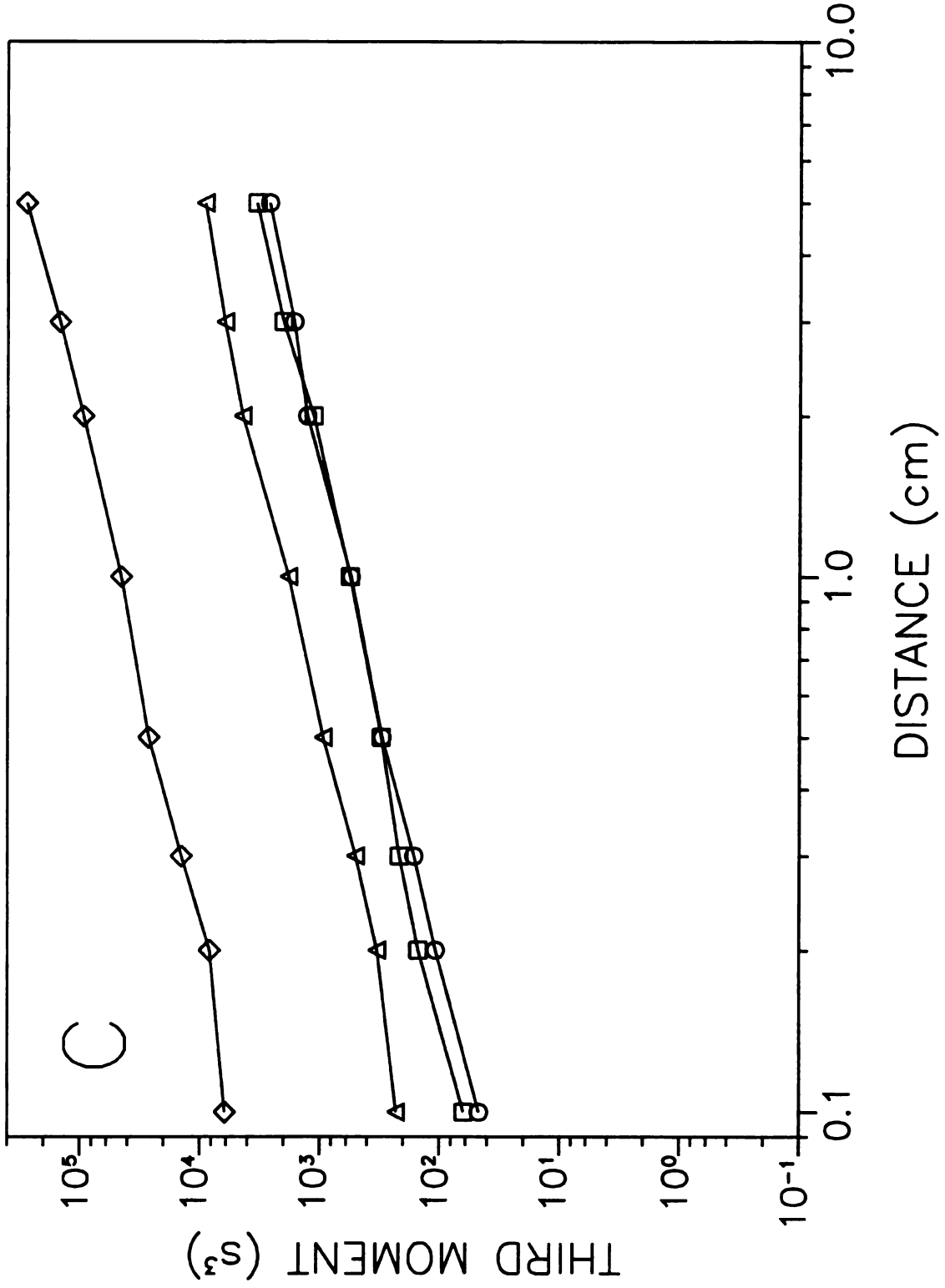

Figure 5.9: The calculated (A) first moment, (B) second moment, and (C) third moment in distance as a function of time for systems with (○) $a_1 = a_2 = 1.0$; (□) $a_1 = 1.0$, $a_2 = 0.1$; (△) $a_1 = 1.0$, $a_2 = 0.01$; (◇) $a_1 = 1.0$, $a_2 = 0.001$. All other conditions as given in Figure 5.7.

Figure 5.9

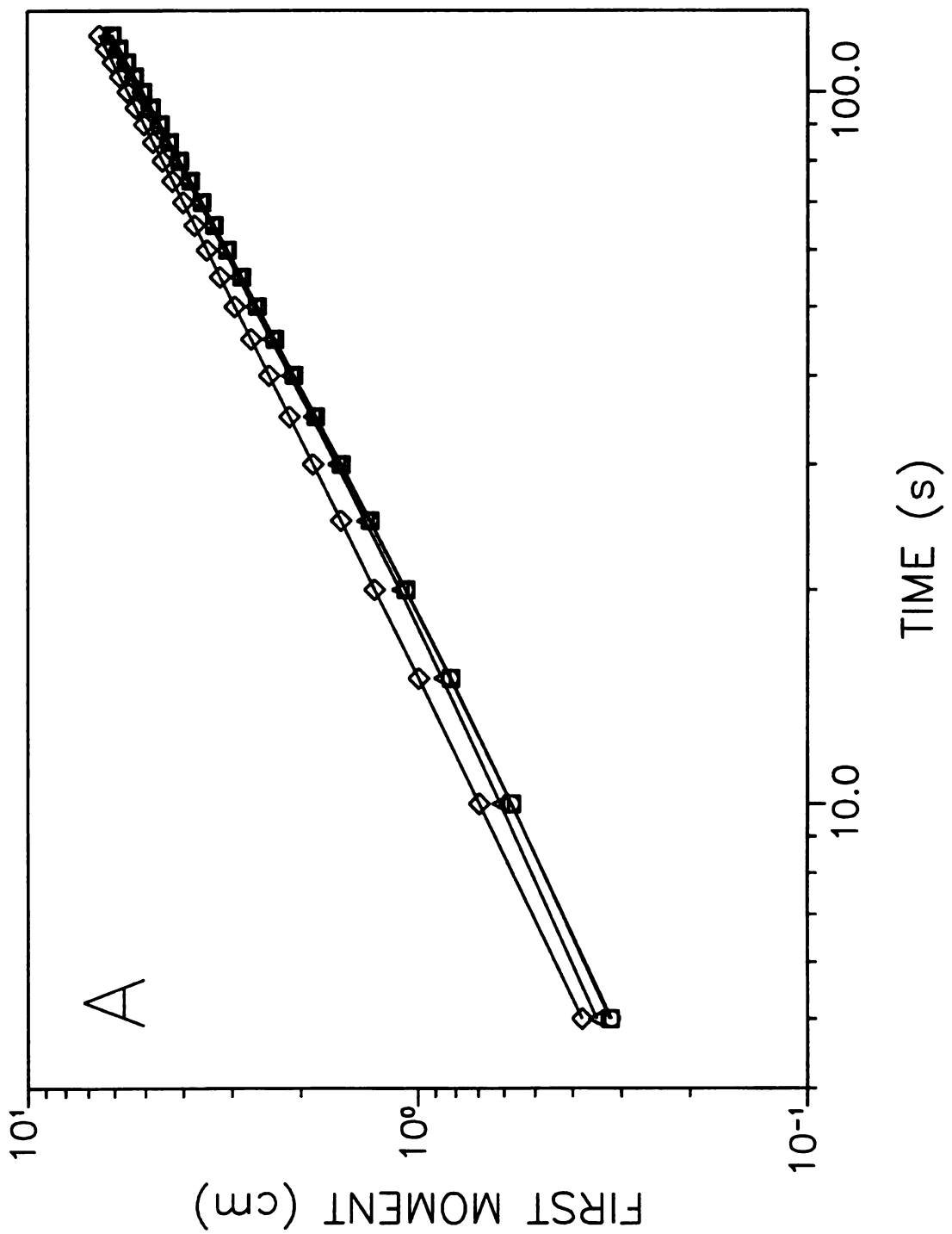

Figure 5.9 cont.

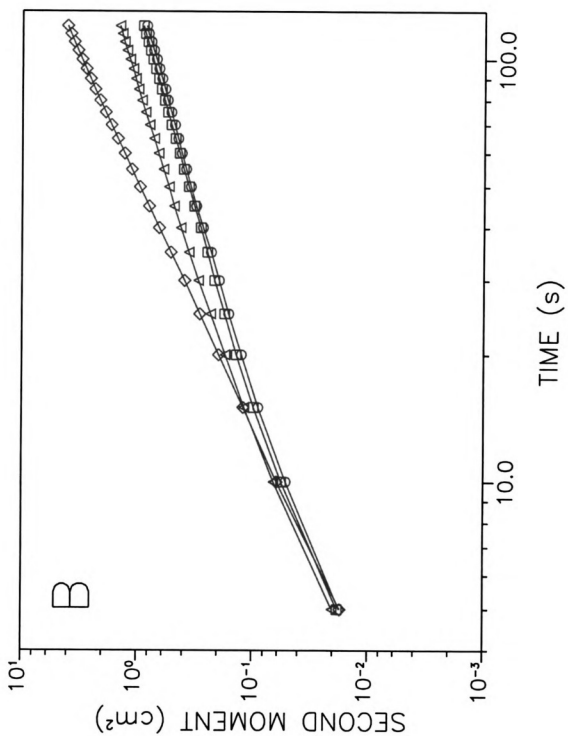

Figure 5.9 cont.

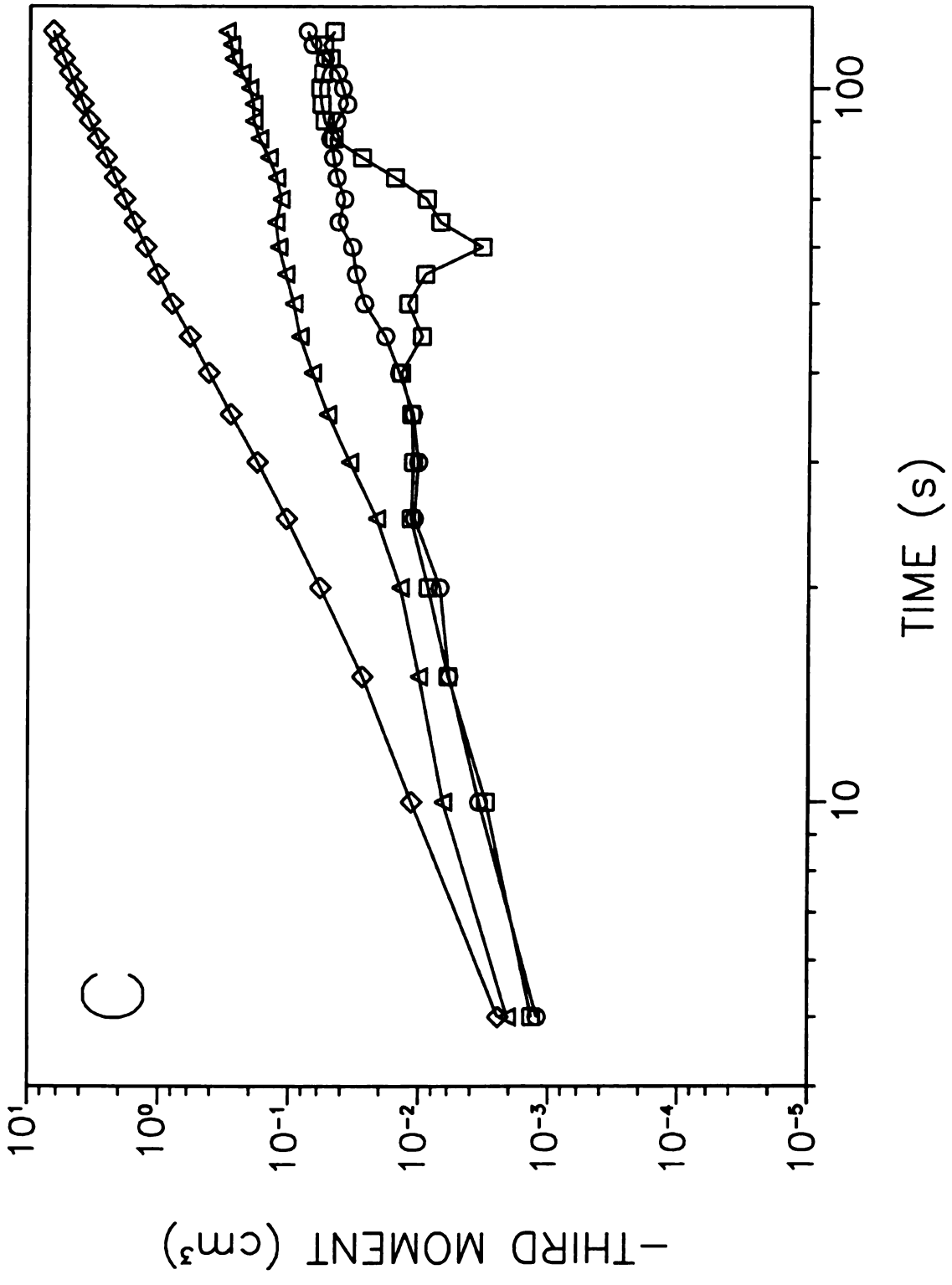

elution time. The first moments in distance as a function of time (Figure 5.9A) are linear but show differences in magnitude, especially at short times. The magnitude of the first moments increases with a decrease in the a parameter and the corresponding mass transfer rate (Table 5.3). This implies that the differences in magnitude are the result of the time required for the mass transfer processes in the system to reach steady state. All of these observations are similar to those in the studies of diffusion coefficient discussed above.

The second moments shown in Figures 5.8B and 5.9B increase as the values of the a parameter for the two sites diverge. However, the effect of the slow mass transfer appears different in the time and distance domains. Figure 5.8B shows linear correlation between the second moments and the column length, indicating that the systems are at steady state. However, Figure 5.9B shows a nonlinear correlation between the second moment and time. The system with $a_1 = 1.0$ and $a_2 = 0.01$ shows curvature, and the system with $a_1 = 1.0$ and $a_2 = 0.001$ has a steeper slope than the other systems. Also, the second moments in Figure 5.9B are initially similar in magnitude and then diverge as time increases. This implies that the initial response of the systems is controlled by the site with fast mass transfer ($a = 1.0$), and that the long-time behavior of the systems is controlled by the site with slower mass transfer. This trend supports the conclusion that the mass transfer of the systems becomes biexponential in character as the two values of the a parameter diverge. These trends in the second moments are similar to those for the diffusion coefficient described above.

The third moments shown in Figures 5.8C and 5.9C increase as the values of the a parameter for the two sites diverge. The greatest asymmetry is produced by the highest barrier to interfacial mass transfer (smallest value of a). The third moments follow the same trends as described for the second moments above. The moments in time are a linear function of distance (Figure 5.8C). The third moments in distance as a function of time (Figure 5.9C) all appear to begin with comparable values, and then diverge as time increases. This indicates that the systems are equivalent initially, but become different at long time as the site with slow mass transfer becomes dominant. The moments also show nonlinear trends with time, especially for the system with $a_1 = 1.0$ and $a_2 = 0.001$.

5.4 Discussion.

The systems studied in this report show the effects of multiple sites on the absorption mechanism in chromatography. Differences in only the absorption coefficients of n different sites creates a system that responds as a homogeneous system with an average absorption coefficient defined as

$$K_{abs,avg} = \sum_{j=1}^{n} P_j K_{abs,j} \qquad [5.6]$$

This occurs because the interactions of the molecules with the surface sites are independent. The system can then be split into n different systems in series such that the separate systems are the fraction P_i of the composite system. However, differences in either the surface-phase diffusion coefficient or the interfacial resistance to mass transfer cause the system to behave as reversible first-order reactions in competition, rather than a

single reversible first-order reaction. These changes in the mass transfer kinetics cause the second and third moments to vary from those of a system with a homogeneous surface phase. These observations agree with previous work on the mass transfer rates of diffusion-limited systems.[24] The mass transfer rate constants k_{fs} and k_{sf} are related to the system parameters in Chapter 4. Equations [4.17], and [4.18] show that the rate constants are proportional to the number of molecules in each phase at equilibrium. This is the only influence of the absorption coefficient on the mass-transfer rate constants. Therefore, the mass transfer rate appears only to be affected by the average absorption coefficient, as defined in Equation [5.6]. It can also be shown that the partial derivative of the characteristic time $\tau = 1/(k_{fs} + k_{sf})$ with respect to K_{abs} is zero (Appendix A). Thus, the mass transfer of the system is not dependent on changes in the absorption coefficient of the individual surface sites so long as the value of $K_{abs,avg}$ is kept constant. This explains the independence of τ with respect to the absorption coefficient already observed in the kinetic and fluid dynamic results presented above (Section 5.3.1). The systems with different absorption coefficients are observed to behave identically to a single site system with an absorption coefficient equal to $K_{abs,avg}$. The logarithmic graphs of the moments are linear with a slope of 1 (Figures 5.2 and 5.3). This indicates that the systems behave as would be expected for a system with a single site at steady state.

The partial derivative of τ with respect to D_s, however, is not zero (Appendix A) because the surface-phase diffusion coefficient affects the mass transfer differently than the absorption coefficient. Unlike the absorption coefficient, changes in the surface-phase diffusion coefficient affect the rate of movement to and from the interface.

Therefore, changes in the surface-phase diffusion coefficient will change the value of τ. This is apparent in the kinetic and fluid dynamic data presented above for systems with different surface-phase diffusion coefficients. As the difference between the diffusion coefficients at each site increases, the difference in τ increases. Once the differences in τ are sufficiently large, the system shows biexponential kinetics for mass transfer between the fluid and surface phases. The data in Table 5.2 and Figures 5.4 to 5.6 show that as the difference between the two diffusion coefficients increases there are larger deviations from the response of a system with a single site. The most noticeable effect of the different diffusion coefficients is the curvature in the second and third moments in Figure 5.6. The second and third moments of systems with 1.0×10^{-7} cm^2 s^{-1} as the smallest diffusion coefficient exhibit a slope of 2 initially that decreases to a value of 1 on the logarithmic graphs as time increases. The second and third moments of systems with 1.0×10^{-8} cm^2 s^{-1} as the smallest diffusion coefficient exhibit a slope of 2 for the entire simulation time. This square dependence of the second moments on time can be explained by the fact that the two absorption sites cause a spatial separation that is similar to that described by Golay and Atwood.[25] Their work describes a non-equilibrium phenomenon in which there is a group of molecules near the wall with zero velocity and a group of molecules in the center of the open tube with a velocity close to the maximum for the laminar profile. This distribution initially causes a zone profile with a "boxcar" shape with a variance that is proportional to the time squared. The profile described by Golay and Atwood is transient, and disappears quickly since the open tube has a very small volume of zero velocity. The systems simulated in this study have a stationary

phase that produces two average velocities of the zone because of the different diffusion coefficients. This condition is probably transient as well but, because the mass transfer within the systems is slow, it requires more time to reach steady state than is simulated herein. The square dependence of the third moment on time further indicates that the systems are not at steady state.

The kinetic and fluid dynamic response of the system to differences in interfacial resistance to mass transfer appears to be similar to differences in diffusion coefficient. This indicates that the changes in mass transfer rate arising from changes in the *a* parameter affect the system in the same manner as those arising from changes in the diffusion coefficient. While it is possible to determine from the system response whether multiple sites with different mass transfer properties exist, the exact number and nature of those sites cannot be determined.

This work also demonstrates the inherent difference between the statistical moments in the time and distance domains. For the data collected at a specified time, each molecule has the same amount of time to interact with the fluid and surface phases. This is different from the data collected at a specified distance, where each molecule has the same amount of time in the fluid phase but different total amounts of time. At steady state, the moments in time and distance are related to each other through the average velocity of the solute zone in the following manner:

$$\frac{M_{n,d}}{M_{n,t}} = \left(\frac{v}{1 + K_{abs}\beta} \right)^n \qquad [5.7]$$

From this equation, it is evident that the higher moments are the most sensitive indication of the steady state. This expectation is verified by comparison of Figures 5.5 and 5.6 or Figures 5.8 and 5.9. When the system is not at steady state, the average velocity of each molecule is not equal to the average velocity of the zone and Equation [5.7] is not satisfied. The moments in time and distance hold different information about a system that is not a steady state and, therefore, do not have a simple relationship to each other.

5.5 Conclusions.

A new theoretical model has been applied to absorption chromatography to study the effects of multiple surface sites. This model follows individual molecules through three-dimensional space, allowing independent interactions with the surface phase. There are many benefits to this kind of simulation. First, this model makes no assumptions about the relative contribution to mass transfer from the processes of diffusion, convection, and interaction with the surface phase. It is not necessary to neglect or to combine any of these processes in order to make the model tractable, as in the case of the mass balance approach. Thus, a detailed and unified model is available to study heterogeneous surfaces over a wide range of mass transfer rates.

Second, each molecule interacts independently with the surface, and any correlation between the different surface sites can be studied without prior knowledge or assumptions. This chapter has shown that a heterogeneous system with differences in absorption coefficient is indistinguishable from a homogeneous system with the same effective absorption coefficient. Differences in the surface-phase diffusion coefficient or

the interfacial resistance to mass transfer, however, result in different kinetic and fluid dynamic responses.

Finally, this model provides a wealth of information. Since the algorithms in the simulation are applied to an ensemble of molecules, it is possible to obtain molecular-level information as well as macroscopic information. The mass transfer curves, zone profiles, and statistical moments can easily be obtained from the same simulation. Thus, it is possible to associate the kinetic regime of the mass transfer curve with the curvature observed in the statistical moments. It is also possible to compare the time and distance moments to determine when the fluid dynamics of the system have reached steady state. The results presented herein suggest that the steady state is achieved when the ratio of the statistical moments in the time and distance domains is related to the average velocity of the solute zone, as given in Equation [5.7]. The findings for this simple two-site system suggest that further study by this method will be beneficial in studying more complicated systems.

5.6 References.

1. Giddings, J.C.; Eyring, H.; J. Phys. Chem. 1955, 59, 416.
2. Giddings, J.C.; J. Chem. Phys. 1957, 26, 169.
3. McQuarrie, D.A.; J. Chem. Phys. 1963, 38, 437.
4. Weiss, G.H.; Sep. Sci. 1970, 5, 51.
5. Cavazzini, A.; Remelli, M.; Dondi, F.; J. Microcolumn Sep. 1997, 9, 295.
6. Cavazzini, A.; Remelli, M.; Dondi, F.; Felinger, A.; Anal. Chem. 1999, 71, 3453.
7. Hilderbrand, G.P.; Reilley, C.N.; Anal. Chem. 1964, 36, 47.

8. Pilgrim, G.W.; Keller, R.A.; J. Chromatogr. Sci. 1973, 11, 206.

9. Zhu, B.Y.; Mant, C.T.; Hodges, R.S.; J. Chromatogr. 1992, 594, 75.

10. Heron, S.; Tchapla, A.; J. Chromatogr. A, 1996, 725, 205.

11. Buszewski, B.; Gadzala-Kopiuch, R.M.; Jaroniec, M.; J. Liq. Chromatogr. Relat. Technol. 1997, 20, 2313.

12. Lochmuller, C.H.; Colborn, A.S.; Hunnicutt, M.L.; Harris, J.M.; Anal. Chem. 1983, 55, 1344.

13. Bereznitski, Y.; Jaroniec, M.; Gangoda, M.E.; J. Chromatogr. A, 1998, 828, 59.

14. Beck, T.L.; Klatte, S.J.; Cole, L.A.; Dorsey, J.G.; J. Chromatogr. A, 1993, 656, 317.

15. Boehm, R.E.; Martire, D.E.; J. Phys. Chem. 1980, 84, 3620.

16. Martire, D.E.; Boehm, R.E.; J. Phys. Chem. 1983, 87, 1045.

17. Yarovsky, I.; Aguilar, M.I.; Hearn, M.T.W.; J. Chromatogr. A, 1994, 660, 75.

18. Yarovsky, I.; Aguilar, M.I.; Hearn, M.T.W.; Anal. Chem. 1995, 67, 2145.

19. Klatte, S.J.; Beck, T.L.; J. Phys. Chem. 1995, 99, 16024.

20. Klatte, S.J.; Beck, T.L.; J. Phys. Chem. 1996, 100, 5931.

21. Slusher, J.T.; Mountain, R.D.; J. Phys. Chem. B, 1999, 103, 1354.

22. Golay, M.J.E.; in Gas Chromatography, Desty, D.H. Ed.; Academic Press: New York, NY, 1958; p. 36.

23. McGuffin, V.L.; Krouskop, P.E.; Hopkins, D.L.; in Unified Chromatography, ACS Symposium Series 748, Parcher, J.F.; Chester, T.L. Eds.; American Chemical Society: Washington DC, 1999; p. 37.

24. McGuffin, V.L.; Krouskop, P.E.; Wu, P.; J. Chromatogr. A, 1998, 82, 37.

25. Golay, M.J.E.; Atwood, J.G.; J. Chromatogr. 1979, 186, 353.

STOCHASTIC SIMULATION OF SEPARATION SYSTEMS

VOLUME 2

By

Peter Edward Krouskop

A DISSERTATION

Submitted to
Michigan State University
in partial fulfillment of the requirements
for the degree of

DOCTOR OF PHILOSOPHY

Department of Chemistry

2002

Chapter 6

A Novel Stochastic Model of Adsorption Chromatography

6.1 Introduction.

Many models have been developed and applied to adsorption that provide varying degrees of insight into the process. These models can be grouped into two main categories: empirical or semi-empirical models and stochastic models. The empirical and semi-empirical models are commonly used to fit isotherm data to obtain information about the adsorbent (such as total surface area) or the adsorbate (such as interaction energies). Among these types of models are the Langmuir isotherm,[1] the Brunauer-Emmett-Teller (BET) equation,[2] two-dimensional equations of state,[3] and potential models.[3,4] The Langmuir isotherm describes a system that forms a monolayer of adsorbate on the surface. The BET, two-dimensional equations of state, and potential models are used to study the formation of multiple layers of adsorbate molecules. The BET equation is the simplest and assumes that only the first layer is affected by the presence of the surface. All subsequent layers are given the properties associated with the liquid form of the adsorbate. Attempts to incorporate long-range effects of the surface in the adsorption process have lead to the two-dimensional equations of state and the potential models. However, these empirical and semi-empirical models do not predict results *a priori*. Experimental measurements must be used to determine the fitting parameters of the models. The parameters are then system specific and do not produce useful results when extended to other systems.

Stochastic models describe the processes involved in adsorption on a molecular basis. These models may be based on random sequential adsorption[5-9] as well as Monte Carlo[10-13] and molecular dynamic simulations.[12] Random sequential adsorption places molecules on a surface until no more molecules can be placed due to size constraints. The limit in the number of molecules on the surface is referred to as the jamming limit. Originally, random sequential adsorption did not account for desorption, molecular movement in the fluid or surface phases, or long-range molecular interactions. It has since been advanced to allow diffusion within both phases,[9,14-16] desorption,[9] and long-range molecular interactions.[9] The results of the simulations based on this model can be used to determine the rate that the jamming limit is reached as well as the physical characteristics of the jammed state. A problem of random sequential adsorption simulations is that slow adsorption processes cannot be modeled, since adsorption is assumed to occur every time that a molecule encounters the surface phase.

The empirical and semi-empirical models of adsorption discussed above have been used in the mass balance and stochastic models of chromatography discussed in Chapter 1. Random sequential adsorption has been used in stochastic models of chromatography as well. Mass balance models have been used to study the causes of asymmetry in solute zones using the empirical and semi-empirical models of adsorption.[17-21] Giddings and Eyring[22] were the first to present a stochastic theory of adsorption chromatography, and other workers have advanced the theory to include multiple sites,[23-27] axial dispersion,[28] and nonlinear isotherms using the empirical and semi-empirical models discussed above.[29] Another approach to modeling the chromatographic system has been presented by Schure and Lenhoff.[30] The model is

similar to random sequential adsorption with diffusion and convection, which introduces a time increment dependence in the adsorption and desorption processes. This chapter extends the model presented in this dissertation to adsorption chromatography. A novel adsorption algorithm that is independent of the time increment will be discussed in detail, and validations of the new chromatographic simulation will be presented.

6.2 Simulation.

Using the algorithms presented in Chapter 2, separation systems based on the processes of diffusion, convection, adsorption, and desorption are modeled within a three-dimensional system as time is incremented. This chapter discusses the validation and application of this simulation to adsorption chromatography. The kinetic and fluid dynamic behavior of chromatographic systems are presented using the methods and equations discussed in Sections 2.3 and 3.2. The chromatographic system consists of an open tube with a radius of 2.0×10^{-3} cm, a fluid-phase diffusion coefficient of 1.0×10^{-5} $cm^2\ s^{-1}$, and a fluid-phase velocity of 0.1 $cm\ s^{-1}$.

6.3 Results and Discussion.

The adsorption algorithm described Section 2.7.2 is validated by demonstrating that the observed adsorption and desorption rates are independent of the time increment of the simulation. Once the algorithm has been validated, simulations of adsorption chromatography are used to compare with existing theory to determine the error in the calculated first and second moments. Finally, the simulation is applied to systems that

are initially far from steady state to explore conditions that have not been previously possible.

6.3.1 Validation of the Probability Expression.

To determine that the probability expression for adsorption in Equation [2.16] is correct, a series of simulations is performed. The first simulations assume that the probability of adsorption is unity ($k_a = k'_a = \infty$), as in random sequential adsorption and the adsorption chromatography simulations based on this model.[9,30] The desorption rate constant has a value of 1.0 s^{-1}. Simulations are then performed using time increments (t) of 1.0×10^{-4}, 1.0×10^{-5}, and 1.0×10^{-6} s. The number of molecules in the fluid phase is recorded at 0.01 s intervals for a period of 5 s. The fraction of molecules remaining in the fluid phase as a function of time is presented in Figure 6.1A. It can be seen clearly that the three systems with different time increments are not equivalent. The initial rate, as observed before 0.5 s, appears to be equivalent, but the systems diverge after that point. As the time increment decreases, so does the fraction of molecules in the fluid phase at long times. The theoretical values for the steady state are related to the ratio of k'_a/k_d.[31,32] Therefore, the trend observed in Figure 6.1A implies that the smaller time increments cause k'_a to increase, since k_d is constant. Although the results of these simulations appear to be dependent on the time increment, this behavior is anomalous because the time increment has no physical meaning in a real experimental system. In experimental systems, the adsorption rate, desorption rate, and diffusion coefficient are the only molecular parameters that affect the system response.

Figure 6.1: The fraction of fluid-phase molecules as a function of time for time increments of $t = 1.00 \times 10^{-4}$ s (○), 1.00×10^{-5} s (□), and 1.00×10^{-6} s (△) and adsorption probability expressions of (A) 1.0, (B) $1-\exp(-100\ t)$, and (C) $1-\exp(-(2\ \pi\ k_a\ R_f)/(2\ D_f\ t)^{0.5}\ t)$. Other simulation conditions as follows: $N = 50000$ (A) and 5000 (B,C), $R_f = 2.00 \times 10^{-3}$ cm, $D_f = 1.0 \times 10^{-5}$ $cm^2\ s^{-1}$, $k_a = 1.0$ $site^{-1}\ s^{-1}$, $k_d = 1.0\ s^{-1}$.

Figure 6.1

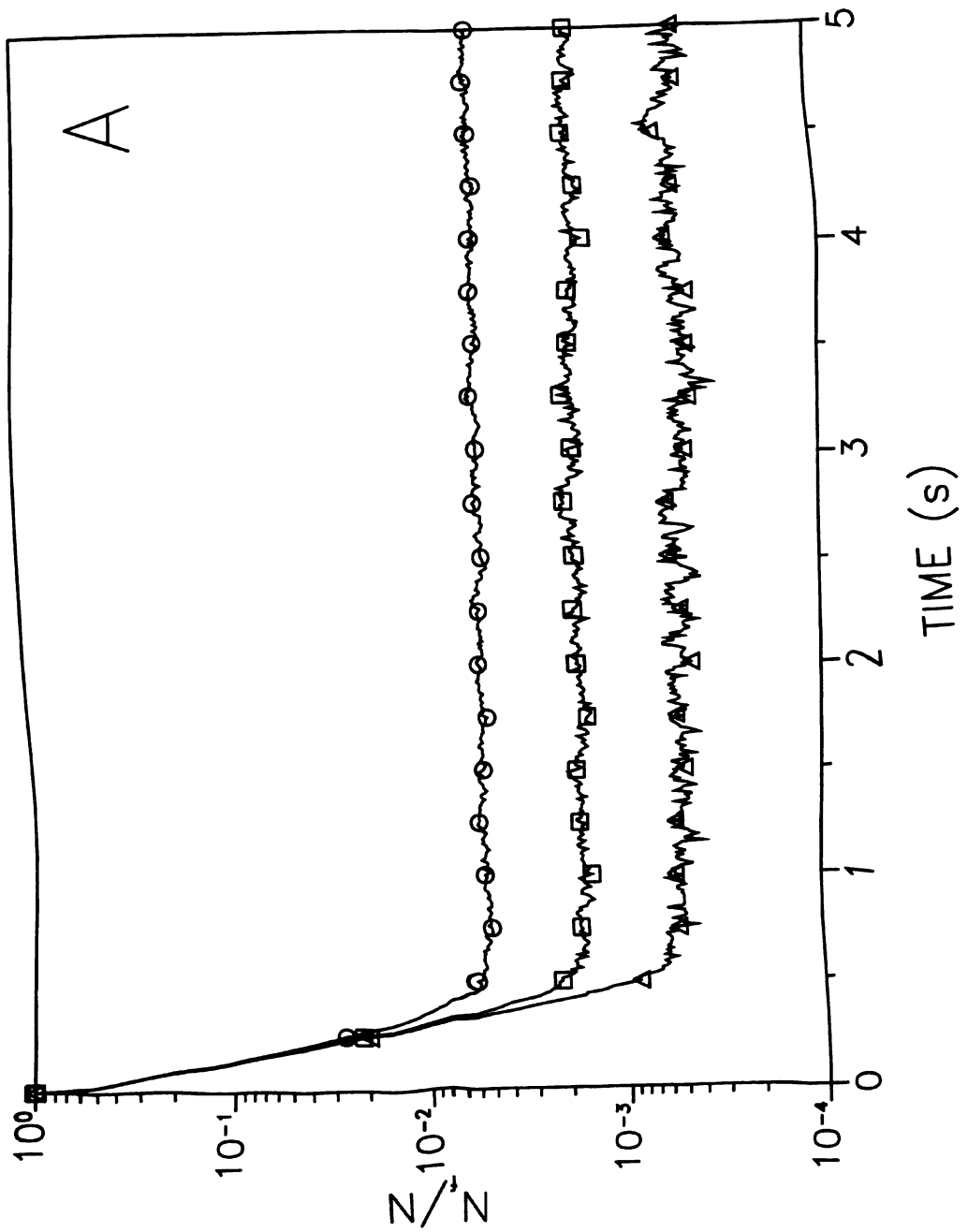

Figure 6.1 cont.

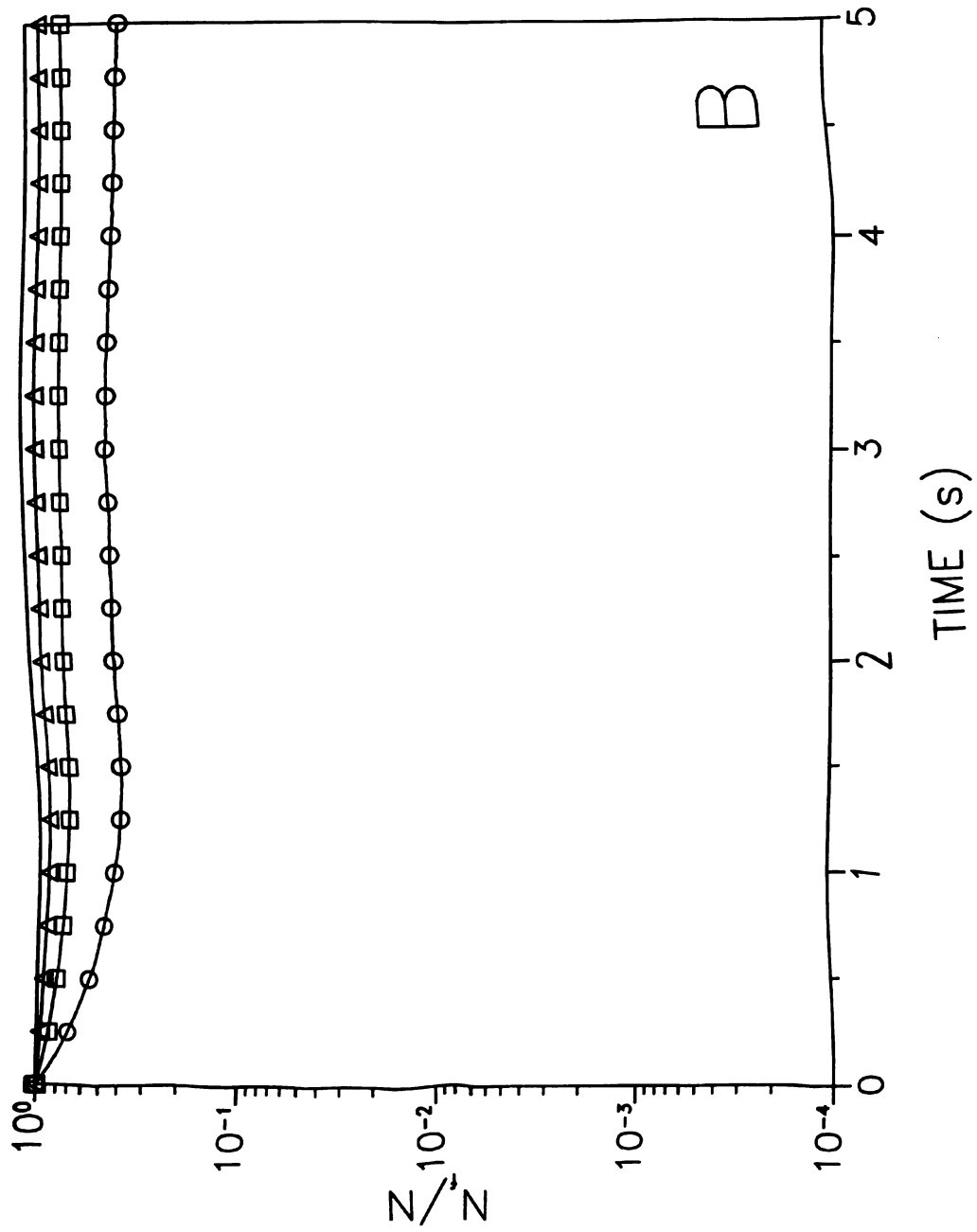

Figure 6.1 cont.

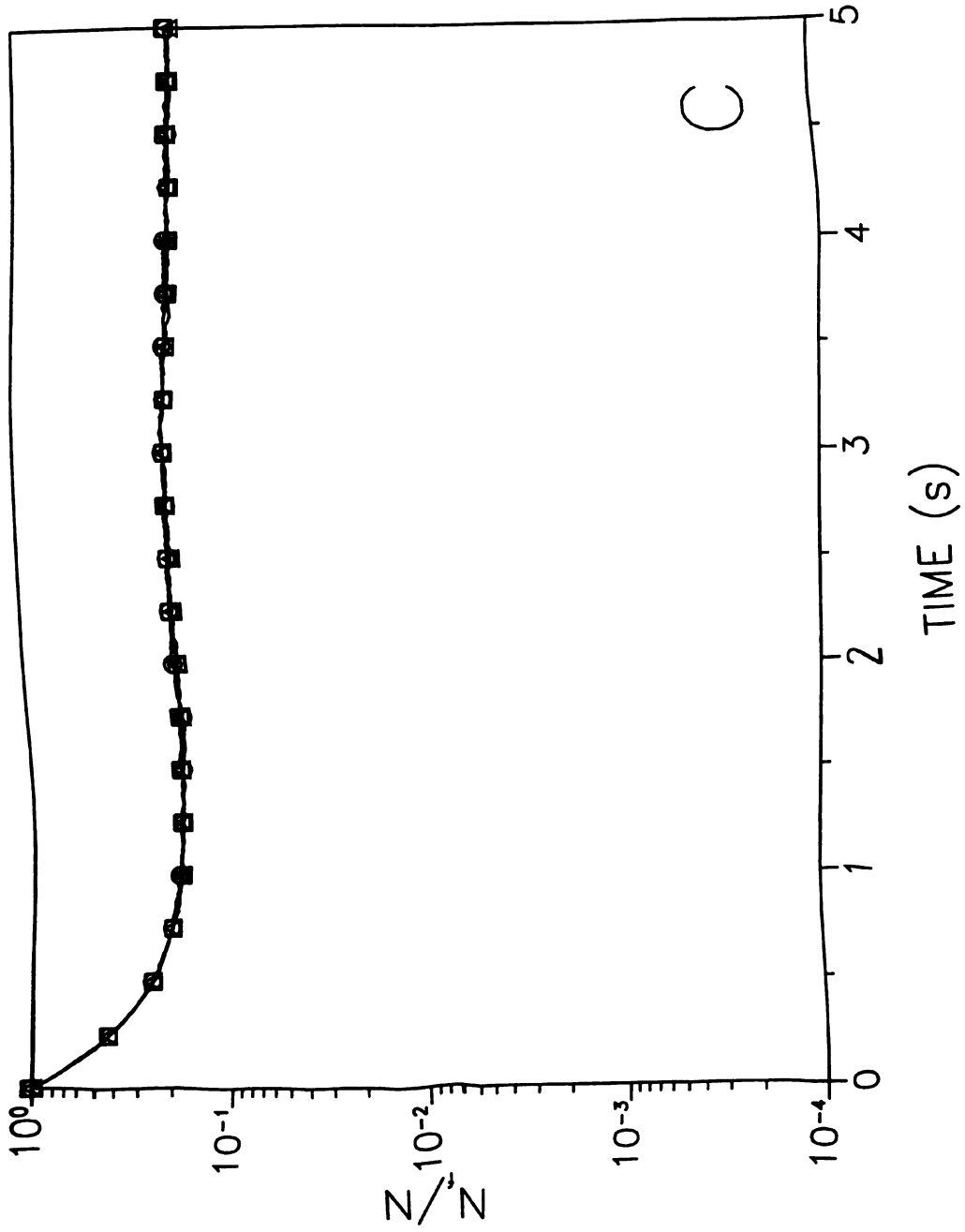

Further simulations are conducted to investigate the origin and magnitude of the time-increment dependence. It has been determined that the number of diffusion steps in a fixed total time is inversely related to the time increment.[33] Thus, studies were conducted to determine the effect of the time increment on the collision rate (Appendix B). From these studies, it has been empirically determined that the frequency of collision (ν_c) with the wall of an open-tubular column per molecule per second is

$$\nu_c = \left(\frac{\pi}{2 R_f}\right)\left(\frac{D_f}{2 t}\right)^{0.5} \qquad [6.1]$$

It is apparent that an increase in the radius of the fluid phase (R_f) decreases the rate of collision, and an increase in the diffusion coefficient (D_f) increases the rate of collision. These trends have physical significance. An increase in the time increment (t) decreases the rate of collision, a trend with no physical significance. It is the time-increment dependence of Equation [6.1] that is responsible for the trend observed in Figure 6.1A.

The absorption systems presented in Chapters 3 through 5 do not show a dependence on the time increment. In absorption systems, the transfer from the fluid to surface phase or the surface to fluid phase is a second-order reaction dependent on the collision frequency. The collision frequency from either side of the interface between the fluid and surface phases is dependent on the time increment in the same manner (Appendix B). Thus, the system response is independent of the time increment. However, the two transfer reactions are not both second-order in adsorption systems. Adsorption is a second-order reaction, and desorption is a first-order reaction. The

collision frequency influences only the second-order reaction causing the system response to be dependent on the time increment.

The time-increment dependence of the collision frequency is the result of the explicit time-increment dependence of the random-walk diffusion step (Equation [2.3]). Thus, it is not possible to remove the time-increment dependence of the collision rate. However, it is possible to compensate for changes in the collision rate by allowing the probability of adsorption to be time-increment dependent as given in Equation [2.16]. The first attempt to accomplish this goal is to reduce the pseudo-first order rate constant k'_a to a finite value. This allows the probability to vary with the time increment in the exponential term of Equation [2.16]. To test this adsorption algorithm, the previous simulations are repeated with a value of 100 s^{-1} for k'_a and 1.0 s^{-1} for k_d, so that adsorption is still faster than desorption. The results of the simulations with varying time increment are presented in Figure 6.1B. It is apparent that these systems are still not equivalent. The trend observed in Figure 6.1B as the time increment is increased is opposite that in Figure 6.1A. The time increment of 1.0×10^{-6} s produces the lowest probability of adsorption and the slowest adsorption rate, whereas the time increment of 1.0×10^{-4} s produces the highest probability of adsorption and the fastest adsorption rate.

The previous studies have shown that an infinite or a finite but static value of the pseudo-first-order adsorption rate constant produces unrealistic results as the time increment is changed. This implies that neither method adequately compensates for the time-increment dependence of the random-walk diffusion process. The adsorption probability expression must be explicitly dependent on the time increment in such a

manner that the simulation results are independent of the time increment. The most obvious parameter to absorb this time-increment dependence is the concentration of surface sites [S] in Equation [2.17]. The dimensions of the surface and the adsorption site determine the value of [S]. If adsorption does not occur at the time of collision with the surface, the molecule will travel an average distance of $(2\,D_f\,t)^{0.5}$ from the original point before another collision may occur. This introduces a lower limit on the dimensions of the adsorption site and, thus, a limit on the concentration of sites [S] that can be simulated for a given value of the time increment. The effective concentration of surface sites is given by

$$[S] = \frac{2\pi R_f}{(2D_f\,t)^{0.5}} \qquad [6.2]$$

where the numerator is the circumference of the interface between the fluid and surface phases and the denominator is the dimension of the adsorption site for a given time increment. Because k'_a is the product of a second-order rate constant (k_a) and the number of surface sites ([S]), the value of k'_a is then a function of the time increment. When k'_a is calculated in this manner, the system response becomes independent of the time increment, as shown in Figure 6.1C. In these simulations, the second-order adsorption rate constant (k_a) is 1.0 $site^{-1}\,s^{-1}$ and the desorption rate constant (k_d) is 1.0 s^{-1}. The previous time increments of 1.0×10^{-4}, 1.0×10^{-5}, and 1.0×10^{-6} s are used. The resulting pseudo-first order adsorption rate constants (k'_a) for these systems are 281, 889, and 2810 s^{-1}, respectively. As seen in Figure 6.1C, all the systems behave equally at both short and

long times. This demonstrates that the probability expression for adsorption given by Equations [2.16] and [6.2] is now independent of the time increment.

6.3.2 Validation of the Steady-State System Response.

The steady state of an adsorption system is defined as the point when the rates of adsorption and desorption are equal, that is

$$k_a[S][A]_c = k_d[AS] \qquad [6.3]$$

where $[A]_c$ is the number of molecules colliding with the surface and [AS] is the number of adsorbed molecules at equilibrium. The values of [S], $[A]_c$, and [AS] are converted into the relevant parameters of the system by means of Equations [6.1] and [6.2]

$$[A]_c = \tilde{N}_f \nu_c t = \left(\frac{\pi}{2R_f}\right)\left(\frac{D_f}{2t}\right)^{0.5} \tilde{N}_f t \qquad [6.4]$$

$$k_a\left(\frac{2\pi R_f}{(2D_f t)^{0.5}}\right)\left(\frac{\pi}{2R_f}\right)\left(\frac{D_f}{2t}\right)^{0.5} \tilde{N}_f t = k_d \tilde{N}_s \qquad [6.5]$$

where $\tilde{N}_f$ and $\tilde{N}_s$ are the number of molecules in the fluid and surface phases, respectively. The ratio of $\tilde{N}_s$ to $\tilde{N}_f$ at steady state is then

$$\frac{\tilde{N}_s}{\tilde{N}_f} = \left(\frac{\pi^2}{2}\right)\left(\frac{k_a}{k_d}\right) = K_{ads} \qquad [6.6]$$

where K_{ads} is the adsorption coefficient for the system. The ratio in Equation [6.6] is dependent only on the adsorption and desorption rate constants, and is independent of the time increment. Thus, the long-time distribution of molecules between the two phases should be independent of the time increment, as verified in Figure 6.1C for time

increments of 1.0×10^{-4} to 1.0×10^{-6} s. However, under closer examination, there is still a slight dependence on the time increment remaining. The dependence is shown in Figure 6.2 using an adsorption rate constant of 1.0 site^{-1} s^{-1}, a desorption rate constant of 1.0 s^{-1}, and time increments ranging from 1.0×10^{-2} to 1.0×10^{-6} s. Table 6.1 shows the simulated steady-state distribution ($\tilde{N}_s/\tilde{N}_f$) and the corresponding error as functions of the time increment. The data presented in Figure 6.2 and Table 6.1 indicate that, as the time increment increases, the error in the $\tilde{N}_s/\tilde{N}_f$ ratio increases as well. This implies that small time increments will simulate systems that appear independent of the time increment.

To determine the magnitude of the time increment necessary for the simulation to correctly simulate adsorption, the real adsorption rate is compared to the simulated adsorption rate. The rate of adsorption (r_a) in a real system is

$$r_a = k_a[S][A]_c \qquad [6.7]$$

The rate represented by Equation [6.7] needs to be independent of the time increment of the simulation. The rate of adsorption in the simulation is

$$r_a = P_{ads}\, \nu_c\, N_f = \left(1 - \exp\left(-k'_a\, t\right)\right)\left(\frac{\pi N_f}{2R_f}\right)\left(\frac{D_f}{2t}\right)^{0.5} \qquad [6.8]$$

where k'_a is the pseudo-first-order rate constant equal to k_a [S]. Equation [6.8] becomes independent of time increment when the expression $1 - \exp(-k'_a\, t)$ can be approximated by $k'_a\, t$. For example, Table 6.1 shows that a time increment one order of magnitude smaller than the characteristic time for adsorption (calculated as $1/k'_a$) simulates the adsorption coefficient with -2.17% error, and the approximation of $k'_a\, t$ is within 4.51% error.

Figure 6.2: The fraction of fluid-phase molecules as a function of time for time increments of $t = 1.00 \times 10^{-2}$ s (○), 1.00×10^{-3} s (□), 1.00×10^{-4} s (△), 1.00×10^{-5} s (◇), and 1.00×10^{-6} s (●) and an adsorption probability expression of $1-\exp(-(2\,\pi\,k_a\,R_f)/(2\,D_f\,t)^{0.5}\,t)$. Other simulation conditions as follows: N = 5000, $R_f = 2.00 \times 10^{-3}$ cm, $D_f = 1.0 \times 10^{-6}$ cm^2 s^{-1}, $k_a = 1.0$ site^{-1} s^{-1}, $k_d = 1.0$ s^{-1}.

Figure 6.2

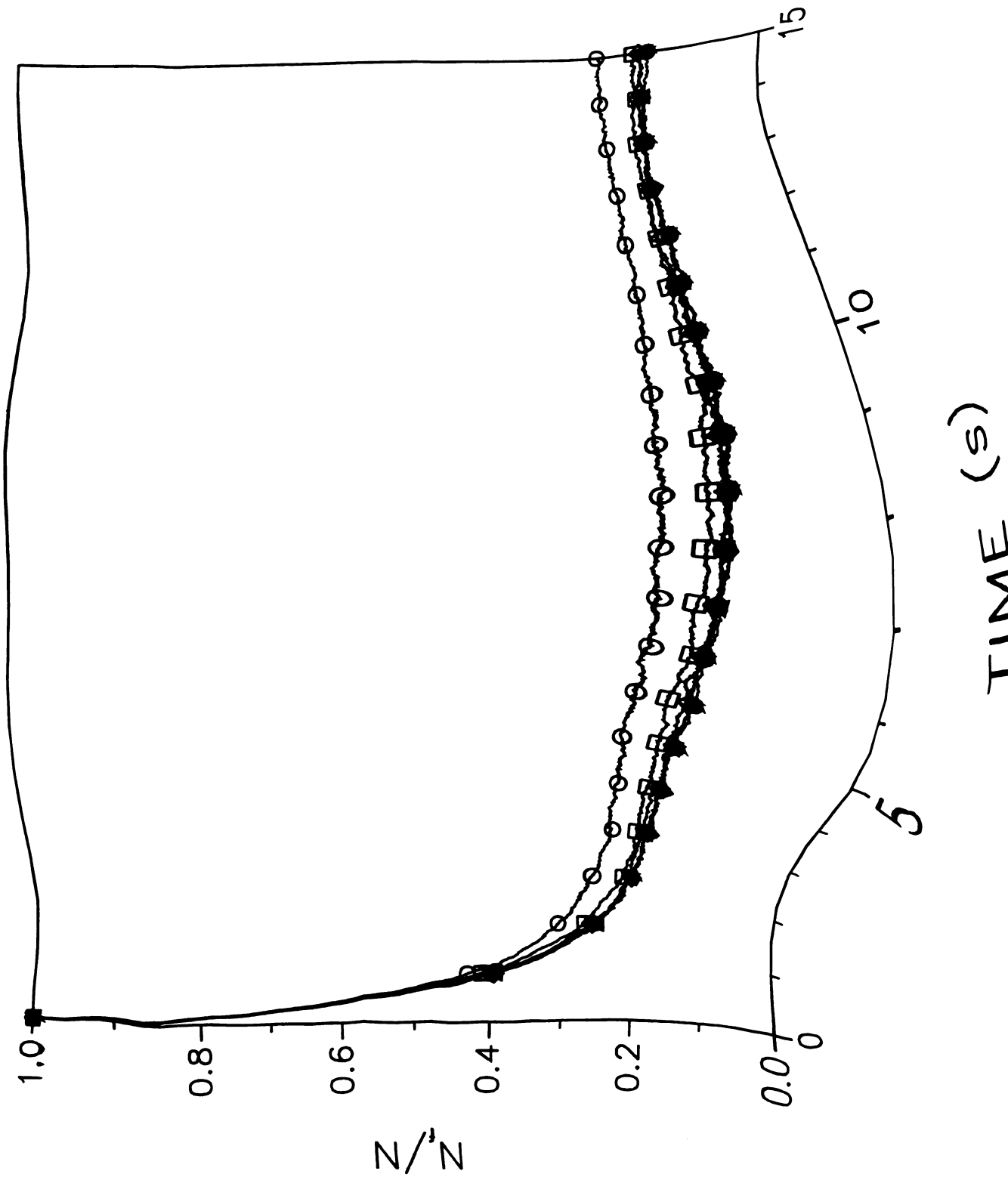

Table 6.1 Ratio of the Steady-State Number of Molecules in the Fluid ($\tilde{N}_f$) and Surface ($\tilde{N}_s$) Phases and the Approximation of the Adsorption Probability (k_a [S] t) as a Function of Time Increment.[a]

t (s)	$\tilde{N}_s/\tilde{N}_f$ Simulation	$\tilde{N}_s/\tilde{N}_f$ Theory[b]	Error (%)	[S]	k_a [S] t	1 – exp(–k_a [S] t)	Error (%)
1.0×10^{-2}	3.48 ± 0.04	4.93	-29.4	88.86	0.889	0.589	50.9
1.0×10^{-3}	4.52 ± 0.07	4.93	-8.37	281.0	0.281	0.245	14.7
1.0×10^{-4}	4.83 ± 0.11	4.93	-2.17	888.6	0.0889	0.0850	4.51
1.0×10^{-5}	4.94 ± 0.09	4.93	0.0214	2810	0.0281	0.0277	1.41
1.0×10^{-6}	5.04 ± 0.08	4.93	2.07	8886	0.00889	0.00885	0.445

[a] Other simulation conditions given in Figure 6.2.
[b] Calculated using Equation [6.6].

This source of error imposes an upper limit on the time increment that can be used to simulate adsorption using Equations [2.16] and [6.2].

To examine the effects of the rate constants on the kinetic and steady-state behavior, systems with equal values for k_a (site^{-1} s^{-1}) and k_d (s^{-1}) of 0.001, 0.01, 0.1, and 1.0 are simulated. The fraction of molecules in the fluid phase as a function of time is presented in Figure 6.3 for these systems. To study the steady-state behavior of these systems, the ratio of the average number of molecules in the surface and fluid phases is calculated and compared to the theoretical value, as shown in Table 6.2. For the systems with equal values of k_a and k_d (Case 1 of Table 6.2), the value of $\tilde{N}_s/\tilde{N}_f$ is statistically equivalent and within ±2.92% of the theoretically predicted value from Equation [6.6]. The values of the mass-transfer rate constants for these systems are determined by nonlinear regression to Equation [3.1] and are presented in Case 1 of Table 6.3. It should be noted that the values of the mass-transfer rate constants are different than the adsorption and desorption rate constants used as input for the simulation.

Figure 6.3: The fraction of fluid-phase molecules as a function of time for adsorption and desorption rate constants of $k_a = 0.001$ site^{-1} s^{-1}, $k_d = 0.001$ s^{-1} (◇); $k_a = 0.01$ site^{-1} s^{-1}, $k_d = 0.01$ s^{-1} (△); $k_a = 0.1$ site^{-1} s^{-1}, $k_d = 0.1$ s^{-1} (□); $k_a = 1.0$ site^{-1} s^{-1}, $k_d = 1.0$ s^{-1} (○). Other simulation conditions as follows: $t = 1.00 \times 10^{-3}$ s (◇, △), 1.00×10^{-4} s (□), 1.00×10^{-6} s (○), $N = 5000$, $R_f = 2.00 \times 10^{-3}$ cm, $D_f = 1.0 \times 10^{-5}$ cm^2 s^{-1}.

Figure 6.3

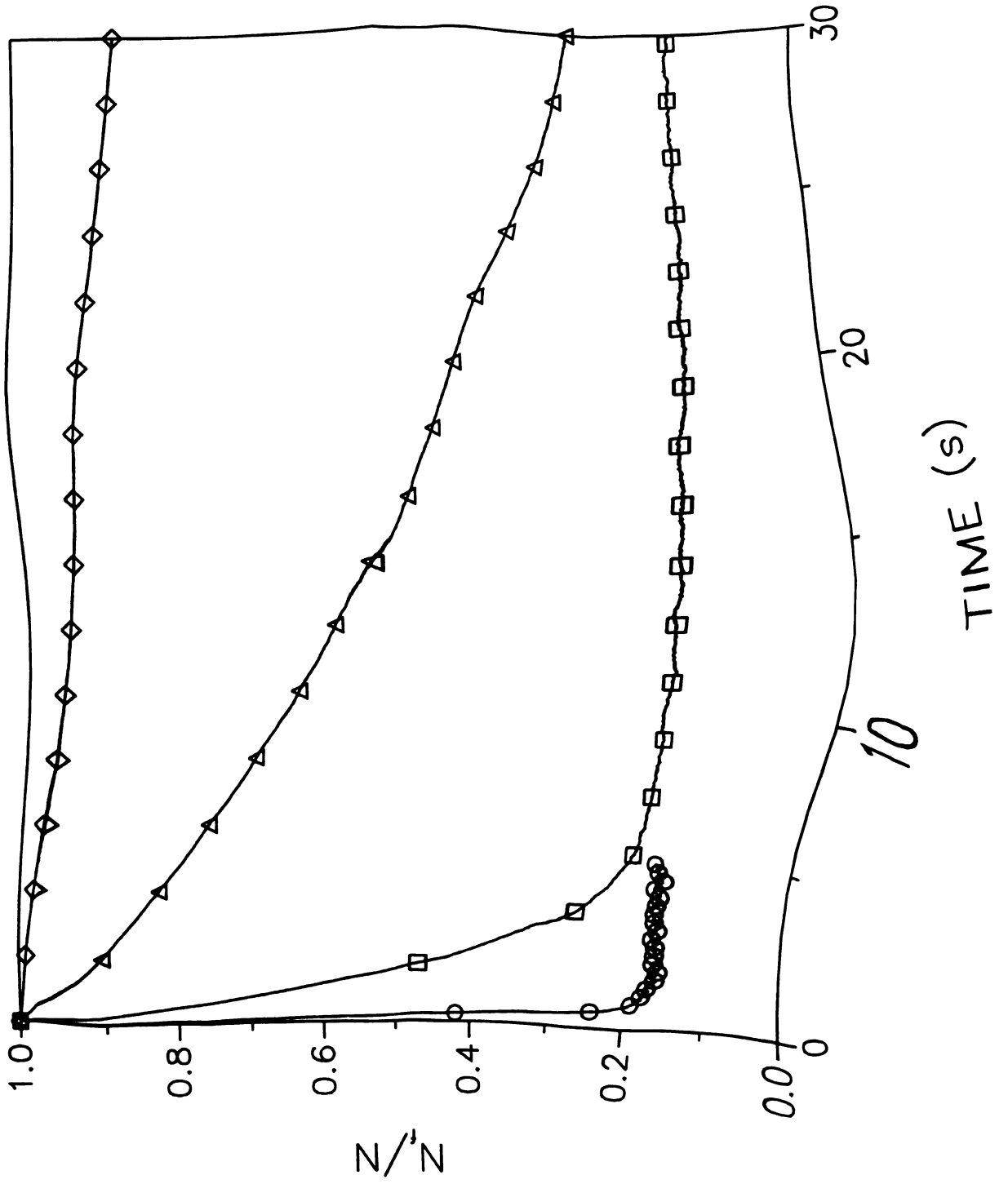

Table 6.2 Ratio of the Steady-State Number of Molecules in the Fluid ($\tilde{N}_f$) and Surface ($\tilde{N}_s$) Phases as a Function of the Adsorption and Desorption Rate Constants (k_a, k_d).

Case	t (s)	k_a (site^{-1} s^{-1})	k'_a (s^{-1})	k_d (s^{-1})	$\tilde{N}_s/\tilde{N}_f$ Simulation	$\tilde{N}_s/\tilde{N}_f$ Theory[a]	Error (%)
1[b]	1.0×10^{-3}	0.001	0.0889	0.001	4.88 ± 0.05	4.93	-1.11
	1.0×10^{-3}	0.01	0.889	0.01	5.08 ± 0.08	4.93	2.92
	1.0×10^{-4}	0.1	28.1	0.1	5.03 ± 0.08	4.93	1.99
	1.0×10^{-6}	1.0	2810	1.0	5.00 ± 0.08	4.93	1.26
2[c]	1.0×10^{-3}	0.001	0.0889	0.1	0.050 ± 0.001	0.049	2.01
	1.0×10^{-3}	0.01	0.889	0.1	0.508 ± 0.002	0.493	3.01
	1.0×10^{-4}	0.1	28.1	0.1	5.03 ± 0.08	4.93	1.99
	1.0×10^{-6}	1.0	2810	0.1	53 ± 5	49	7.99
3[d]	1.0×10^{-4}	0.1	28.1	0.001	471 ± 39	493	-4.50
	1.0×10^{-4}	0.1	28.1	0.01	51 ± 3	49	3.74
	1.0×10^{-4}	0.1	28.1	0.1	5.03 ± 0.08	4.93	1.99
	1.0×10^{-4}	0.1	28.1	1.0	0.501 ± 0.005	0.493	1.51
	1.0×10^{-4}	0.1	28.1	10.0	0.051 ± 0.001	0.049	3.38
4	1.0×10^{-5}[e]	0.203	180	1.0	1.02 ± 0.01	1.00	2.37
	1.0×10^{-4}[f]	0.0203	5.69	0.1	1.01 ± 0.01	1.00	0.701
	1.0×10^{-3}[g]	0.00203	0.180	0.01	1.020 ± 0.007	1.000	1.99
5	1.0×10^{-3}[c]	0.01	0.889	0.1	0.508 ± 0.002	0.493	3.01
	1.0×10^{-4}[f]	0.0203	5.69	0.1	1.01 ± 0.01	1.00	0.701
	1.0×10^{-4}[c]	0.1	28.1	0.1	5.03 ± 0.08	4.93	1.99

[a] Calculated using Equation [6.6].
[b] Simulation conditions given in Figure 6.3.
[c] Simulation conditions given in Figure 6.4.
[d] Simulation conditions given in Figure 6.5.
[e] Other simulation conditions: N = 5000, $D_f = 1.0 \times 10^{-5}$ cm^2 s^{-1}, $R_f = 2.0 \times 10^{-3}$ cm, T = 15.0 s.
[f] Other simulation conditions: N = 5000, $D_f = 1.0 \times 10^{-5}$ cm^2 s^{-1}, $R_f = 2.0 \times 10^{-3}$ cm, T = 140.0 s.
[g] Other simulation conditions: N = 5000, $D_f = 1.0 \times 10^{-5}$ cm^2 s^{-1}, $R_f = 2.0 \times 10^{-3}$ cm, T = 1.0×10^3 s.

Table 6.3 The Fluid to Surface Phase and Surface to Fluid Phase Mass-Transfer Rate Constants (k_{fs}, k_{sf}) as a Function of the Adsorption and Desorption Rate Constants (k_a, k_d).

Case	t (s)	k_a (site^{-1} s^{-1})	k'_a (s^{-1})	k_d (s^{-1})	k_{fs} (s^{-1})	k_{sf} (s^{-1})	k_{fs}/k_{sf} Simulation	k_{fs}/k_{sf} Theory[a]	Error (%)
1[b]	1.0×10^{-3}	0.001	0.0889	0.001	0.005107 ± 0.000002	0.0010406 ± 0.0000007	4.91	4.93	-0.55
	1.0×10^{-3}	0.01	0.889	0.01	0.04994 ± 0.00003	0.010032 ± 0.000007	4.98	4.93	0.88
	1.0×10^{-4}	0.1	28.1	0.1	0.4814 ± 0.0002	0.09750 ± 0.00006	4.94	4.93	0.06
	1.0×10^{-6}	1.0	2810	1.0	4.004 ± 0.007	0.802 ± 0.002	4.99	4.93	1.10
2[c]	1.0×10^{-3}	0.001	0.0889	0.1	0.00482 ± 0.00003	0.0948 ± 0.0006	0.051	0.049	2.94
	1.0×10^{-3}	0.01	0.889	0.1	0.04767 ± 0.00004	0.09529 ± 0.00008	0.500	0.493	1.37
	1.0×10^{-4}	0.1	28.1	0.1	0.4814 ± 0.0002	0.09750 ± 0.00006	4.94	4.93	0.06
	1.0×10^{-6}	1.0	2810	0.1	3.986 ± 0.003	0.0802 ± 0.0003	49.7	49.3	0.71
3[d]	1.0×10^{-4}	0.1	28.1	0.001	0.48345 ± 0.00007	0.000983 ± 0.000008	492	493	-0.32
	1.0×10^{-4}	0.1	28.1	0.01	0.4833 ± 0.0001	0.00975 ± 0.00001	49.5	49.3	0.40
	1.0×10^{-4}	0.1	28.1	0.1	0.4814 ± 0.0002	0.09750 ± 0.00006	4.94	4.93	0.06
	1.0×10^{-4}	0.1	28.1	1.0	0.496 ± 0.001	0.988 ± 0.002	0.502	0.493	1.71
	1.0×10^{-4}	0.1	28.1	10.0	0.53 ± 0.01	10.5 ± 0.3	0.050	0.049	2.00

[a] $k_{fs}/k_{sf} = \tilde{N}_s/\tilde{N}_f$, calculated using Equation [6.6].
[b] Simulation conditions given in Figure 6.3.
[c] Simulation conditions given in Figure 6.4.
[d] Simulation conditions given in Figure 6.5.

Table 6.3 cont.

Case	t (s)	k_a ($site^{-1}\ s^{-1}$)	k'_a (s^{-1})	k_d (s^{-1})	k_{fs} (s^{-1})	k_{sf} (s^{-1})	k_{fs}/k_{sf} Simulation	k_{fs}/k_{sf} Theory[a]	Error (%)
4	1.0×10^{-5} [e]	0.20264	180	1.0	1.002 ± 0.002	1.013 ± 0.002	0.989	1.00	-1.06
	1.0×10^{-4} [f]	0.020264	5.69	0.1	0.1001 ± 0.0002	0.0987 ± 0.0002	1.01	1.00	1.35
	1.0×10^{-3} [g]	0.002026	0.180	0.01	0.010466 ± 0.000006	0.010396 ± 0.000006	1.01	1.00	0.68
5	1.0×10^{-3} [c]	0.01	0.889	0.1	0.04767 ± 0.00004	0.09529 ± 0.00008	0.500	0.493	1.37
	1.0×10^{-4} [f]	0.020264	5.69	0.1	0.1001 ± 0.0002	0.0987 ± 0.0002	1.01	1.00	1.35
	1.0×10^{-4} [c]	0.1	28.1	0.1	0.4814 ± 0.0002	0.09750 ± 0.00006	4.94	4.93	0.06

[a] Calculated using Equation [6.6].

[c] Simulation conditions given in Figure 6.4.

[e] Other simulation conditions: $N = 5000$, $D_f = 1.0 \times 10^{-5}\ cm^2\ s^{-1}$, $R_f = 2.0 \times 10^{-3}$ cm, $T = 15.0$ s.

[f] Other simulation conditions: $N = 5000$, $D_f = 1.0 \times 10^{-5}\ cm^2\ s^{-1}$, $R_f = 2.0 \times 10^{-3}$ cm, $T = 140.0$ s.

[g] Other simulation conditions: $N = 5000$, $D_f = 1.0 \times 10^{-5}\ cm^2\ s^{-1}$, $R_f = 2.0 \times 10^{-3}$ cm, $T = 1.0 \times 10^{3}$ s.

The discrepancy arises from the inclusion of the diffusion processes as well as the adsorption and desorption processes in the mass-transfer rate constants. The adsorption and desorption rate constants do not contain information about mass transfer. The ratio of the mass-transfer rate constants should be equal to the adsorption coefficient according to kinetic theory.[31,32] The ratio is calculated and presented in Case 1 of Table 6.3 together with the theoretical value calculated from Equation [6.6]. The ratios calculated from the mass-transfer rate constants are within ±1.10% of theory.

Next, the steady-state and kinetic behavior due to changes in the second-order adsorption rate constant are studied. The adsorption rate constant is changed from 0.001 to 1.0 site^{-1} s^{-1} while maintaining the desorption rate constant at 0.1 s^{-1}. The fraction of molecules in the fluid phase as a function of time is presented in Figure 6.4 for these systems. The steady-state behavior shows the expected decrease in the fraction of molecules in the fluid phase as the adsorption rate constant increases. The simulated value of $\tilde{N}_s/\tilde{N}_f$ is within ±7.99% of the theoretically predicted value as seen in Case 2 of Table 6.2. These curves were fit to Equation [3.1] using nonlinear regression, and the calculated values of the mass-transfer rate constants are presented in Case 2 of Table 6.3. The fluid to surface phase mass-transfer rate constant increases by one order of magnitude for each increase in k_a, while the surface to fluid phase mass-transfer rate constant remains unchanged. The ratio of the mass-transfer rate constants is within ±2.94% of the theoretical value, as seen in Case 2 of Table 6.3.

Finally, the desorption rate constant was changed to test that the desorption process is modeled correctly. Figure 6.5 exhibits the fraction of molecules in the fluid

Figure 6.4: The fraction of fluid-phase molecules as a function of time for adsorption rate constants of k_a = 0.001 site^{-1} s^{-1} (◇), 0.01 site^{-1} s^{-1} (△), 0.1 site^{-1} s^{-1} (□), and 1.0 site^{-1} s^{-1} (○). Other simulation conditions as follows: t = 1.00×10^{-3} s (◇,△), 1.00×10^{-4} s (□), 1.00×10^{-6} s (○), k_d = 0.1 s^{-1}, all others as given in Figure 6.3.

Figure 6.4

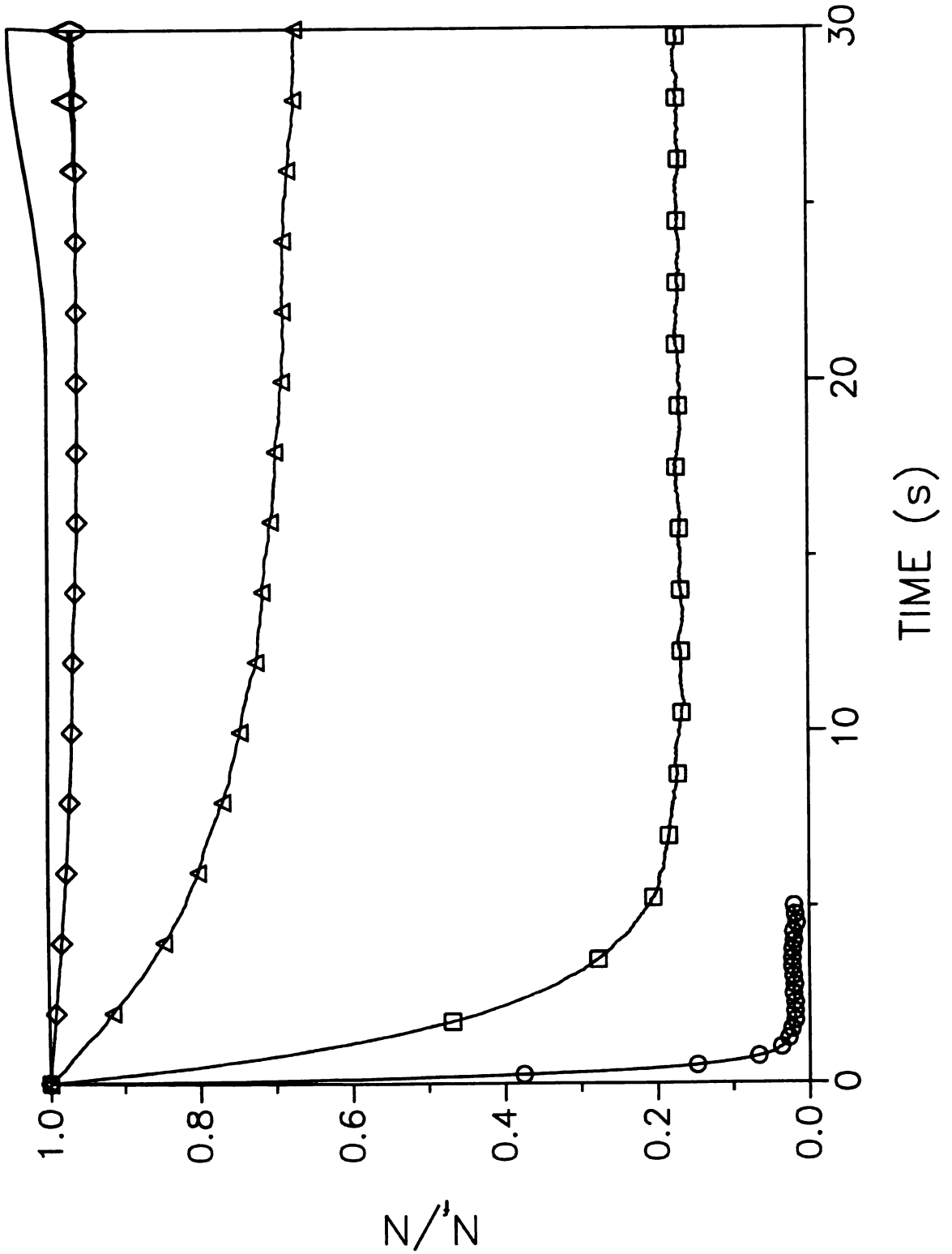

Figure 6.5: The fraction of fluid-phase molecules as a function of time for desorption rate constants of $k_d = 0.001$ s^{-1} (○), 0.01 s^{-1} (□), 0.1 s^{-1} (△), and 1.0 s^{-1} (◇). Other simulation conditions as follows: $t = 1.00 \times 10^{-4}$ s, $k_a = 0.1$ $site^{-1}$ s^{-1}, all others as given in Figure 6.3.

Figure 6.5

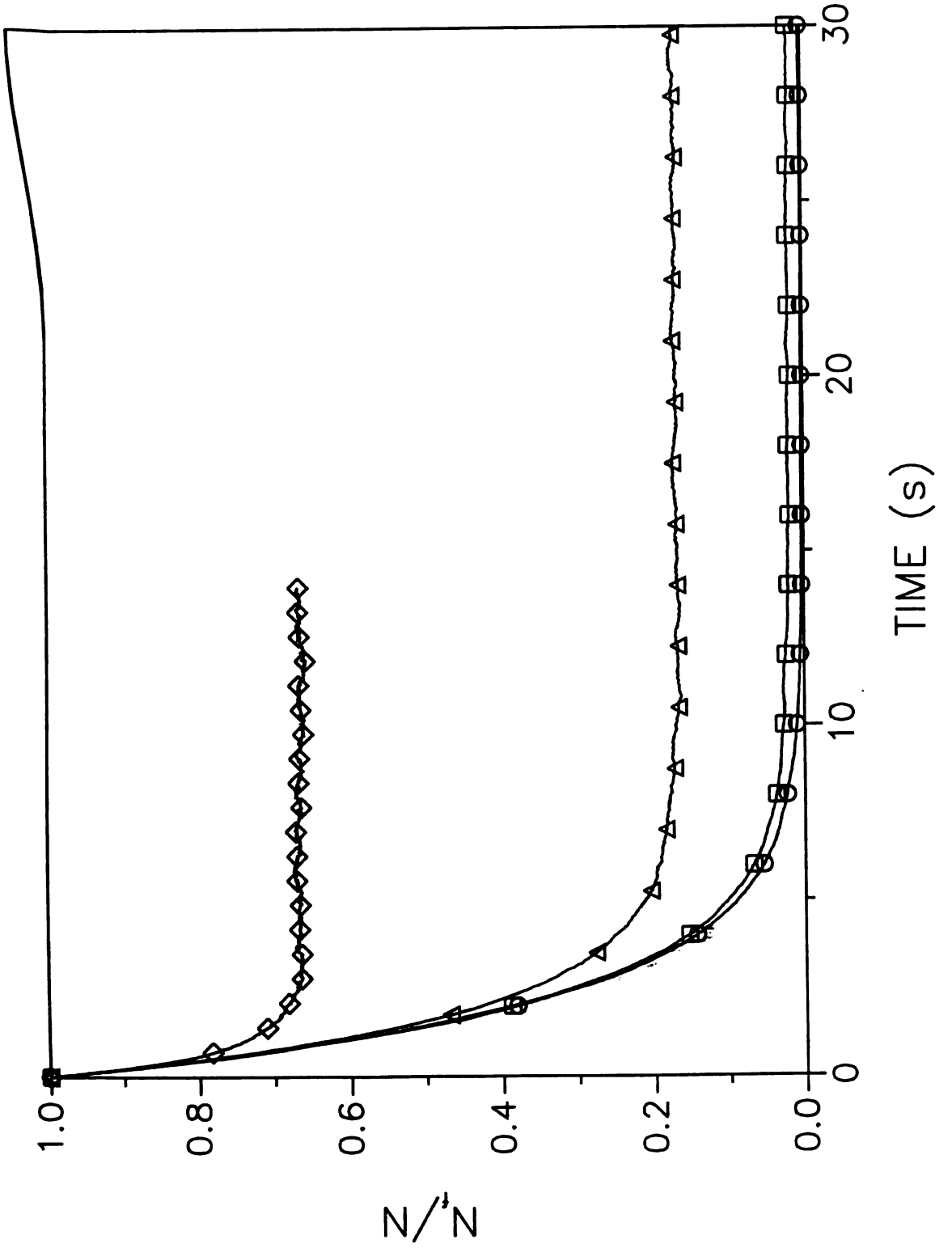

phase for systems with an adsorption rate constant of 0.1 site^{-1} s^{-1} and desorption rate constants ranging from 0.001 to 1.0 s^{-1}. The initial rates of these systems appear to be equivalent since the adsorption rate constant is not changed. The steady-state fraction of molecules in the fluid phase decreases as the desorption rate constant decreases. The simulated value of $\tilde{N}_s/\tilde{N}_f$ is within ±4.50% of the theoretical value, as shown in Case 3 of Table 6.2. The ratio of the mass-transfer rate constants for these systems, displayed in Case 3 of Table 6.3, is within ±2.00% of theory. These data demonstrate that the simulation correctly models the adsorption and desorption processes.

6.3.3 Validation of Adsorption Chromatography.

The adsorption algorithm validated above is used to simulate adsorption chromatography under laminar flow conditions. The molecules are initially distributed between the fluid and surface phases as they would be at steady state. The processes of diffusion, convection, adsorption, and desorption are allowed to progress for 500 s. The position of each molecule is recorded at specified time intervals and the first and second moments are calculated by using Equations [2.1] and [2.2]. These moments in distance are then compared to theoretical values predicted by using steady-state equations adapted from Giddings[34] and given below.

$$M_{1,d} = \frac{v_0 T}{1 + K_{ads}} \qquad [6.9]$$

$$M_{2,d} = \left(\frac{2 D_f}{v_0} + \frac{\left(1 + 6 K_{ads} + 11 K_{ads}^2\right) R_f^2 v_0}{24 \left(1 + K_{ads}\right)^2 D_f} + \frac{2 K_{ads} v_0}{\left(1 + K_{ads}\right)^2 k_d} \right) M_{1,d} \qquad [6.10]$$

The first term in Equation [6.10] describes the axial diffusion in the fluid phase, the second term describes the resistance to mass transfer in the fluid phase, and the final term describes the resistance to mass transfer in the surface phase. The simulated and calculated moments are presented in Figures 6.6 and 6.7 for systems in which k_a was varied from 0.00203 to 0.203 site^{-1} s^{-1} and k_d was varied from 0.01 to 100 s^{-1}, with K_{ads} ranging from 0.01 to 100. The first moments in distance as a function of time are shown in Figure 6.6A for variation in k_a and Figure 6.7A for variation in k_d. As can be seen, good agreement exists between simulation and theory. The average relative errors for each system are shown in Table 6.4. The first moments show errors less than ±0.85% relative to the values predicted by Equations [6.9] and [6.11] for K_{ads} ranging from 0.01 to 100.0 The second moments are shown in Figures 6.6B for variation in k_a and 6.7B for variation in k_d. The observed error in the second moments is less than ±10.1% relative to the values predicted by Equations [6.10] and [6.12], as displayed in Table 4. It appears that the error in the second moment is related to the adsorption rate. As seen in Figure 6.6B and Table 6.4, the difference between simulation and theory increases as the adsorption rate constant decreases. However, it should be pointed out that the apparent error decreases with time (Figure 6.6), so the discrepancies between simulation and theory disappear at long times. The second moments in Figure 6.7B show no such trend with the desorption rate constant and appear to agree well with theory for all values of K_{ads}. The increase in error at small adsorption and desorption rate constants arises because simulation is not at equilibrium initially. It is not sufficient to distribute the molecules between the phases as they would be at steady state to model a system at

Figure 6.6: First (A) and second (B) moments in distance as a function of time for values of $k_a = 0.00203$ site^{-1} s^{-1} (□), 0.0203 site^{-1} s^{-1} (△), and 0.203 site^{-1} s^{-1} (◇). (—) Theory calculated from Equations [6.9] and [6.10]. Other simulation conditions as follows: N = 750, t = 5×10^{-5} s, $k_d = 0.1$ s^{-1}, $R_f = 2.00 \times 10^{-3}$ cm, $D_f = 1.0 \times 10^{-5}$ cm^2 s^{-1}, $v_0 = 0.1$ cm s^{-1}.

Figure 6.6

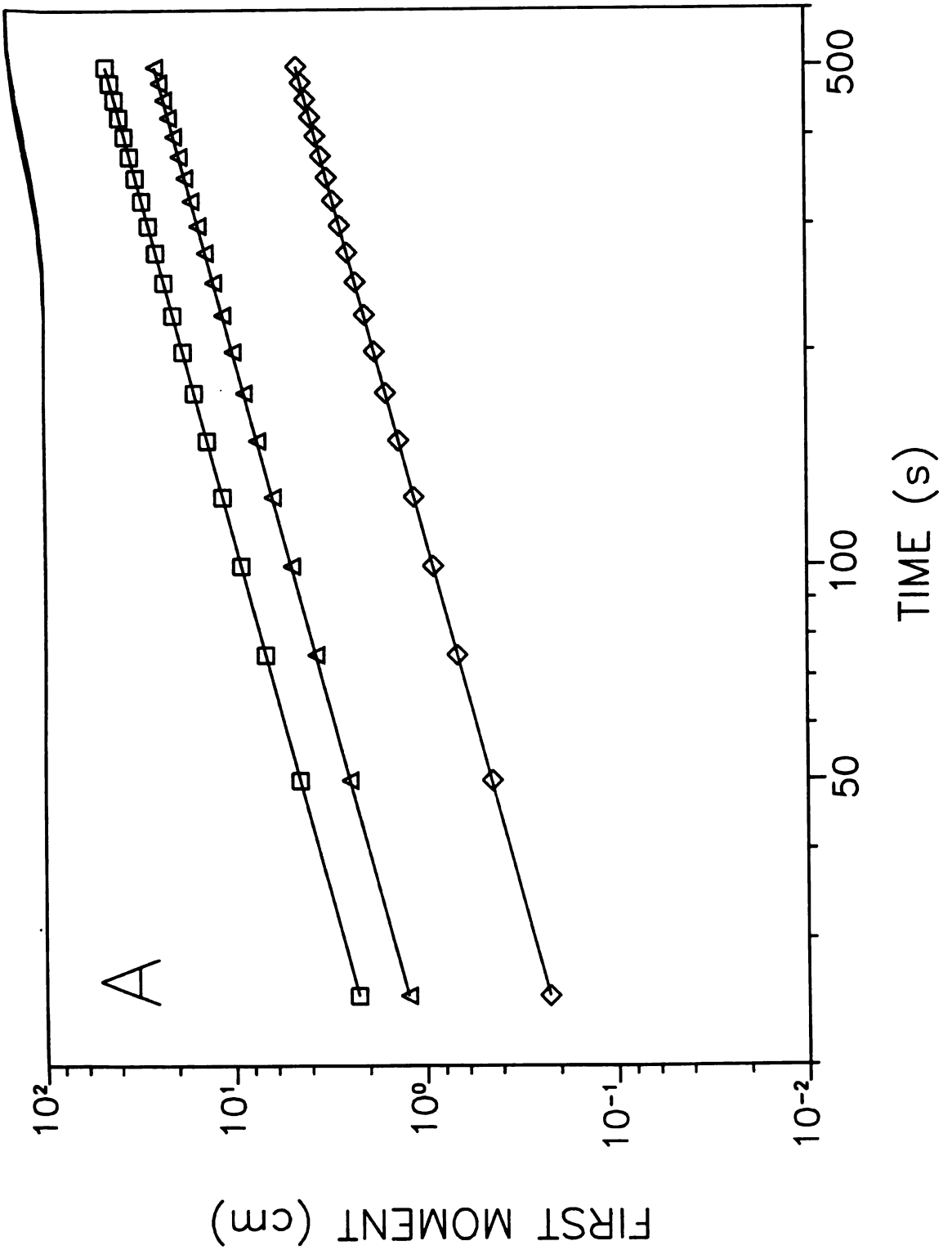

Figure 6.6 cont.

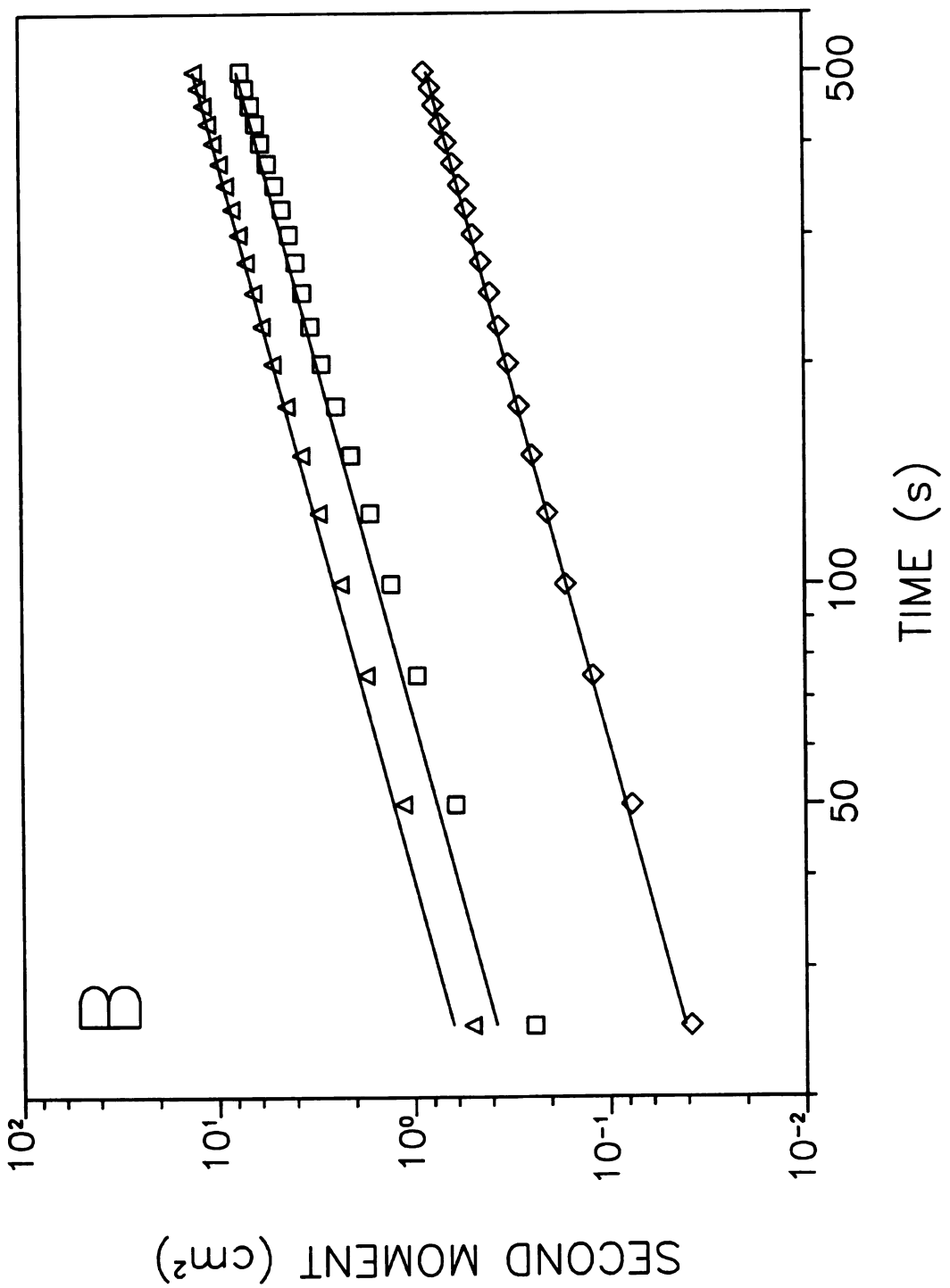

Figure 6.7: First (A) and second (B) moments in distance as a function of time for values of k_d = 100.0 s^{-1} (○), 10.0 s^{-1} (□), 1.0 s^{-1} (△), 0.1 s^{-1} (◇), and 0.01 s^{-1} (●). (—) Theory calculated from Equations [6.9] and [6.10]. Other simulation conditions as follows: k_a = 0.203 $site^{-1}$ s^{-1}, all others as given in Figure 6.6.

Figure 6.7

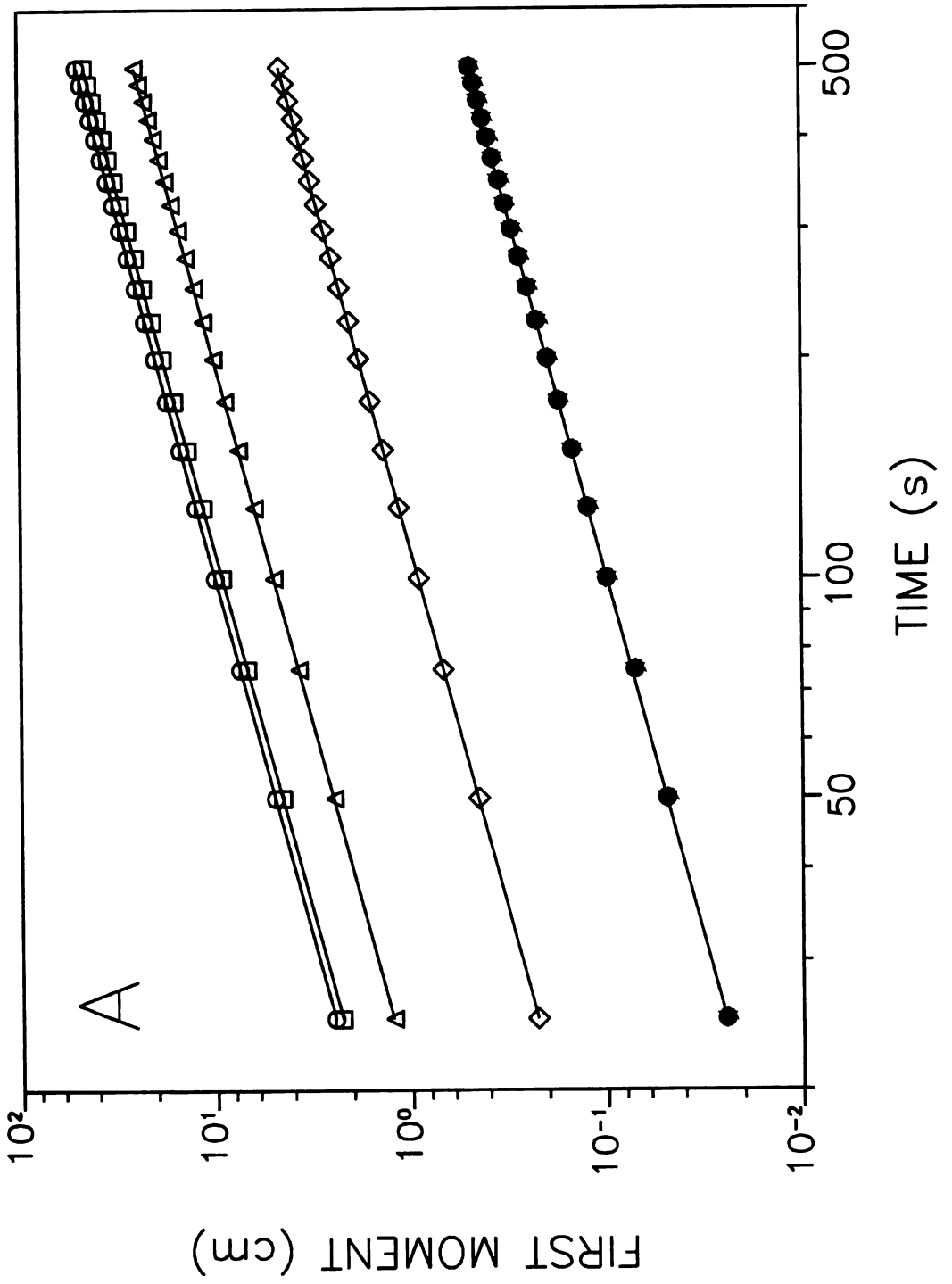

Figure 6.7 cont.

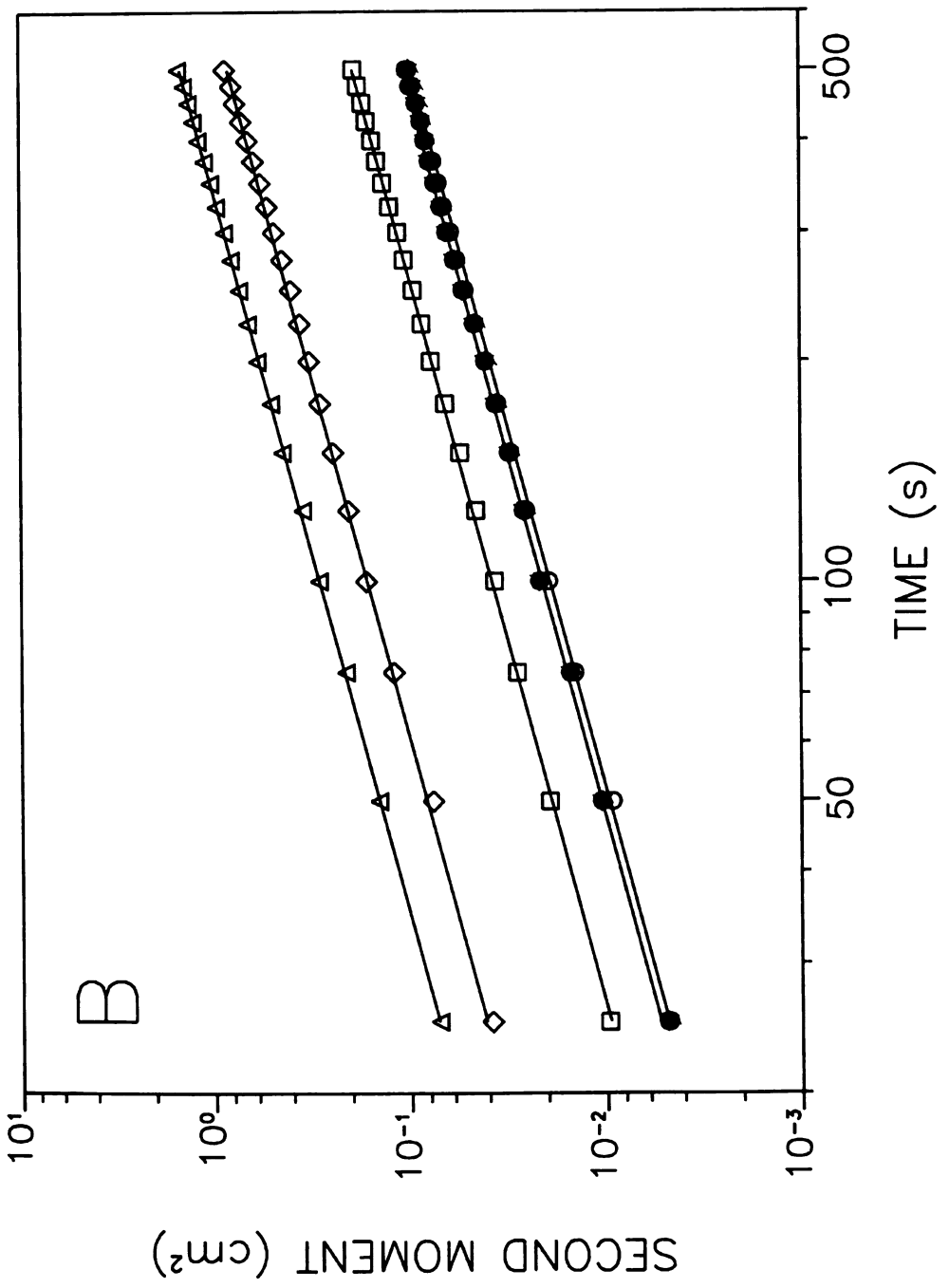

equilibrium. Equilibrium is only attained when all molecules have sampled both the fluid and surface phases such that the average residence time in each phase is the same for each molecule in the ensemble. Since the slow rates of adsorption and desorption require some time to equilibrate, the simulation accurately describes these systems, whereas steady-state theories such as the one presented by Giddings[34] do not. Once steady state has been achieved, the simulation and theory converge, as seen in Figure 6.6 and 6.7.

Table 6.4 Relative Error in the First and Second Moments (M_1, M_2)of Adsorption Chromatography.

				Average Relative Error[c] (%)	
k_a (site^{-1} s^{-1})	k'_a (s^{-1})	k_d (s^{-1})	K_{ads}	M_1 (cm)	M_2 (cm^2)
0.203[a]	80.5	0.1	10.0	0.072	1.3
0.0203[a]	8.05	0.1	1.0	0.44	3.5
0.00203[a]	0.805	0.1	0.1	0.079	10.1
0.203[b]	80.5	0.01	100.0	0.015	4.4
0.203[b]	80.5	0.1	10.0	0.072	1.3
0.203[b]	80.5	1.0	1.0	0.67	1.0
0.203[b]	80.5	10.0	0.1	0.44	2.4
0.203[b]	80.5	100.0	0.01	0.85	2.9

[a] Simulation conditions given in Figure 6.6.
[b] Simulation conditions given in Figure 6.7.
[c] Errors calculated with respect to Equations [6.9] and [6.10].

6.3.4 Simulation of Adsorption Chromatography.

More simulations are conducted to study chromatographic systems as they evolve from an initial state of nonequilibrium in which all the molecules are in the fluid phase to steady state. This initial distribution of molecules is equivalent to introducing the sample to a chromatographic system by injection in the fluid phase. The kinetic and steady-state

behavior is simulated for systems with adsorption rate constants (k_a) varying from 0.203 to 0.00203 site^{-1} s^{-1} and desorption rate constants (k_d) varying from 1.0 to 0.01 s^{-1}, while maintaining a value of 1.0 for the adsorption coefficient (K_{ads}). The steady-state behavior of these systems is presented in Case 4 of Table 6.2. The simulated fraction $\tilde{N}_s/\tilde{N}_f$ agrees well with the theoretical value. The mass-transfer rate constants in Case 4 of Table 6.3 indicate that as the adsorption and desorption rate constants decrease, the mass-transfer rate constants decrease as well.

The hydrodynamic behavior of these systems is studied by determining the zone profiles for these systems with a velocity of 0.1 cm s^{-1} and column lengths of 0.1, 0.2, 0.5, 1.0, 2.0, and 5.0 cm. The zone profiles are shown in Figure 6.8 for a system with an adsorption rate constant of 0.1 site^{-1} s^{-1} and a desorption rate constant of 0.1 s^{-1}. The observed profiles are very sharp and asymmetric at short distances and then broaden and become more symmetric as the distance increases.

The statistical moments of the systems described above are calculated in both the time and distance domains. Moments in time as a function of distance are shown in Figure 6.9 and moments in distance as a function of time are shown in Figure 6.10. The first moments in time or mean elution times shown in Figure 6.9A are equivalent for the three systems in Case 4 of Tables 2 and 3, as expected. The first moments also match well with theory, given in Equation [6.11], which implies that the systems have reached steady state.

$$M_{1,t} = \frac{(1 + K_{ads})L}{v_0} \qquad [6.11]$$

Figure 6.8: Zone profiles as a function of time for column lengths of 0.1, 0.2, 0.5, 1.0, 2.0, and 5.0 cm (left to right). Other simulation conditions as follows: $t = 5.00 \times 10^{-5}$ s, $N = 2000$, $k_a = 0.1$ site^{-1} s^{-1}, $k_d = 0.1$ s^{-1}, $R_f = 2.00 \times 10^{-3}$ cm, $D_f = 1.0 \times 10^{-5}$ cm^2 s^{-1}, $v_0 = 0.1$ cm s^{-1}.

Figure 6.8

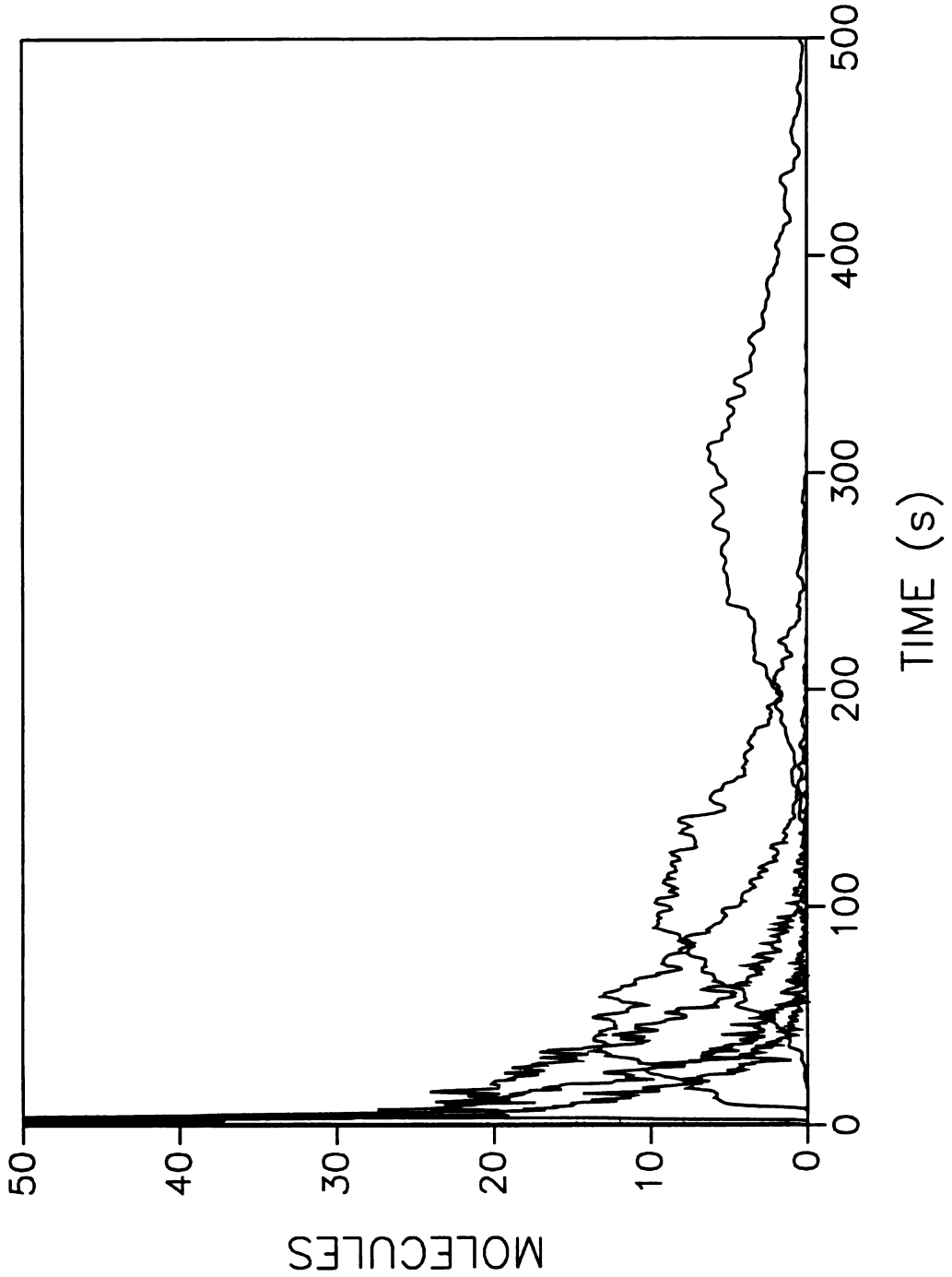

Figure 6.9: First (A), second (B), and third (C) moments in time as a function of distance for values of $k_a = 0.00203$ site^{-1} s^{-1}, $k_d = 0.01$ s^{-1} ($\triangle$); $k_a = 0.0203$ site^{-1} s^{-1}, $k_d = 0.1$ s^{-1} ($\bigcirc$); $k_a = 0.203$ site^{-1} s^{-1}, $k_d = 1.0$ s^{-1} ($\square$). (—) Theory calculated from Equations [6.11] and [6.12]. All other conditions as given in Figure 6.8.

Figure 6.9

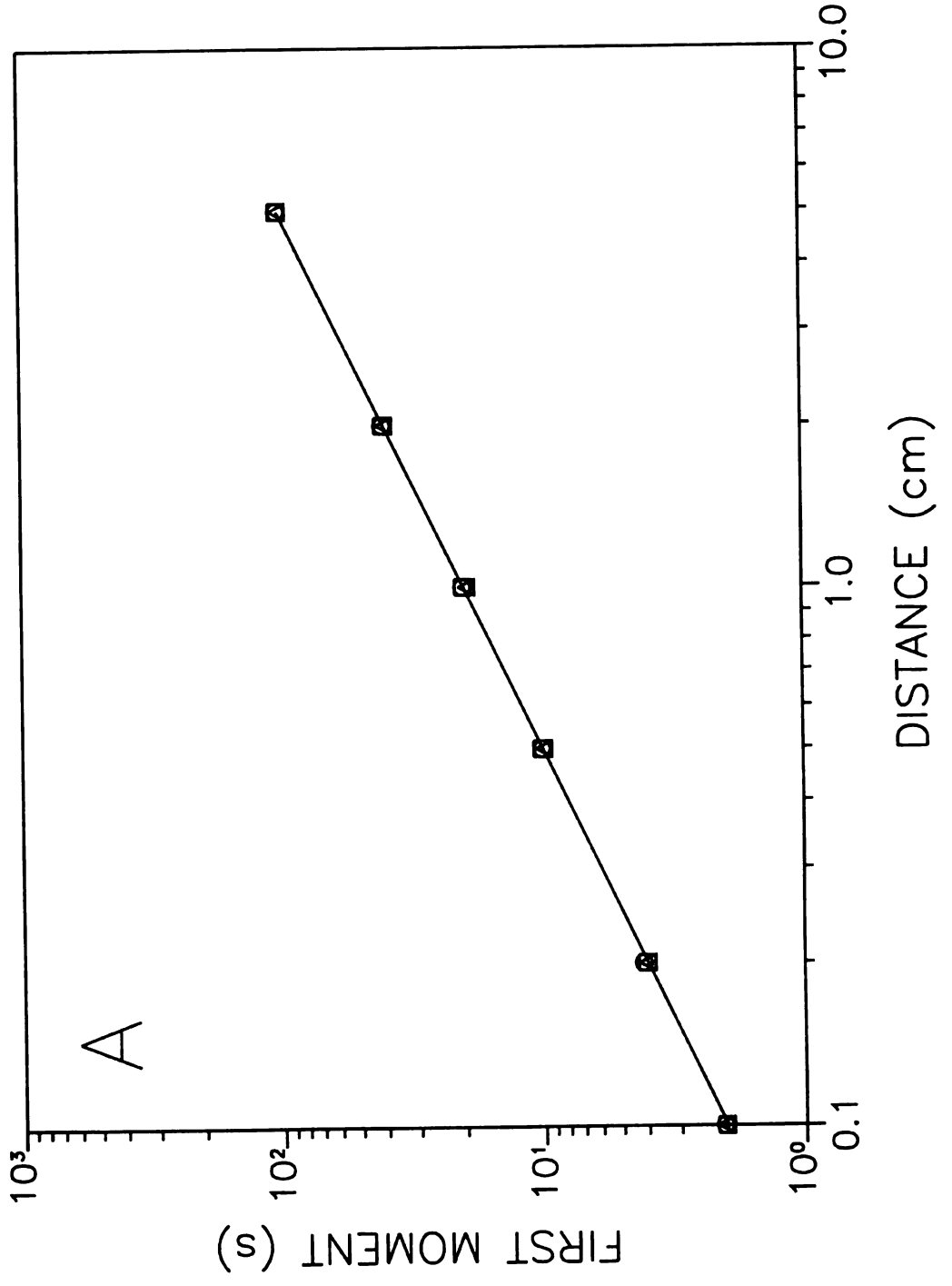

Figure 6.9 cont.

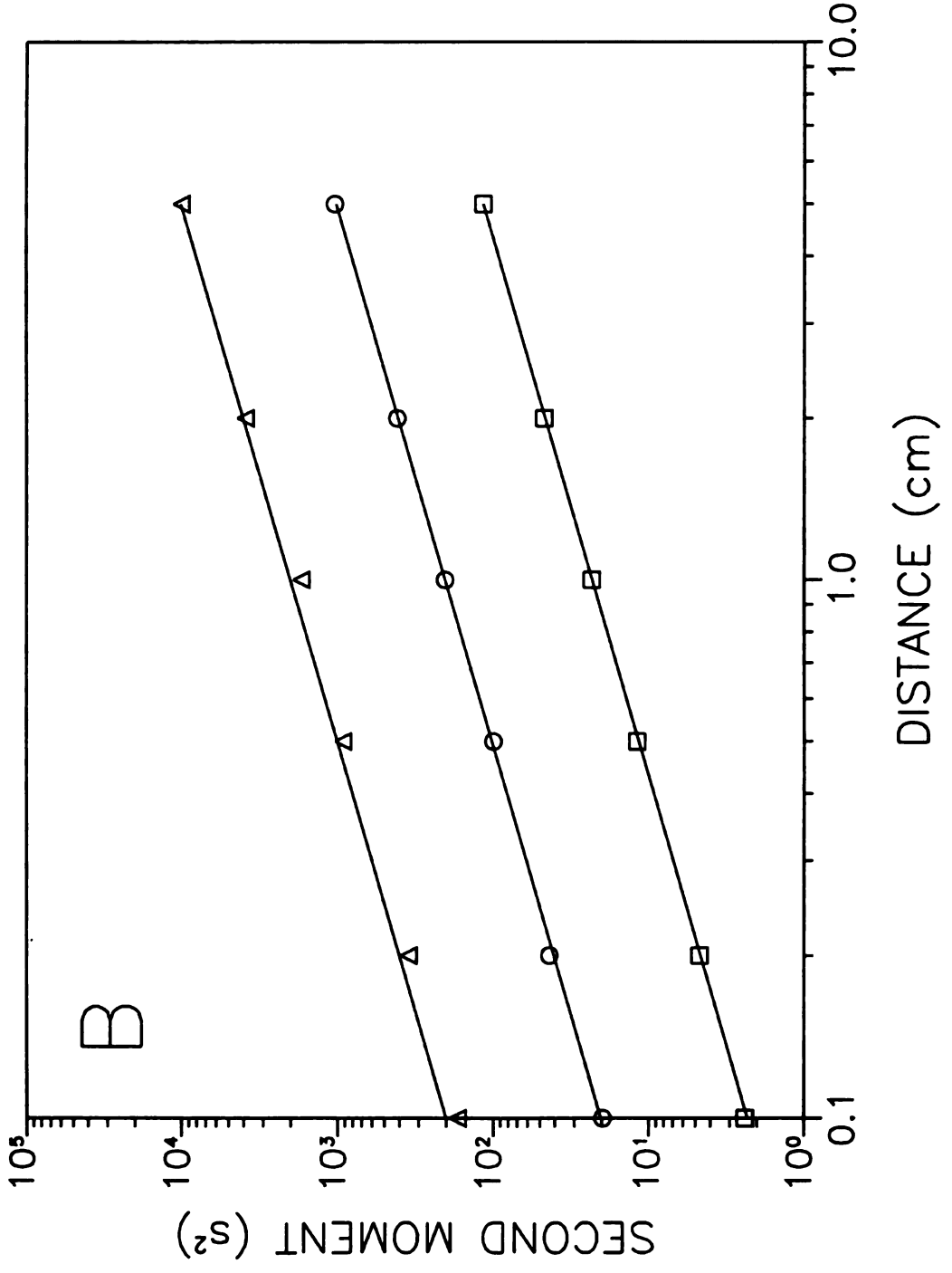

Figure 6.9 cont.

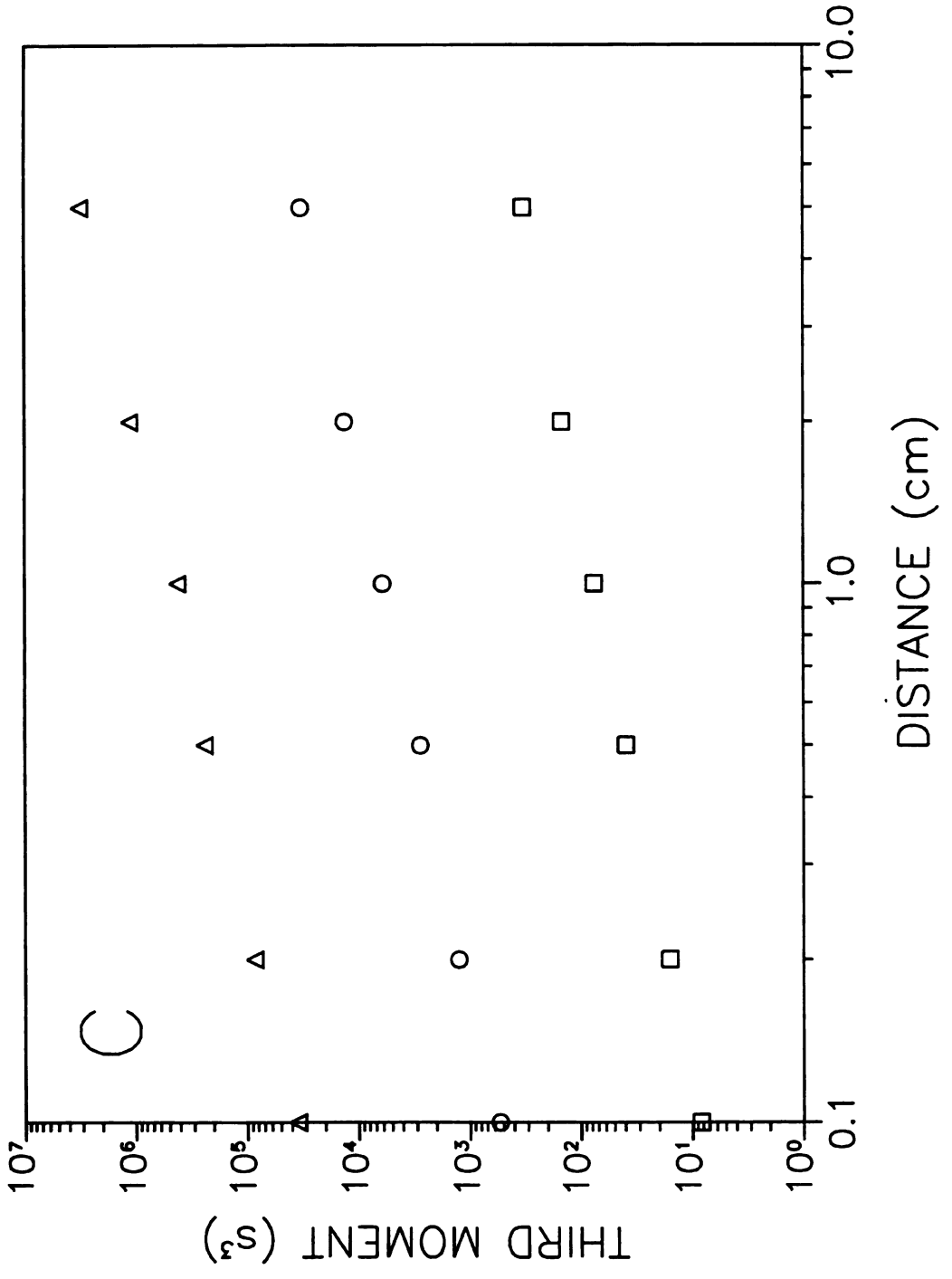

Figure 6.10: First (A), second (B), and third (C) moments in distance as a function of time for values of $k_a = 0.00203$ site^{-1} s^{-1}, $k_d = 0.01$ s^{-1} (△); $k_a = 0.0203$ site^{-1} s^{-1}, $k_d = 0.1$ s^{-1} (○); $k_a = 0.203$ site^{-1} s^{-1}, $k_d = 1.0$ s^{-1} (□). (—) Theory calculated from Equations [6.9] and [6.10]. All other conditions as given in Figure 6.8.

Figure 6.10

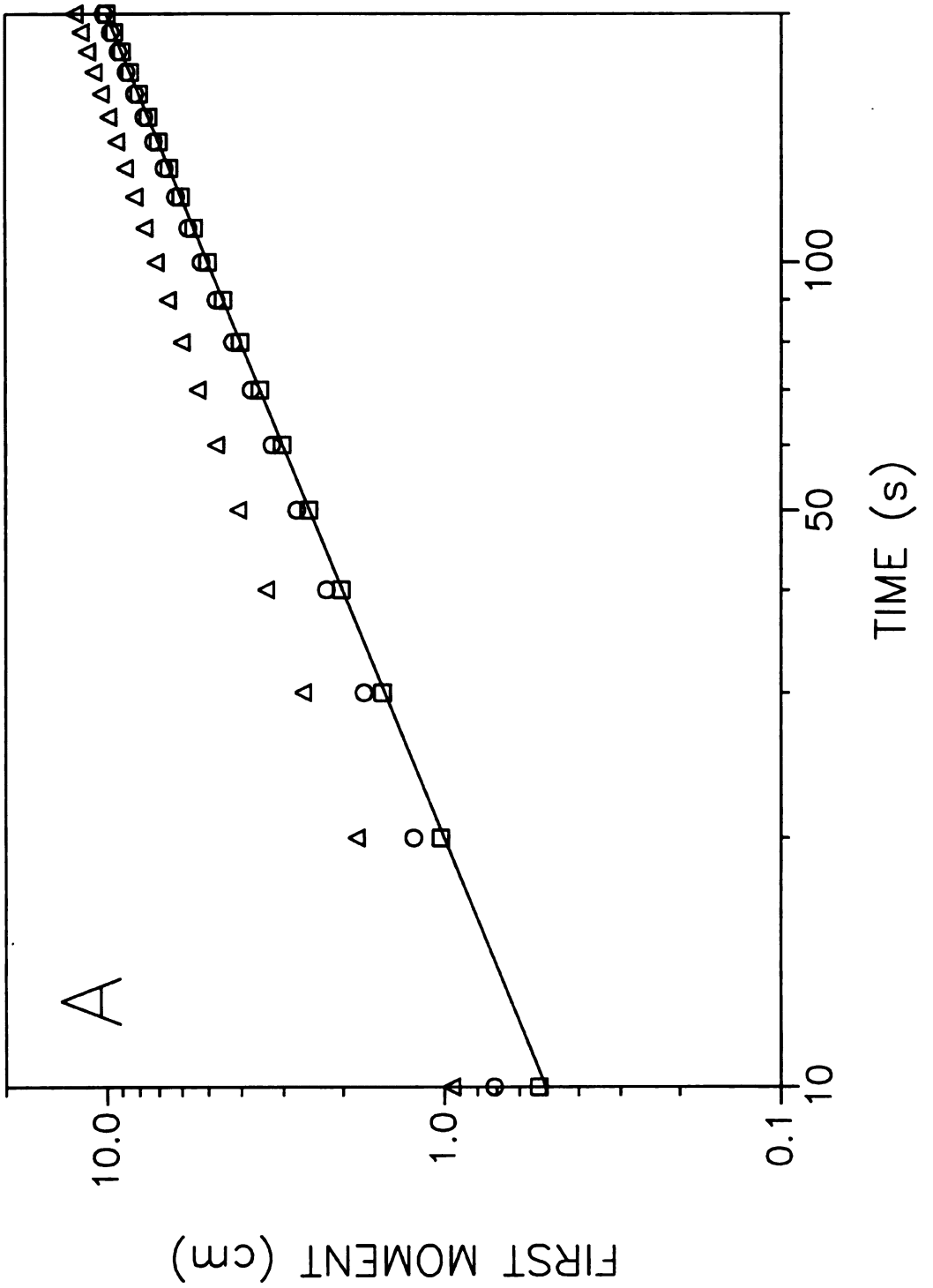

Figure 6.10 cont.

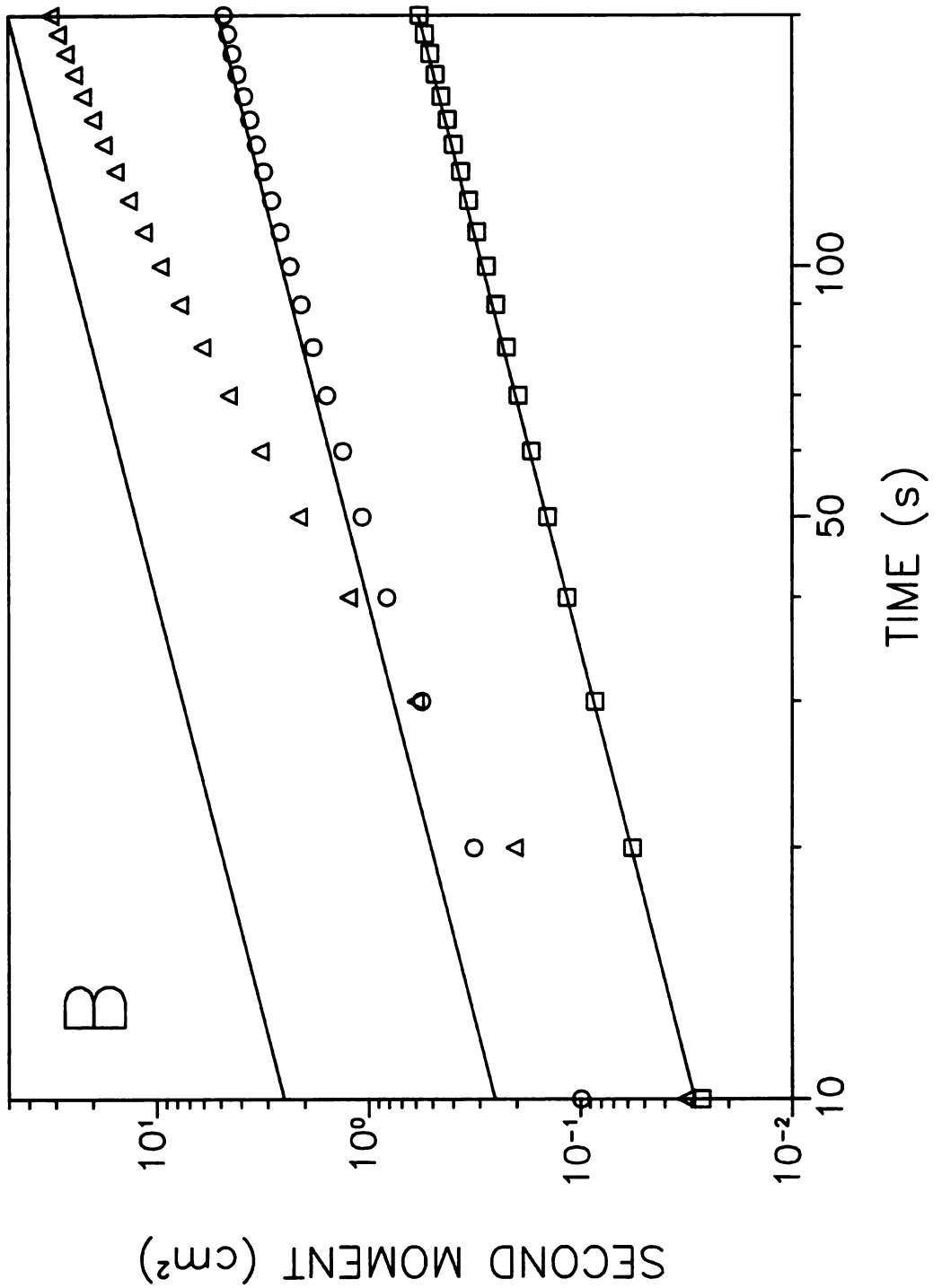

Figure 6.10 cont.

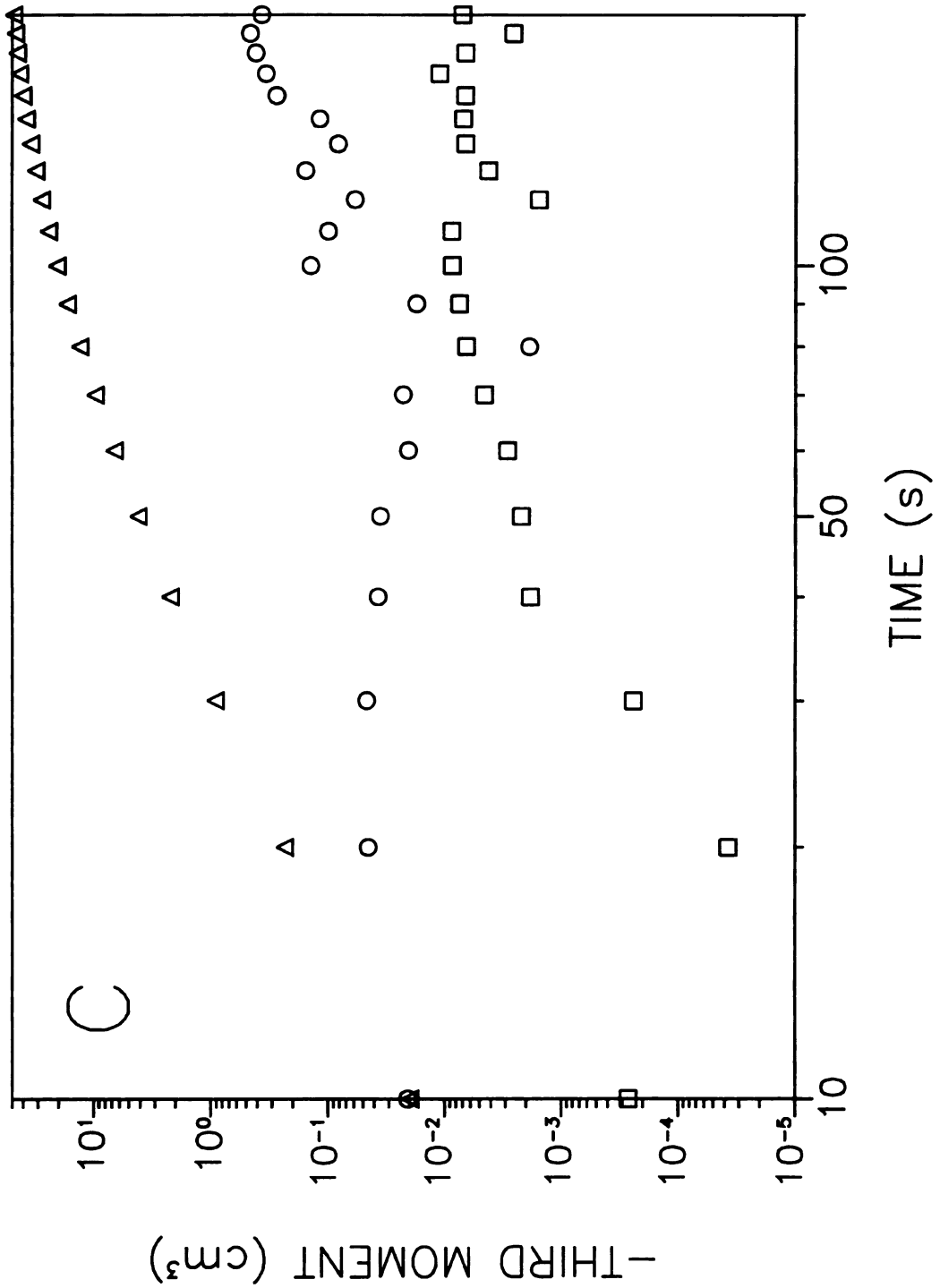

The first moment in distance, or mean position, presented in Figure 6.10A shows some deviation from the expected response. First, the three systems are not collinear as seen in Figure 6.9A. Also, the systems show varying degrees of deviation from the values predicted by Equation [6.9]. The largest adsorption and desorption rate constants show very good agreement with the values predicted by theory. As the adsorption and desorption rate constants decrease, the simulation results deviate from the theory. The deviation results from a break down of the assumption in the theory that the system is at steady-state. At short times, the simulation is still affected by the initial nonequilibrium of the system. As the simulation approaches equilibrium, the first moments for simulation and theory converge. Equilibrium occurs very quickly for the system with an adsorption rate constant of 1.0 $site^{-1}$ s^{-1} and a desorption rate constant of 1.0 s^{-1}, thus the values of the first moment from the simulation and theory are similar. The smaller rate constants require more time to reach equilibrium, which causes the deviations between simulation and theory to increase. Further observation of the deviations in Figure 6.10A show that the first moments predicted by the simulation are always greater than theory. This positive deviation is caused by the initial nonequilibrium. Because the molecules begin in the fluid phase, the convective flow moves them farther down the column than would be expected for a system at equilibrium. There is also a slight negative curvature in the simulation data presented in Figure 6.10A. This negative curvature results from the decrease in the average velocity of the zone as the systems approach steady state.

The second moment or variance of the solute zones is presented in Figures 6.9B and 6.10B. Figure 6.9B shows that the second moments in time as a function of distance agree with the established steady-state theory shown below.

$$M_{2,t} = \left(\frac{2 D_f (1 + K_{ads})}{v_0^2} + \frac{\left(1 + 6 K_{ads} + 11 K_{ads}^2\right) R_f^2}{24 v_0 D_f} + \frac{2 K_{ads}}{v_0 k_d} \right) M_{1,t} \qquad [6.12]$$

However, the smallest adsorption and desorption rate constants result in second moments that are slightly smaller than predicted by theory at the shortest distances. This is believed to result from the time necessary for the system to reach equilibrium. This conclusion is supported by the second moments in distance as a function of time shown in Figure 6.10B. The second moments for the system with the largest adsorption and desorption rate constants show good agreement with theory in Equation [6.10]. As the rate constants decrease, the deviation from theory increases. However, as time increases and the systems approach equilibrium, the difference between simulation and theory decreases for all systems. The negative deviation from theory in Figures 6.9B and 6.10B occurs because of the initial nonequilibrium. The amount of broadening due to processes in the fluid phase alone (first and second terms of Equations [6.10] and [6.12]) is smaller than the sum of fluid and surface phase processes (Equations [6.10] and [6.12]). Thus, the systems that require substantial time to reach steady state will acquire less broadening than predicted for a system at steady state. The simulation and theory converge once steady state is reached, as observed for long distances in Figure 6.9B and long times in Figure 6.10B.

The third moments shown in Figures 6.9C and 6.10C indicate the amount of asymmetry in the zone profiles. Figure 6.9C shows that the third moments in time increase as the rate constants for adsorption and desorption decrease. The third moments appear to be linear in distance, just as the second moments (Figure 6.9B). This indicates that the observed asymmetry or skew, defined as $M_3/(M_2)^{1.5}$, of the zone profiles decreases to zero and the profiles become more Gaussian as distance is increased (Figure 6.8). The third moments in distance presented in Figure 6.10C also increase as the rate constants decrease. The moments also appear to increase nonlinearly with time, just as the second moments (Figure 6.10B). The skew for the two largest adsorption and desorption rate constants is small since the third moments are of equal or lesser magnitude than the second moments over the time simulated. However, the skew for the smallest adsorption and desorption rate constants appears to be larger since the third moment is greater in magnitude than the second moment.

Another series of simulations is performed for systems in which the adsorption coefficient (K_{ads}) is varied from 0.493 to 4.93. This is accomplished by using adsorption rate constants of 0.1, 0.0203, and 1.0 site^{-1} s^{-1} while maintaining a desorption rate constant of 0.1 s^{-1}. The steady-state behavior of these systems is presented in Case 5 of Table 6.2. It can be seen that the simulation value of $\tilde{N}_s/\tilde{N}_f$ is within ±3.01% of the theoretical value. The mass-transfer kinetics of these systems are presented in Case 5 of Table 6.3. The mass-transfer rate constants from the fluid to surface phases increase as K_{ads} increases, and the mass-transfer rate constants from the surface to fluid phase remain constant. These trends mimic the changes in the adsorption and desorption rate constants.

The statistical moments in time and distance for the systems described above are presented in Figures 6.11 and 6.12, respectively. The first moments in time (Figure 6.11A) show the expected increase with an increase in the adsorption coefficient. It is also apparent that the simulation and steady-state theory (Equation [6.11]) are in good agreement. The first moments in distance (Figure 6.12A) decrease as the adsorption coefficient increases. However, the simulation values are larger than those predicted by steady-state theory (Equation [6.8]) at short times. The error is the greatest for the system with the largest adsorption coefficient (K_{ads} = 4.93) and decreases as the adsorption coefficient decreases. The error occurs because of the initial nonequilibrium as discussed previously. The error decreases with time as the adsorption and desorption processes approach steady state.

The second moments in time and distance are presented in Figures 6.11B and 6.12B, respectively. The second moments in time (Figure 6.11B) increase as the adsorption coefficient increases. Again, there is good agreement between simulation and steady-state theory (Equation [6.12]). The second moments in distance (Figure 6.12B) decrease as the adsorption coefficient increases, and show substantial differences between simulation and steady-state theory (Equation [6.10]) at short times. The deviations from theory decrease as the adsorption coefficient increases. The differences also decrease as time increases and the systems approach steady state. The second moments from the simulation are all smaller than the values predicted by steady-state theory. This is caused by the initial nonequilibrium as discussed previously.

Figure 6.11: First (A), second (B), and third (C) moments in time as a function of distance for values of $k_a = 0.1$ site^{-1} s^{-1}, $k_d = 0.1$ s^{-1} ($\triangle$); $k_a = 0.0203$ site^{-1} s^{-1}, $k_d = 0.1$ s^{-1} ($\bigcirc$); $k_a = 0.01$ site^{-1} s^{-1}, $k_d = 0.1$ s^{-1} ($\square$). (—) Theory calculated by Equations [6.11] and [6.12]. All other conditions as given in Figure 6.8.

Figure 6.11

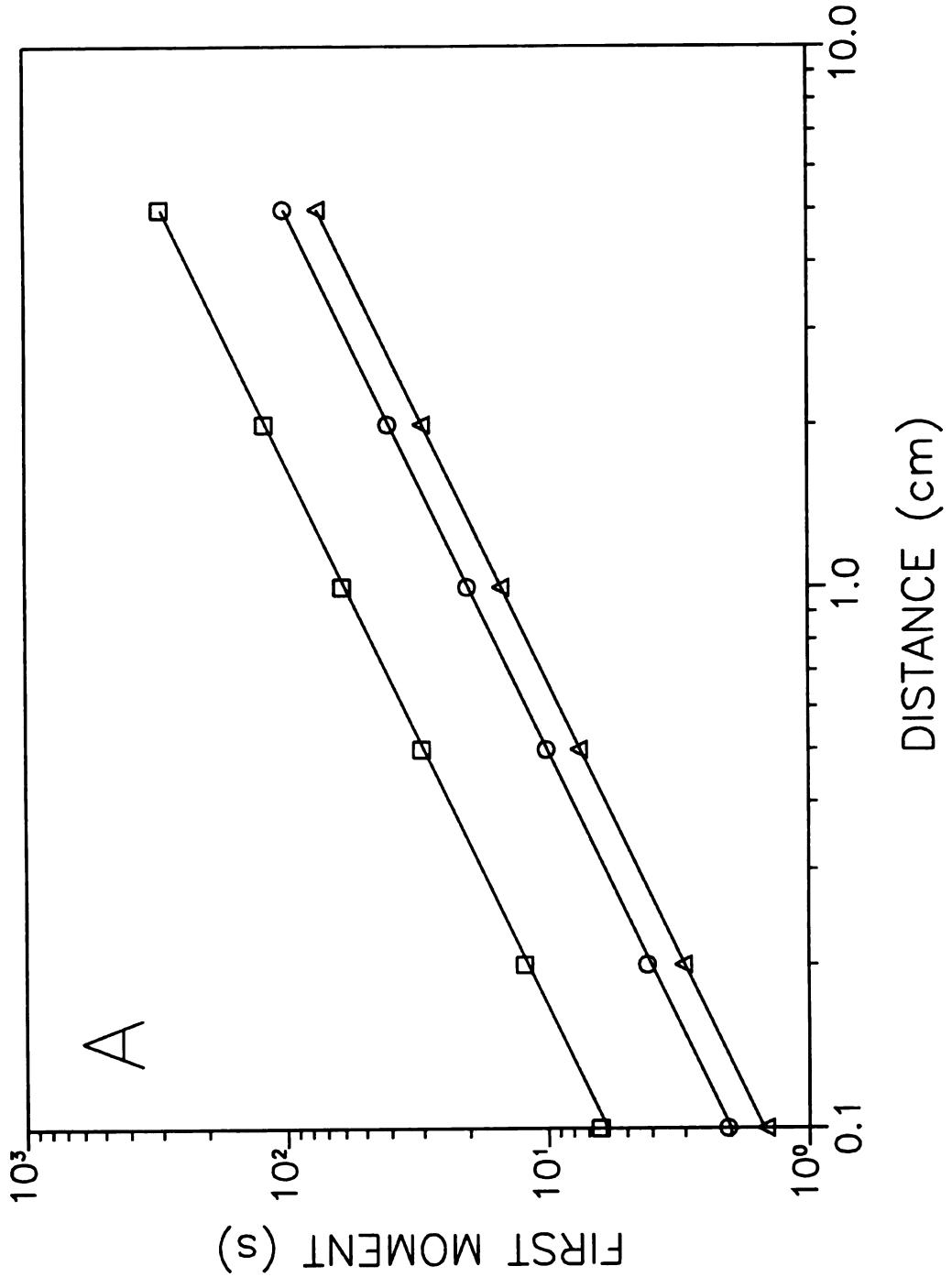

Figure 6.11 cont.

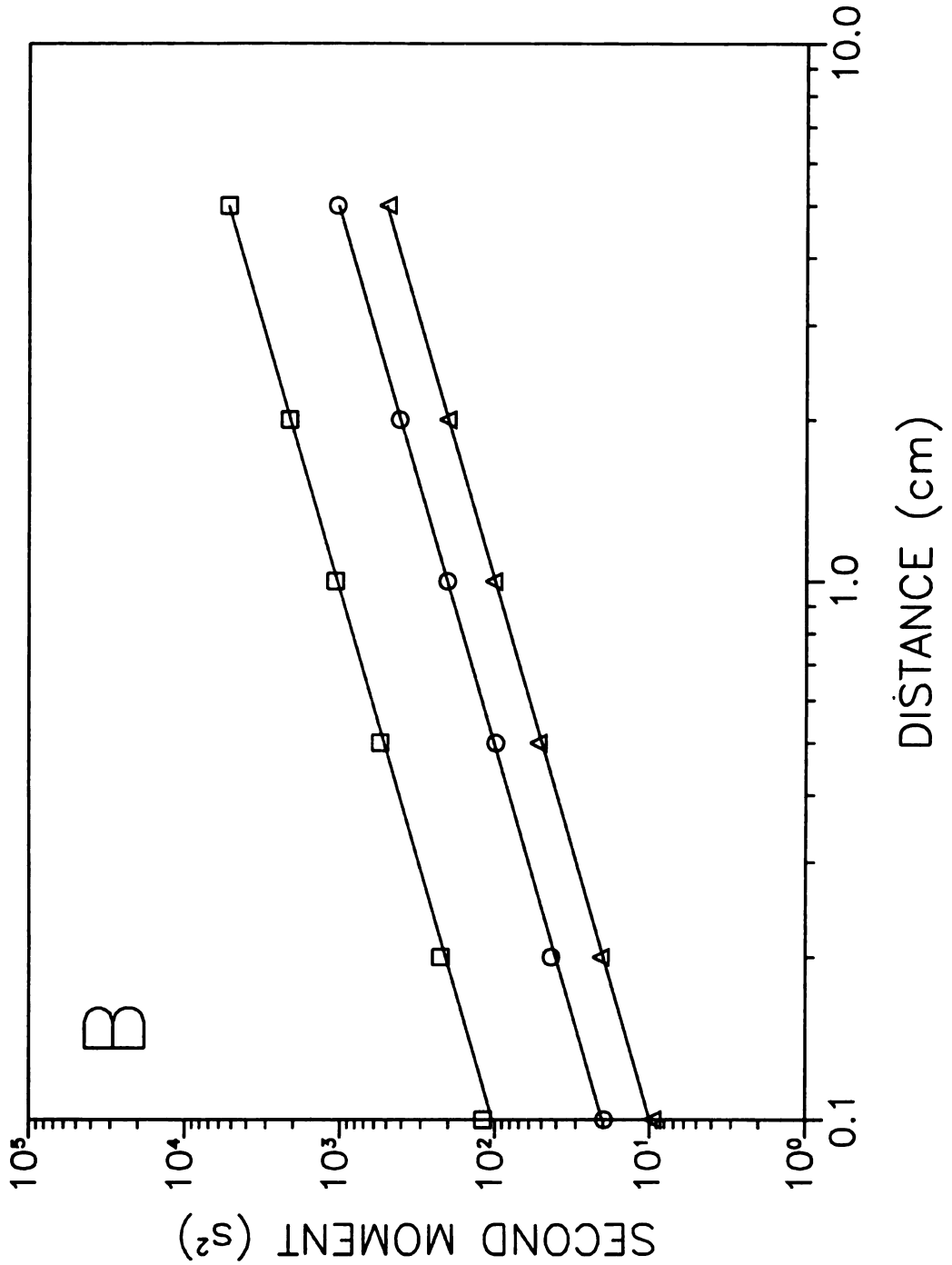

Figure 6.11 cont.

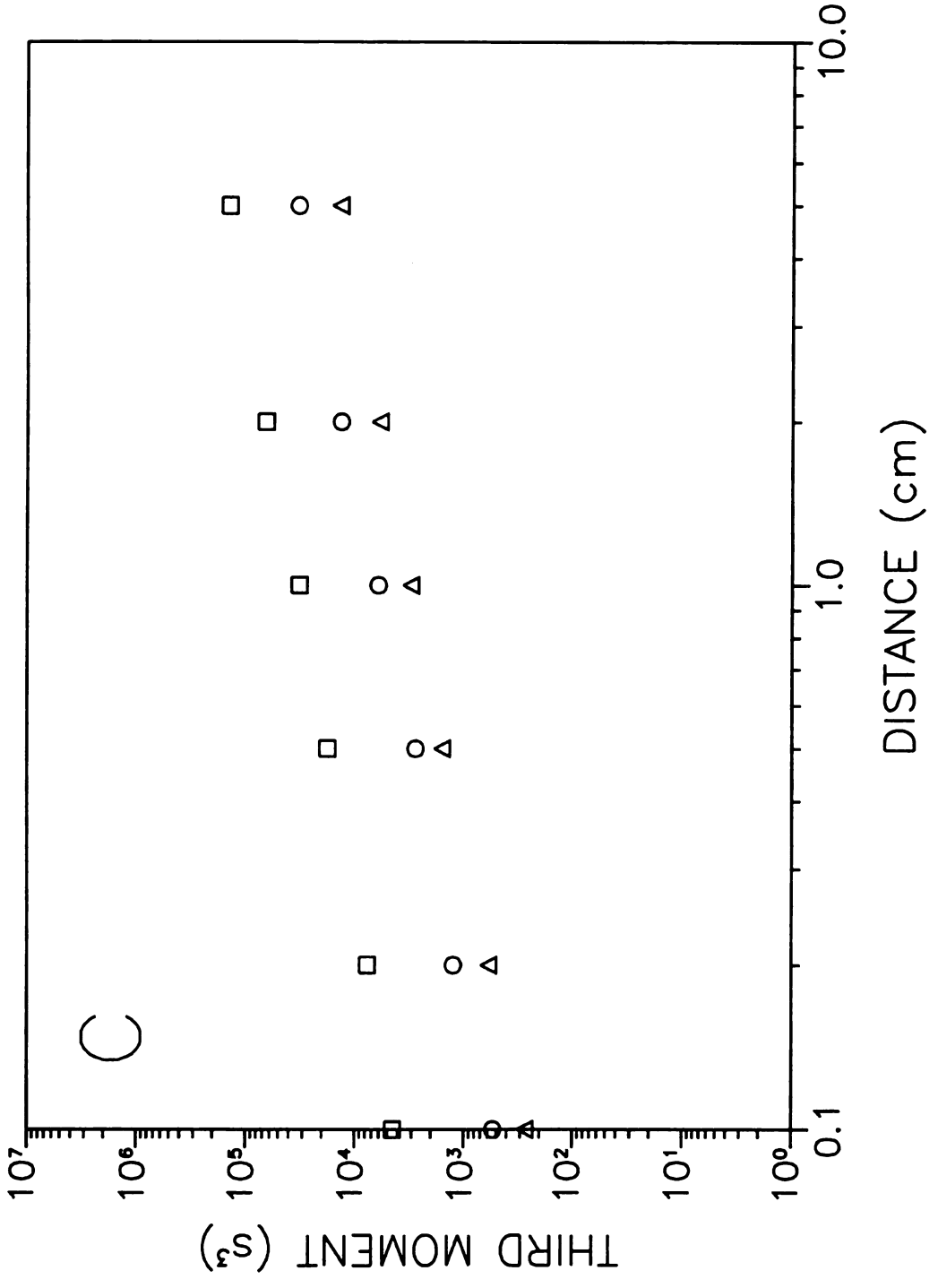

Figure 6.12: First (A), second (B), and third (C) moments in distance as a function of time for values of $k_a = 0.1$ site^{-1} s^{-1}, $k_d = 0.1$ s^{-1} (△); $k_a = 0.0203$ site^{-1} s^{-1}, $k_d = 0.1$ s^{-1} (○); $k_a = 0.01$ site^{-1} s^{-1}, $k_d = 0.1$ s^{-1} (□). (—) Theory calculated from Equations [6.9] and [6.10]. All other conditions as given in Figure 6.8.

Figure 6.12

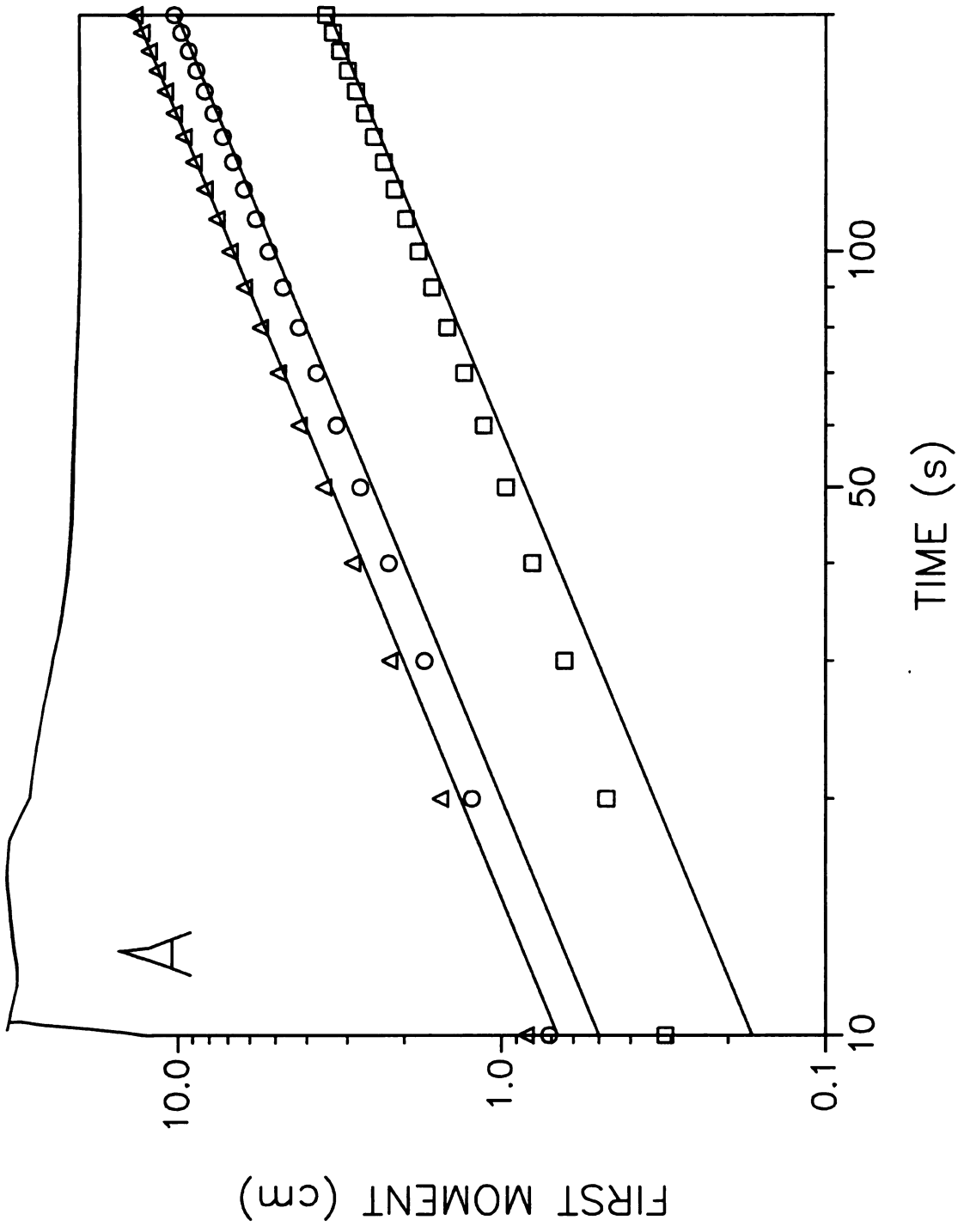

Figure 6.12 cont.

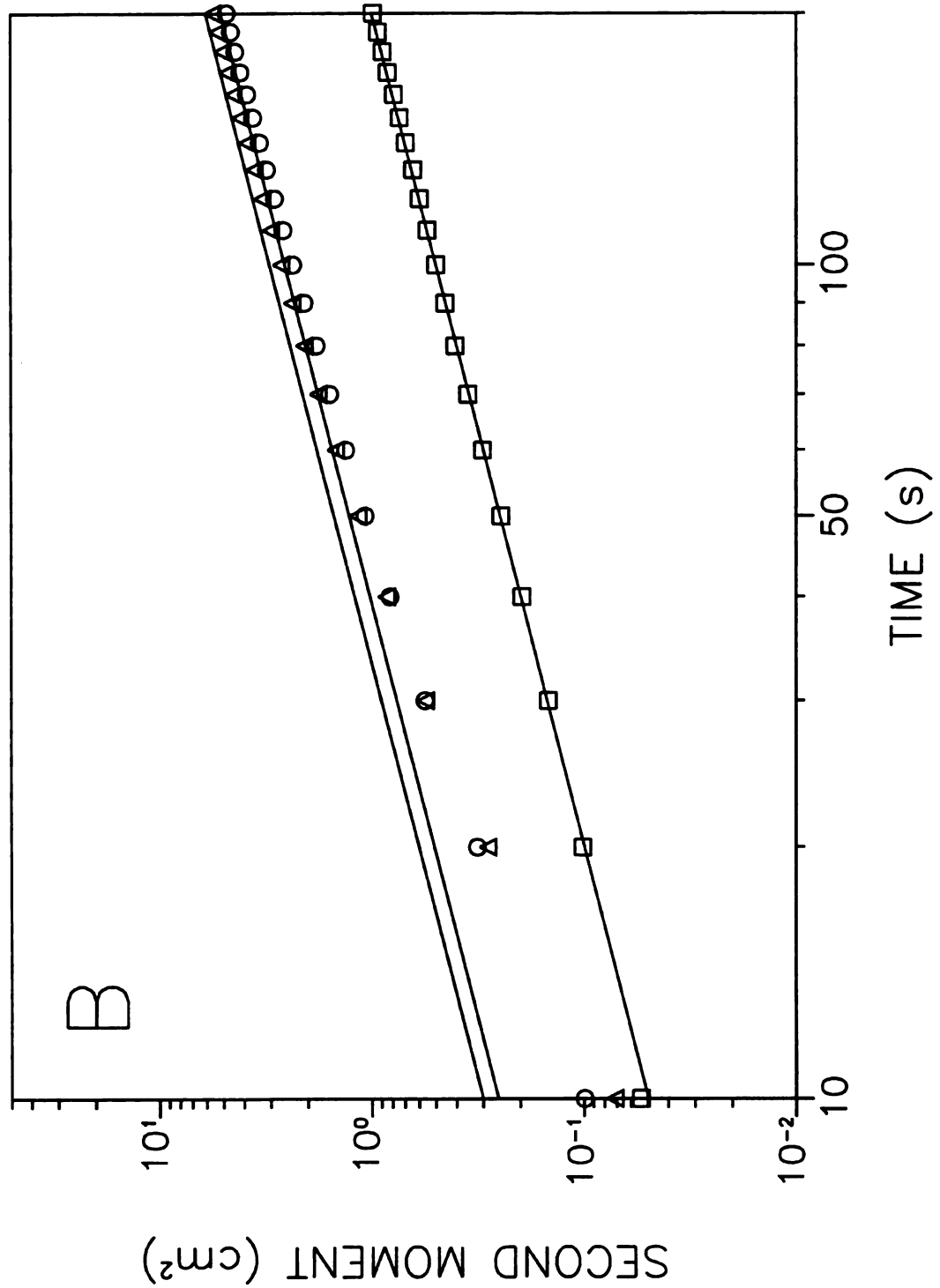

Figure 6.12 cont.

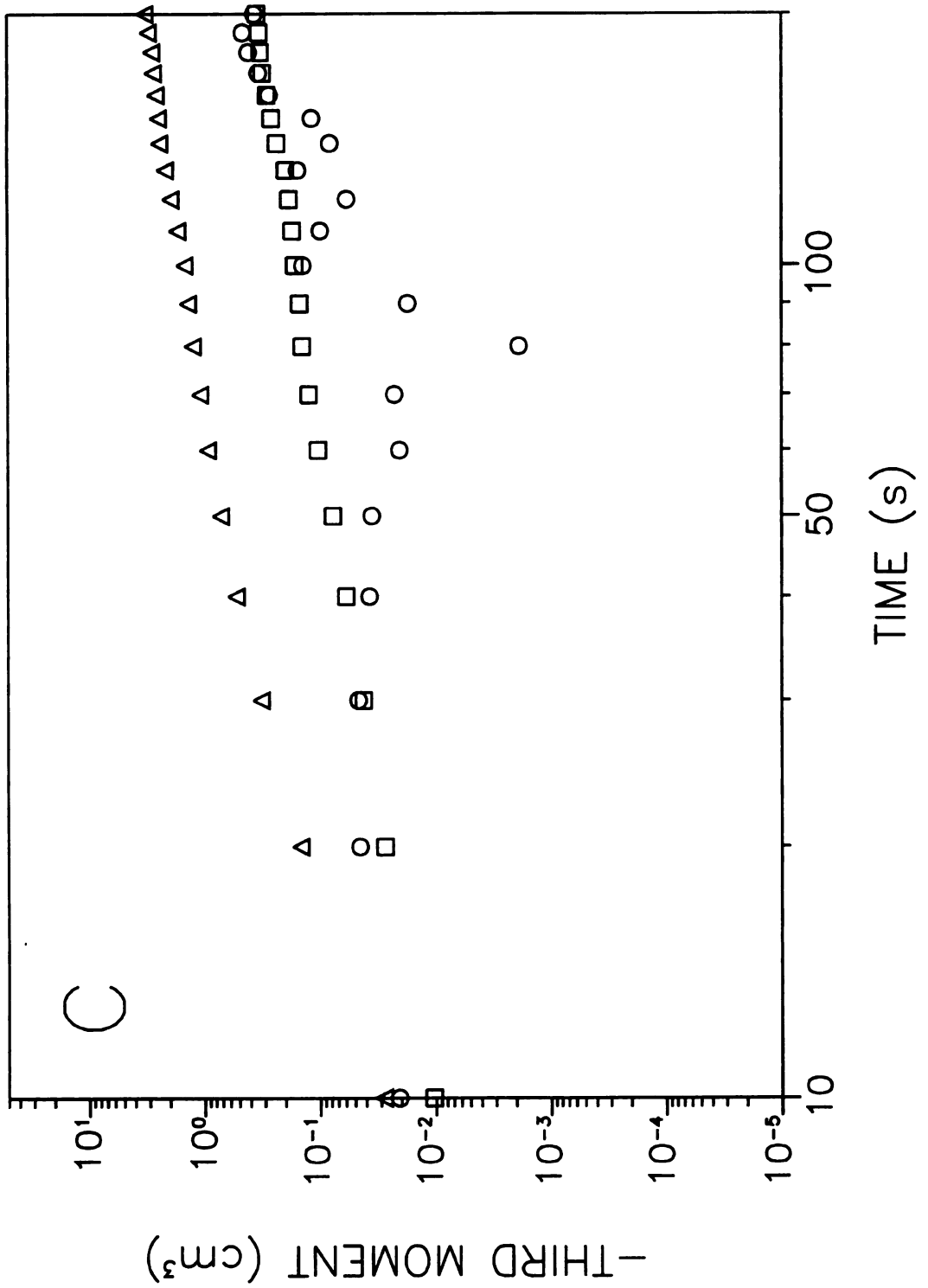

The third moments in time and distance are shown in Figure 6.11C and 6.12C, respectively. The moments in time (Figure 6.11C) increase as the adsorption coefficient increases. The third moments also show a linear dependence on the distance, just as the second moments (Figure 6.11B). The third moment is greater than the second moment for all systems, which implies that the zone profiles will have some asymmetry or skew. The skew will decrease with increasing distance. The third moments in distance (Figure 6.12C) decrease as the equilibrium constant increases. The magnitude of the third moments in distance is smaller than the second moment for all systems. Therefore, the skew will also be small and the zone profiles will be Gaussian.

6.4 Conclusions.

The approach to modeling adsorption presented in this chapter allows the processes of diffusion, convection, adsorption, and desorption to act independently upon individual molecules. This allows systems to be modeled with no assumptions about the relative importance or interaction of any of these processes. It also allows the evolution of a system from some initial state to a steady state to be studied. This is not possible with traditional models that assume the system to be at equilibrium. It has been shown that the adsorption model is independent of the time increment used in the simulation, unlike previous stochastic simulations.[30] The input parameters are the physically measurable values of the second-order adsorption rate constant (k_a) and the first-order desorption rate constant (k_d). The chromatographic capabilities of this simulation have

been proven to agree with established theory, indicating that the simulation correctly models the separation process.

This new model can now be used to explore areas that were not possible by other models. The simulation can be easily modified to accommodate heterogeneous surfaces with different adsorption and desorption rates. This will facilitate the study of the kinetic and steady-state behavior of heterogeneous surfaces in chromatographic systems. The work presented here is indicative of a linear isotherm, but any isotherm can be placed within the frame work of the simulation. Thus, exploration of the different types of isotherms can be accomplished with the same level of detail presented herein. Finally, this simulation can be used to study systems with mixed adsorption and absorption mechanisms, using the algorithms presented in Chapter 2. For example, the simulation can be used to study adsorption to the interface between the fluid and surface phases before partition into the surface phase or to study partition followed by adsorption to the chromatographic support. The capability to incorporate both separation mechanisms into the same model with no assumptions about the relative rates of the adsorption and absorption processes will allow this model to explore areas of separation science beyond the traditional equilibrium models currently in use.

6.5 References.

1. Langmuir, I.; J. Am. Chem. Soc. 1918, 40, 1361.
2. Brunauer, S.; Emmett, P.H.; Teller, E.; J. Am. Chem. Soc. 1938, 60, 309.
3. Adamson, A.W.; Physical Chemistry of Surfaces, 5th ed.; John Wiley: New York, NY, 1990; Chp. 16.

4. Brunauer, S.; The Adsorption of Gases and Vapors, Vol. 1; Princeton University Press: Princeton, NJ, 1945.

5. Feder, J.; J. Theor. Biol. 1980, 87, 237.

6. Swendsen, R.H.; Phys. Rev. A, 1981, 24, 504.

7. Sherwood, J.D.; J. Phys. A, 1990, 23, 2827.

8. Brosilow, B.J.; Ziff, R.M.; Vigil, R.D.; Phys. Rev. A, 1991, 43, 631.

9. Talbot, J.; Tarjus, G.; Van Tassel, P.R.; Viot, P.; Colloids Surf. A, 2000, 165, 287.

10. Borowko, M.; Patrykiejew, A.; Rzysko, W.; Sokolowski, S.; Langmuir, 1997, 13, 1073.

11. Riccardo, J.L.; Steel, W.A.; Ramirez Cuesta, A.J.; Zgrablich, G.; Langmuir, 1997, 13, 1064.

12. Bates, S.P.; Van Santen, R.A.; in Advances in Catalysis, Vol. 42; Academic Press: New York, NY, 1998; 1.

13. Lehner, B.; Hohage, M.; Zeppenfeld, P.; Chem. Phys. Lett. 2001, 336, 123.

14. Senger, B.; Voegel, J.C.; Schaaf, P.; Johner, A.; Schmitt, A.; Talbot, J.; Phys. Rev. A, 1991, 44, 6926.

15. Senger, B.; Schaaf, P.; Voegel, J.C.; Johner, A.; Schmitt, A.; Talbot, J.; J. Chem. Phys. 1992, 97, 3813.

16. Bafaluy, J.; Senger, B.; Voegel, L.C.; Schaaf, P.; Phys. Rev. Lett. 1993, 70, 623.

17. Yun, T.; Smith, M.S.; Guiochon, G.; J. Chromatogr. A, 1998, 828, 19.

18. Smith, M.S.; Guichon, G.; J. Chromatogr. A, 1998, 827, 241.

19. Fornstedt, T.; Zhong, G.M.; Guiochon, G.; J. Chromatogr. A, 1996, 742, 55.

20. Fornstedt, T.; Zhong, G.M.; Guiochon, G.; J. Chromatogr. A, 1996, 741, 1.

21. Fornstedt, T.; Zhong, G.M.; Bensetiti Z.; Guiochon, G.; Anal. Chem. 1996, 68, 2370.

22. Giddings, J.C.; Eyring, H.; J. Phys. Chem. 1955, 59, 416.

23. Giddings, J.C.; J. Chem. Phys. 1957, 26, 169.

24. McQuarrie, D.A.; J. Chem. Phys. 1963, 38, 437.

25. Weiss, G.H.; Sep. Sci. 1970, 5, 51.

26. Cavazzini, A.; Remelli, M.; Dondi, F.; J. Microcolumn Sep. 1997, 9, 295.

27. Cavazzini, A.; Remelli, M.; Dondi, F.; Felinger, A.; Anal. Chem. 1999, 71, 3453.

28. Felinger, A.; Cavazzini, A.; Remelli, M.; Dondi, F.; Anal. Chem. 1999, 71, 4472.

29. Dondi, F.; Munari, P.; Remelli, M.; Cavazzini, A.; Anal. Chem. 2000, 72, 4353.

30. Schure, M.R.; Lenhoff, A.M.; Anal. Chem. 1993, 65, 3024.

31. Steinfeld, J.I.; Francisco, J.S.; Hase, W.L.; Chemical Kinetics and Dynamics; Prentice Hall: Englewood Cliffs, NJ, 1989.

32. Benson, S.W.; Foundations of Chemical Kinetics; McGraw-Hill: New York, NY, 1960.

33. Wu, P.; McGuffin, V.L.; AIChE J. 1998, 44, 2053.

34. Giddings, J.C.; Dynamics of Chromatography; Marcel Dekker: New York, NY, 1965; Chp. 3,4.

Appendix B

Determination of the Collision Frequency as a Function of Molecular and System Parameters

The number of molecular collisions with the wall or any other surface such as the interface between the fluid and surface phases is dependent on the time increment (t), absorption coefficient (K_{abs}), fluid and surface phase diffusion coefficients (D_f and D_s, respectively), and fluid and surface phase radii (R_f and R_s, respectively). The dependence of the collision frequency on the molecular and system parameters is not surprising. However, the dependence on the time increment t is an artifact of the diffusion algorithm. Studies have been performed to determine the dependence of the collision frequency on the parameters listed above to determine the best method to remove the effects of the artificial dependence on t.

Table B.1 shows the collision frequency (ν_c) with a solid wall as simulated by the stochastic model. The data show that the collision frequency is inversely dependent on the square root of t. The data also show an inverse dependence on R_f and direct dependence on the square root of D_f. Combining these observations, the collision frequency is found to be best represented by

$$\nu_c = \frac{\pi}{2R_f}\sqrt{\frac{D_f}{2t}} \qquad [B.1]$$

Using the systems shown in Table B.1, the values of ν_c obtained from the simulation are plotted against those obtained from Equation [B.1] in Figure B.1.

Table B.1 Collision Frequency With the Wall (ν_c) as a Function of Time Increment (t), Fluid-Phase Diffusion Coefficient (D_f), and Fluid-Phase Radius (R_f).

t (s)	D_f ($cm^2\ s^{-1}$)	R_f (cm)	ν_c ($molecule^{-1}\ s^{-1}$)
1.00×10^{-6} [a]	1.00×10^{-5}	2.00×10^{-3}	1800 ± 300
1.00×10^{-5} [a]	1.00×10^{-5}	2.00×10^{-3}	560 ± 90
1.00×10^{-4} [a]	1.00×10^{-5}	2.00×10^{-3}	180 ± 30
1.00×10^{-3} [b]	1.00×10^{-5}	2.00×10^{-3}	56 ± 9
1.00×10^{-3} [b]	1.00×10^{-8}	2.00×10^{-3}	2 ± 2
1.00×10^{-3} [b]	1.00×10^{-7}	2.00×10^{-3}	6 ± 3
1.00×10^{-3} [b]	1.00×10^{-6}	2.00×10^{-3}	18 ± 6
1.00×10^{-3} [b]	1.00×10^{-5}	2.00×10^{-3}	56 ± 9
1.00×10^{-3} [b]	1.00×10^{-5}	2.00×10^{-3}	56 ± 9
1.00×10^{-3} [b]	1.00×10^{-5}	4.00×10^{-3}	28 ± 7
1.00×10^{-3} [b]	1.00×10^{-5}	2.00×10^{-2}	6 ± 4
1.00×10^{-3} [b]	1.00×10^{-5}	5.00×10^{-2}	2 ± 2

[a] Other simulation conditions as follows: N = 5000, T = 10 s.
[b] Other simulation conditions as follows: N = 10000, T = 10 s.

The data fall along a line that has a slope of 1.01 and an intercept of 0.02. This indicates that the equation fully accounts for the observed dependencies of the collision frequency on the simulation parameters.

The collision frequencies for both sides of the interface between fluid and surface phases are shown in Table B.2. The collision frequencies on both sides of the interface are inversely dependent on the square root of t, just as observed above. The data also show the fluid-phase collision frequencies ($\nu_{c,f}$) decrease and the surface-phase collision frequencies ($\nu_{c,s}$) increase non-linearly as K_{abs} increases. The following relationships appear applicable

Figure B.1: Relationship between the collision frequency determined by stochastic simulation and predicted by Equation [B.1]. Simulation conditions given in Table B.1.

Figure B.1

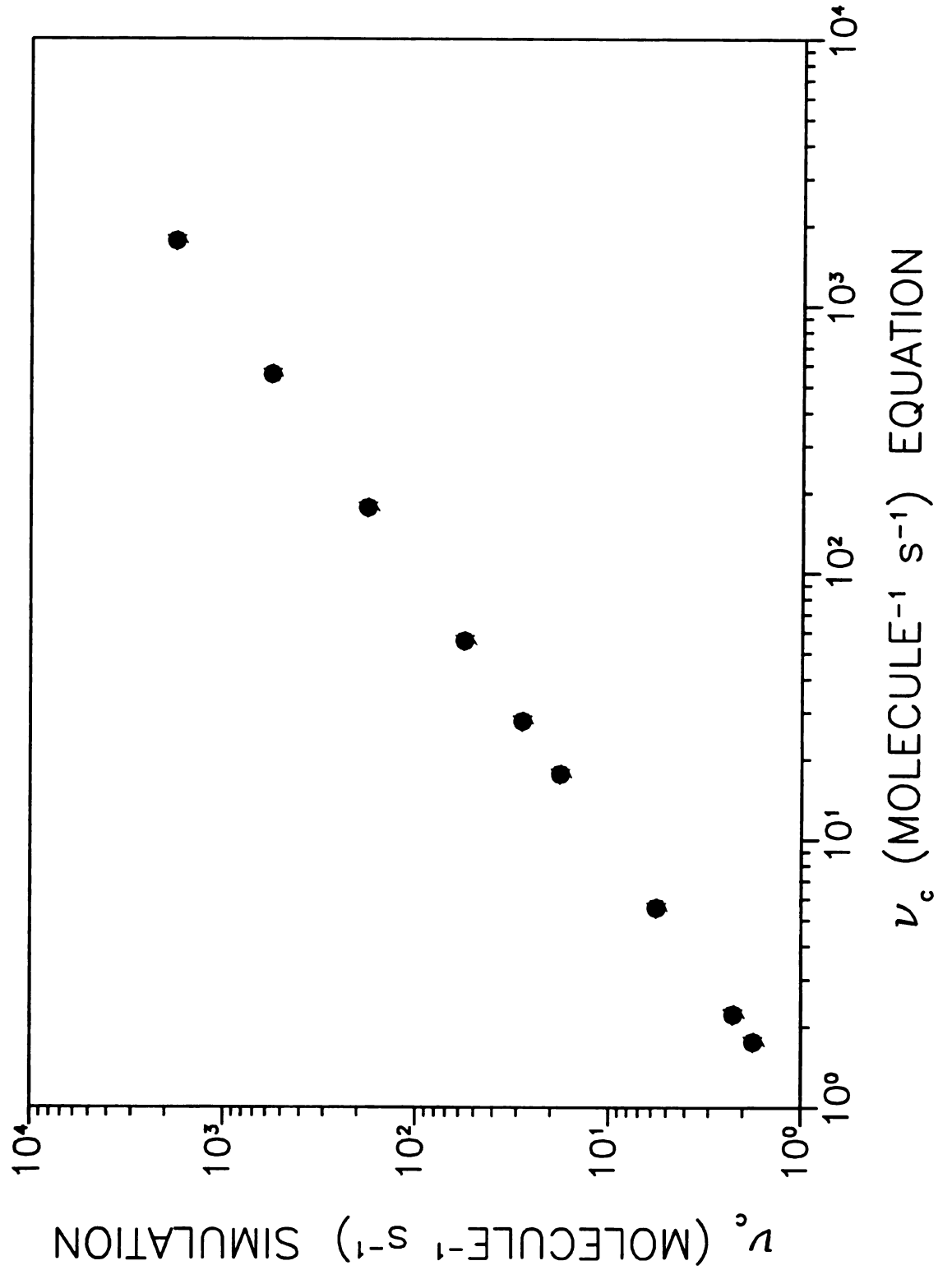
ν_c (MOLECULE^{-1} s^{-1}) EQUATION
ν_c (MOLECULE^{-1} s^{-1}) SIMULATION
10^0
10^1
10^2
10^3
10^4

Table B.2 ***Fluid and Surface Phase Collision*** **Frequencies ($\nu_{c,f}$, $\nu_{c,s}$) With the Interface as a Function of the Time Increment (t), Absorption Coefficient (K_{abs}), Fluid and Surface Phase Diffusion Coefficients (D_f, D_s), and Fluid and Surface Phase Radii (R_f, R_s)**

t (s)	K_{abs}	D_f ($cm^2\ s^{-1}$)	D_s ($cm^2\ s^{-1}$)	R_f (cm)	R_s (cm)	$\nu_{c,f}$ ($molecule^{-1}\ s^{-1}$)	$\nu_{c,s}$ ($molecule^{-1}\ s^{-1}$)
5.00×10^{-14} [a]	1	1.00×10^{-5}	1.00×10^{-7}	2.00×10^{-3}	8.28×10^{-4}	5490000 ± 70000	553000 ± 7000
5.00×10^{-12} [b]	1	1.00×10^{-5}	1.00×10^{-7}	2.00×10^{-3}	8.28×10^{-4}	380000 ± 20000	38000 ± 2000
5.00×10^{-10} [c]	1	1.00×10^{-5}	1.00×10^{-7}	2.00×10^{-3}	8.28×10^{-4}	42000 ± 2000	4200 ± 200
5.00×10^{-8} [d]	1	1.00×10^{-5}	1.00×10^{-7}	2.00×10^{-3}	8.28×10^{-4}	4000 ± 2000	400 ± 200
5.00×10^{-6} [e]	1	1.00×10^{-5}	1.00×10^{-7}	2.00×10^{-3}	8.28×10^{-4}	400 ± 200	40 ± 20
5.00×10^{-5} [e]	1	1.00×10^{-5}	1.00×10^{-7}	2.00×10^{-3}	8.28×10^{-4}	130 ± 50	13 ± 6
5.00×10^{-5} [f]	0.01	1.00×10^{-7}	1.00×10^{-7}	2.00×10^{-3}	8.28×10^{-4}	30 ± 30	0.2 ± 0.5
5.00×10^{-5} [f]	0.02	1.00×10^{-7}	1.00×10^{-7}	2.00×10^{-3}	8.28×10^{-4}	20 ± 40	0.5 ± 1
5.00×10^{-5} [f]	0.05	1.00×10^{-7}	1.00×10^{-7}	2.00×10^{-3}	8.28×10^{-4}	20 ± 20	1 ± 1
5.00×10^{-5} [f]	0.1	1.00×10^{-7}	1.00×10^{-7}	2.00×10^{-3}	8.28×10^{-4}	20 ± 30	2 ± 3
5.00×10^{-5} [f]	0.2	1.00×10^{-7}	1.00×10^{-7}	2.00×10^{-3}	8.28×10^{-4}	20 ± 20	4 ± 4
5.00×10^{-5} [f]	0.5	1.00×10^{-7}	1.00×10^{-7}	2.00×10^{-3}	8.28×10^{-4}	20 ± 20	9 ± 9
5.00×10^{-5} [f]	1	1.00×10^{-7}	1.00×10^{-7}	2.00×10^{-3}	8.28×10^{-4}	10 ± 20	10 ± 20
5.00×10^{-5} [f]	2	1.00×10^{-7}	1.00×10^{-7}	2.00×10^{-3}	8.28×10^{-4}	8 ± 10	20 ± 20
5.00×10^{-5} [f]	5	1.00×10^{-7}	1.00×10^{-7}	2.00×10^{-3}	8.28×10^{-4}	4 ± 5	20 ± 30
5.00×10^{-5} [f]	1	1.00×10^{-7}	1.00×10^{-7}	2.00×10^{-3}	8.28×10^{-4}	10 ± 20	10 ± 20
5.00×10^{-5} [f]	1	1.00×10^{-6}	1.00×10^{-7}	2.00×10^{-3}	8.28×10^{-4}	40 ± 30	10 ± 10
5.00×10^{-5} [f]	1	1.00×10^{-5}	1.00×10^{-7}	2.00×10^{-3}	8.28×10^{-4}	130 ± 50	13 ± 6

Table B.2 cont.

t (s)	K_{abs}	D_f ($cm^2\ s^{-1}$)	D_s ($cm^2\ s^{-1}$)	R_f (cm)	R_s (cm)	$\nu_{c,f}$ ($molecule^{-1}\ s^{-1}$)	$\nu_{c,s}$ ($molecule^{-1}\ s^{-1}$)
5.00×10^{-5} [f]	1	1.00×10^{-7}	1.00×10^{-9}	2.00×10^{-3}	8.28×10^{-4}	10 ± 20	1 ± 2
5.00×10^{-5} [f]	1	1.00×10^{-7}	1.00×10^{-8}	2.00×10^{-3}	8.28×10^{-4}	10 ± 20	4 ± 6
5.00×10^{-5} [f]	1	1.00×10^{-7}	1.00×10^{-7}	2.00×10^{-3}	8.28×10^{-4}	10 ± 20	10 ± 20
5.00×10^{-5} [f]	1	1.00×10^{-7}	1.00×10^{-7}	3.68×10^{-4}	8.28×10^{-4}	10 ± 10	10 ± 10
5.00×10^{-5} [f]	1	1.00×10^{-7}	1.00×10^{-7}	2.00×10^{-3}	8.28×10^{-4}	10 ± 20	10 ± 20
5.00×10^{-5} [f]	1	1.00×10^{-7}	1.00×10^{-7}	3.69×10^{-3}	8.28×10^{-4}	9 ± 10	9 ± 10
5.00×10^{-5} [f]	1	1.00×10^{-7}	1.00×10^{-7}	8.68×10^{-3}	8.28×10^{-4}	5 ± 9	5 ± 9
5.00×10^{-5} [f]	1	1.00×10^{-7}	1.00×10^{-7}	1.70×10^{-2}	8.28×10^{-4}	3 ± 7	3 ± 7
5.00×10^{-5} [f]	1	1.00×10^{-7}	1.00×10^{-7}	2.00×10^{-3}	9.76×10^{-5}	20 ± 20	20 ± 20
5.00×10^{-5} [f]	1	1.00×10^{-7}	1.00×10^{-7}	2.00×10^{-3}	1.91×10^{-4}	20 ± 20	20 ± 20
5.00×10^{-5} [f]	1	1.00×10^{-7}	1.00×10^{-7}	2.00×10^{-3}	4.49×10^{-4}	20 ± 20	20 ± 20
5.00×10^{-5} [f]	1	1.00×10^{-7}	1.00×10^{-7}	2.00×10^{-3}	8.28×10^{-4}	10 ± 20	10 ± 20
5.00×10^{-5} [f]	1	1.00×10^{-7}	1.00×10^{-7}	2.00×10^{-3}	1.46×10^{-3}	8 ± 10	8 ± 10
5.00×10^{-5} [f]	1	1.00×10^{-7}	1.00×10^{-7}	2.00×10^{-3}	2.90×10^{-3}	4 ± 8	4 ± 8
5.00×10^{-5} [f]	1	1.00×10^{-7}	1.00×10^{-7}	2.00×10^{-3}	4.63×10^{-3}	2 ± 6	2 ± 6

[a] Other simulation conditions as follows: N = 1000, T = 5.8×10^{-6} s

[b] Other simulation conditions as follows: N = 1000, T = 4.8×10^{-4} s

[c] Other simulation conditions as follows: N = 1000, T = 2.53×10^{-3} s

[d] Other simulation conditions as follows: N = 1000, T = 1.8 s

[e] Other simulation conditions as follows: N = 1000, T = 20.0 s

[f] Other simulation conditions as follows: N = 1000, T = 10.0 s

$$\nu_{c,f} \propto \frac{1}{1+K_{abs}} \qquad [B.2]$$

$$\nu_{c,s} \propto \frac{K_{abs}}{1+K_{abs}} \qquad [B.3]$$

It appears that $\nu_{c,f}$ is directly proportional to the square root of D_f and is independent of D_s. Conversely, $\nu_{c,s}$ is directly proportional to the square root of D_s and is independent of D_f. The values of $\nu_{c,f}$ and $\nu_{c,s}$ show a nonlinear decrease as the value of R_f increases. The same phenomena occur for R_s, as seen at the bottom of Table B.2. The following relationships are applicable

$$\nu_{c,f} \propto \frac{R_f}{R_f+R_s} \qquad [B.4]$$

$$\nu_{c,s} \propto \frac{R_f}{R_f+R_s} \qquad [B.5]$$

By combining the relationships presented above, the following relationships are obtained

$$\nu_{c,f} = \left(\frac{\pi R_f}{R_f+R_s}\right)\left(\frac{1}{1+K_{abs}}\right)\sqrt{\frac{D_f}{2t}} \qquad [B.6]$$

$$\nu_{c,s} = \left(\frac{\pi R_f}{R_f+R_s}\right)\left(\frac{K_{abs}}{1+K_{abs}}\right)\sqrt{\frac{D_s}{2t}} \qquad [B.7]$$

The values of $\nu_{c,f}$ and $\nu_{c,s}$ obtained from the simulation and Equations [B.6] and [B.7] are plotted against each other in Figures B.2A and B.2B, respectively. Figure B.2A shows that the data from the systems in Table B.2 create a line with a slope of 1.3 and an intercept of -2.1. Figure B.2B shows a line with a slope of 1.3 and an intercept of -0.3. Thus, Equations [B.6] and [B.7] adequately describe the dependence of the collision frequencies from the fluid and surface phases.

Figure B.2: Relationship between the individual collision frequencies $\nu_{c,f}$ (A) and $\nu_{c,s}$ (B) determined by stochastic simulation and predicted by Equations [B.6] and [B.7]. Simulation conditions given in Table B.2.

Figure B.2

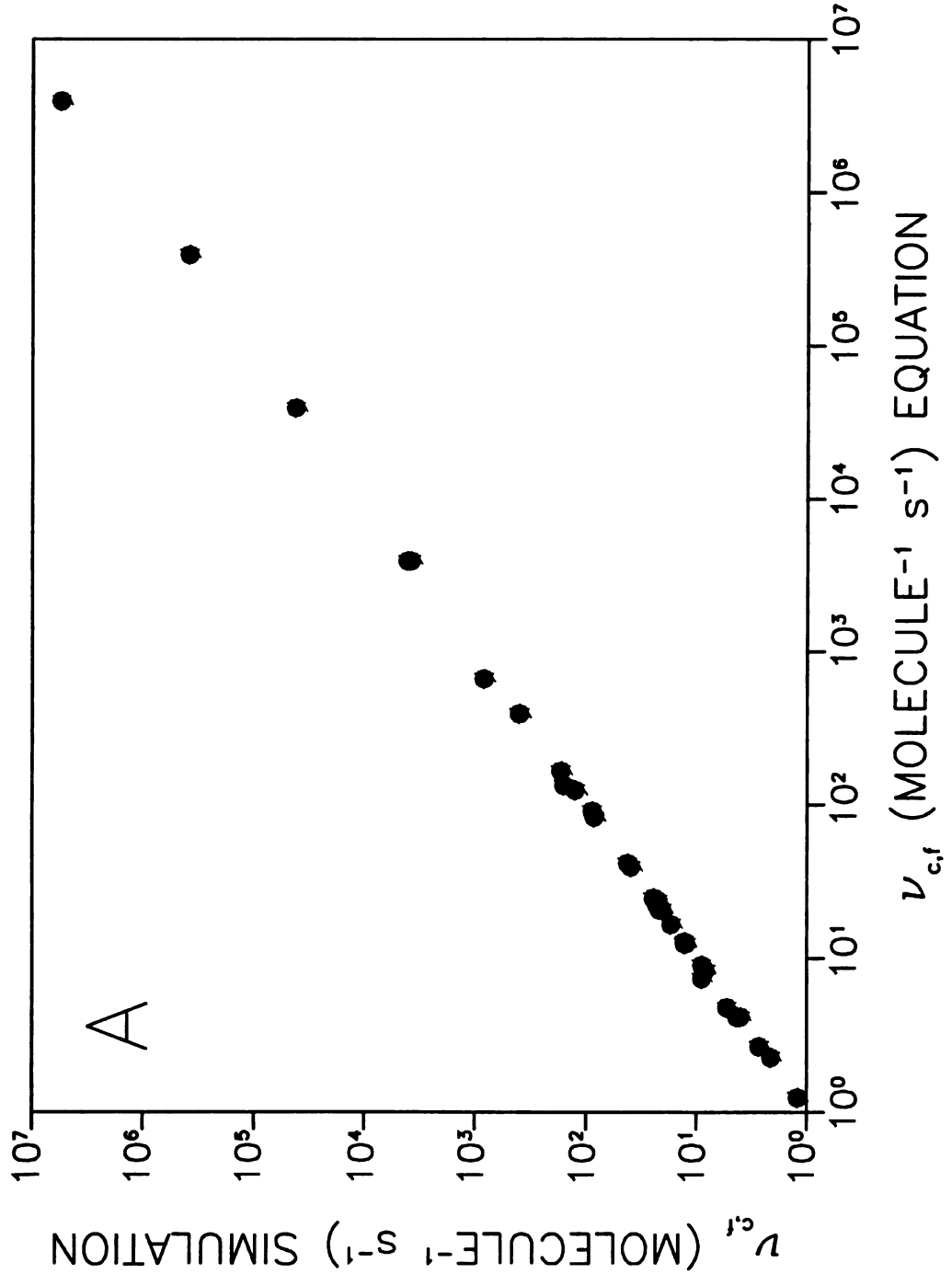
A
$\nu_{c,f}$ (MOLECULE^{-1} S^{-1}) SIMULATION
$\nu_{c,f}$ (MOLECULE^{-1} S^{-1}) EQUATION
10^0
10^1
10^2
10^3
10^4
10^5
10^6
10^7

Figure B.2 cont.

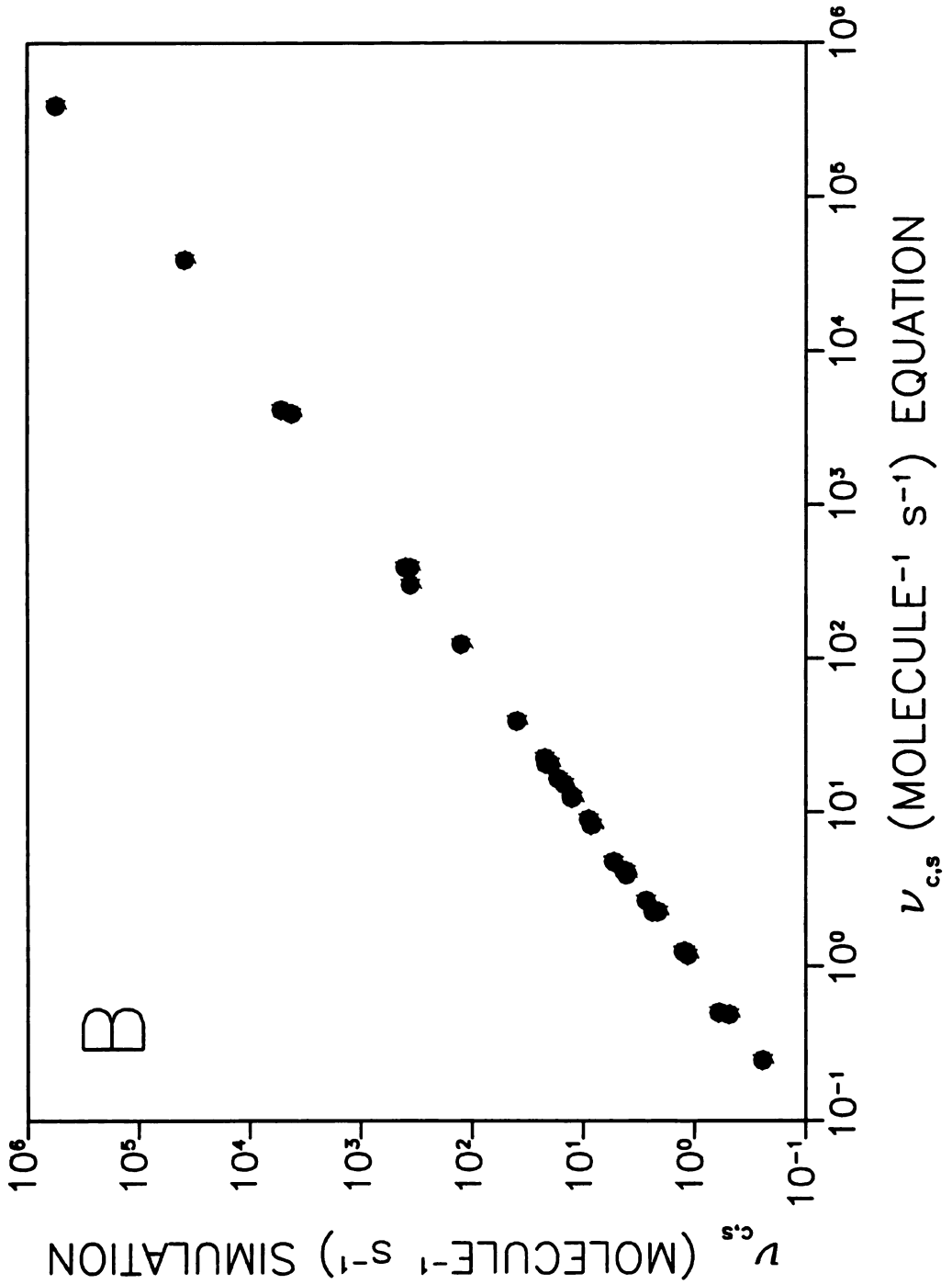

Chapter 7

Stochastic Simulation of Concurrent Reaction and Separation: The A → B Reaction

7.1 Introduction.

The most common method of producing large amounts of a product is to place the reactants in a reactor vessel and allow the reaction to proceed. Then, the desired product is separated from any reactant that is left and any by-products that have been produced. These separate unit operations of reaction and separation can be combined, and the result can be very beneficial. Reactions that are limited by low equilibrium values of product can produce more than theoretically expected as the reactants and products are separated during the reaction (Le Châtelier's principle). The combination of the two operations can also reduce the size and amount of instrumentation necessary for the two processes. One combination of these reactive separation techniques is the chromatographic reactor. Since the inception of the chromatographic reactor column in the 1960s,[1] it has been used in many different fields. It has been used to measure reaction rates and other physicochemical properties of various analytes.[2-6] It has also been used to increase the yield and selectivity of products in biological and organic synthesis reactions.[4,7-9] The recent interest has been in developing continuous systems that can be used in preparative and production scale equipment. The rotating cylindrical annulus reactor, countercurrent moving bed reactor, and simulated countercurrent moving bed reactor have resulted from the work of many investigators.[10-15]

Theoretical models of these systems have also been created so that better understanding of the underlying processes may be realized. The increase in understanding will allow investigators to develop systems with better yield, selectivity, and purity of product. It will also enable the judicious use of chromatographic reactors in areas that will most benefit from the unique capabilities of these systems. Most of the models of chromatographic reactors to date have been derived from a classical mass balance approach. Magee presented one of the first models of a batch chromatographic reactor to demonstrate the abilities of the combined processes.[16] Several models have been developed for specific types of reversible and irreversible reactions, which have been reviewed by Sardin *et al.*[17] These models invoke assumptions about the relationship between the rates of reaction and mass transfer between the fluid and surface phases. The most common models for chromatographic reactors assume that mass transfer is faster than the reaction and can be treated as if it were at equilibrium.[16,18-22] Another approach is to treat the reaction as fast and at equilibrium, while the chromatographic aspects are modeled through the mass transfer equations.[23,24] A few researchers have attempted to explore systems where neither mass transfer nor reaction are limiting.[24-28] Within these systems, axial dispersion is either assumed to be negligible or is treated by using an effective dispersion term in the mass balance equations. The mass transfer coefficient is assumed to be independent of the reaction in all of these theoretical approaches.

Recently, stochastic and random walk models have been applied to mass transfer systems with reactions.[29] The present chapter introduces a stochastic model that can be used to explore pulsed and batch chromatographic reactors.[30-32] The processes of

diffusion, convection, absorption, and reaction are applied to individual molecules as time is incremented. Treating individual molecules in this manner reduces the number of assumptions or simplifications in the model. For instance, the evolution of the system over time and distance is easily simulated by removing the steady-state assumptions of other models. Axial dispersion is easily incorporated into the model through the inclusion of all relevant mass transfer processes. Also, the mass transfer and reaction processes are not isolated from each other, since each molecule is treated individually, thereby allowing the interplay of the two processes to be investigated. This simulation can be used to study reactive separations in gas, supercritical fluid, and liquid systems, thus providing a unified approach to their study. The model will be described in detail, and the results of simulations ranging from reaction-limited to mass-transfer-limited systems will be presented.

7.2 Results and Discussion.

Using the algorithms of Chapter 2, systems with an irreversible (A→B) first-order or pseudo-first-order reaction in the surface phase are modeled. The systems consist of individual molecules that absorb (partition) between a fluid phase with a radius of 2.00×10^{-3} cm and a homogeneous surface phase with thickness of 8.2843×10^{-4} cm. The values for the fluid-phase radius and surface-phase thickness were chosen to obtain a ratio of the phase volumes equal to 1.0. The fluid-phase diffusion coefficient is 1.00×10^{-5} cm^2 s^{-1} and the surface-phase diffusion coefficient is 1.00×10^{-7} cm^2 s^{-1}. Simulations of reaction and separation are presented individually to demonstrate and validate the

performance of the simulation as well as to provide a basis for comparison to the reactive separations. Reactive separations are presented for systems that vary in rate constant (k_r), absorption coefficient ($K_{abs,A}$ for species A and $K_{abs,B}$ for species B), and fluid-phase velocity (v_0).

7.2.1 Simulation of Reactions.

To demonstrate the case of chemical reaction alone, simulations are performed in which the reaction rate constant is varied from 0.01 to 10.0 s^{-1}. The number of molecules of each species in the system is recorded as a function of time. Figure 7.1A shows the decay of species A and Figure 7.1B shows the production of species B with respect to time for the simulated rate constants. The different rates of decay and production can be easily seen in this figure. The curves can be described by a single exponential function having a characteristic time $\tau_r = 1/k_r$, where k_r is the rate constant.[33] However, to allow comparison to the more complicated reactive separation systems, the characteristic T_{10} and T_{90} times at which species A and B reach 10% and 90%, respectively, of the number of molecules present at steady state are calculated from the curves. These characteristic times, summarized in Table 7.1, show the expected order of magnitude decrease for each order of magnitude increase in the rate constant. The times measured for species A and B agree well with each other, which is another indication that the simulation is appropriately modeling the chemical reaction. The simulated T_{10} and T_{90} values exhibit ± 5.1% and ± 1.2% average relative errors, respectively, when compared to the theoretically calculated times.

Figure 7.1: Stochastic simulation of chemical reaction (A→B) alone showing the decay curves for species A (A) and the production curves for species B (B) as a function of time for the following rate constants: (○) $k_r = 0.01\ s^{-1}$, (□) $k_r = 0.1\ s^{-1}$, (△) $k_r = 1.0\ s^{-1}$, (◇) $k_r = 10.0\ s^{-1}$. Other simulation conditions as follows: $t = 1.00 \times 10^{-3}$ s, N = 10000.

Figure 7.1

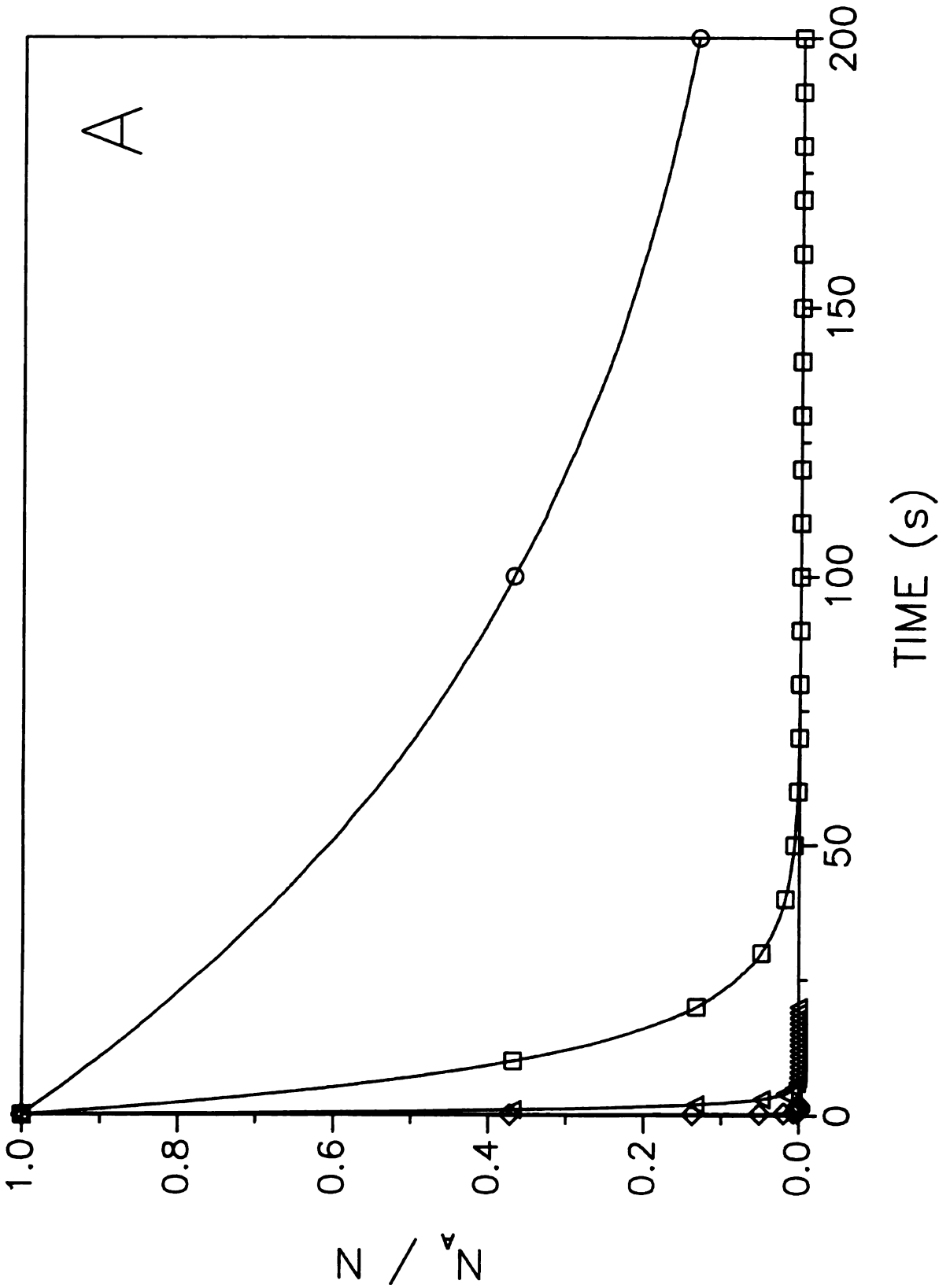

Figure 7.1 cont.

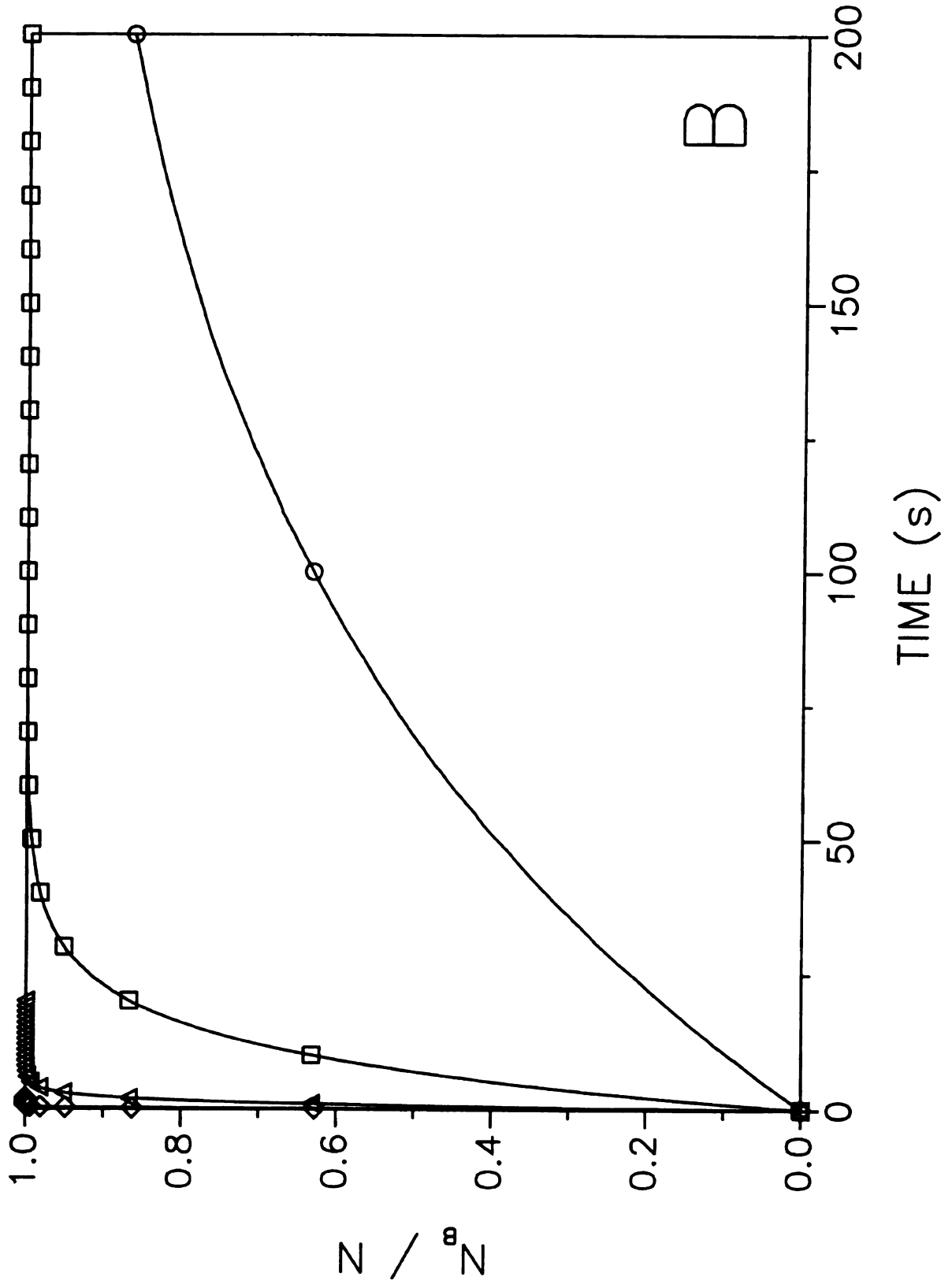

Table 7.1 Characteristic Times for Chemical Reaction Alone as a Function of the Rate Constant (k_r).[a]

	Species A		Species B		Theory	
k_r (s^{-1})	T_{10} (s)	T_{90} (s)	T_{10} (s)	T_{90} (s)	T_{10} (s)	T_{90} (s)
0.01	10.0	229	11	230	10.5	230
0.1	1.0	22.9	1.1	23.0	1.1	23.0
1.0	0.10	2.28	0.11	2.29	0.11	2.30
10.0	0.010	0.232	0.011	0.233	0.011	0.230

[a] Simulation conditions given in Figure 7.1.

7.2.2 Simulation of Separations.

To illustrate the case of separation alone, simulations are performed with absorption coefficients varying from 0.1 to 5.0. Since the three-dimensional position of each molecule is known, the phase in which it resides can easily be ascertained at any time during the simulation. The data shown in Figure 7.2 are obtained by counting the number of molecules present in the fluid phase as a function of time. The steady-state number of molecules in the fluid phase as well as the rate at which the steady state is established are seen to be dependent on the absorption coefficient. The curves in Figure 7.2 can be described by a single exponential function with a characteristic time $\tau_m = 1/(k_{fs} + k_{sf})$, where k_{fs} is the rate constant for mass transfer from the fluid to surface phase and k_{sf} is the rate constant for mass transfer from the surface to fluid phase.[34] Again, characteristic T_{10} and T_{90} times for the system to reach 10% and 90%, respectively, of the steady-state distribution were calculated from the curves in Figure 7.2 for comparison to the more complex reactive separation systems. The characteristic times in Table 7.2 show that the rate at which molecules enter the surface phase increases as the absorption coefficient increases. The rate of transfer into the surface phase has been found to be

Figure 7.2: Stochastic simulation of separation alone showing the fraction of molecules in the fluid phase as a function of time for the following absorption coefficients: (○) $K_{abs} = 0.1$, (□) $K_{abs} = 0.2$, (△) $K_{abs} = 0.5$, (◇) $K_{abs} = 1.0$, (●) $K_{abs} = 2.0$, (■) $K_{abs} = 5.0$. Other simulation conditions as follows: $t = 1.00\times10^{-3}$ s, $N = 10000$, $R_f = 2.00\times10^{-3}$ cm, $R_s = 8.2843\times10^{-4}$ cm, $D_f = 1.00\times10^{-5}$ cm^2 s^{-1}, $D_s = 1.00\times10^{-7}$ cm^2 s^{-1}.

Figure 7.2

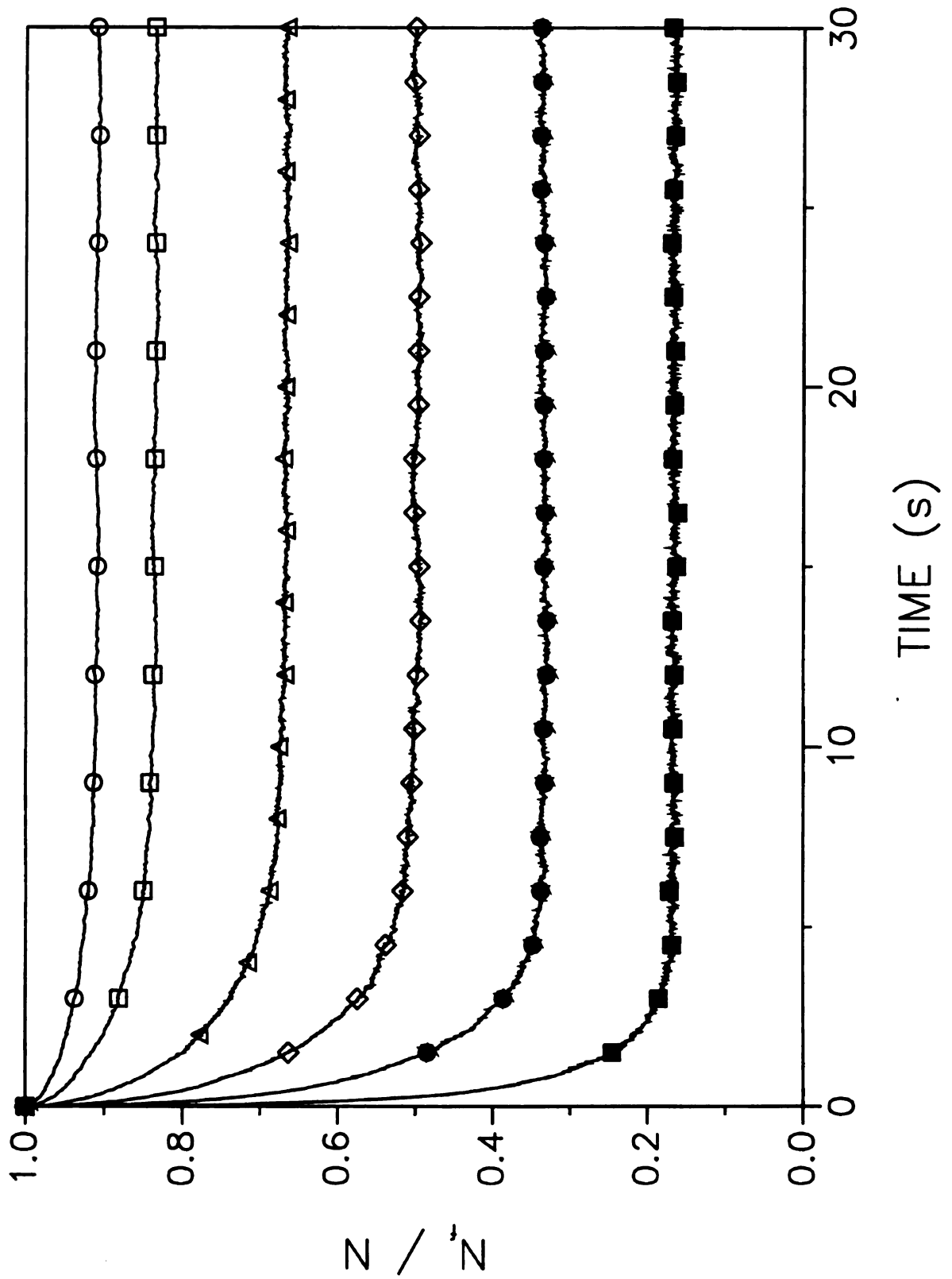

proportional to the ratio $K_{abs}/(1 + K_{abs})$.[35] The characteristic times for mass transfer in these systems are comparable to those for chemical reactions that have rate constants in the range of 1.0 to 10.0 s^{-1}, as is evident by comparison of Tables 7.1 and 7.2.

Table 7.2 Characteristic Times and Steady-State Distributions for Separation Alone as a Function of the Absorption Coefficient (K_{abs}).[a]

K_{abs}	T_{10} (s)	T_{90} (s)	$\tilde{N}_s/\tilde{N}_f$
0.1	0.08	6.54	0.10
0.2	0.07	6.09	0.20
0.5	0.05	4.92	0.50
1.0	0.03	3.75	0.99
2.0	0.02	2.63	1.97
5.0	0.012	1.42	5.08

[a] Simulation conditions given in Figure 7.2.

In addition, the steady-state distribution of molecules between the two phases is obtained. The data are presented in Table 7.2 as the ratio of the average number of molecules in the surface and fluid phases at steady state ($\tilde{N}_s/\tilde{N}_f$). This ratio defines the capacity factor (k') in chromatography, which is equal to the absorption coefficient (K_{abs}) multiplied by the ratio of the volumes of the surface phase (V_s) and fluid phase (V_f)

$$k' \equiv \frac{\tilde{N}_s}{\tilde{N}_f} = K_{abs}\left(\frac{V_s}{V_f}\right) = K_{abs}\left(\frac{R_s^2 + 2R_f R_s}{R_f^2}\right) \qquad [7.1]$$

where R_f is the radius of the fluid phase and R_s is the thickness of the surface phase. The radii used in these simulations were chosen such that the ratio of the volumes of the two phases is equal to unity, thus the ratio $\tilde{N}_s/\tilde{N}_f$ is equal to the absorption coefficient. The values determined from the simulation, summarized in Table 7.2, show good agreement with the expected values to within ±1.6% average relative error.

The effects of the rate of mass transfer are also investigated under dynamic conditions. To study these effects, an average laminar velocity of 0.1 cm s^{-1} is imposed on the fluid phase. The time at which each molecule elutes is recorded for column lengths of 0.01, 0.1, 0.2, 0.5, 1.0, 2.0, and 5.0 cm. The recorded times for a column of 1.0 cm length are used to create the zone profiles shown in Figure 7.3 as the absorption coefficient is varied from 0.1 to 5.0. The maxima of the zone profiles tend toward longer times as the absorption coefficient increases. The profiles also diminish in height and increase in width as the absorption coefficient increases. It is noticeable that the profiles show varying degrees of asymmetry. The most asymmetric zones are observed for the systems with the smallest absorption coefficients.

The changes in the shape of the zone profiles are quantified through the statistical moments in Figure 7.4. Figure 7.4A shows the first moment or mean elution time as a function of the absorption coefficient. Two items of interest can be seen. First, the first moments for all systems appear to increase linearly with distance. The slope of the first moments on the logarithmic graph is unity, suggesting that the average movement of the zone through the column is at steady state. Second, the solute zones with smaller absorption coefficients elute sooner than those with larger absorption coefficients. This occurs because molecules with smaller absorption coefficients spend more time in the fluid phase and less time in the surface phase. The average elution time at steady state is given by $L\,(1+k')/v_0$, where L is the column length, v_0 is the linear velocity, and k' is the capacity factor. The average elution time (first moment) is directly related to the capacity factor, which is also directly related to the absorption coefficient according to Equation [7.1].

Figure 7.3: Zone profiles for separation systems with absorption coefficients of 0.1, 0.2, 0.5, 1.0, 2.0, and 5.0 (left to right). Other simulation conditions as follows: $t = 5.00\times10^{-5}$ s, N = 2000, $R_f = 2.00\times10^{-3}$ cm, $R_s = 8.2843\times10^{-4}$ cm, L = 1.0 cm, $D_f = 1.00\times10^{-5}$ cm^2 s^{-1}, $D_s = 1.00\times10^{-7}$ cm^2 s^{-1}, $v_0 = 0.1$ cm s^{-1}.

Figure 7.3

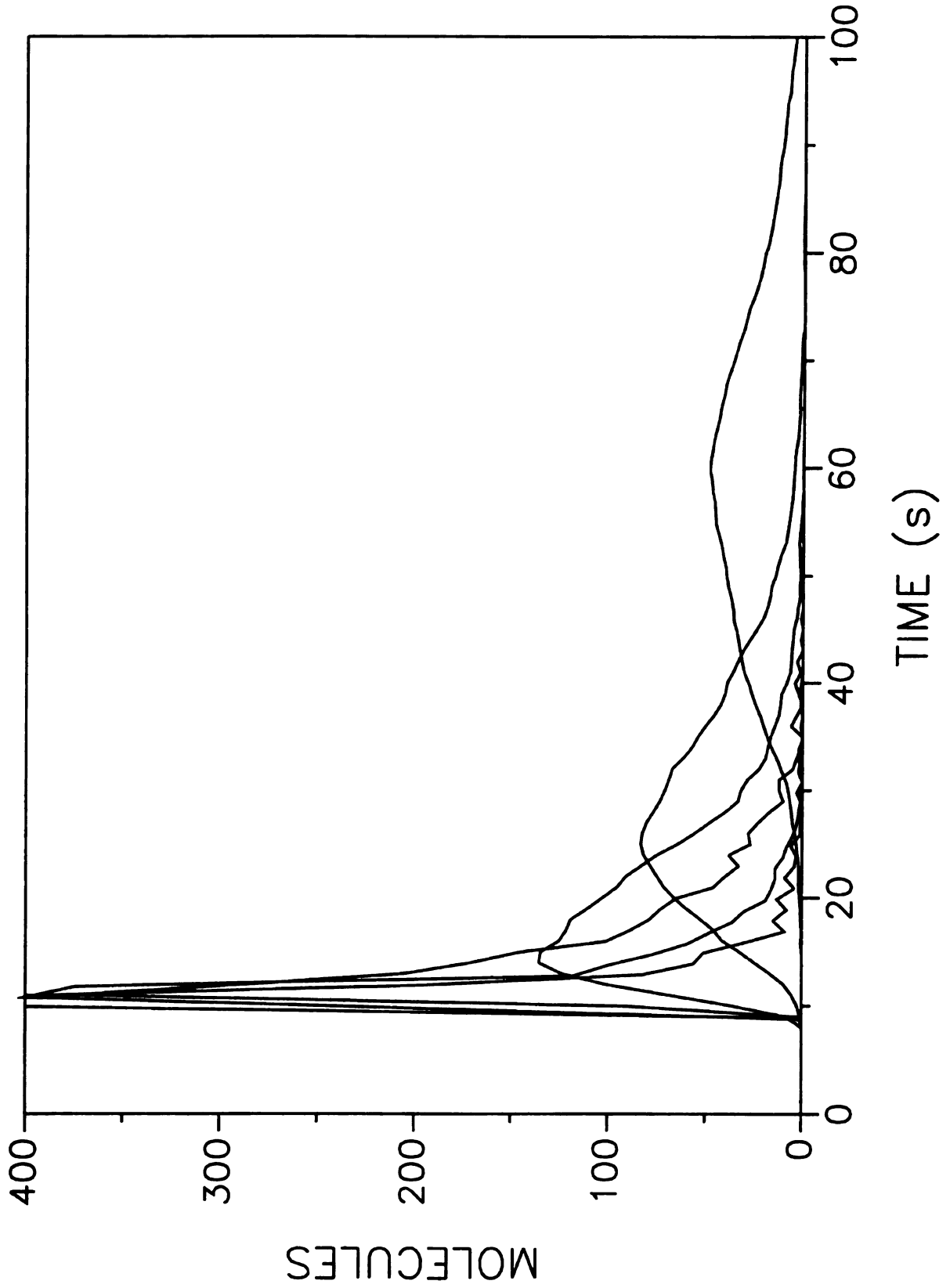

Figure 7.4: First (A), second (B), and third (C) statistical moments as a function of distance for separation systems with the following absorption coefficients: (○) K_{abs} = 0.1, (□) K_{abs} = 0.2, (△) K_{abs} = 0.5, (◇) K_{abs} = 1.0, (●) K_{abs} = 2.0, (■) K_{abs} = 5.0. Other simulation conditions as given in Figure 7.3.

Figure 7.4

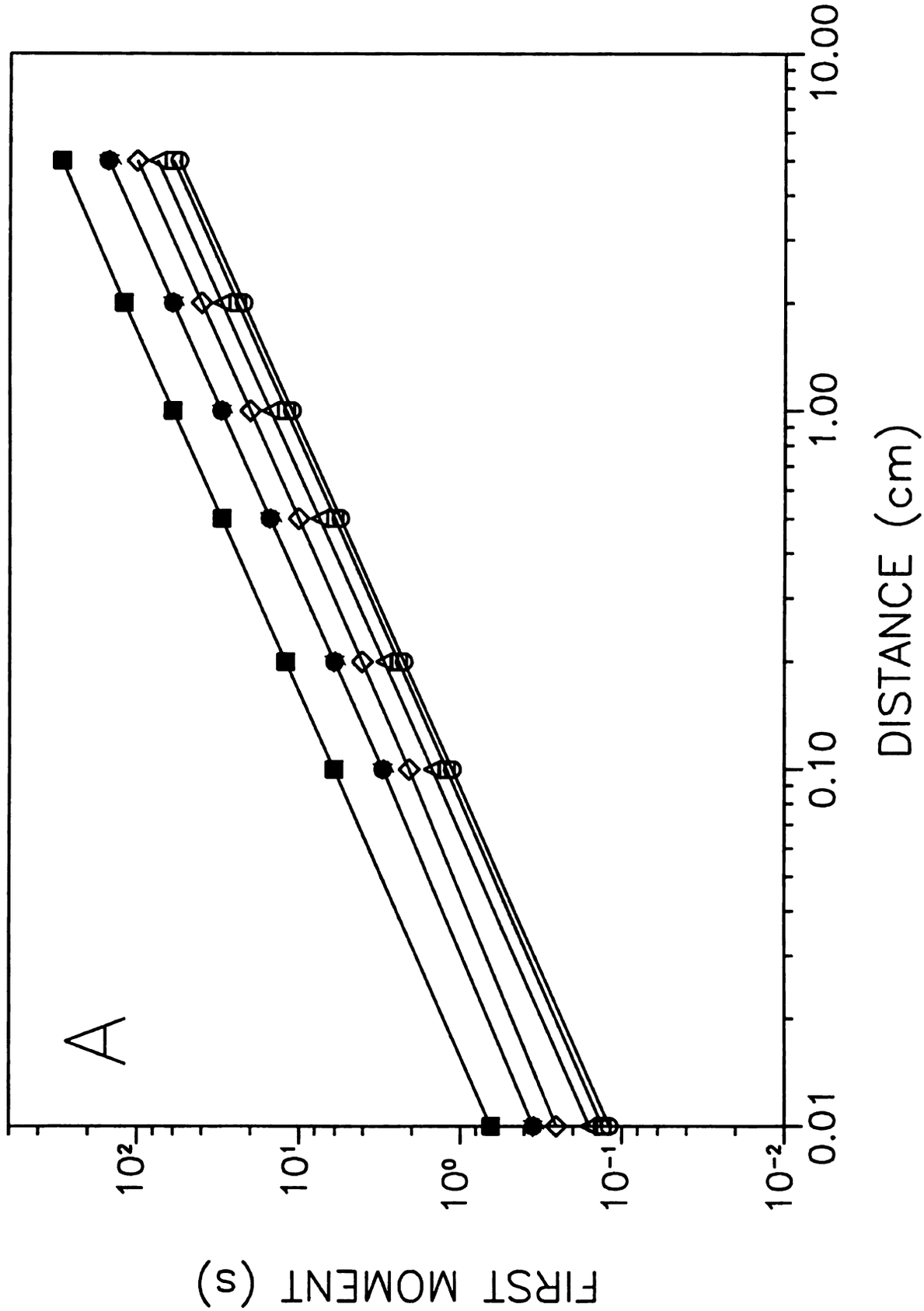
A
FIRST MOMENT (s)
10^{2}
10^{1}
10^{0}
10^{-1}
10^{-2}
0.01
0.10
1.00
10.00
DISTANCE (cm)

Figure 7.4 cont.

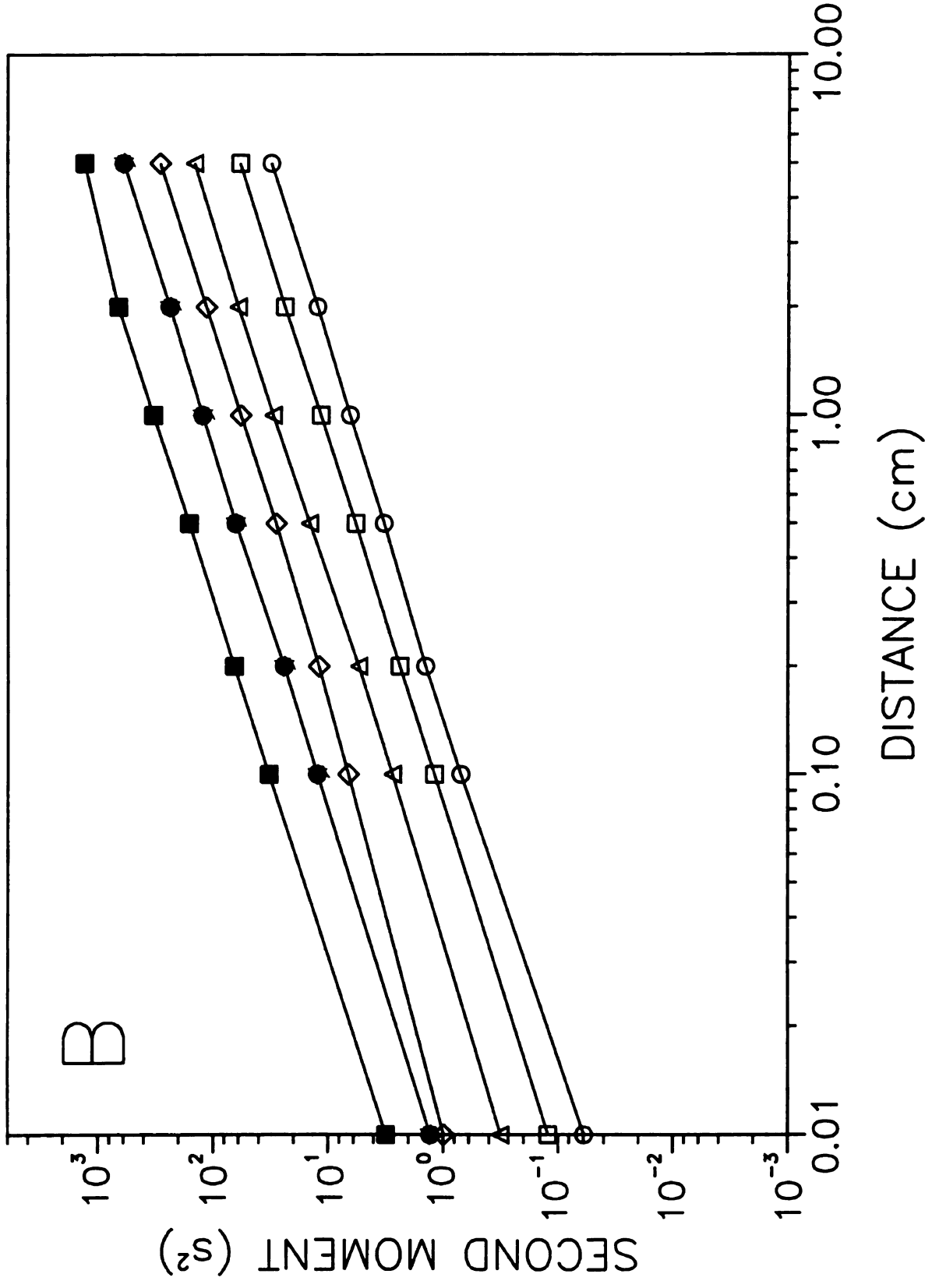

Figure 7.4 cont.

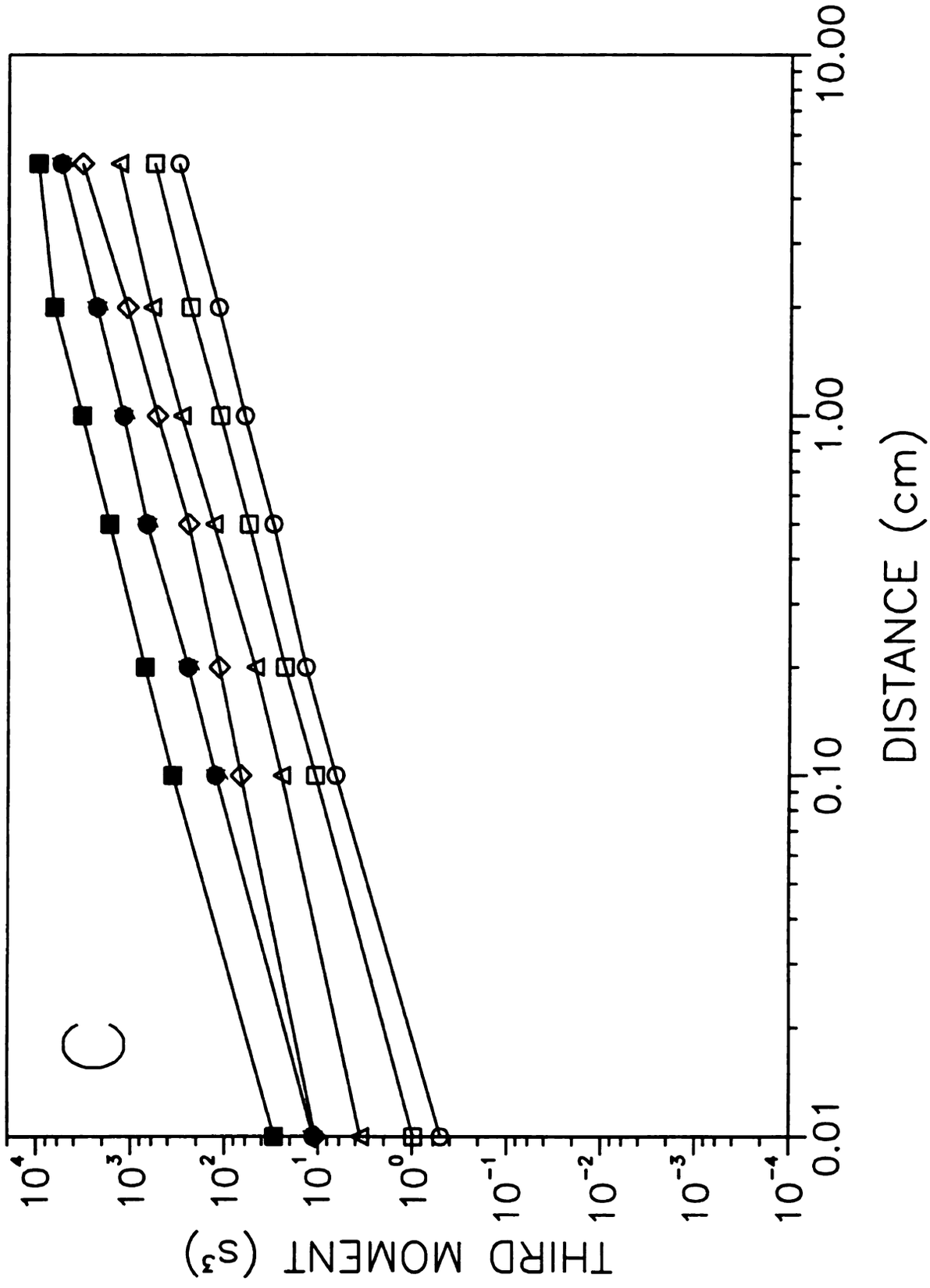

The second moment or variance of the zones is shown in Figure 7.4B. These plots are also linear with distance, indicating that the variance of the zones has also achieved steady state. The second moment also increases as the absorption coefficient increases. This change in shape is dependent on the length of time that the molecules remain on column and the rate of the mass transfer processes. Longer time on column and slower rate of mass transfer cause an increase in broadening. Both of these observations agree with chromatographic theory,[36] where the variance in time units is given by

$$\sigma_t^2 = \frac{(2D_f + 2D_s k')(1+k')^2 L}{v_0^3} + \frac{(1+6k'+11k'^2)R_f^2 L}{24 v_0 D_f} + \frac{2k' R_s^2 L}{3 v_0 D_s} \qquad [7.2]$$

where the first term arises from diffusion in the fluid and surface phases, the second term from mass transfer in the fluid phase, and the third term from mass transfer in the surface phase.

The third moment, which is related to the asymmetry, is shown in Figure 7.4C. The third moments exhibit the same trend as the second moments in that they increase with the absorption coefficient. However the skewness, which is expressed as the ratio of $M_3/M_2^{3/2}$, decreases. Hence, the zones with greatest skewness are observed for the smallest absorption coefficients, which have the slowest mass transfer rates according to Table 7.2.

7.2.3 Simulation of Reactive Separations.

A reactive separation system was simulated by combining the simple first-order A→B reaction and mass transfer processes already discussed. The systems used to study the interplay of the two processes initially contained all molecules in the fluid phase as species A. Changes in the rates of decay of species A, production of species B, and axial distributions of both species are presented for variations in the rate constant (k_r), the absorption coefficient ($K_{abs,A}$ and $K_{abs,B}$), and the velocity (v_0) of the fluid phase.

7.2.3.1 Effect of Changes in Reaction Rate Constant.

The kinetic behavior of reactive separation systems is investigated for rate constants from 0.01 to 10.0 s^{-1}. The absorption coefficient is 1.0 for both species A and B. Curves following the decay of species A and the production of species B in the fluid phase can be seen in Figures 7.5A and 7.5B, respectively. It is obvious that these curves are not single exponential functions like the cases of reaction alone (Figure 7.1) and separation alone (Figure 7.2). From the curves in Figure 7.5, the kinetic behavior and the equilibrium distribution between the phases are determined and the results are summarized in Table 7.3. These data represent the limiting cases as well as those that fall in between. For example, the system with rate constant of 0.01 s^{-1} is reaction-rate limited. The curve for species A (Figure 7.5A) shows a distinct change in the rate of decay at the time when this system reaches the expected steady-state fraction of molecules in the fluid phase for a system with separation alone (i.e. $\tilde{N}_{f,A}/N = 0.5$). The rate of decay before this point is mainly due to mass transfer between the phases, whereas

Figure 7.5: Stochastic simulation of reactive separations showing the decay curves for species A (A) and the production curves for species B (B) in the fluid phase for the following rate constants: (○) $k_r = 0.01\ s^{-1}$, (□) $k_r = 0.1\ s^{-1}$, (△) $k_r = 1.0\ s^{-1}$, (◇) $k_r = 10.0\ s^{-1}$. Other simulation conditions as follows: $t = 1.00\times10^{-3}$ s, N = 10000, $R_f = 2.00\times10^{-3}$ cm, $R_s = 8.2843\times10^{-4}$ cm, $D_f = 1.00\times10^{-5}\ cm^2\ s^{-1}$, $D_s = 1.00\times10^{-7}\ cm^2\ s^{-1}$, $K_{abs,A} = K_{abs,B} = 1.00$.

Figure 7.5

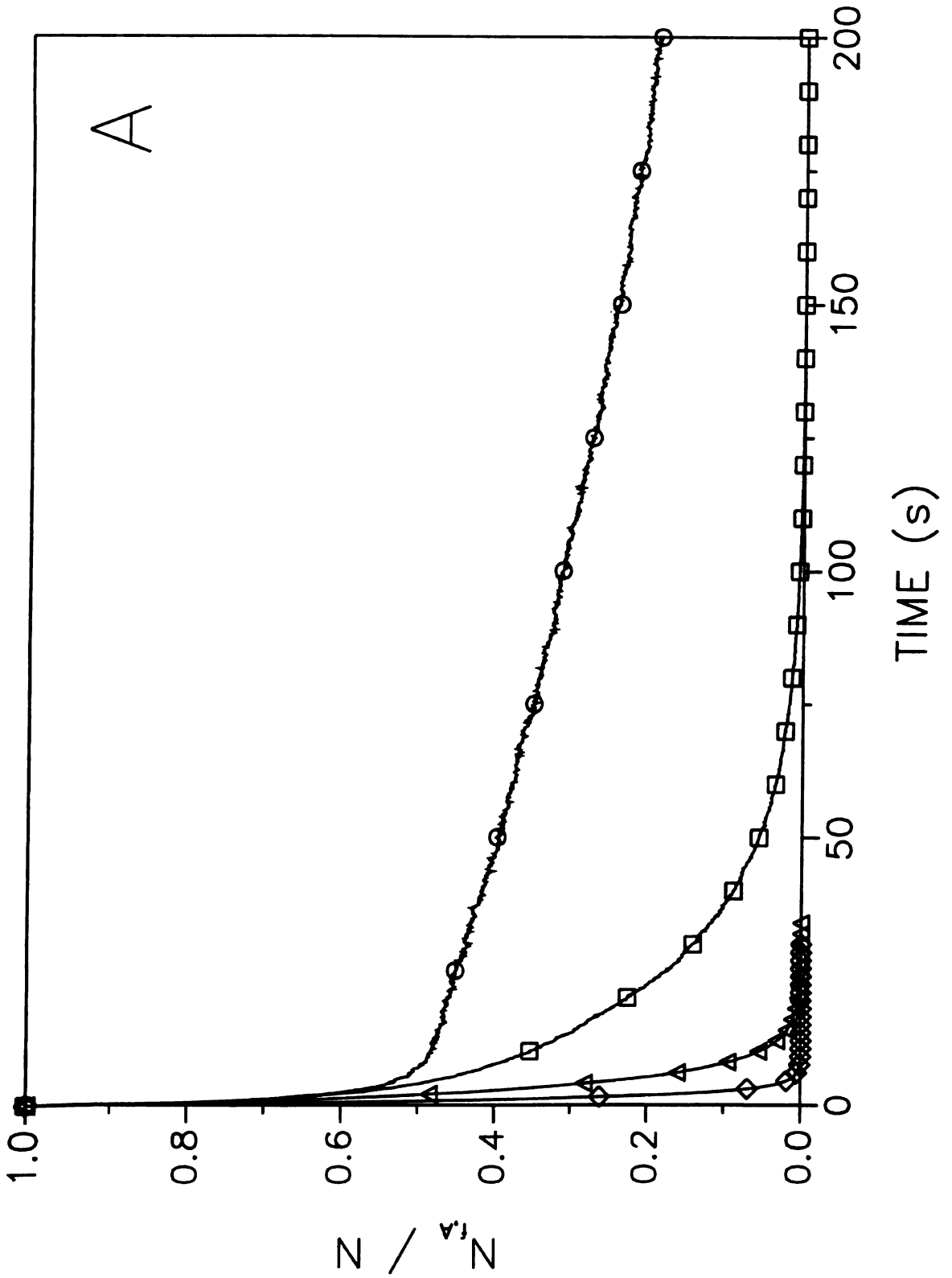

Figure 7.5 cont.

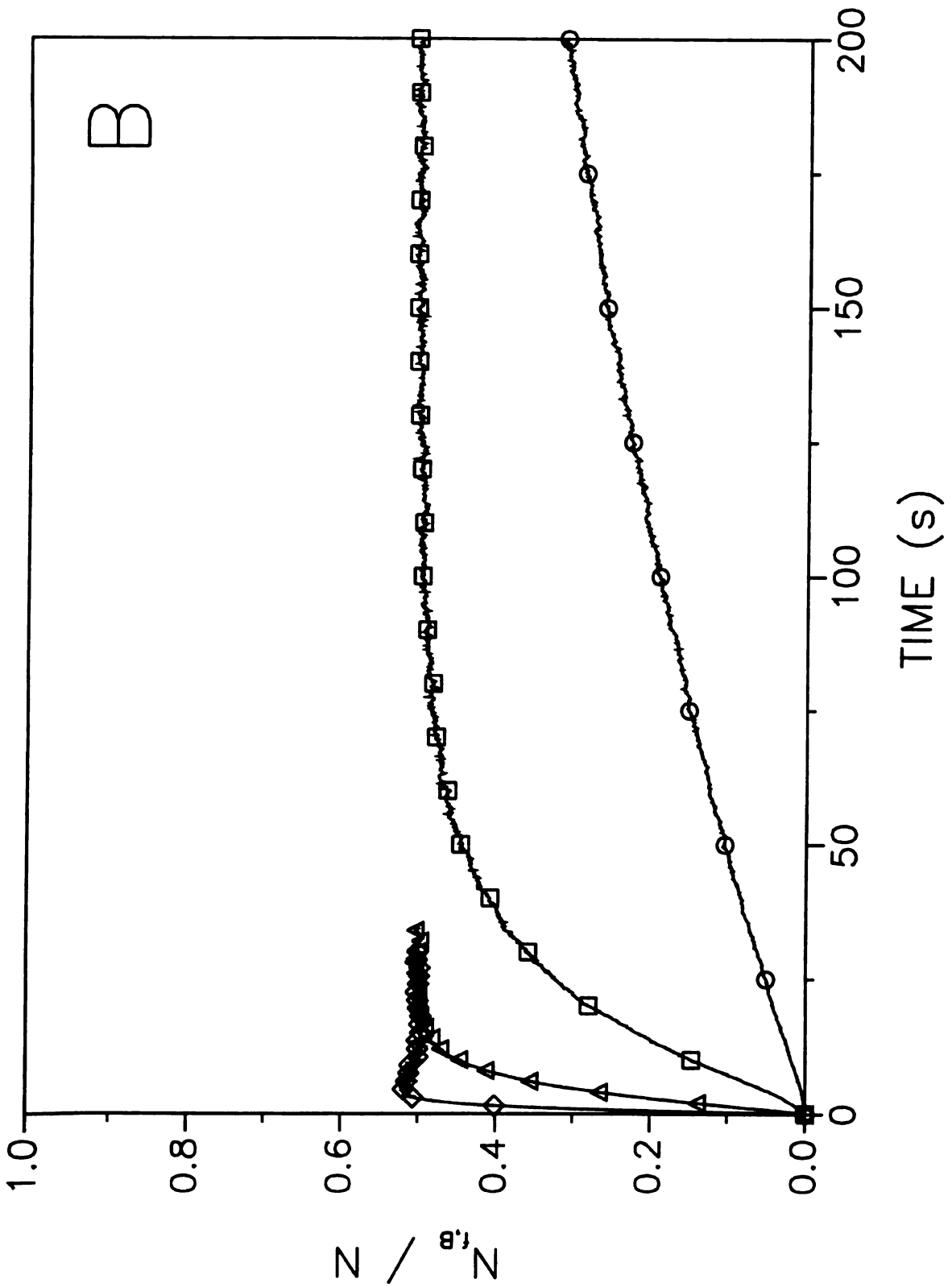

the rate of decay after this point is mainly due to reaction kinetics.

Table 7.3 Characteristic Times and Steady-State Distributions for Reactive Separations as a Function of Rate Constant (k_r).[a]

	Species A			Species B		
k_r (s^{-1})	T_{10} (s)	T_{90} (s)	$\tilde{N}_{A,s}/\tilde{N}_{A,f}$	T_{10} (s)	T_{90} (s)	$\tilde{N}_{B,s}/\tilde{N}_{B,f}$
0.01	0.121	329	–	22.0	463	1.000
0.1	0.115	37.3	–	4.40	52.4	0.995
1.0	0.105	7.10	–	1.00	10.4	0.995
10.0	0.079	2.55	–	0.15	1.85	0.993

[a] Simulation conditions given in Figure 7.5.

The data for species A presented in Table 7.3 also confirm these differences between the short- and long-time behavior for a rate constant of 0.01 s^{-1}. The characteristic T_{10} time is comparable to that shown in Table 7.2 for separation alone. However, the characteristic T_{90} time is more similar to that shown in Table 7.1 for reaction alone with a rate constant of 0.01 s^{-1}. These data support the conclusion that the decay curve shows two regions, one that is related to mass transfer and one that is related to reaction kinetics. The system with rate constant of 10.0 s^{-1} represents the other limiting case. The reaction depletes the A molecules as rapidly as they enter the surface phase and, thus, the system is limited by mass transfer. This is confirmed by the data presented in Table 7.3. The characteristic T_{10} and T_{90} times for species A are comparable to those shown in Table 7.2 for separation alone. The intermediate rate constants of 0.1 and 1.0 s^{-1} represent systems that are between the limiting cases. The characteristic T_{10} times for species A are shorter than those for reaction alone, but longer than those for separation alone. The T_{90} times for species A are longer than those for either reaction alone or separation alone. This is

believed to result from coupling of the mass transfer and reaction rates. The general trends in Table 7.3 indicate that an increase in rate constant reduces the T_{90} time. The T_{10} time shows much less dependence on the rate constant. This occurs because mass transfer is the dominant process at short times and, hence, the reaction rate has little ability to influence the initial response of the system.

The production curves for species B are shown in Figure 7.5B for each of the reaction rates. All the systems exhibit curves that asymptotically approach the expected steady-state values for the systems with separation alone ($\tilde{N}_{f,B}/N = \tilde{N}_{s,B}/N = 0.5$). An interesting phenomenon occurs at approximately 5 – 10 s for the system with rate constant of 10.0 s^{-1}. The curve shows that slightly more B molecules are present in the fluid phase than at equilibrium. This phenomenon arises because species B is formed faster than the system can equilibrate due to the mass-transfer-limited conditions. The characteristic times for the production of species B are also summarized in Table 7.3. Both T_{10} and T_{90} times show a definite decrease as the rate constant increases. This trend suggests that kinetics play a more significant role in the overall appearance of species B both at short and long times. This is different from the trend shown for species A. The reason for this difference is that the reaction cannot occur until species A has interacted with the surface phase, which is controlled solely by the mass transfer rate of the system. Once species A has crossed the interface between the fluid and surface phases, the reaction rate controls the system dynamics for both species, as exhibited by the trend in the T_{90} times. The production of species B is dominated by the reaction rate at early times because the reaction is the only source of B in the system. As the rate constant

increases, species B becomes less dependent on the reaction rate and more dependent on the mass transfer rate. The larger the rate constant, the smaller the difference between the characteristic times of the two species. As shown in Table 7.3, the largest rate constant results in T_{10} and T_{90} times similar to those for mass transfer alone (Table 7.2) for both species A and B.

The long-time or steady-state behavior of these systems is also determined from the decay curves in Figure 7.5. Since species A disappears from the systems at the long-time limit, the phase distribution is not calculable. For species B, the phase distribution is presented in Table 7.3 as the ratio of the steady-state number of molecules in the surface and fluid phases. The calculated ratio agrees with the capacity factor ($k' = 1.0$), as defined in Equation [7.1]. This ratio shows that these systems are equivalent at steady state. The reaction and mass transfer aspects of the system have no effect because all of species A is converted to species B, and the mass transfer between the phases for species B has reached equilibrium.

The fluid dynamic behavior of these systems is then simulated with laminar flow at an average linear velocity of 0.1 cm s^{-1}. The resulting zone profiles in the time domain are shown in Figures 7.6A and 7.6B for species A and B, respectively, for a column length of 1.0 cm. Only three zone profiles are shown in Figure 7.6A because the system with a rate constant of 10.0 s^{-1} does not have any A molecules remaining by the time the zone reaches 1.0 cm. The profiles decrease in area, mean elution time, and width as the reaction rate increases. It is noteworthy that all of these profiles share a common rising edge. The zone profiles for species B, shown in Figure 7.6B, exhibit a different trend.

Figure 7.6: Zone profiles for species A (A) and species B (B) in reactive separation systems with rate constants of 0.01, 0.1, 1.0, and 10.0 s^{-1} (right to left). Other simulation conditions as follows: $t = 5.00\times10^{-5}$ s, N = 2000, $R_f = 2.00\times10^{-3}$ cm, $R_s = 8.2843\times10^{-4}$ cm, L = 1.0 cm, $D_f = 1.00\times10^{-5}$ cm^2 s^{-1}, $D_s = 1.00\times10^{-7}$ cm^2 s^{-1}, $K_{abs,A} = 1.00$, $K_{abs,B} = 1.00$, $v_0 = 0.1$ cm s^{-1}.

Figure 7.6

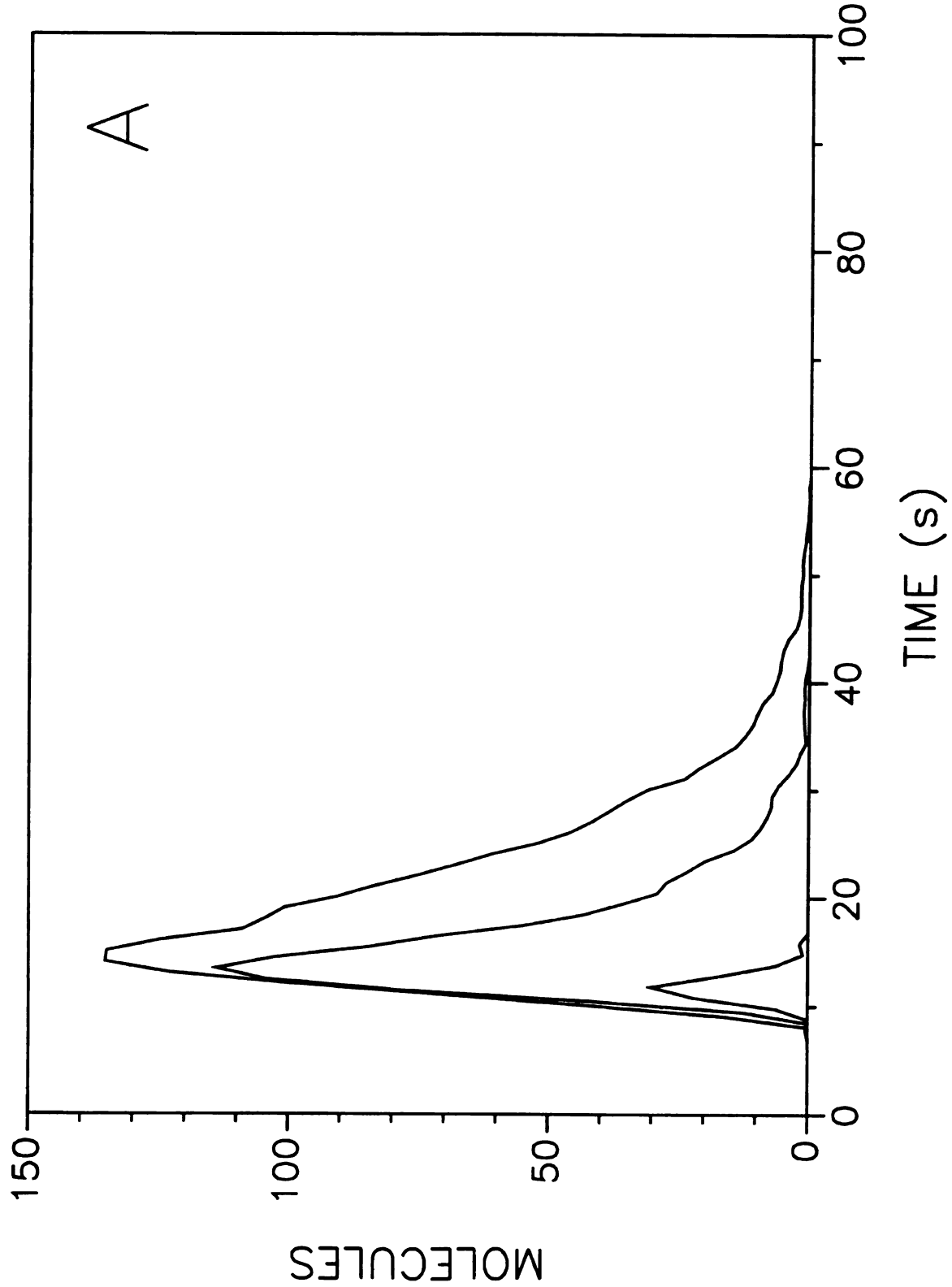

Figure 7.6 cont.

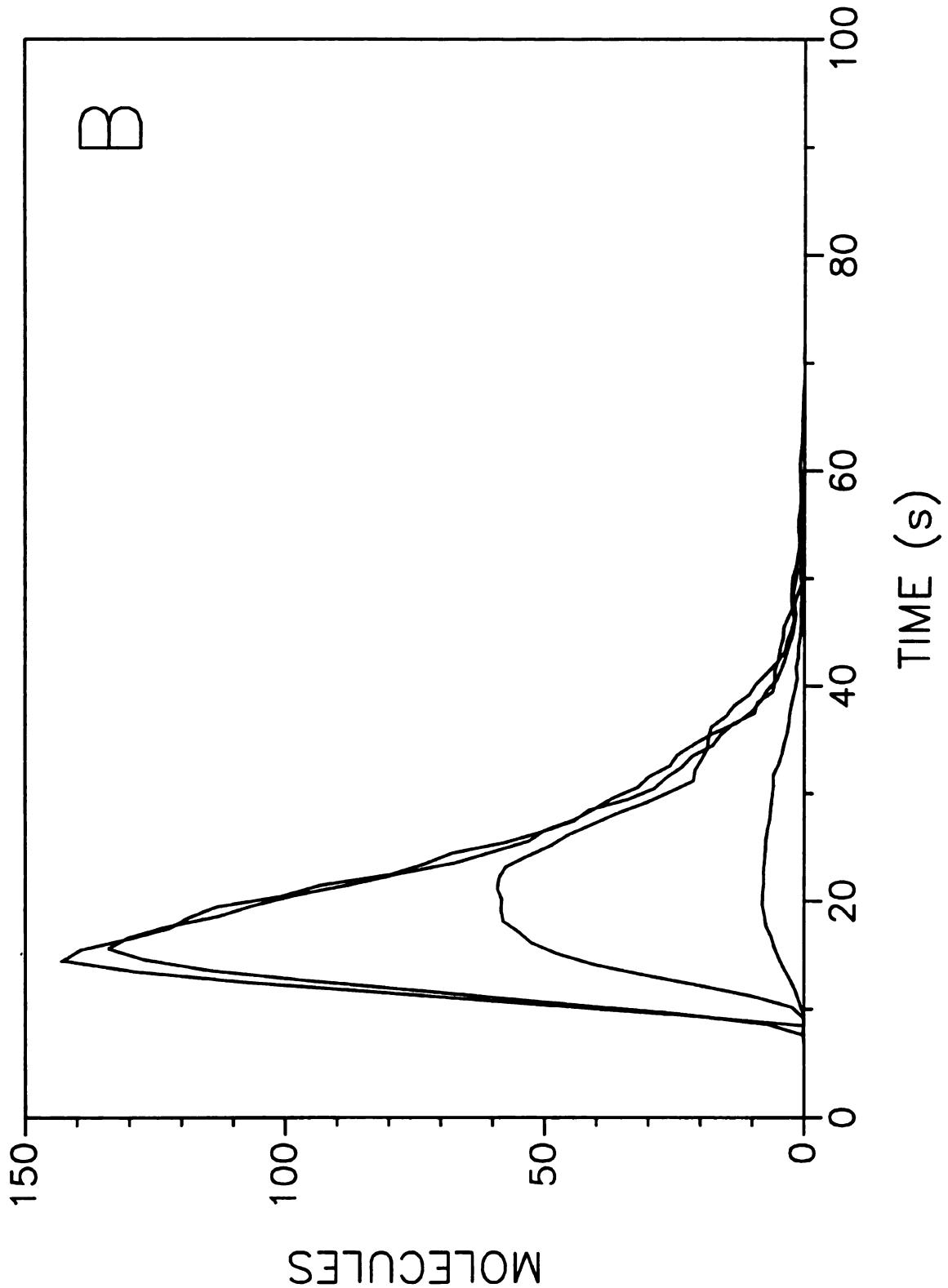

The area increases, whereas the mean elution time and width decrease as the rate constant increases. These zone profiles appear to share a common falling edge. To understand the observed trends in the zone profiles, consider the zone profile for the system with separation alone (Figure 7.3). Molecules that elute in the early portion of the zone profile (i.e., before the mean) have spent more time in the fluid phase, whereas those that elute in the later portion have spent more time in the surface phase. Because the reaction occurs in the surface phase, molecules that have spent more time in the surface phase are more likely to react. Thus, species A is gradually depleted from the later portion of the zone, leading to progressively shorter elution time and narrower zones as the reaction rate increases. This explains why there is a common leading edge in the zones for species A. Species B will exhibit zones that decrease in elution time and increase in width, since the later portion of the zone is produced first. This explains the common edge in the later part of the zones for species B.

The statistical moments are calculated for species A and B to quantitate the phenomena observed in the zone profiles and are shown in Figures 7.7 and 7.8, respectively. The curves shown in Figure 7.7A represent the first moment or mean elution time. All the systems show a linear trend with distance, implying that the mean elution time for species A has reached steady state for all values of the rate constant. However, the first moments also show that the reactive separation systems do not behave the same as systems with separation alone (Figure 7.4A). As the only parameter changing is the rate constant, these systems would be expected to have the same first moment if the reaction and separation processes were independent. However, the first moments appear

Figure 7.7: First (A), second (B), and third (C) statistical moments as a function of distance for species A in reactive separations with the following rate constants: (○) k_r = 0.01 s^{-1}, (□) k_r = 0.1 s^{-1}, (△) k_r = 1.0 s^{-1}, (◇) k_r = 10.0 s^{-1}. Other simulation conditions as given in Figure 7.6.

Figure 7.7

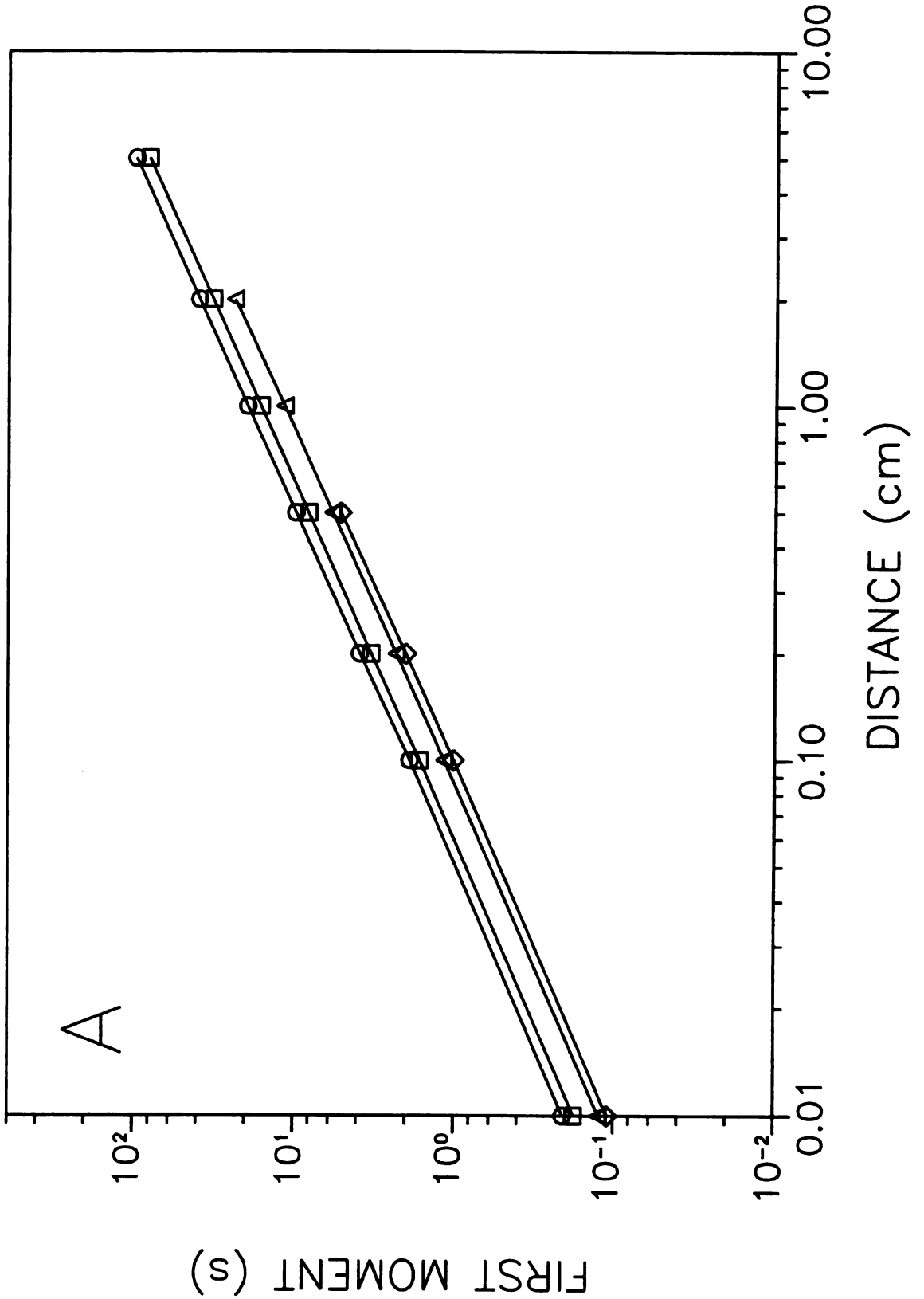
A
FIRST MOMENT (s)
10^{2}
10^{1}
10^{0}
10^{-1}
10^{-2}
0.01
0.10
1.00
10.00
DISTANCE (cm)

Figure 7.7 cont.

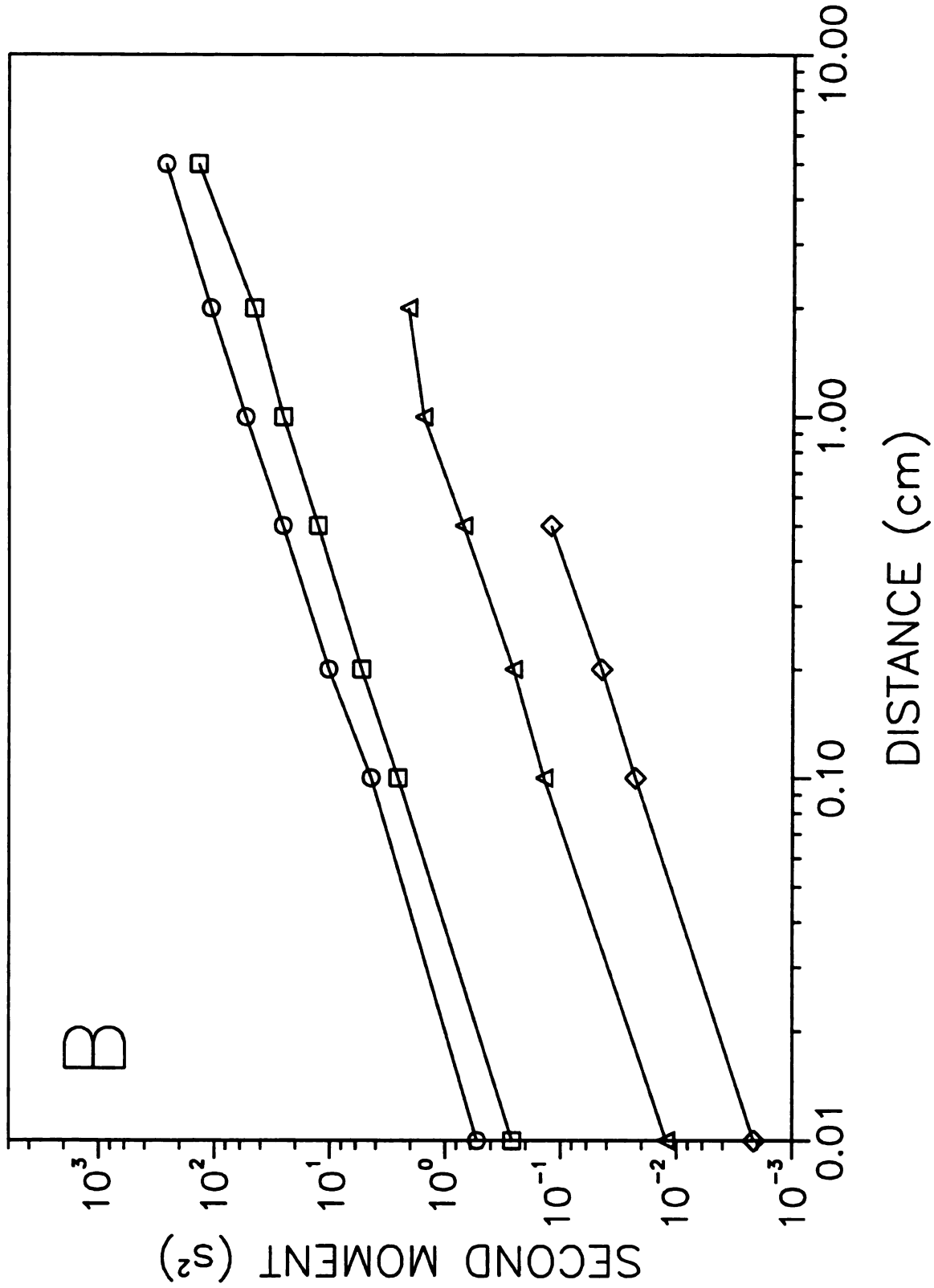

Figure 7.7 cont.

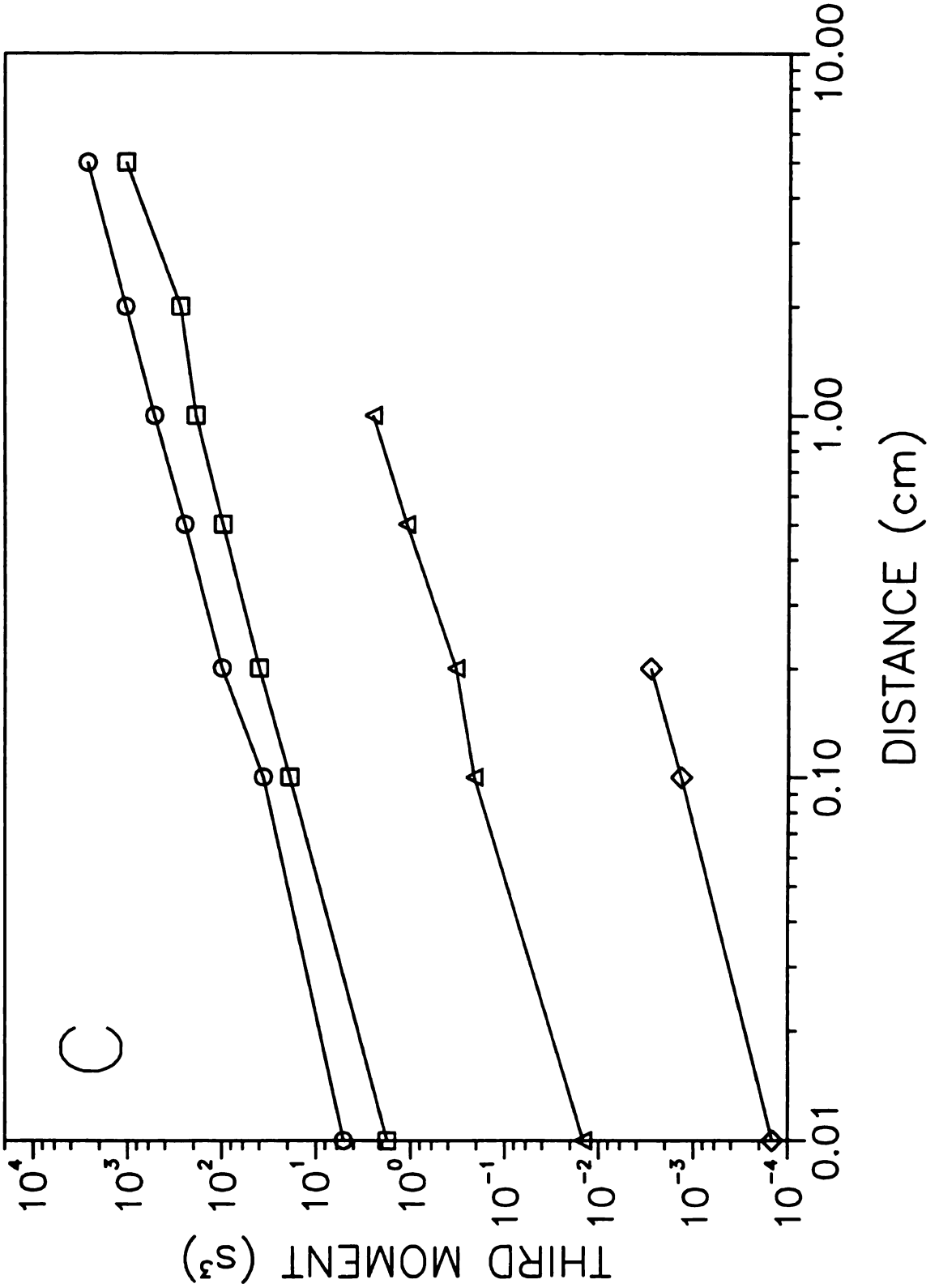

Figure 7.8: First (A), second (B), and third (C) statistical moments as a function of distance for species B in reactive separations with the following rate constants: (○) k_r = 0.01 s^{-1}, (□) k_r = 0.1 s^{-1}, (△) k_r = 1.0 s^{-1}, (◇) k_r = 10.0 s^{-1}. Other simulation conditions as given in Figure 7.6.

Figure 7.8

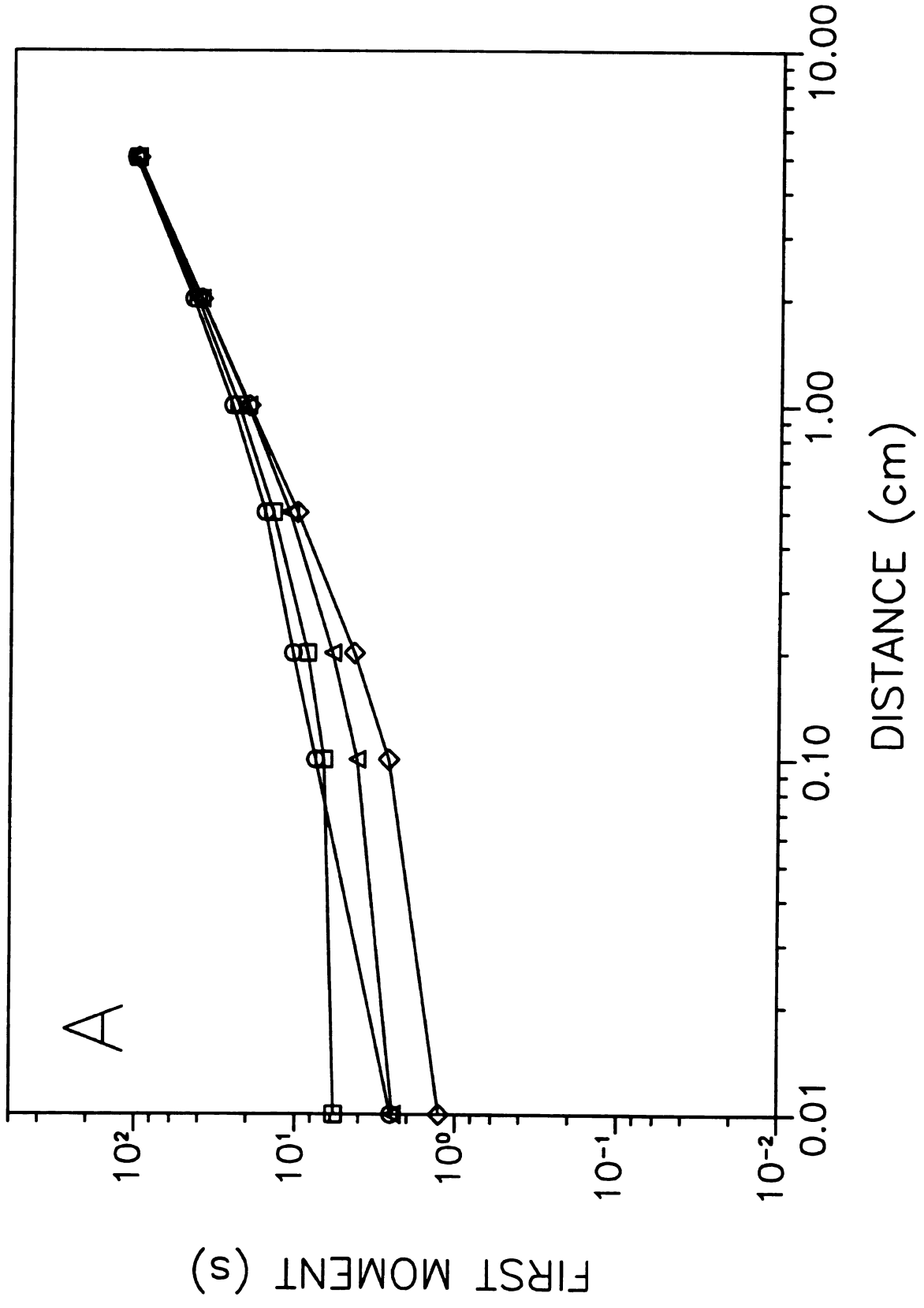
A
FIRST MOMENT (s)
10^{2}
10^{1}
10^{0}
10^{-1}
10^{-2}
0.01
0.10
1.00
10.00
DISTANCE (cm)

Figure 7.8 cont.

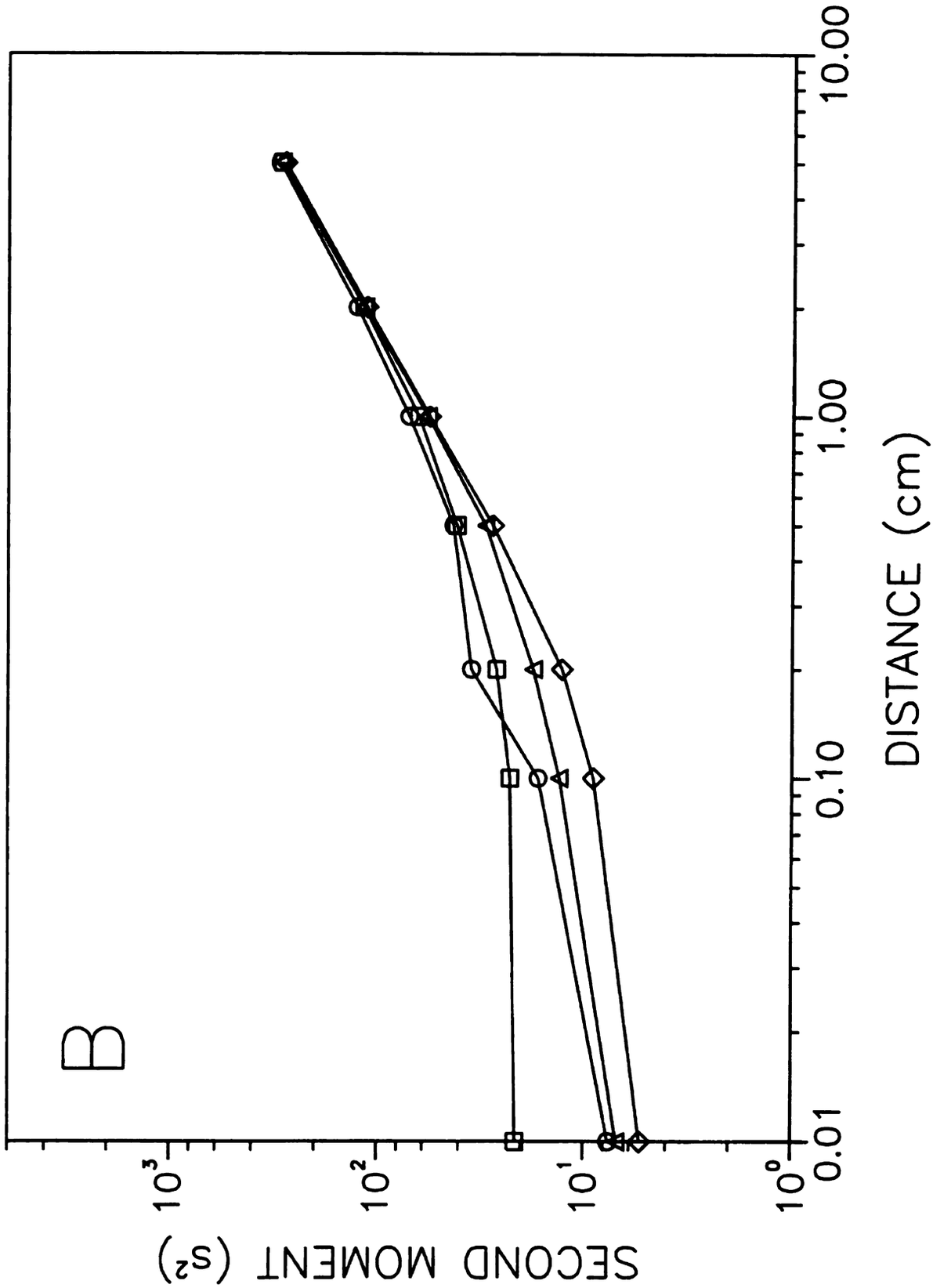

Figure 7.8 cont.

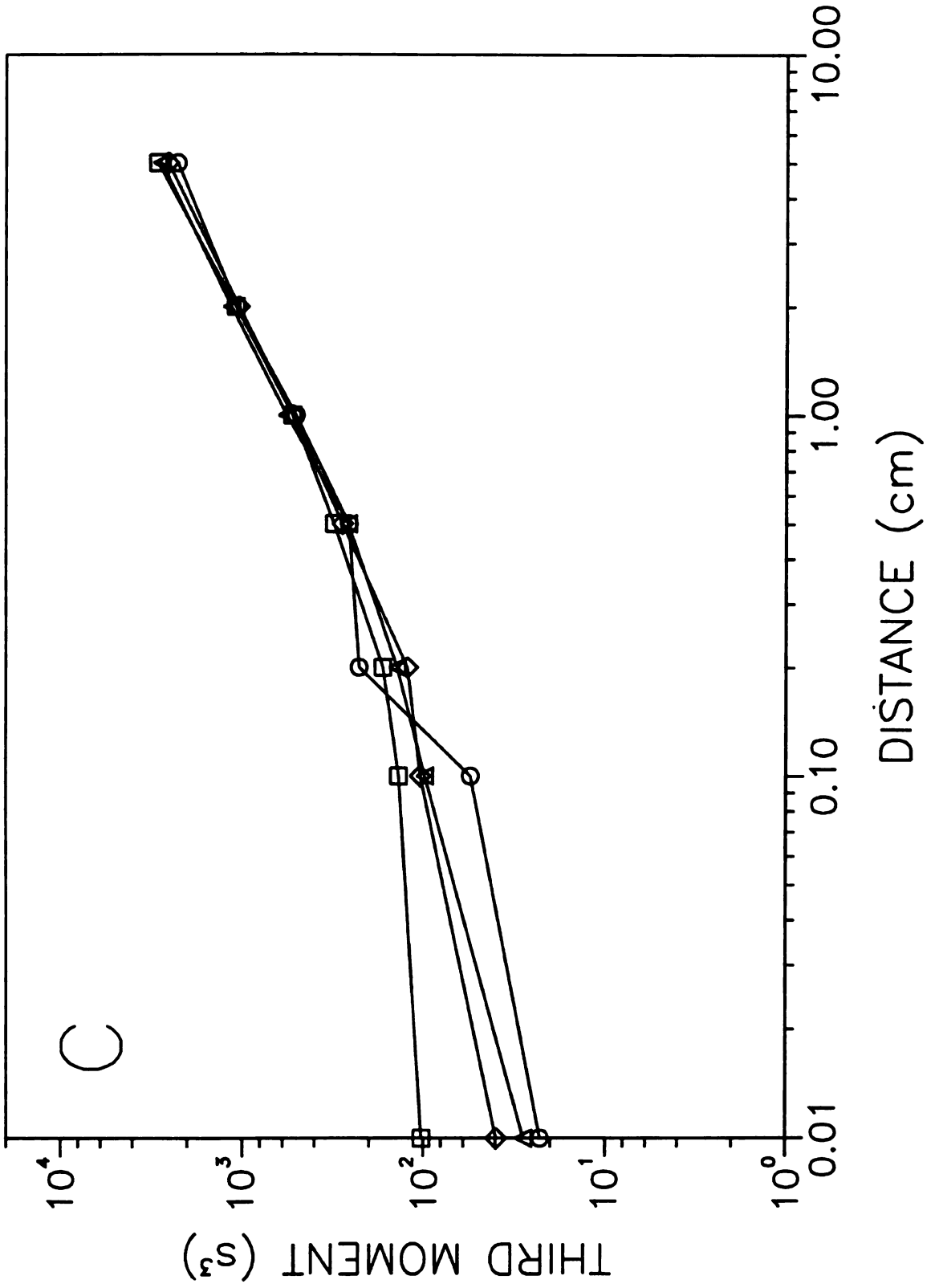

to decrease as the rate constant increases. This shift in elution time is caused by the reaction in the surface phase as already discussed. The two fastest reaction rates have fewer data than the other systems since all of species A has been consumed at the longer distances. Figure 7.8A shows that the first moments for species B are not linear with distance. This nonlinearity arises because of the manner in which the reaction creates B molecules. Since species A must enter the surface phase and remain there to react, the molecules that have long residence times in the surface phase will become species B initially. As the system proceeds toward steady state and the average residence time of species B becomes less dominated by the initial production, the first moments become more linear. It is also noticeable that the first moments for all systems converge with increasing distance and are statistically indistinguishable at 5.0 cm. At this point, all of the molecules have been converted to species B. The systems become equivalent and are expected to have the same first moments as the systems with separation alone, since species A and B have the same molecular properties.

The second moment or variance is also different in the reactive separation systems compared to systems with separation alone. The second moments for species A, shown in Figure 7.7B, appear to increase linearly with distance and, hence, have achieved steady state. All the variances are smaller than the corresponding system with separation alone (Figure 7.4B). The systems with rate constants of 0.01 and 0.1 s^{-1} are the most similar to the system with separation alone, while the other rate constants produce variances that are much smaller. The systems with large rate constants do not exhibit much broadening from resistance to mass transfer in the surface phase, since the molecules of species A

that enter the surface phase react quickly to form species B. The second moments for species B are shown in Figure 7.8B. The nonlinear second moments are caused by the same processes that caused curvature in the first moments, as discussed previously. The slowest reaction rates result in larger second moments until the systems converge. It is noteworthy that these systems converge to the second moment of the system with separation alone with no offset due to reaction. This occurs because species A and B have the same molecular properties, just as in the case of the first moment.

The third moments for species A and B are shown in Figures 7.7C and 7.8C, respectively, and exhibit the same general trends already discussed. The magnitude of the third moments for species A indicates that the amount of asymmetry in the zone profiles is relatively small. The third moments for species A in the systems with the large rate constants of 1.0 and 10.0 s^{-1} are very close to zero. The third moments for the systems with the smallest rate constants are the most similar to those for the system with separation alone (Figure 7.4C). The third moments for species B are all greater than those for the system with separation alone until the reaction has reached completion. Once the systems have converged, the third moments appear to be equivalent to those for the system with separation alone.

7.2.3.2 Effect of Changes in Absorption Coefficient.

To investigate the effect of the absorption coefficient on reactive separation systems, the value of $K_{abs,B}$ is changed over the range of 0.1 to 5.0 while the value of $K_{abs,A}$ is held constant at 1.0. The rate constant for the A→B reaction is 0.1 s^{-1}. These conditions were chosen to produce systems that were not limited by either reaction or

mass transfer kinetics so that the interplay of the two processes could be examined. The curves in Figure 7.9A show the decay of species A in the systems under investigation. It is evident that species A does not show any kinetic dependence on the absorption coefficient of species B. This demonstrates that the properties of the product have no effect on the behavior of the reactant, which is as expected for an irreversible A→B reaction. This conclusion is supported by the data presented in Table 7.4, which confirm that the characteristic T_{10} and T_{90} times for species A do not change. These times are comparable to those found in Table 7.3 for the rate constant of 0.1 s^{-1}. The production curves for species B (Figure 7.9B), however, show effects of the change in absorption coefficient. The T_{10} times for these curves (Table 7.4) decrease as the absorption coefficient increases, just as in the case of separation alone (Table 7.2). However, the T_{90} times for species B in these systems do not show the same trend as the system with separation alone. These systems produce the same characteristic times, indicating that the long-time behavior of these systems is dominated by the reaction rate rather than mass transfer processes. The steady-state behavior of these systems is quantified in Table 7.4 as the ratio of fluid to surface phase molecules ($\tilde{N}_s/\tilde{N}_f$). The phase distribution for species A is not calculable since there are no molecules remaining at the long-time limit. The phase distribution for species B reflects the expected dependence upon the absorption coefficient, according to Equation [7.1].

Figure 7.9: Stochastic simulation of reactive separations showing the decay curves for species A (A) and the production curves for species B (B) in the fluid phase as a function of time for the following absorption coefficients: (○) $K_{abs,B} = 0.1$, (□) $K_{abs,B} = 0.2$, (△) $K_{abs,B} = 0.5$, (◇) $K_{abs,B} = 1.0$, (●) $K_{abs,B} = 2.0$, (■) $K_{abs,B} = 5.0$. Other simulation conditions as follows: $t = 1.00\times10^{-3}$ s, $N = 10000$, $R_f = 2.00\times10^{-3}$ cm, $R_s = 8.2843\times10^{-4}$ cm, $D_f = 1.00\times10^{-5}$ cm^2 s^{-1}, $D_s = 1.00\times10^{-7}$ cm^2 s^{-1}, $K_{abs,A} = 1.00$, $k_r = 0.1$ s^{-1}.

Figure 7.9

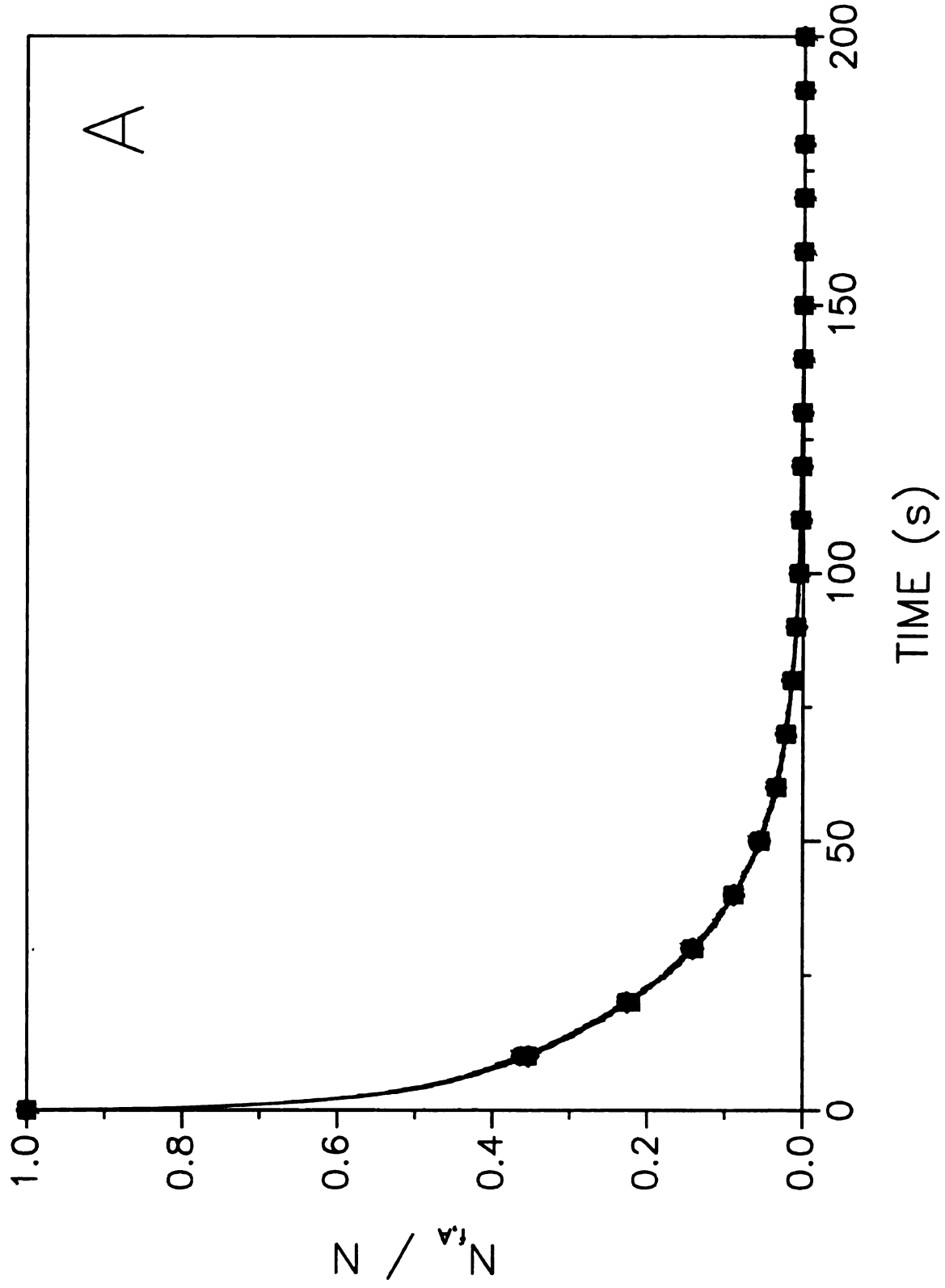

Figure 7.9 cont.

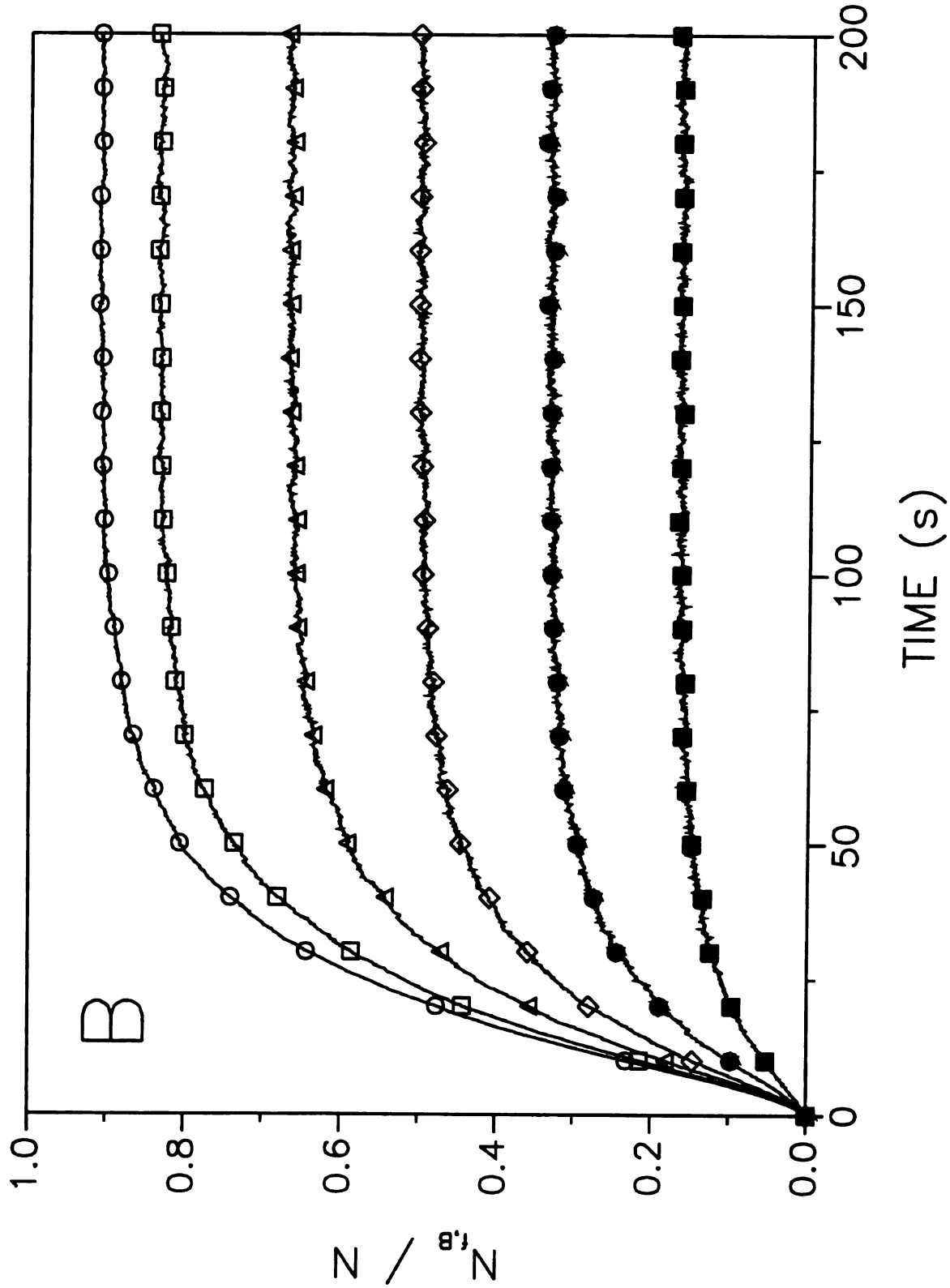

Table 7.4 Characteristic Times and Steady-State Distributions for Reactive Separations as a Function of the Absorption Coefficient (K_{abs}) for Species B.[a]

		Species A			Species B		
$K_{abs,A}$	$K_{abs,B}$	T_{10} (s)	T_{90} (s)	$\tilde{N}_{A,s}/\tilde{N}_{A,f}$	T_{10} (s)	T_{90} (s)	$\tilde{N}_{B,s}/\tilde{N}_{B,f}$
1.0	0.1	0.109	37.0	–	5.10	53.3	0.10
1.0	0.2	0.100	37.2	–	5.00	53.1	0.20
1.0	0.5	0.122	37.1	–	4.80	53.0	0.50
1.0	1.0	0.115	37.3	–	4.40	52.4	0.99
1.0	2.0	0.119	37.5	–	4.30	52.2	2.00
1.0	5.0	0.121	37.2	–	2.50	53.3	5.01

[a] Simulation conditions given in Figure 7.9.

The fluid dynamic behavior of systems in which the absorption coefficient of species B is changed can be seen in Figure 7.10. The average linear velocity of the laminar flow is 0.1 cm s^{-1}. Since species A does not experience any change in reaction or separation properties, the zone profiles at 1.0 cm, seen in Figure 7.10A, all overlap. The behavior of species B, however, shows some differences in these systems. Figure 7.10B shows that the mean elution time changes as a function of the absorption coefficient. There is also a noticeable change in the width and asymmetry of these zones.

The statistical moments of the zone profiles for species A and B quantify the extent of the changes as a function of the absorption coefficient. Figure 7.11A shows the first moment or mean elution time for species A. It is apparent that the change in the value of $K_{abs,B}$ does not affect the mean elution time of species A. However, the first moments are smaller in magnitude than the first moments for a system with separation alone (Figure 7.4A). The smaller magnitude is the result of the same processes described previously in relation to Figure 7.7A. The first moments for species B in Figure 7.12A have the characteristic curvature associated with reactive separation systems, as discussed

Figure 7.10: Zone profiles for species A (A) and species B (B) in reactive separation systems with absorption coefficients of 0.1, 0.2, 0.5, 1.0, 2.0, and 5.0 (left to right). Other simulation conditions as follows: $t = 5.00\times10^{-5}$ s, N = 2000, $R_f = 2.00\times10^{-3}$ cm, $R_s = 8.2843\times10^{-4}$ cm, L = 1.0 cm, $D_f = 1.00\times10^{-5}$ cm^2 s^{-1}, $D_s = 1.00\times10^{-7}$ cm^2 s^{-1}, $K_{abs,A} = 1.00$, $k_r = 0.1$ s^{-1}, $v_0 = 0.1$ cm s^{-1}.

Figure 7.10

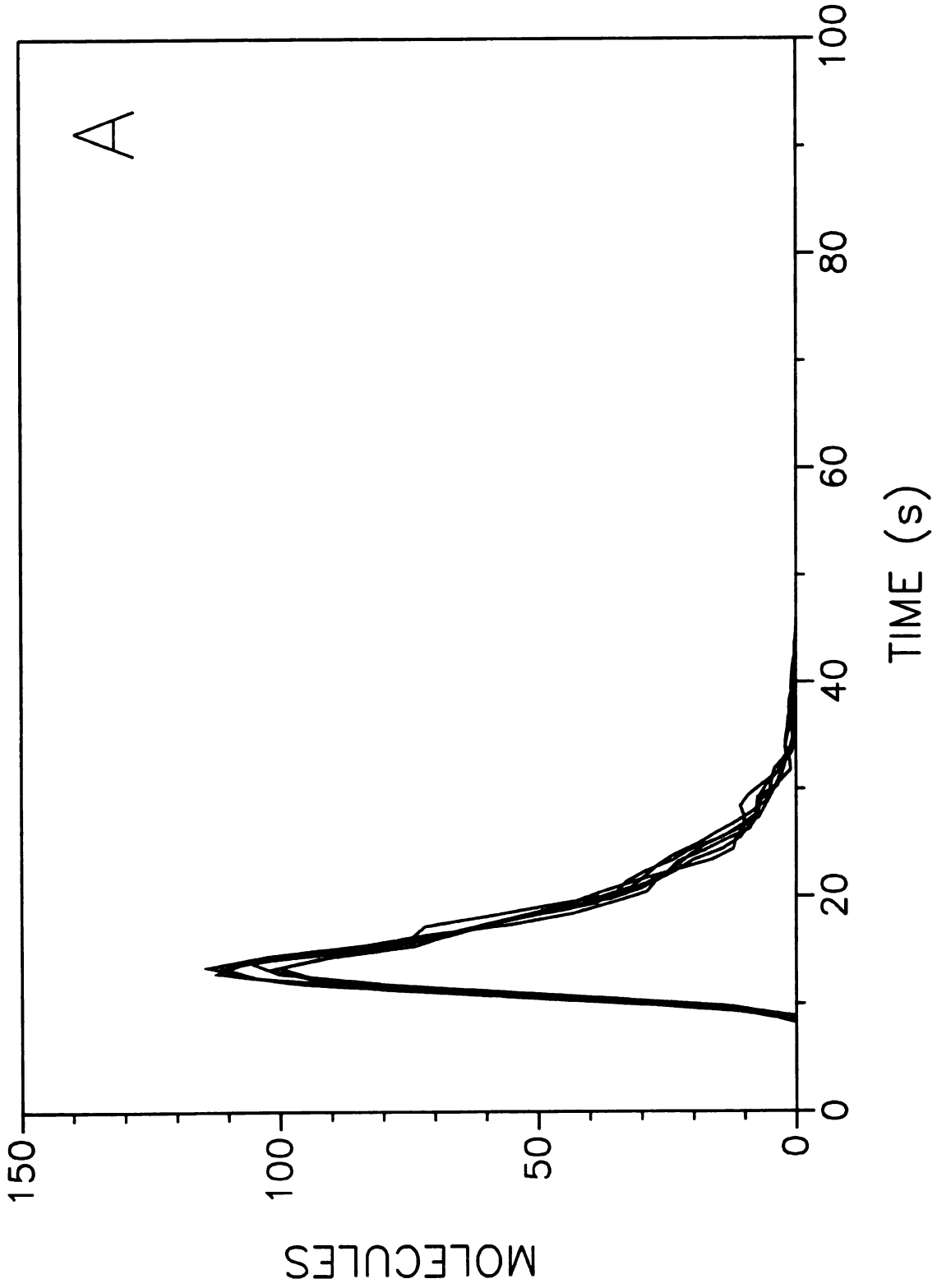

Figure 7.10 cont.

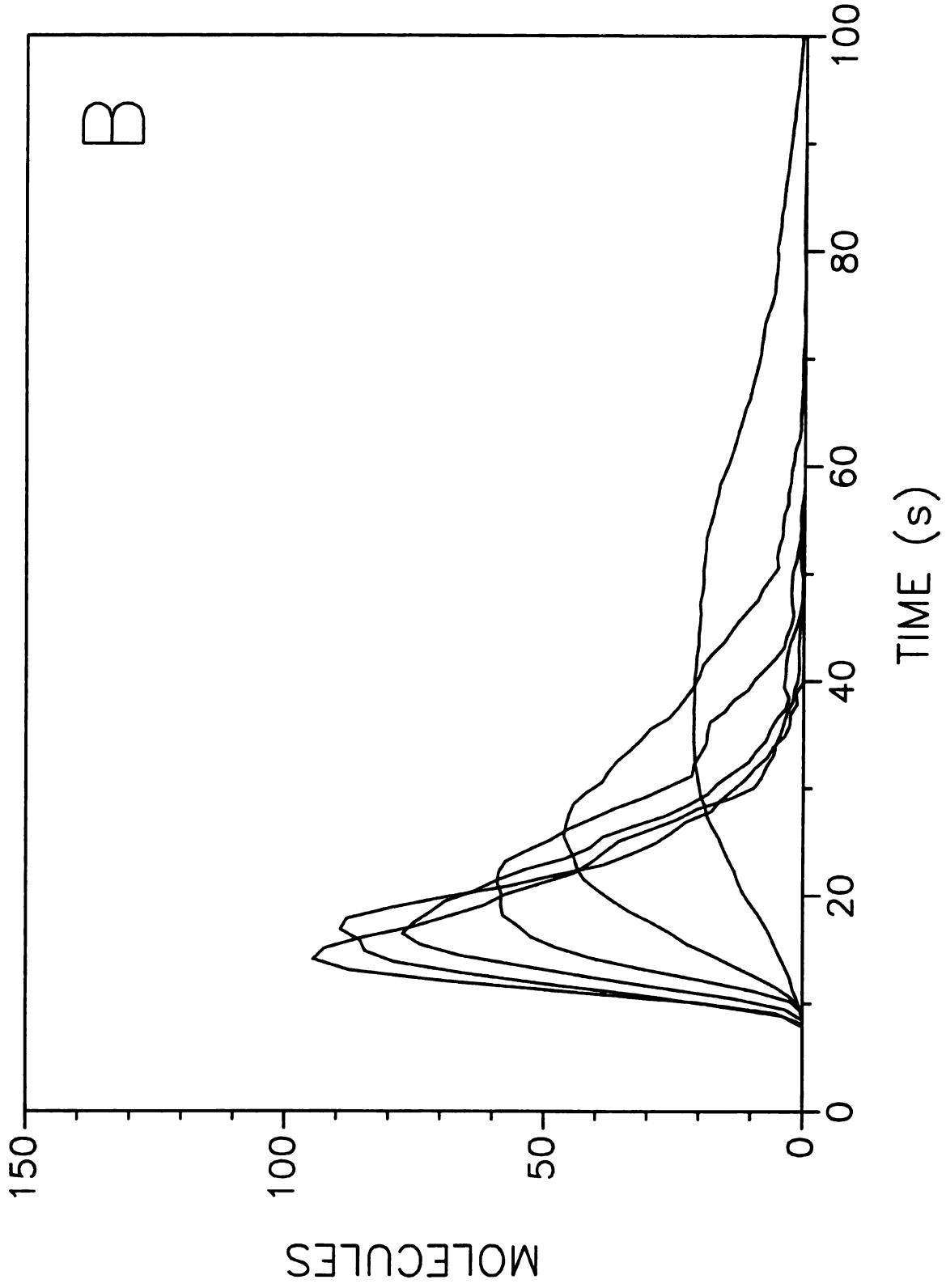

Figure 7.11: First (A), second (B), and third (C) statistical moments as a function of distance for species A in reactive separations with the following absorption coefficients: (○) $K_{abs,B} = 0.1$, (□) $K_{abs,B} = 0.2$, (△) $K_{abs,B} = 0.5$, (◇) $K_{abs,B} = 1.0$, (●) $K_{abs,B} = 2.0$, (■) $K_{abs,B} = 5.0$. Other simulation conditions as given in Figure 7.10.

Figure 7.11

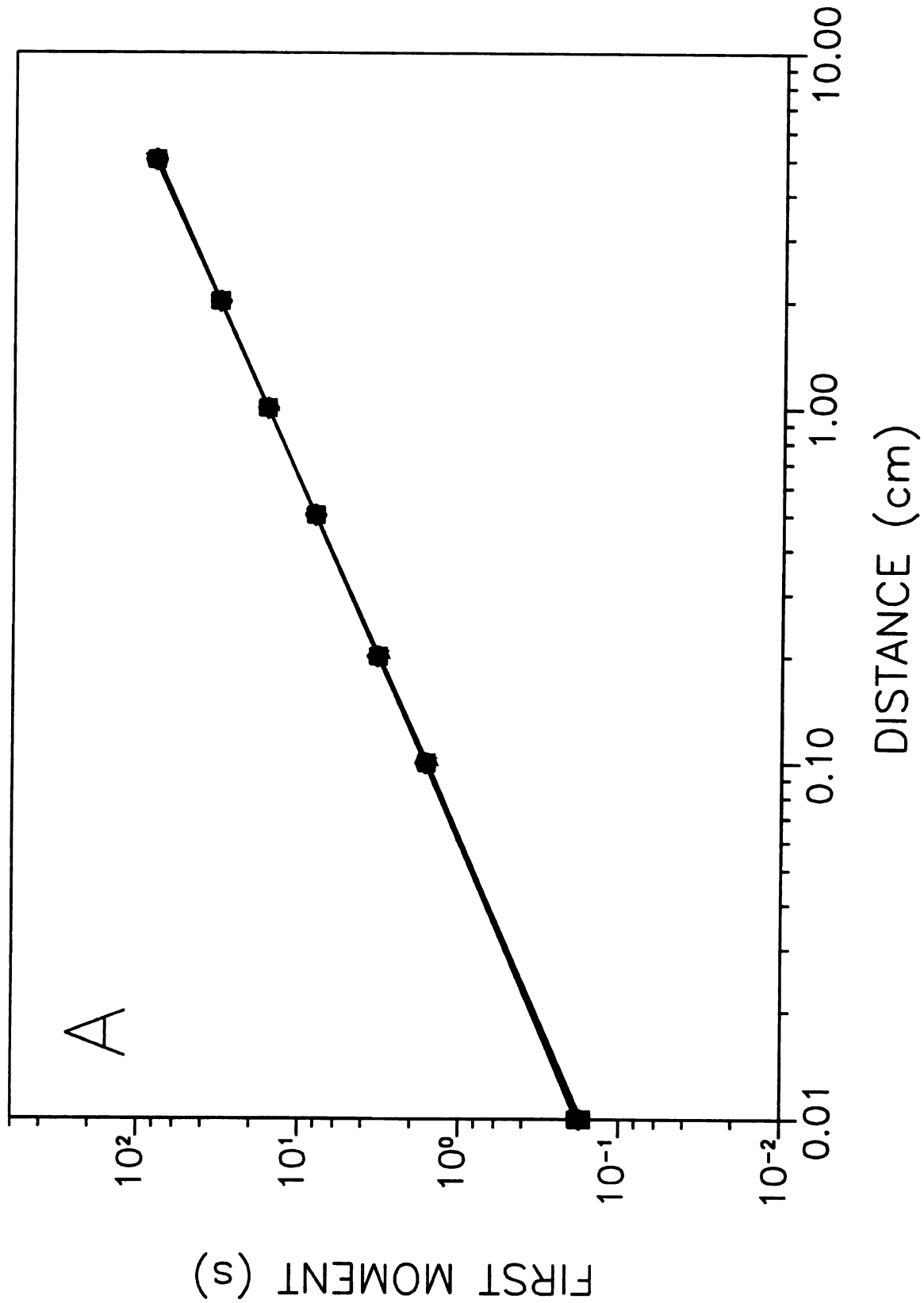
A
FIRST MOMENT (s)
DISTANCE (cm)
10²
10¹
10⁰
10⁻¹
10⁻²
0.01
0.10
1.00
10.00

Figure 7.11 cont.

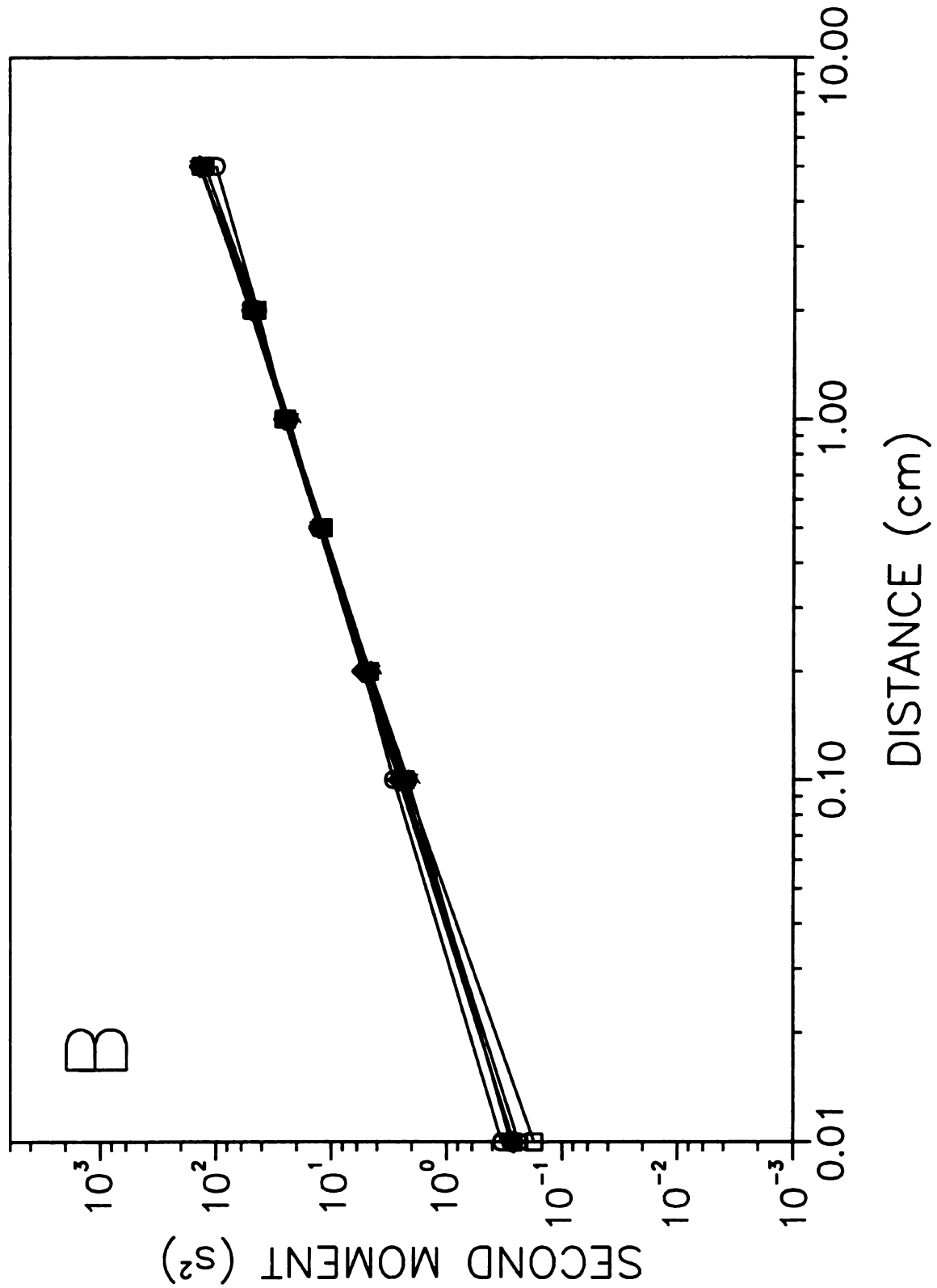

Figure 7.11 cont.

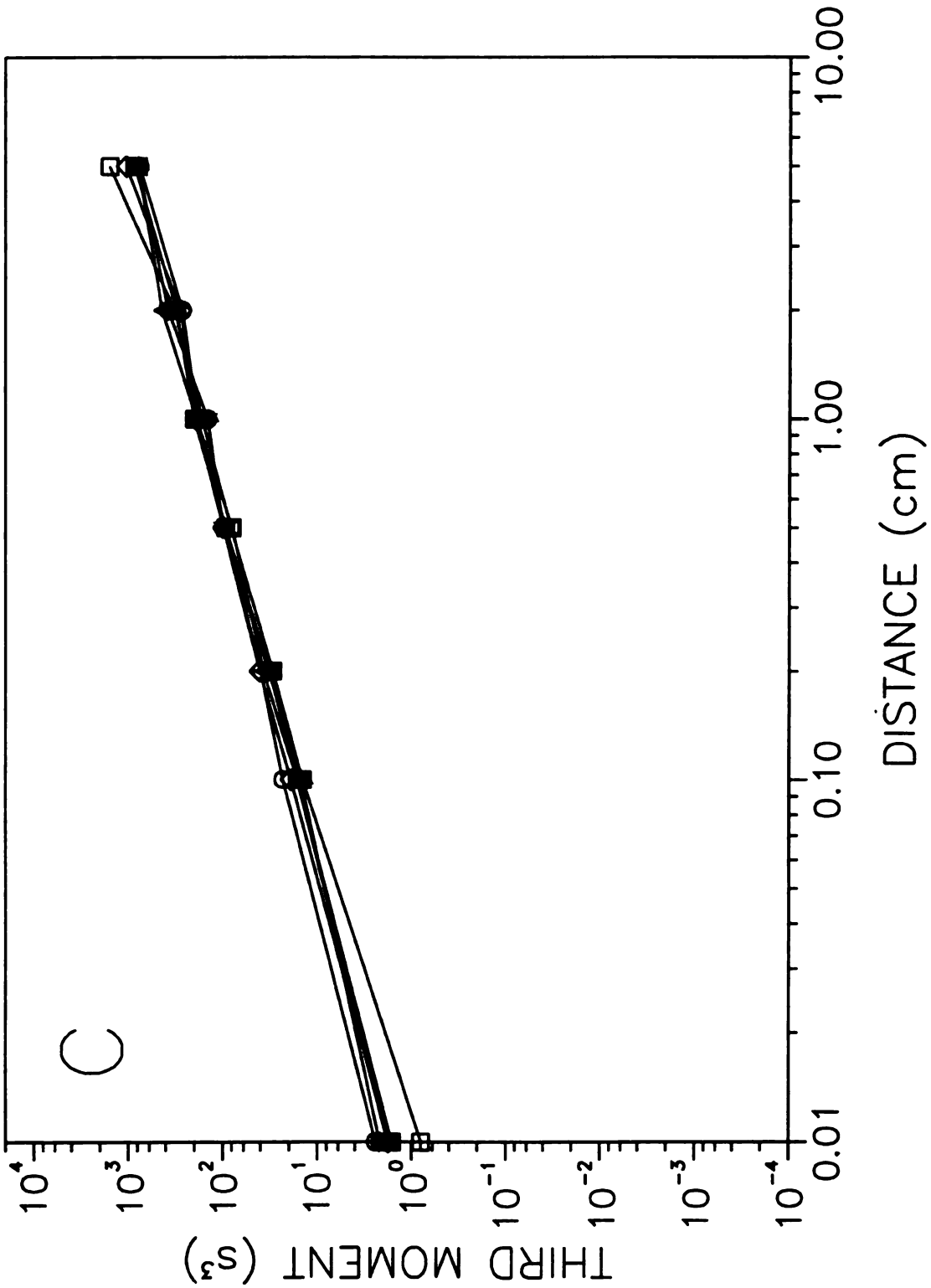

Figure 7.12: First (A), second (B), and third (C) statistical moments as a function of distance for species B in reactive separations with the following absorption coefficients: (○) $K_{abs,B} = 0.1$, (□) $K_{abs,B} = 0.2$, (△) $K_{abs,B} = 0.5$, (◇) $K_{abs,B} = 1.0$, (●) $K_{abs,B} = 2.0$, (■) $K_{abs,B} = 5.0$. Other simulations conditions as given in Figure 7.10.

Figure 7.12

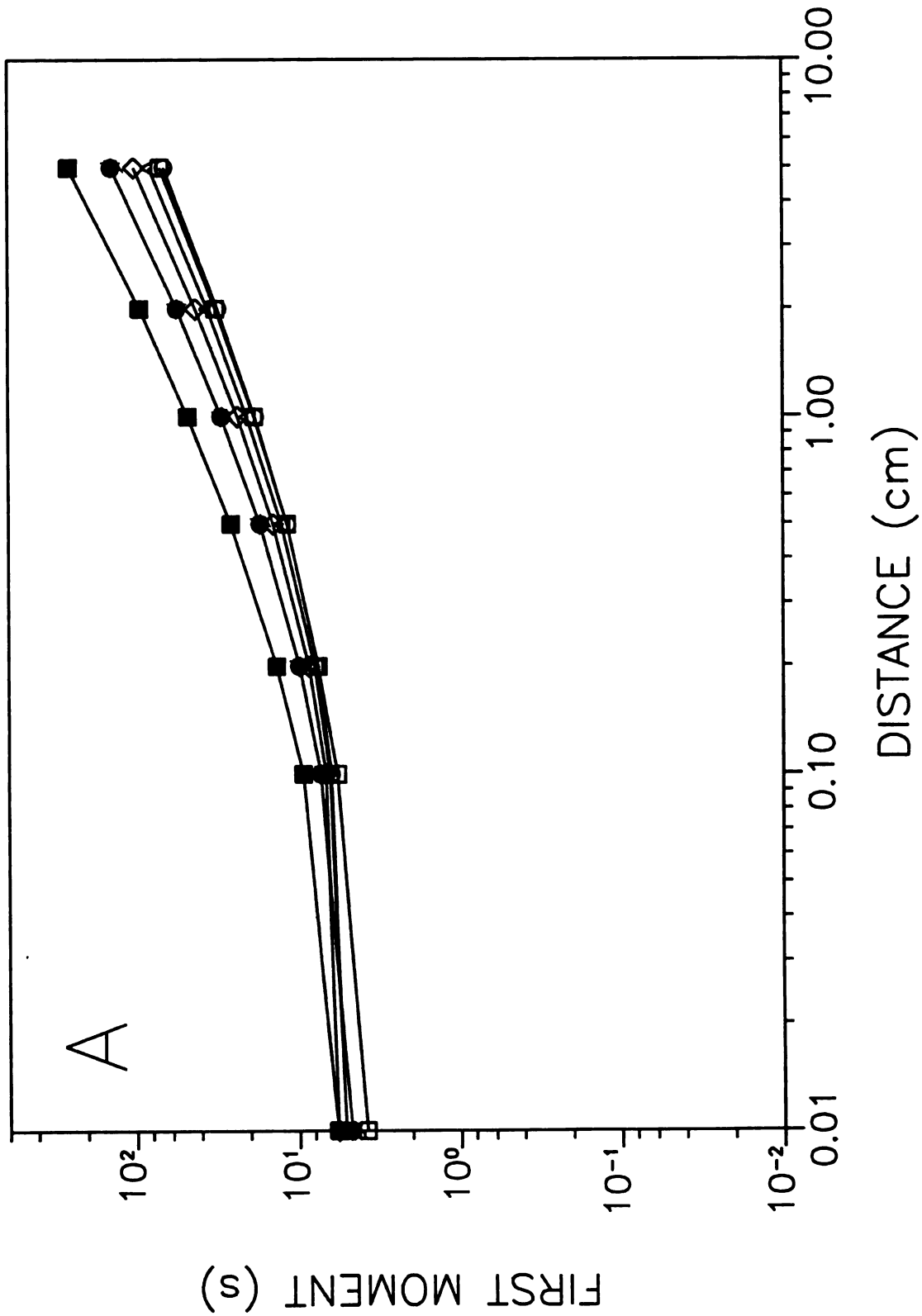
A
FIRST MOMENT (s)
10^{2}
10^{1}
10^{0}
10^{-1}
10^{-2}
0.01
0.10
1.00
10.00
DISTANCE (cm)

Figure 7.12 cont.

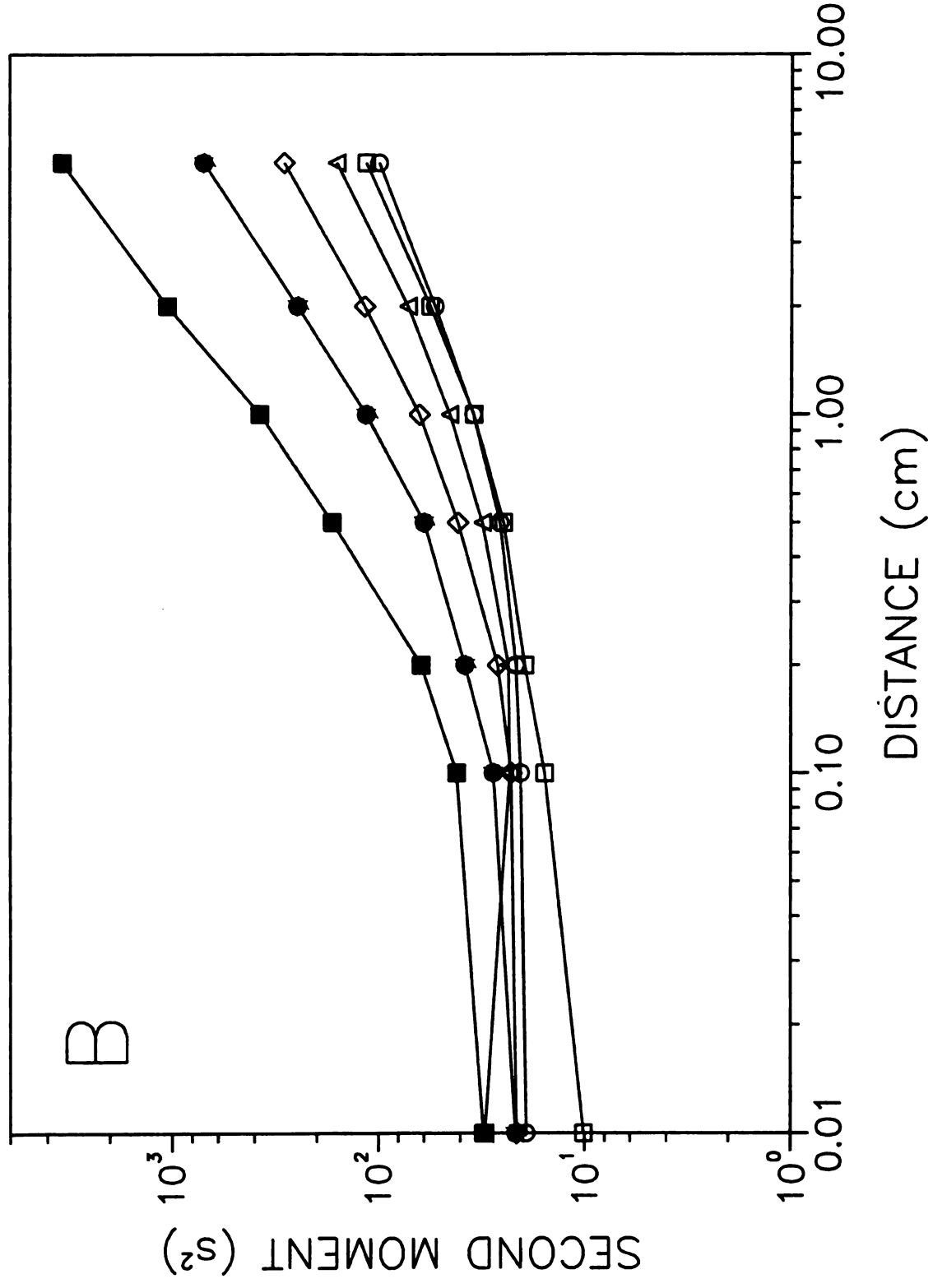

Figure 7.12 cont.

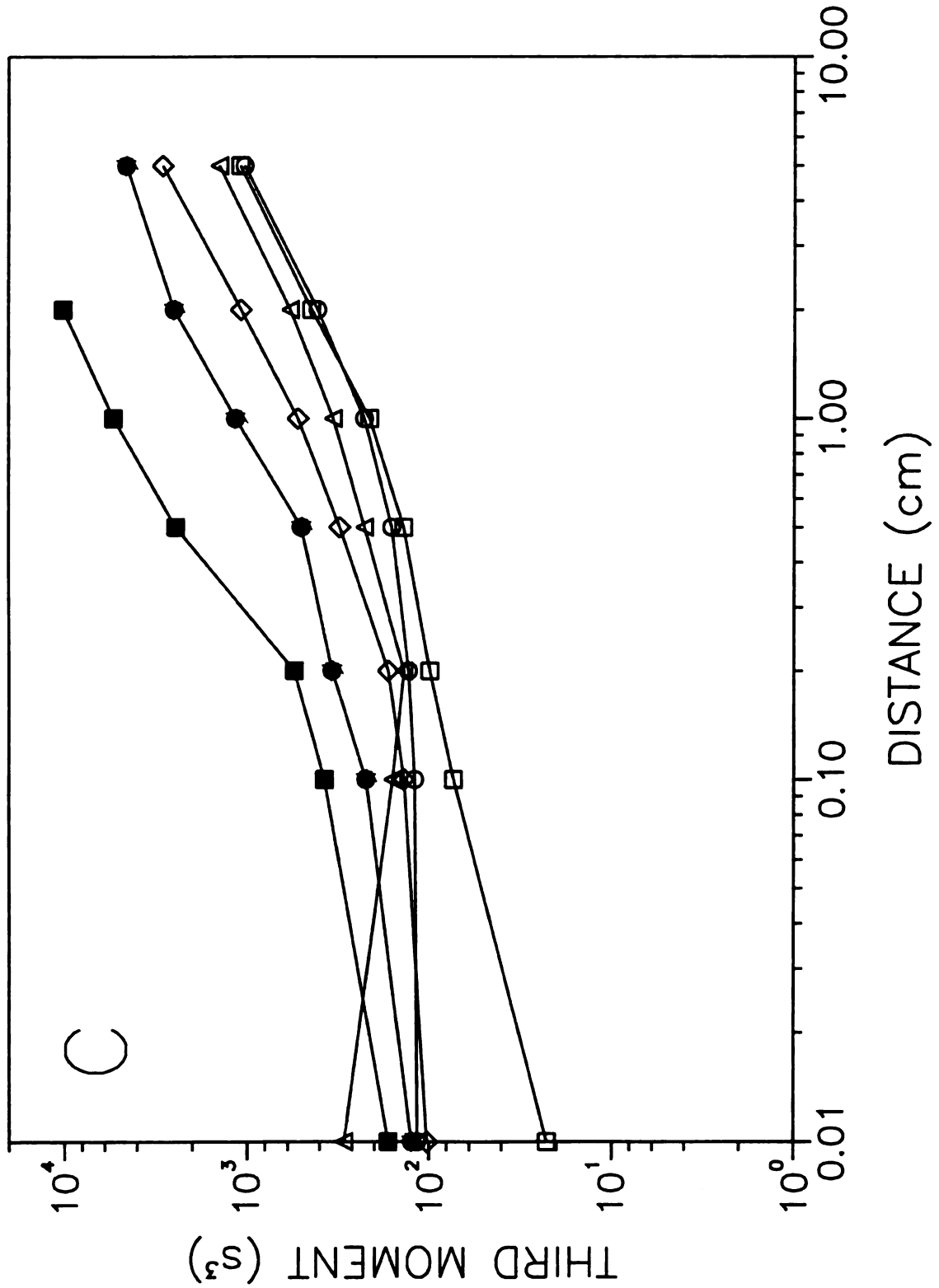

previously. The systems appear to behave similarly to systems with separation alone (Figure 7.4A) at long column lengths in that the mean elution time increases as the absorption coefficient increases. However, the absolute magnitude of the first moments for these systems is different than that for the system with separation alone. For reactive separation systems in which the absorption coefficient for species A is less than that for species B ($K_{abs,A} < K_{abs,B}$), the first moments are smaller than those for the systems with separation alone. For reactive separation systems in which the absorption coefficient for species A is greater than that for species B ($K_{abs,A} > K_{abs,B}$), the first moments are larger than those for the systems with separation alone.

The second moment or variance for species A and B is presented in Figures 7.11B and 7.12B, respectively. Figure 7.11B shows that the absorption coefficient of species B has no affect on the variance of species A. The variance is also smaller in magnitude than the system with separation alone (Figure 7.4B). This results from the same processes described earlier in relation to Figure 7.7B. Figure 7.12B shows the expected curvature in the variance of species B due to the reaction. It also shows that at long column lengths, the variance increases with the absorption coefficient. Once the reaction has reached completion, the systems behave similarly to systems with separation alone (Figure 7.4B). However, as in the case of the first moments, the absolute magnitude of the second moments for these systems is larger than that for systems with separation alone. The increase in the magnitude of the moments can be attributed to the interaction of the reaction and separation processes. For values of $K_{abs,A} \neq K_{abs,B}$, species A and B move through the system at different rates. The difference in absorption coefficients causes B

molecules to be produced at shorter distances than the mean position of the zone ($K_{abs,A} < K_{abs,B}$) or at longer distances than the mean position of the zone ($K_{abs,A} > K_{abs,B}$). The amount of broadening due to this effect is dependent on the magnitude of the difference in absorption coefficients between species A and B. By comparing Figures 7.4B and 7.12B, it can be seen that the greatest changes in the second moment occur for the systems with the greatest difference in absorption coefficients (i.e., $K_{abs,A} = 1.0$, $K_{abs,B} = 0.1, 5.0$).

The third moment or asymmetry for species A and B is shown in Figures 7.11C and 7.12C, respectively. Figure 7.11C shows that the absorption coefficient of species B has no effect on the asymmetry of species A. Again, the magnitude of the third moment is smaller than the corresponding system with separation alone (Figure 7.4C). The third moment for species B exhibits an increase with the absorption coefficient, similar to that for separation alone. However, the absolute magnitude of the third moment for these systems is larger than that for separation alone, as described previously for the second moments in Figure 7.12B. This implies that the interaction between the reaction and separation processes causes both the variance and asymmetry for species B to increase.

7.2.3.3 Effect of Changes in Fluid-Phase Velocity.

Another parameter that affects reactive separations is the velocity of the fluid phase. To study these effects, the linear velocity is changed over the range of 0.02 to 0.5 cm s^{-1}. The rate constant is 0.1 s^{-1}, the absorption coefficient for species A is 1.0, and the absorption coefficient for species B is 0.1. The combined mass transfer and reaction

kinetics of this system is shown in Figures 7.9A and 7.9B. The resulting characteristic T_{10} and T_{90} times are 0.1 and 37.0 s for species A and 5.1 and 53.3 s for species B, as seen in Table 7.4. These parameters were chosen to investigate a system that had comparable reaction and mass transfer rates, as well as a system that would lead to the separation of the two species. The ensuing fluid dynamic performance for species A and B can be seen in Figures 7.13A and 7.13B, respectively. As expected, the slower velocities cause the zones of the two species to elute at longer times. Since the two species have spent more time on the column, a greater number of molecules are converted from species A to B. This results in smaller area of the zones for species A and larger area for species B as the velocity decreases. Figure 7.13B shows that the number of B molecules increases more rapidly than the chromatographic broadening, resulting in greater height of the profiles (v_0 = 0.5 to 0.02 cm s^{-1}). Once the rate of production of B molecules diminishes because the reactant (species A) is no longer present in large quantity, the chromatographic broadening causes the height of the profile to decrease again (v_0 = 0.01 cm s^{-1}).

The statistical moments of these systems for species A and B can be seen in Figures 7.14 and 7.15, respectively. Figure 7.14A shows that the first moment or mean elution time for species A increases linearly with distance. This implies that the systems are at steady state, even for the fastest velocity. The first moments also increase as the velocity decreases, which is consistent with the average elution time of $L(1+k')/v_0$ for separation alone. The magnitude of the first moments for these systems is smaller than that for separation alone, as discussed previously. The first moments for species B in

Figure 7.13: Zone profiles for species A (A) and species B (B) in reactive separation systems with linear velocities of 0.02, 0.05, 0.1, 0.2, and 0.5 cm s^{-1} (right to left). Other simulation conditions as follows: $t = 5.00\times10^{-5}$ s, N = 2000, $R_f = 2.00\times10^{-3}$ cm, $R_s = 8.2843\times10^{-4}$ cm, L = 1.0 cm, $D_f = 1.00\times10^{-5}$ cm^2 s^{-1}, $D_s = 1.00\times10^{-7}$ cm^2 s^{-1}, $K_{abs,A} = 1.00$, $K_{abs,B} = 0.1$, $k_r = 0.1$ s^{-1}.

Figure 7.13

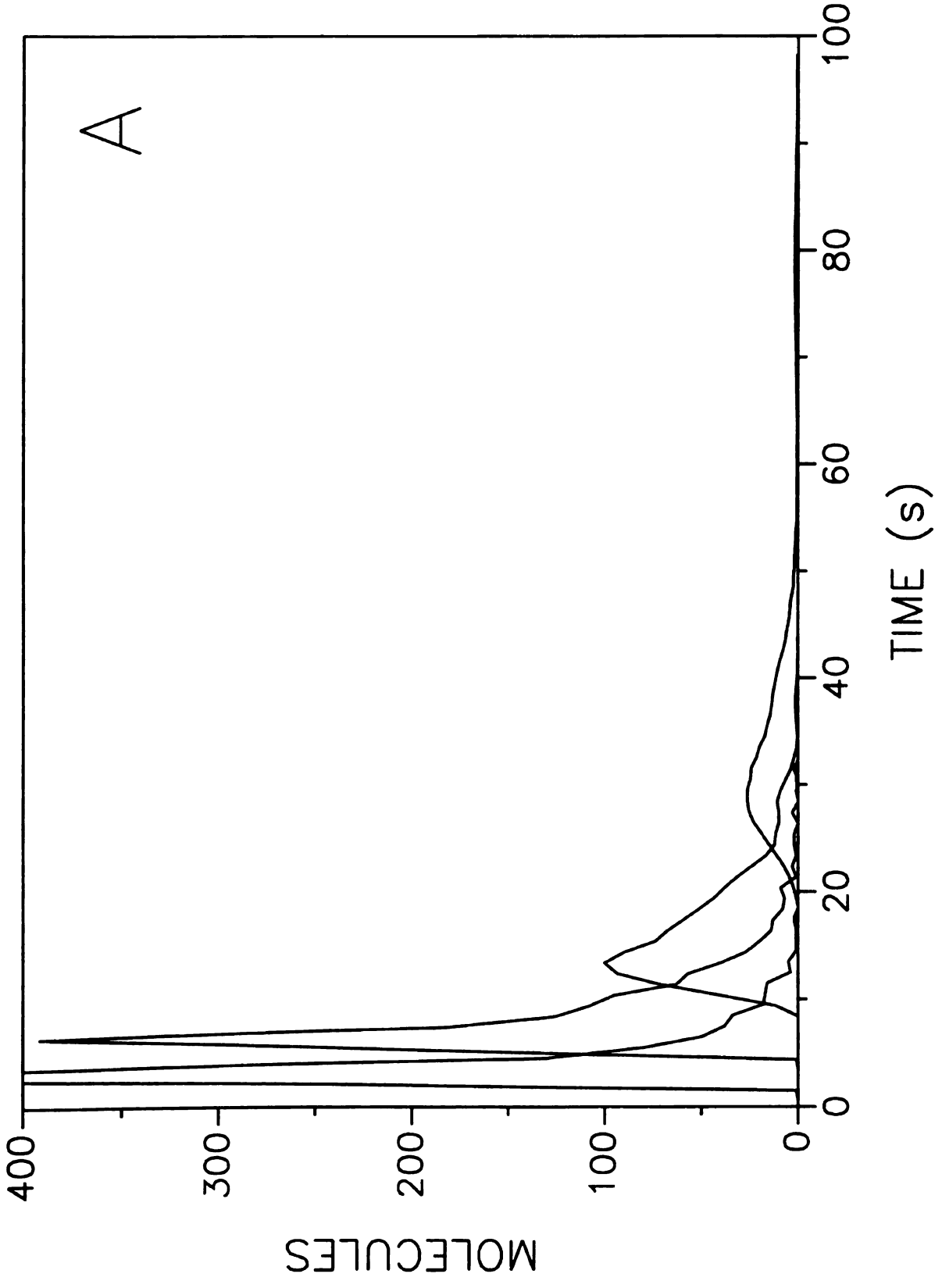

Figure 7.13 cont.

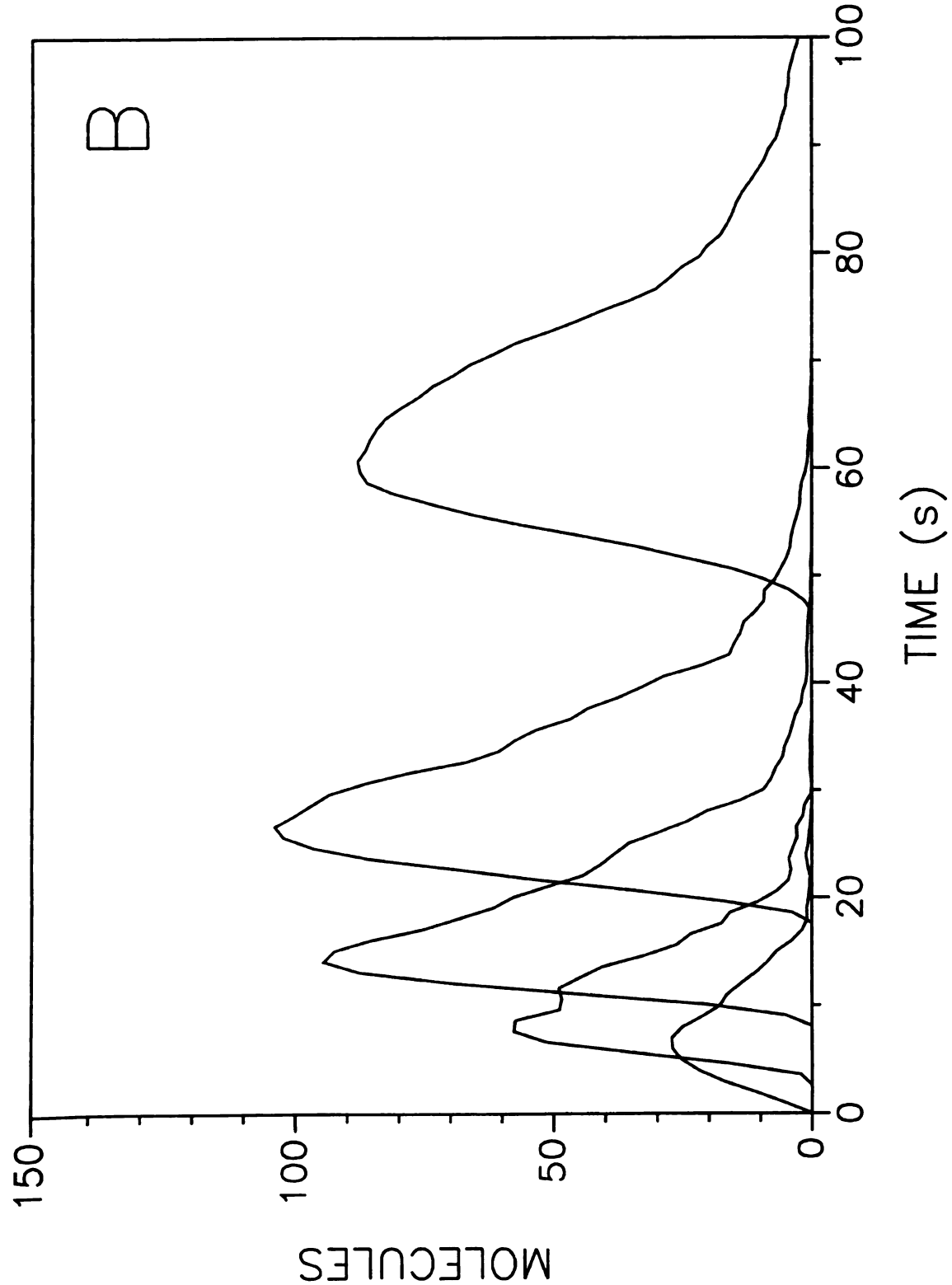

Figure 7.14: First (A), second (B), and third (C) statistical moments as a function of distance for species A in reactive separations with the following average linear velocities: (○) $v_0 = 0.02$ cm s^{-1}, (□) $v_0 = 0.05$ cm s^{-1}, (△) $v_0 = 0.1$ cm s^{-1}, (◇) $v_0 = 0.2$ cm s^{-1}, (●) $v_0 = 0.5$ cm s^{-1}. Other simulation conditions as given in Figure 7.13.

Figure 7.14

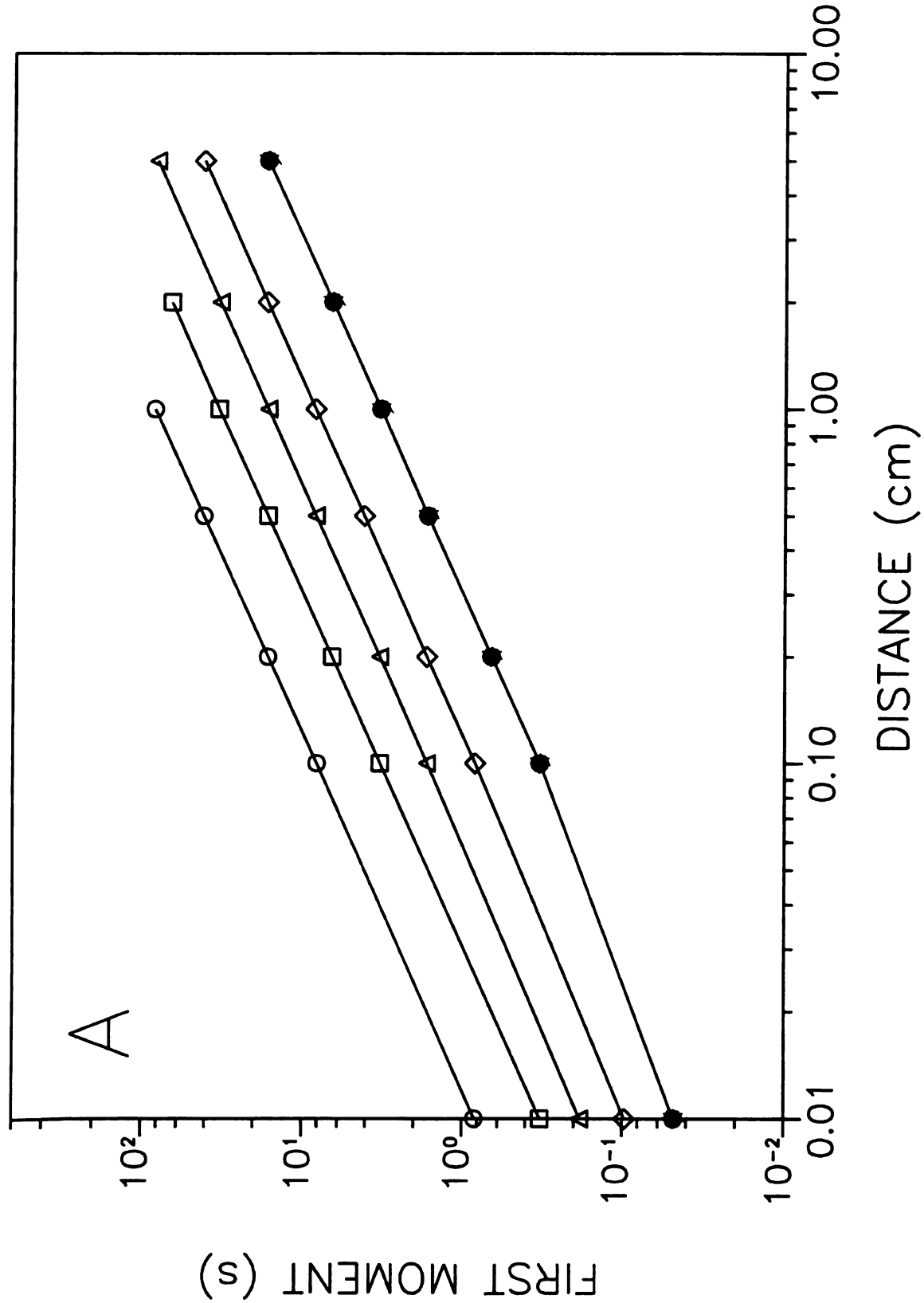
A
FIRST MOMENT (s)
10^{2}
10^{1}
10^{0}
10^{-1}
10^{-2}
0.01
0.10
1.00
10.00
DISTANCE (cm)

Figure 7.14 cont.

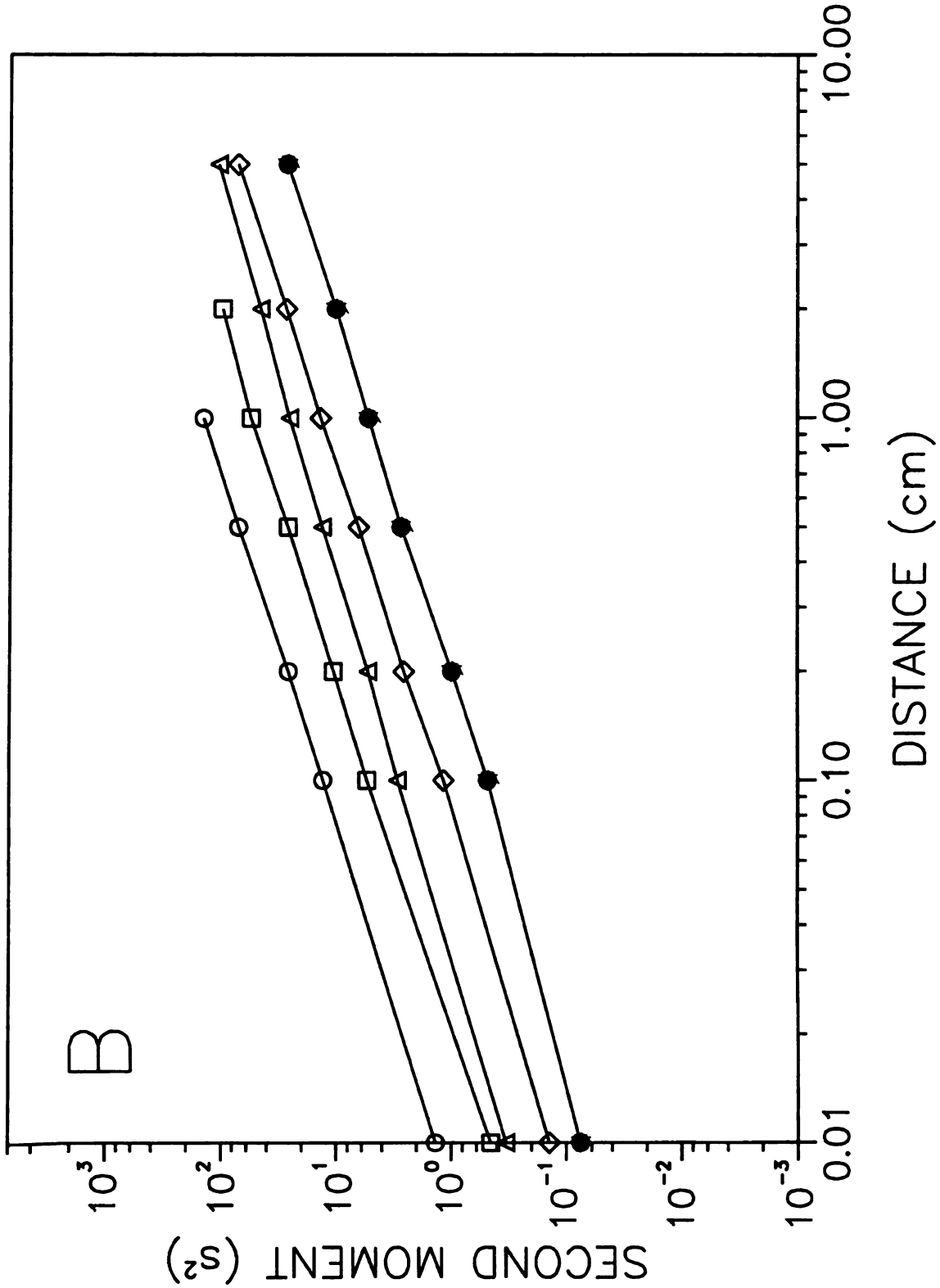

Figure 7.14 cont.

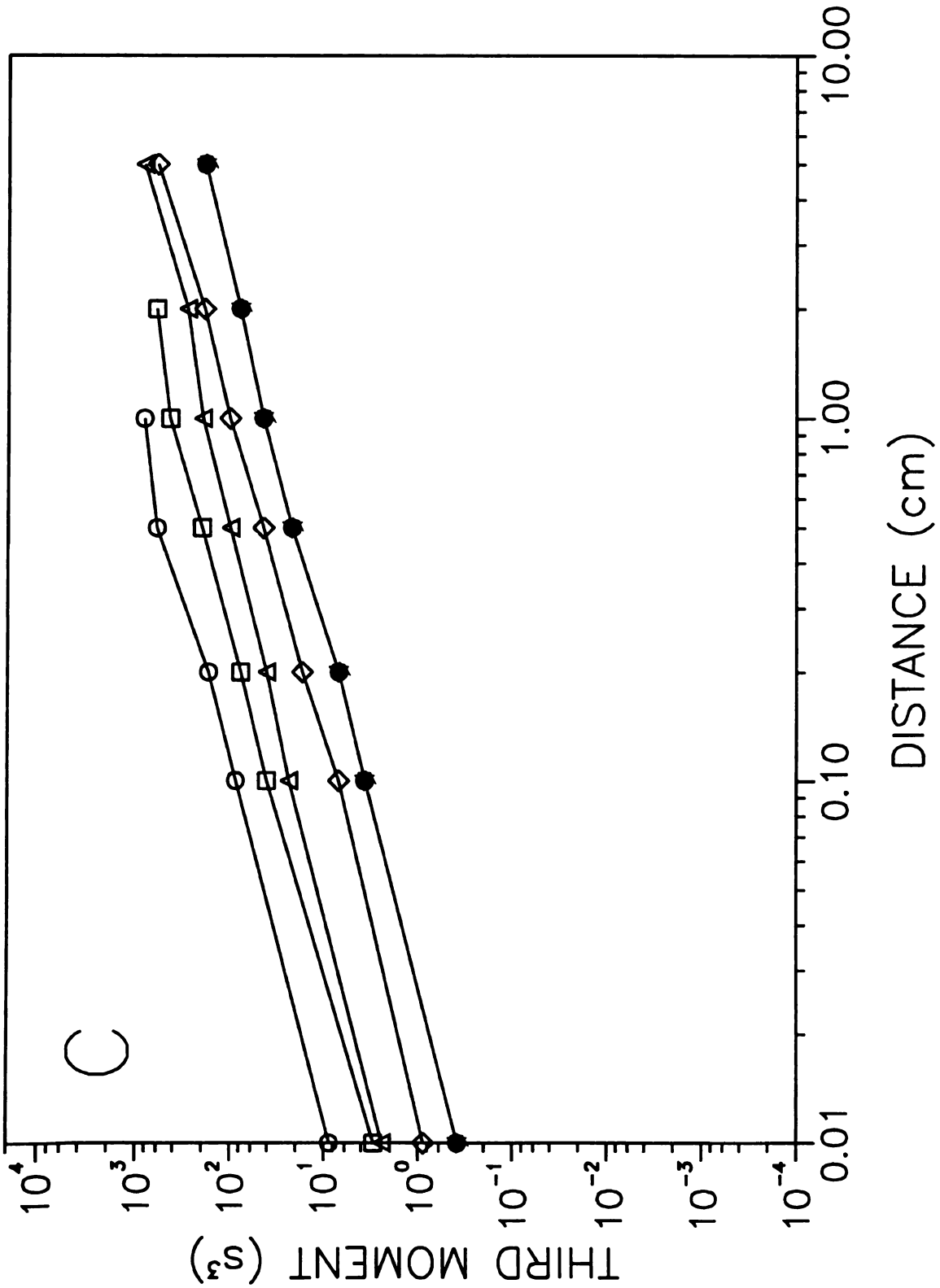

Figure 7.15: First (A), second (B), and third (C) statistical moments as a function of distance for species B in reactive separations with the following average linear velocities: (○) $v_0 = 0.02$ cm s^{-1}, (□) $v_0 = 0.05$ cm s^{-1}, (△) $v_0 = 0.1$ cm s^{-1}, (◇) $v_0 = 0.2$ cm s^{-1}, (●) $v_0 = 0.5$ cm s^{-1}. Other simulation conditions as given in Figure 7.13.

Figure 7.15

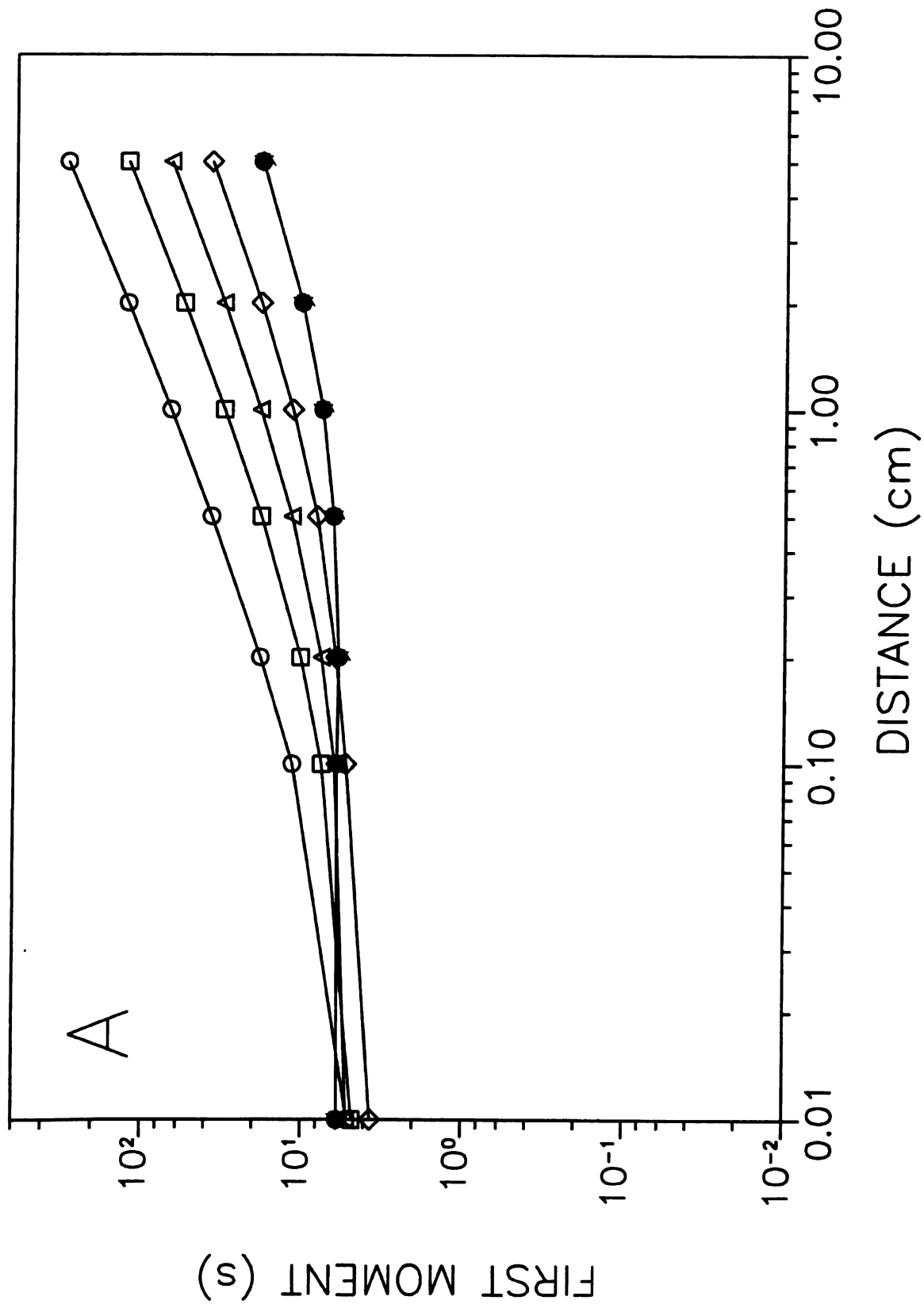
A
FIRST MOMENT (s)
10^{2}
10^{1}
10^{0}
10^{-1}
10^{-2}
0.01
0.10
1.00
10.00
DISTANCE (cm)

Figure 7.15 cont.

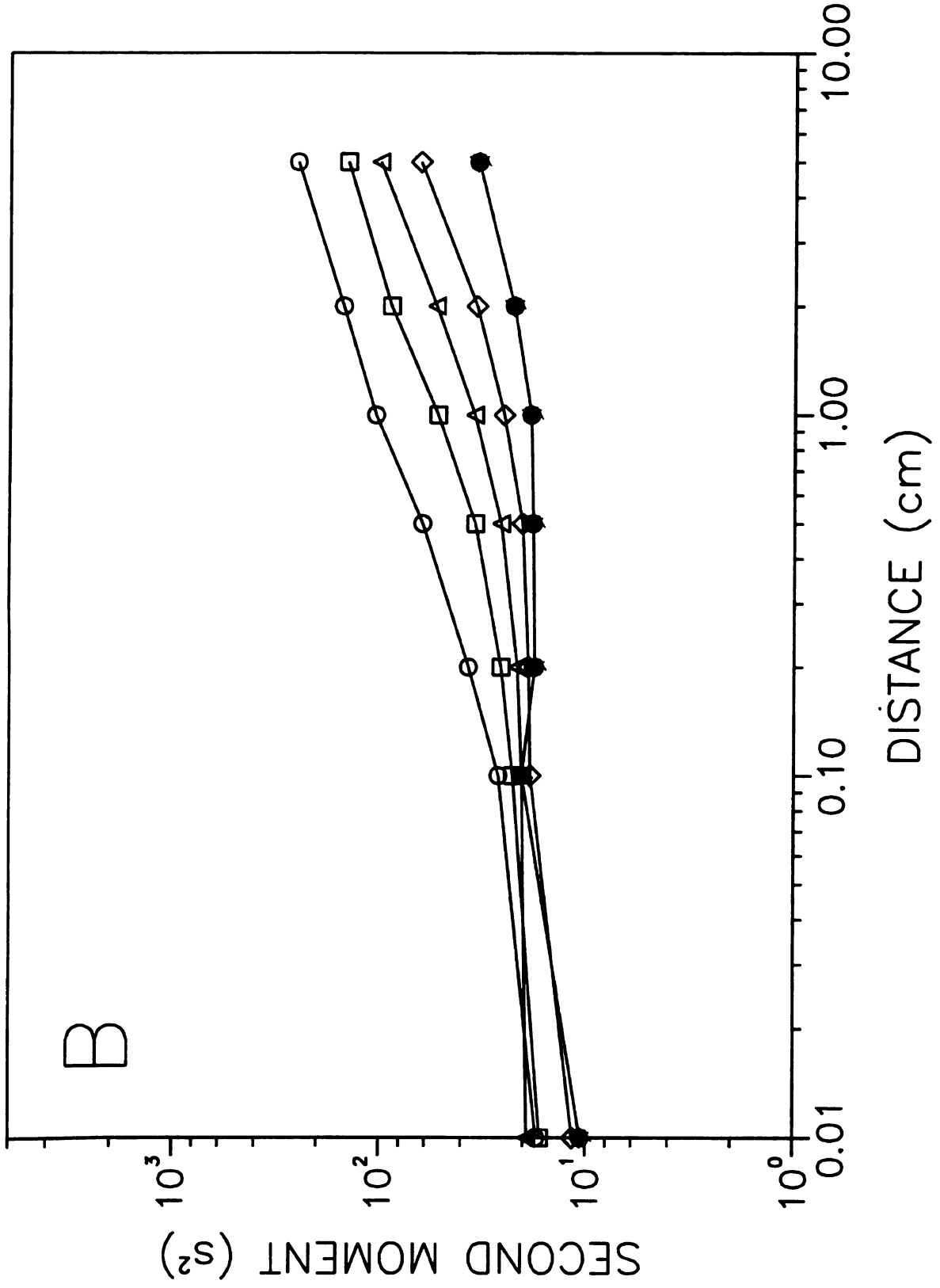

Figure 7.15 cont.

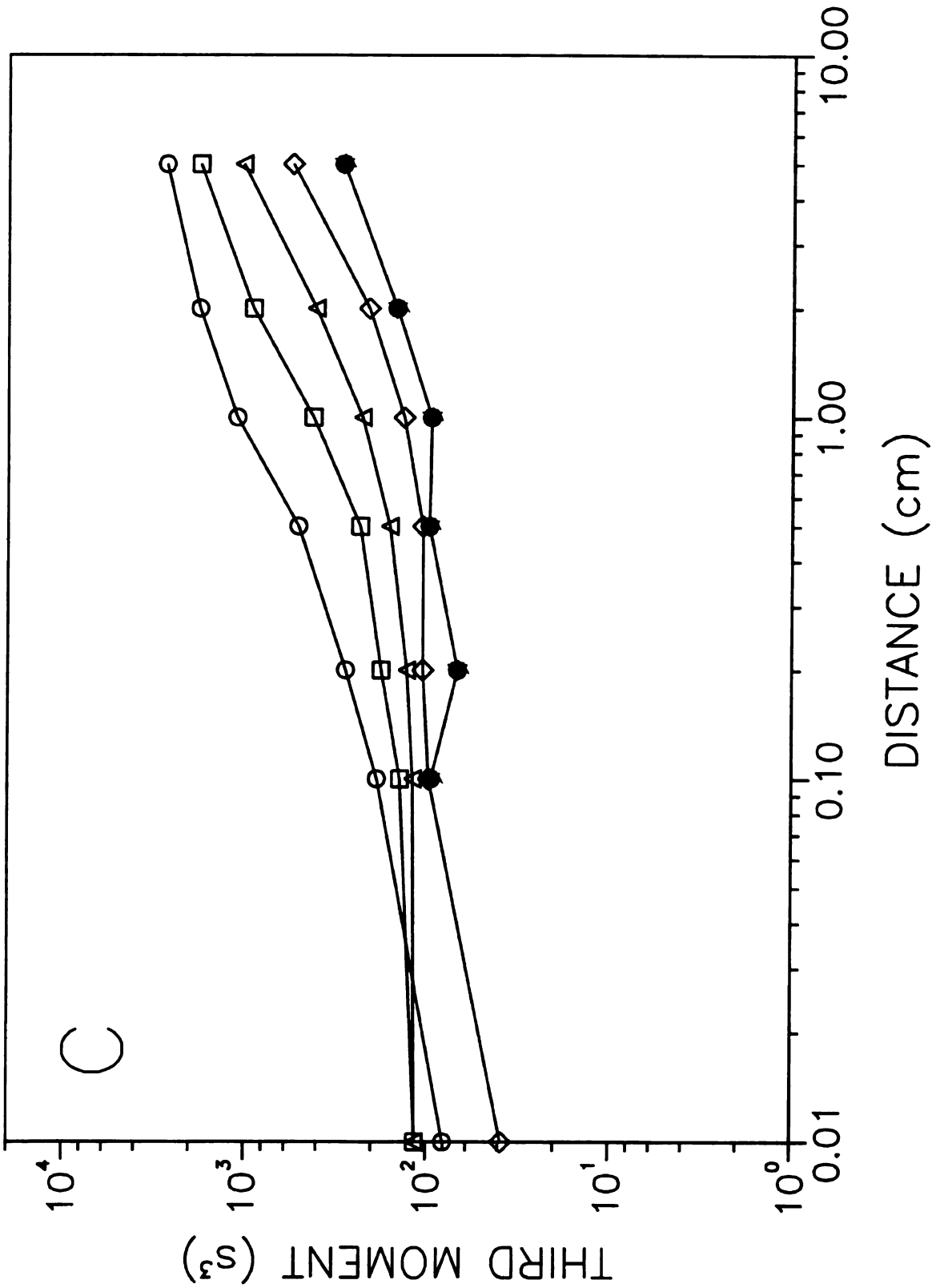

Figure 7.15A show the characteristic curvature due to the reaction. It appears that all the systems have a similar first moment at the shortest column length. This occurs because the systems are reaction-rate limited at short distances and, therefore, are independent of velocity. However, as the column length increases, the first moments of the systems diverge. The trend observed at long column lengths is that the fastest velocity produces the smallest first moment for species B, similar to that seen for species A. The magnitude of these values is greater than that for separation alone, as discussed previously.

The second moment or variance for species A, displayed in Figure 7.14B, also appears to be linear with respect to the distance traveled. The variance increases as the velocity decreases, as predicted from Equation [7.2] for separation alone. The absolute magnitude is again smaller than for the corresponding system with separation alone (Figure 7.4B). The second moments for species B in Figure 7.15B show the curvature that results from the coupling of the reaction and separation processes. At short column lengths, all the systems appear to produce similar second moments for species B. The cause of this has been discussed previously in conjunction with Figure 7.15A. The second moments for species B at long column lengths decrease as the velocity increases, as seen for species A (Figure 7.14B). This implies that changes in the velocity affect the zones of species A and B in a similar manner. The magnitude of the variance for species B is greater than that for a system with separation alone, as seen previously. The increase in variance is caused by the coupling of the reaction and the movement of the zones of species A and B. Since $K_{abs,A} \neq K_{abs,B}$, an increase in the velocity enhances the difference

in the average velocity of the two species and increases the variance, as discussed previously.

The third moment or asymmetry for species A, shown in Figure 7.14C, also appears to be linearly related to distance. The third moments show the same general trends as the first and second moments. The third moments are smaller that those observed for systems with separation alone (Figure 7.4C). This results from the consumption of species A, as discussed previously. The third moments for species B in Figure 7.15C show that the faster velocities produce larger third moments. The third moments are much larger than those for systems with separation alone because of the greater difference in the average velocity of the two species, as discussed previously.

7.2.4 Comparison of Simulation and Theory.

Villermaux has presented a theory for reactive chromatography that allows for facile determination of the moments for a zone of species A as it elutes from a column.[24] The theory has been developed for systems with and without axial dispersion. The axial dispersion is either determined empirically for a given system, or it can be determined from the Peclet number. The results of the present simulation are compared to the theories with and without axial dispersion for systems with changes in the rate constant (k_r) and the column length (L).

The first simulations show the result of changes in the rate constant over the range of 0.01 to 10.0 s^{-1}, with absorption coefficients for species A and B of 1.0, a column length of 0.01 cm, and a velocity of 0.1 cm s^{-1}. The resulting moments for species A can

be seen in Table 7.5. As the rate constant is increased, the theory with axial dispersion predicts that the average velocity of the zone also increases. The largest rate constant results in a zone that moves through the column faster than the velocity of the fluid phase. The theory without axial dispersion also predicts that the average velocity of the zone increases as the rate constant increases. The largest rate constant results in a zone that moves through the column at the velocity of the fluid phase. The first moments from the simulation show a trend that is more similar to the theory without axial dispersion than the theory that includes axial dispersion. However, the first moments from the simulation are larger than those predicted by either theory.

The second and third moments from the simulation appear to be larger than those predicted by the theory without axial dispersion, but smaller than those predicted by the theory with axial dispersion. This trend suggests that there is some effect of axial dispersion on the second and third moments, as expected, but that the amount of axial dispersion is less than that predicted by the theory with axial dispersion. The latter theory assumes that mass transfer and reaction contribute independently to the axial dispersion in the system. The simulation does not make this assumption, so the discrepancy may be an indication of the interaction of mass transfer and reaction rates.

The statistical moments from the simulation are also calculated at different distances and are presented in Table 7.5. The distances range from 0.01 to 1.0 cm for a rate constant of 0.01 s^{-1}, with all other parameters as previously described. The first moments from all three approaches increase as the distance increases. The first moments from the simulation appear to be most similar in magnitude to those predicted by the

Table 7.5 Comparison of the Statistical Moments as Calculated From Classical Mass Balance[24] and Stochastic Simulation Approaches for Species A at Various Distances and Rate Constants (k_r).[a]

k_r (s^{-1})	Distance (cm)	Theory without axial dispersion			Theory with axial dispersion			Simulation		
		First Moment (s)	Second Moment (s^2)	Third Moment (s^3)	First Moment (s)	Second Moment (s^2)	Third Moment (s^3)	First Moment (s)	Second Moment (s^2)	Third Moment (s^3)
0.01	0.01	0.20	0.3	1.0	0.19	0.7	5.0	0.22 ± 0.01	0.6 ± 0.1	5 ± 2
0.1	0.01	0.177	0.19	0.7	0.160	0.48	2.8	0.181 ± 0.002	0.28 ± 0.05	1.8 ± 0.5
0.5	0.01	0.134	0.06	0.14	0.100	0.16	0.54	0.140 ± 0.007	0.04 ± 0.02	0.09 ± 0.07
1.0	0.01	0.117	0.020	0.04	0.078	0.087	0.20	0.125 ± 0.002	0.014 ± 0.004	0.02 ± 0.01
10	0.01	0.1004	0.00008	0.00002	0.0561	0.03758	0.05031	0.1090 ± 0.0004	0.00217 ± 0.00005	0.00019 ± 0.00003
0.01	0.01	0.20	0.3	1.0	0.19	0.7	5.0	0.22 ± 0.01	0.6 ± 0.1	5 ± 2
0.01	0.1	1.97	2.7	11	1.95	7.2	51	1.95 ± 0.04	4.9 ± 0.4	44 ± 12
0.01	1.0	19.72	27	113	19.49	72	508	19.31 ± 0.09	51 ± 3	471 ± 62

[a] Simulation conditions as described in Figure 7.6.

theory without axial dispersion at the shortest column length (0.01 cm). However, they appear to be most similar to the theory with axial dispersion at the longest column length (1.0 cm). This suggests that the first moment is affected by axial dispersion through a combination of reaction and mass transfer processes. The theory with axial dispersion due to independent contributions from reaction and mass transfer again overestimates the effect of these processes. The interaction of these processes is important, even in the first moment. The second and third moments for these simulations also fall between the two theoretical predictions, as seen previously.

7.3 Conclusions.

In this work, a novel stochastic simulation has been used to elucidate the effects of the different processes in reactive separations. This approach can be used to study the interaction of the processes of reaction and mass transfer with no implicit assumptions about their independence or interdependence. Since no assumptions are made, the simulation can be used to study systems that are limited by reaction or mass transfer as well as systems in which both processes are important. Any coupling of these processes occurs naturally within the framework of the simulation so that empirical fitting parameters are not necessary in determining the overall response of a reactive separation system. This is an improvement over existing theories that make simplifying assumptions about how the processes couple or which process is dominant within the system. Another benefit of this simulation method is that systems can be studied that are near to or far from steady-state conditions. The system is allowed to progress from the

kinetic region to the steady-state region with no inherent assumptions about the time evolution.

The most fundamental processes in reactive separations are reaction, mass transfer, and convective flow. These three processes couple to produce the zone profiles and moments that have been presented in this chapter. The dependence of the system response is best described by formulating a characteristic time for each process. The characteristic time for reaction can be defined as $\tau_r = 1/k_r$. The characteristic time for mass transfer can be defined as $\tau_m = 1/(k_{fs} + k_{sf})$, where k_{fs} and k_{sf} are the mass transfer rate constants from fluid to surface phase and from surface to fluid phase, respectively. Finally, the characteristic time for convective flow can be defined as $\tau_f = R_f/v_0$. The characteristic time that is the largest will have the greatest influence on the kinetic response of the system. The characteristic time can also elucidate the process that would most benefit from the use of optimization methods.

Some general points can be made about the relationship between the characteristic times for reaction, mass transfer, and convective flow. First, systems with irreversible reactions that are dominated by τ_r will produce zones for the reactant (species A) that are less broad and less asymmetric than the corresponding system with separation alone. Zones for the product (species B) will be broader and more asymmetric than the corresponding system with separation alone until the reactant has been consumed. Thereafter, a system with an irreversible reaction is no longer a reactive system and behaves as a system with separation alone. Second, the reactants in systems dominated by τ_m will appear less broad and less asymmetric than the corresponding system with

separation alone. The product zones in such systems will show more broadening and asymmetry over a period of the first few multiples of τ_m, but the zones will eventually become symmetric. Third, if τ_f dominates there will be negligible difference between the reactive separation and the system with separation alone. This insight can be used to optimize the reactive separation to obtain systems that produce higher yield and purity.

7.4 References.

1. Basset, D.N.; Habgood, H.W.; J. Phys. Chem. 1960, 64, 769.

2. Collins, C.G.; Dean, H.A.; AIChE J. 1968, 14, 25.

3. Coca, J.; Langer, S.H.; Chemtech 1983, 13, 682.

4. Coca, J.; Adrio, G.; Jeng, C.Y.; Langer, S.H.; in Preparative and Production Scale Chromatography, Chromatographic Science Series 61, Ganetsos, G.; Barker, P.E., Eds.; Marcel Dekker: New York, NY, 1993; p.449.

5. Yonovskii, M.I.; Berman, A.D.; in Preparative and Production Scale Chromatography, Chromatographic Science Series 61, G. Ganetsos and P.E. Barker, Eds.; Marcel Dekker: New York, NY 1993; p.523.

6. Katsanos, N.A.; Thede, R.; Roubani-Kalantzopoulou, F.; J. Chromatogr. A 1998, 795, 133.

7. Ganetsos, G.; Barker, P.E.; Ajongwen, J.N.; in Preparative and Production Scale Chromatography, Chromatographic Science Series 61, Ganetsos, G.; Barker, P.E. Eds.; Marcel Dekker: New York, NY 1993; p.375.

8. Hashimoto, K.; Adachi, S.; Shirai, Y.; in Preparative and Production Scale Chromatography, Chromatographic Science Series 61, Ganetsos, G.; Barker, P.E. Eds.; Marcel Dekker: New York, NY 1993; p.395.

9. Mazzotti, M.; Neri, B.; Gelosa, D.; Morbidelli, M.; Ind. Eng. Chem. Res. 1997, 36, 3163.

10. Barker, P.E.; Ganetsos, G.; Sep. Pur. Mthds. 1988, 17, 65.

11. Carr, R.W.; in Preparative and Production Scale Chromatography, Chromatographic Science Series 61, Ganetsos, G.; Barker, P.E. Eds.; Marcel Dekker: New York, NY, 1993; p.421.

12. Ray, A.K.; Carr, R.W.; Aris, R.; Chem. Eng. Sci. 1994, 49, 469.

13. Ray, A.K.; Carr, R.W.; Chem. Eng. Sci. 1995, 50, 2195.

14. Mazzotti, M.; Kruglov, A.; Neri, B.; Gelosa, D.; Morbidelli, M.; Chem. Eng. Sci. 1996, 51, 1827.

15. Kruglov, A.V.; Bjorklund, M.C.; Carr, R.W.; Chem. Eng. Sci. 1996, 51, 2945.

16. Magee, E.M.; Ind. Eng. Chem. Fundam. 1963, 2, 32.

17. Sardin, M.; Schweich, D.; Villermaux, J.; in Preparative and Production Scale Chromatography, Chromatographic Science Series 61, Ganetsos, G.; Barker, P.E. Eds.; Marcel Dekker: New York, NY 1993; p.477.

18. Keller, R.A.; Giddings, J.C.; Chromatogr. Rev. 1961, 3, 1.

19. Klinkenberg, A.; Chem. Eng. Sci. 1961, 15, 255.

20. Hattori, T.; Murakami, Y.; J. Catal. 1968, 12, 166.

21. Schweich, D.; Villermaux, J.; Ind. Eng. Chem. Fundam. 1978, 17, 1.

22. Binous, H.; McCoy, B.J.; Chem. Eng. Sci. 1992, 47, 4333.

23. Schweich, D.; Villermaux, J.; Sardin, M.; AIChE J. 1980, 26, 477.

24. Villermaux, J.; in Percolation Processes: Theory and Applications, Rodrigues, A.E.; Tondeur, D. Eds.; Sijthoff en Noordhoff, Alpen aan den Rijn, the Netherlands 1981; p.539.

25. Gore, F.E.; Ind. Eng. Proc. Des. Devel. 1967, 6, 10.

26. Kocirik, M.; J. Chromatogr. 1967, 30, 459.

27. Chu, C.; Tsang, L.C.; Ind. Eng. Chem. Proc. Des. Devel. 1971, 10, 47.

28. Carta, G.; Mahajan, A.J.; Cohen, L.M.; Byers, C.H.; Chem. Eng. Sci. 1992, 47, 1645.

29. Yang, H.; Peters, J.L.; Allen, C.; Chern, S.S.; Coalson, R.D.; Michael, A.C.; Anal. Chem. 2000, 72, 2042.

30. McGuffin, V.L.; Wu, P.; J. Chromatogr. A 1996, 722, 3.

31. McGuffin, V.L.; Krouskop, P.E.; Hopkins, D.L.; in Unified Chromatography, ACS Symposium Series 748, Parcher, J.F.; Chester, T.L. Eds.; American Chemical Society: Washington, DC 2000; p.37.

32. Krouskop, P.E.; McGuffin, V.L.; manuscript submitted, J. Chromatogr. A. 2001.

33. Steinfeld, J.I.; Francisco, J.S.; Hase, W.L.; Chemical Kinetics and Dynamics, Prentice Hall: Englewood Cliffs, NJ, 1989.

34. Wu, P.; McGuffin, V.L.; AIChE J. 1998, 44, 2053.

35. McGuffin, V.L.; Krouskop, P.E.; Wu, P. J.; Chromatogr. A 1998, 828, 37.

36. Golay, M.J.E.; in Gas Chromatography 1958; Desty, D.H., Ed.; Academic Press: New York, NY, 1958; p.36.

Chapter 8

Stochastic Simulation of Concurrent Reaction and Separation: The A ↔ B Reaction

8.1 Introduction.

The theories that have been developed to model reactive separation systems can be classified as those that solve mass balance equations and those that treat the system stochastically. The mass balance models are solved exactly or by various numerical methods to obtain zone profiles in distance and time together with the statistical moments. These models have been reviewed by Jeng and Langer.[1] These theories differ in the kinds of reactions that are simulated as well as the assumptions made about the system. One common assumption is that the mass transfer processes are at equilibrium and the reaction processes limit the system response.[2-6] Another common assumption is that the reaction processes are at equilibrium and the mass transfer processes limit the system response.[6-8] Some theories model both the mass transfer and reaction processes explicitly, but assume that axial dispersion is negligible or can be modeled by an effective dispersion term that is independent of the reaction.[8-12]

Recently, stochastic and random walk models have been applied to reactive separation systems.[13-15] In Chapter 7, the simulation was applied to a simple first-order irreversible reaction (A→B) and, in the present chapter, to a first-order reversible reaction (A↔B). There are several benefits that come from applying a stochastic model to reactive separations. First, stochastic simulations require few, if any, simplifying assumptions and can be designed to include all relevant reaction and mass transfer

processes. Accordingly, the systems may have reaction and mass transfer processes that are interdependent and may be near to or far from steady state. In addition, information concerning the molecular and macroscopic response of the systems can be readily obtained from the same simulation. Molecular-level information, such as residence times and reaction times of the individual molecules, can be determined by following the molecular trajectories through three-dimensional space and time. This detailed information about the history of each molecule can be used to elucidate how the individual molecules create the macroscopic response, such as zone profiles and statistical moments. The current chapter will demonstrate the power of this simulation by determining the molecular and macroscopic behavior of A $\leftrightarrow$ B reactive separation systems as a function of the rate constants, equilibrium constants, and absorption coefficients.

8.2 Results and Discussion.

The systems studied in this work begin with all molecules as species A in the fluid phase, and a reversible A$\leftrightarrow$B reaction occurs in the surface phase. The inner radius of the open tubular column is 2.00×10^{-3} cm and the thickness of the surface phase is 8.2834×10^{-4} cm, which yields a ratio of the phase volumes of 1.0. The diffusion coefficients for both species A and B are 1.00×10^{-5} and 1.00×10^{-7} cm^2 s^{-1} in the fluid and surface phases, respectively. The data presented in this chapter represent the average of triplicate simulations unless otherwise stated.

8.2.1 Molecular-Level Response.

Changes in the forward and reverse rate constants, equilibrium constant, and absorption coefficient affect the behavior of the individual molecules in the system. The results of changes in the parameters listed above on the molecular steady state and kinetics observed within the system are investigated below.

8.2.1.1 Steady-State Response.

The evolution of the system from the starting conditions to equilibrium or steady-state conditions can be studied.[16] To illustrate the data obtained from the simulation, Figure 8.1 shows the fraction of molecules in the fluid and the surface phases as a function of time for species A and B. The species simulated have a absorption coefficient of 1.0 and forward (k_f) and reverse (k_r) rate constants of 0.1 s^{-1}. Two distinct regions are evident, one where mass transfer and reaction kinetics are dominating, and one where the system is at steady state. In the kinetic region, the fraction of species A decreases and the fraction of species B increases in the fluid phase (Figure 8.1A). The graph for the surface phase (Figure 8.1B) shows that the fraction of species A initially increases as the molecules diffuse into the phase, but then decreases as the chemical reaction converts species A to B. The long-time data presented in Figure 8.1 also show the steady-state fractions of species A and B in each phase. These fractions are dependent on the equilibrium constant for the reaction and the absorption coefficient for each species as seen in Table 8.1. The theoretical steady-state distribution of molecules is given by

Figure 8.1: Stochastic simulation of (A↔B) reactive separations showing the fraction of molecules in the fluid phase (A) and surface phase (B) as species A (○) and species B (□). Other simulation conditions as follows: $t = 5.00\times10^{-4}$ s, N = 10000, $R_f = 2.00\times10^{-3}$ cm, $R_s = 8.2843\times10^{-4}$ cm, $D_f = 1.00\times10^{-5}$ cm^2 s^{-1}, $D_s = 1.00\times10^{-7}$ cm^2 s^{-1}, $K_{abs,A} = K_{abs,B} = 1.00$, $k_f = k_r = 0.1$ s^{-1}.

Figure 8.1

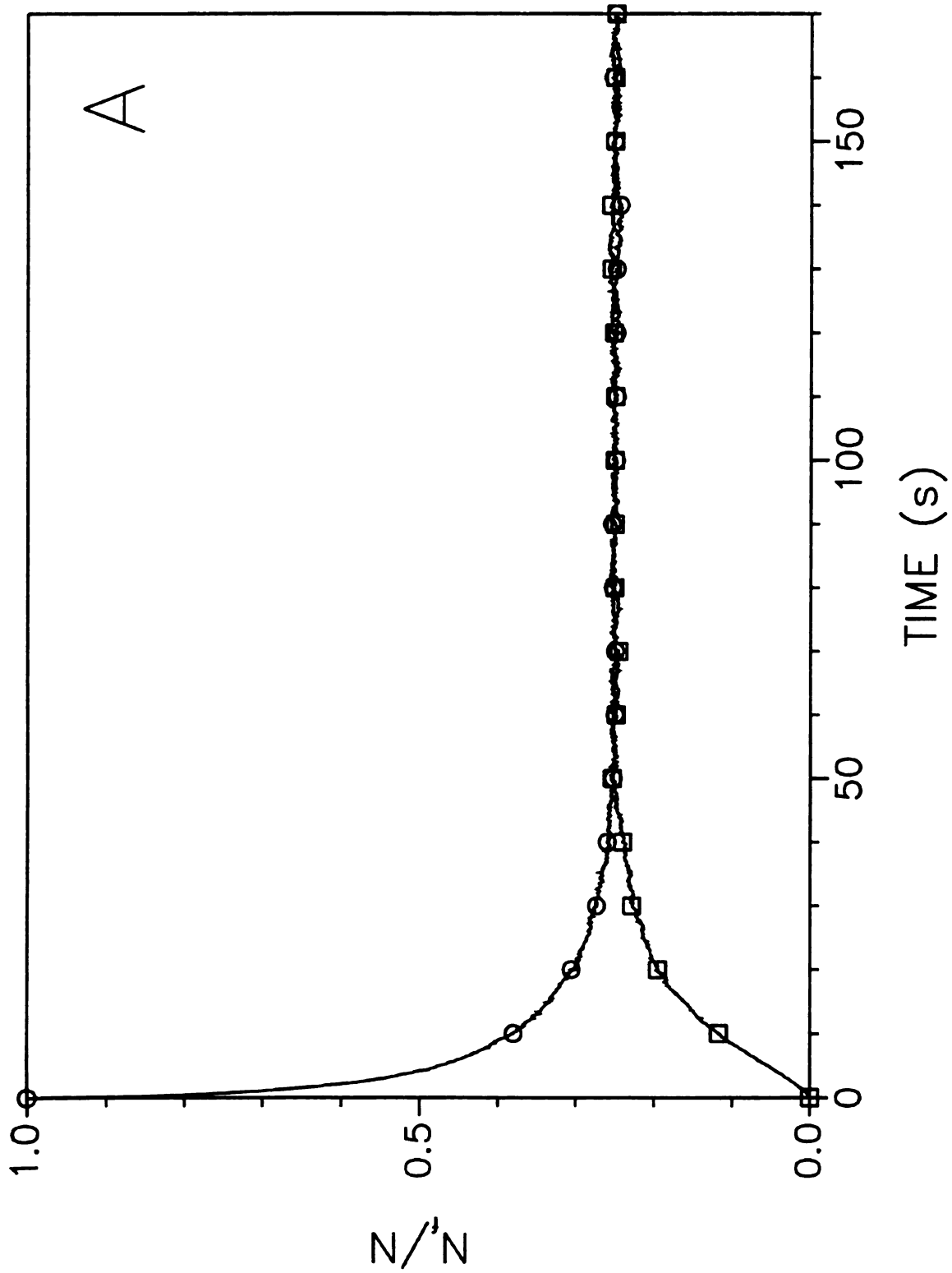

Figure 8.1 cont.

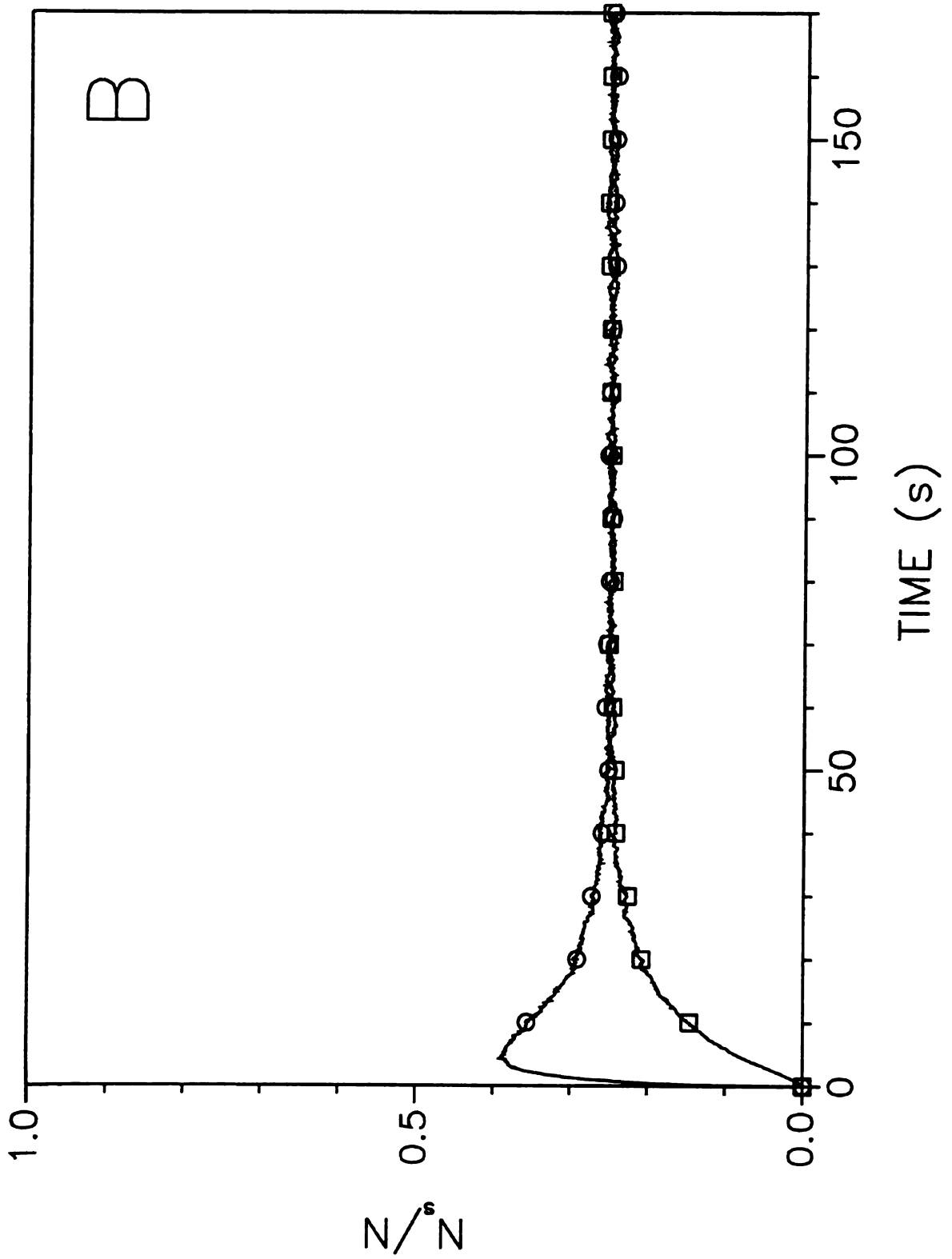

Table 8.1 Fraction of Species A and B in the Fluid and Surface Phases at Steady State as a Function of the Rate Constants (k_f, k_r) and the Absorption Coefficient for Species B ($K_{abs,B}$).[a]

					Fraction of Species A				Fraction of Species B			
					Fluid Phase		Surface Phase		Fluid Phase		Surface Phase	
$K_{abs,A}$	$K_{abs,B}$	k_f (s^{-1})	k_r (s^{-1})	K_{eq}	Simulation	Theory[b]	Simulation	Theory[c]	Simulation	Theory[d]	Simulation	Theory[e]
1.0	1.0	0.01	0.01	1.0	0.2541 ± 0.0014	0.2500	0.2513 ± 0.0015	0.2500	0.2469 ± 0.0016	0.2500	0.2476 ± 0.0012	0.2500
1.0	1.0	0.1	0.1	1.0	0.2494 ± 0.0010	0.2500	0.2512 ± 0.0023	0.2500	0.2494 ± 0.0021	0.2500	0.2499 ± 0.0014	0.2500
1.0	1.0	1.0	1.0	1.0	0.2496 ± 0.0009	0.2500	0.2499 ± 0.0017	0.2500	0.2513 ± 0.0020	0.2500	0.2491 ± 0.0008	0.2500
1.0	1.0	10.0	10.0	1.0	0.2487 ± 0.0011	0.2500	0.2514 ± 0.0012	0.2500	0.2491 ± 0.0009	0.2500	0.2507 ± 0.0003	0.2500
1.0	1.0	0.01	0.1	0.1	0.4571 ± 0.0029	0.4545	0.4551 ± 0.0031	0.4545	0.0440 ± 0.0012	0.0455	0.0439 ± 0.0002	0.0455
1.0	1.0	0.1	0.1	1.0	0.2494 ± 0.0010	0.2500	0.2512 ± 0.0023	0.2500	0.2494 ± 0.0021	0.2500	0.2499 ± 0.0014	0.2500
1.0	1.0	1.0	0.1	10.0	0.0457 ± 0.0004	0.0455	0.0449 ± 0.0007	0.0455	0.4558 ± 0.0034	0.4545	0.4536 ± 0.0028	0.4545
1.0	1.0	10.0	0.1	100	0.0048 ± 0.0002	0.0050	0.00495 ± 0.00007	0.00495	0.4960 ± 0.0007	0.4950	0.4943 ± 0.0010	0.4950
1.0	0.1	0.1	0.1	1.0	0.0770 ± 0.0010	0.0769	0.0775 ± 0.0006	0.0769	0.7790 ± 0.0180	0.7692	0.0763 ± 0.0005	0.0769
1.0	0.5	0.1	0.1	1.0	0.2017 ± 0.0012	0.2000	0.2014 ± 0.0044	0.2000	0.3964 ± 0.0040	0.4000	0.2004 ± 0.0008	0.2000
1.0	1.0	0.1	0.1	1.0	0.2494 ± 0.0010	0.2500	0.2512 ± 0.0023	0.2500	0.2494 ± 0.0021	0.2500	0.2499 ± 0.0014	0.2500
1.0	5.0	0.1	0.1	1.0	0.3101 ± 0.0021	0.3125	0.3138 ± 0.0008	0.3125	0.0620 ± 0.0007	0.0625	0.3141 ± 0.0024	0.3125

[a] Other simulation conditions as given in Figure 8.1.
[b] Calculated from Equation [8.1].
[c] Calculated from Equation [8.2].
[d] Calculated from Equation [8.3].
[e] Calculated from Equation [8.4].

$$\frac{\tilde{N}_{A,f}}{N} = \frac{K_{abs,B}}{K_{abs,B}\left(1+K_{abs,A}\right)+K_{abs,A}\,K_{eq}\left(1+K_{abs,B}\right)} \quad [8.1]$$

$$\frac{\tilde{N}_{B,f}}{N} = \frac{K_{abs,A}\,K_{abs,B}\,K_{eq}}{K_{abs,B}\left(1+K_{abs,A}\right)+K_{abs,A}\,K_{eq}\left(1+K_{abs,B}\right)} \quad [8.2]$$

$$\frac{\tilde{N}_{A,s}}{N} = \frac{K_{abs,A}\,K_{abs,B}}{K_{abs,B}\left(1+K_{abs,A}\right)+K_{abs,A}\,K_{eq}\left(1+K_{abs,B}\right)} \quad [8.3]$$

$$\frac{\tilde{N}_{B,s}}{N} = \frac{K_{abs,A}\,K_{eq}}{K_{abs,B}\left(1+K_{abs,A}\right)+K_{abs,A}\,K_{eq}\left(1+K_{abs,B}\right)} \quad [8.4]$$

where N is the total number of molecules, $\tilde{N}_{A,f}$ and $\tilde{N}_{B,f}$ are the steady-state number of molecules of A and B in the fluid phase, respectively, $\tilde{N}_{A,s}$ and $\tilde{N}_{B,s}$ are the steady-state number of molecules of A and B in the surface phase, respectively, $K_{abs,A}$ and $K_{abs,B}$ are the absorption coefficients for species A and B, respectively, and K_{eq} is the reaction equilibrium coefficient, which is equal to the ratio of the forward (k_f) and reverse (k_r) rate constants. It can be observed by comparison of simulation and theoretical results in Table 8.1 that the steady-state behavior of these systems is simulated accurately. The top of Table 8.1 shows that a change in the rate constants from 0.01 to 10.0 s^{-1} while keeping K_{eq} constant at 1.0 does not change the fraction of species A and B in each phase at steady state. The values of k_f and k_r affect the rate at which steady state is achieved, whereas the values of K_{eq} and $K_{abs,B}$ affect the steady-state fraction of species A and B in the fluid and surface phases. For systems in which K_{eq} increases from 0.1 to 100, shown in the middle of Table 8.1, the fraction of species A decreases in both phases while the fraction of species B increases in both phases. For systems in which $K_{abs,B}$ increases from 0.1 to 5.0, shown at the bottom of Table 8.1, the fraction of species A increases in both

phases. The fraction of species B decreases in the fluid phase and increases in the surface phase over the same range.

8.2.1.2 Kinetic Response.

To compare the rates at which the systems reach steady state, characteristic times are determined from data similar to those shown in Figure 8.1A. Times that correspond to 10% (T_{10}), 50% (T_{50}), and 90% (T_{90}) of the change from initial to steady-state conditions in the fluid phase are recorded. The average and standard deviation of the characteristic times are presented in Table 8.2. The value of T_{10} for species A is relatively constant for the systems that change k_f and k_r over the range from 0.01 to 10.0 s^{-1}, while keeping K_{eq} constant at 1.0. This indicates that the initial change in the concentration of species A in the fluid phase is not dependent on the rate of the reaction. The T_{10} times for species A are probably related to the mass transfer rate, which is the same for these systems. The values of T_{50} and T_{90} for species A decrease as the rate constants increase. This is expected, since faster reactions should reach steady state more rapidly. The characteristic times for species B all show a decrease with increasing rate constant. This is again expected, since the faster reaction rates equilibrate more rapidly. It is interesting to note that the characteristic T_{10} times for species B are not constant like those for species A. The T_{10} times for species B are dependent on the rate constant because the reaction to create species B is the limiting process, rather than mass transfer as in the case for species A.

Table 8.2: Characteristic Relaxation Times for Species A and B as a Function of the Rate Constants (k_f, k_r) and the Absorption Coefficient for Species B ($K_{abs,B}$).[a]

					Species A			Species B		
$K_{abs,A}$	$K_{abs,B}$	k_f (s^{-1})	k_r (s^{-1})	K_{eq}	T_{10} (s)	T_{50} (s)	T_{90} (s)	T_{10} (s)	T_{50} (s)	T_{90} (s)
1.0	1.0	0.01	0.01	1.0	0.063 ± 0.006	2.00 ± 0.06	121 ± 2	13.7 ± 0.8	71.8 ± 0.6	231 ± 2
1.0	1.0	0.1	0.1	1.0	0.060 ± 0.010	1.83 ± 0.04	16.4 ± 0.7	2.84 ± 0.09	10.7 ± 0.4	30 ± 1.1
1.0	1.0	1.0	1.0	1.0	0.063 ± 0.003	1.19 ± 0.01	4.9 ± 0.14	0.54 ± 0.03	2.22 ± 0.05	6.8 ± 0.3
1.0	1.0	10.0	10.0	1.0	0.055 ± 0.005	0.588 ± 0.008	2.5 ± 0.10	0.152 ± 0.008	0.48 ± 0.02	1.09 ± 0.05
1.0	1.0	0.01	0.1	0.1	0.033 ± 0.003	0.90 ± 0.01	6.0 ± 0.3	4.3 ± 0.1	15.3 ± 0.3	41 ± 4
1.0	1.0	0.1	0.1	1.0	0.060 ± 0.010	1.83 ± 0.04	16.4 ± 0.7	2.84 ± 0.09	10.7 ± 0.4	30 ± 1.1
1.0	1.0	1.0	0.1	10.0	0.097 ± 0.003	1.773 ± 0.006	7.14 ± 0.02	0.88 ± 0.04	3.37 ± 0.07	9.8 ± 0.3
1.0	1.0	10.0	0.1	100	0.078 ± 0.003	0.73 ± 0.010	2.56 ± 0.05	0.230 ± 0.005	0.74 ± 0.012	1.78 ± 0.03
1.0	0.1	0.1	0.1	1.0	0.100 ± 0.005	3.18 ± 0.04	36.2 ± 0.2	4.81 ± 0.08	19.1 ± 0.2	56.7 ± 0.5
1.0	0.5	0.1	0.1	1.0	0.06 ± 0.03	1.98 ± 0.05	21.2 ± 0.3	3.4 ± 0.12	12.82 ± 0.06	35.4 ± 0.9
1.0	1.0	0.1	0.1	1.0	0.060 ± 0.010	1.83 ± 0.04	16.4 ± 0.7	2.84 ± 0.09	10.7 ± 0.4	30 ± 1.1
1.0	5.0	0.1	0.1	1.0	0.048 ± 0.02	1.43 ± 0.04	11.5 ± 0.1	1.8 ± 0.2	7.25 ± 0.07	20.8 ± 0.2

[a] Other simulation conditions as given in Figure 8.1.

The value of K_{eq} is varied from 0.1 to 100 and the data can be seen in the middle of Table 8.2. The changes in K_{eq} are achieved by maintaining the reverse rate constant (k_r) at a value of 0.1 s^{-1} and allowing the forward rate constant (k_f) to vary from 0.01 to 10.0 s^{-1}. The characteristic times (T_{10}, T_{50}, and T_{90}) for species A attain a maximum value when k_f is between 0.1 and 1.0 s^{-1}. This maximum is caused by the combination of reaction and mass transfer rates. Since both rates are the same order of magnitude within this range (see Section 7.2.3),[14] the effect on the system is to increase the time for species A to reach equilibrium. When reaction is the rate-limiting process, as for the case with $k_f = 0.01$ s^{-1}, the characteristic times are equivalent to those for the reaction alone (see Section 7.2.1). When mass transfer is the rate-limiting process, as for the case with $k_f = 10.0$ s^{-1}, the system reaches equilibrium based on the mass transfer times (see Section 7.2.2). The characteristic times for species B are also presented in Table 8.2. The trends are similar to those seen previously for the systems with changes in both rate constants. This implies that K_{eq} as well as the individual values of k_f and k_r continue to play an important role in the development of the steady state for species B.

Finally, several systems are simulated with different absorption coefficients. The absorption coefficient for species B ranges from 0.1 to 5.0, while the absorption coefficient for species A remains constant at a value of 1.0. The data from these systems show that the characteristic times for both species decrease as the absorption coefficient for species B increases. This trend is related to the change in the fraction of molecules in each phase, as shown in Table 8.1. The decrease in the fraction of species A and B in the fluid phase with increasing $K_{abs,B}$ value serves to decrease the difference between the

initial and equilibrium conditions, thereby reducing the time required to achieve steady state.

8.2.1.3 Determination of Reaction Location.

To understand the reason for some of the trends discussed above, the simulation is used to determine the positions in the surface phase where the reaction occurs. The radial profiles are shown in Figures 8.2 and 8.3. The interface between the fluid and surface phase occurs at a radial distance of 2.00×10^{-3} cm. Radial distances less than this value are in the fluid phase where no reaction occurs, and distances greater are in the surface phase. Figures 8.2A and 8.2B show the number of A→B and B→A reactions, respectively, at times of 0.5, 1.0, 2.0, 5.0, and 10.0 τ. The characteristic time $\tau = 1/(k_f + k_r)$ is determined from the reaction rate constants ($k_f = k_r = 0.1\ s^{-1}$), which is 5.0 s for this system. The figures show that the total number of reactions in both directions increases as time increases. Figure 8.2A reveals that the mass transfer of the system causes the A→B reactions to occur near the interface at short times. Figure 8.2B exhibits little effect of mass transfer on the position of the B→A reaction in the surface phase.

The effects of mass transfer on the position of the reaction can be seen more clearly in Figure 8.3. In this figure, the radial profile of the A→B (Figure 8.3A) and B→A (Figure 8.3B) reactions occurring in 1.0 τ are displayed. It can be seen in Figure 8.3A that most of the A→B reactions occur very close to the interface for the fastest rate ($k_f = k_r = 10.0\ s^{-1}$). The reactions occur farther into the surface phase and become less concentrated at the interface as the rate constant decreases. The slowest reaction

Figure 8.2: Number of molecules of species A (A) and species B (B) reacting in the surface phase as a function of the radial position at 0.5 τ = 2.5 s ($\bigcirc$), 1.0 τ = 5.0 s ($\square$), 2.0 τ = 10.0 s ($\triangle$), 5.0 τ = 25.0 s ($\diamond$), 10.0 τ = 50.0 s ($\triangledown$). Other simulation conditions as given in Figure 8.1.

Figure 8.2

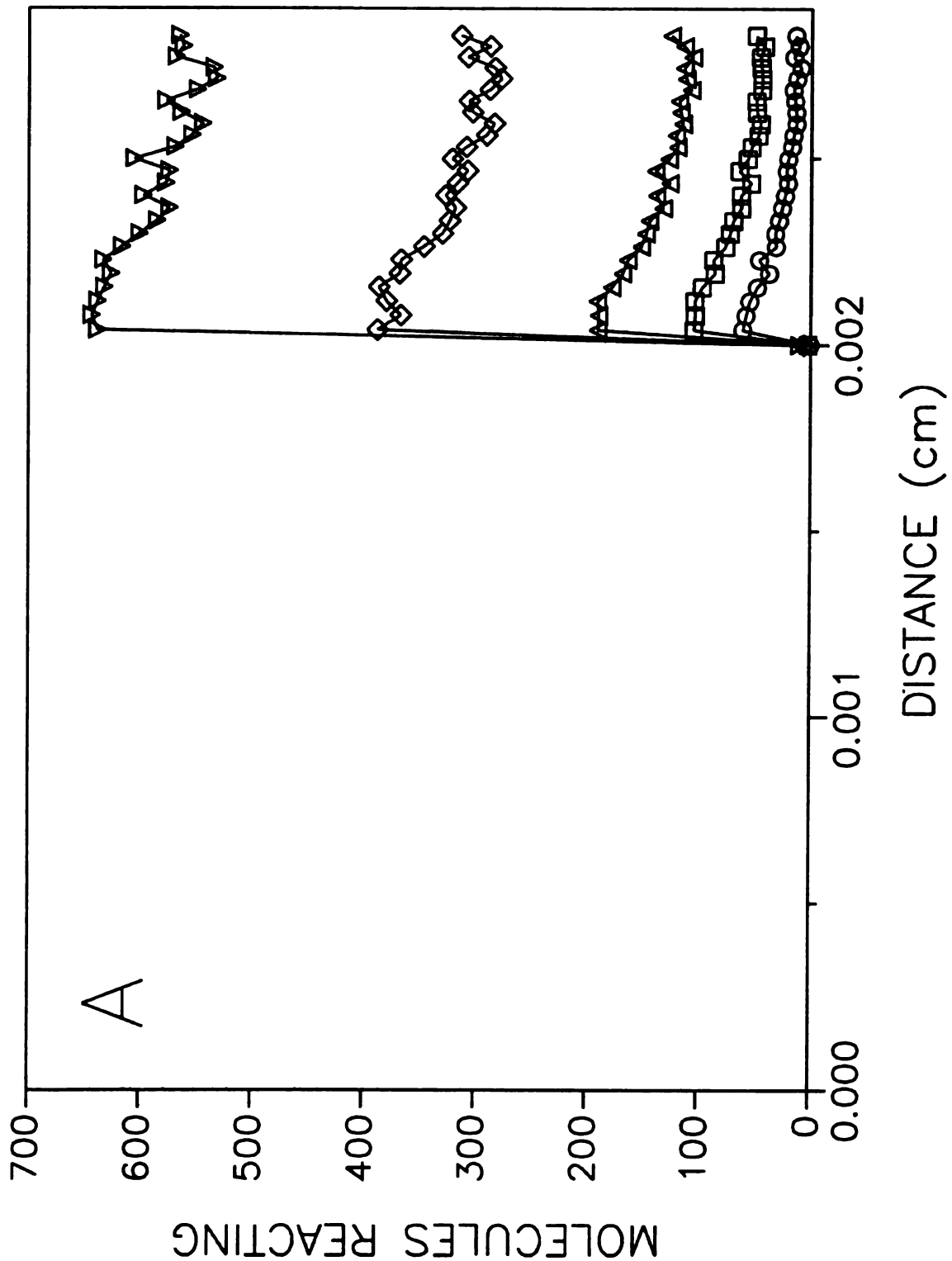
A
MOLECULES REACTING
700
600
500
400
300
200
100
0
0.000
0.001
0.002
DISTANCE (cm)

Figure 8.2 cont.

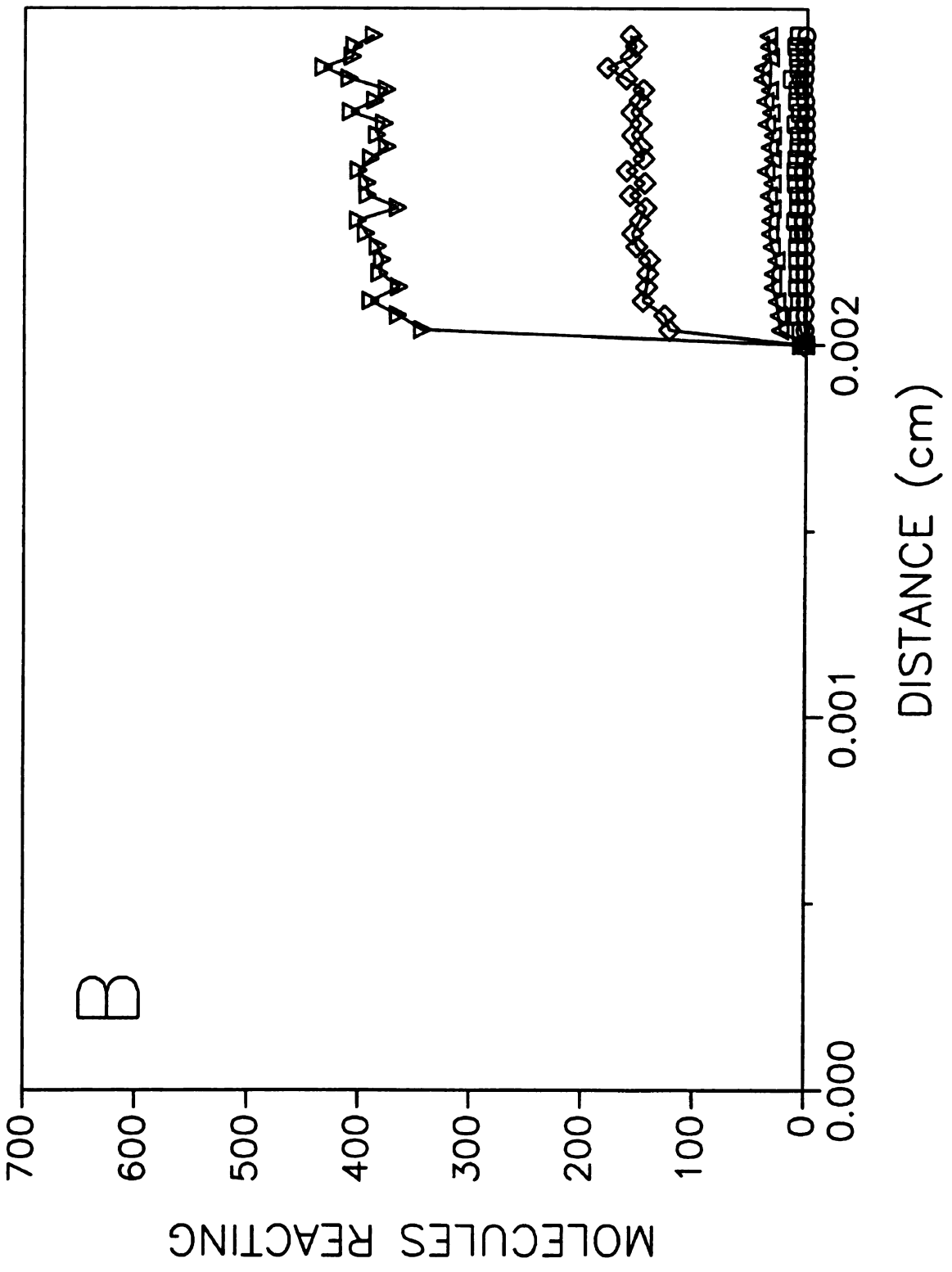

Figure 8.3: Number of molecules of species A (A) and species B (B) reacting within 1.0 τ in the surface phase as a function of the radial position for rate constants of $k_f = k_r = 0.01\ s^{-1}$ (○), $k_f = k_r = 0.1\ s^{-1}$ (□), $k_f = k_r = 1.0\ s^{-1}$ (△), $k_f = k_r = 10.0\ s^{-1}$ (◇). Other simulation conditions as given in Figure 8.1.

Figure 8.3

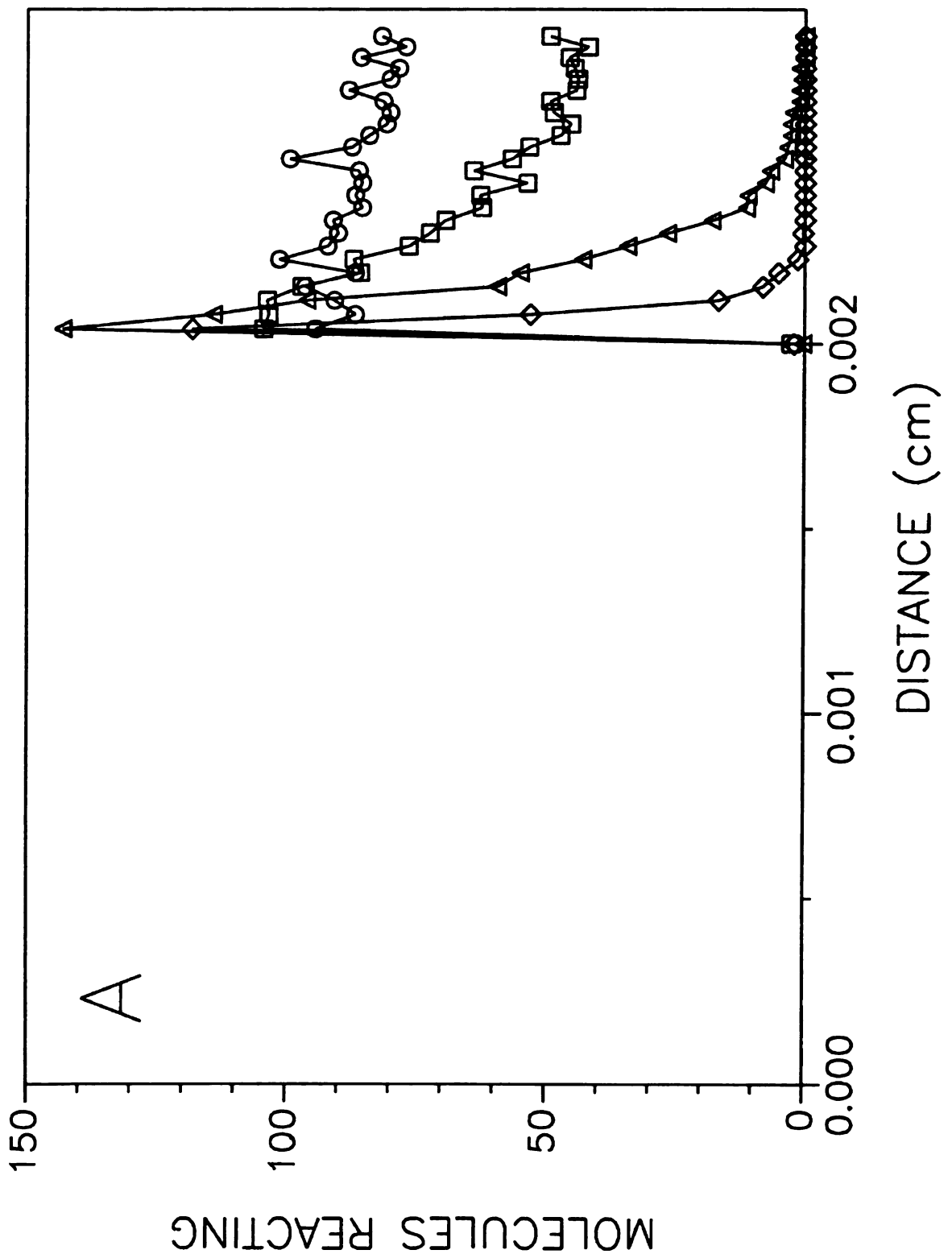

Figure 8.3 cont.

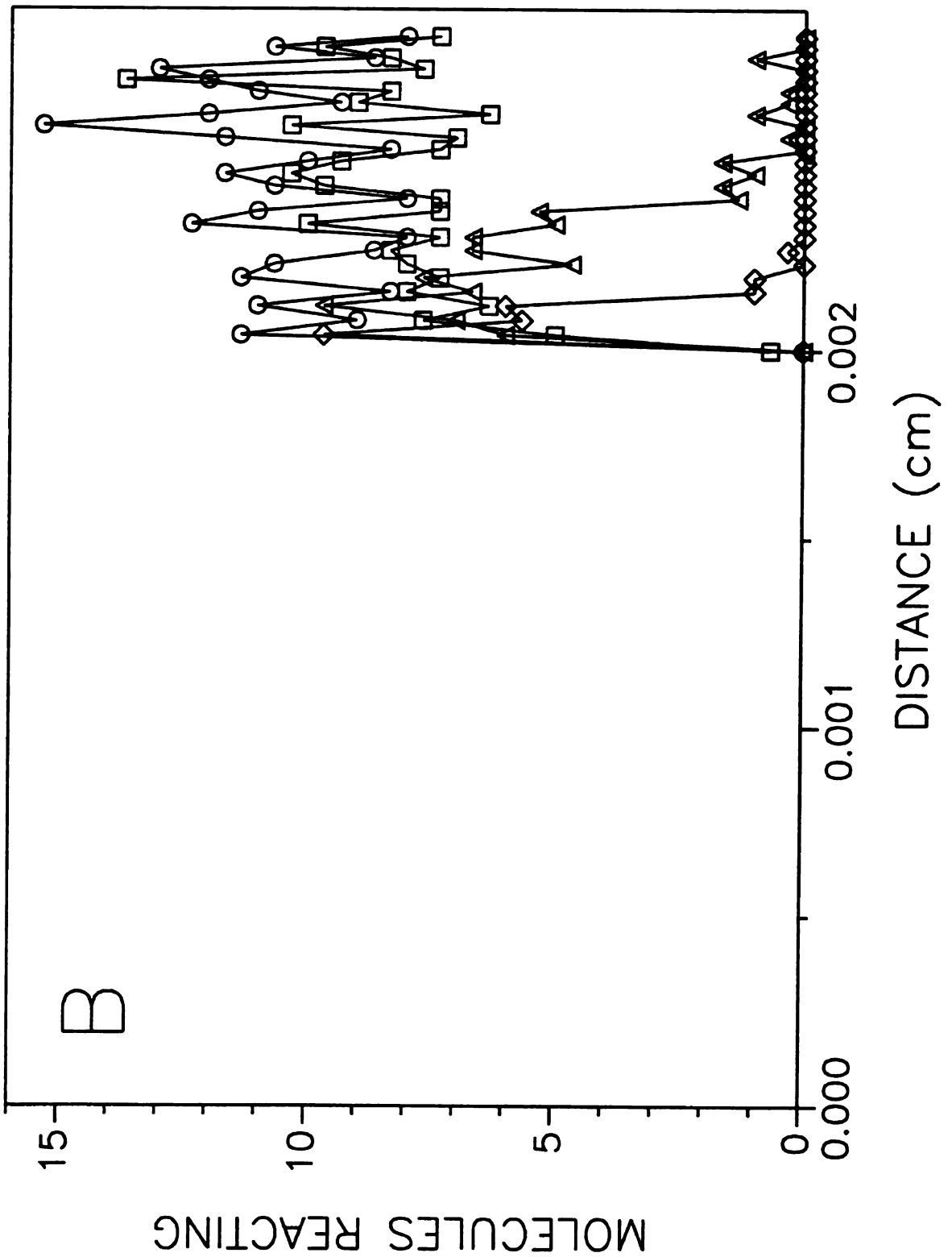

($k_f = k_r = 0.01\ s^{-1}$) has a flat profile, signifying that the A→B reaction occurs uniformly throughout the surface phase. This suggests that the position of the reaction is no longer dependent on mass transfer. The same general trends are shown for the B→A reaction in Figure 8.3B, but a flat profile is reached in a system with larger rate constants ($k_f = k_r = 0.1\ s^{-1}$). Figure 8.3 also shows that there are fewer B→A reactions than A→B reactions within 1.0 τ. The large difference in the number of reactions is a result of the delay introduced by the lack of species B at the beginning of the simulation. Finally, the data presented in this figure show that the system with $k_f = k_r = 0.01\ s^{-1}$ can be treated with equilibrium theories of separation, and the system with $k_f = k_r = 10.0\ s^{-1}$ can be treated with equilibrium theories of reaction. The systems between these two will show deviations from either theory, since both mass transfer and reaction rate are important in the progression of the system to steady state.

8.2.1.4 Determination of Residence Times.

The simulation can also be used to determine the time that each molecule resides in each phase as well as the average time. Figures 8.4A and 8.4B display the fluid-phase residence time distribution for species A and B, respectively, for a system with forward and reverse rate constants of $0.1\ s^{-1}$ and absorption coefficients of 1.0 for both species. These distributions indicate that the most probable residence time is one time increment (5.0×10^{-5} s), and that the probability decreases as the residence time increases for both species. Figures 8.5A and 8.5B depict the surface-phase residence time distribution for species A and B, respectively, for the same system. The most probable residence time in

Figure 8.4: Fluid-phase residence time distribution for species A (A) and species B (B). Other simulation conditions as given in Figure 8.1.

Figure 8.4

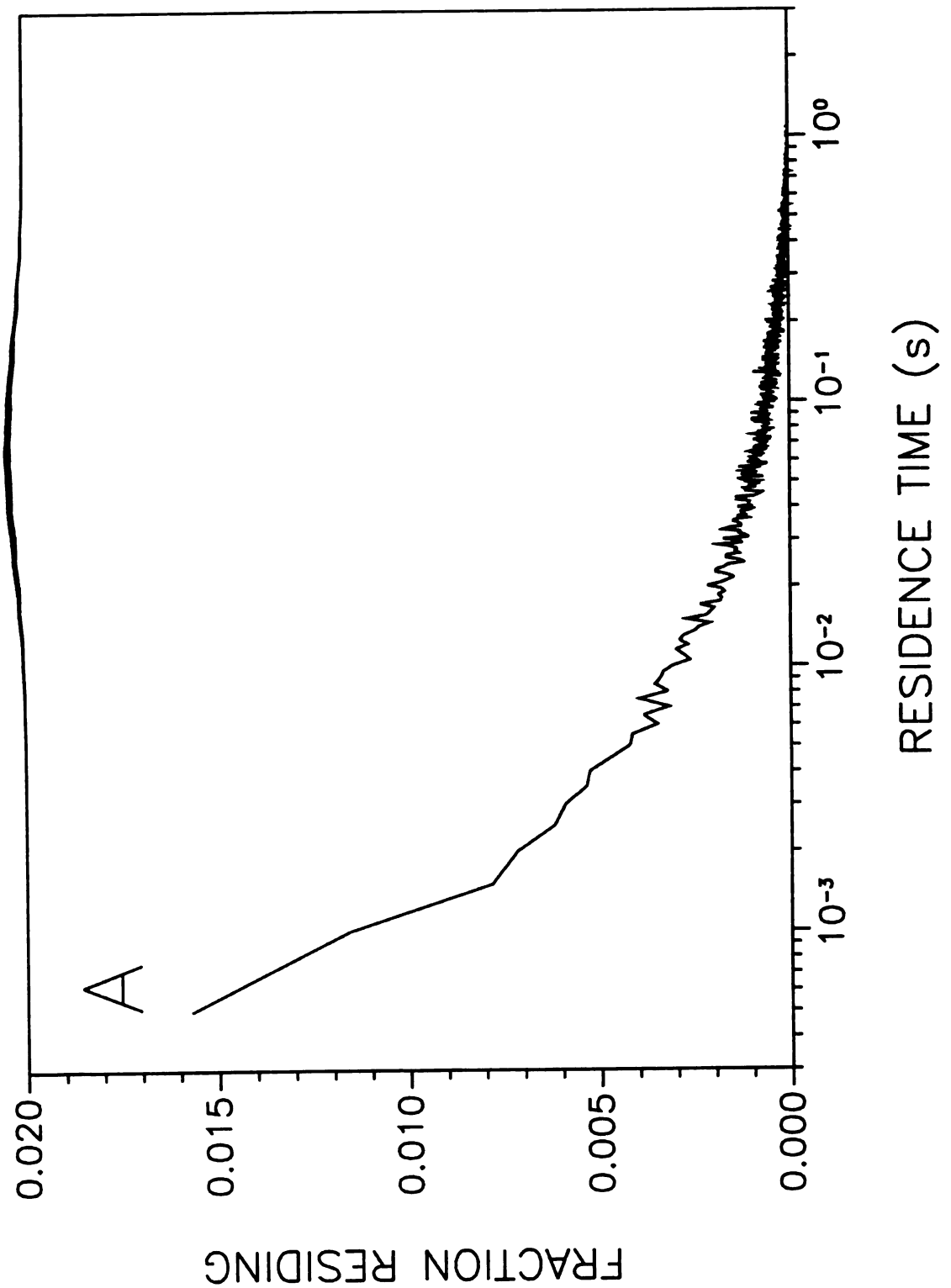
A
0.020
0.015
0.010
0.005
0.000
FRACTION RESIDING
10^{-3}
10^{-2}
10^{-1}
10^{0}
RESIDENCE TIME (s)

Figure 8.4 cont.

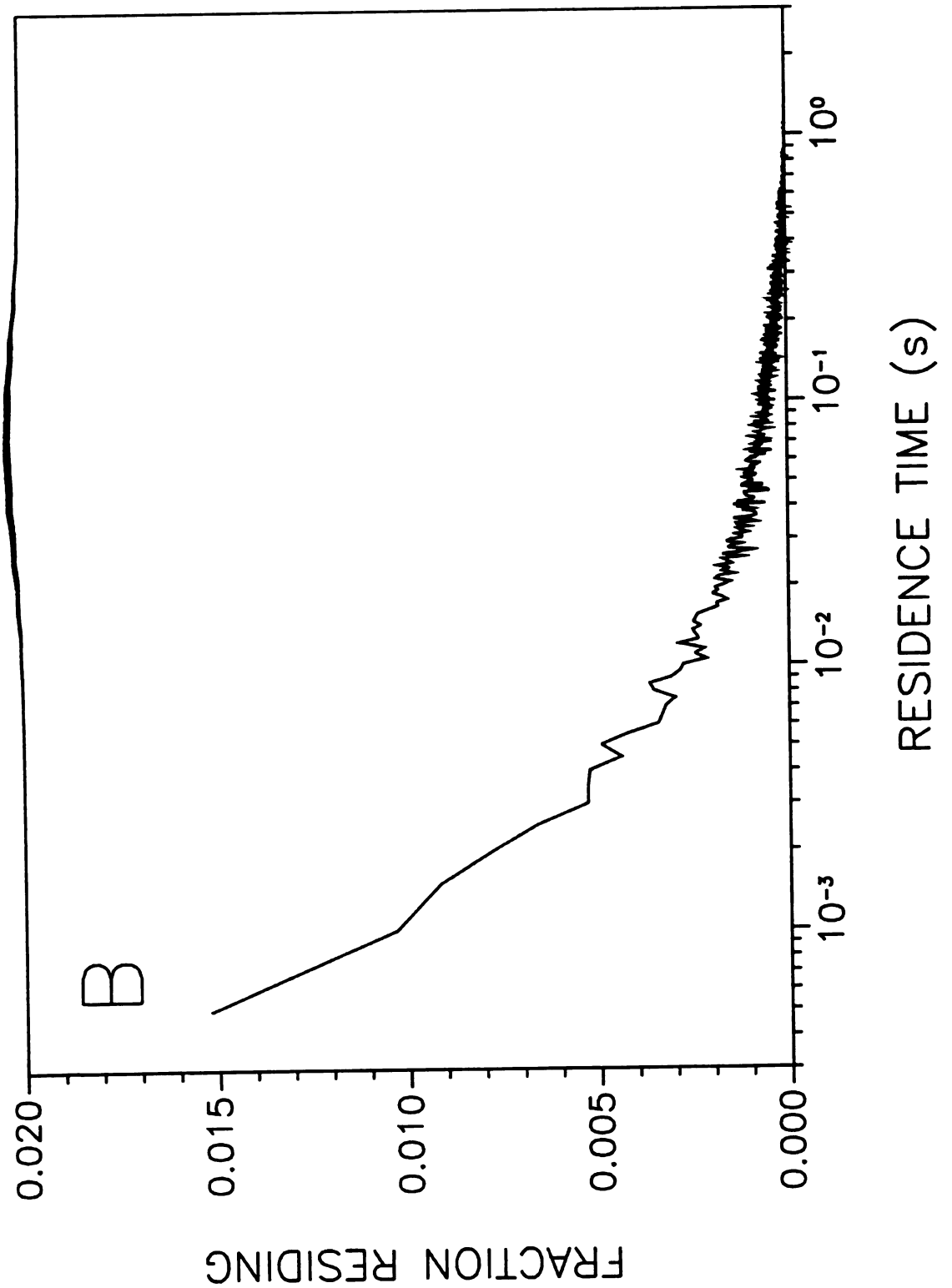

Figure 8.5: Surface-phase residence time distribution for species A (A) and species B (B) (——) together with the fraction of molecules reacting as a function of the surface-phase residence time (○). Other simulation conditions as given in Figure 8.1.

Figure 8.5

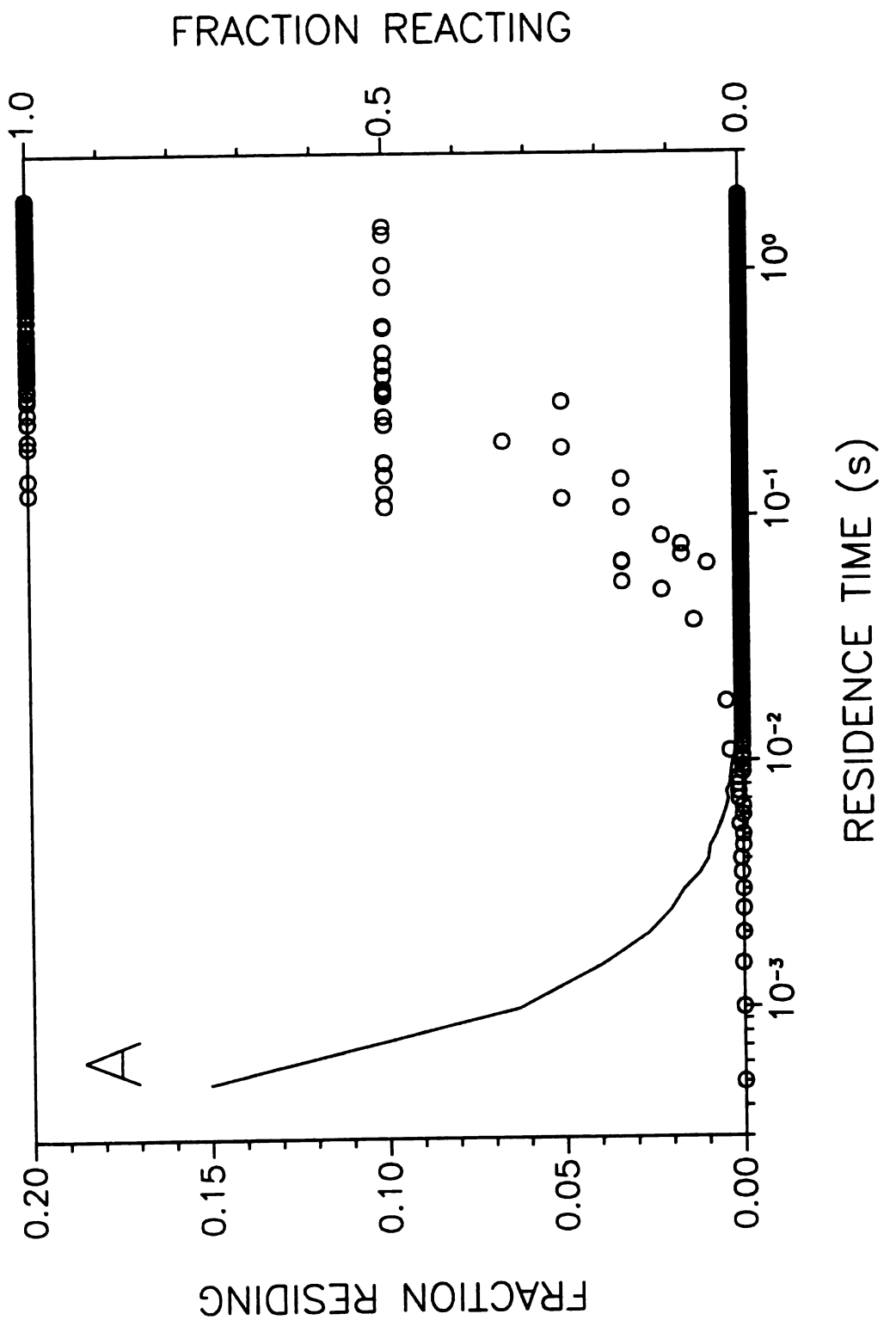
FRACTION REACTING
1.0
0.5
0.0
0.20
0.15
0.10
0.05
0.00
FRACTION RESIDING
10^{0}
10^{-1}
10^{-2}
10^{-3}
RESIDENCE TIME (s)
A

Figure 8.5 cont.

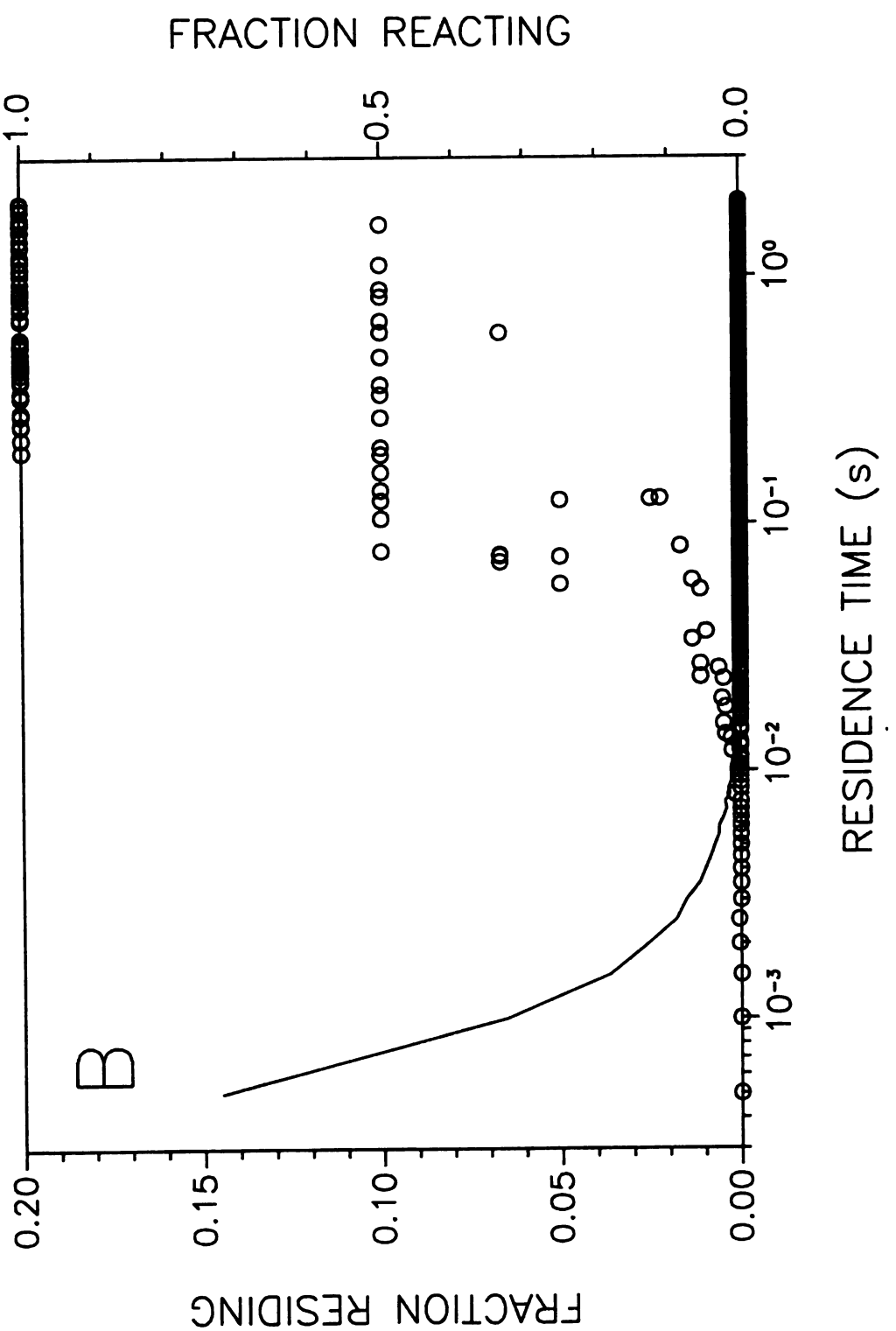

the surface phase is also one time increment. The most probable residence times in the fluid and surface phases indicate that the molecules remain close to the interface and usually transfer across the interface several times before diffusing away. The residence time distributions in Figure 8.4 and 8.5 are used to obtain the average residence time for each species. These averages are presented in Table 8.3 for systems in which the rate constants, equilibrium constants, and absorption coefficients are varied. It is noteworthy that the average residence time for each species is much greater than one time increment. This implies that there are some molecules of each species that remain in the fluid and surface phases much longer than the most probable time. The molecules with long residence times appear to be the driving force behind the average response of the systems. The average residence times in the fluid phase for species A do not appear to vary. However, the average residence times in the surface phase decrease slightly with increasing rate constant and increasing K_{eq}. The average residence times for species B are generally similar to those for species A, except for systems in which $K_{abs,B}$ changes. The average fluid-phase residence times for species B appear to vary inversely with $K_{abs,B}$, while the surface-phase residence times remain constant. Accordingly, the ratio of the average time in the surface and fluid phases is equal to $K_{abs,B}$, as expected. It is interesting to note that the time in the fluid phase is changing to accommodate the change in absorption coefficient, rather than the time in the surface phase.

Figure 8.5 also portrays the probability that a molecule will react as a function of the residence time in the surface phase. The graphs illustrate that the most probable sojourn time in the surface phase is the least likely to produce a reaction. The probability

Table 8.3 Average Residence Times for Species A and B in the Fluid and Surface Phases as a Function of the Rate Constants (k_f, k_r) and the Absorption Coefficient for Species B ($K_{abs,B}$).[a]

					Residence Times for Species A (s)		Residence Times for Species B (s)	
$K_{abs,A}$	$K_{abs,B}$	k_f (s^{-1})	k_r (s^{-1})	K_{eq}	Fluid phase	Surface phase	Fluid phase	Surface phase
1.0	1.0	0.01	0.01	1.0	0.13 ± 0.16	0.13 ± 0.8	0.13 ± 0.16	0.13 ± 0.8
1.0	1.0	0.1	0.1	1.0	0.13 ± 0.16	0.12 ± 0.7	0.13 ± 0.16	0.13 ± 0.7
1.0	1.0	1.0	1.0	1.0	0.13 ± 0.16	0.12 ± 0.6	0.13 ± 0.16	0.12 ± 0.6
1.0	1.0	10.0	10.0	1.0	0.13 ± 0.16	0.11 ± 0.6	0.13 ± 0.16	0.11 ± 0.6
1.0	1.0	0.01	0.1	0.1	0.13 ± 0.16	0.12 ± 0.8	0.13 ± 0.16	0.12 ± 0.7
1.0	1.0	0.1	0.1	1.0	0.13 ± 0.16	0.12 ± 0.7	0.13 ± 0.16	0.13 ± 0.7
1.0	1.0	1.0	0.1	10.0	0.13 ± 0.16	0.11 ± 0.4	0.13 ± 0.16	0.12 ± 0.8
1.0	1.0	10.0	0.1	100	0.13 ± 0.16	0.06 ± 0.10	0.13 ± 0.16	0.13 ± 0.8
1.0	0.1	0.1	0.1	1.0	0.13 ± 0.16	0.12 ± 0.7	1.3 ± 1.3	0.12 ± 0.7
1.0	0.5	0.1	0.1	1.0	0.13 ± 0.16	0.12 ± 0.7	0.3 ± 0.3	0.13 ± 0.7
1.0	1.0	0.1	0.1	1.0	0.13 ± 0.16	0.12 ± 0.7	0.13 ± 0.16	0.13 ± 0.7
1.0	5.0	0.1	0.1	1.0	0.13 ± 0.16	0.12 ± 0.7	0.03 ± 0.05	0.12 ± 0.7

[a] Other simulation conditions as given in Figure 8.1.

of reacting within one sojourn reaches unity at a time much longer than the most probable residence time (5.0×10^{-5} s) and slightly longer than the average residence time (~ 0.13 s). The residence time required to guarantee that reaction occurs is 0.197 s for both species A and B.

8.2.2 Macroscopic-Level Response.

The fluid dynamic response of the reactive separation systems is studied by recording the time that each molecule elutes from column lengths of 0.1, 0.2, 0.5, 1.0, 2.0, and 5.0 cm. The recorded times are then used to create zone profiles and to calculate the corresponding statistical moments. Zone profiles obtained at these distances for a system with $k_f = k_r = 0.1\ s^{-1}$ and $K_{abs,A} = K_{abs,B} = 1.0$ can be viewed in Figures 8.6A and 8.6B for species A and B, respectively. Since the system begins with all molecules as species A, the zones of species A are expected to show a decrease in height due to the reaction. However, it is difficult to distinguish the cause of the decrease in peak height in Figure 8.6A, since both reaction and broadening cause the same effect. It is apparent that the initial profiles for species A are very asymmetric, and do not become symmetric until 5.0 cm. Species B is expected to increase in height due to the reaction as shown in the initial profiles (0.1 to 1.0 cm) in Figure 8.6B. The decrease in height at longer column lengths (2.0 and 5.0 cm) is the result of broadening of the zone profile without an increase in the number of B molecules. The 1.0 cm distance corresponds to a time that is on the order of T_{90} for the system. Thus, the system has nearly reached steady state and there will be little further increase in the number of B molecules in the system. Figure 8.6B

Figure 8.6: Zone profiles for species A (A) and species B (B) in reactive separation systems with column lengths of 0.1, 0.2, 0.5, 1.0, 2.0, and 5.0 cm (left to right). Other simulation conditions as follows: $t = 5.00\times10^{-5}$ s, N = 4000, $R_f = 2.00\times10^{-3}$ cm, $R_s = 8.2843\times10^{-4}$ cm, $D_f = 1.00\times10^{-5}$ cm^2 s^{-1}, $D_s = 1.00\times10^{-7}$ cm^2 s^{-1}, $K_{abs,A} = K_{abs,B} = 1.00$, $k_f = k_r = 0.1$ s^{-1}.

Figure 8.6

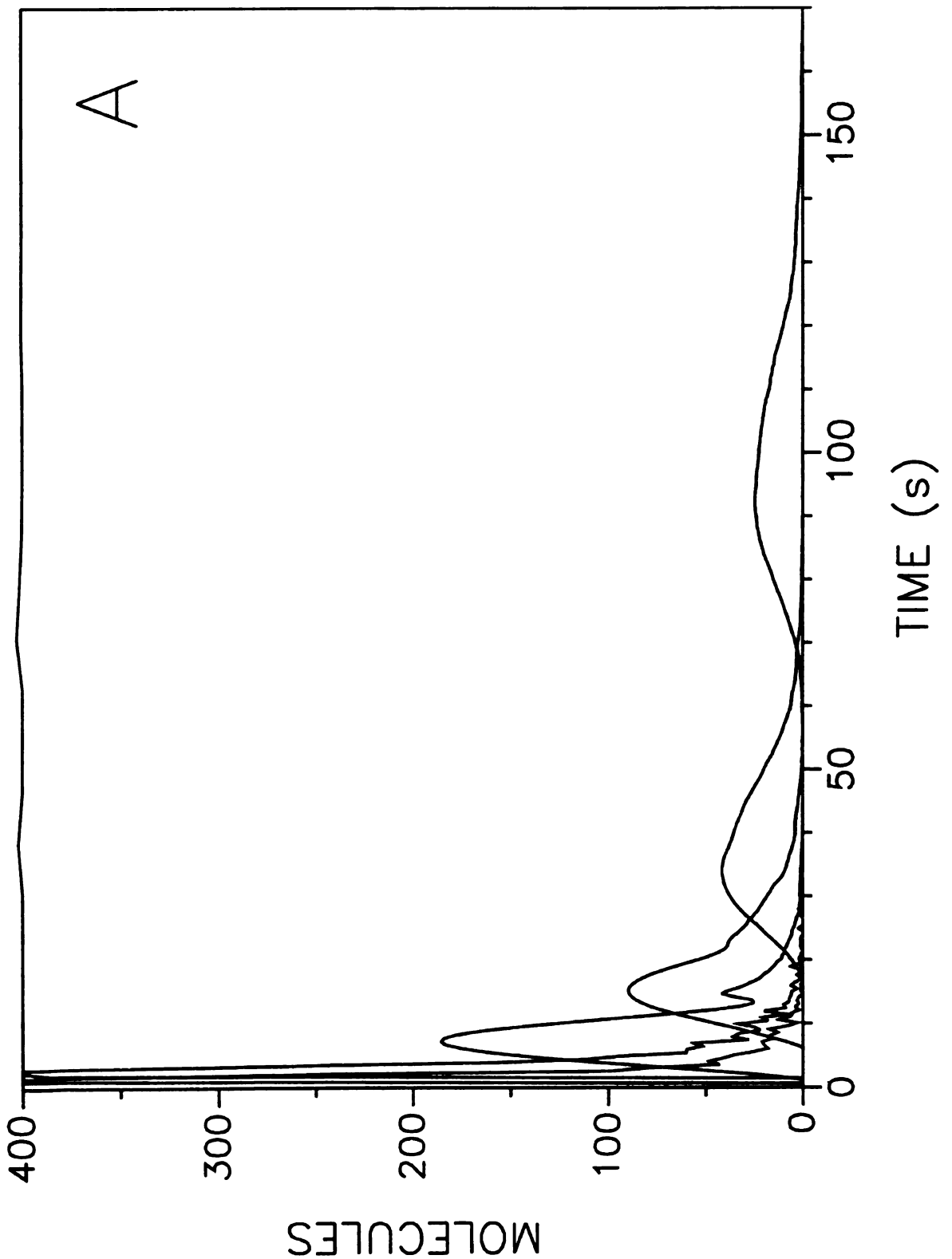

Figure 8.6 cont.

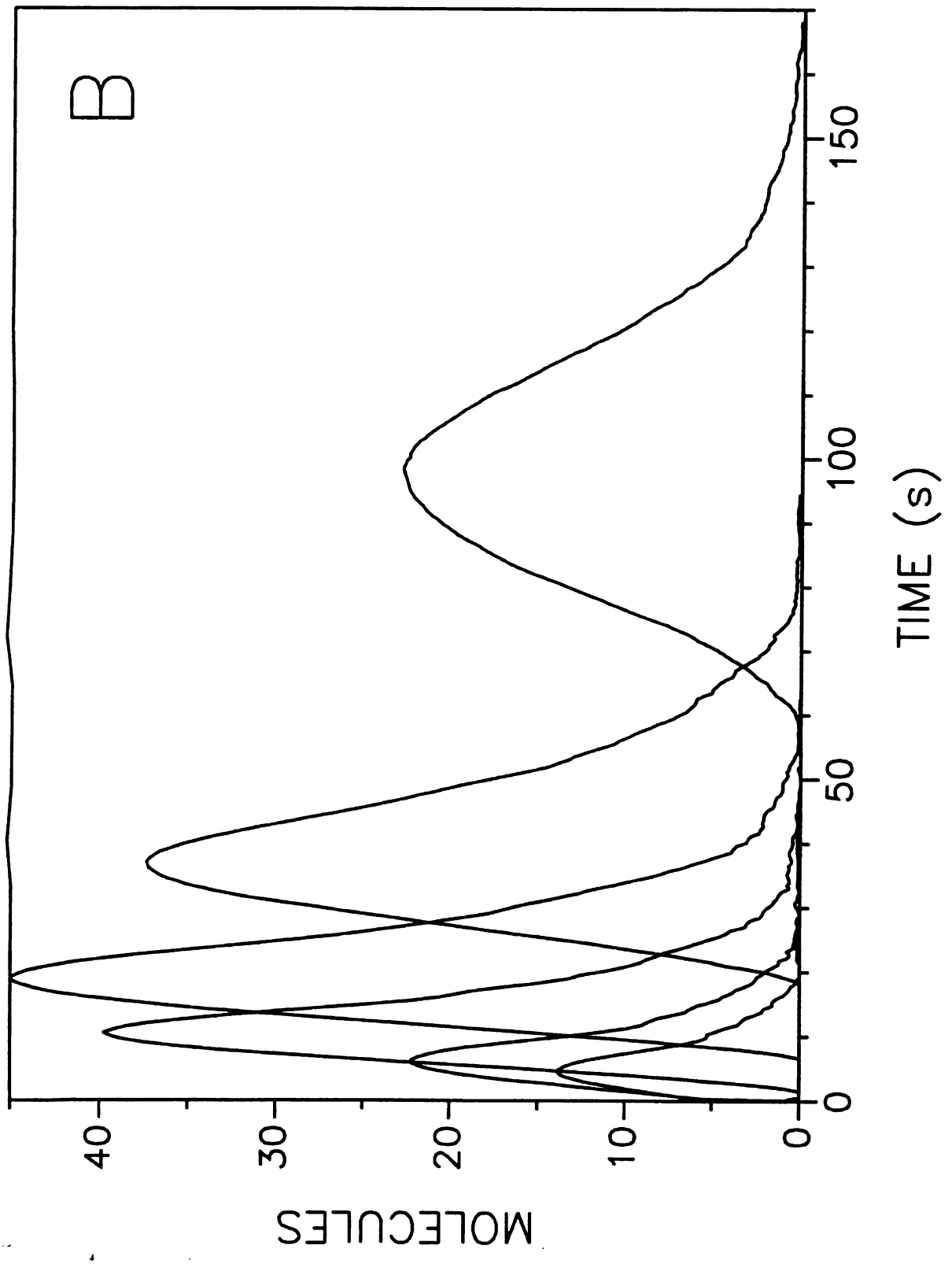

also shows that the initial zones for species B are asymmetric, although not as pronounced as for species A. The profiles for species B become symmetric at the same time as those for species A, since the two species are linked through the chemical reaction.

8.2.2.1 Effect of Changes in Reaction Rate Constant.

The statistical moments for the system discussed above as well as others in which the forward and reverse rate constants are equal are presented in Figures 8.7 and 8.8. The values of k_f and k_r for these systems range from 0.01 to 10.0 s^{-1}. Figure 8.7A shows that the first moment or mean elution time for species A in each system is relatively constant. Although the first moments show a slight difference at a column length of 0.1 cm, they are statistically equivalent by 2.0 cm. This illustrates that the velocity of species A through the column is not greatly affected by the change in rate constant. The first moments for species B in Figure 8.8A, however, show a substantial dependence on the rate constant, especially at short column lengths (0.1 to 0.5 cm). As the rate constant decreases, the time required for species A to react to form species B increases. This implies that molecules must remain in the surface phase longer to react, resulting in the increase in the mean elution time. Moreover, the elution time for species B is substantially greater than that for species A at short column lengths. As column length increases and the systems reach steady state, these differences disappear and the first moments of the systems converge.

Figure 8.7: First (A), second (B), and third (C) statistical moments as a function of distance for species A in reactive separations with the following rate constants: $k_f = k_r =$ 0.01 s^{-1} (○), $k_f = k_r = 0.1$ s^{-1} (□), $k_f = k_r = 1.0$ s^{-1} (△), $k_f = k_r = 10.0$ s^{-1} (◇). Other simulation conditions as given in Figure 8.6.

Figure 8.7

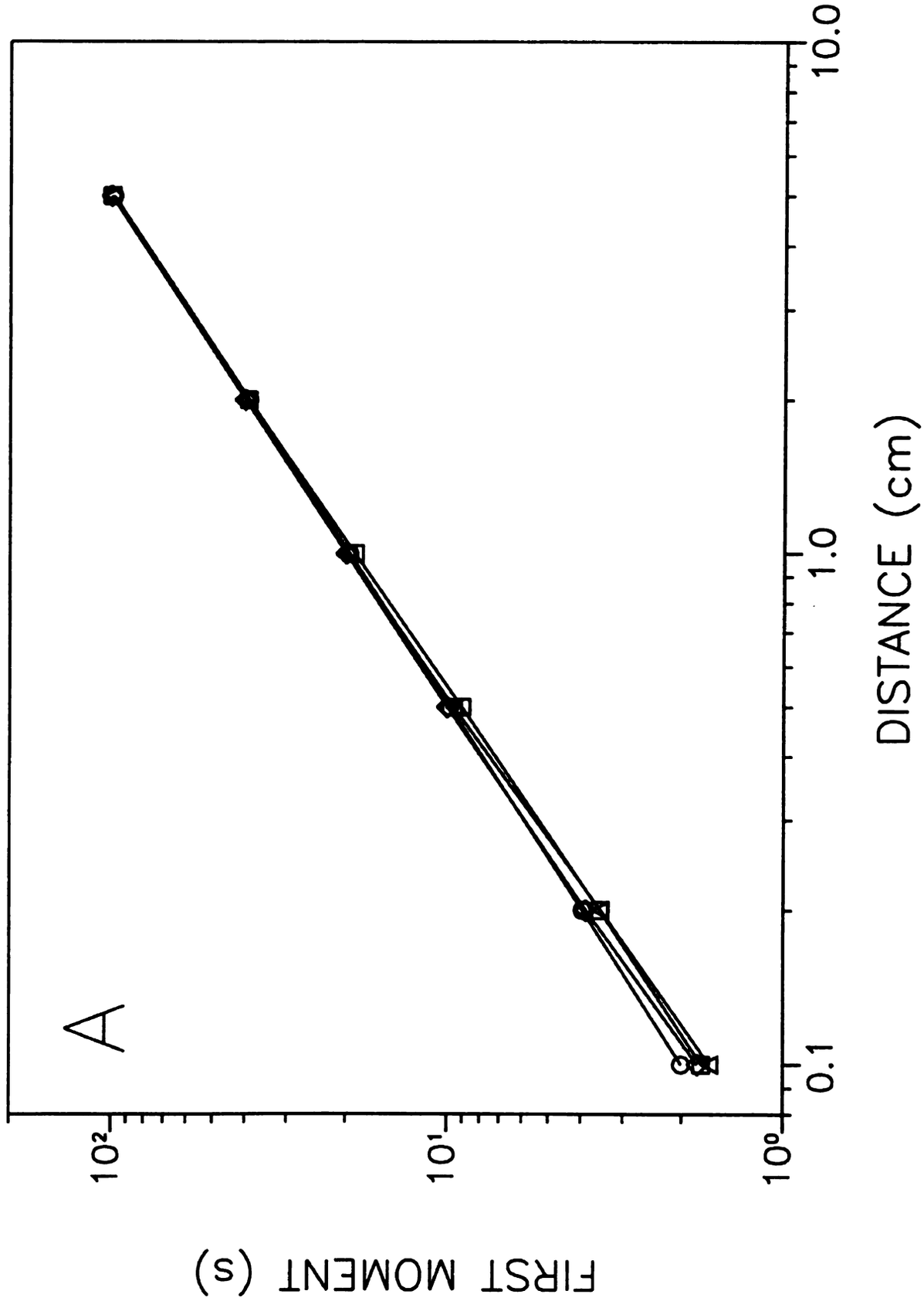

Figure 8.7 cont.

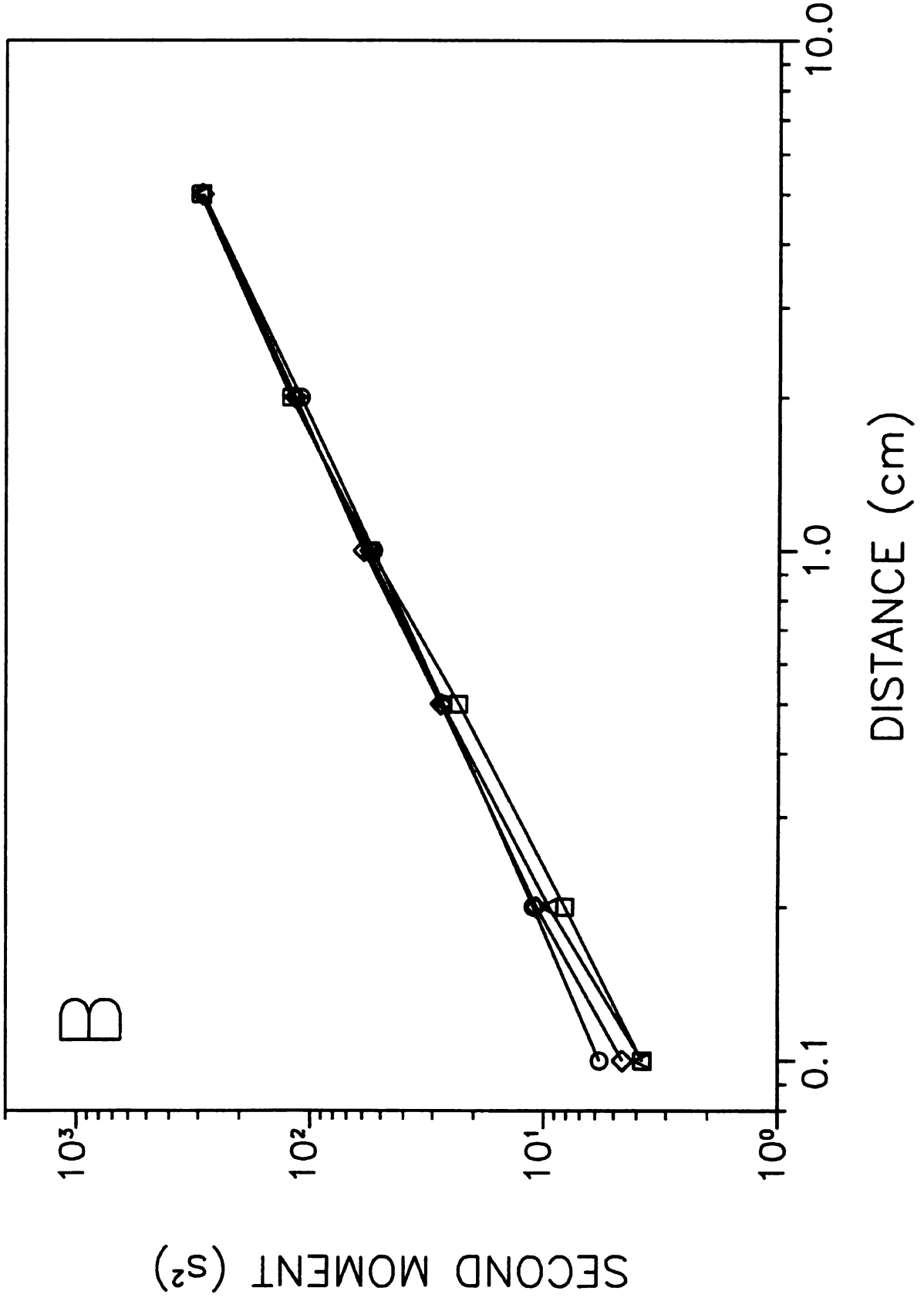

Figure 8.7 cont.

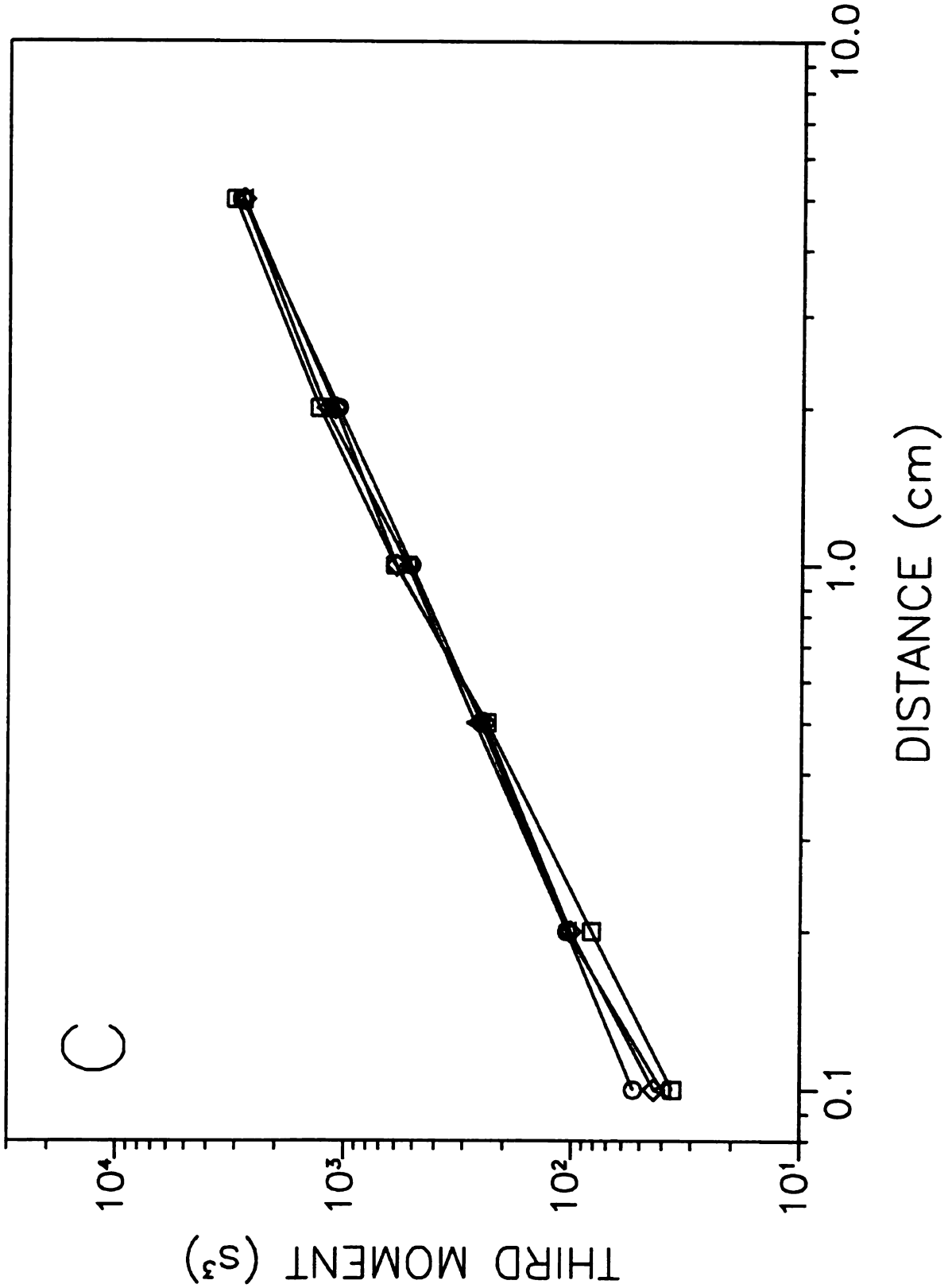

Figure 8.8: First (A), second (B), and third (C) statistical moments as a function of distance for species B in reactive separations with the following rate constants: $k_f = k_r =$ 0.01 s^{-1} (○), $k_f = k_r = 0.1$ s^{-1} (□), $k_f = k_r = 1.0$ s^{-1} (△), $k_f = k_r = 10.0$ s^{-1} (◇). Other simulation conditions as given in Figure 8.6.

Figure 8.8

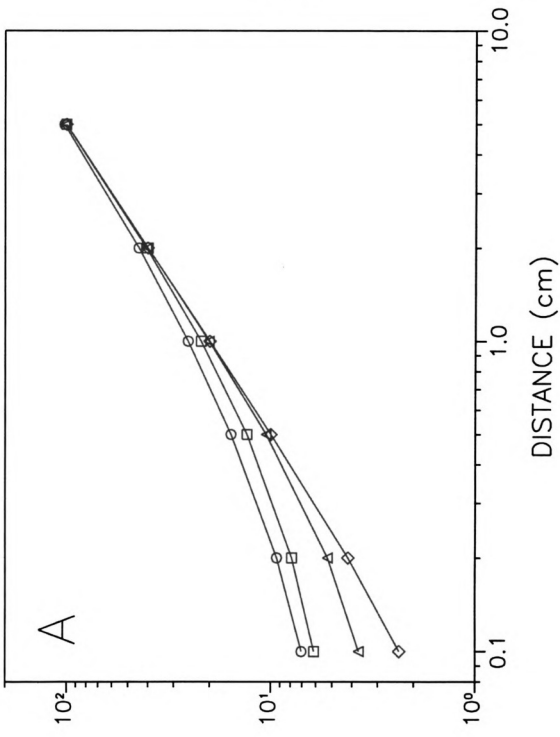

Figure 8.8 cont.

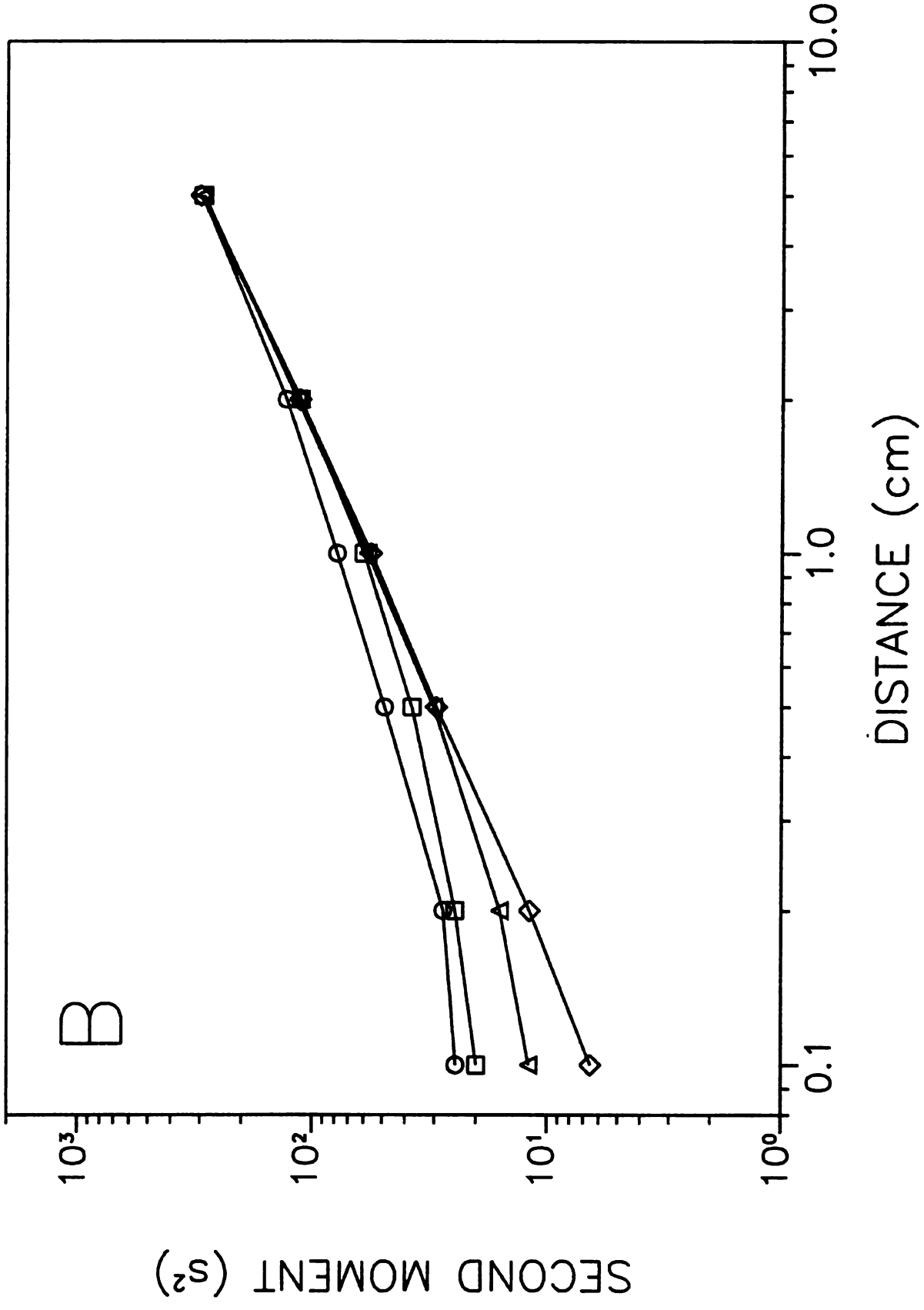

Figure 8.8 cont.

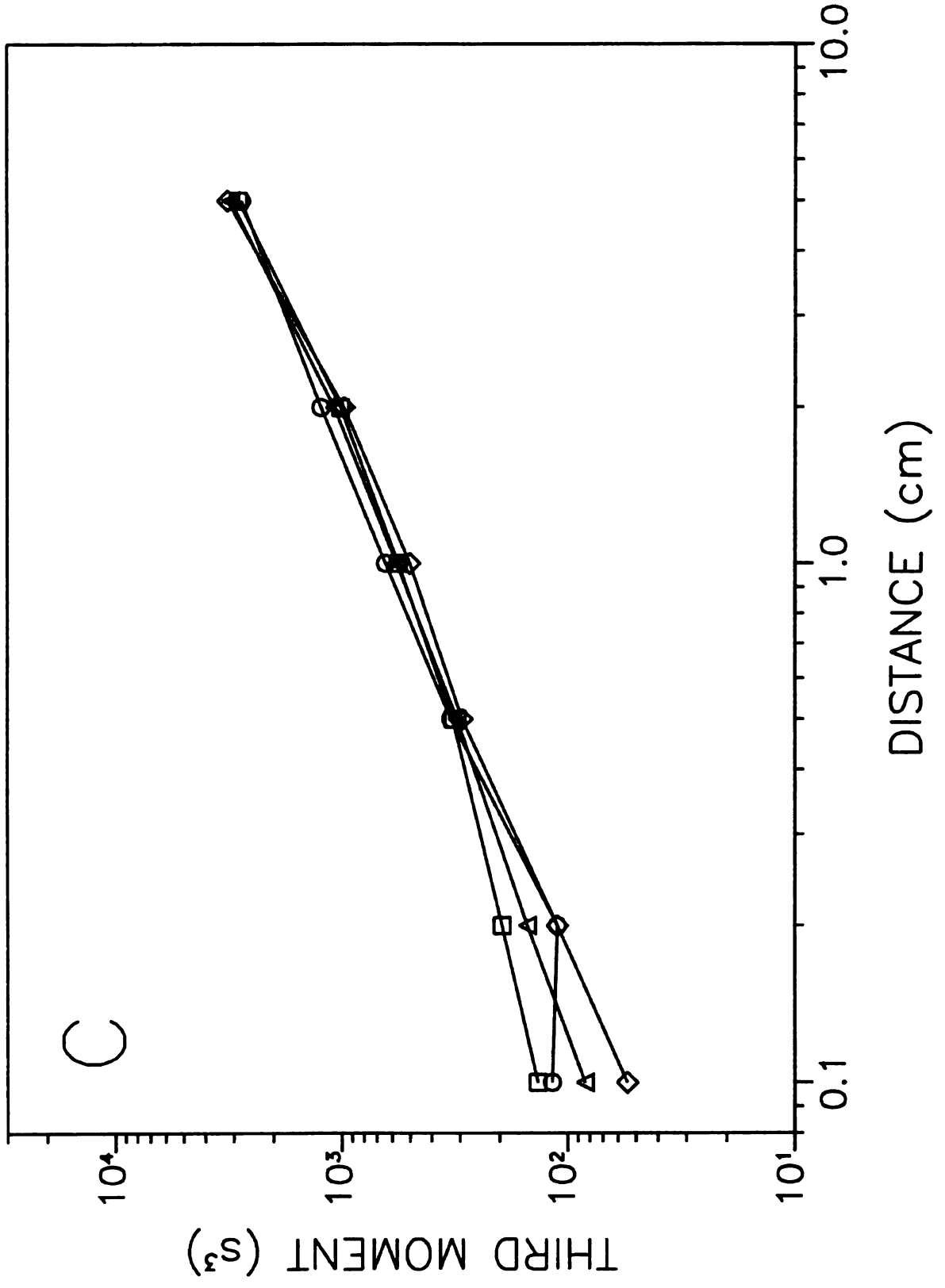

The second moment or variance for species A and B is shown in Figures 8.7B and 8.8B, respectively. The second moments for species A appear to increase linearly with distance. There is little difference between the systems, which implies that the width of the zones of species A is not dependent on the rate constant. The second moments for species B show a marked increase in variance with decreasing rate constant, especially at short column lengths. Once the systems have reached steady state, the difference in the variance of species B disappears. The widths of the zones of species A and B become equal once the systems have achieved steady state. This is expected since species A and B have the same molecular properties in these systems.

The third moment or asymmetry for species A and B is shown in Figures 8.7C and 8.8C, respectively. The third moments for all systems appear to be similar in magnitude and increase with distance. Initially, the third moments for species B are larger than those for species A, but become indistinguishable by 2.0 cm. This implies that the asymmetry in these systems is only influenced by the rate constant during the period in which the reaction is out of equilibrium. Once the reaction has achieved steady state, the third moments of the system are only influenced by mass transfer processes, as in the case of a system with separation alone.[14]

8.2.2.2 Effect of Changes in Reaction Equilibrium Constant.

Figures 8.9 and 8.10 present the statistical moments for systems in which K_{eq} has been varied from 0.1 to 100. This range is obtained by holding k_r constant at 0.1 s^{-1} while k_f is changed from 0.01 to 10.0 s^{-1}. The first moments for species A and B (Figures 8.9A and 8.10A, respectively) show much the same trend as seen in Figures 8.7A and 8.8A.

Figure 8.9: First (A), second (B), and third (C) statistical moments as a function of distance for species A in reactive separations with the following reaction equilibrium constants: $K_{eq} = 0.1$ (○), $K_{eq} = 1.0$ (□), $K_{eq} = 10.0$ (△), $K_{eq} = 100$ (◇). Other simulation conditions as follow: $t = 5.00\times10^{-5}$ s, $N = 4000$, $R_f = 2.00\times10^{-3}$ cm, $R_s = 8.2843\times10^{-4}$ cm, $D_f = 1.00\times10^{-5}$ cm^2 s^{-1}, $D_s = 1.00\times10^{-7}$ cm^2 s^{-1}, $K_{abs,A} = K_{abs,B} = 1.00$, $k_r = 0.1$ s^{-1}.

Figure 8.9

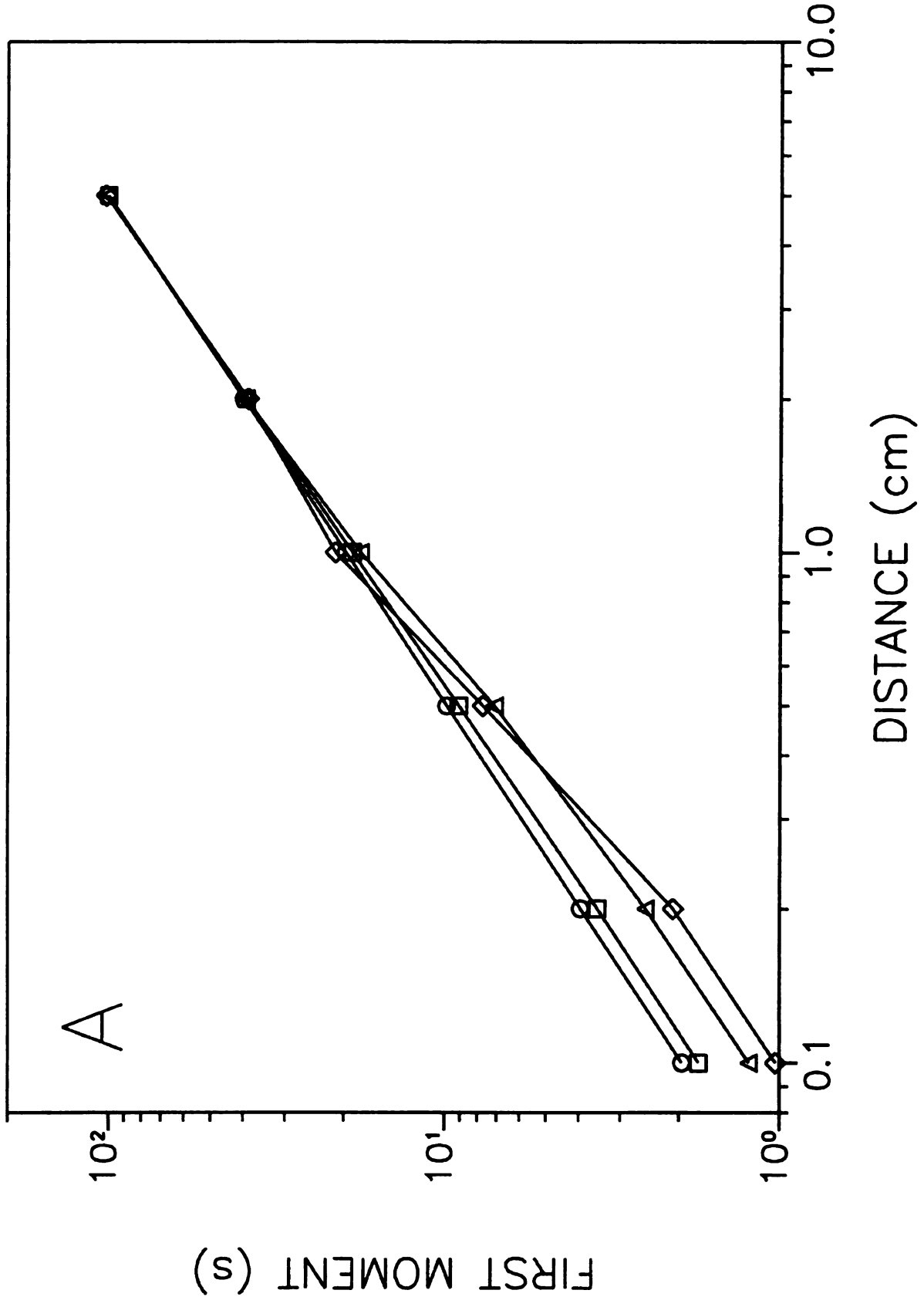

Figure 8.9 cont.

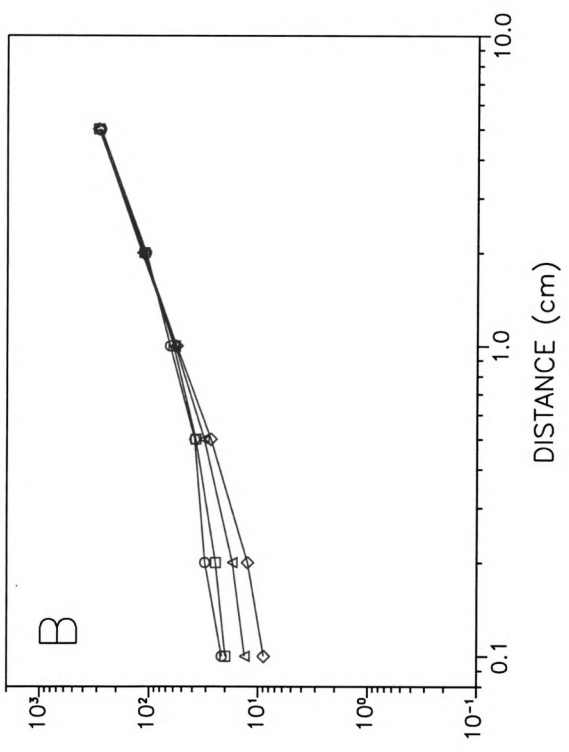

Figure 8.9 cont.

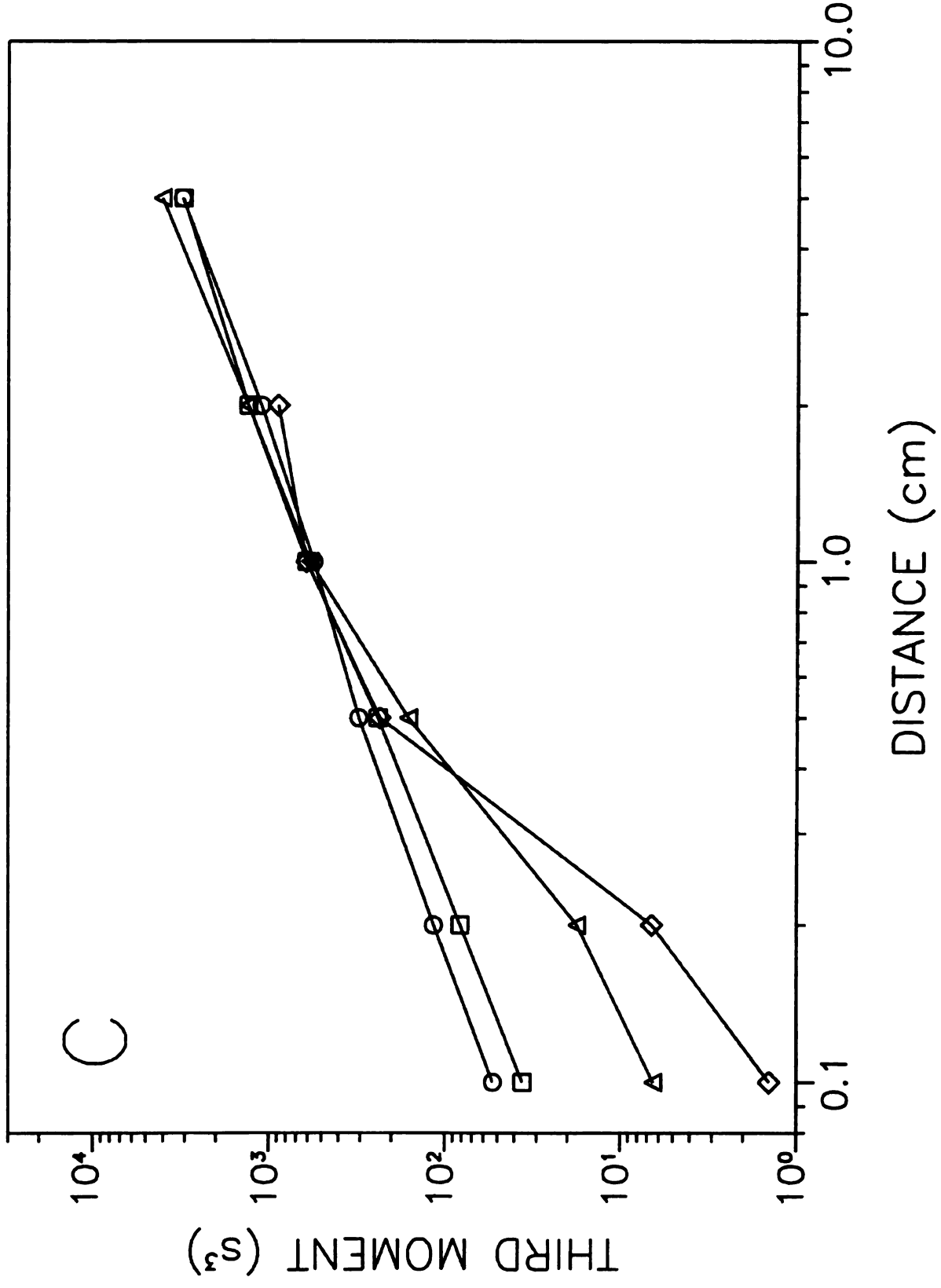

Figure 8.10: First (A), second (B), and third (C) statistical moments as a function of distance for species B in reactive separations with the following reaction equilibrium constants: $K_{eq} = 0.1$ (○), $K_{eq} = 1.0$ (□), $K_{eq} = 10.0$ (△), $K_{eq} = 100$ (◇). Other simulation conditions as given in Figure 8.9.

Figure 8.10

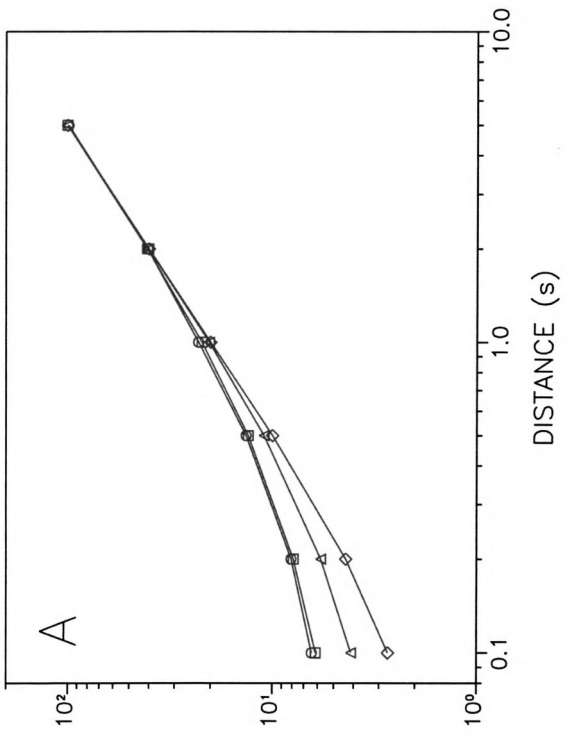

Figure 8.10 cont.

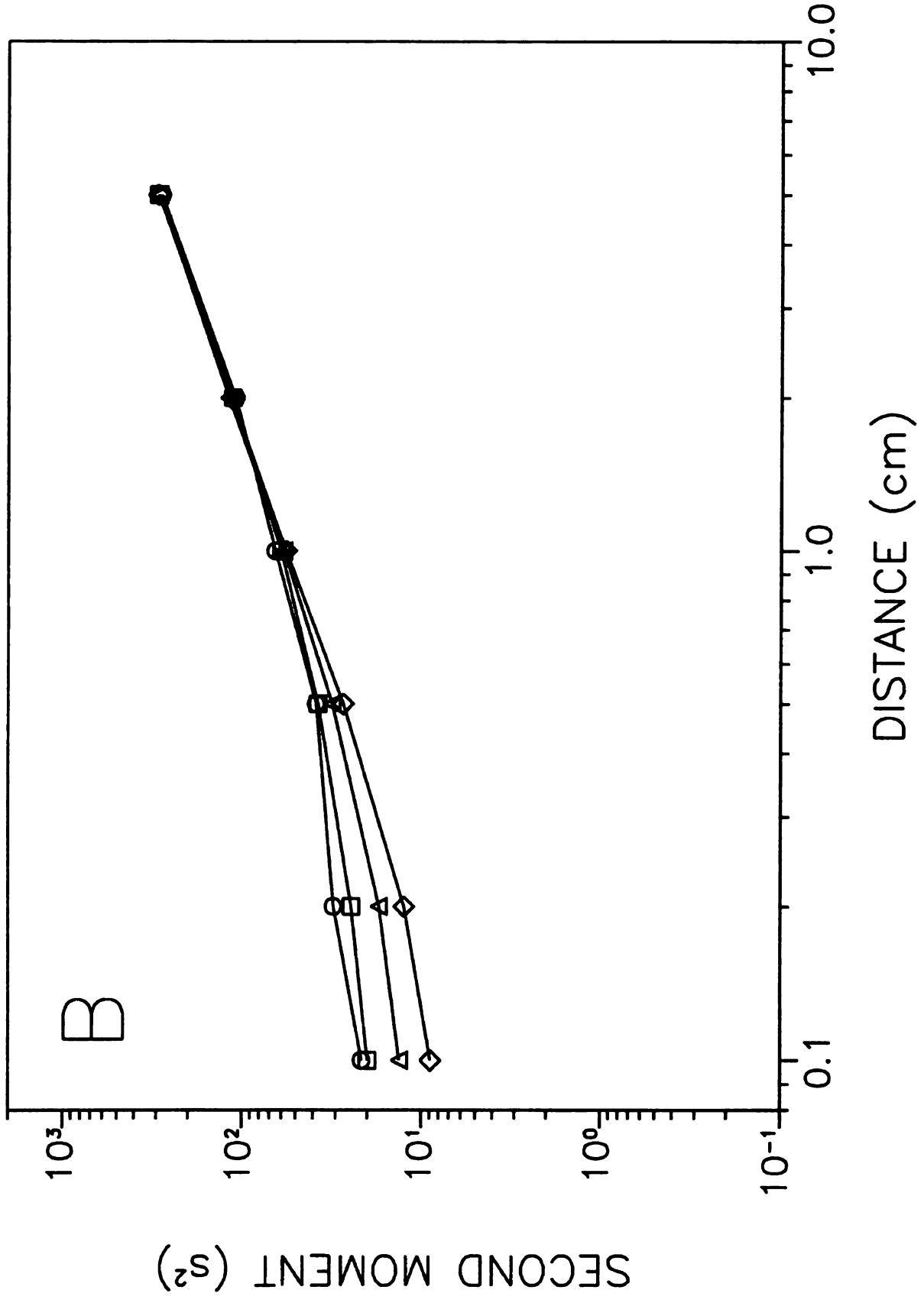

Figure 8.10 cont.

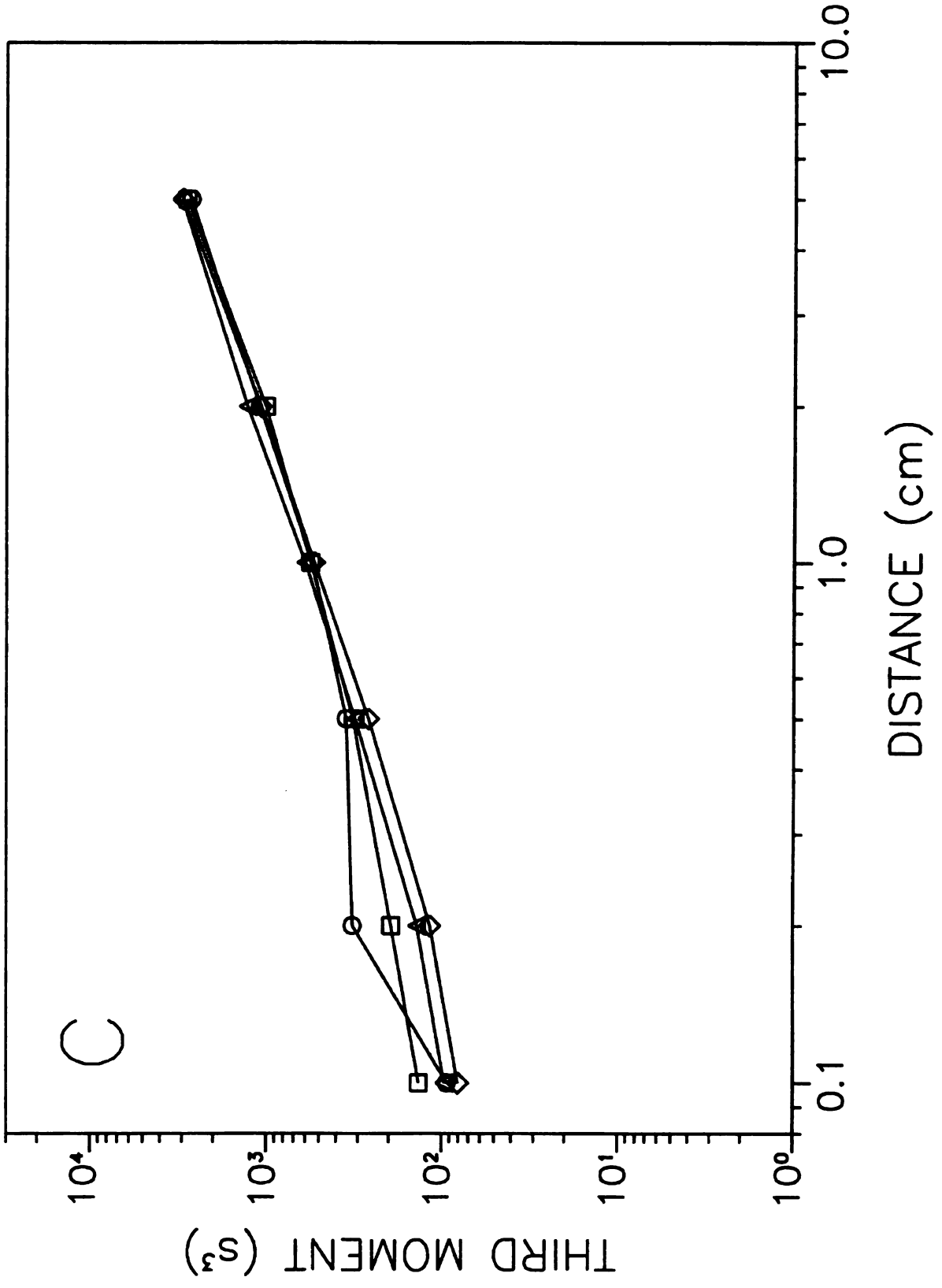

Species A also shows an interesting trend at short column lengths, where the zones elute at shorter times as K_{eq} increases. This trend occurs because species A reacts more rapidly as k_f increases, so the molecules of species A that elute at short column lengths are those that have spent the most time in the fluid phase. Eventually, the systems reach steady state as column length increases, where the mean elution times become indistinguishable. It is interesting to note that these systems have very different numbers of molecules of species A and B at equilibrium (see Table 8.1), yet they all appear to have the same steady-state response. This occurs because species A and B have the same molecular properties. Species B also elutes at decreasing times as K_{eq} increases (Figure 8.10A). However, the elution times for species B are longer than those for species A at the same distances, as noted in the previous study. As before, the observed differences in the first moments of species A and B result from the time required to enter the surface phase and react.

The second moment or variance for species A and B is shown in Figures 8.9B and 8.10B, respectively. The variance for species A decreases as K_{eq} increases, especially at short column lengths. The reason for this observation is similar to that described for Figure 8.9A. The A molecules that have passed these distances have spent most of the time in the fluid phase, and there is little variance increase due to mass transfer in the surface phase. Species B also shows decreasing second moments as K_{eq} increases (Figure 8.10B), although to a lesser extent than species A (Figure 8.9B). However, the zones of species B are much broader than those of species A at the same distances. The increase in breadth is caused by the increased time that species B has spent in the surface phase

and the correspondingly greater contribution to mass transfer. The variance of species A and B becomes equal as the systems reach steady state. This is expected since the molecular properties for species A and B are equal.

The third moment or asymmetry for species A and B is shown in Figures 8.9C and 8.10C, respectively. Many of the trends are similar to those for the second moments in Figures 8.9B and 8.10B. At short column lengths (0.1 to 0.5 cm), the third moments for species A and B decrease with increasing K_{eq}. The systems eventually attain steady state as the column length increases and the third moments converge. Again, since species B spends more time in the surface phase initially, the asymmetry is much greater than that for species A during the time that the reaction is not at steady state. Once the reaction has reached steady state, the third moments for species A and B become equivalent in magnitude.

8.2.2.3 Effect of Changes in Absorption Coefficient.

The statistical moments for systems with $K_{abs,B}$ values of 0.1 to 5.0 are presented in Figures 8.11 and 8.12. The first moments for species A and B, presented in Figure 8.11A and 8.12A, respectively, show that the mean elution time increases as $K_{abs,B}$ increases. This is expected since the zones of species A and B travel at a slower average velocity as $K_{abs,B}$ increases. However, the elution times for species B are larger in magnitude and show more curvature at short column lengths (0.1 to 0.5 cm) than those for species A. The curvature is the result of the chemical reaction, as discussed previously in relation to Figures 8.8A and 8.10A. This phenomenon has also been observed for the irreversible A→B reaction in Chapter 7 and occurs because of the

Figure 8.11: First (A), second (B), and third (C) statistical moments as a function of distance for species A in reactive separations with the following absorption coefficients: $K_{abs,B} = 0.1$ (○), $K_{abs,B} = 0.5$ (□), $K_{abs,B} = 1.0$ (△), $K_{abs,B} = 5.0$ (◇). Other simulation conditions as follows: $t = 5.00\times10^{-5}$ s, $N = 4000$, $R_f = 2.00\times10^{-3}$ cm, $R_s = 8.2843\times10^{-4}$ cm, $D_f = 1.00\times10^{-5}$ cm^2 s^{-1}, $D_s = 1.00\times10^{-7}$ cm^2 s^{-1}, $K_{abs,A} = 1.00$, $k_f = k_r = 0.1$ s^{-1}.

Figure 8.11

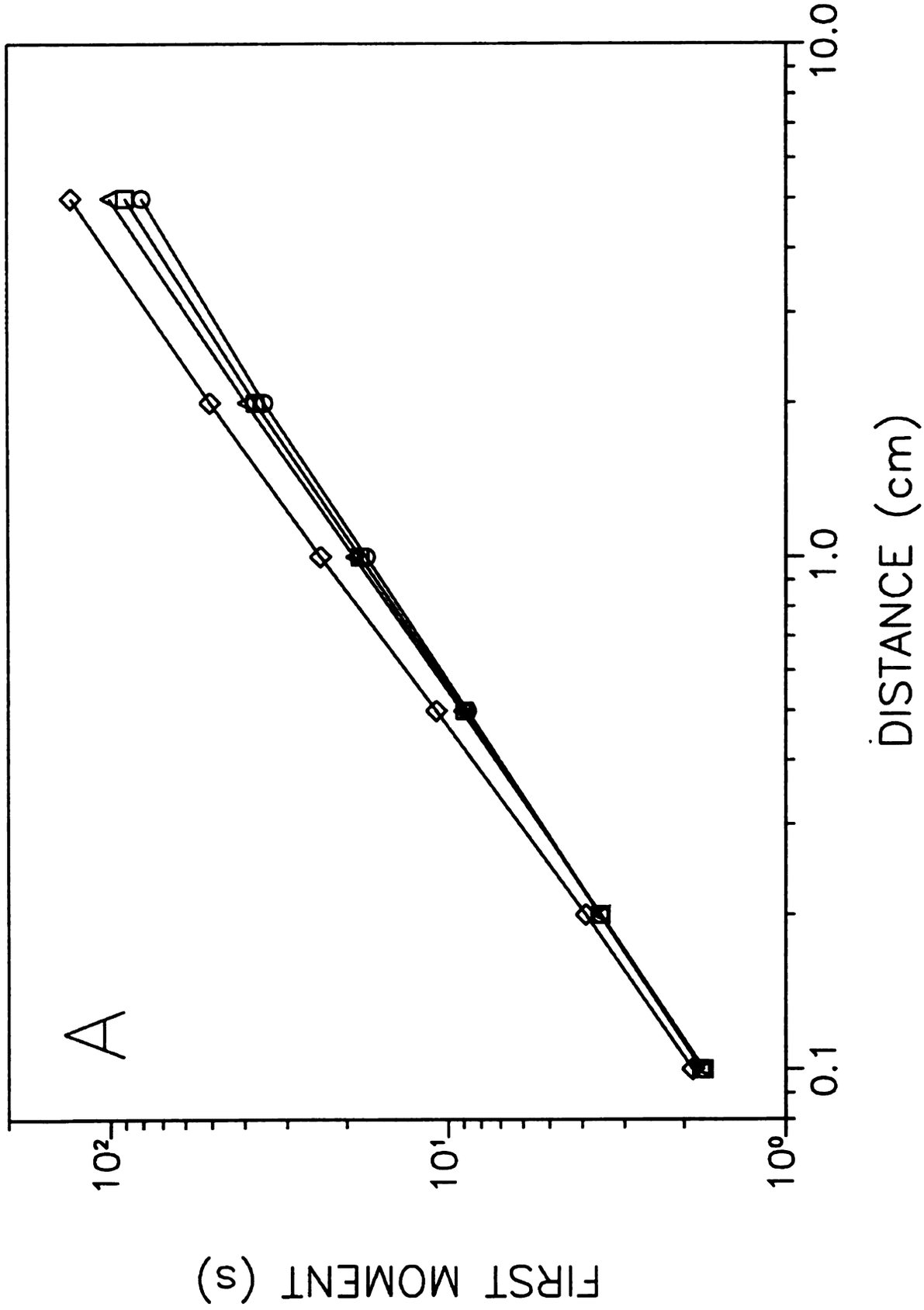

Figure 8.11 cont.

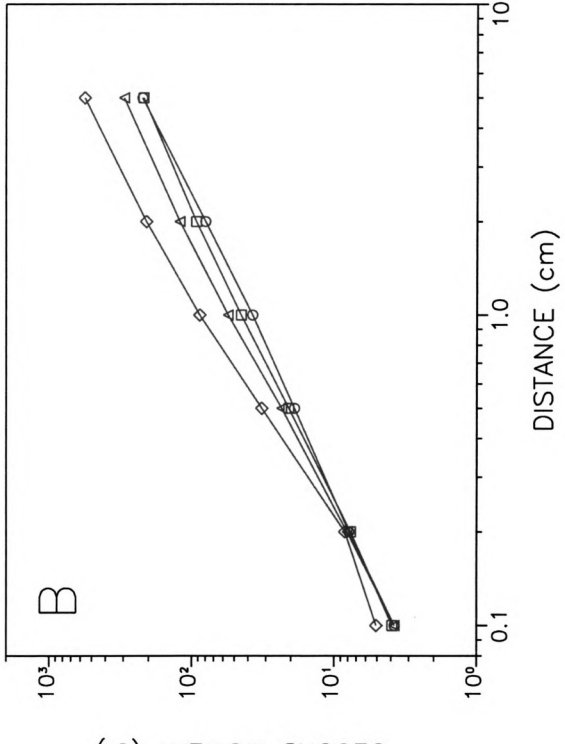

Figure 8.11 cont.

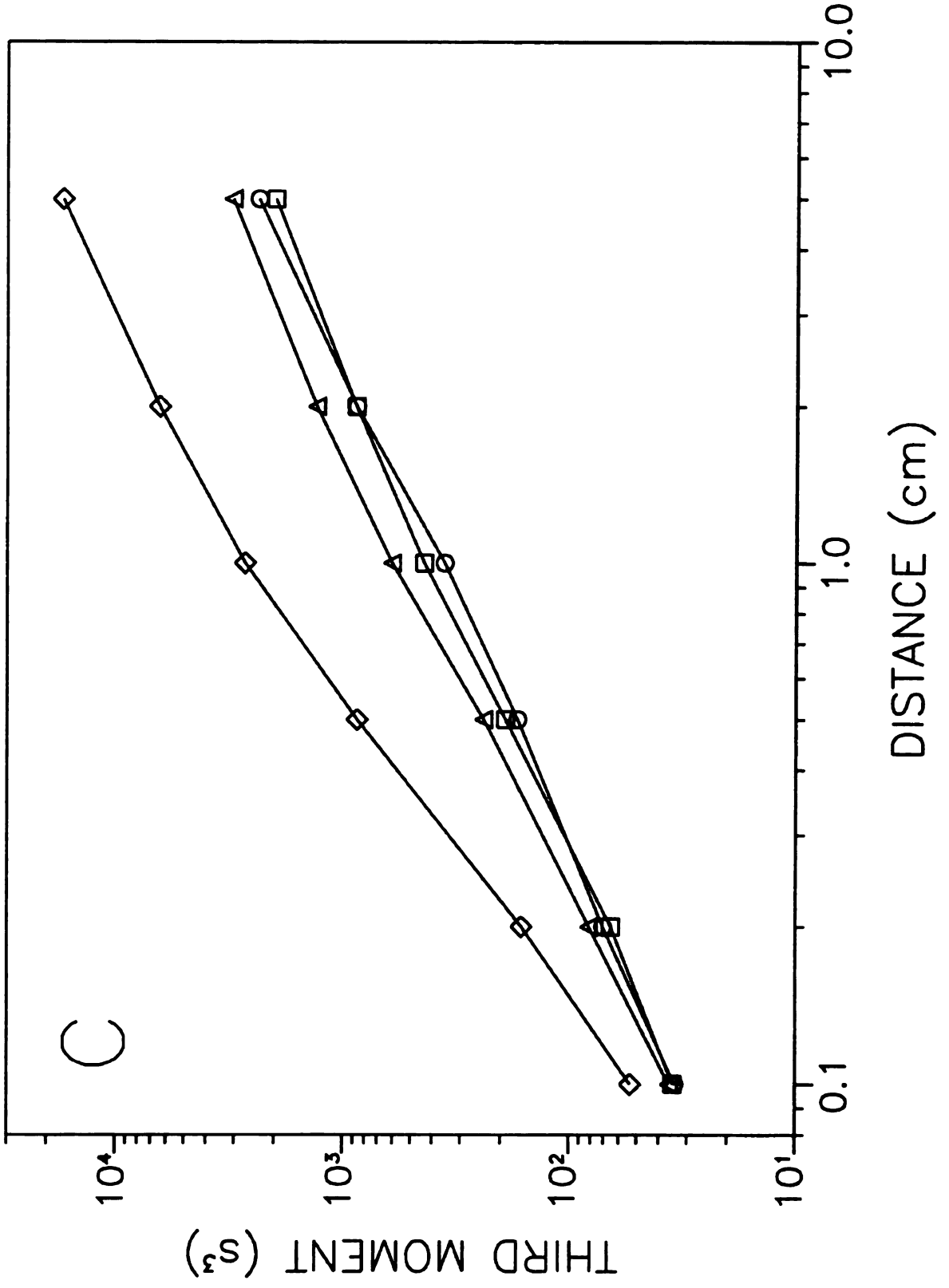

Figure 8.12: First (A), second (B), and third (C) statistical moments as a function of distance for species B in reactive separations with the following absorption coefficients: $K_{abs,B} = 0.1$ (○), $K_{abs,B} = 0.5$ (□), $K_{abs,B} = 1.0$ (△), $K_{abs,B} = 5.0$ (◇). Other simulation conditions as given in Figure 8.11.

Figure 8.12

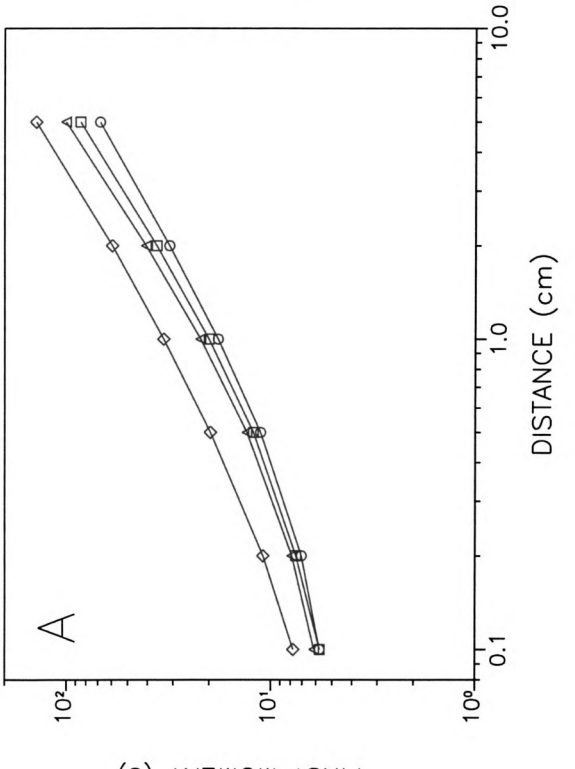

Figure 8.12 cont.

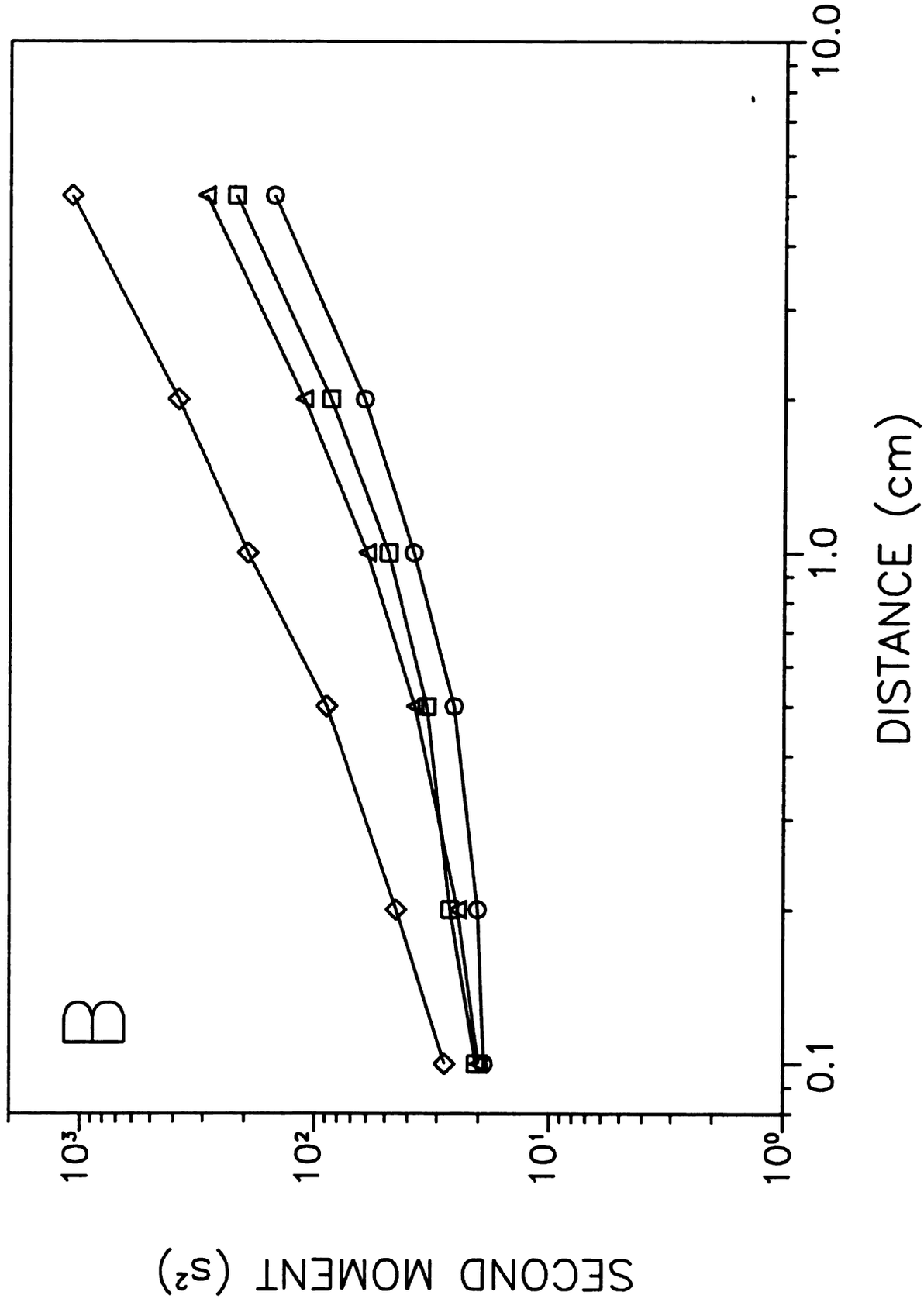

Figure 8.12 cont.

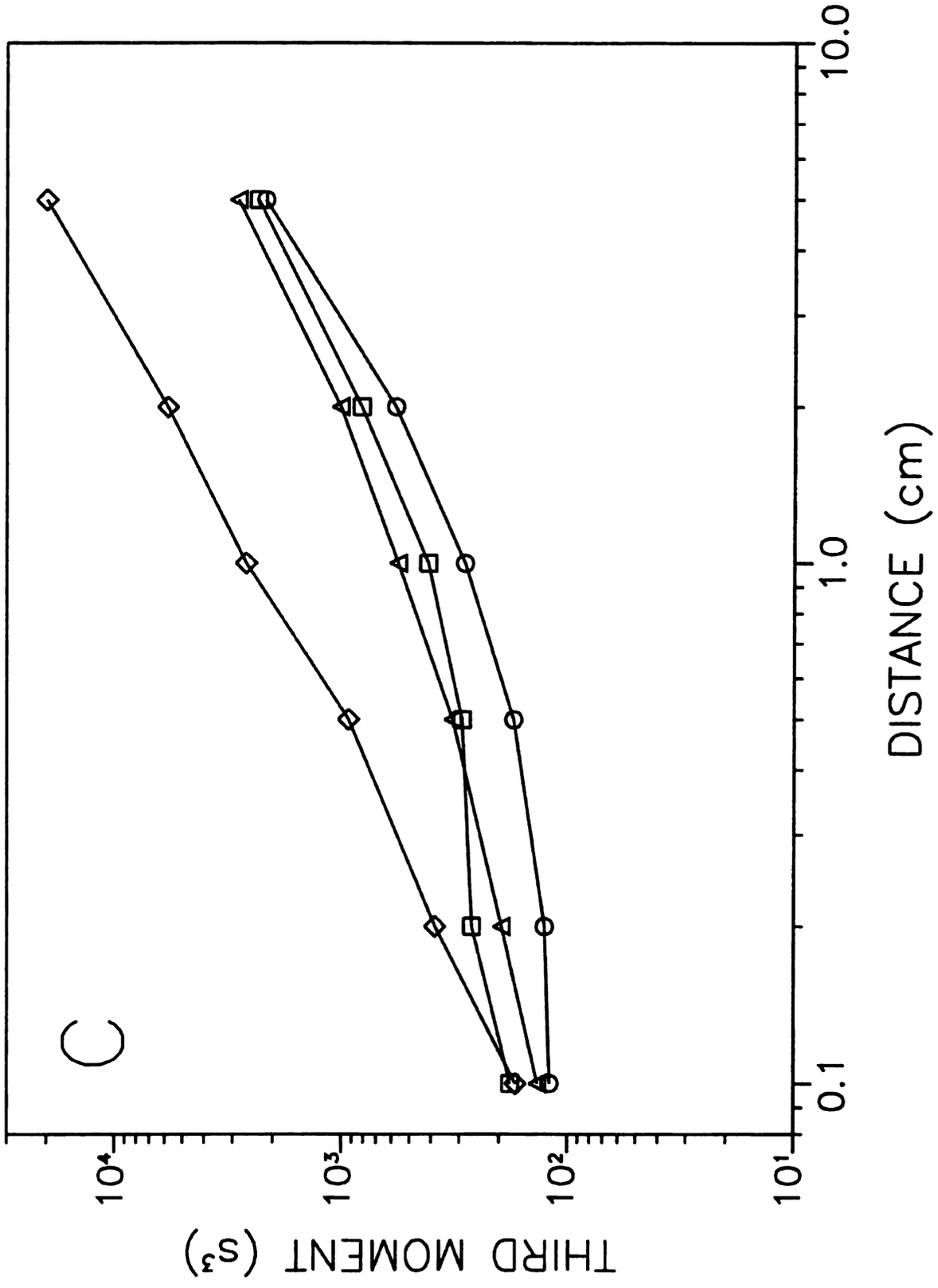

difference in the average velocities of the two species resulting from the different absorption coefficients.[14] Once the reaction in these systems reaches steady state, the first moments become linear as seen at the distances of 1.0 to 5.0 cm in Figure 8.11A and 8.12A. More notably, the first moments for species A and B do not converge as column length increases when $K_{abs,B}$ is varied, in direct contrast to the cases when k_f, k_r, and K_{eq} were varied.

The second moment or variance for species A and B is presented in Figures 8.11B and 8.12B, respectively. Both species show an increase in variance as $K_{abs,B}$ increases. This trend is consistent with non-reactive separation systems (see Equation [7.2] and Section 7.2.2).[14,17,18] At short column lengths, species B has larger second moments than species A for all values of $K_{abs,B}$. At the longest column length, however, the second moments for species B are slightly less than those for species A in systems with $K_{abs,B} < K_{abs,A}$. In systems with $K_{abs,B} > K_{abs,A}$, the second moments for species B remain larger than those for species A. The second moments of species A and B converge to a common value for the system with $K_{abs,A} = K_{abs,B} = 1.0$. The second moments in Figure 8.11B and 8.12B also show varying degrees of curvature for the systems studied. The moments for species A show a sigmoidal shape, while those for species B show only positive curvature. The curvature results from the interplay of the reaction and mass transfer processes within the system, which has been seen previously for species B in the irreversible A→B reaction[14] (Chapter 7) as well as the other studies presented herein. The previously unobserved sigmoidal shape in the variance for species A is caused by the reverse B→A reaction. Initially, the only reaction possible is the conversion of A to B,

which reduces the variance of species A in the same manner as for the irreversible reaction (Chapter 7).[14] However, as the reverse reaction occurs, the variance of species A is affected by the molecular properties of species B, unlike the irreversible case, causing the variance to increase. Once steady state has been achieved, the variances for both species A and B become linear with distance, as seen in the previous studies (Figures 8.7B-8.10B).

The third moment or asymmetry for species A and B is presented in Figures 8.11C and 8.12C, respectively. The third moments for both species A and B increase as $K_{abs,B}$ increases. This is the same trend seen for the second moments and implies that the third moments are also dependent on the reaction and mass transfer processes. The sigmoidal curvature of the third moments for species A is again indicative of the effect of the B→A reaction on the response of species A. The positive curvature of the third moments for species B indicates that the asymmetry of the zones is affected by the reaction in the same manner as the second moment. The third moments of species B are larger than those for species A at short column lengths (0.1 to 0.5 cm). Once the systems have equilibrated, the third moments for the two species appear to converge, and the difference in the magnitude disappears.

8.2.3 Determination of Purity and Yield.

The simulation results for the reactive separation systems discussed above can be used to predict the purity and yield of the product (species B). The relative purity (P) and the relative yield (Y) are determined by

$$P = \frac{N_{B,T}}{N_{A,T} + N_{B,T}} \qquad [8.5]$$

$$Y = \frac{N_{B,T}}{\tilde{N}_B} \qquad [8.6]$$

where $N_{A,T}$ and $N_{B,T}$ are the number of A and B molecules, respectively, that have traversed the column length in time T, and $\tilde{N}_B$ is the number of B molecules predicted by steady-state theory (Equations [8.1] and [8.3]). The values of $N_{A,T}$ and $N_{B,T}$ are obtained from the zone profiles by summing the number of molecules of each species that elute from the column between 0.0 s and time T. Graphs of the relative purity as a function of the relative yield for column lengths of 0.1 to 5.0 cm are presented in Figure 8.13. Three systems are presented in which the absorption coefficient ($K_{abs,B}$) is varied and the rate constants are not changed ($k_f = k_r = 0.1\ s^{-1}$). Figure 8.13A shows the purity and yield for the case where $K_{abs,A} = 1.0$ and $K_{abs,B} = 0.1$. The purity and yield both increase as the column length increases, because more time is available for the reaction to produce species B. The longest column length of 5.0 cm is able to achieve a purity close to the theoretical value of 85% B. Figure 8.13B shows the relationship between the purity and yield for the case where $K_{abs,A} = K_{abs,B} = 1.0$. The purity and yield for this system also increase with increasing column length. The purity of this system tends toward the theoretically expected value of 50% B. It can be seen that the purity of species B may be higher than 50% for very small fractional yields (< 0.1). This increase in purity is the result of non-equilibrium of the mass transfer processes in the system. The non-equilibrium causes a slight separation of the two species, as seen in the first moments (Figures 8.11A and 8.12A) at short column lengths. If fractions are collected during this

Figure 8.13: Relative purity as a function of the relative yield for column lengths of 0.1, 0.2, 0.5, 1.0, 2.0, and 5.0 cm (right to left) for systems with $K_{abs,A} = 1.0$ and $K_{abs,B} = 0.1$ (A), $K_{abs,B} = 1.0$ (B), and $K_{abs,B} = 5.0$ (C). Other simulation conditions as given in Figure 8.11.

Figure 8.13

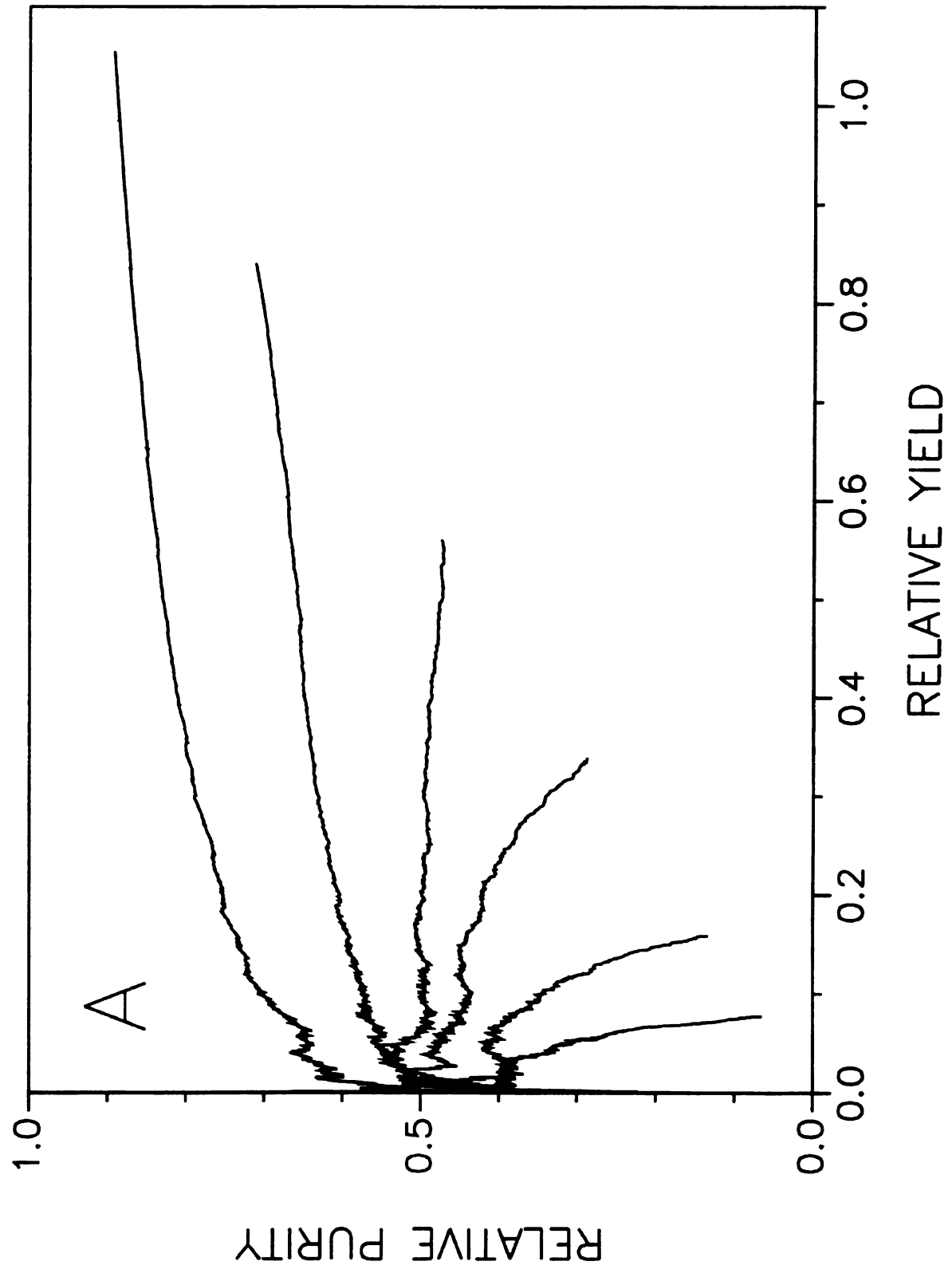

Figure 8.13 cont.

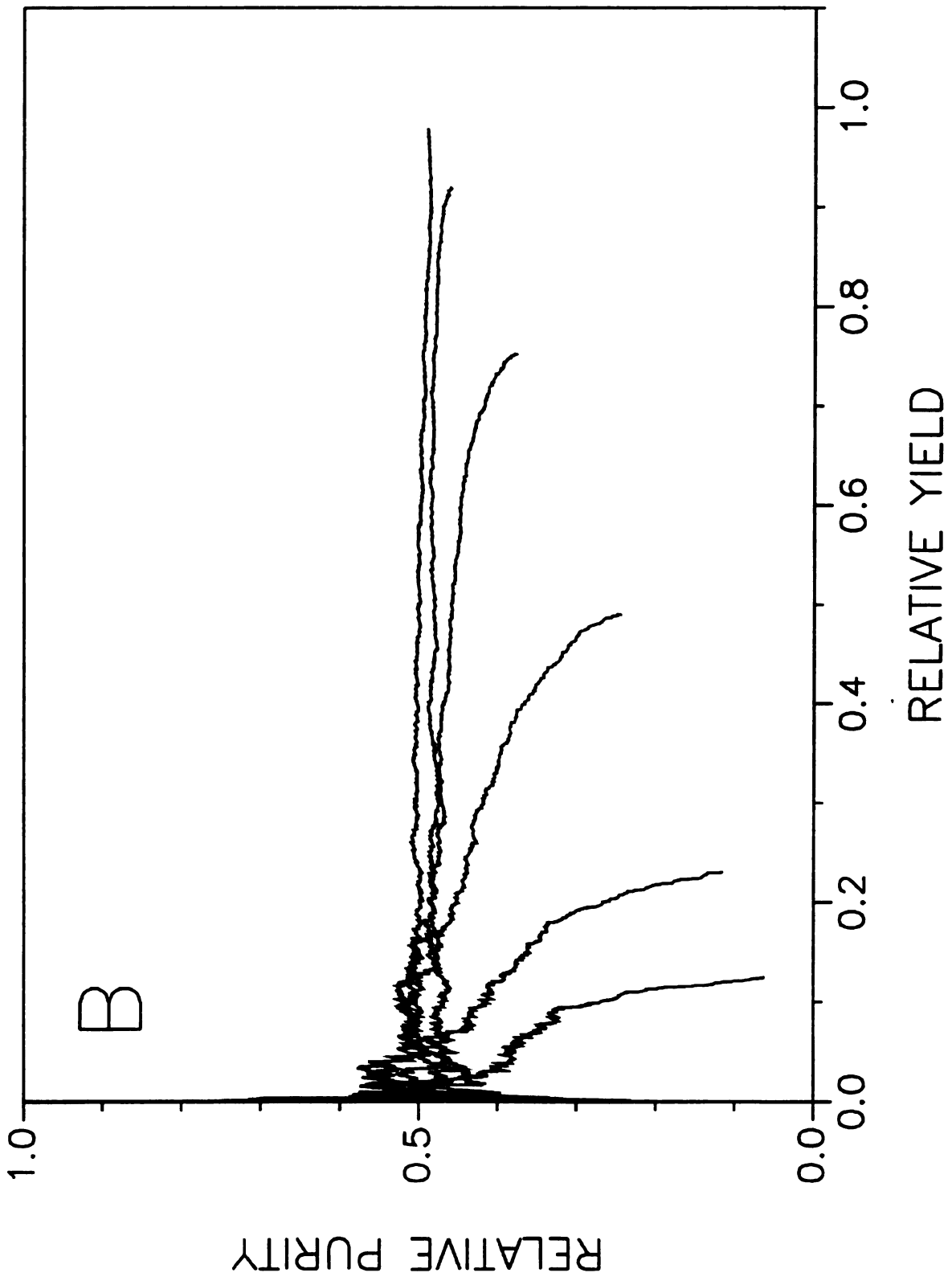

Figure 8.13 cont.

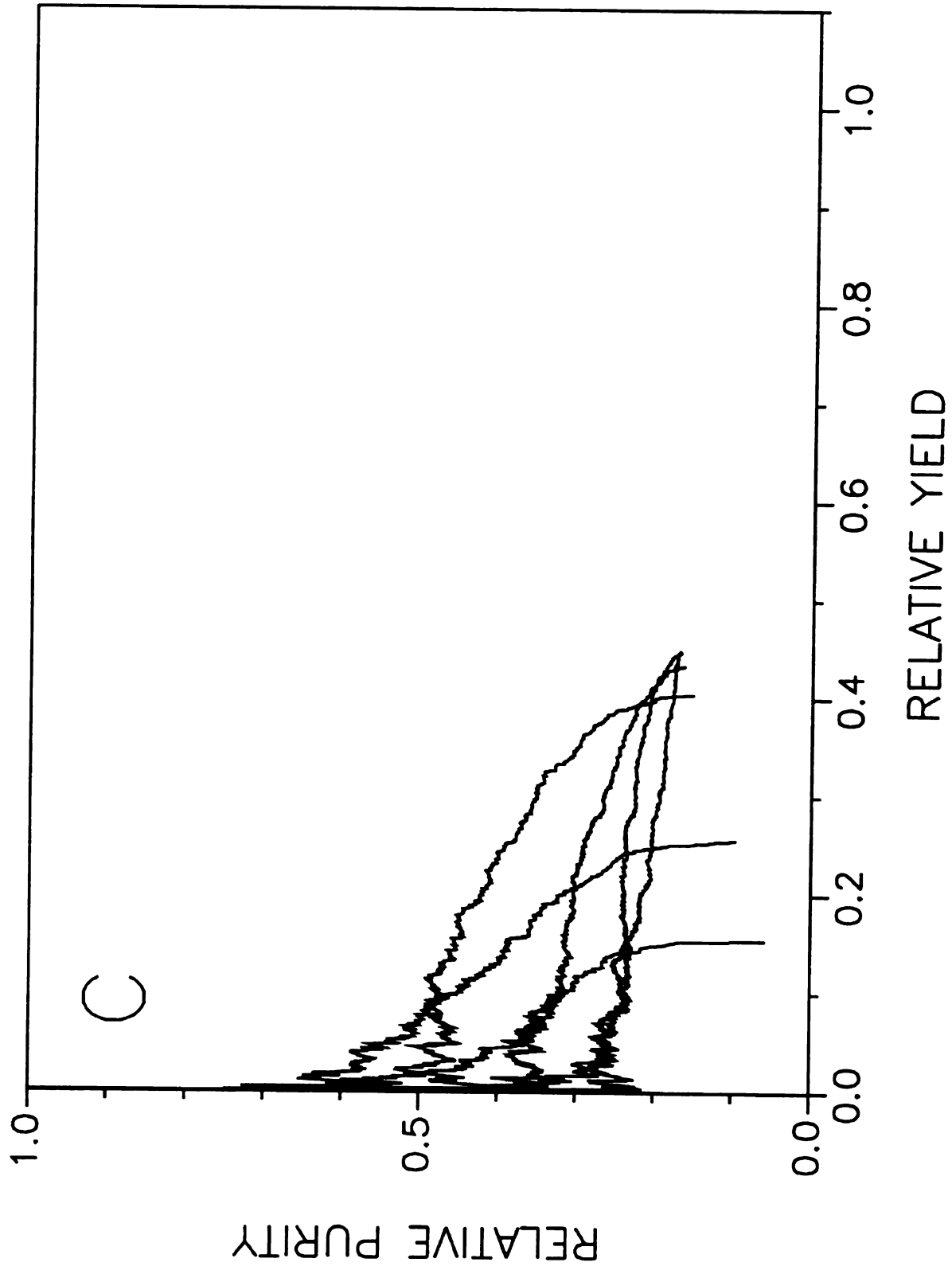

time, an increase in the purity can be achieved albeit at the expense of yield. As more of the zone is collected, the small degree of separation between the species becomes negligible and the purity decreases. Figure 8.13C shows the case where $K_{abs,A} = 1.0$ and $K_{abs,B} = 5.0$. The purity does not constantly increase with respect to column length, as seen in the previous two systems. The purity of species B appears to go through a maximum that is greater than the theoretical value of 37% at a column length of 0.2 cm. The decrease in purity after this length is caused by the B→A reaction, which causes mixing of the zones for species A and B. The yield in this system increases with column length, as observed for the other systems.

Figure 8.13 shows another interesting trend. The relative yield from the longest column length decreases as the absorption coefficient increases. This observation appears to be related to the total residence time for each species on the column. The relative yield is the greatest for the case where the residence time for species B is less than that for species A (i.e., $K_{abs,B} < K_{abs,A}$), and it is the smallest for the systems where the residence time for species B is greater than that for species A (i.e., $K_{abs,B} > K_{abs,A}$). This is an interesting observation as it implies that the purity and yield of a simple reversible reaction can be changed by altering the chromatography of the system.

8.3 Conclusions.

This chapter shows that the stochastic simulation approach can expand the understanding of reactive separations by providing both molecular-level and macroscopic-level information. Since the three-dimensional position of each molecule is

followed through time, it is possible to monitor the residence times and the progress of the reaction in the fluid and surface phases. The ensemble of molecules can be used to generate zone profiles and statistical moments, which provide information on the fluid dynamic behavior for each species. The interaction of the reaction and mass transfer processes is easily explored, and the effects of this interaction can be elucidated as a function of the rate constants, equilibrium constants, and absorption coefficients of the system. For the A↔B reaction, the combination of reaction and mass transfer processes is seen to cause curvature in the statistical moments until steady state is reached. Separation of the species occurs during the time in which the two processes are not at equilibrium. This implies that both the purity and yield of the product could be improved if a system could be devised that was constantly out of equilibrium. This challenges the view that the yield of first-order and pseudo-first-order reversible reactions cannot be increased above the equilibrium value.[19,20] This new insight is made possible through the stochastic model because the temporal evolution of the system can be studied without involving the steady-state assumption.

8.4 References.

1. Jeng, C.Y.; Langer, S.H.; J. Chromatogr. 1992, 589, 1.
2. Klinkenberg, A.; Chem. Eng. Sci. 1961, 15, 255.
3. Magee, E.M.; Ind. Eng. Chem. Fundam. 1963, 2, 32.
4. Hattori, T.; Murakami, Y.; J. Catal. 1968, 12, 166.
5. Schweich, D.; Villermaux, J.; Ind. Eng. Chem. Fundam. 1978, 17, 1.

6. Binous, H.; McCoy, B.J.; Chem. Eng. Sci. 1992, 47, 4333.

7. Schweich, D.; Villermaux, J.; Sardin, M.; AIChE J. 1980, 26, 477.

8. Villermaux, J.; in Percolation Processes: Theory and Applications, Rodrigues, A.E.; Tondeur, D. Eds.; Sijthoff en Noordhoff: Alpen aan den Rijn, the Netherlands 1981; p.539.

9. Gore, F.E.; Ind. Eng. Proc. Des. Devel. 1967, 6, 10.

10. Kocirik, M.; J. Chromatogr. 1967, 30, 459.

11. Chu, C.; Tsang, L.C.; Ind. Eng. Chem. Proc. Des. Devel. 1971, 10, 47.

12. Carta, G.; Mahajan, A.J.; Cohen, L.M.; Byers, C.H.; Chem. Eng. Sci. 1992, 47, 1645.

13. Yang, H.; Peters, J.L.; Allen, C.; Chern, S.S.; Coalson, R.D.; Michael, A.C.; Anal. Chem. 2000, 72, 2042.

14. Krouskop P.E.; McGuffin, V.L.; submitted to AIChE J. 2001.

15. Krouskop, P.E.; McGuffin, V.L.; submitted to AIChE J. 2001.

16. Wu, P.; McGuffin, V.L.; AIChE J. 1998, 44, 2053.

17. Golay, M.J.E.; in Gas Chromatography 1958; Desty, D.H., Ed.; Academic Press: New York, NY, 1958; p.36.

18. McGuffin, V.L.; Wu, P.; J. Chromatogr. A 1996, 722, 3.

19. Sardin, M.; Schweich, D.; Villermaux, J.; in Preparative and Production Scale Chromatography, Chromatographic Science Series 61, Ganetsos, G.; Barker, P.E. Eds.; Marcel Dekker: New York, NY 1993; p.477.

20. Yonovskii, M.I.; Berman, A.D.; in Preparative and Production Scale Chromatography, Chromatographic Science Series 61, Ganetsos, G. and Barker, P.E. Eds.; Marcel Dekker: New York, NY 1993; p.523.

Chapter 9

Conclusions and Future Directions

9.1 Introduction.

Chromatography is a widely used separation and purification technique. The effects of diffusion, convection, and absorption or adsorption have been studied at length from macroscopic representations of the system. To date, chromatography has not been extensively studied at the microscopic or molecular scale. This dissertation presents a novel modeling program that can be used to study all chromatographic systems at microscopic and molecular levels.

9.2 Absorption Chromatography.

A stochastic simulation using the algorithms presented in Chapter 2 is applied to absorption chromatography in Chapters 3 through 5. The systems that are investigated have homogeneous and heterogeneous surface phases. The simulation is also applied to absorption chromatography systems with a reaction in the surface phase that occurs concurrently with the separation processes (Chapters 7 and 8). The findings of these studies are presented below along with some future applications of the simulation in the area of absorption chromatography.

9.2.1 Separation Systems.

The simulation is used to model simple absorption systems in Chapters 3 and 4. The algorithms are shown to be applicable to all forms of chromatography from gas chromatography to liquid chromatography in Chapter 3. The ability to obtain mass transfer rate constants from simulation data is also demonstrated. The mass transfer rate constants give insight into the evolution of the system from initial to steady-state conditions. The mass transfer rates are shown to be dependent on the diffusion coefficients in the fluid and surface phases as well as the interfacial resistance to mass transfer. The transition from initial to steady-state conditions is shown to create zone profiles that are asymmetric. The amount of asymmetry in the profile, and thus the degree of equilibrium within the system, can be inferred from the inverse of the Stanton number. In Chapter 4 the simulation is used to obtain empirical relationships between the molecular and system parameters and the observed mass transfer rate constants. The relationships show that the mass transfer rates have a complex dependence on the diffusion coefficients in the fluid and surface phases and the radii of the system. The studies also show that the mass transfer rate is not affected by the diffusion coefficients and the system radii independently. The empirical equation that is developed in Chapter 4 allows the mass transfer rate to be predicted from basic system parameters. Thus, the mass transfer rate of the system can be computed. Such information gives the investigator the ability to choose the appropriate simplifying assumptions if other models of chromatography are to be used. The mass transfer rate constants also allow easy computation of the inverse Stanton number, which can be used to determine the

parameters necessary (e.g. flow rate, and column length) for the system to reach steady state. Other studies in Chapter 4 indicate that electrochromatography and traditional liquid chromatography produce peaks with the same amount of broadening under most chromatographic conditions. The broadening in both systems is dominated by the mass transfer rates between the fluid and surface phases. This reduces the benefit the flat electroosmotic flow profile has over the parabolic laminar flow profile. The systems that will most benefit from the different flow profile are those with fast mass transfer between the fluid and surface phases.

Chapter 5 presents simulations of a chromatographic system with a heterogeneous surface phase. The data show that changes in the absorption coefficient alone do not cause changes in the observed absorption coefficient of the solute. This observation is believed to be the result of the independence of the characteristic time $\tau = 1/(k_{fs} + k_{sf})$ with respect to the absorption coefficient (see Chapter 4 and Appendix A). However, changes in the surface-phase diffusion coefficient or changes in the interfacial resistance to mass transfer coefficient (the *a* parameter) cause observable changes in the mass transfer rates of the heterogeneous systems. The data show that, as the difference in the mass transfer properties of the different surface sites increases, the zone profiles become more asymmetric. The statistical moments also show deviations from ideal behavior over short times and distances. The deviations from ideality observed in the moments and zone profiles, however, are found to be temporary, and disappear once a steady state has been achieved. The difference between the moments in the time and distance domains while the system is not at steady sate is also elucidated.

In future studies of absorption systems, it will be possible to use *ab initio* and molecular dynamic simulations to obtain the input parameters. This connection with the atomic and molecular based theories will allow a complete study of chromatography at molecular, microscopic, and macroscopic levels. The cause and effect of changes in mass transfer rate can then be determined.

9.2.2 Reactive Separation Systems.

The simulation also models first-order and pseudo-first-order reactions occurring concurrently with separation. The reaction can occur in the fluid or surface phase, and can consist of three consecutive reactions with one side reaction. Chapter 7 presents studies of a separation system in which an irreversible, first-order A $\rightarrow$ B reaction occurs in the surface phase. This work shows that the simulation accurately models such systems, and is able to provide mass transfer and fluid dynamic data about the system with no assumptions made about the relative importance of the reaction rate and mass transfer rate. The data collected show that the reactant molecules pass through the system with a faster velocity than predicted by chromatographic theory while the product moves with a slower velocity than predicted by chromatographic theory. These observations are found to be in good agreement with established theories of reactive separations. This work further indicates that the processes of mass transfer and reaction do not independently contribute to the observed deviations from chromatographic theory.

Chapter 8 presents the wealth of data that can be obtained from a stochastic model of the system. A system consisting of a simple first-order reversible A $\leftrightarrow$ B reaction

occurring in the surface phase of a separation column is studied in detail. The molecular-level data obtained from the simulation show that the location of the reaction is dependent on the relative magnitude of the mass transfer rate and the reaction rate. The data also indicate that the location of the reaction becomes evenly distributed through the surface phase once the mass transfer in the system has reached steady state. It appears that the mass transfer and reaction rates contribute in a dependent fashion on the relaxation time of the system. The macroscopic behavior of the system, as represented by zone profiles and their statistical moments, show that separation of the two species occurs during the initial period of non-equilibrium. The extent and duration of the separation is dependent on the reaction rate and partition coefficient. Thus, the purity and yield of the product show dependence on the column length as well as the rate constants and partition coefficient. The initial period of non-equilibrium is found to provide an increase in the product purity collected at small yields. It is shown that by simply changing the chromatographic parameters of the system, specifically the absorption coefficient of one of the species, it is possible to alter the yield and purity of the product. The best yield and purity are obtained for systems in which the product is less retained than the reactant.

Further application of this model to reactive separations will elucidate the interaction of the mass transfer and reaction rates and the resulting dependence of the statistical moments on those parameters. It will also be possible to determine an empirical relationship between the simulation parameters and the resulting yield and purity. The relationship will then allow the prediction of yield and purity results from molecular and system parameters such as column length and radii as well as absorption

coefficient, diffusion coefficient, and rate constant. Eventually, by combining the absorption and adsorption capabilities of this model, it will be possible to study reactive separations in such materials as zeolites, where the molecules must first pass through a non-reactive layer before adsorbing and reacting.

9.3 Adsorption Chromatography.

This dissertation presents a novel algorithm for modeling adsorption in Chapter 6. The algorithm is validated for adsorption rate constants ranging from 1.0 to 0.001 $site^{-1}$ s^{-1} and desorption rate constants ranging from 0.01 to 10.0 s^{-1}. The algorithm is checked for accuracy by comparing the simulated steady state to that predicted by established theory. The ratio of the number of molecules in the surface phase to the number of molecules in the fluid phase at steady state is found to be within 5.0 % relative error of the expected value. Adsorption chromatography simulations are used to determine the accuracy of the algorithm in modeling a separation system. The first and second moments as calculated from the simulation are within 1.0 % relative error and 10.1 % relative error, respectively, of the values predicted by Giddings. One of the strengths of the new model is shown by following the progression of adsorption chromatography systems from an initial state far from equilibrium to steady state.

Since the simulation can now be used to simulate adsorption chromatography, it is possible to explore the adsorption system at the same level of detail that absorption is presented within this dissertation. Future studies of mass transfer can determine the relationships of the system and molecular parameters to the observed mass transfer rate of

the system. It is also possible to explore the effects of a heterogeneous surface phase on the system response. Further work on the adsorption algorithm to incorporate non-linear adsorption isotherms will allow the simulation to model non-linear and preparative chromatography.

Combining the adsorption and absorption processes will allow the exploration of a mixed retention mechanism. Such a mechanism has been discussed in relation to poor column performance in silica-based chromatographic systems.[1-3] The simulation will be able to explore adsorption to the wall of the tube after the molecule has absorbed into a surface phase. The study of a mechanism in which adsorption to the interface occurs before absorption into the surface phase can also be studied.

9.4 Conclusions.

The work presented in this dissertation has shown that a simulation of a chromatographic system can provide insight into the intricate processes involved. The interaction of the different processes can be studied in detail from the molecular level to the macroscopic level, providing a complete view of the system. Moreover, the methods used within this dissertation can be applied to many different surface science studies. The methodology can be employed to model catalysis, condensation, crystallization, and other processes that have a physical boundary within the system. By employing these methods in the study of other surface phenomena, a model can be created that bridges the molecular descriptions of *ab initio* and molecular dynamic simulations with the macroscopic descriptions obtained from mass balances and thermodynamics.

9.5 References.

1. Nahum, A.; Horvath, C.; J. Chromatogr. 1981, 203, 53.

2. Bereznitski, Y.; Jaroniec, M.; Kruk, M.; J. Liq. Chromatogr. Relat. Technol. 1996, 19, 2767.

3. Ciolino, L.A.; Dorsey, J.G.; J. Chromatogr. A 1994, 678, 201.